Heat Production and Transfer in Earth's Continental Crust

by

Carson Kinney

A thesis

presented to the University of Waterloo

in fulfilment of the

thesis requirement for the degree of

Doctor of Philosophy

in

Earth and Environmental Science

Waterloo, Ontario, Canada, 2025

© Carson Kinney 2025

Examining Committee Membership

The following served on the Examining Committee for this thesis. The decision of the Examining Committee is by majority vote.

External Examiner	Dr. Aphrodite Indares Professor
Supervisor	Dr. Chris Yakymchuk Associate Professor
Internal Member	Dr. Shoufa Lin Professor
Internal-external Member	Dr. Sander Rhebergen Associate Professor
Other Member(s)	Dr. Cees Van Staal Adjunct Professor

Author's Declaration

This thesis consists of material I authored or co-authored: see Statement of Contributions included in the thesis. This is a true copy of the thesis, including any required final revisions, as accepted by my examiners.

I understand that my thesis may be made electronically available to the public.

Statement of Contributions

Carson Kinney is the sole author of thesis chapters 1 and 6, with input provided by Chris Yakymchuk. Chapters 2–5 are manuscripts that have been prepared for submission to academic journals; writing, data interpretation, and figure preparation were primarily done by Carson Kinney. All samples collected and analysed for chapters 2 and 5 were done so by Carson Kinney; the contributions of various co-authors for each chapter are summarized below:

Chapter 2 was submitted to and accepted by the *Journal of Metamorphic Petrology* (Kinney et al. 2023). Samples were collected by Carson Kinney, Jillian Kendrick, Sophie Gagnon, and Chris Yakymchuk. Carson Kinney primarily completed modelling, figure preparation, and writing with contributions from Jillian Kendrick (co-author), Manuel Duguet (co-author, Ontario Geological Survey), and Chris Yakymchuk (supervisor). Manuel Duguet was responsible for whole-rock lithogeochemical analysis and thin section preparation at the Ontario Geological Survey labs and for providing comments and edits on the manuscript. The manuscript includes revisions based on comments from an anonymous reviewer and Chris Clark during the peer-review process for the *Journal of Metamorphic Petrology*.

Citation:

> Kinney, C., Kendrick, J., Duguet, M., and Yakymchuk, C. 2023. Redistribution of heat-producing elements during melting of Archean crust. Journal of Metamorphic Geology: jmg.12751. doi:10.1111/jmg.12751.

Chapter 3 was written in preparation for submission to *Geology*. Carson Kinney primarily completed this manuscript, including modelling, figure preparation, and writing, with guidance and contributions from supervisor Chris Yakymchuk.

Chapter 4 was written and submitted to the *Geological Journal.* This manuscript, including data compilation, modelling, figure preparation, and writing, was primarily completed by Carson Kinney with contributions from supervisor Chris Yakymchuk. Holden Little (co-author) assisted in data compilation, modelling, and manuscript revision. This manuscript includes revisions based on comments from two anonymous *Geological Journal* reviewers.

Manuscript ID:

GJ-24-0338.R1

Chapter 5 was written in preparation for submission to the *Canadian Journal of Earth Sciences*. This manuscript, including data collection and compilation, modelling, interpretation, figure preparation, and writing, was completed by Carson Kinney. Samples were collected by Carson Kinney, Sabastien Dyer, Zachary Adam, and Chris Yakymchuk. Carson Kinney conducted electron microprobe analyses at the University of Toronto with assistance from Yanan Liu. Jessica Gareau and Sabina Bergelt (co-authors) assisted in modelling and provided edits and comments on the manuscript. Supervisor Chris Yakymchuk provided guidance, comments, and feedback on interpretations and the manuscript.

Abstract

Planetary differentiation through tectonism reflects heat production and transfer, reducing internal energy and shaping planetary interiors. Geologic heat originates from two primary sources: primordial heat from planetary formation and the radiogenic decay of isotopes like U, Th, and K. Shearing can generate heat on local scales, but heat transfer predominantly occurs through conduction, where energy flows from hotter to cooler regions via atomic vibrations. In tectonically active areas, advection of magma and convection in fluids are more efficient mechanisms. Local heat transfer often relies on one dominant process, while large-scale systems involve a mix of conduction, convection, and advection. The causes and proportions of each heat source and mantle and crustal radiogenic contributions remain challenging to quantify.

Understanding the re-distribution of heat-producing (i.e., radioactive) elements during metamorphism and crustal differentiation is achieved via combining natural observations with trace element and accessory mineral modelling. Six potential end-members were considered for the protolith of mid-crustal tonalite-trondhjemite-granodiorite packages—often considered the product of lower-crustal melting. Model results suggest heat-producing elements partition subequally between solid and melt at typical pressure-temperature conditions for crustal differentiation. Accessory minerals like apatite, feldspar, amphibole, and epidote are primary repositories for radioactive elements, with their stability in pressure-temperature space governing heat removal from the lower crust. Observations from the Archean Kapuskasing uplift reveal a similar partitioning pattern during mafic rock melting, supporting the notion that radiogenic heat equally influences mantle and crustal processes.

Examining the crustal heat-production record provides insights into continental growth, thickness, and preservation. A database of crustal rocks, including trace element compositions and crystallization ages, reveals trends in heat production over time with implications for basalt formation and crustal evolution. While Archean mantle melting produced less heat-producing basalt than today due to higher degrees of partial melting, the total crustal heat-production rate has remained relatively constant. However, modern crust exhibits more significant variability, suggesting recent enrichment in heat-producing elements contrasts with a more homogenized Archean crust. Crustal growth pulses marked by mafic-to-felsic transitions imply a cyclic nature

of crustal differentiation, with crustal thickness remaining stable due to self-organizing thermal processes.

Trace element substitution in autocrystic zircon is a valuable tool for reconstructing deep geologic processes, but some influences on these proxies remain underexplored. Elevated titanium rims on volcanic zircon, often attributed to magma recharge, could also result from adiabatic ascent. Modelling shows that decompression melting and system expansion during ascent drive cooling, while subvolcanic boiling induces crystallization and latent heat release. Zircon growth during ascent can record these processes, and high-titanium rims may form in a single magma pulse without recharge, emphasizing the importance of multiple geochemical tools to interpret magma evolution.

Ultra-high temperature (UHT) metamorphism represents the thermal extreme of crustal processes, yet its mechanisms and energy sources remain debated; common explanations include mafic underplating or mantle upwelling. The Frontenac Terrane in southeastern Ontario records UHT conditions during the Mesoproterozoic. Back-arc sedimentation between 1390–1200 Ma preceded Shawinigan (~1180–1160 Ma) and Ottawan (~1060 Ma) orogenic events. Granitic and minor mafic intrusions during Shawinigan times triggered regionally advective UHT metamorphism preserved through subsequent reheating events. The Frontenac Terrane provides critical insights into the Grenville Province assembly, with felsic intrusions providing a plausible mechanism for UHT conditions during orogenesis.

Heat production and transfer fundamentally shape Earth's structure and behaviour. Radiogenic heat from U, Th, and K and primordial heat drive crustal and mantle dynamics. Although incompatible with most rock-forming minerals, heat-producing elements are preferentially incorporated into accessory minerals like apatite and zircon, depleting their source rocks. Increased melting reduces system-wide heat production as these elements concentrate in the melt. Advective heating is crucial for crustal growth, enabling magmas to ascend nearly adiabatically and providing a heat source for crustal reworking. These processes dictate metallogenic fluid generation, crustal heterogeneity, and long-term crustal stabilization.

Acknowledgements

I am incredibly fortunate for the number and quality of people I want to thank. The contributions of those around me have provided tremendous support, insights, and guidance—it takes a village. Thank you all for making this experience possible.

My supervisor, Chris Yakymchuk, for his unfaltering support, advice, and encouragement. Since I started working with his lab group as an undergraduate student (a quarter of my life ago!), Chris has provided a welcoming environment that fosters curiosity and offers both personal and professional guidance, all while exemplifying the standards and significance of high-quality research. Being mentored by and working with such a remarkable academic and person has been a cherished privilege. The opportunities and support have been one of a lifetime. I want to thank my current and previous co-committee members Shoufa Lin, Cees Van Staal, and (former member) Brian Kendall for their insights throughout the project. I also acknowledge the Ontario Graduate Scholarship program, NSERC, and Alamos Gold Inc. for financial support.

I have met some genuinely inspiring professionals and world-class scientists during my decade (undergraduate and graduate!) at the University of Waterloo. Shaun Frape continues to be a pillar in the community by tirelessly supporting students while providing humorous anecdotes and advice. Although unrelated to this project, I was fortunate to work and live with Alex Krampf-Jones, whose compassionate guidance and teachings have been foundational. John Johnston, Jen Park, and Keith Delaney are other community members who have provided notable support.

The Yak Pak has included many great peers and friends; in particular, Ivan Edgeworth, Quinn Worthington, Sophie Gagnon, Sabina Bergelt, and Jessa Gareau have provided a true sense of community through hockey chats, recipe swaps, baked goods, train appreciation, and music recommendations. Sharing samples, (unfortunate) rental cars, and an office with Jillian Kendrick was the most fun I've ever had learning. My parallel companion, Sabastien Dyer, provided much-needed smooth brain-hit rock field assistance and spirited discussions while developing my appreciation for bike lanes. Although not a member of the Pak, I was equally able to distract and get help from fan tong Qiháng Wú and xiao piao piao Iris Li. Thank you all for the companionship—you know I love to yap!

I've been surrounded by a tremendous group of friends who have provided much-needed support and fun to survive. Megan Thomson, you were a support pillar, listening to many disjointed and half-verbalized theories while forgiving the endless work hours. Thank you, Dani, Dolly, and your family for the encouragement, care, and understanding. I was fortunate to live with 4 (5) of my friends—Phil Braunstein, Tim Shardlow, Natalie Vuong, Alex Umbach, and Rachel Beaver—during the *trying times* of 2020 and 2021. Mid-day Strikers and Galactic Racing, furnace-room carpentry, and family dinners, among so many memorable times, maintained my sanity. We made Drarkomuth's Dwelling a home—additional thanks to Raeana Samuel, Cody Collis, Jessica Tran, and Stevie Lien.

My family has been the ultimate support throughout my life, and I owe much to them. Being surrounded by numerous outstanding grandparents, cousins, aunts, and uncles has provided a life full of laughter, adventure, and guidance. Mom, you have been a hero throughout my entire life, doing the seemingly impossible. Your continued encouragement and confidence have always laid the foundation for me. My father, Poppa, will always be a role model to enjoy the little things in life while working hard. Maggie and Mackenzie, thank you for pushing me (sometimes literally...) throughout life while providing incredible support in my adventures. You were instrumental in developing the perseverance necessary for a PhD, and I'll always appreciate the partners in tomfoolery. A final thank you is reserved for my grandparents, John "Jack" Kinney, Jane "Nanny" Kinney, Wayne Pearson, and Mary Pearson. You all have been incredible role models and have supported my development. It is a privilege to call you all family.

Dedication

To those who measure success not with evaluations but with enthusiasm.

Passion over perfection

Table of Contents

Examining Committee Membership ii
Author's Declaration iii
Statement of Contributions iv
Abstract vi
Acknowledgements viii
Dedication x
List of Figures xv
List of Tables xvi
Chapter 1.0: Introduction 1
1.1 Heat production and transfer 1
1.2 Crustal differentiation and preservation 3
1.3 Investigating the crustal archive across Eons 6
1.4 Thesis format and objectives 9
Chapter 2.0: Redistribution of heat-producing elements during the melting of Archean crust 16
Summary 16
2.1 Introduction 17
2.2 Regional geology 19
2.3 Methodology 21
2.3.1 Whole-rock geochemistry 21
2.3.2 Mineral Liberation Analysis 22
2.3.3 Phase equilibrium modelling 22
2.3.4 Accessory mineral modelling 23
2.3.5 Heat production and thermal buffering times 25
2.4 Results 25
2.4.1 Mineral assemblages and microstructures 25
2.4.2 Whole-rock compositions 27
2.4.3 P–T phase diagrams 28
2.4.4 Accessory mineral modelling 30
2.4.5 Budget of heat-producing elements 31
2.4.6 Metamorphic heat production and heating times 33

2.5 Discussion 34
2.5.1 Model limitations 34
2.5.2 Accessory Minerals and Their Control on HPE Distribution 40
2.5.3 Heat Production and Heating Times 41
2.5.4 Implications for TTG generation and HPE distribution in the crust 43
2.6 Conclusions 44
2.7 References 45
Chapter 3.0: Heat-producing element dilution recording dilating, oscillatory crustal growth 72
Summary 72
3.1 Introduction 72
3.2 Methodology 74
3.3 Results 75
3.4 Discussion 76
3.4.1 Magmatic dilution 77
3.4.2 Is the rock record preservation or creation? 79
3.4.3 The tempo of crustal formation and differentiation 80
3.5 Conclusion 81
3.6 References 82
Chapter 4.0: High-titanium zircon rims in rhyolite—a reflection of adiabatic ascent? 93
Summary 93
4.1 Introduction 93
4.2 Methodology 94
4.3 Results 95
4.3.1 Natural titanium in zircon zoning 95
4.3.2 Temperature changes during adiabatic ascent 96
4.3.3 Thermodynamic Properties of the System 97
4.3.4 Zircon growth during crystallization 98
4.4 Discussion 100
4.4.1 Limitations of the methodology 100
4.4.2 Thermodynamic reasoning of the adiabat 103
4.4.3 What does zircon record? 105
4.5 Conclusion 107

4.6 References 107
Chapter 5.0: The Frontenac Terrane— a record of advective ultra-high temperature metamorphism 122
Summary 122
5.1 Introduction 122
5.2 Regional Geology 124
5.3 Methodology 125
5.4 Results 126
5.4.1 Rock types of the Frontenac Terrane 126
5.4.2 Structural Geology 129
5.4.3 Whole-rock geochemistry 131
5.4.4 Conditions of metamorphism and magma crystallization 136
5.4.5 Geochronology 136
5.5 Discussion 138
5.5.1 Deposition of Frontenac sediments 138
5.5.2 The Shawinigan orogen and Frontenac magmatism 140
5.5.3 Implications for Proterozoic Evolution of the Grenville Province 144
5.5.4 Regional advective ultra-high temperature metamorphism 147
5.6 Conclusions 150
5.7 References 150
Chapter 6.0: Conclusion 180
6.1 Summary of research 180
6.2 Future work and recommendations 182
References 184
Appendices 194
Appendix S1 (Chapter 2 Supplementary Material) 211
Appendix S1.1 211
Appendix S1.2 226
Appendix S1.3 233
Appendix S1.4 237
Appendix S1.5 239
Appendix S1.6 241
Appendix S1.7 244

Appendix S1.8 246
Appendix S1.9 252
Appendix S2 (Chapter 3 Supplementary Material) 254
Appendix S2.1 254
Appendix S2.2 258
Appendix S3 (Chapter 4 Supplementary Material) 260
Appendix S3.1 260
Appendix S3.2 263
Appendix S3.3 282
Appendix S3.4 284
Appendix S3.5 286
Appendix S4 (Chapter 5 Supplementary Material) 291
Appendix S4.1 291
Appendix S4.2 293
Appendix S4.3 335
Appendix S4.4 399
Appendix S4.5 403
Appendix S4.6 411
Appendix S4.7 419
Appendix S4.8 399
Appendix S4.9 431
Appendix S4.10 434
Appendix S4.11 436
Appendix S4.12 439

List of Figures

Figure 1.1: Decay of heat-producing elements. 11
Figure 1.2: Predicted solidi of various crustal endmembers 12
Figure 1.3: Photographs showing crustal differentiation at various scales 13
Figure 1.4: Flow diagram showing the steps and tools used to study deep-crustal processes. 14
Figure 1.5: Schematic showing different steps to modelling deep crustal processes. 15
Figure 2.1: Simplified map of the Kapuskasing uplift 60
Figure 2.2: Representative photographs of rock types in the Kapuskasing uplift. 61
Figure 2.3: Representative microphotographs of metabasites from the Kapuskasing uplift 62
Figure 2.4: Concentrations of trace elements for rock types from the Kapuskasing uplift 63
Figure 2.5: Calculated heat production for rock types from the Kapuskasing uplift 64
Figure 2.6: Simplified pseudosections for modelled metabasite samples 65
Figure 2.7: Metamorphic potassium budget 66
Figure 2.8: Metamorphic uranium budget 67
Figure 2.9: Metamorphic thorium budget 68
Figure 2.10: Calculated heating times and metamorphic heat production 69
Figure 3.1: Crustal composition through time 89
Figure 3.2: Crustal heat production through time 90
Figure 3.3: Modelled heat production during crustal formation and differentiation 91
Figure 3.4: Crustal growth curve 92
Figure 4.1: Ti concentration and recorded temperature of natural zircons 116
Figure 4.2: Adiabatic ascent paths of A- and S-type magma 117
Figure 4.3: Thermodynamic properties of phases and the ascent path 118
Figure 4.4: Predicted Ti-in-zircon for modelled magmas 119
Figure 5.1: Geological map of the Frontenac Terrane 168
Figure 5.2: Representative photographs of Frontenac Terrane rock types 169
Figure 5.3: Photos of structures found in the Frontenac Terrane 171
Figure 5.4: Geochemical plots of metasedimentary rocks from the Frontenac Terrane 172
Figure 5.5: Geochemical plots of granitoid rocks from the Frontenac Terrane 173
Figure 5.6: Mineral compositions from the Frontenac Terrane 174
Figure 5.7: Isotopic composition of rocks from the Frontenac Terrane. 175
Figure 5.8: Thermobarometry of the Frontenac Terrane 176
Figure 5.9: Summary of geochronology of the Frontenac Terrane 177
Figure 5.10: Mesoproterozoic tectonic model of the SW Grenville Province 178

List of Tables

Table 2.1: Major element concentrations of modelled samples 70
Table 2.2: Measured trace element concentrations of modelled samples 71
Table 4.1: Modelled anhydrous compositions for A- and S-type granites 122
Table 4.2: Initial Zr concentrations (mg/kg) of the modelled granites. 123

"Some of these crystalline rocks are amongst the oldest of the globe; their origin is linked with the earth's early history, they are witnesses of the power of that internal heat which has played so notable a part in the growth of the solid land."

— Sir Archibald Geikie, Outlines of field-geology (1891)

Chapter 1.0: Introduction

1.1 Heat production and transfer

The production and transfer of heat within Earth's crust are fundamental in driving geological processes, from the generation of magma to the formation and preservation of the continental crust. There are three basic sources of geologic heat: 1) primordial heat remaining from planetary accretion, 2) radiogenic heat produced primarily through the decay of U, Th, and K, and 3) mechanical heating during deformation. However, considering mechanical heating produces short-term and local heating (e.g. Nabelek et al. 2001), it is likely not an effective mechanism for thermal stabilization of the crust. Heat flow from the mantle through the crust via conduction is a global phenomenon, whereas convection and advection are generally restricted to tectonically active regions (Stüwe 2007). This heat, either produced or transferred, can induce metamorphism and magmatism at higher crustal levels while influencing the strength and stability of the overall crust (Mareschal and Jaupart 2006, Bea 2012). Further, temperature-induced dehydration is an essential source of metallogenic or ligand-rich fluids (e.g. Luo et al. 2007) and global element cycling more broadly (e.g. Halama et al. 2014). Altogether, understanding the mechanisms behind heat production and transfer in Earth's crust is essential for deciphering the formation and evolution of the lithosphere, the cause and effect of tectonic activity, and the genesis of mineral deposits.

The mantle is a thermal battery slowly transferring primordial heat—with minor radiogenic input (Javoy and Kaminski 2014)—into and through the crust. Primordial heat is the result of accretion, core formation, and the decay of short-lived isotopes (Horedt 1980) remaining from planetary formation and early differentiation. Shock melting of accretion bodies provides a molten initial state (Halliday 2006) with crystallization of the core releasing latent heat to surrounding matter (Kleine et al. 2002, 2009). Further, the sinking of dense material (i.e. Fe-Ni core) undergoes exothermic gravitational compression (Horedt 1980). Primordial heat is the dominant source of heat in the mantle (Davies 2001, Javoy and Kaminski 2014), with its loss—alongside decayed U, Th, and K—resulting in a ~200ºC decrease in mantle temperature since the Archean (Keller and Schoene 2018).

Spontaneous ejection of subatomic particles during radioactive decay induces collisions with surrounding particles, transferring energy (i.e. heating). α-decay emits two protons and two

neutrons, whereas an electron/antineutrino or positron/neutrino pair expulsions occur during β–- or β+-decay, respectively (Ruedas 2017). As α- and β-decay often result in excited particles, further emission of gamma particles (γ-decay) is common. The energy released through α-decay is equal to the change in mass between parent and daughter particles multiplied by the speed of light in a vacuum squared. However, energy is lost to neutrinos and antineutrinos during β-decay, which negligibly interact with matter (Ruedas 2017). Electron capture involves the nucleus of the parent atom drawing an electron from an inner shell, which collides with a proton, creating a daughter with an additional neutron, emitting a neutrino (Alvarez 1938, Mougeot 2018). As mass difference determines the energy released coupled with the rate of decay and molar mass determines the power generation, ^{238}U produces the most energy per decay chain (8.29 pJ) and power per kilogram (0.103 mW/kg; Fig. 1.1a) followed by ^{235}U (7.44 pJ; 0.595 mW/kg). ^{232}Th produces 6.83 pJ and 0.0277 mW/kg which is more energy but less power than ^{40}K (0.2 pj and 0.0562 mW/kg respectively) due to Th's long half-life and greater molar mass; the decay of ^{238}U, ^{235}U,^{235}Th, and ^{40}K produces >99% of radiogenic heat (Stüwe 2007, Dickin 2018).

The distribution of heat-producing elements (U, Th, and K) throughout the crustal column has a direct influence on its metamorphic and magmatic potential (Bea 2012, Abbady and Al-Ghamdi 2018) with further implications on crustal strength (Mareschal and Jaupart 2006). K is an essential structural constituent in some rock-forming minerals such as mica and amphibole. In contrast, U and Th are generally concentrated as trace elements in accessory phases such as apatite, zircon, allanite, or monazite (Bea 1996, 2012). Mica and amphibole are reactants during partial melting (e.g. Clemens et al. 1986, Ellis and Thompson 1986); the breakdown of these minerals partitions a more significant proportion of the K budget in the melt as temperature increases. Further, observations of deep crustal exposures paired with experimental and modelling results indicate a decrease in accessory mineral stability with increasing temperature at subsolidus conditions (Klimm et al. 2008, Stepanov et al. 2012, Yakymchuk and Acosta-Vigil 2019). Together, this implies heat-producing elements (K, Th, and U) will be concentrated in the melt phase and transported to generally shallower depths during crustal differentiation; a process likely fundamental for cratonization (Mareschal and Jaupart 2006, Michaut et al. 2009). However, natural evidence is conflicting, not only is the degree and function type (linear, logarithmic, etc.) relating depth and depletion of these elements in the continental crust (e.g. Ashwal et al. 1987, Chamberlain and Sonder 1990), but anatexis may be a

poor mechanism for depleting the lower crust in heat-producing elements (e.g. Alessio et al. 2018). A greater understanding of heat-producing element distribution during crustal building and stabilization is required.

In a stable continental crust, conduction is the dominant heat mechanism as mantle and radiogenic heat is transported towards the surface. However, in active tectonic regions, convection within, and advection of, magma alongside hydrothermal fluid circulation significantly influence thermal conditions (e.g. Luo et al. 2007). Most geologic materials have low thermal conductivity and diffusivity (Vosteen and Schellschmidt 2003)—the ability to transfer heat and develop a steady state respectively—therefore, conductive heat transfer is generally slow. However, contact metamorphic or magma cooling can occur in relatively short timescales of <5 Ma with significant temperature gradients (Annen 2011, Menéndez et al. 2011); increased rates of cooling are likely from convection from hotter interior regions to the cooler margin aids in magma stalling and crystallization (Coulson et al. 2002, Zhang et al. 2024). Advection of magma from the deep crust or mantle into the shallow crust can drive metamorphism and volcanism (Petford et al. 1994, Menéndez et al. 2011, Glazner 2019a) with further heat transfer achieved through magmatic fluid circulation (e.g. Kol'tsov and Bushmin 2022).

1.2 Crustal differentiation and preservation

Crustal differentiation is achieved through partial melting and upward advection of magma; this process has resulted in complementary residual lower-crustal source and enriched upper-crustal stratification (Brown 2001, Sawyer et al. 2011, Hernández-Montenegro et al. 2019). This process generally occurs at convergent margins (Brown 2010)—though intracrustal differentiation can occur in extensional regimes (Rey et al. 2009). Removing melt from the lower crust (and mantle) provides the magmatic middle and upper crust material. It provides increased crustal strength through several mechanisms: 1) changing lower-crustal mineral assemblages, 2) removal of heat-producing elements, and 3) advection of magmatic heat. Solidus temperatures for most crustal compositions range from ~750–850ºC (Fig. 1.2), although the specific temperature is affected by composition; higher concentrations of H_2O and SiO_2 generally lower melting temperature. Crustal anatexis involves a series of reactions commonly involving a combination of quartz, feldspar, and hydrous minerals producing melts typically enriched in volatiles and silica with a

complementary ferromagnesian and aluminous residue (Ellis and Thompson 1986, Stevens et al. 1997, Wei and Wang 2007). The production and storage of melt significantly reduce shear strength (Nabelek et al. 2001, Diener and Fagereng 2014); therefore, melt extraction is likely critical to stabilizing the continental crust.

Incipient melting occurs along grain boundaries (Chantel et al. 2016), eventually forming self-organizing melt pathways (Sawyer 2008, Yakymchuk et al. 2013) for buoyancy- or tectonically-driven ascent (Petford et al. 1994, Brown and Solar 1999). The development of melt films along grain boundaries wets the surface and, with continued melting, forms an interconnected network between mineral grains. These discrete melt pockets can be preserved as anhedral quartz and feldspar crystals generally along peritectic mineral grain boundaries (e.g. Fig. 1.3a). The percentage of the system that needs to be molten to form an interconnected framework depends on several factors, such as viscosity, permeability, and stress regime, with common estimates of 2–10 wt% (Vigneresse and Tikoff 1999). Below the anatectic front—a conceptual line or zone denoting the depth of the solidus—melt will organize and pond into ever-larger melt channels (Fig.1.3c; Yakymchuk et al. 2013), a diminutive example of larger-scale crustal differentiation. However, connected melt requires a positive force and a pathway (i.e. space) to drain from the source, a process achieved through dilatational sites during overall tectonic compression (Brown 2010) or extensional shearing during regional tension. Ascent above the anatectic front must be rapid enough to prevent freezing—largely accomplished through narrow sheets or fractures to be preserved as dykes or sills (Clemens and Mawer 1992, Petford et al. 1993, 1994). However, structural entrapment, loss of buoyancy, or thermal death in the middle crust is common before volcanic eruption or upper crustal emplacement (Brown 2010, Moyen et al. 2021).

The strength of the lower crust is critical when discussing the stabilization and preservation of the continental crust. The crustal base must be sufficiently rigid to support overlying material without lateral collapse while maintaining positive buoyancy to the mantle. Minerals with naturally weak planes, such as sheet or single-chain silicates, are susceptible to activation at lower stress (Mansard et al. 2020). However, these are generally reactants of anatexis with stronger double-chain and neso-silicate products (Fereidooni 2022) remaining in the source region. Further, as melt retention can induce retrograde reactions to weaker mineral

assemblages (e.g. Hernández-Montenegro et al. 2019), melt extraction is key in preserving lower crustal strength. Residual ferromagnesian aluminosilicates generally do not accommodate high concentrations of heat-producing elements with U and Th dominantly partitioned into accessory minerals such as apatite, monazite, and zircon and K hosted within remnant K-feldspar, mica, and amphibole (Bea 1996, Bingen et al. 1996, Williams et al. 2018). Unlike K-feldspar, mica, and amphibole that react to form melt (Clemens et al. 1986, Beard and Lofgren 1991), accessory minerals dissolve to saturate the melt with some trace element such as Zr for zircon, P for apatite, or LREE/P for monazite with the added consequence of U, Th partitioning into the melt phase (Watson 1979b, Stepanov et al. 2012, Boehnke et al. 2013). However, the efficacy of accessory mineral dissolution is uncertain, and evidence exists for high-temperature stability of accessory minerals retaining heat-producing elements in residual material (e.g. Alessio et al. 2018). Regardless, sections of uplifted former lower crust commonly produce less heat than upper-crustal rocks (e.g. Gard et al. 2019), indicating some degree of differentiation of heat-producing elements in the continental crust

The emplacement of hot, heat-producing element-enriched magmas can induce upper-crustal metamorphism, provide increased crustal buoyancy, and circulate metallogenic fluids. As rocks generally have low thermal conductivity and diffusivity (Vosteen and Schellschmidt 2003), appreciable thermal effects from magma emplacement are usually on the order of decimeter to kilometre scale (Stüwe 2007, Annen 2011). Nonetheless, regional-scale effects are possible with large amounts of hot magma intruding (Barton and Hanson 1989, Brown and Walker 1993). Perturbation of the geothermal gradient—either local or regional—increases the rate of planetary cooling as conductive heat loss relies on temperature difference and conductive distance (Stüwe 2007). Although minor for any intrusion, the cumulative effect of faster conduction after granitoid intrusion into the upper crust has likely aided the overall stabilization of continents and planetary cooling. Further, the concentration of lower-density quartzofeldspathic material at higher structural levels aids long-term preservation by providing positive buoyancy to the mantle and oceanic crust. However, the higher density of the residual lower crust can induce delamination with complimentary mantle upwelling and associated crustal softening (Liu et al. 2016).

The differentiation of the continental crust is as much a metamorphic process as it is an igneous one (Jacob et al. 2021, Moyen et al. 2021), resulting in a crustal mosaic with the mantle as the ultimate progenitor. Some crustal material remains essentially unchanged or fractionated and can provide a glimpse into mantle processes (e.g. basalt). In contrast, others are transformed by a myriad of processes to be unrecognizably incompatible with the mantle (e.g. Cs-Ta-Li pegmatites). Each stage of melting, crystallization, erosion, sedimentation, and recrystallization since planetary accretion imprints new characteristics onto the crust—an archive of the geologic record. Over time, this dynamic cycle produced a generally strong residual lower crust capable of supporting a buoyant upper crust above the mantle. However, the crust is the most variable portion of Earth; enriched lower crust and depleted upper crust are common (Dewey 1986) saying nothing of mid-crustal variability (e.g. Karlstrom and Williams 1998), as such, geologic problems—particularly those occurring at great depths and elevated temperatures—are best approached with an appreciation for terrestrial systems' interlinking nature and complexity.

1.3 Investigating the crustal archive across Eons

Reconstructing thousand to million-year processes occurring millions to billions of years ago at directly unobservable depths requires combining simple and sophisticated tools wielded with creative rigour. Rocks were useful for millennia, but with the theory of uniformitarianism and the work of James Hutton (see Bushman 1983), the appreciation and systemic study of the geologic record developed. Plate tectonics theory, a 20th-century addition to our knowledge (see Frankel 1988), further deepened our appreciation for the transience of Earth and provided missing mechanisms for many crustal theories. Ever-increasing compilations of natural and experimental observations paired with geochemical data have allowed for a collection of proxies and tracers (e.g. Kaneko and Miyano 2004, Henry 2005, Ferry and Watson 2007) for deep-crustal processes to be refined. These data are further interrogated by incorporating technology where laborious and complex calculations can be performed with relative ease. For a study with observation scales varying from atomic to planetary, such as geology, it is suitable to have tools ranging from hammers to supercomputers (Fig. 1.4).

Field surveys provide much-needed local and regional context while providing the opportunity to collect samples and structural measurements. Visually inspecting the outcrop can help recognize mesoscale structures and provide broad colour-based lithologic descriptions to be

further refined by inspecting fresh and weathered surfaces. Leucosome–melanosome relationships such as diffuse vs sharp contacts (Fig. 1.3c)—evidence of possible in-situ or injected leucosome respectively (Sawyer 2008), seemingly peritectic minerals including garnet (Fig. 1.3c) and clinopyroxene providing insights into the melting reaction (e.g. Sawyer et al. 2011), or apparent retrogression haloes (Fig. 1.3c) showing the effects of melt retention (e.g. Hernández-Montenegro et al. 2019) can be observed. Together, these features record the production, movement, and emplacement of magma during crustal differentiation. Compass and inclinometer allow for the directionality of lithologic contacts, internal bedding, and tectonic foliation to be measured with samples (liberally!) taken in accordance with the questions asked. Preparing maps by interpolating between individual sites reveals the larger geometric patterns of crustal buildings. Altogether, the quintessential act of field surveys delivers the opportunity to observe deep crustal processes frozen in time and collect samples for further investigation.

When returned from the field, samples are cut, crushed, and milled to be analyzed, and the data are later integrated into larger interpretations. Rectangular slices of rock are generally ground flat and thin, allowing for transmitted light microscopy—a process pioneered by William Nicol in 1815 and made foundational by Henry Clifton Sorby. Minerals and textures invisible to the naked eye reveal sub-millimetre evidence of partial melting such as *films* of former melt (Fig. 1.3a; Sawyer 2008), nanogranite inclusions (e.g. Bartoli 2019), or different generations of hydrous (i.e. melt-reactants) minerals showing breakdown and recrystallization (Fig. 1.3b; Sawyer 2008). Further, evidence of alteration, including xenoblastic biotite, chlorite, or sericite, indicates late-stage fluid fluxing (e.g. Fig. 1.3a; Luo et al. 2007), whereas symplectite coronae formed during retrogression can provide evidence for crustal cooling paths (e.g. Duan et al. 2017). Polished thin sections can be analyzed using scanning electron microscopes, electron/ion microprobes, and laser ablation-mass spectrometer systems, among other instruments, to provide in-situ compositions of minerals. Compositions of co-existing minerals (e.g. biotite-garnet or plagioclase-garnet), exsolution pairs (e.g. perthite or pigeonite), or monomineralic trace element concentrations (e.g. Ti-in-zircon or Zr-in-rutile) can then be used as proxies for temperature and pressure (Ferry and Watson 2007b, Anderson et al. 2008). Further, isotopic analyses of minerals in thin sections using spectrometers allow for texturally inclusive geochronology (e.g. Benn and Kamber 2009). Other subsamples are disaggregated and milled to be fused into glass or dissolved in acid before spectrometer analysis for major, trace, and isotopic composition of the

bulk rock (e.g. Ingamells 1970, Yuguchi et al. 2020). Mineral separates can be made by washing, sieving, separation via paramagnetism, fluid-assisted density separation, and picking (manual or automatic) previously disaggregated material for major and trace elements and isotopic analysis. Together, these approaches allow for extensive interrogation of natural samples and can create a large amount of data for interpretation.

Well over a century of petrologic and calorimetric experiments (e.g. Cusack 1896, Graham et al. 1989, Vielzeuf and Montel 1994, Graphchikov et al. 1999) has provided thermodynamic properties such as entropy, enthalpy, expansivity, and compressibility of geologic phases coupled with observations of experimental and natural phase assemblages. These data can then be compiled into large databases (e.g. Berman 1988, Holland and Powell 2011) and implemented in complex algorithms to calculate either the minimal Gibbs assemblage or a set of user-defined reaction equations across pressure-temperature-compositional space (e.g. Powell and Holland 1988, De Capitani and Petrakakis 2010, Gualda and Ghiorso 2015, Xiang and Connolly 2022). Modern computational abilities have made these complex calculations relatively easy to perform. The underlying databases for these models require an in-depth understanding of the distribution of elements in a system between many possible co-existing phases. For *major elements* such as Na, Ca, K, Fe, Mg, Al, Si, H, Ti, ± Cr and Mn, extensive experimental and natural data provides a strong foundational knowledge for the stability of most rock-forming minerals. However, thermodynamic databases have limited inclusion of *trace elements* including P, Zr, lanthanides, and actinides; some of these elements are the essential structural components of accessory minerals (Bea and Montero 1999, Schwindinger et al. 2020). Therefore, accessory minerals are modelled using the saturation approach, wherein experiments have determined some combination of variables, generally temperature and melt composition, that can be combined into a mathematical expression that approximates observations (Watson 1979b, Stepanov et al. 2012, Boehnke et al. 2013). For most use cases of thermodynamic phase modelling, the addition of accessory mineral modelling is likely unnecessary but, as trace elements—including U and Th—preferentially partition into accessory minerals (Hermann 2002, Bea 2012, Alessio et al. 2018), understanding accessory mineral stability is required to understanding the heat involved during crustal building and stabilization. The composition and proportion of the predicted major phases can be extracted across the desired system conditions (Fig. 1.5); trace elements are modelled by calculating the ratio of the element in different phases or states (Hanson and Langmuir 1978,

Hanson 1980). Fundamental to this approach is the—generally experimentally-derived—distribution coefficients (e.g. McKenzie and O'Nions 1991, Claiborne et al. 2010), which are commonly assumed to be constant across modelled conditions. However, temperature-dependent strain partitioning models (e.g. Taylor et al. 2015) provide an avenue for model refinement and advancement. Trace element modelling of the stability-determining elements for accessory minerals (i.e. Zr for zircon or P for apatite) provides a theoretical framework for accessory mineral stability—key in understanding trace element distribution (e.g. Bea and Montero 1999, Yakymchuk and Brown 2019). Altogether, the development of modelling approaches has dramatically increased our knowledge of subsurface processes and trace element distribution during crustal differentiation. Refining methods and additional research into accessory mineral stability would continue this progress.

The current crustal mosaic results from heat loss and self-organization over billions of years. Though we have only appreciated these processes for a few centuries, the extensive interrogation of the planet and the development of specialized tools have provided insight into the crust's evolution. The process of crustal formation, differentiation, and stabilization is revealed by combining field observations, analytical data, and spatial imagination in fortuitously preserved and exposed crustal sections. Understanding the heterogeneity in element distribution during this process alongside the physiochemical properties of geologic material allows for targeted analyses of mineral separates to interpret. With continued advancements in experimental apparatus, analytical instruments, and computational ability, we are poised to gain deeper insights into the complex interplay of processes that shape Earth's crustal evolution.

1.4 Thesis format and objectives

Six chapters comprise this thesis. Chapters 2–5 are prepared for publication in scientific journals with an introduction (Chapter 1) and conclusion (Chapter 6). Two chapters investigate heat production in crustal rocks (Chapters 2 and 3), whereas the other two data chapters (Chapters 4 and 5) involve the advective transfer of heat during crustal building and reworking. Chapter 5 further provides a new regional-scale study on an underexamined area in southeastern Ontario and explores the mechanisms for extreme thermal regional metamorphism. Each chapter has an associated reference list and an appendix with supplemental data.

This thesis aims to investigate the production and transfer of heat in the continental crust. Active tectonics is the physical manifestation of the global heat flow with crustal building and differentiation acting as heat sink processes—therefore, understanding the flow of heat is fundamental in understanding tectonic processes at large. The research contained within relates field and petrographic observations alongside analytical data with forward phase equilibrium, trace elements, accessory minerals, and thermal modelling. This holistic approach highlights the importance of combining research methods to understand deep crustal processes unavailable for direct observation. Chapters 2 and 3 leverage trace element modelling in understanding their distribution during anatexis and crustal differentiation. Chapter 4 explores the energetics and effects of rapid magma advection on trace element proxies using phase equilibrium, trace element, and accessory mineral modelling. Chapter 5 incorporates new field and petrologic observations, thermobarometry, forward modelling, and historic data to provide a comprehensive review and reinterpretation of the Mesoproterozoic geometry offshore Laurentia while providing a mechanism for ultra-high temperature metamorphism during orogenesis with minimal mafic magma.

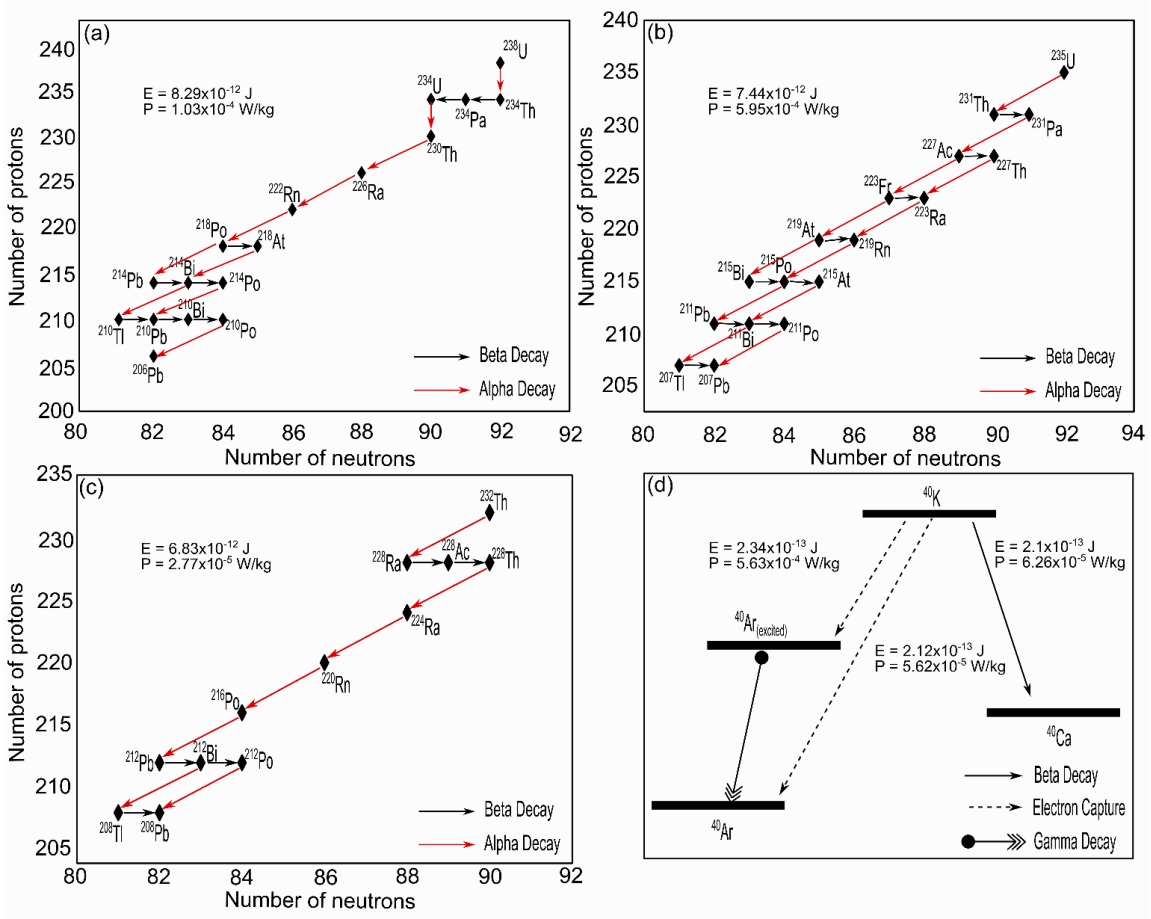


Figure 1.1: Decay chains with total energy and power of heat-producing elements. E–energy, P–power.

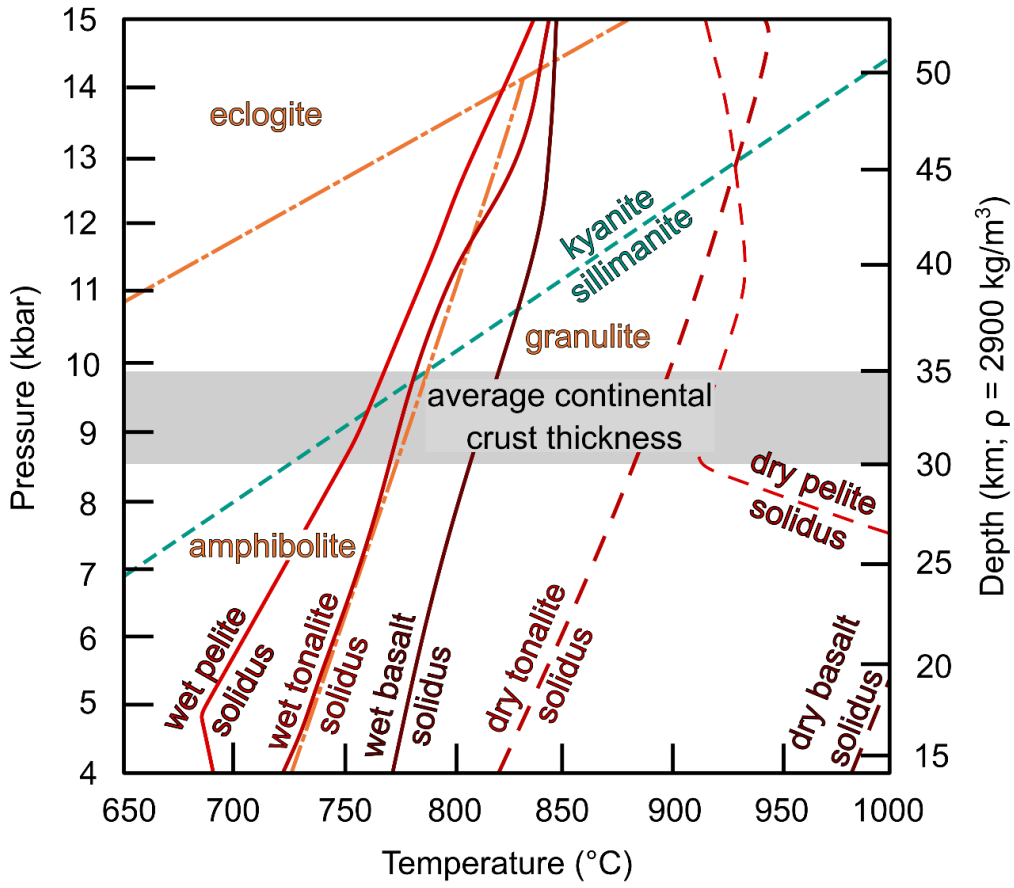


Figure 1.2: Predicted solidi of various crustal end-members with aluminosilicate polymorphs and metamorphic facies shown for reference. Solidi are from Clemens et al. (1986), Scaillet et al. (1995), Palin et al. (2016), and Xiang and Connolly (2022).

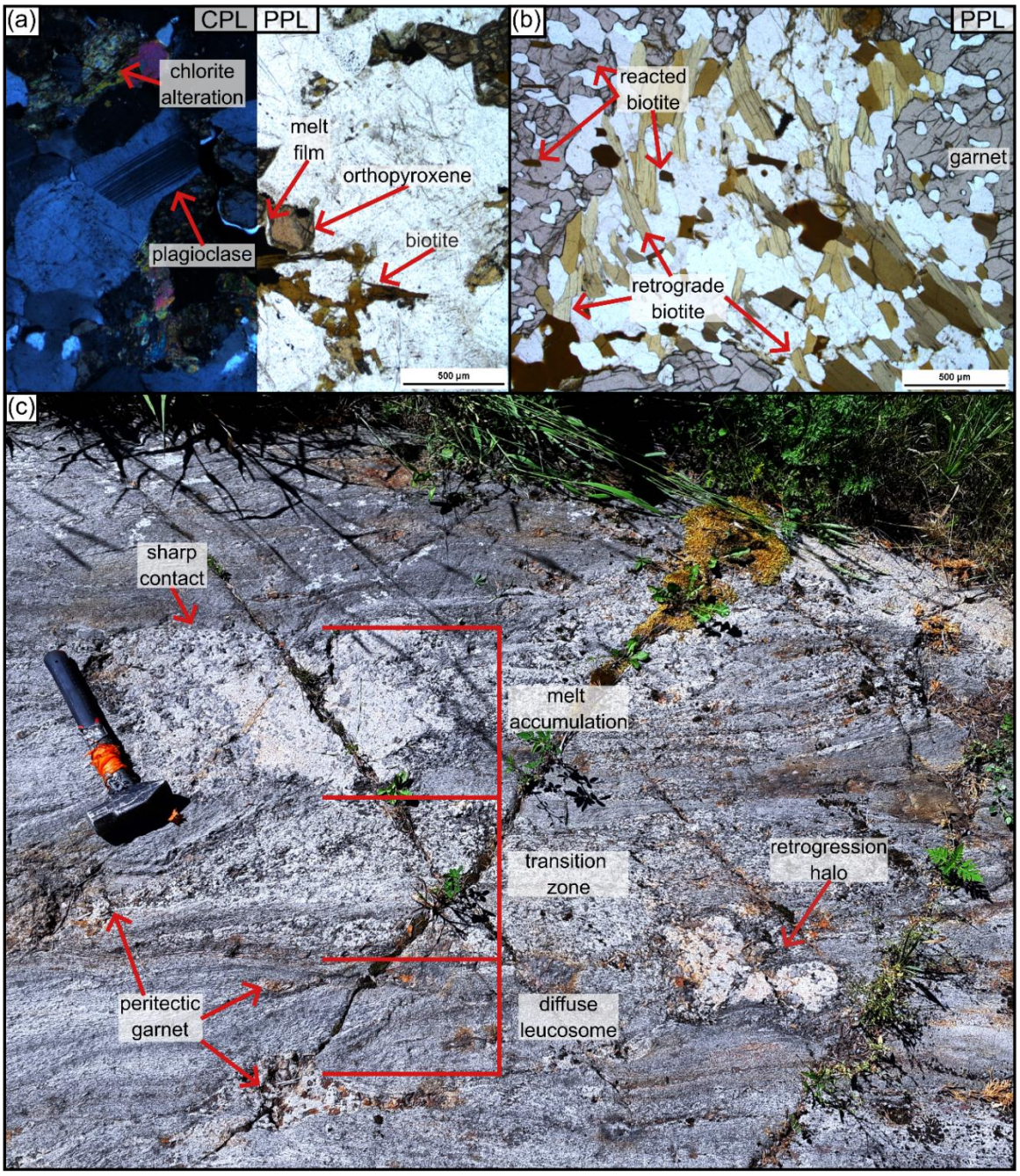


Figure 1.3: (a) Microphotograph of peritectic orthopyroxene with worm-like melt films and complete chlorite replacement of a cryptic mineral. (b) Microphotograph showing xenoblastic reactant biotite commonly enclosed by product garnet and large, sub- to euhedral matrix biotite likely formed during retrogression. (c) The outcrop surface shows melt formation (diffuse leucosome), transport in a transitional zone, and ponding. Peritectic red garnet is common in leucotome; biotite-rich retrogression halo shows the effects of melt retention.

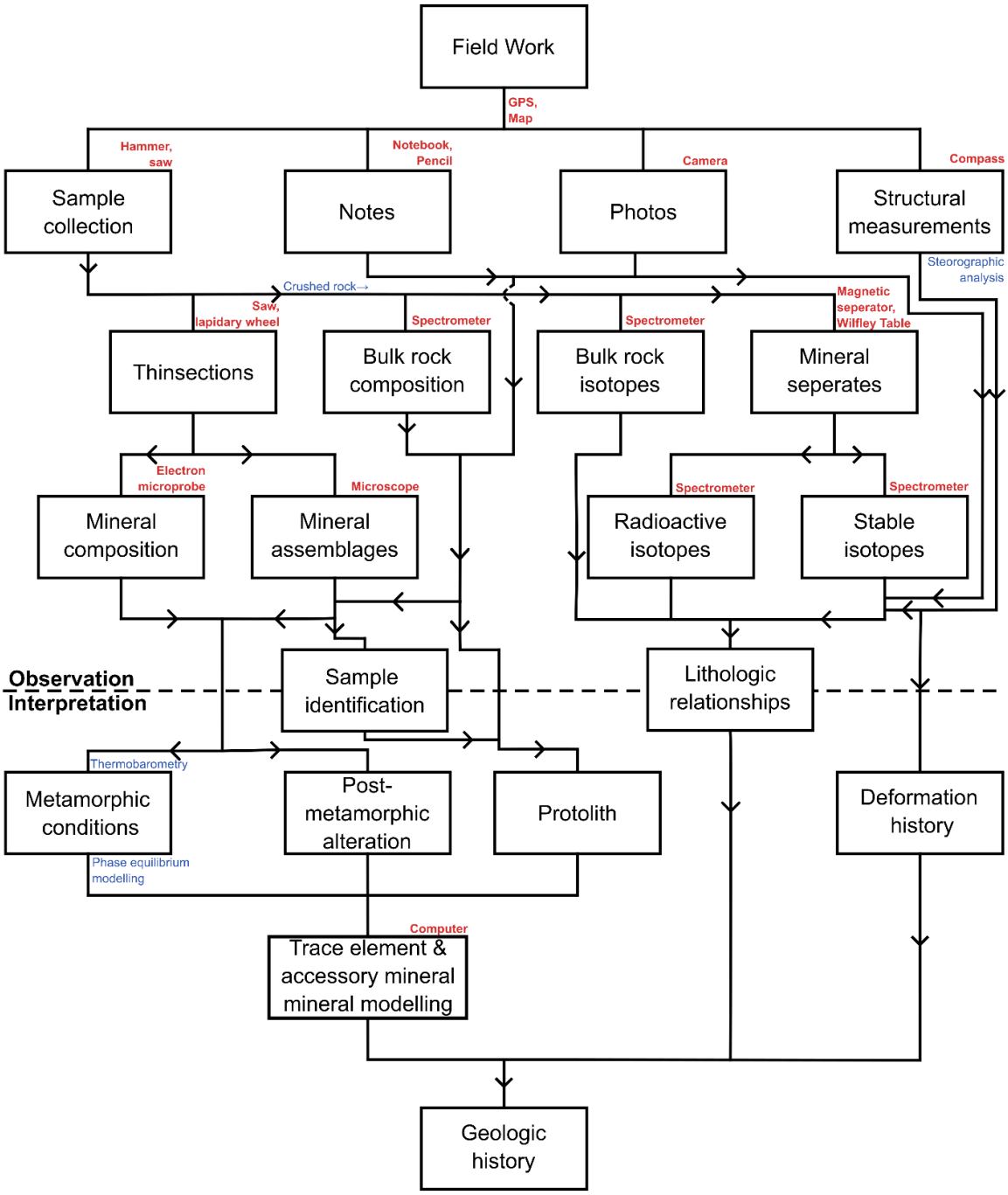


Figure 1.4: Flow diagram showing the steps and tools used to study deep-crustal processes.

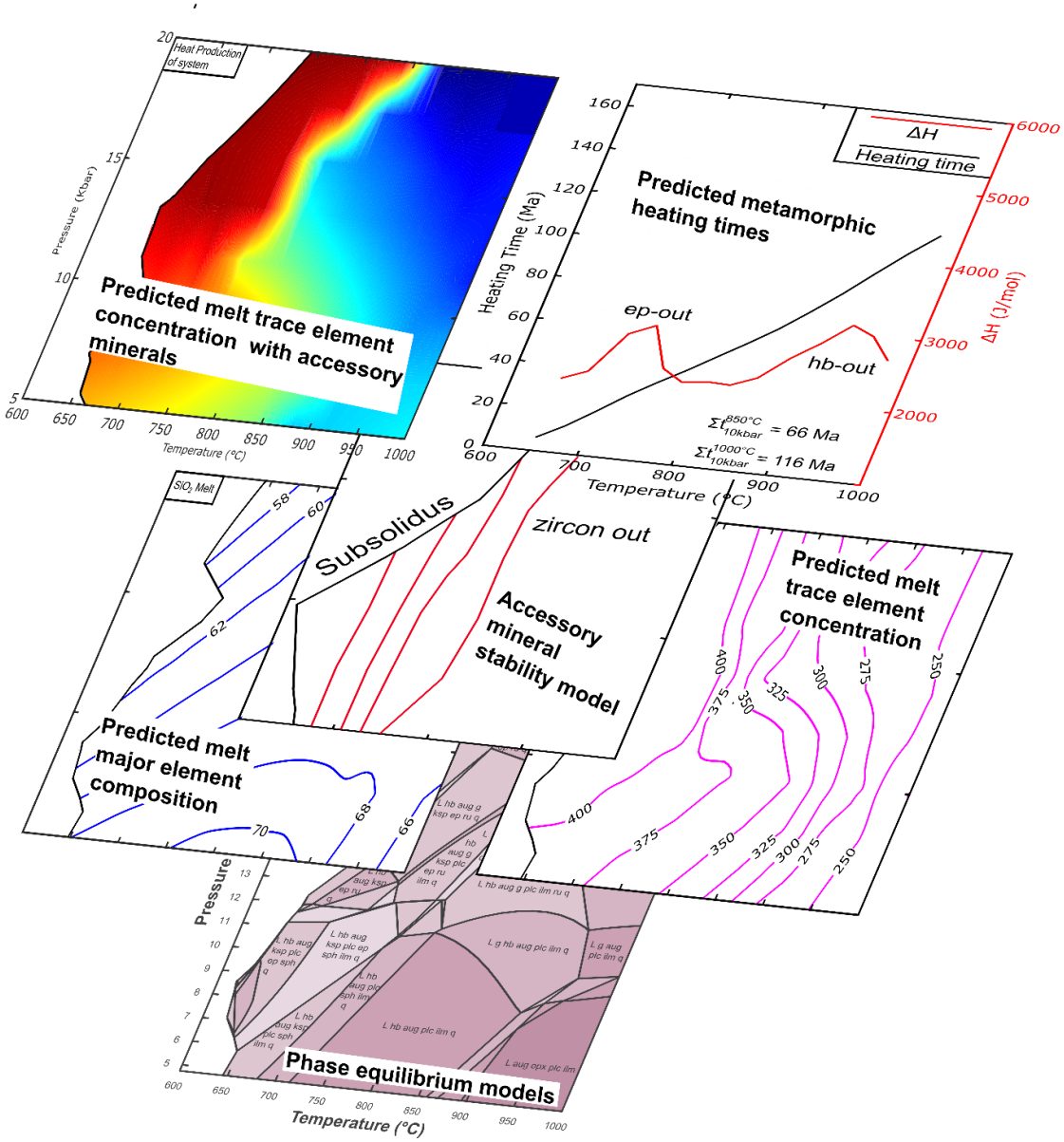


Figure 1.5: Schematic showing different steps to modelling deep crustal processes.

Chapter 2.0: Redistribution of heat-producing elements during the melting of the Archean crust

Summary

The heat generated from the decay of K, Th, and U plays a fundamental role in the differentiation and stabilization of Earth's continental crust. This is particularly important in constructing Archean cratons that form the nuclei of Earth's continents. The Kapuskasing uplift is a rare exposure of an Archean-age crustal cross-section that provides a snapshot of crustal melting, differentiation, and compositional stratification. We integrate field observations, whole-rock compositions, thermodynamic equilibrium, and accessory mineral modelling with heat production and latency time modelling to provide insights into the partitioning of heat-producing elements between residue and melt during anatexis of metabasites as well as the effects on metamorphic timescales and the production of tonalite–trondhjemite–granodiorite (TTG) suites. We model six metabasite compositions ranging from relatively fertile greenschist-facies metabasites to melt-depleted residual mafic (upper-) amphibolites to granulites. Heat-producing elements are modelled to be partitioned between melt and residue; the dominant minerals in the residue that host these elements are apatite, hornblende, K-feldspar, and epidote. At 800–850°C, epidote is no longer stable, and the melt fraction is predicted to contain roughly half of the heat production capacity for the system. Apatite and melt are expected to be the dominant repositories for Th and U during anatexis; zircon is predicted to be wholly consumed by 850°C, whereas apatite persists to higher temperatures, and allanite is expected only in minor modal abundances at high-P, low-T conditions. The partitioning of heat-producing elements into relatively low-density melt decreases the heat production of the residual system during anatexis. Due to their high density and affinity for U and Th, epidote and apatite retain heat production capacity in the residue during metabasite melting. Thermal latency modelling of metamorphism suggests that enriched metabasite compositions require 38–46 My to increase the temperature from ~650 to 850°C —solidus temperature to peak metamorphic temperature of the Kapuskasing uplift— whereas estimates are considerably shorter for depleted compositions (7–25 My). Four of the six samples modelled require 60–70 My to reach 1000°C from the solidus. Our modelling of heat-producing element partitioning and predicted proportions of melt suggest that enriched basaltic compositions are the most reasonable source of TTG magmas, and our heating time modelling

indicates the mantle as an equal to dominant source of heat for metabasite anatexis compared with radiogenic heat production.

2.1 Introduction

Earth's continental crust is thought to be differentiated into a refractory lower part depleted in incompatible elements and a complementary enriched upper part (Taylor and Mclennan, 1981; Rudnick and Gao, 2003). This stratification is the result of intracrustal differentiation, a long-term process that results from the partial melting of deep crust followed by the extraction of melt and ascent to shallower crustal levels (Ashwal et al., 1987; Sawyer et al., 2011; Brown, 2013). The heat-producing (i.e., radioactive) elements U, Th (together producing ~80% of modern radiogenic heat; Arevalo et al., 2009), and K (~20% of modern radiogenic heat) are concentrated in granitic (sensu lato) magmas (Bea, 2012). Therefore, current models of the Earth's crust invoke an upper crust enriched in heat-producing elements (HPE) and a complementary deep crust with low concentrations of HPE (Rudnick and Fountain, 1995); however, the validity of assuming decreasing heat-production with depth is questioned (Bea and Montero, 1999; Hacker et al., 2011; Bea, 2012). The enrichment of HPE (and therefore heat) in upper crustal rocks and sediments is essential for the strength of the crust (Mareschal and Jaupart, 2006), the generation of heat during crustal thickening (Jamieson and Beaumont, 2013), and the stabilization of modern and ancient continental crust (Rudnick and Fountain, 1995; Mareschal and Jaupart, 2006). Archean cratons—remnants of Earth's earliest continents—are proposed to be compositionally layered, composed of greenstone belts (upper crust), grey gneisses (middle crust), and residual mafic granulites or eclogites (lower crust; Percival, 1990; Bédard, 2006; Sizova et al., 2015; Petersson et al., 2020), indicating that crustal differentiation was an early process on Earth. Understanding the role of HPE in craton formation requires knowledge of the behaviour and distribution of these elements among these lithologies and associated minerals. However, exposures of all three levels of the Archean crust are rare and linking these together commonly relies on indirect evidence such as xenoliths, geochemical models or isotopic compositions (Huang et al., 2013; Upadhyay et al., 2014; Manya, 2016; Gardiner et al., 2019).

The redistribution of heat-producing elements during melt extraction out of the partially molten source is controlled by the behaviour of major minerals for K and accessory minerals for Th and U (Iyer et al., 1984; Bingen et al., 1996; Klimm et al., 2008). Understanding the growth

and breakdown of accessory minerals zircon, monazite, apatite, and allanite is crucial for determining whether Th and U remain in the residue or are incorporated into the melt and transferred to shallower crust (Bea, 1996; Alessio et al., 2018; Schwindinger et al., 2020; Williams et al., 2022). Mass balance estimates of the vertical distribution of heat-producing elements in the continental crust suggest limited concentrations of Th and U in the deep crust (Taylor and Mclennan, 1995; Rudnick and Gao, 2003). This contrasts with observations of no appreciable change in their concentrations with depth (Alessio et al., 2018), which is attributed to the behaviour of monazite in the deep crust during partial melting in metasedimentary rocks (Williams et al., 2018; Yakymchuk and Brown, 2019). However, monazite is generally restricted to peraluminous and metaluminous rocks, and the lower crust is generally thought to be dominated by metabasites (Rudnick and Fountain, 1995) that are unlikely to contain monazite.

Apatite, zircon, and allanite are more common accessory mineral hosts for U and Th in metabasites; however, their behaviour during partial melting has received less attention than monazite and zircon—important mineral chronometers—in metasedimentary rocks. Apatite is ubiquitous in metabasites of varying metamorphic grades as these compositions generally have sufficient calcium coupled with a general incompatibility of phosphorous and monovalent anions (Cl^-, OH^-, F^-) in anhydrous silicate minerals (Webster and Piccoli, 2015; Hughes et al., 2018). Zircon is less common in metabasites than other rock types but can form in silica-saturated systems in intermediate to basic melt compositions (Watson and Harrison, 1983; Boehnke et al., 2013; Shao et al., 2019). Allanite forms a solid solution with epidote with comparable stable pressure-temperature conditions (Apted and Liou, 1983; Hermann, 2002; Bushmin and Glebovitsky, 2008). During partial melting, allanite stability increases with pressure and the light rare earth elements (LREE) concentration in the system (Hermann, 2002; Klimm et al., 2008; Gregory et al., 2012).

The heat-producing elements Th and U are concentrated in accessory minerals. Apatite and zircon can have up to 5 wt% U and Th, although concentrations of 10–100 mg/kg in apatite and 100–1000 mg/kg in zircon are more common (Hurley and Fairbairn, 1957; Ahrens, 1965; Cooper and Lovering, 1970; Dupuy and Dostal, 1983; Bingen et al., 1996; Wang et al., 2011). Thorium can act as an essential structural constituent of allanite (Klimm et al., 2008), and allanite may also sequester large proportions of the uranium budget. Considering that the

Archean deep and middle crust is dominated by metabasic rocks and intermediate grey gneisses (product of metabasite anatexis; Moyen and Martin, 2012), furthering our understanding of the suprasolidus behaviour of apatite, zircon and allanite in these lithologies are critical for developing models of melt–residue partitioning of heat-producing elements. This is important for evaluating the nature and timescales of Archean craton stabilization, intracrustal heat production, and the long-term compositional differentiation of Earth's continental crust.

In this contribution, we investigate a suite of samples from a nearly continuous cross-section of Neoarchean crust known as the Kapuskasing uplift to examine the behaviour of heat-producing elements during crustal melting and evaluate the timescales of high-temperature metamorphism. We integrate phase equilibrium modelling of major phases with solubility expressions for accessory minerals (apatite, zircon, and allanite) along with trace element partitioning to quantify the budgets of the heat-producing elements in the residue and melt. These results are used in heat-production and thermal latency calculations to model the capacity for radiogenic heat to drive anatexis of metabasites, providing insights into the Archean continental crust's formation, stabilization, and thermal structure.

2.2 Regional geology

The Kapuskasing uplift, in the central Superior Province (Fig. 2.1), offers a rare opportunity to observe a near-complete section of the Archean crust (Percival and Card, 1983; Percival, 1990; Perry et al., 2006; Kendrick et al., 2022). The metamorphic history is relatively well understood, with the paleo-depth and metamorphic grade increasing from west to east (Percival and West, 1994). Greenstone belts, grey gneiss dominated by tonalite-trondhjemite-granodiorite (TTG), and mafic granulites represent the upper, middle, and lower crust, respectively (Percival and Mcgrath, 1986; Perry et al., 2006). The deepest exposed crust in the east is dominated by mafic granulites with evidence of in situ partial melting (Hartel and Pattison, 1996). These rocks were metamorphosed at 2660–2640 Ma (Krogh, 1993), similar to some crystallization ages obtained from the grey gneisses (Percival and West, 1994). This indicates that the mafic granulites could represent the source of the grey gneiss (e.g., Moyen and Martin, 2012). In contrast, whole-rock oxygen isotopes (Li et al., 1991) and proximal metasedimentary gneisses (Percival, 1983) suggest that the mafic granulites likely have an origin as supracrustal metabasites.

The upper crust in the Kapuskasing uplift is represented by the Michipicoten greenstone belt, which consists of three bimodal volcanic cycles with approximate ages of 2900, 2750, and 2700 Ma (Sage, 1994). Each cycle contains a base of ultramafic to mafic rocks that transition to felsic rocks going up the stratigraphic section (Sage et al., 1996). The oldest of these cycles contains a series of komatiites, whereas the younger cycles contain a base of tholeiitic basalt (Sage, 1994). The 2900 and 2750 Ma cycles are capped with thin beds of iron formation, whereas the youngest cycle is possibly coeval with chemical sediments and interfingered with clastic metasediments (Sage, 1994; Turek et al., 1996). The majority of the Michipicoten Greenstone Belt has been metamorphosed to greenschist facies (Fig. 2.2a) and reaches amphibolite grade near the contact with the Wawa Gneiss Domain (Sage, 1994; Lin and Beakhouse, 2013).

The Wawa Gneiss Domain represents the paleo-middle crust and is metamorphosed to amphibolite-facies conditions (Moser, 1994; Kendrick et al., 2019). The Wawa Gneiss Domain is dominated by hornblende–biotite grey gneisses of mostly tonalite, trondhjemite, and granodiorite (TTG) in composition with minor diorite (Moser, 1994; Kendrick et al., 2019). The Wawa Gneiss Domain is separated from the granulite-facies (deep crust) Kapuskasing Structural Zone to the east by a gradational metamorphic contact (Percival, 1983). Shear zones define the most pervasive fabric in the Wawa Gneiss Domain, becoming ubiquitous and defining the regional scale Saganash Lake fault when approaching the Kapuskasing Structural Zone (Moser, 1994; Nitescu and Halls, 2002). The hornblende–biotite gneisses of the Wawa Gneiss Domain enclose meter- to decameter-sized hornblende–plagioclase–clinopyroxene rafts (Fig. 2.2b) which are commonly crosscut by granodiorite dykes and quartz-monzonite pegmatites (Percival, 1990). The majority of the granitoids crystallized between ca 2700 and ca 2645 Ma (Percival and Krogh, 1983; Moser et al., 1996); rare crystallization ages >2900 Ma have been reported (Moser et al., 1996).

The lower crust in the Kapuskasing uplift is represented by the Kapuskasing Structural Zone which contains upper-amphibolite to granulite-facies metabasites that display petrographic evidence of anatexis (Percival and West, 1994; Hartel and Pattison, 1996) as well as tonalitic gneisses that may have also partially melted (Percival, 1990; Kendrick et al., 2021). Metabasic migmatites are heterogenous with a metamorphic mineral assemblage of plagioclase, hornblende,

quartz, and ilmenite with variable amounts of clinopyroxene and garnet in the melanosome. In contrast, the leucosomes are composed of plagioclase, quartz and clinopyroxene with rare garnet. Gneissic tonalites are heterogenous with leucosomes consisting of plagioclase, quartz, biotite, and hornblende and melanosomes of plagioclase, quartz, garnet, biotite, clinopyroxene, and hornblende in variable amounts (Percival, 1983; Percival and Card, 1983). Garnet-clinopyroxene-plagioclase-quartz thermobarometry indicates granulite-facies metamorphism at 9 kbar and 685–735°C (Percival, 1983). However, based on experimental data, Hartel and Pattison (1996) argue that peak metamorphism was likely closer to 11 kbar for a temperature of 850°C. Krogh (1993) dated regional metamorphism between 2660 and 2640 Ma, although high-temperature conditions may have initiated closer to 2700 Ma (Corfu, 1987; Krogh and Moser, 1994) and probably persisted for ~80 My after peak metamorphism (Bowman et al., 2011). This prolonged thermal history agrees well with the initial interpretation of Percival and West (1994) that the deeper crustal levels experienced protracted cooling rates due to long deep-crustal residence. Although protoliths are uncertain, whole-rock oxygen isotopes ($\delta^{18}O$) of mafic rocks in the Kapuskasing Structural Zone range from +5.6 to 7.1‰ (Li et al., 1991) which were interpreted to indicate that the now mafic granulites originated as sub-aerial or sub-marine volcanic flows, providing evidence of a supracrustal sequence (perhaps similar to the Michipicoten Greenstone Belt) metamorphosed to granulite facies. This interpretation is also supported by supracrustal rocks in the Kapuskasing Structural Zone (Moser, 1994).

2.3 Methodology

2.3.1 Whole-rock geochemistry

Twelve greenstone samples (across all three volcanic cycles in the Michipicoten Greenstone Belt) from the upper crust, 27 TTG samples (Kendrick et al., 2021) from the middle crust, and 23 high-grade metabasites from the lower crust were processed and analysed for whole-rock bulk compositions and density (Appendix S1.1) at room temperature and atmospheric pressure. Weathered surfaces and veins were removed using a rock saw. Whole-rock lithogeochemical analysis of most samples (70 of 72) was performed at the Ontario Geological Survey Geoscience Laboratories (Geolabs), where samples were crushed using an agate mill. Major element concentrations were analyzed by X-ray fluorescence (XRF); samples were heated to 105°C under a nitrogen atmosphere followed by heating to 1000°C under an oxygen atmosphere and fused

with a borate flux. Bulk-rock concentrations were subsequently analyzed using Malvern-Panalytical Axios Advanced WD-XRF spectrometers. For trace element analyses, samples were digested in a closed vessel using a multi-acid solution and analyzed using a Thermo Scientific iCAP-Q inductively coupled plasma mass spectrometer (ICP-MS). For free and crystalline water content, samples were heated to 105°C and 1000°C, respectively and analyzed by infrared absorption. Ferrous iron was measured through potentiometric titration with a permanganate solution standard.

The procedure for analyzing the two other samples at Actlabs is described in Kendrick et al. (2022). Both laboratories inserted duplicates, internal reference materials, and blanks for quality assurance and quality control, which are reported alongside detection limits in Appendix S1.3.

2.3.2 Mineral Liberation Analysis

Mineral maps and modal proportions were collected from Mineral Liberation Analysis (MLA) at Actlabs to complement optical petrology; MLA results of the modelled samples are reported in Appendix S1.5. The mineralogical analysis was done by FEI QEMSCAN 650 F, using Field Image Analysis for modal mineralogy and particle data. The Field Emission Gun was used at an accelerating voltage of 25 kV and a spot size of 6.4μm with a working distance of 13 mm. The mineral reference library was customized for this project. The weight percentage of the mineral was calculated using the area proportion and semi-quantitative mineral compositions.

2.3.3 Phase equilibrium modelling

Six samples were selected for forward-phase equilibrium modelling (Table 2.1); three samples from the Michipicoten greenstone belt were grouped into greenstones, and three from the Kapuskasing Structural Zone were grouped into high-grade metabasites. We selected samples so that an enriched (between median and maximum), intermediate (near median), and depleted (between median and minimum) bulk composition concerning P_2O_5, Zr, LREE, K, U, and Th were modelled to account for the heterogeneity of the sample suite from both the upper and lower crust.

Phase equilibrium modelling calculations were performed using the THERMOCALC (v3.50) software package (Powell and Holland, 1988) with the internally consistent dataset, ds62 (Holland and Powell, 2011) and activity-composition models of Green et al. (2016) for liquid, clinoamphibole, clinopyroxene, White et al. (2014) for orthopyroxene, biotite, muscovite, and garnet, Holland and Powell (2003) for K-feldspar and plagioclase, White et al. (2000) for ilmenite, and Holland and Powell (2011) for epidote; quartz, rutile, titanite (sphene) and H_2O were modelled as pure end-members. Modelling was conducted in the NCKFMASHTO (Na_2O–CaO–K_2O–FeO–MgO–Al_2O_3–SiO_2–H_2O–TiO_2–Fe_2O_3) chemical system (Holland and Powell, 1990) to consider essential components in mafic metamorphic systems. The dataset and chemical activity-composition models are calibrated for tonalitic melt produced through the anatexis of hydrated metabasites. As H_2O content can be affected by hydrothermal fluids and surface processes, minimal free H_2O at the 10 kbar solidus was deemed appropriate. These assumptions are consistent with water-saturated compositions required for TTG melt generation (Moyen and Martin, 2012) while maintaining fluid-absent melting (Palin et al., 2016c; Stuck and Diener, 2018) coupled with peak metamorphic pressure estimates of ~10 kbar for granulites in the Kapuskasing Structural Zone (Hartel and Pattison, 1996). The amounts of ferric and ferrous iron in the modelled composition were determined from the whole-rock values obtained from titration.

2.3.4 Accessory mineral modelling

Accessory minerals are a key repository of heat-producing elements (e.g., Bea, 1996; Yakymchuk and Brown, 2019), and their behaviour must be considered in crustal anatexis studies. Modelling accessory minerals requires using the output from the THERMOCALC calculations coupled with solubility expressions (Kelsey et al., 2008; Johnson et al., 2021). A grid was calculated across each pseudosection at a 0.25 kbar and 25°C resolution to extract the modal amount, density, and composition of melt and minerals and system enthalpy. These data were used to calculate the variables that affect accessory mineral stability and, in turn, to calculate stability and modal amounts of accessory minerals.

For modelling the behaviour of accessory minerals, we focus on the concentrations of trace elements that are essential structural constituents of zircon (Zr), apatite (P), and allanite (LREE) in the melt and residue (Table 2.2). The concentrations of these elements in the melt and

residue were determined for two scenarios. In the first scenario, these elements are only found in the accessory minerals and melt, i.e., these elements are not partitioned into the major (rock-forming) minerals. For this scenario, the saturation of the melt with Zr, P_2O_5, and LREE is calculated, and excess concentrations of these elements are divided by their stoichiometric amounts in the appropriate accessory mineral to determine their proportions in the system (c.f. Kelsey et al., 2008; Yakymchuk and Brown, 2014). In the second scenario, the major minerals are modelled as an additional sink for these elements based on mineral–melt equilibrium partitioning. Concentrations above the saturation concentration of the melt and the amount modelled to reside in the major minerals are then used to calculate the proportions of the accessory minerals in the system. We assume stoichiometric amounts of Zr in zircon (497,600 mg/kg) and P_2O_5 in apatite (418,200 mg/kg). LREE concentration in allanite is variable in natural systems; here, we use 250,000 mg/kg LREE as a baseline, equating to approximately one atom per formula unit (apfu). In both scenarios, if the modelled melt concentration is less than the saturation concentration of the essential structural constituents, the accessory mineral is considered wholly consumed. The solubility expression for each modelled accessory mineral and the procedure for modelling accessory minerals are described in Appendix S1.6.

As each accessory mineral can partition essential structural constituents of the others (i.e., LREE and Zr in apatite, LREE and P_2O_5 in zircon, and Zr and P in allanite), an order of saturation calculations was determined of apatite, then zircon, followed by allanite. This order was chosen as apatite is commonly an accessory mineral in mafic igneous rocks, with zircon rarely present in significant proportions, and allanite is restricted to higher-pressure metamorphism. Although Th can be a significant constituent in allanite and can account for a few weight percent in apatite and zircon, mixing is assumed to be ideal following a constant distribution coefficient (e.g. Yakymchuk et al., 2018).

Partitioning of trace elements into the major minerals is modelled using partition coefficients for the melting of metabasites from (Bédard, 2006). There are no experimentally constrained distribution coefficients for K-feldspar and muscovite in mafic to intermediate systems; therefore, these minerals are not considered repositories for U and Th. The limitations of this approach are discussed later. Partition coefficients are summarized in Appendix S1.7. Contour plots of accessory mineral dissolution are presented in Appendix S1.5.

2.3.5 Heat production and thermal buffering times

The heat generated at the time of metamorphism in the Kapuskasing Structural Zone (c. 2650 Ma) from the radioactive decay of K, Th, and U is calculated using the isotopic decay constants (λ) and measured present-day heat-producing elements concentrations (N_O; Table 2.1 for K_2O, Table 2.2 for U and Th) to calculate the past concentrations (N_t) using the decay equation $N_t = N_O e^{\lambda t}$ (Rutherford and Soddy, 1903). The present-day $^{238}U/^{235}U$, $^{39}K/^{40}K$ and 100% ^{232}Th are assumed. As metamorphism and magmatic emplacement were prolonged in the Kapuskasing Structural Zone, 2650 Ma is used in these calculations as this is during both magmatism and granulite-facies metamorphism at ca 2660–2640 Ma (Krogh, 1993). Concentrations of the HPE can be paired with the heat production equation of Ashwal et al. (1987) to determine radiogenic heat production:

$$A\left(\frac{\mu W}{m^3}\right) = \rho(0.097C_u + 0.036C_K + 0.026C_{Th}) \quad \text{Equation 2.1}$$

Where ρ is rock density ($g \cdot cm^{-3}$), C_U and C_{Th} are concentrations in mg/kg, and C_K is in wt%. The density of the system and each phase were determined across the same P–T grid used for accessory mineral modelling for each pseudosection. We combine the calculated heat production with the modelled enthalpy changes between extracted points (i.e., between 25°C intervals; ΔH), temperature, and system density—from the THERMOCALC output—to determine the buffering time between temperature intervals along model isobaric heating paths at 10 kbar using the formulation of (Stüwe, 2007):

$$\Delta t(s) = \frac{\Delta T \rho C_p}{(A * 10^{-6})}, \text{where } C_p = \frac{\frac{\Delta H}{\Delta T}}{M} \quad \text{Equation 2.2}$$

This equation normalizes the heat capacity to the molar mass of the bulk composition (0.625–0.656 kg/mol for our samples) to calculate the specific heat capacity (J/Kg•K). The units for density (ρ), enthalpy (H), and heat production (A) are kg/m^3, J, and $\mu W/m^3$, respectively.

2.4 Results

2.4.1 Mineral assemblages and microstructures

Mineral proportions reported here are wt% results from MLA reported in Appendix S1.5 and methods described in section 2.3.2. The investigated greenstone samples from the Michipicoten

greenstone belt have varying degrees of visible alteration and preservation of original igneous textures. The three samples have a mineral assemblage of plagioclase, chlorite, Fe-oxides ± clinopyroxene, epidote, quartz, and calcite. The enriched and intermediate greenstone samples are inferred to have preserved igneous textures (Fig. 2.3a-c). Primary igneous microstructures include feldspar laths (Fig 2.4a and c); these are partially replaced by epidote (Fig. 2.3b) or affected by minor sericitization. The enriched greenstone sample comprises over 35 wt% plagioclase, whereas plagioclase content is ~13 wt% of intermediate and depleted greenstone samples. Clinopyroxene is found in the enriched (2.5 wt%) and depleted (0.45 wt%) greenstones and is partially or wholly replaced by chlorite and amphibole (Fig. 2.3a). Matrix chlorite is found in minor proportions in the enriched greenstone but as a major mineral in both the intermediate (22 wt% chlorite) and depleted (21 wt% chlorite) greenstone samples and occurs as discrete grains (Fig. 2.3c) or is interleaved with biotite. Biotite is commonly observed in contact with and surrounding Fe-oxides. Calcite (usually <1 wt%; but 14 wt% in the intermediate greenstone) occurs as discrete matrix grains, not as veins. Apatite occurs as inclusions in matrix minerals and along grain boundaries in proportions of 0.43, 0.33, and 0.04 wt% in the enriched, intermediate, and depleted greenstones, respectively. Zircon is only found in minor (0.01 wt%) proportions in the intermediate greenstone sample; no allanite was observed in any greenstone sample.

Upper amphibolite to granulite-facies (high-grade) metabasite samples modelled from the Kapuskasing Structural Zone have a typical assemblage of plagioclase, quartz, clinopyroxene, and hornblende ± biotite with minor amounts of titanite, ilmenite, and hematite—garnet is observed in one sample (intermediate high-grade metabasite; Fig. 2.3e). Samples are foliated, and compositional banding is observed in the thin section for the enriched and intermediate high-grade metabasite with plagioclase and quartz layers as well as ferromagnesian (clinopyroxene, hornblende) layers (Fig. 2.3d–f). Samples have well-preserved granoblastic microstructures and do not show petrographic evidence of retrogression; however, a small (<0.25 mm wide) calcite + plagioclase veinlet, as well as minor sericitization of plagioclase, is observed in the depleted metabasite sample. The depleted high-grade metabasite is composed of 45 wt% hornblende, and the enriched high-grade metabasite is composed of 27 wt% hornblende, whereas hornblende is a minor constituent of the intermediate high-grade metabasite (1 wt%); in all three samples, hornblende is xenoblastic. Clinopyroxene is >20 wt% of both the enriched and intermediate samples, whereas the depleted high-grade metabasite is 13 wt% clinopyroxene, which is

concentrated in the melanosome. Plagioclase is interstitial and xenoblastic and composes ~30wt% of all samples. Apatite (0.09–1.25 wt%) and minor (<0.05 wt%) zircon are common inclusions in hornblende and quartz (Fig 2.4f). Allanite (determined from the MLA internal mineral library) is only found in the enriched high-grade metabasite in a minor (0.05 wt%) proportion.

2.4.2 Whole-rock compositions

The concentrations of P_2O_5, Zr, $LREE_{(tot)}$, and heat-producing elements in samples from across the Kapuskasing uplift are presented in Fig. 2.4; these values will be compared with model results later. The TTG samples (n=27) show the greatest variability in LREE, U, and Th, whereas the high-grade metabasites (n=23) have lower variability than the greenstone samples (n=13) and the TTGs for all elements of interest. The TTGs are enriched in Zr, LREE, K, U, and Th compared to the greenstones and high-grade metabasite samples (Fig. 2.4). All three rock types have similar median concentrations of P_2O_5; the greenstone has the highest median compared to the high-grade metabasites and TTGs.

The higher concentrations of heat-producing elements in the TTGs correspond to higher calculated present-day heat production (Fig. 2.5a) than the high-grade metabasite and greenstone samples. Calculated heat production from present to 3.0 Ga using the measured concentrations of the heat-producing elements (HPE), decay constants, and the median densities are shown for the TTGs, greenstones, and high-grade metabasites in Figure 2.5b–d. The relative proportion of radiogenic heat from the decay of K and Th decreases with increasing age with an increasing proportion of heat produced by U from the present to 3.0 Ga (Fig. 2.5b–d). At 3.0 Ga, ancient heat production is calculated to be ~30% greater in the TTGs, 20% higher in the high-grade metabasites and 36% higher in the greenstone samples than current heat production. Present and past heat production in the TTG samples is primarily produced through Th-decay, followed by the decay of U and K. Current radiogenic heat production in the high-grade metabasites is dominated by K decay. In contrast, U-decay is the most important at >2.7 Ga for these rocks. The proportion of current radiogenic heat production in the greenstone samples is similar for U, Th, and K.

2.4.3 P–T phase diagrams

Simplified P–T pseudosections for each of the six investigated metabasite samples are shown in Figure 2.6, fully labelled figures are in Appendix S1.9; mineral abbreviations are from (Holland and Powell, 2011) except we use titanite (ttn) instead of sphene. Enriched samples (see Fig. 2.6a and 2.6d) have calculated solidus temperatures of 610–775°C compared to 640–775°C and 650–850°C for intermediate samples (Fig. 2.6b and 6e) and depleted samples (Fig. 2.6c and 6f), respectively. K-feldspar is generally stable at temperatures between the solidus and 800–850°C at pressures less than 18 and 16 kbar for enriched greenstone (Fig. 2.6a) and high-grade metabasite (Fig. 2.6d), respectively. K-feldspar is not predicted to be stable in depleted samples or the intermediate high-grade metabasite. For the intermediate greenstone composition (Fig. 2.6b), K-feldspar is predicted to be stable for pressures between 6 and 20 kbar and at temperatures between 675 and 925°C.

Hornblende is stable for all modelled pressures and temperatures for the enriched high-grade metabasite. In contrast, hornblende is stable for the enriched greenstone sample at temperatures below 950°C, though the stability limit decreases to ~800°C at 20 kbar and 850°C at 5 kbar. For the intermediate high-grade metabasite sample (Fig. 2.6d), hornblende is stable at temperatures below ~925°C at low pressures, decreasing to 710°C at 20 kbar. Comparatively, hornblende stability is pressure-dependent for the intermediate greenstone; hornblende is predicted at pressures less than 15 to 10 kbar, decreasing with temperature. For depleted samples, hornblende is stable across all modelled pressures and temperatures below 11 kbar and 950°C. Biotite is predicted for the intermediate greenstone compositions at temperatures below 875–975°C.

Plagioclase is generally predicted to be stable at higher pressures in high-grade metabasite compositions compared to the greenstone samples. For the enriched greenstone, plagioclase is stable at pressures less than 11 kbar at the solidus (~650°C) and temperatures above 875°C at 20 kbar. Plagioclase is stable only at low pressures (<7 kbar) and temperatures (<875°C) for the intermediate greenstone. For the depleted greenstone (Fig. 2.6c), the plagioclase-out boundary is an upward closing curve crossing the solidus at 12 kbar and 850°C, reaching a maximum pressure of 18 kbar at ~930°C and ~15.5 kbar at 1000°C. At the solidus, plagioclase is predicted to be stable at pressures less than 13 kbar for the enriched (~700°C), 15.5

kbar for the intermediate (~750°C), and 18 kbar for the depleted (~850°C) mafic high-grade metabasite (Fig. 2.6f). At 20 kbar, plagioclase is predicted to be stable at temperatures greater than ~915°C for the three modelled high-grade metabasite compositions.

Garnet is predicted to be stable at lower pressures in the greenstone compositions than in high-grade metabasite samples. The garnet-out field boundary is a downward closing curve reaching a minimum pressure at 900–925°C for the modelled greenstone compositions. At the solidus, garnet is stable at pressures above 15 kbar for the enriched (675°C), 9 kbar for the intermediate (675°C), and 10.5 kbar for the depleted (825°C) greenstone composition. At 1000°C, garnet is predicted to be stable at pressures above 9.5 kbar, 7.5 kbar, and 9.5 kbar for enriched, intermediate, and depleted greenstone compositions (Fig. 2.6a–c), respectively. At the solidus, garnet is stable at pressures greater than 18 kbar for the enriched (790°C), 11 kbar for the intermediate (750°C), and 15 kbar for the depleted (850°C) high-grade metabasite. The garnet-out boundary for all three modelled high-grade metabasite samples has a negative dP/dT slope crossing 1000°C at 13.5, 11, and 11.5 kbar for the enriched, intermediate, and depleted high-grade metabasite compositions (Fig. 2.6d–f), respectively.

Except for the intermediate greenstone composition (Fig. 2.6b), epidote is restricted to pressures greater than 5.5–6 kbar at the solidus with the epidote-out line having a positive dP/dT slope crossing 20 kbar at 925–975°C. For the intermediate greenstone composition, epidote is predicted over a small P–T range between 6.5 and 14 kbar at <700°C. Augite is stable across all modelled pressures and temperatures for all pseudosections except for the depleted greenstone (Fig. 2.6c), where augite is absent from high pressure (>12 kbar) and low temperature (<850°C) conditions. Orthopyroxene is predicted for all greenstone compositions and the depleted high-grade metabasite at temperatures above 800–900°C and pressures below 8–10 kbar. If present, titanite is predicted to be stable at pressures less than 12 kbar and temperatures below 800°C. In the greenstone samples (Fig 2.7a-c), rutile is generally stable above 11 kbar, although it requires higher pressures with increasing temperature in the intermediate greenstone. Rutile is predicted to be stable in the high-grade metabasites (Fig 2.7d-f) above 12 kbar at temperatures less than ~775°C and pressures greater than 15 kbar at higher temperatures.

2.4.4 Accessory mineral modelling

Predicted accessory mineral stabilities are plotted as contours over the modelled P–T range for each sample; a summary is provided below, although plots and a full description are provided in Appendix S1.8. Contours represent the percentage of the accessory mineral that has been dissolved normalized to the whole-rock concentration of the essential structural component (P_2O_5, Zr, LREE; Table 2.2) divided by the amount of that element in the accessory mineral (e.g., 0% $diss_{apatite}$ = whole rock P_2O_5/418,200; Kelsey et al., 2008). Results for two scenarios are presented: (1) the trace element essential structural constituents of the accessory minerals are only found in that accessory mineral and melt (e.g., Zr found only in zircon and melt) and, (2) all investigated trace elements are partitioned between the major minerals, accessory minerals and melt based on equilibrium partitioning. We present both scenarios to assess the influence of major minerals sequestering P_2O_5, Zr, and LREE during anatexis on accessory mineral stability, affecting HPE distribution.

Apatite is predicted to be <20% dissolved at temperatures <800°C for all compositions and both modelled scenarios, and the stability of apatite is decreased by 25–50°C for scenario 2 relative to scenario 1. Apatite is expected to be wholly dissolved in intermediate compositions at equal or lower temperatures than in depleted compositions. The apatite stability field is predicted to extend to higher temperatures for enriched compositions. Apatite is expected to have increased stability for most high-grade metabasites compared to the greenstone counterparts (i.e., depleted, intermediate and enriched). This point will be further discussed in section 2.5.2. In general, the sequestration of P_2O_5 in major minerals minimally affects the stability of apatite.

Zircon stability is temperature-dependent, and zircon is expected to be dissolved entirely at temperatures near 900°C for all modelled compositions and both scenarios. For scenario 2 (i.e., Zr distributed in major minerals), zircon is not predicted to be stable for the depleted compositions except at low temperatures and pressure for the depleted high-grade metabasite. For intermediate and enriched compositions, the difference for modelled zircon-out contours between Scenario 1 and Scenario 2 can be greater than 200°C. The stability of zircon is comparable between greenstone and high-grade metabasite compositions. In general, the sequestration of Zr in major minerals considerably affects the stability of zircon.

Allanite is generally predicted to be stable at pressures greater than 5.5 kbar and temperatures between 650 and 950°C. It is generally predicted to be stable at higher temperatures in the modelled high-grade metabasite compositions compared to the greenstone compositions. However, the melt is always predicted to be supersaturated with LREE; an explanation and implications of this are discussed later. The 100% dissolved contour is predicted at higher temperatures for depleted than modelled enriched compositions. However, allanite is predicted to completely dissolve at lower temperatures for intermediate greenstone and high-grade metabasite compared to depleted and enriched compositions. In general, the sequestration of LREE in major minerals minimally affects the stability of allanite.

2.4.5 Budget of heat-producing elements

The proportion of K, U, and Th in the melt across the modelled P–T range and the distribution between the melt and residual mineral assemblage along an isobaric heating path at 10 kbar are shown in Figures 2.7–9. The contours on these figures represent the weight proportion of K, U, and Th partitioned into the melt. K concentration in phases is retrieved from THERMOCALC and converted to wt%. The calculated modes of apatite, zircon, and allanite for partitioning U and Th account for P_2O_5, Zr, and LREE partitioning into major minerals (i.e., scenario 2). For all further results and discussion, only scenario 2 (trace elements partitioning into major minerals) is considered because it is a closer approximation to natural systems.

The contours representing the proportion of potassium in the melt have a steep dP/dT slope and are broadly sympathetic to the solidus. Ranked by decreasing potassium affinity, biotite, K-feldspar, hornblende, and plagioclase are predicted to be dominant mineral repositories for potassium in all modelled rock types (Fig. 2.7); the proportion of the K budget in the melt increases with temperature. K-feldspar hosts >50 % (by weight) of the potassium in the system, as can biotite at temperatures <750–800°C. Biotite—though is only predicted as part of the suprasolidus assemblage for the intermediate greenstone—is expected to host a smaller proportion of potassium as temperature increases with K-feldspar and the melt of the primary repositories for K. Once the temperature is above biotite stability for the intermediate greenstone (and well above K-feldspar stability), >70 % of potassium is predicted to be hosted in the melt.

For all compositions modelled, there is a steep increase in the proportion of potassium hosted in the melt as the temperature approaches 750–800°C. This coincides with the breakdown

of K-feldspar and 10–20 wt% melt. The greater proportion of melt predicted for the greenstone compositions coincides with slightly greater proportions of the K budget hosted in the melt. Hornblende and plagioclase generally contain 10–15% of the K budget at most temperatures, with the proportion of the potassium budget in hornblende and plagioclase steadily decreasing with temperature. An exception to this is the depleted greenstone, where hornblende can contain ~80% of the system K budget.

The contours representing the proportion of uranium hosted in the melt have a steep dP/dT slope and are broadly sympathetic to the solidus (Fig. 2.8). Uranium is modelled to be strongly partitioned into a few minerals, particularly apatite and epidote; however, zircon, allanite, hornblende, and plagioclase can each contain 5–10 wt% of the uranium in the system. The proportion of U hosted in hornblende and plagioclase is due to their relatively high modal proportion. At 850°C and 10 kbar, the maximum concentration of U in plagioclase and hornblende is 0.2 mg/kg and 0.1 mg/kg, though they compose 35 wt% and 64 wt% of the system, respectively. The U budget is predicted to be hosted by order of decreasing amounts into epidote, apatite, zircon, melt, plagioclase, hornblende, and augite. Epidote is predicted to sequester up to 50 wt% of the uranium, though it is restricted to temperatures <800°C. Apatite can sequester >40 wt% of the uranium in the system; if temperatures exceed apatite or epidote stability, >75 wt% of the uranium is hosted in the melt.

The primary mineral repositories for thorium are predicted to be epidote, allanite, and apatite. Contours for the proportion of the thorium budget hosted in the melt have steep and generally positive dP/dT slopes. The Th budget is predicted to be hosted preferentially in epidote with an order of decreasing affinity of epidote, allanite, apatite, melt, hornblende, plagioclase, and augite. If present (<800°C), epidote and allanite can sequester >95 wt% of the thorium budget of the system—apatite is predicted to be the dominant mineral repository of thorium when temperatures exceed that of epidote and allanite stability (Fig. 2.9). Hornblende can sequester up to 40 wt% of the thorium. However, this is only predicted for the depleted greenstone. Hornblende, plagioclase, and augite generally contain <15 wt% of the thorium each; the maximum concentration of Th in hornblende, plagioclase, and augite is 0.45, 0.78, and 0.85 mg/kg, respectively. The proportion of thorium in the melt increases with temperature. At

~750°C, the melt is predicted to contain ~25 wt% of the Th budget—the proportion increases to ~50 wt% at 850°C.

2.4.6 Metamorphic heat production and heating times

Heat production is calculated from measured concentrations of whole-rock samples and modelled for the six compositions during metamorphism. We differentiate the modelled radiogenic heat production predicted in the system (melt–restite) during anatexis—called metamorphic heat production (MHP)—from radiogenic heat production calculated using measured whole-rock specific gravity and bulk composition concentrations of K, U, and Th, which we call past heat production (PHP). MHP is calculated by modelling the distribution of HPE during metamorphism to calculate the heat production of each phase in the system using the predicted densities and HPE concentrations of each phase (eq. 2.1); the weighted average of heat production and phase proportion provide the heat production of the system during metamorphism. These two values for heat production are compared in Figure 2.10, along with the relative value of heat production from HPE in the melt. All heat production calculations are time-corrected to 2650 Ma, broadly the timing of high-temperature metamorphism and crystallization of TTGs (Krogh, 1993; Percival and West, 1994) in the Kapuskasing uplift.

Metamorphic heat production decreases with increasing melt proportion and the proportion of radiogenic heat in the melt. Heat-producing elements are expected to preferentially partition into the melt, which has a lower density (ρ=2.1–2.6 g/cm^3) than the restite (>2.6 g/cm^3) and the bulk rock at room temperature and modern atmospheric pressure (>2.9 g/cm^3). As heat production is a function of density and HPE concentration, the modelled heat production of the system (melt and restite) decreases as temperature and HPE content in the melt increases. The difference between the PHP and the MHP is most pronounced for the intermediate greenstone, which has a PHP of 0.66 μW/m^3 and is reduced to 0.16–0.11 μW/m^3 during metamorphism (Fig. 2.10b). Although not as extreme, a decrease in radiogenic heat production with increasing melt fraction during prograde metamorphism is predicted for all samples. The enriched greenstone has a PHP of 0.56 μW/m^3 and is predicted to be reduced to 0.5–0.39 μW/m^3 during metamorphism, whereas the enriched high-grade metabasite has a PHP of 0.53 μW/m3, which is reduced to 0.37–0.29 μW/m^3 during metamorphism. The intermediate high-grade metabasite has a PHP of 0.23 μW/m^3 and metamorphic heat production ranging from 0.18 to 0.14 μW/m^3. The depleted

high-grade metabasite has a PHP of 0.2 μW/m^3, which is reduced to 0.12–0.11 μW/m^3 during metamorphism. The depleted greenstone has the lowest discrepancy between PHP (0.07 μW/m^3) and metamorphic heat production (0.06–0.05 μW/m^3).

The calculated time required to raise the temperature from the solidus to 1000°C along a 10 kbar isobaric heating path for the modelled samples is presented in Figure 2.10. These calculations consider the endothermic nature of partial-melting reactions (e.g., Bea, 2012; Schorn et al., 2018) by using the enthalpy of reaction to progress metamorphism in 25°C increments and consider both radiogenic (internally derived) heating as well as an estimated mantle heat flux; heating times not accounting for mantle heat are also displayed. The thermal contribution from the mantle is calculated using an Archean Moho temperature of 850°C (Mareschal and Jaupart, 2006; Sun et al., 2021), Moho depth of 40 km, and thermal conductivity of 2 W/mK (Pasquale et al., 2015) resulting in a mantle heat flux of 42.5 mW/m^2.

The enriched greenstone sample (Fig. 2.10a) is predicted to have a shorter heating time than the enriched high-grade metabasite (Fig. 2.10d). In contrast, the intermediate and depleted greenstone compositions are predicted to require more time than the high-grade metabasites of similar composition. For example, the time required to heat the greenstone samples from the solidus to 1000°C requires ~65 Ma for the enriched (Fig. 2.10a), ~111 Ma for the intermediate (Fig. 2.10b), and ~82 Ma for the depleted (Fig. 2.10c) compositions. Comparatively, the enriched (Fig. 2.10d), intermediate (Fig. 2.10e), and depleted (Fig. 2.10f) high-grade metabasite compositions are predicted to require ~71, ~67, and ~60 Ma, respectively, to reach 1000°C from the solidus.

2.5 Discussion

2.5.1 Model limitations

Several assumptions and necessary simplifications exist in our modelling of accessory mineral behaviour during partial melting in metabasites and calculating heat production. The first relates to the possible alteration of the protoliths. The second is the limitations of the thermodynamic database and activity–composition models used in the calculations. The third relates to the assumed equilibrium partitioning of trace elements between minerals and melt.

Fluid-related alteration can mobilize heat-producing elements and change the heat production of rock from that of the protolith. Acidic hydrothermal fluids can mobilize potassium through the dissolution of K-feldspar to produce muscovite + quartz and lead to potassic alteration further along the flow path (Frank et al., 1998; Frank and Vaccaro, 2012) and uranium is soluble in oxidizing fluids and the degree of U solubility in hydrothermal systems decreases with temperature (Timofeev et al., 2018). Although thorium is often considered insoluble in hydrothermal systems, it can be selectively leached from rocks in acidic fluids carrying SO_4^{2+}, F, and OH^- (Ekberg et al., 2000; Nisbet et al., 2018, 2019).

Some metabasites in the Michipicoten greenstone belt that hosts gold mineralization show compositional changes during metamorphism and silicic alteration that resulted in a minor removal of U (<10%) and Th (<4%) coupled with enrichment in K_2O, occasionally greater by a factor of 2 in some samples (Ciufo et al., 2020). Carbonate alteration is also observed in the intermediate greenstone sample, which contains particularly high (2.49 wt%) K_2O and low (42.59 wt%) SiO_2. This composition lies within the median range for U, Th, P_2O_5, Zr, and LREE (Fig. 2.4) as well as heat production (Fig. 2.5a), metamorphic heat production and metamorphic heat time (Fig. 2.10b). Greenstone belts commonly exhibit evidence of metasomatism, including carbonate alteration. Metasomatism—particularly hydration—of metabasites is a requirement for TTG formation (Moyen and Martin, 2012); therefore, even though the intermediate greenstone sample may have high K_2O and carbonate compared to the rest of the sample suite, it still represents a possible TTG source. Our phase equilibrium modelling does not consider C-bearing species, mainly due to the uncertainties around CO_2 solubility in silicate melt (e.g. Carvalho et al. 2023). However, suppose carbonate alteration occurred before high-grade metamorphism. In that case, the presence of carbonate should decrease water activity and increase the solidus temperature (Khitarov and Kadik, 1973), resulting in less melting and, therefore, greater retention of HPE in the source.

Limited subsolidus alteration was observed in the other greenstone and high-grade metabasite samples; nonetheless, any other potential effects of fluid infiltration at high temperatures are uncertain. The high-grade metabasites did, however, undergo high-temperature metamorphism and display evidence of anatexis, including clinopyroxene and garnet associated with leucosome (Fig. 2.2c; Ellis and Thompson, 1986; Hartel and Pattison, 1996). Although we

did not model the effects of melt loss (c.f. Yakymchuk and Brown, 2014; Stuck and Diener, 2018), we consider modelling both the low-grade greenstone compositions and the residual mafic high-grade metabasites as a reasonable approximation to the range of compositions in the Kapuskasing Structural Zone. If melt loss did occur, the major mineral assemblages would likely change very little (Palin et al., 2016c); however, trace element distribution would be affected. Yakymchuk and Brown (2014) and Yakymchuk (2017) modelled the behaviour of zircon+monazite and apatite+monazite, respectively, during the crustal melting of metapelitic rocks. They determined that melt loss would cause a decrease in accessory mineral proportions—relative to the undrained scenario—and therefore, the results depicted in Appendix S1.8 and Figure 2.10 should be considered maxima. Further, the effects of melt loss and garnet fractionation were studied by Kendrick & Yakymchuk (2020), who determined that garnet has a more extensive control on the trace elements for those readily partitioned into garnet than melt. Therefore, it may be reasonable to conclude that the stability of HPE-rich minerals is the most important control on the heat production of a system during anatexis. This being said, if melt loss did occur, the dissolution of zircon, apatite, and allanite (HPE-rich minerals) may occur to saturate the next batch of melt in Zr, P_2O_5, and LREE, respectively, decreasing the heat production of the solid proportion of the system.

We use the median values for U, Th, K, and bulk rock density in Fig. 2.5 and relative proportions of U, Th, and K in Figures 2.7, 2.8, and 2.9 to limit sample-specific bias. Finally, the modelled compositions encompass a range of heat-producing element concentrations to evaluate the sensitivity of our results to these variations. However, if younger (<2650 Ma) fluids or melt loss removed K, Th, or U from the rocks, heat production would be lower and heating times greater than predicted in Figure 2.10; the opposite would occur if fluids (or melt) introduced heat-producing elements to the samples. We are unaware of younger alteration events that would have mobilized the HPE in the study area. The widespread preservation of high-temperature mineral assemblages (e.g. garnet and clinopyroxene) suggests that late-stage fluid/melt infiltration was negligible.

The position of phase stability boundaries in pressure-temperature space depends on a confluence of factors, including the activity–composition models, which likely result in uncertainty of 50–100°C and 1–2 kbar (Green et al., 2016). These activity-composition

uncertainties are of similar magnitude to the uncertainties related to the reaction enthalpy (Powell and Holland, 1988), which is believed to be the most uncertain thermodynamic parameter due to slight differences between large values in enthalpy calculations (Powell and Holland, 1985) and the inability to calculate absolute enthalpies (Holland and Powell, 1985). Furthermore, the method of bulk composition determination (XRF for our samples) and hand sample heterogeneities could introduce an uncertainty of ±1 kbar in pressure calculations through phase equilibrium modelling (Palin et al., 2016a). When considering the uncertainties related to mineral stabilities and system enthalpy changes, the values for the modelled buffering times presented in Figure 2.10 and discussed further are considered reasonable first-order estimates and are likely best used to compare modelled samples.

There are minor discrepancies between the observed mineral assemblage in the samples and the predictions of the phase equilibrium models. Biotite is predicted only for the intermediate greenstone composition but is observed in all samples; however, only the enriched samples have biotite modes >1 wt%, and all are <5 wt% (Appendix S2.2). Quartz is observed in all samples but is predicted to be <1 wt% for the enriched and depleted high-grade metabasites. Neither biotite nor quartz is a significant repository for U or Th. However, biotite is an important host of K, and biotite-breakdown melting reactions will produce relatively K-rich melt. However, biotite and quartz may be the product of subsolidus reactions, in which case their presence in the samples but not in the models is not an issue for suprasolidus HPE calculations.

We make several assumptions to calculate the partitioning of trace elements between minerals and melt and predict the stability of accessory minerals. In our models, we assume the mineral–melt distribution coefficients are constant regardless of changing melt composition, temperature, or pressure even though these variables likely affect distribution coefficients (Klein et al., 1997; Wilke and Behrens, 1999). There are no known experimentally-constrained distribution coefficients for K-feldspar and muscovite in metabasite compositions however, published values for P, Zr, LREE, Th, and U partitioning in K-feldspar are less than 0.1 in rhyolite-dacite derived melts (Philpotts and Schnetzler, 1970; Stix and Gorton, 1990)—though some natural samples of K-feldspar in peraluminous granites contain up to 0.5 wt% P_2O_5 (London, 1992). In the modelling, partitioning trace amounts of P, Zr, or LREE into K-feldspar or muscovite would only slightly reduce the amount of apatite, zircon, or allanite in the modelled

system. Concentrations of the LREE in the system would be reduced ($Kd^{plg/melt}$ = 0.23–0.36), which would reduce the stability of allanite—this is explored in more detail below. However, K-feldspar is not predicted in either depleted composition and is predicted to be <10 wt% in the other compositions. Further, if the distribution coefficients for K-feldspar are like plagioclase, the heat production in the system would be slightly higher as the distribution coefficients of Th and U between plagioclase and melt are 0.1. Muscovite is only predicted at high pressure and low temperatures for the enriched and intermediate high-grade metabasite and intermediate greenstone compositions with a maximum predicted proportion of 11 wt% (intermediate greenstone). Biotite (the most similar mineral in terms of composition and structure) has a mineral/melt distribution coefficient of 0.1 for U and Zr, 0.18 for P, and 0.01 for Th, which when paired with the limited stability field of muscovite across the modelled P–T conditions, muscovite is considered to have only minor effects in the generation of Archean crust. Considering the restricted stability of muscovite and K-feldspar predicted in our models paired with limited partitioning of HPE, Zr, P, and LREE in compositionally and structurally similar minerals, the lack of well-constrained partition coefficients for the HPE and Zr, P, and LREE for muscovite and K-feldspar is not expected to influence the general results of this study significantly.

Allanite is compositionally more complex than apatite or zircon and is more challenging to model. Allanite saturation of melt involves the solubility of multiple trace elements in the melt (La–Sm) and considering Th, which can act as an essential structural constituent of allanite (Klimm et al., 2008). Even though modelled allanite stability was restricted to epidote-present P–T fields in our models, the modelled melt was always slightly supersaturated in the LREE with respect to allanite. This supersaturation is likely within model uncertainty, considering distribution coefficient and saturation expression limitations. The model predictions are generally consistent with the observation of allanite in low- to medium-temperature, high-pressure metabasites (Sorensen, 1991; Hermann, 2002; Loury et al.., 2016; Tamblyn et al.., 2019). Although allanite can be an important host of Th in some circumstances, it is a minor contributor to the total heat budget modelled for the various rock types (Figs 2.7–9) due to its low modal proportions and limited stability. Nonetheless, we treat modelled allanite stability with caution, given the relatively few studies of allanite solubility (e.g., Klimm et al., 2008) that we can integrate with the phase equilibrium modelling.

Maximum amounts of modelled apatite, zircon, and allanite across the P–T grid is 0.49, 0.025, and 0.042 wt%, respectively. The occurrence of apatite in all 6 modelled samples, and minor zircon in three of the samples (intermediate greenstone, enriched/intermediate high-grade metabasites; Fig. 2.3, Appendix S1.5), indicate sufficient P_2O_5 and Zr in the bulk composition to stabilize these minerals when accounting for trace elements partitioning into major minerals (scenario 2). When present, apatite and zircon occur along grain boundaries and as inclusions within other minerals (Fig 2.4f); no microstructural preference (restite or leucosome) for either is observed. Although bulk-rock compositions were modelled, apatite and zircon may be armoured as inclusions in stable or growing minerals during heating (Watson et al., 1989; Bea, 1996; Bea and Montero, 1999) and be unavailable to release heat-producing elements into the melt. Further, armoured grains decrease the amount of P_2O_5 and Zr available to saturate the melt. A discrepancy between the model predictions and natural systems could also result from disequilibrium. Clemens et al. (2020) highlight the undersaturation of magma in trace elements and discuss the low magma temperature generally predicted by the Zr-saturation thermometer in granitoids. Acosta-Vigil et al. (2012) quantified disequilibrium in sedimentary-derived melts and determined the melt to be undersaturated in Zr and LREE. Undersaturation would limit accessory mineral growth and result in trace element disequilibrium at the magma source—an observation supported by Bea (1996), Storkey et al. (2005), and Bea et al. (2006). In such disequilibrium scenarios, our models (Appendix S1.8) overestimate the dissolution of accessory minerals in the melt and underestimate the heat production during prograde metamorphism. When comparing our model results with natural systems, there are possibilities for underestimation of accessory mineral dissolution resulting from our closed-system model (i.e., no melt loss) and overestimation of accessory mineral dissolution resulting from armouring and disequilibrium.

We make several necessary simplifications to provide a baseline for understanding the stability of zircon, apatite, and allanite, the redistribution of heat-producing elements, and the time required for TTG-magma generation through the anatexis of mafic rocks. Further, we assume negligible alteration after the closed-system melting of metabasites and equilibrium. Our model results correlate well with observations from the Kapuskasing uplift (discussed later), which suggests that the simplifications are reasonable, and our results provide a baseline for studying HPE redistribution during crustal anatexis in the Kapuskasing uplift and Archean terranes in general.

2.5.2 Accessory Minerals and Their Control on HPE Distribution

Modelled accessory mineral stabilities and trace element concentrations are similar to our observations of natural metabasite samples. Apatite is predicted to be stable across a more extensive range of pressure and temperature conditions than either zircon or allanite. The median concentration of P_2O_5 (~0.1 wt%) is comparable across mafic lithologies and is slightly lower in natural TTG samples (Fig. 2.4), which is consistent with the predicted high-temperature persistence of apatite (<20% dissolution below 850°C; Appendix S1.8) across all modelled samples. Comparatively, zircon is predicted to dissolve entirely by 850°C, while allanite is restricted to high pressures and low temperatures (Appendix S1.8).

The presence of accessory minerals in the MLA results (Appendix S1.5) agrees well with the model results presented in Appendix S1.8. Zircon is observed in only 3 samples with a maximum proportion of 0.02 wt%, and allanite is only reported in one sample comprising 0.05 wt% of the sample. Comparatively, apatite is observed in all samples (0.04–1.25 wt%) with a median proportion of 0.39 wt%, similar but less than the maximum predicted apatite across the six samples (0.49 wt%). The dissolution of zircon and allanite can explain the higher concentrations of Zr and LREE in the TTGs and the corresponding depletion (relative to greenstones) in the lower-crustal metabasites.

Apatite is a key repository for U and Th (Figs 2.8, 2.9) and is predicted to be stable to relatively high temperatures (Appendix S1.8). The presence of apatite in the residue is expected to buffer the loss of U and Th to the melt and retain these elements in the residue; this is compounded by an increase in system density due to the extraction of relatively low-density melt. Twenty to forty percent of U and Th is predicted to be sequestered in apatite for the estimated temperatures of TTG formation in the Kapuskasing uplift (~850°C) with a greater proportion of U and Th stored in apatite for enriched compositions compared to intermediate and depleted compositions (likely due to high P_2O_5 in the latter). As none of the mineral-melt distribution coefficients for major minerals and P_2O_5, Zr, LREE, U, or Th is >1 (Bédard, 2006), the calculated bulk distribution coefficients are, on average, 2–3 times greater when apatite is considered than when apatite is omitted from the modelling. Thus, the melt is expected to accommodate more U and Th during anatexis of metabasites when apatite is unstable. Therefore,

it is important to consider the proportion of apatite in a system when discussing heat-producing element redistribution during metabasite anatexis.

2.5.3 Heat Production and Heating Times

The heat-producing element that produces the greatest proportion of radiogenic heat in each rock type influences the amount of heat produced and the heat production trend through time (Fig. 2.5). The concentration of potassium changes very little through time as only 0.01% of present-day potassium is radioactive, contrasting with the natural isotopes of U and Th which are all radioactive. Both isotopes of U have shorter half-lives than either ^{232}Th or ^{40}K—U also has a larger mass difference between parent and daughter isotopes, therefore producing more energy (Einstein, 1905). Together, these decay differences lead to inequalities in present heat production as 1 mg/kg of U produces almost 4 times more heat than 1 wt% K or 1mg/kg of Th (Bea, 2012) and with the relatively short decay of ^{235}U, this difference would have been greater in the past. As U produced the greatest proportion of heat before 400 Ma in greenstone samples from the Michipicoten Greenstone Belt (Fig. 2.5), the upper crust has experienced the greatest relative reduction in heat production through time although a larger absolute change is experienced by the greater heat-producing middle crust and, to a lesser extent, lower crust.

The greater calculated heat production (past and present) of the high-grade metabasites compared to the greenstones could be the result of several variables. If the high-grade metabasites were originally enriched in HPE compared to the greenstones, the higher heat production is a relict property of the igneous protoliths. However, the results in Figures 2.7–9 suggest other explanations assuming the protoliths of the greenstones and high-grade metabasites had roughly equivalent HPE concentrations. The high-grade metabasites have a greater density (~3.05 g/cm^3) compared to greenstones (~2.95 g/cm^3) resulting in greater calculated heat production in the high-grade samples (eq. 2.1, Fig. 2.5) even if they had similar concentrations of the HPE. Another reason to explain the heat-production difference between the greenstones and high-grade metabasites is the behaviour of the HPE-bearing minerals during anatexis discussed above causing the greater concentration of HPE in the high-grade metabasites compared to the greenstones. With apatite stable during anatexis at high temperatures, HPE can be retained in the residue upon melt loss, resulting in the enrichment of U and Th in the residual high-grade metabasites compared to their precursors at subsolidus conditions (i.e., greenstones). The higher

median concentration of K in the high-grade metabasites relative to the greenstones (Fig. 2.4) could result from a similar mechanism; plagioclase and hornblende retain a significant proportion of K in the restite at high temperature (>850°C). The high-temperature stability of these heat-producing element-sequestrating minerals (e.g., apatite, hornblende, plagioclase) can explain why the residual high-grade metabasites may have higher heat-production than greenstone samples from the same crustal cross-section.

The temperature dependence on heat production and heating times is primarily the result of melt and accessory mineral proportions (Fig. 2.10). At temperatures of TTG magma formation in the Wawa Gneiss Domain (800–850°C; Hartel and Pattison, 1996), heat-producing elements are sub-equally partitioned into liquid and solid phases (Figs 2.7–9), nonetheless which phases HPE are partitioned into is critical to the heat-production of the system. If high-density (and HPE-compatible) phases persist (e.g., epidote and apatite), the effects of HPE partitioning into a low-density melt are expected to be reduced, resulting in higher heat production in the system. For example, the enriched high-grade metabasite composition is predicted to have relatively constant heat production of ~0.38 $\mu W/m^3$ when the melt proportion is <10 wt% (Fig. 2.10d) and a large proportion of U and Th is expected to be sequestered by epidote (Figs 2.8, 2.9). The complete dissolution of epidote below peak metamorphic temperatures (e.g. during prograde metamorphism) of the Kapuskasing Structural Zone is expected to drastically decrease (~20%) the metamorphic heat production of the residue for this composition (Fig. 2.10d). In general, the majority of HPE in the residue resides in apatite, zircon, and hornblende (Figs 2.7–9); these minerals are denser than melt, however, all three minerals are predicted to decrease in modal proportion during prograde metamorphism. Apatite and zircon are predicted in minor modal proportions but sequester a large proportion of U and Th, therefore contributing significant amounts of heat production. However, as the proportion of HPE-compatible minerals decreases in the system, the (low-density) melt becomes the phase in which the greatest proportion of heat is produced as temperatures exceed 800°C (Fig. 2.10).

Several variables influence heating time during metamorphism, particularly the change in enthalpy of the system, the concentrations of K, U, and Th, as well as the density of the phases that host the HPE (Stüwe, 2007; Schorn et al., 2018). For example, the enriched greenstone has higher heat production and is expected to require ~8 My less to reach 850°C than the enriched

high-grade metabasite whereas the intermediate high-grade metabasite has a shorter heating time than the intermediate greenstone. The temperature difference between the solidus and 850°C is smaller for the depleted compared to the intermediate compositions and therefore, the depleted compositions require a shorter amount of time than the intermediate compositions to reach peak-metamorphic temperatures (850°C). Figure 2.10 highlights the importance of mantle heat for the generation of TTGs in geologically reasonable timescales. When only radiogenic heat is considered, metamorphic heating paths require more than double the time compared to heating paths that include mantle heat, thus indicating the mantle as an equal and possible main source of heat during metabasite melting in the Archean.

2.5.4 Implications for TTG generation and HPE distribution in the crust

Many Archean terranes show evidence of TTG generation/crystallization over tens to hundreds of millions of years but the reasons for this suspected protracted crystallization are unclear. However, in some cases, protracted crystallization ages are interpreted as multiple pulses of magmatism (Kröner et al., 1996; Upadhyay et al., 2014; Gardiner et al., 2019). An example of this protracted crystallization is the TTGs of the Wawa Gneiss Domain where U–Pb zircon geochronology indicates crystallization over ~100 Ma (Percival and West, 1994; Moser et al., 1996). If similar rocks to the high-grade metabasites of the Kapuskasing Structural Zone were the parental material to the TTG complexes of the Wawa Gneiss Domain (Kendrick et al., 2019, 2022), the heat-producing element and metamorphic heat production calculations presented here imply that syn-metamorphic melt loss would remove considerable HPE from the system which in turn would leave colder residual. However, Figures 2.4 and 2.5, show that the average HPE and heat production are higher in the high-grade metabasites compared to the greenstones. This can be explained through the melting of particularly enriched greenstones to produce TTGs, as the greenstones have higher third-quartile HPE concentrations compared to the high-grade metabasites (Fig. 2.4).

Considering the difficulty of sampling the lower crust, the distribution of HPE and overall heat production of the lower crust is often inferred based on indirect methods (mass balance, geophysical surveys) or the interrogation of inherently unique samples (e.g. xenoliths) which indicate that the lower crust is depleted in HPE (Rudnick and Fountain, 1995; Rudnick et al., 1998) and is often approximated as such in mathematical and geodynamic models (Bodri and

Čermák, 1993; Sizova et al., 2015). However, we observe higher heat production in the high-grade metabasites compared to the greenstones (Fig. 2.5) showing that the deep crust is not necessarily depleted in HPE (compared to their protoliths), agreeing with the interpretation of Alessio et al. (2018) who concluded that HPE is retained in the residue during the melting of metasedimentary rocks. Moreover, most geodynamic models assume constant heat production based on lithology without regard for HPE partitioning into a lower-density melt (Gerdes et al., 2000; Sizova et al., 2015). This contrasts with the model results presented in Figure 2.10 where heat production is lower in the suprasolidus system, indicating potentially erroneously high heat production in geodynamic models that include partially molten crust. Further, at least in Archean terranes, the TTG-dominated middle crust is likely to be the most radiogenic as opposed to the commonly assumed upper crust. This hot and higher heat-producing middle crust can be a source of heat for middle- and upper-crustal metamorphism as well as be a rheological weak layer in the crust and a focus for deformation.

Although complex geodynamic models such as Sizova et al. (2015) incorporate the thermal effects of hot magmatic emplacement in the middle to the upper crust, the release of the latent heat of fusion and resulting geotherm perturbations should be considered when discussing syn-magmatic metamorphism such as the amphibole-facies halo surrounding the Michipicoten Greenstone Belt. Altogether, when discussing lower crustal heat production and the modelling of geodynamic processes, varying compositional enrichment within a lithology (enriched, intermediate, and depleted concerning HPE) and their respective proportions within the crust should be considered as well as decreasing heat production during anatexis. Finally, depth is a poor proxy for HPE concentration in the crust.

2.6 Conclusions

The redistribution of heat-producing elements (HPE) during anatectic metamorphism of metabasites and the resulting thermal effects are examined through a thermodynamic and petrologic lens providing insights into the internal differentiation of cratons. We combined thermodynamic modelling of phase assemblages for six Archean metabasites from the Kapuskasing uplift with accessory mineral solubility expressions, trace element partitioning calculations, and heat production estimates to evaluate the re-distribution of heat-producing elements between residue and melt during anatexis. Apatite persists well above the solidus and

acts as the main repository (alongside hornblende) for the HPE; zircon and allanite sequester smaller amounts and are expected to be absent at high temperatures. Retention of the HPE in apatite during anatexis can produce residual high-grade metabasites with higher concentrations of HPE relative to their subsolidus equivalents. During anatexis, heat-producing elements sub-equally partition into the low-density melt phase and solids, which reduces heat production and increases heating times with increasing temperature for a melt-bearing crust. Sub-equal partitioning of HPE between melt and residue and comparisons between natural TTG/high-grade metabasites indicate that particularly enriched sources (with respect to HPE, P, Zr, and LREE) are required for TTG magma generation. HPE concentrations in metabasites are not a function of crustal depth but are primarily controlled by the protolith and restite mineral assemblage; these are the determinant factors for heat production. However, due to roughly equal HPE–mantle heat contributions, the differences in heat production expected from metabasites of different compositions do not greatly affect the overall heating times (Kröner et al., 1996; Gardiner et al., 2019). Metabasites that have not experienced previous partial melting (greenstones) are favourable for TTG formation.

2.7 References

Acosta-Vigil, A., Buick, I., Cesare, B., London, D., Morgan, G. (VI), The extent of Equilibration between melt and residuum during regional anatexis and its implications for differentiation of the continental crust: a study of partially melted metapelitic enclaves: Journal of Petrology, v. 53, p. 1319-1356, doi: 10.1093/petrology/egs018

Ahrens, L.H., 1965, Some observations on the uranium and thorium distributions in accessory zircon from granitic rocks: Geochimica et Cosmochimica Acta, v. 29, p. 711–716, doi:10.1016/0016-7037(65)90064-5.

Alessio, K.L., Hand, M., Kelsey, D.E., Williams, M.A., Morrissey, L.J., and Barovich, K., 2018, Conservation of deep crustal heat production: Geology, v. 46, p. 335–338, doi:10.1130/G39970.1.

Apted, M., and Liou, J., 1983, Phase relationships among greenschist, epidote-amphibolite, and amphibolite in a basaltic system: American Journal of Science, v. 283, p. 328–354.

Arevalo, R., McDonough, W.F., and Luong, M., 2009, The K/U ratio of the silicate Earth: Insights into mantle composition, structure and thermal evolution: Earth and Planetary Science Letters, v. 278, p. 361–369, doi:10.1016/j.epsl.2008.12.023.

Ashwal, L.D., Morgan, P., Kelley, S.A., and Percival, J.A., 1987, Heat production in an Archean crustal profile and implications for heat flow and mobilization of heat-producing elements: Earth and Planetary Science Letters, v. 85, p. 439–450, doi:10.1016/0012-821X(87)90139-7.

Bea, F., Fershtater, G., Corretge, L.G., The geochemistry of phosphorus in granite rocks and the effect of aluminium: Lithos, v. 29, p. 43-56,

Bea, F., 1996, Residence of REE, Y, Th and U in granites and crustal protoliths: Implications for the chemistry of crustal melts: Journal of Petrology, v. 37, p. 521–552, doi:10.1093/petrology/37.3.521.

Bea, F., 2012, The sources of energy for crustal melting and the geochemistry of heat-producing elements: Lithos, v. 153, p. 278–291, doi:10.1016/j.lithos.2012.01.017.

Bea, F., Montero, P., Ortega, M., 2006, A LA-ICP-MS evaluation of Zr reservoirs in common crustal rocks: Implications for Zr and Hf geochemistry, and zircon-forming processes: The Canadian Mineralogist, v. 44, p. 693-714, doi: 10.2113/gscanmin.44.3.693

Bea, F., and Montero, P., 1999, Behavior of accessory phases and redistribution of Zr, REE, Y, Th, and U during metamorphism and partial melting of metapelites in the lower crust: An example from the Kinzigite Formation of Ivrea-Verbano, NW Italy: Geochimica et Cosmochimica Acta, v. 63, p. 1133–1153, doi:10.1016/S0016-7037(98)00292-0.

Bédard, J.H., 2006, A catalytic delamination-driven model for coupled genesis of Archaean crust and sub-continental lithospheric mantle: Geochimica et Cosmochimica Acta, v. 70, p. 1188–1214, doi:10.1016/j.gca.2005.11.008.

Bingen, B., Demaiffe, D., and Hertogen, J., 1996, Redistribution of rare earth elements, thorium, and uranium over accessory minerals in the course of amphibolite to granulite facies metamorphism: The role of apatite and monazite in orthogneisses from southwestern

Norway: Geochimica et Cosmochimica Acta, v. 60, p. 1341–1354, doi:10.1016/0016-7037(96)00006-3.

Bodri, L., and Čermák, V., 1993, Heat production in the continental lithosphere, part II: variational approach: Tectonophysics, v. 225, p. 29–34, doi:10.1016/0040-1951(93)90245-F.

Boehnke, P., Watson, E.B., Trail, D., Harrison, T.M., and Schmitt, A.K., 2013, Zircon saturation re-revisited: Chemical Geology, v. 351, p. 324–334, doi:10.1016/j.chemgeo.2013.05.028.

Borisov, A., Aranovish, L., 2019, Zircon solubility in silicate melts: New experiments and probability of zircon crystallization in deeply evolved basic melts: Chemical Geology, v. 510, p. 103-112, doi: 10.1016/j.chemgeo.2019.02.019

Bowman, J.R., Moser, D.E., Valley, J.W., Wooden, J.L., Kita, N.T., and Mazdab, F.K., 2011, Zircon U-Pb isotope, $\delta^{18}O$ and trace element response to 80 m.y. of high temperature metamorphism in the lower crust: Sluggish diffusion and new records of Archean craton formation: v. 311, 719–772 p., doi:10.2475/09.2011.01.

Brown, M., 2013, Granite: From genesis to emplacement: Bulletin of the Geological Society of America, v. 125, p. 1079–1113, doi:10.1130/B30877.1.

Bushmin, S.A., and Glebovitsky, V.A., 2008, Scheme of mineral facies of metamorphic rocks: Geology of Ore Deposits, v. 50, p. 659–669, doi:10.1134/S1075701508080011.

Carvalho, B.B., Bartoli, O. and Cesare, B., 2023, C–O–H fluid-melt-rock interaction in graphitic granulites and problems of quantifying carbon budget in the lower continental crust. Chemical Geology, v. 631, 121503. https://doi.org/10.1016/j.chemgeo.2023.121503

Ciufo, T.J., Jellicoe, K., Yakymchuk, C., Lin, S., Mercier-Langevin, P., and Wodicka, N., 2020, Gold through space and time in the Archean: Geology, structural evolution and hydrothermal alteration of the Island Gold deposit, Michipicoten greenstone belt, Ontario, in Targeted Geoscience Initiative 5: contributions to the understanding of Canadian gold systems, v. 8712, p. 328, doi:10.5382/econgeo.116.1.br01.

Clemens, J., Stevens, G., Bryan, S., 2020, Conditions during the formation of granitic magmas by crustal melting – Hot or cold; drenched, damp or dry?, Earth-Science Reviews, doi: 10.1016/j.earscirev.2019.102982

Cooper, A.F., and Lovering, J.F., 1970, Greenschist amphiboles from Haast river, New Zealand: Contributions to Mineralogy and Petrology, v. 27, p. 11–24, doi:10.1007/BF00539538.

Corfu, F., 1987, Inverse age stratification in the archaean crust of the superior province: Evidence for infra- and subcrustal accretion from high resolution U-Pb zircon and monazite ages: Precambrian Research, v. 36, p. 259–275, doi:10.1016/0301-9268(87)90024-6.

Dupuy, C., and Dostal, J., 1983, Uranium and thorium in paleozoic basalts of Nova Scotia (Canada): Bulletin Volcanologique, v. 46, p. 125–133, doi:10.1007/BF02597581.

Einstein, A., 1905, Ist die trägheit eines körpers von seinem energieinhalt abhängig? Annalen der Physik, v. 18, p. 639–641.

Ekberg, C., Albinsson, Y., Comarmond, M.J., and Brown, P.L., 2000, Studies on the complexation behavior of thorium(IV). 1. Hydrolysis equilibria: Journal of Solution Chemistry, v. 29, p. 63–86, doi:10.1023/A:1005166517699.

Ellis, D.J., and Thompson, A.B., 1986, Subsolidus and partial melting reactions in the quartz-excess $CaO+MgO+Al_2O_3+SiO_2+H_2O$ system under water-excess and water-deficient conditions to 10 kb: Some implications for the origin of peraluminous melts from mafic rocks: Journal of Petrology, v. 27, p. 91–121, doi:10.1093/petrology/27.1.91.

Frank, M.R., Candela, P.A., and Piccoli, P.M., 1998, K-feldspar-muscovite-andalusite-quartz-brine phase equilibria: An experimental study at 25 to 60 MPa and 400 to 550°C: Geochimica et Cosmochimica Acta, v. 62, p. 3717–3727, doi:10.1016/S0016-7037(98)00261-0.

Frank, M.R., and Vaccaro, D.M., 2012, An experimental study of high temperature potassic alteration: Geochimica et Cosmochimica Acta, v. 83, p. 195–204, doi:10.1016/j.gca.2011.12.007.

Gardiner, N.J., Kirkland, C.L., Hollis, J., Szilas, K., Steenfelt, A., Yakymchuk, C., and Heide-Jørgensen, H., 2019, Building Mesoarchaean crust upon Eoarchaean roots: the Akia Terrane, West Greenland: Contributions to Mineralogy and Petrology, v. 174, p. 1–19, doi:10.1007/s00410-019-1554-x.

Gerdes, A., Worner, G., Henk, A., 2000, Post-collisional granite generation and HT-LP metamorphism by radiogenic heating: the Variscan South Bohemian Batholith: Journal of the Geological Society. V. 157, p. 577–587, doi:10.1144/jgs.157.3.577

Green, E.C.R., White, R.W., Diener, J.F.A., Powell, R., Holland, T.J.B., and Palin, R.M., 2016, Activity–composition relations for the calculation of partial melting equilibria in metabasic rocks: Journal of Metamorphic Geology, v. 34, p. 845–869, doi:10.1111/jmg.12211.

Gregory, C.J., Rubatto, D., Hermann, J., Berger, A., and Engi, M., 2012, Allanite behaviour during incipient melting in the southern Central Alps: Geochimica et Cosmochimica Acta, v. 84, p. 433–458, doi:10.1016/j.gca.2012.01.020.

Hacker, B.R., Kelemen, P.B., and Behn, M.D., 2011, Differentiation of the continental crust by relamination: Earth and Planetary Science Letters, v. 307, p. 501–516, doi:10.1016/j.epsl.2011.05.024.

Harrison, M., Watson, B., 1984, The behavior of apatite during crustal anatexis: Equilibrium and kinetic considerations: Geochemica et Cosmichimica Acta, v. 48, p/ 1467-1477

Hartel, T.H.D., and Pattison, D.R.M., 1996, Genesis of the Kapuskasing (Ontario) migmatitic mafic granulites by dehydration melting of amphibolite: The importance of quartz to reaction progress: Journal of Metamorphic Geology, v. 14, p. 591–611, doi:10.1046/j.1525-1314.1996.00404.x.

Hermann, J., 2002, Allanite: Thorium and light rare earth element carrier in subducted crust: Chemical Geology, v. 192, p. 289–306, doi:10.1016/S0009-2541(02)00222-X.

Holland, T., and Powell, R., 2003, Activity-compositions relations for phases in petrological calculations: An asymetric multicomponent formulation: Contributions to Mineralogy and Petrology, v. 145, p. 492–501, doi:10.1007/s00410-003-0464-z.

Holland, T.J.B., and Powell, R., 1990, An enlarged and updated internally consistent thermodynamic dataset with uncertainties and correlations: the system K_2O–Na_2O–CaO–MgO–MnO–FeO–Fe_2O_3–Al_2O_3–TiO_2–SiO_2–C–H_2–O_2: Journal of Metamorphic Geology, v. 8, p. 89–124, doi:10.1111/j.1525-1314.1990.tb00458.x.

Holland, T.J.B., and Powell, R., 2011, An improved and extended internally consistent thermodynamic dataset for phases of petrological interest, involving a new equation of state for solids: Journal of Metamorphic Geology, p. 333–383, doi:10.1111/j.1525-1314.2010.00923.x.

Holland, T.J.B., and Powell, R., 1985, An internally consistent thermodynamic dataset with uncertainties and correlations: 2. Data and results: Journal of Metamorphic Geology, v. 3, p. 343–370, doi:10.1111/j.1525-1314.1985.tb00325.x.

Huang, H., Fryer, B., and Polat, A., 2013, Origin of Archean tonalite–trondhjemite–granodiorite (TTG) suites and granites in the Fiskenæsset region, southern West Greenland: Implications for continental growth: Gondwana Research, v. 12, p. 85–93, doi:10.1016/j.gr.2011.12.001.

Hughes, L., Burgess, R., Chavrit, D., Pawley, A., Tartèse, R., Droop, G., Ballentine, C.J., and Lyon, I., 2018, Halogen behaviour in subduction zones: Eclogite facies rocks from the Western and Central Alps: Geochimica et Cosmochimica Acta, v. 243, p. 1–23, doi:10.1016/j.gca.2018.09.024.

Hurley, P.M., and Fairbairn, H.W., 1957, Abundance and distribution of uranium and thorium in zircon, sphene, apatite, epidote, and monazite in granitic rocks: Eos, Transactions American Geophysical Union, v. 38, p. 939–944, doi:10.1029/TR038i006p00939.

Iyer, S.S., Choudhuri, A., Vasconcellos, M.B.A., and Cordani, U.G., 1984, Radioactive element distribution in the Archean granulite terrane of Jequié-Bahia, Brazil: Contributions to Mineralogy and Petrology, v. 85, p. 95–101, doi:10.1007/BF00380226.

Jamieson, R.A., and Beaumont, C., 2013, On the origin of orogens: Bulletin of the Geological Society of America, v. 125, p. 1671–1702, doi:10.1130/B30855.1.

Johnson, T.E., Brown, M., Gardiner, N.J., Kirkland, C.L., and Smithies, R.H., 2017, Earth's first stable continents did not form by subduction: Nature Publishing Group, v. 543, p. 239–242, doi:10.1038/nature21383.

Johnson, T., Yakymchuk, C., and Brown, M., 2021, Crustal melting and suprasolidus phase equilibria: From first principles to the state-of-the-art: Earth-Science Reviews, v. 221, p. 103778, doi:10.1016/j.earscirev.2021.103778.

Kelsey, D.E., Clark, C., and Hand, M., 2008, Thermobarometric modelling of zircon and monazite growth in melt-bearing systems: Examples using model metapelitic and metapsammitic granulites: Journal of Metamorphic Geology, v. 26, p. 199–212, doi:10.1111/j.1525-1314.2007.00757.x.

Kendrick, J., Duguet, M., and Yakymchuk, C., 2022, Diversification of Archean tonalite-trondhjemite-granodiorite suites in a mushy middle crust: Geology, v. 50, p. 76–80, doi:10.1130/g49287.1.

Kendrick, J., Yakymchuk, C., and Duguet, M., 2019, Tectonometamorphic history of the Wawa–Abitibi Terrane: Crustal differentiation and low-grade metamorphism in the Kapuskasing Uplift, in Summary of Field Work and Other Activities 2019, Sudbury, ON, Ontario Geologic Survey, p. 107–113.

Kendrick, J., Yakymchuk, C., 2020, Garnet fractionation, progressive melt loss and bulk composition variations in anatectic metabasites: Complications for interpreting the geodynamic significance of TTGs, Geoscience Frontiers, v. 11, p. 745-763, doi: 10.1016/j.gsf.2019.12.001

Khitarov, N.I., Kadik, A.A., 1973, Water and carbon dioxide in magmatic melts and peculiarities of the melting process, Contributions to Mineralogy and Petrology, v. 41, p. 205-215, doi: 10.1007/BF00371031

Klein, M., Stosch, H.G., and Seek, H.A., 1997, Partitioning of high field-strength and rare-earth elements between amphibole and quartz-dioritic to tonalitic melts: An experimental study: Chemical Geology, v. 138, p. 257–271, doi:10.1016/S0009-2541(97)00019-3.

Klimm, K., Blundy, J.D., and Green, T.H., 2008, Trace element partitioning and accessory phase saturation during H_2O-saturated melting of basalt with implications for subduction zone chemical fluxes: Journal of Petrology, v. 49, p. 523–553, doi:10.1093/petrology/egn001.

Krogh, T.E., 1993, High precision U-Pb ages for granulite metamorphism and deformation in the Archean Kapuskasing structural zone, Ontario: implications for structure and development of the lower crust: Earth and Planetary Science Letters, v. 119, p. 1–18, doi:10.1016/0012-821X(93)90002-Q.

Krogh, T.E., and Moser, D.E., 1994, U-Pb zircon and monazite ages from the Kapuskasing uplift: Age constraints on deformation within the Ivanhoe Lake fault zone: Canadian Journal of Earth Sciences, v. 31, p. 1096–1103, doi:10.1139/e94-098.

Kröner, A., Hegner, E., Wendt, J.I., and Byerly, G.R., 1996, The oldest part of the Barberton granitoid-greenstone terrain, South Africa: Evidence for crust formation between 3.5 and 3.7 Ga: Precambrian Research, v. 78, p. 105–124, doi:10.1016/0301-9268(95)00072-0.

Li, H., Schwarcz, H.P., and Shaw, D.M., 1991, Deep crustal oxygen isotope variations: The Wawa-Kapuskasing crustal transect, Ontario: Contributions to Mineralogy and Petrology, v. 107, p. 448–458, doi:10.1007/BF00310679.

Lin, S., and Beakhouse, G.P., 2013, Synchronous vertical and horizontal tectonism at late stages of Archean cratonization and genesis of Hemlo gold deposit, Superior craton, Ontario, Canada: Geology, v. 41, p. 359–362, doi:10.1130/G33887.1.

London, D., 1992, Phosphorus in S-type magmas: the P_2O_5 content of feldspars from peraluminous granites, pegmatites, and rhyolites: American Mineralogist, v. 77, p. 126–145.

Loury, C., Rolland, Y., Cenki-Tok, B., Lanari, P., and Guillot, S., 2016, Late Paleozoic evolution of the South Tien Shan: Insights from P-T estimates and allanite geochronology on retrogressed eclogites (Chatkal range, Kyrgyzstan): Journal of Geodynamics, v. 96, p. 62–80, doi:10.1016/j.jog.2015.06.005.

Manya, S., 2016, Petrogenesis and emplacement of the TTG and K-rich granites at the Buzwagi gold mine, northern Tanzania: Implications for the timing of gold mineralization: Lithos, v. 256–257, p. 26–40, doi:10.1016/j.lithos.2016.03.025.

Mareschal, J.C., and Jaupart, C., 2006, Archean thermal regime and stabilization of the cratons: Archean Geodynamics and Environments, p. 61–73, doi:10.1029/164GM06.

Martin, H., Moyen, J.F., Guitreau, M., Blichert-Toft, J., and le Pennec, J.L., 2014, Why Archaean TTG cannot be generated by MORB melting in subduction zones: Lithos, v. 198–199, p. 1–13, doi:10.1016/j.lithos.2014.02.017.

Montsion, R.M., Thurston, P., and Ayer, J., 2018, 1:2 000 000 Scale Geological Compilation of the Superior Craton:

Moser, D.E., 1994, The geology and structure of the mid-crustal Wawa gneiss domain: A key to understanding tectonic variation with depth and time in the late Archean Abitibi-Wawa Orogen: Canadian Journal of Earth Sciences, v. 31, p. 1064–1080, doi:10.1139/e94-096.

Moser, D.E., Heaman, L.M., Krogh, T.E., and Hanes, J.A., 1996, Intracrustal extension of an Archean orogen revealed using single-grain U-Pb zircon geochronology: Tectonics, v. 15, p. 1093–1109, doi:10.1029/96TC00130.

Moyen, J., and Martin, H., 2012, Forty years of TTG research: Lithos, v. 148, p. 312–336, doi:10.1016/j.lithos.2012.06.010.

Nisbet, H., Migdisov, A.A., Williams-Jones, A.E., Xu, H., van Hinsberg, V.J., and Roback, R., 2019, Challenging the thorium-immobility paradigm: Scientific Reports, v. 9, p. 8–13, doi:10.1038/s41598-019-53571-x.

Nisbet, H., Migdisov, A., Xu, H., Guo, X., van Hinsberg, V., Williams-Jones, A.E., Boukhalfa, H., and Roback, R., 2018, An experimental study of the solubility and speciation of thorium in chloride-bearing aqueous solutions at temperatures up to 250°C: Geochimica et Cosmochimica Acta, v. 239, p. 363–373, doi:10.1016/j.gca.2018.08.001.

Nitescu, B., and Halls, H.C., 2002, A gravity profile across southern Saganash Lake fault: Implications for the origin of the Kapuskasing Structural Zone: Canadian Journal of Earth Sciences, v. 39, p. 469–480, doi:10.1139/e01-100.

Ontario Geologic Survey, 2011, MRD 126 - 1:250 000 Scale Bedrock Geology of Ontario.:

Palin, R.M., Weller, O.M., Waters, D.J., and Dyck, B., 2016a, Quantifying geological uncertainty in metamorphic phase equilibria modelling; A Monte Carlo assessment and implications for tectonic interpretations: Geoscience Frontiers, v. 7, p. 591–607, doi:10.1016/j.gsf.2015.08.005.

Palin, R.M., White, R.W., and Green, E.C.R., 2016b, Partial melting of metabasic rocks and the generation of tonalitic–trondhjemitic–granodioritic (TTG) crust in the Archaean: Constraints from phase equilibrium modelling: Precambrian Research, v. 287, p. 73–90, doi:10.1016/j.precamres.2016.11.001.

Palin, R.M., White, R.W., Green, E.C.R., Diener, J.F.A., Powell, R., and Holland, T.J.B., 2016c, High-grade metamorphism and partial melting of basic and intermediate rocks: Journal of Metamorphic Geology, v. 34, p. 871–892, doi:10.1111/jmg.12212.

Pasquale, V., Verdoya, M., Choizzi, P., 2015, Measurements of rock thermal conductivity with a transient divided bar: Geothermics, v. 53, p. 183-189, doi: 10.1016/j.geothermics.2014.05.008

Percival, J.A., 1990, A field guide to the Kapuskasing Uplift, A cross section through the Archean Superior Province: Exposed Cross-Sections of the Continental Crust, p. 227–283.

Percival, J.A., 1983, High-grade metamorphism in the Chapleau-Foleyet Area, Ontario: American Mineralogist, v. 68, p. 667–686.

Percival, J.A., and Card, K.D., 1983, Archean crust as revealed in the Kapuskasing uplift, Superior province, Canada: Geology, v. 11, p. 323, doi:10.1130/0091-7613.

Percival, J.A., and Krogh, T.E., 1983, U-Pb zircon geochronology of the Kapuskasing structural zone and vicinity in the Chapleau-Foleyet area, Ontario.: Canadian Journal of Earth Sciences, v. 20, p. 830–843, doi:10.1139/e83-073.

Percival, J.A., and Mcgrath, P.H., 1986, Deep crustal structure and tectonic history of the northern Kapuskasing Uplift of Ontario: An integrated petrological-geophysical study: Tectonics, v. 5, p. 553–572.

Percival, J.A., and West, G.F., 1994, The Kapuskasing uplift: a geological and geophysical synthesis: Canadian Journal of Earth Sciences, v. 31, p. 1256–1286, doi:10.1139/e94-110.

Perry, H.K.C., Mareschal, J.-C., and Jaupart, C., 2006, Variations of strength and localized deformation in cratons: The 1.9 Ga Kapuskasing uplift, Superior Province, Canada: Earth and Planetary Science Letters, v. 249, p. 216–228, doi:10.1016/j.epsl.2006.07.013.

Petersson, A., Kemp, A.I.S., Gray, C.M., and Whitehouse, M.J., 2020, Formation of early Archean granite-greenstone terranes from a globally chondritic mantle: Insights from igneous rocks of the Pilbara Craton, Western Australia: Chemical Geology, v. 551, p. 119757, doi:10.1016/j.chemgeo.2020.119757.

Philpotts, J.A., and Schnetzler, C.C., 1970, Phenocryst-matrix partition coefficients for K, Rb, Sr and Ba, with applications to anorthosite and basalt genesis: Geochimica et Cosmochimica Acta, v. 34, p. 307–322, doi:10.1016/0016-7037(70)90108-0.

Powell, R., and Holland, T.J.B., 1988, An internally consistent dataset with uncertainties and correlations: 3. Applications to geobarometry, worked examples and a computer program: Journal of Metamorphic Geology, v. 6, p. 173–204.

Powell, R., and Holland, T.J.B., 1985, An internally consistent thermodynamic dataset with uncertainties and correlations: 1. Methods and a worked example: Journal of Metamorphic Geology, v. 3, p. 327–342, doi:10.1111/j.1525-1314.1985.tb00324.x.

Rudnick, R.L., and Fountain, D., 1995, Nature and composition of the continental crust: A lower crustal perspective: Physics of the Earth and Planetary Interiors, v. 145, p. 267–309.

Rudnick, R.L., and Gao, S., 2003, Composition of the continental crust: Elsevier Ltd., v. 4, 1–51 p., doi:10.1016/B978-0-08-095975-7.00301-6.

Rudnick, R.L., McDonough, W.F., and O'Connell, R.J., 1998, Thermal structure, thickness and composition of continental lithosphere: Chemical Geology, v. 145, p. 395–411, doi:10.1016/S0009-2541(97)00151-4.

Rutherford, E., and Soddy, F., 1903, Radioactive Change: The London, Edinburgh, and Dublin Philosophical Magazine and Journal of Science, v. 5, p. 576–591, doi:10.1080/14786440309462960.

Sage, R.P., 1994, Geology of the Michipicoten Greenstone Belt: Ontario Geologic Survey, p. 671.

Sage, R.P., Lightfoot, P.C., and Doherty, W., 1996, Bimodal cyclical Archean basalts and rhyolites from the Michipicoten (Wawa) greenstone belt, Ontario: Geochemical evidence for magma contributions from the asthenospheric mantle and ancient continental lithosphere near the southern margin of the Superior: Precambrian Research, v. 76, p. 119–153, doi:10.1016/0301-9268(95)00020-8.

Sawyer, E.W., Cesare, B., and Brown, M., 2011, When the continental crust melts: Elements, v. 7, p. 229–234, doi:10.2113/gselements.7.4.229.

Schorn, S., Diener, J.F.A., Powell, R., and Stüwe, K., 2018, Thermal buffering in the orogenic crust: The Geological Society of America, v. 46, p. 643–646.

Schwindinger, M., Weinberg, R.F., and White, R.W., 2020, The fate of accessory minerals and key trace elements during anatexis and magma extraction: Journal of Petrology, v. 61, doi:10.1093/petrology/egaa031.

Shao, T., Xia, Y., Ding, X., Cai, Y., and Song, M., 2019, Zircon saturation in terrestrial basaltic melts and its geological implications: Solid Earth Sciences, v. 4, p. 27–42, doi:10.1016/j.sesci.2018.08.001.

Sizova, E., Gerya, T., Stüwe, K., and Brown, M., 2015, Generation of felsic crust in the Archean: A geodynamic modeling perspective: Precambrian Research, v. 271, p. 198–224, doi:10.1016/j.precamres.2015.10.005.

Sorensen, S.S., 1991, Petrogenetic significance of zoned allanite in garnet amphibolites from a paleo-subduction zone: Catalina Schist, southern California: American Mineralogist, v. 76, p. 589–601.

Stix, J., and Gorton, M.P., 1990, Variations in trace element partition coefficients in sanidine in the Cerro Toledo Rhyolite, Jemez Mountains, New Mexico: Effects of composition, temperature, and volatiles: Geochimica et Cosmochimica Acta, v. 54, p. 2697–2708, doi:10.1016/0016-7037(90)90005-6.

Storkey, A. C., Hermann, J., Hand, M., Buick, I. S., 2005, Using in situ trace-element determinations to monitor partial-melting processes in metabasites, Journal of Petrology, v. 46, p. 1283-1308, doi: 10.1093/petrology/egi017

Stuck, T.J., and Diener, J.F.A., 2018, Mineral equilibria constraints on open-system melting in metamafic compositions: Journal of Metamorphic Geology, v. 36, p. 255–281, doi:10.1111/jmg.12292.

Stüwe, K., 2007, Energetics: Heat and Temperature, in Geodynamics of the Lithosphere, Springer-Verlag, p. 51–137.

Sun, G., Lio, S., Cawood, P., Tang, M., van Hunen, J., Gao, L., Hu, Y., and Hu, F., 2021, Thermal state and evolving geodynamic regimes of the Meso- to Neoarchean North China Craton: Nature Communications, v. 12, doi: 10.1038/s41467-021-24139-z

Tamblyn, R., Zack, T., Schmitt, A.K., Hand, M., Kelsey, D., Morrissey, L., Pabst, S., and Savov, I.P., 2019, Blueschist from the Mariana forearc records long-lived residence of material in the subduction channel: Earth and Planetary Science Letters, v. 519, p. 171–181, doi:10.1016/j.epsl.2019.05.013.

Taylor, S.R., and Mclennan, S.M., 1981, The composition and evolution of the continental crust: rare earth element evidence from sedimentary rocks: Philosophical Transactions of the Royal Society of London. Series A, Mathematical and Physical Sciences, v. 301, p. 381–399, doi:10.1098/rsta.1981.0119.

Taylor, S.R., and Mclennan, S.M., 1995, The geochemical the continental evolution crust: Reviews in Mineralogy and Geochemistry, v. 33, p. 241–265.

Timofeev, A., Migdisov, A.A., Williams-Jones, A.E., Roback, R., Nelson, A.T., and Xu, H., 2018, Uranium transport in acidic brines under reducing conditions: Nature Communications, v. 9, p. 2–8, doi:10.1038/s41467-018-03564-7.

Turek, A., Heather, K.B., Sage, R.P., and Van Schmus, W.R., 1996, U-Pb zircon ages for the Missanabie-Renabie area and their relation to the rest of the Michipicoten greenstone belt, Superior Province, Ontario, Canada: Precambrian Research, v. 76, p. 191–211, doi:10.1016/0301-9268(95)00063-1.

Upadhyay, D., Chattopadhyay, S., Kooijman, E., Mezger, K., and Berndt, J., 2014, Magmatic and metamorphic history of Paleoarchean tonalite-trondhjemite-granodiorite (TTG) suite from the Singhbhum craton, eastern India: Precambrian Research, v. 252, p. 180, doi:10.1016/j.precamres.2014.07.011.

Wang, X., Griffin, W.L., Chen, J., Huang, P., and Li, X., 2011, U and Th contents and Th/U ratios of zircon in felsic and mafic magmatic rocks: Improved zircon-melt distribution coefficients: Acta Geologica Sinica, v. 84, p. 164–174.

Watson, E.B., and Harrison, T.M., 1983, Zircon saturation revisited: temperature and composition effects in a variety of crustal magma types: Earth and Planetary Science Letters, v. 64, p. 295–304, doi:10.1016/0012-821X(83)90211-X.

Watson, E.B., Vicenzi, E.P., and Rapp, R.P., 1989, Inclusion/host relations involving accessory minerals in high-grade metamorphic and anatectic rocks: Contributions to Mineralogy and Petrology, v. 101, p. 220–231, doi:10.1007/BF00375308.

Webster, J.D., and Piccoli, P.M., 2015, Magmatic apatite: A powerful, yet deceptive, mineral: Elements, v. 11, p. 177–182, doi:10.2113/gselements.11.3.177.

White, R.W., Powell, R., Holland, T.J.B., Johnson, T.E., and Green, E.C.R., 2014, New mineral activity-composition relations for thermodynamic calculations in metapelitic systems: Journal of Metamorphic Geology, v. 32, p. 261–286, doi:10.1111/jmg.12071.

White, Powell, Holland, and Worley, 2000, The effect of TiO_2 and Fe_2O_3 on metapelitic assemblages at greenschist and amphibolite facies conditions: Mineral equilibria calculations in the system K_2O-FeO-MgO-Al_2O_3-SiO_2-H_2O-TiO_2-Fe_2O_3: Journal of Metamorphic Geology, v. 18, p. 497–511, doi:10.1046/j.1525-1314.2000.00269.x.

Wilke, M., and Behrens, H., 1999, The dependence of the partitioning of iron and europium between plagioclase and hydrous tonalitic melt on oxygen fugacity: Contributions to Mineralogy and Petrology, v. 137, p. 102–114, doi:10.1007/s004100050585.

Williams, M.A., Kelsey, D.E., Baggs, T., Hand, M., and Alessio, K.L., 2018, Thorium distribution in the crust: Outcrop and grain-scale perspectives: Lithos, v. 320–321, p. 222–235, doi:10.1016/j.lithos.2018.09.016.

Williams, M.A., Kelsey, D.E., and Rubatto, D., 2022, Thorium zoning in monazite: a case study from the Ivrea–Verbano Zone, NW Italy: Journal of Metamorphic Geology, p. 0–2, doi:10.1111/jmg.12656.

Yakymchuk, C., Behaviour of apatite during partial melting of metapelites and consequences for prograde suprasolidus monazite growth: Lithos, v. 274-275, p. 412-426, doi: 10.1016/j.lithos.2017.01.009

Yakymchuk, C., and Brown, M., 2014, Consequences of open-system melting in tectonics: Journal of the Geological Society, v. 171, p. 21–40, doi:10.1144/jgs2013-039.

Yakymchuk, C., and Brown, M., 2019, Divergent behaviour of Th and U during anatexis: Implications for the thermal evolution of orogenic crust: Journal of Metamorphic Geology, v. 37, p. 899–916, doi:10.1111/jmg.12469.

Yakymchuk, C., Kirkland, C.L., and Clark, C., 2018, Th/U ratios in metamorphic zircon: Journal of Metamorphic Geology, v. 36, p. 715–737, doi:10.1111/jmg.12307.

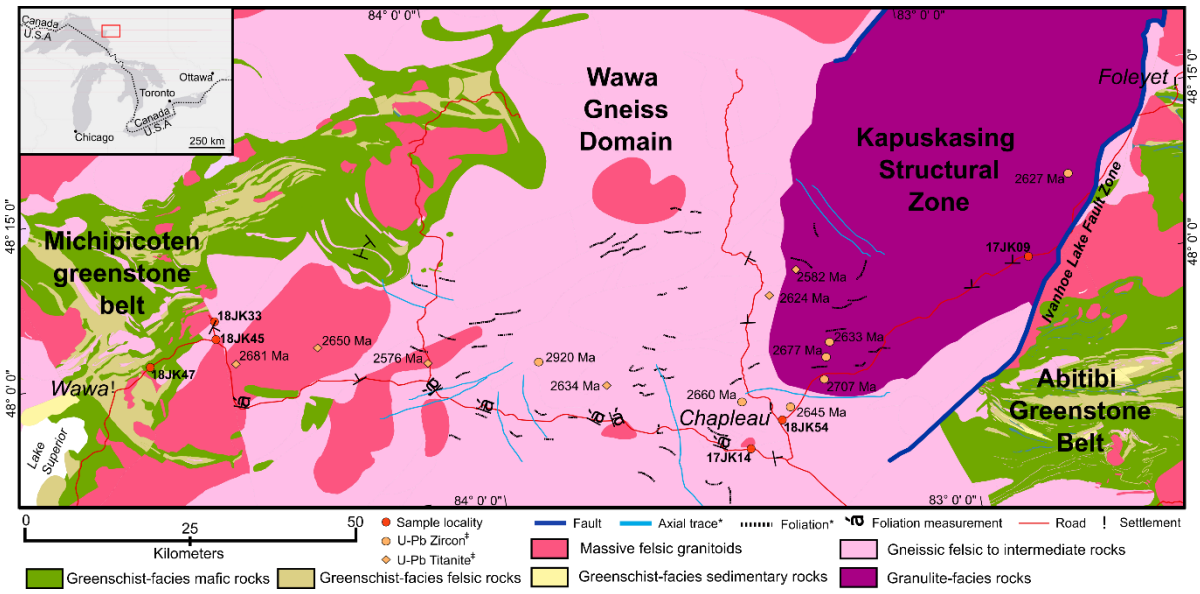


Figure 2.1: Simplified map of the Kapuskasing uplift comprised of three domains: Michipicoten Greenstone Belt (MGB) representing the upper crust, Wawa Gneiss Domain (WGD) representing the middle crust, and Kapuskasing Structural Zone (KSZ) representing the lower crust. The geological map is modified from the Ontario Geological Survey (2011). *Structural measurements and interpretations from Moser (1994), geochronology data from Percival and West (1994).

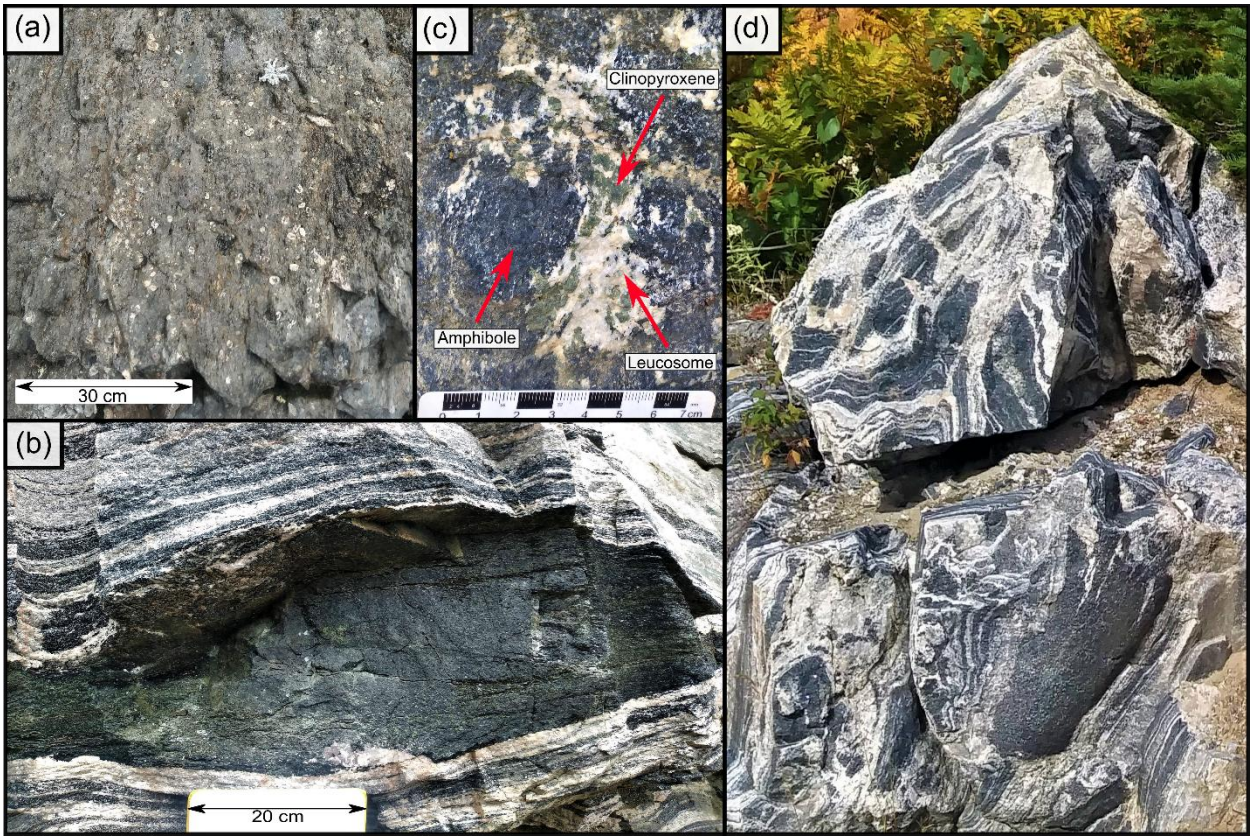


Figure 2.2: Representative photos of rock types in the Kapuskasing uplift. (a) Outcrop of greenstone rocks found in the Michipicoten greenstone belt with a well-developed foliation. (b) Grey gneiss outcrop enclosing a metabasite raft from the Wawa Gneiss Domain. (c) Leucosome with clinopyroxene and amphibole in high-grade metabasite of the Kapuskasing Structural Zone. (d) High-grade metabasite outcrop with abundant grey granitoid leucosome in the Kapuskasing Structural Zone.

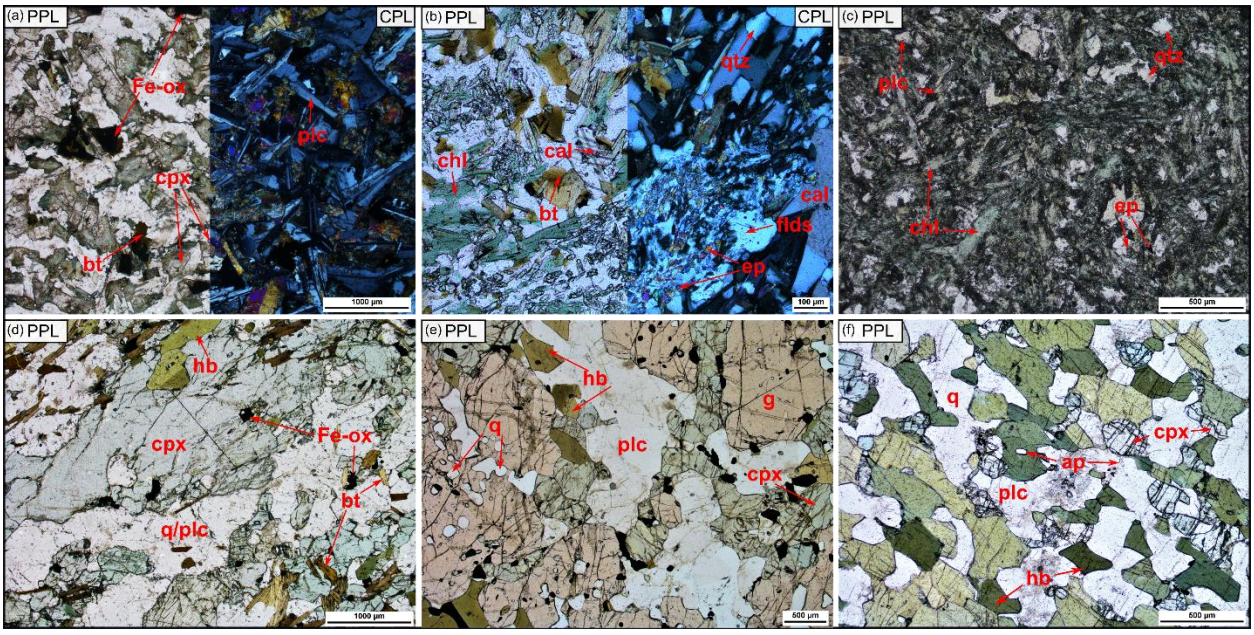


Figure 2.3: Mineral assemblages and microstructures of the investigated metabasite samples from the Michipicoten greenstone belt (a–c) and the Kapuskasing Structural Zone (d–f). (a) 18JK45 (enriched greenstone) with feldspar lathes, clinopyroxene is partially replaced by chlorite and amphibole; biotite is observed surrounding Fe-oxides. (b) 18JK33 (intermediate greenstone) with complete chlorite replacement and minor calcite. Plagioclase is partially replaced by epidote, and chlorite is intergrown with biotite. (c)18JK47 (depleted greenstone) with matrix chlorite, epidote, and feldspar lathes. (d) 18JK54 (enriched high-grade metabasite) with matrix biotite and compositional banding defined by domains rich in clinopyroxene, biotite and hornblende and domains rich in quartz and plagioclase (e) 17JK09 (intermediate high-grade metabasite) garnet with inclusions of quartz and hornblende. Matrix clinopyroxene, plagioclase, and amphibole are granoblastic. (f) 18JK14 (depleted high-grade metabasite) with apatite inclusions in hornblende and quartz with granoblastic texture. plc – plagioclase, cpx – clinopyroxene, bt – biotite, hb – hornblende, g – garnet, q – quartz, chl – chlorite, ep – epidote, ap– apatite, Fe-ox – iron oxide.

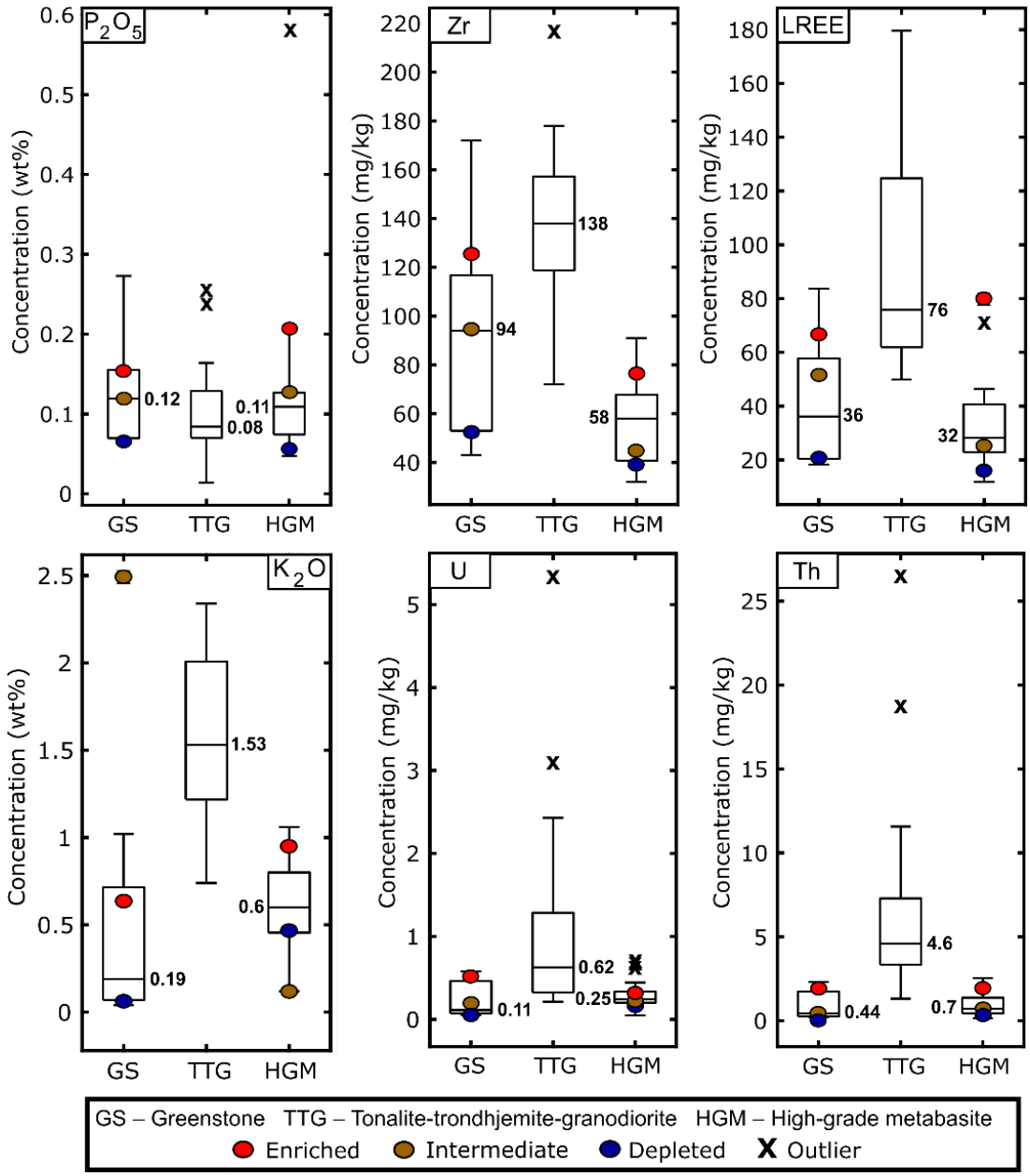


Figure 2.4: Concentrations of select trace elements for rock types from the Kapuskasing uplift. TTGs are enriched in Zr, LREE, K2O, U, and Th compared to greenstones and high-grade metabasites. High-grade metabasite samples have lower variability than either greenstone or TTG samples. GS: Greenstone; TTG: Tonalite-trondhjemite-granodiorite; HGM: high-grade metabasite. The boxes extend to the interquartile range, and the whiskers extend to the furthest data point up to 1.5 times the interquartile range. Crosses represent outliers and are outside of this range. Coloured circles represent the modelled compositions, and numbers beside boxes are the median values.

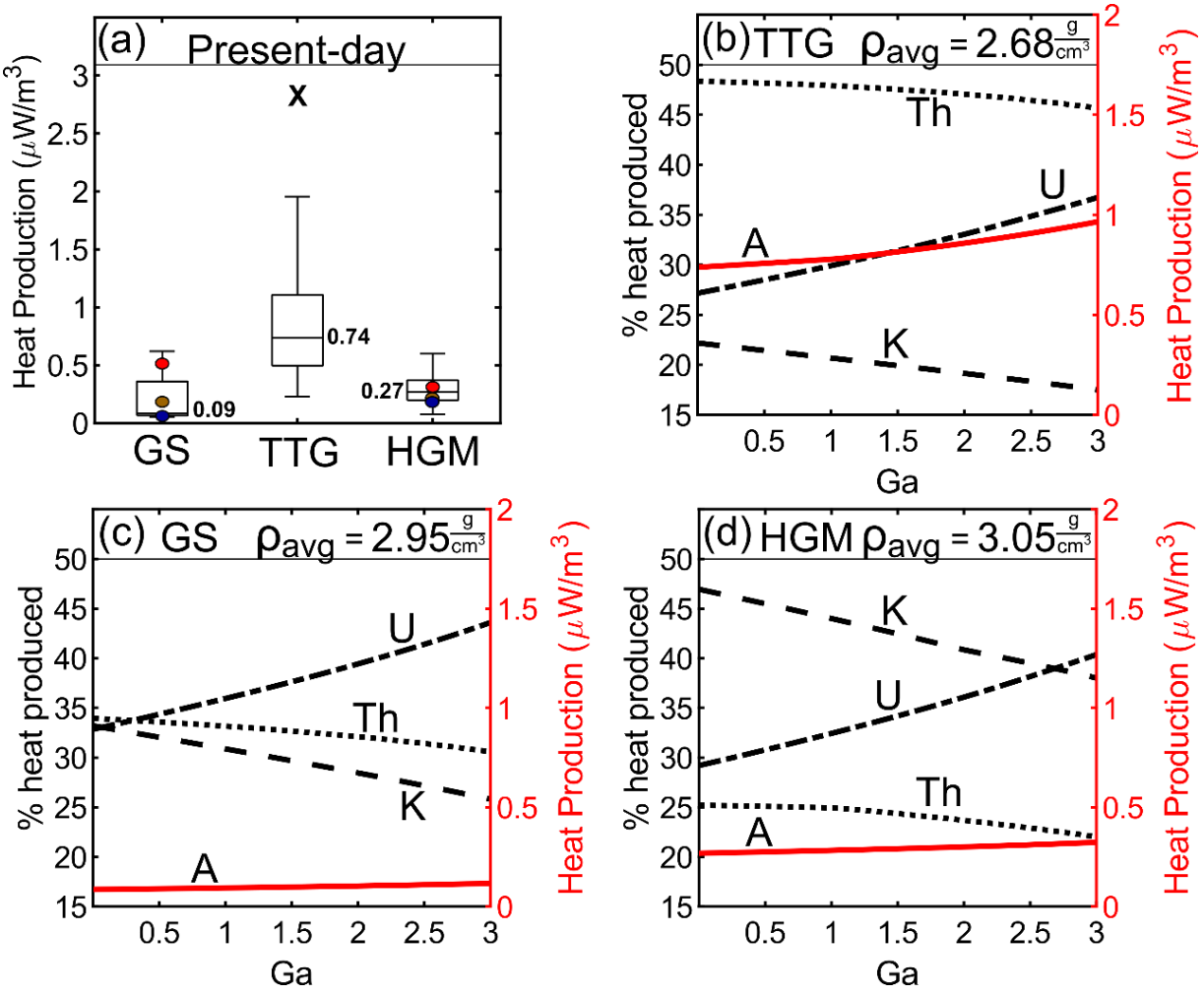


Figure 2.5: Calculated modern heat production and heat production through time for each rock type. ρ_{avg} is the median density of rock types. (a) Box and whisker plot for calculated present-day heat production. The boxes extend to the interquartile range, and the whiskers extend to the furthest data point up to 1.5 times the interquartile range. Crosses represent outliers and are outside of this range. (b) Relative contributions of K, U, and Th to the heat production (A) for tonalite-trondhjemite-granodiorite (TTG) in the Wawa Gneiss Domain. (c) Relative contributions of K, U, and Th to the heat production (A) for greenstone (GS) in the Michipicoten greenstone belt. (d) Relative contributions of K, U, and Th to the heat production (A) for high-grade metabasite (HGM) in the Kapuskasing Structural Zone.

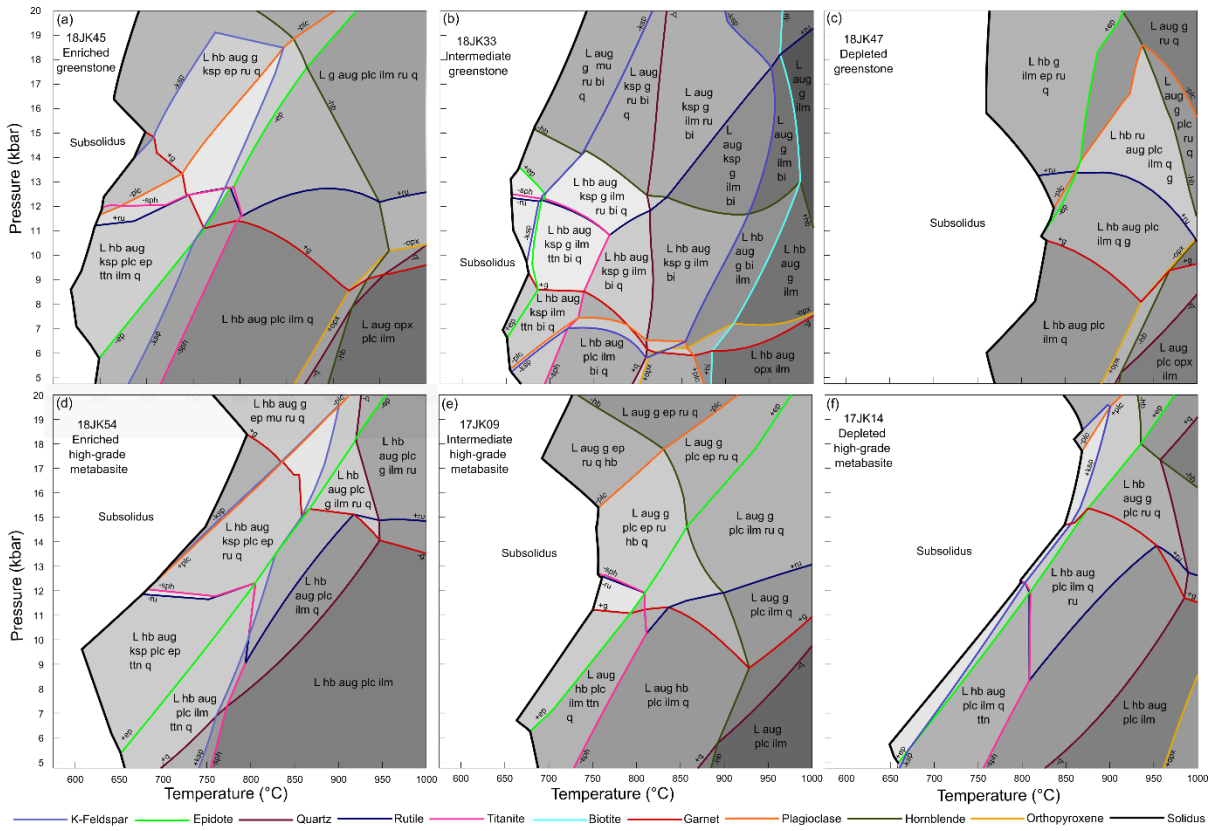


Figure 2.6: Simplified pseudosections for the six metabasite samples modelled in this study. Coloured lines indicate the stability boundaries for selected minerals, whereas the shading intensity is counter-proportional to the variance, except for the subsolidus field, which was not modelled. The thick, solid black line is the solidus. The fully labelled pseudosections are found in Appendix S1.9. Mineral abbreviations are from Holland and Powell (2011), except plagioclase (plc) and titanite (ttn).

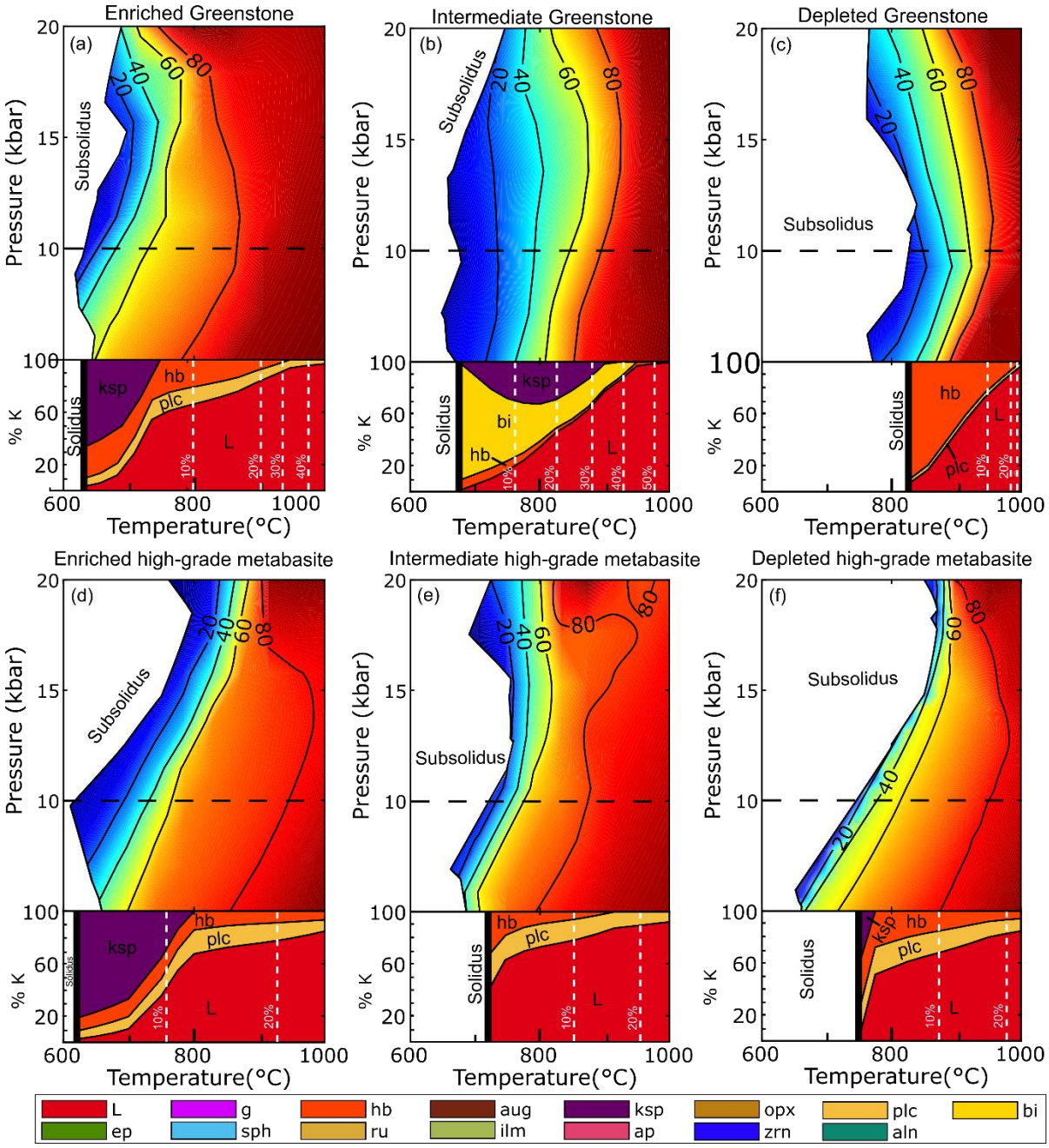


Figure 2.7: Contour plots for percent of the total potassium budget predicted to be in the melt and mode box diagrams showing the percent of the potassium budget in phases at 10 kbar for (a) enriched greenstone, (b) intermediate greenstone, (c) depleted greenstone, (d) enriched high-grade metabasite, (e) intermediate high-grade metabasite, and (f) depleted high-grade metabasite. White contour lines on the mode box diagram show the melt percent (10 wt% intervals). Mineral abbreviations from Holland and Powell (2011), except for plagioclase (plc).

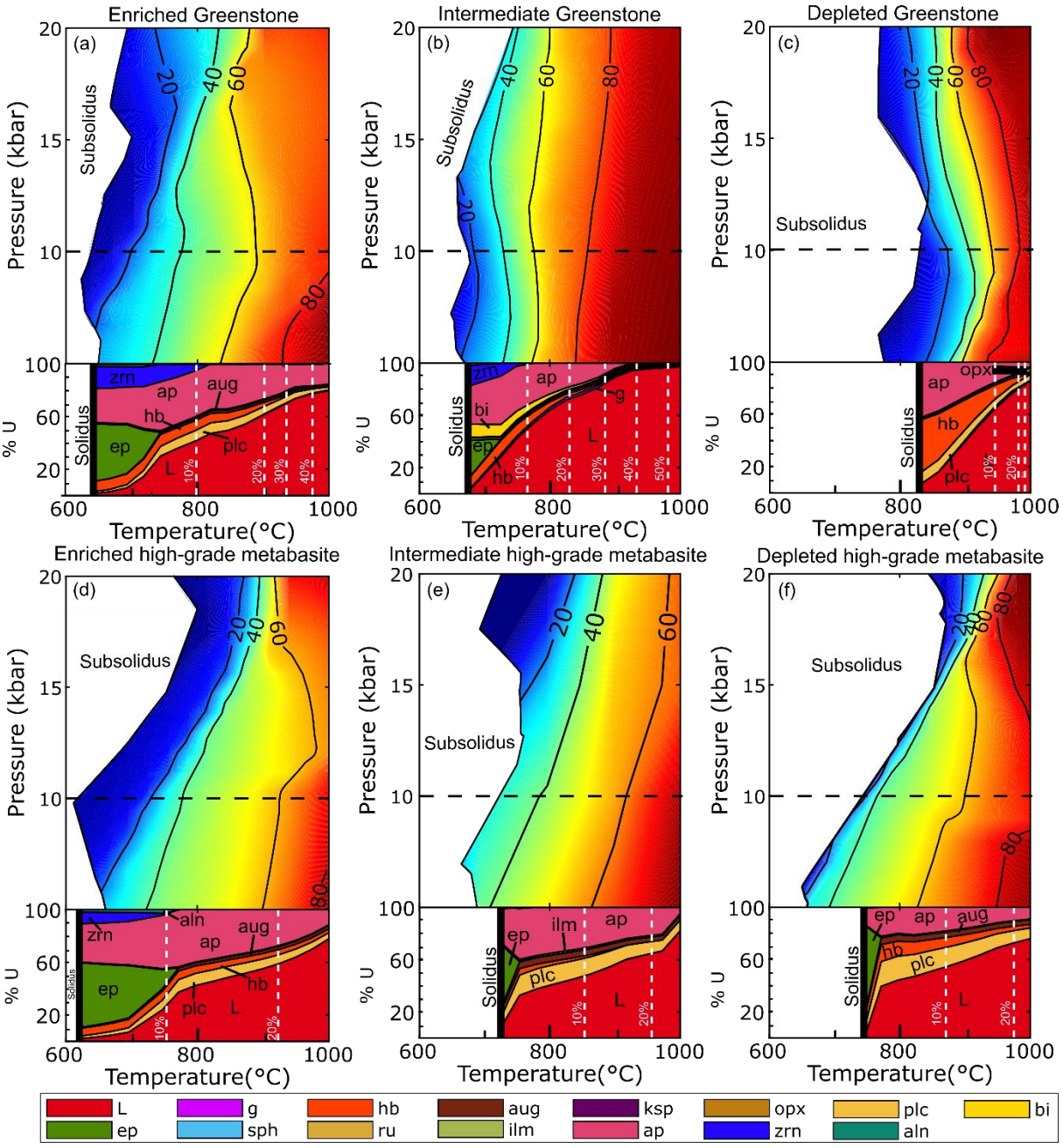


Figure 2.8: Contour plots for percent of the total uranium budget predicted to be in the melt and mode box diagrams showing percent uranium in phases at 10 kbar for (a) enriched greenstone, (b) intermediate greenstone, (c) depleted greenstone, (d) enriched high-grade metabasite, (e) intermediate high-grade metabasite, and (f) depleted high-grade metabasite. White contour lines on the mode box diagram show the melt weight percent (10 wt% intervals). Mineral abbreviations from Holland and Powell (2011), except for plagioclase (plc).

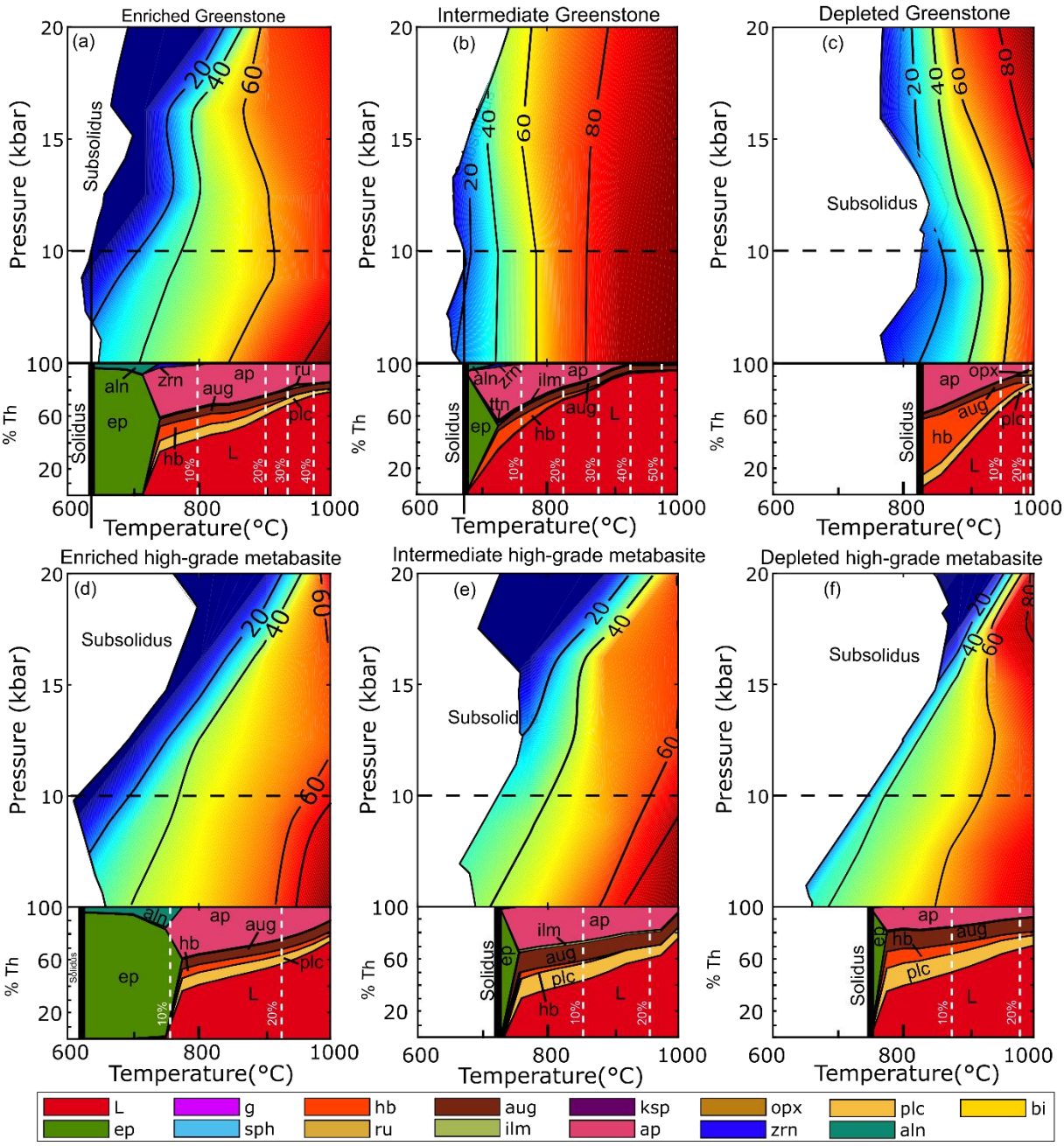


Figure 2.9: Contour plots for percent of the total thorium budget predicted to be in the melt and mode box diagrams showing percent thorium in phases at 10 kbar for (a) enriched greenstone, (b) intermediate greenstone, (c) depleted greenstone, (d) enriched high-grade metabasite, (e) intermediate high-grade metabasite, and (f) depleted high-grade metabasite. White contour lines on the mode box diagram show the melt weight percent (10 wt% intervals). Mineral abbreviations from Holland and Powell (2011), except for plagioclase (plc) and titanite (ttn).

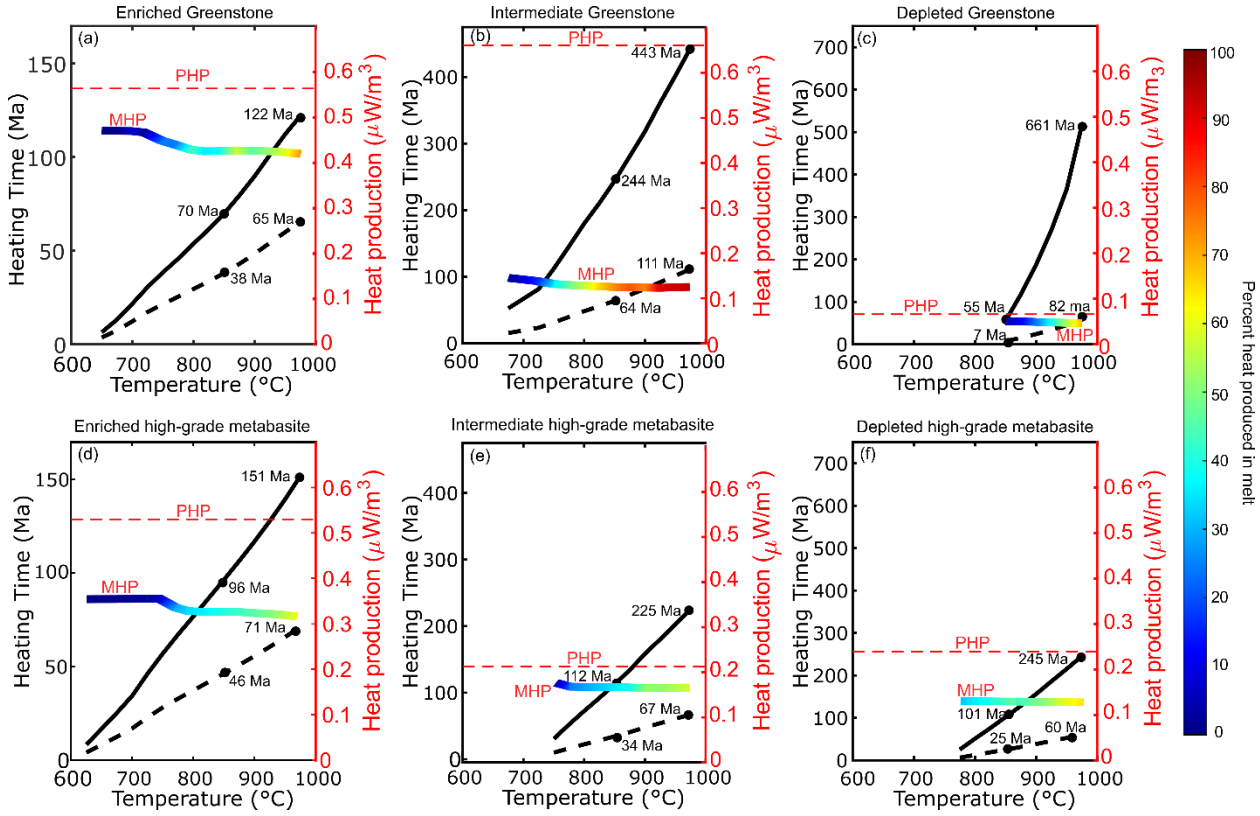


Figure 2.10: Calculated heating times and metamorphic heat production against temperature with the metamorphic heat production line colour representing the percent of radiogenic heat produced in the melt for (a) enriched greenstone, (b) intermediate greenstone, (c) depleted greenstone, (d) enriched high-grade metabasite, (e) intermediate high-grade metabasite, and (f) depleted high-grade metabasite. Past heat production (red dashed line) is calculated using whole-rock HPE concentrations calculated at 2650 Ma, with density calculated at 25°C and modern atmospheric pressure and is plotted for reference. Metamorphic heat production (MHP) is calculated using heat-producing element concentrations at 2650 Ma and partitioned through trace element calculations (c.f. Figures 2.7–9). Circles with durations beside show the time required to reach 850°C and 1000°C from the solidus. The solid black line is the heating times calculated only accounting for radiogenic heat. In contrast, the dashed black line shows the calculated heating time when accounting for radiogenic heat and mantle heat flux.

Table 2.1: Major element concentrations (wt% and mol%) of modelled samples. enr – enriched, int – intermediate, dep – depleted.

Sample	H_2O	SiO_2	Al_2O_3	CaO	MgO	FeO	K_2O	Na_2O	TiO_2	Fe_2O_3	O*
					wt%						
High-grade metabasite samples											
18JK54 (enr)	-	48.4	14.5	11.2	7.55	8.41	0.95	3.24	0.97	3.25	-
17JK09 (int)	-	47.7	14.7	13.2	4.1	11.3	0.12	2.31	1.49	3.33	-
17JK14 (dep)	-	47.7	15.1	12.3	7.17	7.78	0.47	2.63	0.8	2.94	-
Greenstone samples											
18JK45 (enr)	-	51.3	13.6	9.4	5.19	11.4	0.64	2.53	1.54	3	-
18JK33 (int)	-	42.6	11.8	8.02	4.97	9.8	2.49	1.27	2.32	2.62	-
18JK47 (dep)	-	50.8	13.4	8.68	7.97	9.75	0.07	1.7	0.88	2.68	-
					mol%						
High-grade metabasite samples											
18JK54 (enr)	4.75	50.2	8.78	12.3	11.6	7.23	0.62	3.23	0.75	-	2.5
17JK09 (int)	3.2	49.3	9.61	12	11.7	9.62	0.39	4.66	1.93	-	0.5
17JK14 (dep)	3.75	49.6	9.23	13.7	11.1	6.76	0.31	2.65	0.62	-	2.3
Greenstone samples											
18JK45 (enr)	4.9	54.4	8.47	10.7	8.2	10.1	0.43	2.6	1.23	-	2.4
18JK33 (int)	5.91	45.9	7.47	9.25	7.99	16.4	1.71	1.32	1.88	-	2.2
18JK47 (dep)	4.32	52.9	8.23	9.69	12.4	8.5	0.04	1.72	0.69	-	2.1

Table 2.2: Measured trace element concentrations of modelled samples. All values are in mg/kg except for P_2O_5 (wt%).

Sample	P_2O_5	Zr	La	Ce	Pr	Sm	Nd	Th	U
High-grade metabasite samples									
18JK54 (enr)	0.21	77	19	46.1	6.6	5.8	28	1.9	0.3
17JK09 (int)	0.13	45	4.3	12	2	3.5	11	0.7	0.2
17JK14 (dep)	0.06	40	3.2	7.87	1.2	1.9	5.9	0.4	0.2
Greenstone samples									
18JK45 (enr)	0.15	126	12	28.1	4	4.7	18	2	0.5
18JK33 (int)	0.12	95	8	20.9	3.2	4.2	16	0.5	0.2
18JK47 (dep)	0.07	53	3.1	8.13	1.3	2.1	6.3	0.3	0.1

Chapter 3.0: Heat-producing element dilution recording dilating, oscillatory crustal growth

Summary

The rhythm and timing of continental crustal building are key to understanding Earth's planetary heat budget and the degree of preservation bias in the modern continental mosaic. By interrogating the crustal record of a temporally comprehensive database, discrete pulses of marked crustal growth and subsequent differentiation are revealed. The time between these pulses of crustal growth is increasing, a reflection of long-term loss of interior heat. The time-corrected heat production of primitive (mafic) crust decreases with time, whereas siliceous and intermediate-silica compositions show no correlation between heat production and crystallization age. Through a combination of phase equilibrium and trace element modelling, we show that the low heat production of primitive Archean rocks is a result of greater mantle melting—a product of higher ambient temperature—and the reworking of enriched metabasite to form tonalite-trondhjemite-granodiorite suites during cratonization. However, these enriched metabasites are a low proportion of preserved ancient crust, and their paucity in the geologic record has a limited effect on understanding broad temporal trends in crustal composition. The mechanism for pulsive crustal growth remains enigmatic, though it may be explained via slab avalanches across mantle transition zone or variable subduction rates inducing thermochemical mantle plumes and related magmatism producing new crustal material.

3.1 Introduction

The reworking of mantle-derived material (i.e. primitive mafic rocks) has produced a crustal mosaic recording geologic time; however, the rate, duration, and timing of continental crust formation and preservation are contentious. Currently, most new continental crust is formed at convergent margins (Hawkesworth and Kemp 2006, Brown 2010)—these margins are also focal points for reworking of preexisting crust where positive buoyancy prevents subduction-related destruction (Von Huene and Scholl 1991). As such, it has been suggested that >50% of all crustal material has an Archean origin (e.g. Taylor and McLennan 1995, Dhuime et al. 2012) though others consider crustal growth to be a more pulsive and gradual process (e.g. Parman 2007, Condie and Aster 2010). The uncertainty revolves around whether the natural record is of crustal preservation or creation (Condie et al. 2017), a problem rooted in the effects of heat and heat

production on the preservation potential of existing crustal material (Morgan 1985, Gard et al. 2019).

Heat-producing elements (K, U, and Th) are preferentially concentrated in the continental crust compared with the oceanic crust and the mantle. These elements were ~4 times more abundant in the Archean compared to the present; yet Archean terranes often have low age-corrected radiogenic heat production based on current heat-producing element concentrations back-calculated to the time of formation (Jaupart and Mareschal 2014, Gard et al. 2019). One explanation is that the Archean continental crust was composed of mafic rocks with low heat production (Hawkesworth and Jaupart 2021) and contained only minor amounts of granitic and clastic sedimentary rocks that are generally enriched in heat-producing elements (Bea 2012, Jaupart and Mareschal 2014). Alternatively, high heat-producing rocks may have been present in the Archean but were reworked and eroded, perhaps preferably due to their upper crustal positions (Hasterok et al. 2019). The modern continental crust is expected to be stratified with heat production being greater in the upper crust than in the lower crust (Taylor and McLennan 1995, Jaupart and Mareschal 2014). Therefore, if the Archean upper crust was comprised of high heat-producing rocks, the eroded remnants should be recorded in the sedimentary record—contrary to observations from Precambrian sedimentary rocks (Taylor and McLennan 1986). Challenges in assessing crustal growth or reworking through geological time are exacerbated by the episodic nature of preserved crust, with distinct peaks and troughs in the frequency of data such as U–Pb zircon and monazite ages (e.g. Condie et al. 2017, Mulder and Cawood 2022) or hafnium isotopes in zircon (e.g. Kemp et al. 2007). The cyclicity of data raises the question of preservation vs creation (Morgan 1985, Mulder and Cawood 2022), with supercontinent cycles (Condie and Aster 2010, Wang et al. 2020), changes in subduction regimes (O'Neill et al. 2007), or deep-seated mantle dynamics (Galer et al. 1989, Rampino and Prokoph 2013) proposed as mechanisms for both the selective preservation of crust as well as episodic creation of continental crust.

Here, we consider the complete sequence from mantle melting creating juvenile (i.e. mafic) crust, and subsequent reworking to form intermediate middle to upper crust to assess the heat production of these different components during crustal differentiation. We compare measured and extrapolated concentrations of the heat-producing elements from a database of

samples with the predictions of phase equilibrium and trace element modelling to evaluate if low heat-producing Archean crustal material resulted from increased mantle melting or if Archean processes should have produced a crust with similar heat production or higher to modern day. We can further use this crustal record to understand the long-term crustal growth patterns and track the cooling history of Earth.

3.2 Methodology

We approximate crustal heat production trends through time using a broad database of age-constrained igneous crustal compositions from Keller & Schoene (2018). Samples with null concentrations of U, Th, and K were removed; the resultant database is comprised of ~69,000 whole-rock compositions. The concentration of heat-producing elements was back-calculated to the assumed age of crystallization, and heat production was calculated using the formulation of Ashwal et al. (1987). Whole-rock density was approximated based on silica content with ultra-low (40—50 wt% SiO_2; ρ=3.2 g/cm^3), low (50—55 wt% SiO_2; ρ=3.1 g/cm^3), intermediate (55—65 wt% SiO_2; ρ=2.9 g/cm^3), and high (65—75 wt% SiO_2; ρ=2.85 g/cm^3) SiO_2 groupings. The limitations of these assumptions are discussed in Appendix 2.1, although slight variations in density or the groupings based on silica content have negligible influence on the broader results and implications.

Evaluating the redistribution of heat-producing elements during crustal building and differentiation requires a combination of phase equilibrium and trace element modelling of mantle compositions undergoing anatexis and subsequent reworking of basaltic material. Concentrations of the heat-producing elements and estimated heat production of mantle-derived melts are modelled with the GeoPS software package (Xiang and Connolly 2022) using appropriate activity–composition models in the Na_2O-CaO-K_2O-FeO-MgO-Al_2O_3-SiO_2-TiO_2-O_2-Cr_2O_3 system coupled with bulk rock compositions (Appendix 2.2) approximating modern upper mantle (KLB-1; Davis et al. 2009) and estimated Archean mantle (AP; Green, 1974). Trace element modelling using the predicted phase assemblages followed a mass balance approach (i.e. Johnson et al. 2021). Similarly, the effects of crustal differentiation are simulated by modelling the partial melting of mafic Archean crust in the generation of TTG magmas using the composition of the enriched Archean tholeiite (e.g. Palin et al. 2016, Kendrick et al. 2022) in the Na_2O-CaO-K_2O-FeO-MgO-Al_2O_3-SiO_2-TiO_2-O_2 system. U and Th concentrations of mantle

systems are assumed to be pyrolytic (McDonough and Sun 1995); values for enriched Archean tholeiite are from Condie (1976).

3.3 Results

The database used to calculate crustal composition through time is predominately comprised of samples <200 Ma (Fig. 3.1a) but has a temporal resolution spanning into the Eoarchean. Crustal building and differentiation are recorded by a common sequence from mafic to intermediate to felsic rocks (Fig. 3.1b); the database is predominantly low silica rocks, though the proportion decreases (~55% to ~45%) with younger crystallization ages (Fig. 3.1c). In samples older than ~200 Ma, the proportion of high silica samples increases from 25 to 35% over time, with a relatively constant (~15%) proportion of intermediate rocks. Oscillations between periods of high and low sample counts are observed with peaks occurring ca 3320–3180, 2860–2640, 2120–2030, 1480–1330, and 450–330 Ma. Periods with a high number of samples span ~120–240 Ma and are separated by periods of low sample counts; these periods increase in duration (i.e. dilate) from ~300 Ma in the Archean to ~800 Ma in the meso- to neo-Proterozoic. We interpret periods with high sample counts to indicate pulsed crustal growth events—the reasoning and implications of this interpretation are discussed later.

Rocks with higher concentrations of silica have greater calculated heat production (Fig. 3.2), which is expected (e.g. Hasterok et al. 2018). High silica rocks have a median heat production of 1.5–2.2 $\mu W/m^3$ whereas intermediate and low silica compositions have median values of 1–1.4 and 0.1–0.6 $\mu W/m^3$ respectively (Fig. 3.2). Heat production of intermediate and high silica compositions vary with time but have no systematic trends (Fig. 3.2a, b). Comparatively, the calculated heat production of low silica compositions increases from ~0.3 $\mu W/m^3$ at ca 2750 Ma to ~0.6 $\mu W/m^3$ currently (Fig. 3.2c). There is no correlation between crustal heat production and pulses of crustal growth; heat production is stable during a single event.

The modelled heat production of crystallized partial melts of mantle sources for modern and Archean primitive mantle decreases with melt fraction (Fig. 3.3a). Mantle melting was modelled at 10, 15, 20, and 25 kbar; however, as pressure does not noticeably affect modelled heat production, we focus on the results for 20 kbar. Models of modern mantle melting produce melt with lower heat production compared to Archean systems with modelled heat production

exponentially decreasing with increasing melt proportion. At 10 wt% melt—the amount suggested for most modern basalts (Keller and Schoene 2018)—in a KLB-1 system, resultant basalts would produce 0.15 μW/m^3 of heat compared to 0.32 μW/m^3 for Archean pyrolite-derived melts. Alternatively, 40 wt% melting of KLB-1 and Archean pyrolite would produce rocks with a heat production of 0.04 and 0.08 μW/$m^{3,}$ respectively (Fig. 3.3a). Komatiitic magmas can be produced by 20–40 wt% peridotite melting (Herzberg 1992, Rollinson 2010, Keller and Schoene 2018). Therefore, we estimate Archean mantle melting to 15–40 wt%, consistent with lower melting to produce basaltic magma. Our model results are comparable to the range of low-silica post-Archean compositions (Fig. 3.3a) but generally underestimate the heat production of Archean compositions, with the natural median corresponding to ~17 wt% melt.

Heat production of tonalite-trondhjemite-granodiorite (TTG) magma produced from partial melting of a hydrated and enriched Archean tholeiite (e.g. Martin et al. 2005, Moyen 2011, Laurent et al. 2024) increases slightly up to melt proportions of ~2 wt% and then decreases with increasing melt fraction (Fig. 3.3b). Modelled heat production produced through melting of the tholeiite increases at low melt proportion due to the preferential breakdown of epidote and biotite (minerals with relatively high concentrations of heat-producing elements; Bea 1996, Kinney et al. 2023) with continued melting producing lower heat-producing melt due to dilution. Except at very low melt fractions, the modelled heat production of the resultant TTGs is similar when derived from different depths (5, 10 and 15 kbar) (Fig. 3.3b). The interquartile range for natural Archean intermediate silica compositions is reproduced for 5–35 wt% melting of an enriched Archean tholeiite—the median heat production of the natural record corresponding to ~10–15 wt% melt in the model. These proportions of melt are within a reasonable range of temperatures (750–950ºC) and melt fraction for Archean TTGs genesis (Laurent et al. 2024).

3.4 Discussion

Collating large natural datasets and modelling heat production require several assumptions and limitations, and these are presented in Appendix 2.1. We were successful in recreating the Archean mafic crust with lower heat production than modern basalts; however, our model results underestimate heat production in both systems compared to the natural record (Fig. 3.3a). The modelled heat production of Archean and modern basalts (0.08 and 0.15 μW/m3 respectively)

are less than the calculated natural values (0.3 and 0.6 μW/m3 respectively), showing a possible systematic underestimation in the models. Further, we use the same concentrations of U and Th for ancient and modern mantle systems (McDonough and Sun 1995), disregarding the effects of decay throughout time, which would result in 30–40% greater heat production in the mantle at 3000 Ma. We do not attempt to estimate the effects of fractionation of heat-producing elements during crustal formation; though considering their incompatibility in mantle minerals, the pyrolytic model would be an underestimate of the U and Th concentrations. The degree of depletion would depend on the total mass extracted from the mantle when that mass was extracted, and similarly for any rejuvenation of the mantle by crustal inputs. However, the Archean Pyrolite composition tries to account for K-depletion (Green 1975), resulting in predicted heat production of Archean systems being ~2x that of KLB-1 derived melts (Fig. 3.3a). Altogether, the Archean heat-production models are underestimates of the natural record, though we believe these combined effects of fractionation during crustal formation and radioactive decay may help explain the difference. Our models can, however, correctly produce basaltic melt if most natural modern basalts are formed via melting less than the inflection point of 5–8 wt% (Fig. 3.3a)—aligning with some previous estimates (Takahashi et al. 1993, Keller and Schoene 2018).

3.4.1 Magmatic dilution

Variations in radiogenic heat production throughout Earth's history have been attributed to decay (Jaupart and Mareschal 2014), the removal/reworking of a high heat-producing upper crust (Vitorello and Pollack 1980, Hasterok et al. 2019), a more mafic crust in the past compared to the modern crust (Hawkesworth and Jaupart 2021), and/or some fortuitous process that produces low heat-producing rocks (Morgan 1985). Heat-producing elements are generally incompatible in minerals except for feldspar, amphibole, and mica for K and accessory minerals (zircon, monazite, apatite) for U and Th (Bea 2012, Alessio et al. 2018). Consequently, silicate melt is often enriched in heat-producing elements compared to the solid residue in mantle and crustal systems (Bea and Montero 1999, Kinney et al. 2023). However, the heat production of intermediate and felsic rocks does not show the same decrease of heat-producing elements as mafic rocks over geological time (Fig. 3.2). We discuss the importance of high-heat-producing metabasites during cratonization later, however, we propose that the "fortuitous processes" resulting in low-heat producing Archean crust mentioned by Morgan (1985) may be magmatic

dilution during mantle melting. For mantle melting, the heat-producing elements are highly concentrated in low melt fractions with further melting (>20–30 wt%; Fig. 3.3), exponentially decreasing the heat production of the resultant mafic rocks. Modern basalt results from <10 wt% mantle melting compared to 15–40 wt% for Archean basalts and komatiites (Herzberg 1992, Rollinson 2010, Keller and Schoene 2018) There is an apparent trade-off between higher magmatic dilution, but the higher abundance of Th, U and K in the Archean, and modern basalts that formed at lower melt fractions in sources with low concentrations of heat-producing elements; this has compounded into a slight increase in the age-corrected heat production of mafic rocks throughout time (Fig. 3.2c).

The differentiation of crust by reworking lower crust, evident by voluminous TTG suites, is a fundamental process in cratonization and the preservation of continents (e.g. Bédard et al. 2003, Robin and Bailey 2009). During crustal stabilization, the removal of heat-producing elements in the source (e.g. Kinney et al. 2023) and the advection of resultant melt to higher crustal levels decreases the heat content and heat potential of the lower crust, resulting in a stronger crustal base (Mareschal and Jaupart 2006). Though the tectonic environment responsible for TTG formation is debated (e.g. Smithies 2000, Bédard 2006, Deng et al. 2019), their sources are hydrated mafic rocks enriched in incompatible elements (Moyen 2011, Moyen and Martin 2012)—including the heat-producing elements. The variable heat production of intermediate and high silica compositions, not correlated with age (Fig. 3.2b, c), provides evidence for a quasi-minimum heat production needed for anatexis of mafic rocks during crustal differentiation. The melting of enriched mafic compositions during cratonization has certainly produced a preservation bias towards lower heat-producing Archean basalts. However, these enriched metabasites were likely a subordinate component of the Archean crust considering heat production (enrichment) decreases exponentially with melt fraction (Fig. 3.3a) and there was ~4 times more mantle melting in the past (Korenaga 2008, Keller and Schoene 2018) with ~6 wt% of Archean mantle melting producing the equivalent heat to modern day basalts (Fig. 3.3a). With over three-quarters of the melting resulting in lower heat-producing basaltic crust, the composite Archean crust would have a low average heat production. This interpretation is further supported by a larger interquartile range for Archean compositions in the rock record (Fig. 3.3a).

3.4.2 Is the rock record preservation or creation?

Uncertainty on whether the rock record is one of preservation or creation arises from episodic temporal trends with distinct peaks and troughs observed in mineral chronometer abundance (e.g. Condie and Aster 2010, Mulder and Cawood 2022) as well as bulk rock radiogenic and stable isotopes (e.g. Parman 2007, Garçon 2021). The dataset of ~69,000 age-constrained, crustal bulk-rock compositions interrogated here exhibits peaks of data of ca 3320–3180, 2860–2640, 2120–2030, 1480–1330, and 450–330 Ma (Fig. 3.1a). The supercontinent cycle provides a potential mechanism for increased crustal reworking through collisional assembly and preservation by isolation within the heart of the continent (Hinderer 2012). However, only the last two pulses of crustal growth are associated with known supercontinents and no associations are shown between crust formation and the supercontinents Rodinia or Superia/Slavia (Fig. 3.1). Furthermore, respective peaks and troughs between datasets do not align with each other, with some proxies such as detrital zircon (Condie and Aster 2010) or monazite (Mulder and Cawood 2022) aligning well with the supercontinent cycle whereas others are seemingly independent (e.g. $^{4}He/^{3}He_{Basalt}$; Parman 2007, εHf_{Zircon}; Roberts 2012). Altogether, using multiple proxies, each capturing distinct aspects of crustal formation, may offer a more comprehensive understanding of continental crust creation.

Our whole-rock database differs from the detrital zircon record, which tracks the formation of sedimentary (i.e., upper-crustal) material, and the monazite record, which, considering monazite is generally formed in evolved or fractionated systems (Zhu and O'Nions 1999), likely better records the crustal reworking and differentiation. High rates of erosion along arc systems before supercontinent assembly, extensive reworking during collision, and selective preservation of material in continental interiors may explain the correlation between accessory mineral records and supercontinent cycles (Cawood et al. 2013). In contrast, Hafnium isotope ratios in zircon can be tied to the general timing of mantle extraction (e.g. Kemp et al. 2007), whereas the high volatility and limited recycling of He during subduction (Lan et al. 2010) allows $^{4}He/^{3}He$ of basalt to track mantle composition throughout time. The peaks of data presented in Figure 3.1 defining our proposed pulses of crustal growth are like those (Fig. 3.4a) proposed based on $^{4}He/^{3}He$ of basalts (Parman 2007) and $^{187}Re/^{187}Os$ of ophiolites recording mantle extraction periodicity (Pearson et al. 2007) while aligning well with zircon εHf records (Roberts 2012). Altogether, these data and correlations between proxies are interpreted as a

resolvable, preserved crustal record with evidence for pulsive crustal growth throughout Earth's history (Fig. 3.4). Though the mechanism for such events remains uncertain, we consider the mantle to be building crustal potential internally before marked crustal building events.

3.4.3 The tempo of crustal formation and differentiation

The extraction of material from the mantle to create the continental crust is the physical manifestation of planetary heat loss, with periods of marked crustal building (Figs 3.1 and 3.4) being catastrophic heat loss events. Several mechanisms have been proposed for episodic crustal growth including supercontinent blanketing of the mantle with voluminous magmatism during break-up (Lenardic et al. 2011), supercontinent amalgamation (Condie and Aster 2010, Wang et al. 2020), intermittent subduction (O'Neill et al. 2007), and mantle avalanches with subducted slabs piling at the mantle transition zone before catastrophically puncturing the boundary (Rampino and Prokoph 2013)—a possible mechanism for some (super)plumes (e.g. Condie 1998). Large continents are proposed to thermally isolate the underlying mantle, which can induce catastrophic mantle melting subjacent to supercontinents (e.g. Coltice et al. 2007). However, such thermal isolation is unlikely with lateral convection unless the landmass is circumvented by subduction zones (Lenardic et al. 2011). The supercontinents Gondwana and Nuna are associated with marked crustal growth (Fig. 3.4), whereas the three preceding (>2000 Ma) pulses of growth have no temporal associations with supercontinents, nor does the supercontinent Rodinia with crustal growth. This may indicate a change in the mechanism that induces crustal formation (discussed below), provide insights into the initiation of global "modern style" tectonics (e.g. Brown 2008), and show that the formation of a supercontinent is not deterministic of mass crustal growth.

Thermochemical plumes rising from the lower mantle are often invoked for marked crustal building (Stein and Hofmann 1994, Albarède 1998, Zhong et al. 2024) with continuous mass transfer between upper and lower mantle resulting in continuous crustal growth (e.g. Galer et al. 1989) or episodic transfer resulting in pulsive crustal growth (e.g. Stein and Hofmann 1994). The mechanism for episodic transfer across mantle boundaries remains abstract, though an accumulation of subducted slabs at the mantle transition zone before reaching some critical mass has been proposed (Rampino and Prokoph 2013). In this scenario, the dilation observed between pulses of crustal growth may represent increased mantle viscosity, slowing the descent and

accumulation of subducted material. Alternatively, intermittent or variable subduction (e.g. O'Neill et al. 2007, Garçon 2021) with continuous mass transfer could induce pulsive crustal growth. Though these mechanisms invoke subduction—the global initiation of which is contentious (e.g. Tang et al. 2016, Kusky et al. 2018, Harrison 2024)—we consider lithospheric floundering in vertical tectonic models (e.g. Bédard 2006, Robin and Bailey 2009) to be an appropriate substitute to overload the discontinuity with dense, former crustal material. Regardless of the transfer mechanism, we suggest that crustal formation is a bottom-up process with periodic, deep-mantle mass exchange inducing dilating, episodic crustal growth. The dilation between growth pulses represents the heat previously lost—now evident in mantle temperature ~200ºC cooler than the Archean (Korenaga 2008, Keller and Schoene 2018) and further by komatiites and high-Mg basalts in the Archean rock record (Grove and Parman 2004). However, the variable amount of crust produced during any single building event (Fig. 3.1c) indicates the energetic (or crustal potential) threshold for such events may be non-constant.

3.5 Conclusion

The timing, duration, and continuity of crustal growth remain contentious, with uncertainties arising from potential preservation biases in the crustal record. To address these uncertainties, we interrogate a temporally comprehensive database of crustal compositions with a focus on heat-producing elements and reproduce natural trends using thermodynamic and trace element modelling. The low heat production of preserved Archean rocks is reflective of greater mantle melting, diluting heat-producing elements in the resultant primitive (i.e. mafic) crust. Subsequent reworking of volumetrically minor enriched compositions during cratonization further produced a mafic record with low heat production. Our analysis identifies five pulses of marked crustal growth, evident by significant contributions of low-silica, mantle-derived magmas possibly related to episodic transfer of material between the lower and upper mantle. This process may be now related to supercontinents but not systematically nor before 2000 Ma. Following these influxes of low-silica magma to make the primitive crust, reworking of enriched compositions during crustal differentiation produced intermediate and high-silica rocks. Historic heat loss during crustal formation and differentiation increases the duration of subdued magmatism between pulses of crustal growth. Altogether, we determine crustal growth to be a dilating, episodic process driven by mantle cooling operative since the Archean.

3.6 References

Albarède, F. 1998. The growth of continental crust. Tectonophysics, 296: 1–14. doi:10.1016/S0040-1951(98)00133-4.

Alessio, K.L., Hand, M., Kelsey, D.E., Williams, M.A., Morrissey, L.J., and Barovich, K. 2018. Conservation of deep crustal heat production. Geology, 46: 335–338. Geological Society of America. doi:10.1130/G39970.1.

Ashwal, L.D., Morgan, P., Kelley, S.A., and Percival, J.A. 1987. Heat production in an Archean crustal profile and implications for heat flow and mobilization of heat-producing elements. Earth and Planetary Science Letters, 85: 439–450. doi:10.1016/0012-821X(87)90139-7.

Bea, F. 1996. Residence of REE, Y, Th and U in granites and crustal protoliths; Implications for the chemistry of crustal melts. Journal of Petrology, 37: 521–552.

Bea, F. 2012. The sources of energy for crustal melting and the geochemistry of heat-producing elements. Lithos, 153: 278–291. doi:10.1016/j.lithos.2012.01.017.

Bea, F., and Montero, P. 1999. Behavior of accessory phases and redistribution of Zr, REE, Y, Th, and U during metamorphism and partial melting of metapelites in the lower crust: an example from the Kinzigite Formation of Ivrea-Verbano, NW Italy. Geochimica et Cosmochimica Acta, 63: 1133–1153. doi:10.1016/S0016-7037(98)00292-0.

Bédard, J.H. 2006. A catalytic delamination-driven model for coupled genesis of Archaean crust and sub-continental lithospheric mantle. Geochimica et Cosmochimica Acta, 70: 1188–1214. doi:10.1016/j.gca.2005.11.008.

Bédard, J.H., Brouillette, P., Madore, L., and Berclaz, A. 2003. Archaean cratonization and deformation in the northern Superior Province, Canada: an evaluation of plate tectonic versus vertical tectonic models. Precambrian Research, 127: 61–87. doi:10.1016/S0301-9268(03)00181-5.

Brown, M. 2008. Geodynamic regimes and tectonic settings for metamorphism: Relationship to the supercontinent cycle. Indian Journal of Geology, 80: 3–21.

Brown, M. 2010. Melting of the continental crust during orogenesis: the thermal, rheological, and compositional consequences of melt transport from lower to upper continental crust. Canadian Journal of Earth Sciences, 47: 655–694. doi:10.1139/E09-057.

Cawood, P.A., Hawkesworth, C.J., and Dhuime, B. 2013. The continental record and the generation of continental crust. Geological Society of America Bulletin, 125: 14–32. doi:10.1130/B30722.1.

Coltice, N., Phillips, B.R., Bertrand, H., Ricard, Y., and Rey, P. 2007. Global warming of the mantle at the origin of flood basalts over supercontinents.

Condie, K. 1976. Trace-element geochemistry of Archean greenstone belts. Earth-Science Reviews, 12: 393–417. doi:10.1016/0012-8252(76)90012-X.

Condie, K.C. 1998. Episodic continental growth and supercontinents: a mantle avalanche connection? Earth and Planetary Science Letters, 163: 97–108. doi:10.1016/S0012-821X(98)00178-2.

Condie, K.C., Arndt, N., Davaille, A., and Puetz, S.J. 2017. Zircon age peaks: Production or preservation of continental crust? Geosphere, 13: 227–234. doi:10.1130/GES01361.1.

Condie, K.C., and Aster, R.C. 2010. Episodic zircon age spectra of orogenic granitoids: The supercontinent connection and continental growth. Precambrian Research, 180: 227–236. doi:10.1016/j.precamres.2010.03.008.

Deng, Z., Chaussidon, M., Guitreau, M., Puchtel, I.S., Dauphas, N., and Moynier, F. 2019. An oceanic subduction origin for Archaean granitoids revealed by silicon isotopes. Nature Geoscience, 12: 774–778. doi:10.1038/s41561-019-0407-6.

Dhuime, B., Hawkesworth, C.J., Cawood, P.A., and Storey, C.D. 2012. A Change in the Geodynamics of Continental Growth 3 Billion Years Ago. Science, 335: 1334–1336. doi:10.1126/science.1216066.

Galer, S.J.G., Goldstein, S.L., and O'Nions, R.K. 1989. Limits on chemical and convective isolation in the Earth's interior. Chemical Geology, 75: 257–290. doi:10.1016/0009-2541(89)90001-6.

Garçon, M. 2021. Episodic growth of felsic continents in the past 3.7 Ga. Science Advances, 7: eabj1807. doi:10.1126/sciadv.abj1807.

Gard, M., Hasterok, D., Hand, M., and Cox, G. 2019. Variations in continental heat production from 4 Ga to the present: Evidence from geochemical data. Lithos, 342–343: 391–406. doi:10.1016/j.lithos.2019.05.034.

Green, D.H. 1975. Genesis of Archean peridotitic magmas and constraints on Archean geothermal gradients and tectonics. Geology, 3: 15–18.

Grove, T.L., and Parman, S.W. 2004. Thermal evolution of the Earth as recorded by komatiites. Earth and Planetary Science Letters, 219: 173–187. doi:10.1016/S0012-821X(04)00002-0.

Harrison, T.M. 2024. We don't know when plate tectonics began. Journal of the Geological Society, 181: jgs2023-212. doi:10.1144/jgs2023-212.

Hasterok, D., Gard, M., Cox, G., and Hand, M. 2019. A 4 Ga record of granitic heat production: Implications for geodynamic evolution and crustal composition of the early Earth. Precambrian Research, 331: 105375. doi:10.1016/j.precamres.2019.105375.

Hasterok, D., Gard, M., and Webb, J. 2018. On the radiogenic heat production of metamorphic, igneous, and sedimentary rocks. Geoscience Frontiers, 9: 1777–1794. doi:10.1016/j.gsf.2017.10.012.

Hawkesworth, C., and Jaupart, C. 2021. Heat flow constraints on the mafic character of Archean continental crust. Earth and Planetary Science Letters, 571: 117091. doi:10.1016/j.epsl.2021.117091.

Hawkesworth, C.J., and Kemp, A.I.S. 2006. Evolution of the continental crust. Nature, 443: 811–817. doi:10.1038/nature05191.

Herzberg, C. 1992. Depth and degree of melting of komatiites. Journal of Geophysical Research: Solid Earth, 97: 4521–4540. doi:10.1029/91JB03066.

Hinderer, M. 2012. From gullies to mountain belts: A review of sediment budgets at various scales. Sedimentary Geology, 280: 21–59. doi:10.1016/j.sedgeo.2012.03.009.

Jaupart, C., and Mareschal, J.-C. 2014. Constraints on crustal heat production from heat flow data. In Treatise on Geochemistry. Elsevier. pp. 53–73. doi:10.1016/B978-0-08-095975-7.00302-8.

Johnson, T., Yakymchuk, C., and Brown, M. 2021. Crustal melting and suprasolidus phase equilibria: From first principles to the state-of-the-art. Earth-Science Reviews, 221: 103778. doi:10.1016/j.earscirev.2021.103778.

Keller, B., and Schoene, B. 2018. Plate tectonics and continental basaltic geochemistry throughout Earth history. Earth and Planetary Science Letters, 481: 290–304. Elsevier B.V. doi:10.1016/j.epsl.2017.10.031.

Kemp, A.I.S., Hawkesworth, C.J., Foster, G.L., Paterson, B.A., Woodhead, J.D., Hergt, J.M., Gray, C.M., and Whitehouse, M.J. 2007. Magmatic and crustal differentiation history of granitic rocks from Hf-O Isotopes in zircon. Science, 315: 980–983. doi:10.1126/science.1136154.

Kendrick, J., Duguet, M., and Yakymchuk, C. 2022. Diversification of Archean tonalite-trondhjemite-granodiorite suites in a mushy middle crust. Geology, 50: 76–80. doi:10.1130/G49287.1.

Kinney, C., Kendrick, J., Duguet, M., and Yakymchuk, C. 2023. Redistribution of heat-producing elements during melting of Archean crust. Journal of Metamorphic Geology,: jmg.12751. doi:10.1111/jmg.12751.

Korenaga, J. 2008. Urey ratio and the structure and evolution of Earth's mantle. Reviews of Geophysics, 46: 2007RG000241. doi:10.1029/2007RG000241.

Kusky, T.M., Windley, B.F., and Polat, A. 2018. Geological Evidence for the Operation of Plate Tectonics throughout the Archean: Records from Archean Paleo-Plate Boundaries. Journal of Earth Science, 29: 1291–1303. doi:10.1007/s12583-018-0999-6.

Lan, T.F., Sano, Y., Yang, T.F., Takahata, N., Shirai, K., and Pinti, D.L. 2010. Evaluating Earth degassing in subduction zones by measuring helium fluxes from the ocean floor. Earth and Planetary Science Letters, 298: 317–322. doi:10.1016/j.epsl.2010.07.049.

Laurent, O., Guitreau, M., Bruand, E., and Moyen, J.-F. 2024. At the dawn of continents: Archean Tonalite-Trondhjemite-Granodiorite Suites. Elements, 20: 174–179. doi:10.2138/gselements.20.3.174.

Lenardic, A., Moresi, L., Jellinek, A.M., O'Neill, C.J., Cooper, C.M., and Lee, C.T. 2011. Continents, supercontinents, mantle thermal mixing, and mantle thermal isolation: Theory, numerical simulations, and laboratory experiments: Continents and mantle thermal mixing. Geochemistry, Geophysics, Geosystems, 12. doi:10.1029/2011GC003663.

Mareschal, J.-C., and Jaupart, C. 2006. Archean thermal regime and stabilization of the cratons. In Geophysical Monograph Series. American Geophysical Union, Washington, D. C. pp. 61–73. doi:10.1029/164GM06.

Martin, H., Smithies, R.H., Rapp, R., Moyen, J.-F., and Champion, D. 2005. An overview of adakite, tonalite–trondhjemite–granodiorite (TTG), and sanukitoid: relationships and some implications for crustal evolution. Lithos, 79: 1–24. doi:10.1016/j.lithos.2004.04.048.

McDonough, W.F., and Sun, S.-S. 1995. The composition of the Earth. Chemical Geology,: 223–253.

Morgan, P. 1985. Crustal radiogenic heat production and the selective survival of ancient continental crust. Journal of Geophysical Research, 90: C561. American Geophysical Union (AGU). doi:10.1029/jb090is02p0c561.

Moyen, J.-F. 2011. The composite Archaean grey gneisses: Petrological significance, and evidence for a non-unique tectonic setting for Archaean crustal growth. Lithos, 123: 21–36. doi:10.1016/j.lithos.2010.09.015.

Moyen, J.-F., and Martin, H. 2012. Forty years of TTG research. Lithos, 148: 312–336. doi:10.1016/j.lithos.2012.06.010.

Mulder, J.A., and Cawood, P.A. 2022. Evaluating preservation bias in the continental growth record against the monazite archive. Geology, 50: 243–247. doi:10.1130/G49416.1.

O'Neill, C., Lenardic, A., Moresi, L., Torsvik, T.H., and Lee, C.-T.A. 2007. Episodic precambrian subduction. Earth and Planetary Science Letters, 262: 552–562. doi:10.1016/j.epsl.2007.04.056.

Palin, R.M., White, R.W., and Green, E.C.R. 2016. Partial melting of metabasic rocks and the generation of tonalitic–trondhjemitic–granodioritic (TTG) crust in the Archaean: Constraints from phase equilibrium modelling. Precambrian Research, 287: 73–90. doi:10.1016/j.precamres.2016.11.001.

Parman, S.W. 2007. Helium isotopic evidence for episodic mantle melting and crustal growth. Nature, 446: 900–903. doi:10.1038/nature05691.

Pearson, D.G., Parman, S.W., and Nowell, G.M. 2007. A link between large mantle melting events and continent growth seen in osmium isotopes. Nature, 449: 202–205. doi:10.1038/nature06122.

Rampino, M.R., and Prokoph, A. 2013. Are mantle plumes periodic? Eos, Transactions American Geophysical Union, 94: 113–114. doi:10.1002/2013EO120001.

Roberts, N.M.W. 2012. Increased loss of continental crust during supercontinent amalgamation. Gondwana Research, 21: 994–1000. doi:10.1016/j.gr.2011.08.001.

Robin, C.M.I., and Bailey, R.C. 2009. Simultaneous generation of Archean crust and subcratonic roots by vertical tectonics. Geology, 37: 523–526. doi:10.1130/G25519A.1.

Rollinson, H. 2010. Coupled evolution of Archean continental crust and subcontinental lithospheric mantle. Geology, 38: 1083–1086. doi:10.1130/G31159.1.

Smithies, R.H. 2000. The Archaean tonalite–trondhjemite–granodiorite (TTG) series is not an analogue of Cenozoic adakite. Earth and Planetary Science Letters, 182: 115–125. doi:10.1016/S0012-821X(00)00236-3.

Stein, M., and Hofmann, A.W. 1994. Mantle plumes and episodic crustal growth. Nature, 372: 63–68. doi:10.1038/372063a0.

Takahashi, E., Shimazaki, T., Tsuzaki, Y., and Yoshida, H. 1993. Melting study of a peridotite KLB-1 to 6.5 GPa, and the origin of basaltic magmas. Philosophical Transactions of the

Royal Society of London. Series A: Physical and Engineering Sciences, 342: 105–120. doi:10.1098/rsta.1993.0008.

Tang, M., Chen, K., and Rudnick, R.L. 2016. Archean upper crust transition from mafic to felsic marks the onset of plate tectonics. Science, 351: 372–375. doi:10.1126/science.aad5513.

Taylor, S.R., and McLennan, S.M. 1986. The chemical composition of the Archaean crust. Geological Society, London, Special Publications, 24: 173–178. doi:10.1144/GSL.SP.1986.024.01.16.

Taylor, S.R., and McLennan, S.M. 1995. The geochemical evolution of the continental crust. Reviews of Geophysics, 33: 241–265. doi:10.1029/95RG00262.

Vitorello, I., and Pollack, H.N. 1980. On the variation of continental heat flow with age and the thermal evolution of continents. Journal of Geophysical Research, 85: 983. doi:10.1029/JB085iB02p00983.

Von Huene, R., and Scholl, D.W. 1991. Observations at convergent margins concerning sediment subduction, subduction erosion, and the growth of continental crust. Reviews of Geophysics, 29: 279–316. doi:10.1029/91RG00969.

Wang, X.-C., Wilde, S.A., Li, Z.-X., Li, S., and Li, L. 2020. Do supercontinent-superplume cycles control the growth and evolution of continental crust? Journal of Earth Science, 31: 1142–1169. doi:10.1007/s12583-020-1077-4.

Xiang, H., and Connolly, J.A.D. 2022. GeoPS: An interactive visual computing tool for thermodynamic modelling of phase equilibria. Journal of Metamorphic Geology, 40: 243–255. doi:10.1111/jmg.12626.

Zhong, X., Li, Z.-H., and Wang, Y. 2024. Evaluation of plume-induced continental crust growth rate in early Earth: Insight from integrated petrological-thermo-mechanical modeling. Precambrian Research, 410: 107506. doi:10.1016/j.precamres.2024.107506.

Zhu, X.K., and O'Nions, R.K. 1999. Monazite chemical composition: some implications for monazite geochronology. Contributions to Mineralogy and Petrology, 137: 351–363. doi:10.1007/s004100050555.

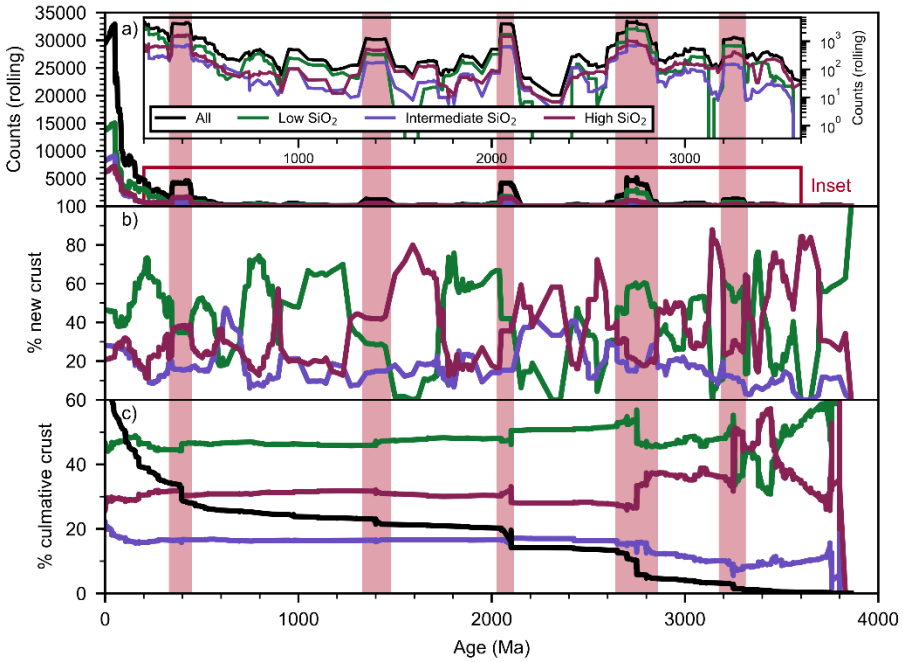


Figure 3.1: Age–composition summary of Keller and Schoene (2018) database; all lines are calculated using a moving median bin of 100 Ma. (a) Number of whole-rock samples for different silica contents. The inset shows all data >200 Ma. (b) Percentage of samples from the various silica content groups through time. (c) Cumulative counts of samples (black line) and the percentage of these samples allocated to the three silica groups. Shaded vertical fields highlight the time and duration of high counts and are interpreted as pulses of crustal building.

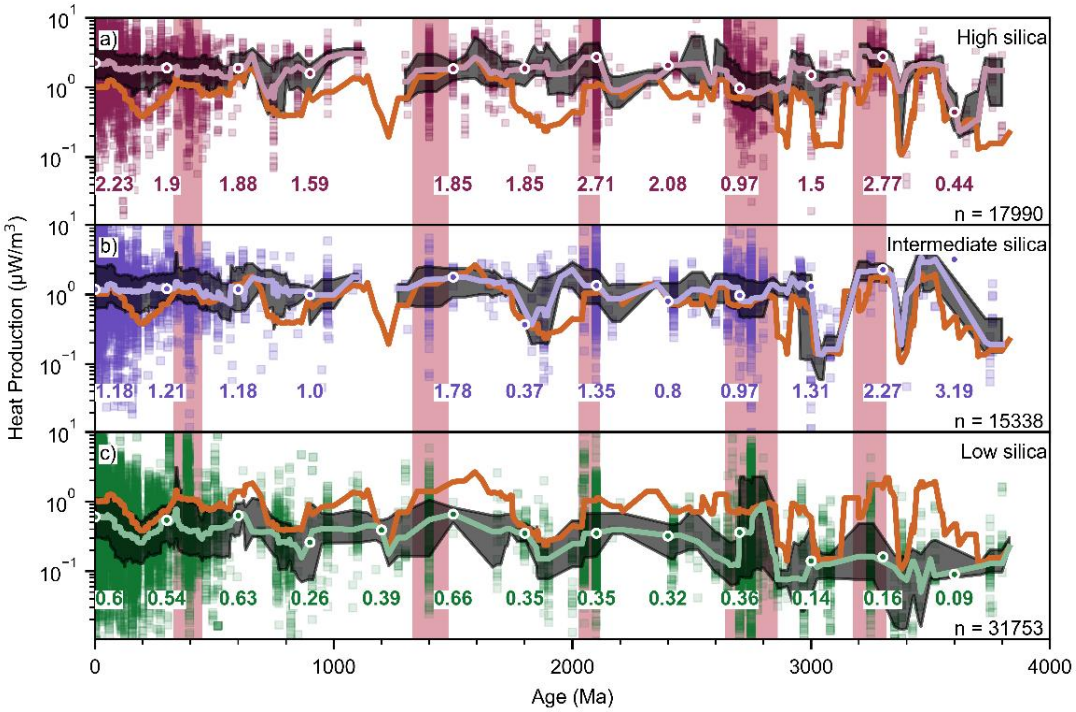


Figure 3.2: Age-corrected heat production of (a) high, (b) intermediate, and (c) low silica compositions through time. A moving median (bin = 100 Ma) is shown for each enclosed in a black field showing the interquartile range. The median of the entire database is shown for reference in orange in (a)–(c). Bold numbers denote the moving median at that time (circle marker). The vertical shaded fields are the same as in Figure 3.1.

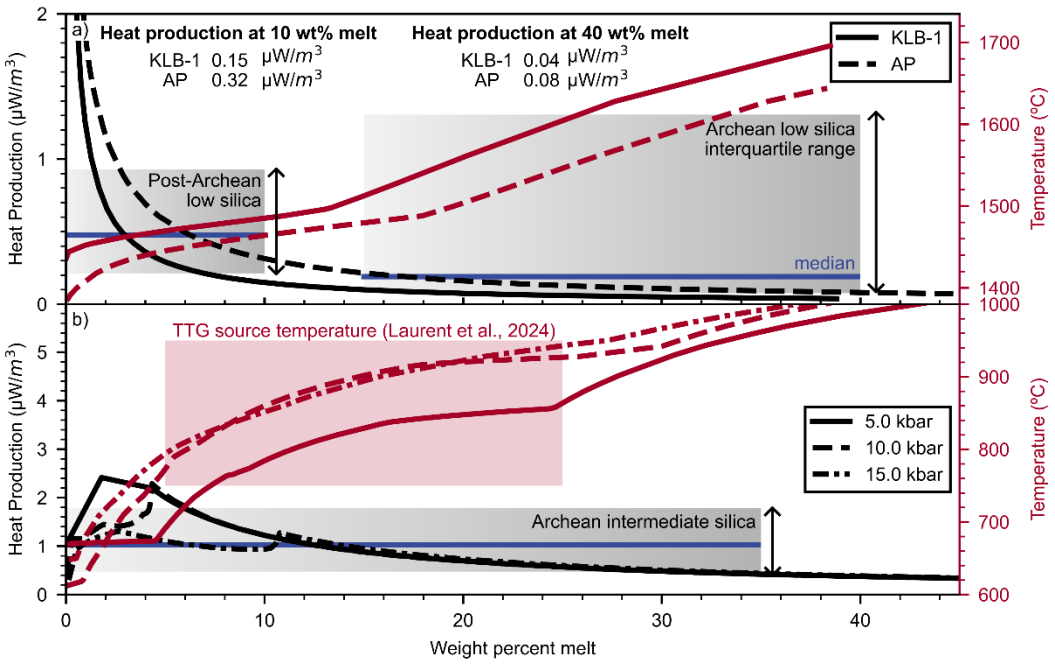


Figure 3.3: Modelled heat production of the melt and temperature against melt fraction of (a) modern (KLB-1) and Archean (AP) mantle (ρ=3.0 g/cm^3) for 20 kbar and (b) enriched Archean tholeiite (ρ=2.85 g/cm^3) for 5, 10, and 15 kbar. The grey box is the interquartile range of heat production of (a) low and (b) intermediate silica compositions with the median denoted by a solid blue line. The red box in (b) denotes the temperatures of TTG generation (Laurent et al. 2024). The width of grey boxes denotes source melting of modern (Keller and Schoene 2018) and Archean (Herzberg 1992, Rollinson 2010, Keller and Schoene 2018) basalts and Archean TTGs (Palin et al. 2016, Laurent et al. 2024).

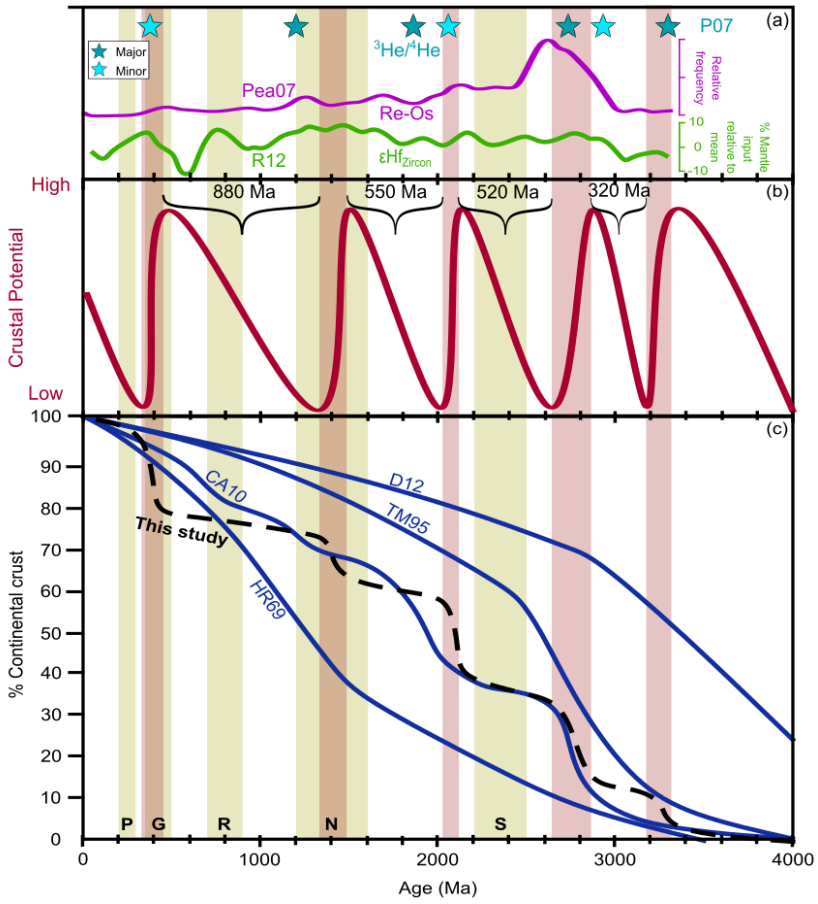


Figure 3.4: (a) Frequency curves for Re-Os model ages of southern African cratonic peridotites (Pea07; Pearson et al. 2007) and primitive εHf_{zircon} (R12; Roberts 2012) signatures with stars denoting proposed periods of major and minor crustal growth based on combined $^3He/^4He$ basalt and U–Pb zircon data (P07; Parman 2007). (b) Schematic diagram showing the proposed crustal potential of the mantle through time. (c) Published crustal growth curves with proposed semi-quantitative curves corresponding to crustal building pulses. The red bars are from Figures 3.1 and 3.2; the yellow fields correspond to supercontinents from Bradley (2011). P–Pangea, G–Gondwana, R–Rodinia, N–Nuna, S–Superia/Sclavia. HR69–Hurley and Rand 1969, CA10–Cawood and Aster (2010), TM95–Taylor and McLennan (1995), D12–Dhuime et al. (2012).

Chapter 4.0: High-titanium zircon rims in rhyolite—a reflection of adiabatic ascent?

Summary

Autocrystic zircon formed during magma crystallization provides crucial information for understanding the long-term evolution of the Earth's crust. Due to the factors that control zircon solubility in silicate melt (e.g. temperature and melt composition), zircon crystallization may occur during magma ascent, emplacement, and eruption. Zircon sourced from volcanic rocks can have rims with elevated concentrations of titanium relative to zircon cores; this has been linked to temperature changes associated with recharge events in magma chambers. An alternative cause of temperature shifts in subvolcanic systems is adiabatic ascent without magma mixing or recharge. Here, we simulate the adiabatic ascent of rhyolitic magmas to model the growth and dissolution of zircon during ascent from the mid-crust to sub-volcanic depths and access the Ti-in-zircon record. Decompression melting and system expansion drive cooling before fluid saturation; sub-volcanic boiling induces magma crystallization and heating. Zircon growth is predicted throughout ascent for both A- and S-type magmas. Our results suggest that high-titanium rims of autocrystic zircon can form through the protracted evolution of a single magmatic pulse without the need for magmatic recharge.

4.1 Introduction

Understanding the igneous and metamorphic processes that produce rhyolite volcanism requires applying mineral compositions as a proxy for system parameters and composition. As zircon is a ubiquitous accessory mineral in felsic to intermediate igneous rocks, zircon crystallized during ascent (autocrysts; Miller et al. 2007) is used as a record of thermochemical changes in a melt parcel (Claiborne et al. 2010a, Chen et al. 2021). One common proxy is the increasing affinity of Ti in zircon with increasing temperature (Ferry and Watson 2007). Ti-in-zircon thermometry is commonly used to infer the injection of magma pulses in the building of composite magmas (Miller et al. 2007, Schaltegger et al. 2009) and sub-volcanic recharge (Barboni et al. 2016, Yan et al. 2018, Chen et al. 2021). However, one aspect of magma transport and emplacement that is commonly overlooked using Ti-in-zircon thermometry is the isentropic, or adiabatic, ascent of felsic magma before emplacement in sub-volcanic magma chambers and subsequent eruption (Glazner 2019).

Magma ascends through the crust at rates between 10^{-8}–10^{-2} m/s (Brown 1994, Clemens 2005, Brugger and Hammer 2010); considering the low thermal conductivity of geologic materials, this process is effectively adiabatic (Clemens and Mawer 1992, Glazner 2019). As an isolated system, temperature variations are only internally derived; changes in pressure result in changing volume (hence internal energy) and pressure-sensitive phase stability will consume or release heat during fusion or fission, respectively (Blundy et al. 2006, Hale et al. 2007, Glazner 2019). Although recharge is observable in active magma chambers (e.g. Chang et al. 2007), this rearrangement of energy during adiabatic ascent may also produce resolvable temperature changes and deserves investigation.

In this contribution, we evaluate how internal processes can affect emplacement temperature and how this can be recorded in autocrystic zircon. We model A- and S-type magmas forming in the middle to lower crust that subsequently ascend adiabatically to subvolcanic levels. We explore various concentrations of H_2O in silicate melt and evaluate the predicted Ti-in-zircon concentrations that crystallize from these magmas during ascent. Our results provide an alternative mechanism for high-titanium rims on zircon in volcanic rocks, and we discuss the implications for understanding volcanic–magmatic systems, zircon growth from source to eruption, as well as the use and limitations of Ti-in-zircon thermometry.

4.2 Methodology

Ascent of A-type (Clemens et al. 1986) and S-type (Scaillet et al. 1995) granitic magma was modelled from 7 to 0.3 kbar with 0.1 kbar resolution representing a mid-crustal source and subvolcanic emplacement. A-type magmas are assumed to be formed through amphibole melting at 850°C (Clemens et al. 1986), whereas S-type magmas are produced through biotite melting (825°C; Clemens and Wall 1981). These experimentally determined starting conditions agree well with a database of 253 A-type and 187 S-type zircon saturation temperatures of natural granites (Appendix 3.1). We use rhyolite-MELTS version 1.1x (Gualda et al. 2012) implemented through the easyMELTS program. System water contents of 1, 3, and 6 wt% H_2O are considered; anhydrous compositions are reported in Table 4.1. Both the A-type and S-type initial compositions were assumed to be saturated in Zr with respect to zircon (in both melt and major minerals) from the source (Table 4.2); we also present zircon saturation models of varying amounts of saturation from the source.

Zircon solubility was simulated using the calculated composition of the modelled melt and temperature. The saturation concentration of Zr (with respect to zircon) was calculated using the expression of Boehnke et al. (2013), assuming the stoichiometric amount of Zr in zircon to be 497,600 mg/kg. This expression refines that of Harrison and Watson (1983) and carries an uncertainty of 2–25%. Zirconium concentrations in minerals and melt were calculated using mass balance (e.g. Hanson,1980) and distribution coefficients of Bacon and Druitt (1988), with mineral weight fractions from the easyMELTS output. If the concentration of Zr in the melt was predicted to be greater than the saturation concentration, the excess Zr was divided by the concentration in zircon (497600 mg/kg) to calculate the weight fraction of zircon. If zircon was predicted to be stable, the concentration of titanium in zircon was calculated using the Ti-in-zircon thermometer of Ferry and Watson (2007). Though this thermometer has multiple calibrations (e.g. Borisov and Aranovich 2020), Ferry and Watson's (2007) expression is the most cited and presents the most relatable results. Quartz is expected to be present throughout crystallization, and therefore, a_{SiO2} (relative to quartz) is set to 1 for all modelled scenarios. Modelling a_{TiO2} is more complex because of the absence of rutile in the assemblage. The MELTS uses the rutile melting point from Samsonov (1973), which mislabelled temperature units; therefore, rutile is unlikely to be predicted by the model (Borisov and Aranovich 2020). This results in unrealistically low a_{TiO2} values predicted by the MELTS model. Experiments of A-(Clemens et al. 1986) and S-type (Clemens and Wall 1981, Scaillet et al. 1995) magmas do not report rutile, though it is noted in some natural granitic systems (e.g. Antunes et al. 2008, Yadav et al. 2020). Therefore, we consider a range of a_{TiO2} values that envelop those expected during granitoid melt crystallization.

4.3 Results

4.3.1 Natural titanium in zircon zoning

We present titanium concentrations of zircon from 70 natural samples (1810 analyses) comprising both rim and core analyses of (assumed) autocrystic zircons from rhyolites and subvolcanic granites as a benchmark for modelling results (see Appendix S3.2). In general, zircon cores—inferred to be older than the rims—have concentrations of Ti that vary from 2.5 to 35.1 mg/kg; rims vary from 3.1 to 30.3 mg/kg. Considering the variability between volcanic suites, comparing the differences between the cores and rims of individual zircon is more useful.

Differences between concentrations of titanium in rims and cores of zircon typically range from -20 to 36 mg/kg (median of -0.7 mg/kg), indicating that cores with greater Ti concentrations compared to the rims (inferred as cooling) are more common than vice versa.

Converting concentrations of Ti to the temperature of zircon growth/equilibration requires an assumption of a_{TiO2} relative to rutile. Differences in apparent temperature for a realistic range of a_{TiO2} values are shown in Fig. 4.1b. The temperature difference becomes more extreme for lower a_{TiO2} values. For a system with low a_{TiO2} (0.4), the temperature discrepancy can range from -118 to 92°C, with a median of -10°C. In contrast, a system with a_{TiO2} = 0.7 could have zircon rims recording temperatures from -104 °C to 82°C relative to the core, with a median value of -9°C. When rutile is present (a_{TiO2} = 1), the temperature difference between the rim and the core can range from -97 to 77°C, with a median difference of -8°C.

Assuming a_{TiO2} is not appreciably different during the growth of cores and rims in autocrystic zircon, most core–rim comparisons show that the rims generally record lower temperatures than the cores; this is expected for protracted zircon crystallization during cooling. However, ~40% of zircon records higher temperatures in rims than cores. These suggest an increase in temperature during the evolution of the magmatic–volcanic system that could represent magma recharge (e.g. hot magmas injecting into the chamber from below (Caricchi et al. 2021); or an isochemical increase in temperature during ascent. We discuss the effects of transient a_{TiO2} later.

4.3.2 Temperature changes during adiabatic ascent

All modelled adiabats undergo cooling during ascent before boiling, crystallization, and heating initiating at ~0.8–1.8 kbar (Fig. 4.2); H_2O-rich compositions undergo boiling and crystallization earlier in the ascent path. For both A- and S-type magmas, the most hydrous magmas reach the highest temperature during crystallization, and the driest compositions have the least change in temperature. In contrast, the composition with 3 wt% H_2O has the most significant cooling and undergoes the most considerable difference in temperature during ascent. For brevity, we focus on the 3 wt% H_2O systems as they are most realistic (discussed later) but present 1 and 6 wt% results as end-member cases, making mention of when appropriate.

A-type magmas with 3 wt% H_2O start ascent with 61 wt% melt, cool to 803°C at 1 kbar (82 wt% melt), with subsequent heating to 879°C (0.3 kbar, 4 wt% melt). Comparatively, the S-type magma initially contained 52 wt% melt before cooling to a thermal minimum of 785°C (1.4 kbar) and a melt maximum of 68 wt% melt preceding the peak temperature of 827°C at 0.3 kbar depth with 18 wt% melt. The 1 wt% H_2O systems start as 21 wt% and 20 wt% melt for A- and S-type, respectively, compared to 98 wt% and 93 wt% for the 6 wt% systems. All compositions are predicted to reach their thermal peaks simultaneously with the minimum pressure and proportion of melt. In contrast, the lowest predicted temperatures are associated with the maximum amount of melt.

4.3.3 Thermodynamic Properties of the System

An adiabatic system has two mechanisms that change temperature: 1) internal energy is used to compress or expand the system (through pressure-volume work), or 2) changes of state (e.g. melting or crystallization) release or consume the latent heat of fusion. The temperature change resulting from the crystallization or melting of mineral assemblages can be estimated by dividing the heat of fusion (ΔH_f) by the heat capacity (C_P) of minerals and multiplying the resultant by the cumulative weight proportion of the phase crystallized or melted. This represents the maximum absolute temperature change due to a change in state. The modelled temperature change predicted by EasyMELTS (ΔT_{model}) is subtracted from this "heat of fusion temperature change" ($T_{\Delta Hf}$) to approximate the change in temperature due to internal energy work ($T_{\Delta U}$); $\Delta T_{model} = T_{\Delta H_f} + T_{\Delta U};\ therefore,\ T_{\Delta U} = \Delta T_{model} - T_{\Delta H_f}$. The expression $T_m = \frac{T_{\Delta H_f}}{T_{\Delta U}}$ Indicates the dominant mechanism for temperature change. If $T_m > 0$, then $T_{\Delta U}$ and $T_{\Delta Hf}$ are heating or cooling the system. If $T_m < 0$ indicates one mechanism is using energy (cooling) and the other mechanism is providing some energy (heating); if $-1<T_m<1$ (denoted by grey shaded area on Fig. 4.3a and b), then pressure-volume work influences temperature more than changes in state.

Aside from some modelling anomalies discussed later, the temperature change from using internal energy is predicted to be negative for both S- and A-type compositions and all water contents (Fig. 4.3a, b). The temperature change is expected to be less than 2ºC per 0.1 kbar interval and negative before crystallization, during which the predicted temperature change from pressure-volume work is between -1ºC and -12ºC. In general, the expected $T_{\Delta U}$ increases with water content and is greater for A-type granites compared to S-type granites. T_m is predicted to

be positive during ascent before fluid saturation as both pressure-volume work and decompression melting of entrained crystals use energy and decrease temperature. Once fluid is exsolved from the magma, crystallization commences (Fig. 4.2), and T_m became negative (Fig. 4.3a, b). The T_m of the 6 wt% H_2O magmas are between -1 and 1 before crystallization, whereas the T_m for magmas with 3 or 1 wt% H_2O is generally >>1 or <<-1.

The coefficient of expansivity describes the positive volume change with increasing temperature, and the coefficient of compressibility describes the negative volume change with increasing pressure—expansivity and compressibility for modelled phases are presented in Figure 3d. The expansivity and compressibility coefficients of the melt are greater than the solids; however, it is greatest for fluid (H_2O) by a factor of ~100. Therefore, systems with more melt (and H_2O; Fig. 4.2) will use more energy through pressure-volume work than through changes in state due to greater expansivity/compressibility and therefore, temperature change is driven mainly by using internal energy ($-1<T_m<1$; Fig. 4.3a, b). However, regardless of composition during crystallization, the latent heat of fusion is the primary driver of temperature change.

4.3.4 Zircon growth during crystallization

Zircon solubility decreases with decreasing temperature, M value—a proxy for Zr-alkali complexing (Watson 1979)—and, as Zr is generally incompatible in rock-forming minerals, melt proportion. The model predicts a decrease in M-value throughout ascent, which is coupled with decreasing temperature to decrease zirconium solubility—leading to zircon growth—during ascent. The increasing stability of zircon is slightly buffered by increasing melt proportion before boiling; however, only H_2O-poor compositions undergo significant melting during ascent (Fig. 4.2). As such if the system is saturated in Zr at the source, zircon is generally predicted to crystallize throughout the ascent (right-hand side plots in Fig. 4.4); a greater proportion of zircon is predicted to record heating in S-type magmas compared to A-type. If the melt is undersaturated in Zr at the source, a greater proportion of zircon records heating. We present scenarios where the magma is 100, 90, and 80% saturated in Zr at the source.

For a dry (1 wt% H_2O) A-type magma saturated in Zr at the source, 90% of zircon formed during cooling compared to 95% in the moderately hydrated composition and 70% in the H_2O-rich composition. If the melt is 80% saturated at the source in Zr, the dry A-type magma is

not expected to crystallize zircon before eruption. 30% and 60% of zircon in 3 wt% and 6 wt% H_2O A-type magmas are predicted to record heating at 80% saturation of Zr at the source.

As zircon is expected to be partially resorbed during the ascent of a dry (1 wt% H_2O; Fig. 4.4b) S-type magma, <10% of zircon is expected to record cooling if saturated in Zr at the source; if the melt is undersaturated at the source, all zircon will record heating. Comparatively, ~50% and 90% of zircon are expected to record heating in S-type magma with 3 wt% H_2O either 100% or 80% saturated in Zr at the source, respectively. For an S-type magma with 6 wt% H_2O, 60% and >90% of zircon are expected to record heating if 100% or 80% saturated in Zr, respectively. A reference for zircon volume is presented in Figure 4.4g; red dashed lines denote 10 vol%, and the three grey shaded zones are 1/3 vol% so that Ac=Am=Ar.

During decompression cooling and subsequent crystallization-driven heating, the concentration of Ti in zircon is expected to decrease, followed by an increase (Fig. 4.4). Moderately hydrated (3 wt% H_2O) compositions are predicted to exhibit the most significant relative difference between core and rim Ti concentrations. In the case of the 1 wt% H_2O A-type magma (Fig. 4.4a), the Ti concentration initially decreases to 77% of the starting content before rising to 98%. This would correspond to a zircon with 16 mg/kg decreasing to 12 mg/kg and increasing to 16 mg/kg with an a_{TiO2} = 0.6 or 27 mg/kg decreasing to 21 mg/kg and finishing at 26 mg/kg titanium if rutile is present (i.e. a_{TiO2} = 1.0). Conversely, the H_2O-rich A-type composition (Fig. 4.4e) with an a_{TiO2}= 0.6 is expected to start with 16 mg/kg Ti (27 mg/kg; values in brackets are if a_{TiO2} = 1) and decrease to 10 (17) mg/kg before subsequent heating increasing the titanium concentration to 19 (32) mg/kg. Similarly, in the moderately hydrated composition (3 wt%), the Ti concentration in zircon was modelled to decrease from 16 to 10 (27 to 17) mg/kg and increase during crystallization to 19 (32) mg/kg (Fig. 4.4c).

Zircon in an S-type magma with 1 wt% H_2O and a_{TiO2} = 0.6 only records heating with a final Ti concentration of 11 mg/kg (19.7 mg/kg if a_{TiO2} = 1). The “starting” concentration is measured at 0.9 kbar as zircon was expected to be wholly dissolved and reprecipitated during ascent (Fig. 4.4b). In contrast, the H_2O-rich (6 wt%) S-type composition is predicted to see a decrease to 10.2 mg/kg from the initial Ti concentration of 13.1 mg/kg before subsequent heating elevated it to 14.83 mg/kg (17.1, 21.8, and 24.7 mg/kg if a_{TiO2} = 1). For the moderately hydrated

composition (3 wt%), the Ti concentration in zircon is predicted to start at 13.1 (21.6) mg/kg and decline to 9.0 (15.0) mg/kg, followed by an increase to 13.4 (22.3) mg/kg during crystallization.

4.4 Discussion

4.4.1 Limitations of the methodology

Several necessary assumptions were made to provide some insights into the consequences of the adiabatic ascent of magma on the concentrations of Ti in autocrystic zircon. The first set of assumptions relates to the limitations of the thermodynamic data and modelling program, whereas the other set relates to the simplification of magmatic systems.

The proportion and compositions of the phases are reliant on a confluence of factors, including the activity-composition models used in rhyolite-MELTS (Berman 1988, Gualda et al. 2012, Ghiorso and Gualda 2015) and the Gibbs-solving algorithm. Rhyolite-MELTS assumes ideal mixing behaviour, disregarding the complexities of non-ideal solid solution behaviours that occur in natural magmatic systems (Holland and Blundy 1994, Graphchikov et al. 1999, Abart et al. 2009). Further, the modelling software does not account for any kinetic processes, such as diffusion and nucleation, which are critical in the growth of crystals and overall magmatic evolution. Gualda et al. (2012) quantified the temperature discrepancy between the modelled and experimental invariant crystallization point to be 30–40°C. As the temperature discrepancies are likely systematic, they are considered a minor issue, and the entire model simulations could be up or down shifted 30–40°C with the difference in temperature along the ascent path being the same. Another slight discrepancy is the higher water content in modelled melts compared to experimental observations. Although thought to be a slight difference (Ghiorso and Gualda 2015), boiling at greater pressures in natural systems would initiate crystallization and subsequent heating—likely recorded by a greater proportion of zircon.

The modelling presented here is a simplistic view of complex natural volcanic–magmatic systems. Equilibrium is assumed throughout the ascent, which would entail crystallization (and melting) occurring faster than the ascent rate and complete chemical equilibration between minerals and melt. Granitic magmas ascend through dyking at rates of 10^{-8}–10^{-2} m/s (Clemens 2005, Rutherford 2008, Brugger and Hammer 2010), whereas quartz and feldspar crystallize at rates of 10^{-10}–10^{-9} m/s and degassing occurs at rates of 10^{-6}–10^{-4} m/s (Clemens 2005, La Spina et

al. 2016). Using these values, the modelled magmas would take 3 days to 8000 years to ascend from 7 kbar (25 km) to subvolcanic (0.3 kbar) depths. Considering that plagioclase can reach equilibrium with magma in the order of hours (La Spina et al. 2016) and phenocrysts are millimetres or centimetres in scale, it is possible for magma ascent can occur under equilibrium conditions (e.g. Clemens 2005, Rutherford 2008, Brugger and Hammer 2010).

Another simplification implemented in our modelling was that of an isochemical system, which excludes any wall rock–magma interaction such as thermal erosion. Although wall-rock assimilation in magma has been recorded, these instances are often either at deep crustal levels with already hot country rock (Perry et al. 1993) or assimilation by hot mantle-derived magmas (Hayes et al. 2015, Borisova et al. 2017). A parcel of granitic magma rising from 7 to 0.3 kbar presents an energetics problem as it does not contain enough thermal energy to assimilate significant amounts of crustal material without fully crystallizing or becoming too viscous (Kerr et al. 1995, Thompson 2002, Glazner 2007) and is therefore considered a minor issue.

Another simplification of this study is the assumption that the magma chamber is either quite shallow and/or the magma does not spend any significant time in the magma chamber. Although subvolcanic storage is common (Ishii 1991, Allard 1997, Pasqualon et al. 2020), it often occurs at pressures of 2.0 ± 0.5 kbar (Huber et al. 2019) before ascent. If this does occur, it is still possible for the model results of 2–0.1 kbar to be valid when the magma reaches volcanic levels. In this scenario, the magma is still expected to heat up after storage and before eruption due to the loss of a fluid phase—this relationship is explored in detail later.

The models presented assume the parcel of melt is separated from the source saturated in zirconium and all initial zircon is antecrystic. Granite magmas are generally undersaturated in Zr (with respect to zircon) at the source (Siégel et al. 2018, Clemens et al. 2020) which would delay the crystallization of autocrystic zircon and ultimately result in a greater proportion of zircon recording crystallization-driven heating; this relationship is shown in Fig. 4.4. Further, inherited zircons are common in granitic magmas and can be the only population of zircons in some granitic compositions (Siégel et al. 2018, Olierook et al. 2020). In this case, epitaxial growth will record the ascent of magma but will require chemical investigation such as Hf content, rare earth element patterns, Th/U ratios, and age, if possible.

We have simulated granitic magma across a spectrum of water contents to encompass the variation observed in natural rhyolite samples. Erupted rhyolites range from effectively anhydrous to containing ~5 wt% H_2O (Di Muro et al. 2006, Wadsworth et al. 2020)—however, the typical range for natural rhyolites falls between 1.5 and 3.5 wt% H_2O. A-type magmas generally contain 2–4 wt% H_2O (Clemens et al. 1986, Hervig et al. 1989), which is comparable to or slightly less than S-type magmas (Clemens and Wall 1981, Mo et al. 2023). For this reason, it can be assumed that the models with 3 wt% H_2O presented here are the most representative of the average rhyolite with the dry (1 wt% H_2O) and H_2O-rich model results being extreme end-member cases. For comparison, magma at the Alid Volcanic Center in Eritrea intruded a shallow chamber (2–4 km; 0.5–1.25 kbar) at approximately 870°C with 2.6 wt% H_2O (Lowenstern et al. 1997); our A-type model with 3 wt% H_2O predicts temperatures ranging from 805 to 845°C at these pressures. Considering boiling-driven crystallization is delayed in the models and the models are often downshifted 30–40ºC, the temperatures of the Alid Volcanic Center suggest that the system is nearing or experiencing boiling and is comparable to our models.

Our models have minor modelling artefacts for compositions with low (1 wt%) and high (6 wt%) H_2O for both compositions. The most hydrated A-type magma is expected to undergo boiling at pressures less than 2.3 kbar however is not expected to heat up until <1.1 kbar (Fig. 4.2a); comparatively, all other compositions undergo heating at the boiling pressure (Fig. 4.2). This is likely explained by expansion of fluid and melt being greater than the heat of crystallization (T_m; Fig. 4.3a). The hydrous A-type magma is predicted to be closest to the liquidus compared to all other compositions and undergo minor (<2 wt%) melting during post-boiling cooling. Another inconsistency is the fluctuations in $T_{\Delta U}$ (and T_m) between negative and positive values (Fig. 4.3a, b) that are followed by an equal and opposite oscillation for the dryest modelled magmas before boiling. These oscillations correlate with aluminium partitioning between feldspar and spinel, the former releasing double the latent heat of fusion than the latter (Holland and Powell 1998). This sporadic stability of spinel at the expense of feldspar—based on Gibbs Free Energy minimization—is likely due to the adjusted enthalpies for feldspar to better fit experimental data and similar crystallization temperatures of spinel and feldspar (Gualda et al. 2012). A final inconsistency in the modelling is the complete dissolution of zircon before boiling for the 1 wt% H_2O S-type magma. This is due to the minor (<2 wt%) orthopyroxene going from product to reactant during ascent and the low solubility of Zr in orthopyroxene. Orthopyroxene

has a lower Zr distribution coefficient than feldspar, and therefore, the consumption of orthopyroxene has a lower impact on the bulk distribution coefficient of Zr. An additional consequence is a greater relative proportion of feldspar in the normalized bulk coefficient. The fluctuations are likely unrealistic; however, the overall trend of the models aligns well between water contents, and the most representative composition (3 wt% H2O) is without these inconsistencies, indicating a broad realism in the results.

We present the concentration of Ti in zircon as a proxy for temperature using the expression of Ferry and Watson (2007). This thermometer was calibrated using experimental and natural data across 580–1070ºC and 7–30 kbar with an uncertainty of 10–15ºC or 0.5–3 mg/kg of Ti in zircon ($0.4< a_{TiO2}<1$), uncertainty increasing with temperature. These temperatures span those predicted by the models (Fig. 4.2) though we model pressure conditions outside the calibration (Watson et al. 2006); a change in pressure on the order of 10 kbar would underestimate temperature estimates by ~50ºC or 2–20 mg/kg of Ti for $0.4< a_{TiO2}<1$. Although the models presented in Fig. 4 assume a constant activity of titania, a_{TiO2} is transient with changing temperature, pressure, and throughout crystallization (Thomas and Watson 2012, Ghiorso and Gualda 2013). Minor changes in a_{TiO2}, on the order of 0.05–0.1, during cooling could counterintuitively produce high Ti rims during pre-boiling ascent. Although the a_{TiO2} predicted by MELTS is erroneous (Borisov and Aranovich 2020), a_{TiO2} is expected to increase as the magma undergoes crystallization (i.e. during heating), which agrees with natural and experimental data (Fonseca Teixeira et al. 2024). This increase in titania activity could counteract any decrease in Ti concentration predicted before boiling and crystallization.

In summary, there are several necessary assumptions in the modelling, and there remain some artefacts in the results for the more extreme compositions (e.g. 1 and 6 wt% H_2O systems). Nonetheless, these are not expected to change the general results and broader implications of the modelling. We now use these model results to explore the consequences of inferring magmatic–volcanic processes from the zircon archive.

4.4.2 Thermodynamic reasoning of the adiabat

As an adiabatic system is isolated, all changes in enthalpy (and temperature) are due to pressure-volume work or changes in state (melting/crystallization; Glazner 2019). Without a change in state, expansion or compression distributes the same energy across greater or smaller volumes resulting

in heating or cooling respectively ($d\Delta H = PdV$). The changing equilibrium with pressure and resultant reactions produces an adiabat following $\frac{dT}{dP} = \frac{V}{\gamma C_V} + \frac{d\Delta H}{C_V dP}$, where γ is the adiabatic index and C_V is the heat capacity at a constant volume (opposed to C_P, which is at constant pressure). Changes in state are energetically expensive—the production of silicate melts requires 900–4000 kJ/mol (Holland and Powell 1998)—and are reversible in isolated systems. The heat consumed or released due to a change in state is described by $\Delta H = c_p \Delta T$. If we take the greatest ΔH of 2285 J and the lowest heat capacity (121 J/K), a 19 K change in temperature is expected whereas the temperature change with the greatest heat capacity (138 J/K) corresponds with a 17 K temperature change—this 2 K difference indicates that ΔH is a greater determinator of temperature change than heat capacity.

The models presented predict minimal pressure-volume work as the change in volume is <0.1 J/bar between 100 bar increments: expansion work results in cooling (Fig. 4.3a, b). The pressure-volume work done by the system increases with the separation of a fluid phase as the compressibility of the fluid is orders of magnitude greater than for melt and solid phases (Fig. 4.3c). The change in volume before boiling ranges from 0.1–0.5 J/bar for a 0.1 kbar change, although it increases to 2–4 J/bar after fluid separation (Fig. 4.3a, b). Altogether, this expansion provides cooling to the system, however, temperature change is either more negative than pressure-volume work can account for or predict a positive temperature change (during crystallization; Fig. 4.2); these discrepancies are due to $T_{\Delta H}$.

Before fluid release, decompression melting of entrained crystals consumes heat and causes a decrease in temperature. However, boiling of H_2O from the melt increases the solidus temperature (Holtz et al. 2001), encouraging crystallization (Fig. 4.2). As H_2O is an order of magnitude more compressible and expandable (Fig. 4.3c), pressure-volume work increases dramatically after boiling when the fluid phase is in equilibrium with the magma; though crystallization supplies significantly more energy (T_m<<-1 Fig. 4.3a, b). Before boiling-driven crystallization, the most hydrous magmas are predicted to change temperature largely due to the use of internal energy more so than from the heat of fusion (-1<T_m<1, Fig. 4.3a, b). This is likely due to the large expansivity of water (Fig. 4.3c)—even if it is dissolved in melt—coupled with the small changes in melt proportion before H_2O saturation. In contrast, the temperature changes of 1 wt% H_2O compositions are expected to be driven by a change of state. A particularly notable model

result is 3 wt% H_2O magmas reaching the lowest temperature (785ºC) whereas the 1 wt% and 6 wt% magmas cool to similar temperatures (±5ºC) of each other. This trend is likely explained by greater overall change in state predicted for the 3 wt% composition considering wet magmas have limited possible pre-boiling fission (initially >90% melt) and dry magmas are closer to their solidus conditions.

4.4.3 What does zircon record?

High titanium rims in rhyolites are often used as evidence for subvolcanic magmatic recharge (e.g. Claiborne et al. 2010, Chen et al. 2021) or the building of composite plutons (Claiborne et al. 2010b). Magma recharge is thought to be required to maintain a partially molten state at shallow depths (Townsend and Huber 2020), though the feasibility of maintaining a shallow magma chamber is questioned (Annen 2011). Claiborne et al. (2010) argue that zircon from Mount St. Helens records protracted (>100 ka) magma accumulation and storage before eruption with repeated rejuvenation and reheating. However, maintaining a molten state at shallow crustal conditions may require >10 km of crustal thickening—a process which is not recorded (Glazner 2021). Chen et al. (2021) consider similar U-Pb ages for high Ti-rims and low Ti-cores to record multiple pulses of magma in the formation of high-silica rhyolites. Similarly, Bolhar et al. (2008) argue that U-Pb ages spanning >10 Ma recording temperature reversals are evidence for the building of shallow magma chambers via the repeated injection of hotter magma to maintain a molten state. Ultimately, understanding the different mechanisms responsible for the high Ti rims in zircon will help provide greater geologic context and allow for better interpretation of trace element data.

For systems with 3 wt% H_2O—the most representative of natural systems modelled here—<10% of zircon crystallizing during the ascent of an A-type magma was predicted to record heating compared to >50% of zircon in S-type magmas (Fig. 4.4). However, due to the nature of rim thickness misleading the volume (Fig. 4.4g), 10% and 50% volume would be reflected as 3% and 25% of the cross-sectional thickness of a zircon grain. However, these zircon proportions likely represent a minimum as there are a few processes that could result in a greater amount of zircon to record heating. We consider a parcel of melt remaining isochemical and in equilibrium throughout the ascent. If hydrofracturing removes fluid from boiling (e.g. Oliver et al. 2006), crystallization would still occur as the solidus of the magma is shifted up in

temperature during dehydration. Similarly, crystal settling or filter pressing separates solids from the rest of the system, inducing a new equilibrium state (Petford 2003, Fernández and Castro 2018). Generally, melt becomes increasingly hydrous during fractionation as anhydrous minerals are crystallized earlier than hydrous minerals (Petrelli et al. 2018); the increasing water content will lead to earlier boiling and crystallization-driven heating.

Recent appreciation for the adiabatic crystallization of granitic systems (Thomas and Watson 2012, Glazner 2019) has provided an isochemical mechanism for the heating, which may be recorded in zircon grains. The models presented in this study predict a temperature change of 11ºC to 31ºC from the source temperature and 15–86 ºC from the coldest temperature along the adiabat. Specifically, the moderately hydrated (3 wt% H_2O) A- and S-type compositions are predicted to experience a cooling of 47ºC and 40ºC, respectively, before subsequently warming by 76ºC and 42ºC. During this ascent, ~10% of zircon in A-type and ~50% of zircon in S-type magma record late-stage heating. Of the compositions modelled, the 3 wt% H_2O system provides the greatest variability in temperature, though a greater proportion of zircon is expected to record heating in more hydrous magmas due to the colder solidus (e.g. Clemens and Wall 1981). However, these values are likely minimums as granitic magmas are generally considered undersaturated in Zr at the source (Siégel et al. 2018, Clemens et al. 2020), and the modelling program tends to predict fluid saturation at lower pressures than natural or experimental results (Ghiorso and Gualda 2015). Further, a greater proportion of A-type magmas are expected to record cooling compared to S-type. We speculate this is due to a greater change in M-value during cooling for the A-type granite (1.45 to 1.39 or 5.8% change for 3 wt% H_2O) than that for the S-type composition (1.1–1.07 or 3% change for 3 wt% H_2O) coupled with a greater (i.e. earlier) boiling pressure (Fig. 4.2) predicted for the S-type granite.

As the 3 wt% H_2O modelled compositions are likely the most representative of natural eruptive rhyolites (Clemens and Wall 1981, Clemens et al. 1986, Hervig et al. 1989, Mo et al. 2023), some high titanium rims on zircon are not necessarily the result of subvolcanic replenishment but may record adiabatic ascent of magma. Although magma recharge is a viable mechanism for high Ti rims and certainly occurs, we propose an isochemical reasoning for high Ti rims on zircons found in some rhyolites—boiling-driven crystallization. Using a suite of trace

elements such as Hf content or rare earth element patterns in zircon paired with geochronology are likely useful tools in determining between ascent vs recharge rims in natural systems.

4.5 Conclusion

Zircon crystallization during magma emplacement offers valuable insights into the dynamic processes shaping Earth's upper crust. Our study highlights the importance of discerning the temporal relationship of magma ascent, emplacement, and eruption with zircon growth. The models presented here provide a theoretical framework for pairing the growth and titanium content in zircon with the ascent and emplacement of magma. During ascent, the system undergoes cooling as internal work and decompression melting consume thermal energy before fluid saturation. Boiling-induced crystallization contributes to heat generation, resulting in magma entering a subvolcanic chamber hotter than the source region. The modelling predicts that zircon growth is continuous during the ascent of both A- and S-type magmas, regardless of the water content variations. This underscores the utility of zircon as a valuable tool for tracing the origin and emplacement of rhyolites. Significant zircon growth is predicted during the heating of the most realistic water contents, resulting in paradoxically thin rims enriched with titanium. Therefore, the utilization of trace elements and age constraints is recommended to discern if zircons are autocrystic and if high titanium rims formed through processes in an isolated (adiabatic ascent) or open (magma recharge) system.

4.6 References

Abart, R., Petrishcheva, E., Käßner, S., and Milke, R. 2009. Perthite microstructure in magmatic alkali feldspar with oscillatory zoning; Weinsberg Granite, Upper Austria. Mineralogy and Petrology, 97: 251–263. doi:10.1007/s00710-009-0090-1.

Allard, P. 1997. Endogenous magma degassing and storage at Mount Etna. Geophysical Research Letters, 24: 2219–2222. doi:10.1029/97GL02101.

Annen, C. 2011. Implications of incremental emplacement of magma bodies for magma differentiation, thermal aureole dimensions and plutonism–volcanism relationships. Tectonophysics, 500: 3–10. doi:10.1016/j.tecto.2009.04.010.

Bacon, C.R., and Druitt, T.H. 1988. Compositional evolution of the zoned calcalkaline magma chamber of Mount Mazama, Crater Lake, Oregon. Contributions to Mineralogy and Petrology, 98: 224–256. doi:10.1007/BF00402114.

Barboni, M., Boehnke, P., Schmitt, A.K., Mark Harrison, T., Shane, P., Bouvier, A.S., and Baumgartner, L. 2016. Warm storage for arc magmas. Proceedings of the National Academy of Sciences of the United States of America, 113: 13959–13964. doi:10.1073/pnas.1616129113.

Berman, R.G. 1988. Internally-consistent thermodynamic data for minerals in the system Na_2O-K_2O-CaO-MgO-FeO-Fe_2O_3-Al_2O_3-SiO_2-TiO_2-H_2O-CO_2. Journal of Petrology, 29: 445–522. doi:10.1093/petrology/29.2.445.

Blundy, J., Cashman, K., and Humphreys, M. 2006. Magma heating by decompression-driven crystallization beneath andesite volcanoes. Nature, 443: 76–80. doi:10.1038/nature05100.

Boehnke, P., Watson, E.B., Trail, D., Harrison, T.M., and Schmitt, A.K. 2013. Zircon saturation re-revisited. Chemical Geology, 351: 324–334. Elsevier B.V. doi:10.1016/j.chemgeo.2013.05.028.

Bolhar, R., Weaver, S.D., Palin, J.M., Cole, J.W., and Paterson, L.A. 2008. Systematics of zircon crystallisation in the Cretaceous Separation Point Suite, New Zealand, using U/Pb isotopes, REE and Ti geothermometry. Contributions to Mineralogy and Petrology, 156: 133–160. doi:10.1007/s00410-007-0278-5.

Borisov, A., and Aranovich, L. 2020. Rutile solubility and TiO_2 activity in silicate melts: An experimental study. Chemical Geology, 556: 119817. doi:10.1016/j.chemgeo.2020.119817.

Borisova, A.Y., Bohrson, W.A., and Grégoire, M. 2017. Origin of primitive ocean island basalts by crustal gabbro assimilation and multiple recharge of plume-derived melts. Geochemistry, Geophysics, Geosystems, 18: 2701–2716. doi:10.1002/2017GC006986.

Brown, M. 1994. The generation, segregation, ascent and emplacement of granite magma: the migmatite-to-crustally-derived granite connection in thickened orogens. Earth Science Reviews, 36: 83–130. doi:10.1016/0012-8252(94)90009-4.

Brugger, C.R., and Hammer, J.E. 2010. Crystallization kinetics in continuous decompression experiments: Implications for interpreting natural magma ascent processes. Journal of Petrology, 51: 1941–1965. doi:10.1093/petrology/egq044.

Caricchi, L., Townsend, M., Rivalta, E., and Namiki, A. 2021. The build-up and triggers of volcanic eruptions. Nature Reviews Earth & Environment, 2: 458–476. doi:10.1038/s43017-021-00174-8.

Chen, S.R., Wang, Q., Zhu, D.C., Weinberg, R.F., Zhang, L.L., and Zhao, Z.D. 2021. Reheating and magma mixing recorded by zircon and quartz from high-silica rhyolite in the Coqen region, southern Tibet. American Mineralogist, 106: 112–122. doi:10.2138/am-2020-7426.

Claiborne, L.L., Miller, C.F., Flanagan, D.M., Clynne, M.A., and Wooden, J.L. 2010a. Zircon reveals protracted magma storage and recycling beneath Mount St. Helens. Geology, 38: 1011–1014. doi:10.1130/G31285.1.

Claiborne, L.L., Miller, C.F., and Wooden, J.L. 2010b. Trace element composition of igneous zircon: a thermal and compositional record of the accumulation and evolution of a large silicic batholith, Spirit Mountain, Nevada. Contributions to Mineralogy and Petrology, 160: 511–531. doi:10.1007/s00410-010-0491-5.

Clemens, J.D. 2005. Granites and granitic magmas: strange phenomena and new perspectives on some old problems. Proceedings of the Geologists' Association, 116: 9–16. doi:10.1016/S0016-7878(05)80013-6.

Clemens, J.D., Holloway, J., and White, A.J.R. 1986. Origin of an A-type granite: Experimental constraints. American Mineralogist, 71: 317–324.

Clemens, J.D., and Mawer, C.K. 1992. Granitic magma transport by fracture propagation. Tectonophysics, 204: 339–360. doi:10.1016/0040-1951(92)90316-X.

Clemens, J.D., Stevens, G., and Bryan, S.E. 2020. Conditions during the formation of granitic magmas by crustal melting – Hot or cold; drenched, damp or dry? Earth-Science Reviews, 200: 102982. doi:10.1016/j.earscirev.2019.102982.

Clemens, J.D., and Wall, V.J. 1981. Origin and crystallization of some peraluminous (S-Type) granitic magmas. Canadian Mineralogist, 19: 111–131.

Di Muro, A., Villemant, B., Montagnac, G., Scaillet, B., and Reynard, B. 2006. Quantification of water content and speciation in natural silicic glasses (phonolite, dacite, rhyolite) by confocal microRaman spectrometry. Geochimica et Cosmochimica Acta, 70: 2868–2884. doi:10.1016/j.gca.2006.02.016.

Fernández, C., and Castro, A. 2018. Mechanical and structural consequences of magma differentiation at ascent conduits: A possible origin for some mafic microgranular enclaves in granites. Lithos, 320–321: 49–61. doi:10.1016/j.lithos.2018.09.004.

Ferry, J.M., and Watson, E.B. 2007. New thermodynamic models and revised calibrations for the Ti-in-zircon and Zr-in-rutile thermometers. Contributions to Mineralogy and Petrology, 154: 429–437. doi:10.1007/s00410-007-0201-0.

G. Pasqualon, N., Savian, J.F., F. Lima, E., R. Luz, F., R. Moncinhatto, T., and F. Trindade, R.I. 2020. Emplacement dynamics of alkaline volcanic and subvolcanic rocks in Trindade Island, Brazil. Journal of Volcanology and Geothermal Research, 406: 107078. doi:10.1016/j.jvolgeores.2020.107078.

Ghiorso, M.S., and Gualda, G.A.R. 2013. A method for estimating the activity of titania in magmatic liquids from the compositions of coexisting rhombohedral and cubic iron–titanium oxides. Contributions to Mineralogy and Petrology, 165: 73–81. doi:10.1007/s00410-012-0792-y.

Ghiorso, M.S., and Gualda, G.A.R. 2015. An H_2O–CO_2 mixed fluid saturation model compatible with rhyolite-MELTS. Contributions to Mineralogy and Petrology, 169: 53. doi:10.1007/s00410-015-1141-8.

Glazner, A.F. 2007. Thermal limitations on incorporation of wall rock into magma. Geology, 35: 319. doi:10.1130/G23134A.1.

Glazner, A.F. 2019. The ascent of water-rich magma and decompression heating: A thermodynamic analysis. American Mineralogist, 104: 890–896. De Gruyter Open Ltd. doi:10.2138/am-2019-6925.

Glazner, A.F. 2021. Thermal constraints on the longevity, depth, and vertical extent of magmatic systems. Geochemistry, Geophysics, Geosystems, 22: e2020GC009459. doi:10.1029/2020GC009459.

Graphchikov, A.A., Konilov, A.N., and Clemens, J.D. 1999. Biotite dehydration, partial melting, and fluid composition; experiments in the system $KAlO_2$ -FeO-MgO-SiO_2 -H_2O-CO_2. American Mineralogist, 84: 15–26. doi:10.2138/am-1999-1-202.

Gualda, G.A.R., Ghiorso, M.S., Lemons, R. V., and Carley, T.L. 2012. Rhyolite-MELTS: A modified calibration of MELTS optimized for silica-rich, fluid-bearing magmatic systems. Journal of Petrology, 53: 875–890. doi:10.1093/petrology/egr080.

Hale, A.J., Wadge, G., and Mühlhaus, H.B. 2007. The influence of viscous and latent heating on crystal-rich magma flow in a conduit: Viscous and latent heating in crystal-rich magma. Geophysical Journal International, 171: 1406–1429. doi:10.1111/j.1365-246X.2007.03593.x.

Hanson, G.N. 1980. Rare earth elements in petrogenetic studies of igneous systems. Annual Review of Earth and Planetary Sciences, 8: 371–406. doi:10.1146/annurev.ea.08.050180.002103.

Harrison, T.M., and Watson, E.B. 1983. Kinetics of zircon dissolution and zirconium diffusion in granitic melts of variable water content. Contributions to Mineralogy and Petrology, 84: 66–72. doi:10.1007/BF01132331.

Hayes, B., Bédard, J.H., Hryciuk, M., Wing, B., Nabelek, P., MacDonald, W.D., and Lissenberg, C.J. 2015. Sulfide immiscibility induced by wall-rock assimilation in a fault-guided basaltic feeder system, Franklin Large Igneous Province, Victoria Island (Arctic Canada). Economic Geology, 110: 1697–1717. doi:10.2113/econgeo.110.7.1697.

Hervig, R.L., Dunbar, N., Westrich, H.R., and Kyle, P.R. 1989. Pre-eruptive water content of rhyolitic magmas as determined by ion microprobe analyses of melt inclusions in phenocrysts. Journal of Volcanology and Geothermal Research, 36: 293–302. doi:10.1016/0377-0273(89)90075-9.

Holland, T., and Blundy, J. 1994. Non-ideal interactions in calcic amphiboles and their bearing on amphibole-plagioclase thermometry. Contributions to Mineralogy and Petrology, 116: 433–447. doi:10.1007/BF00310910.

Holland, T.J.B., and Powell, R. 1998. An internally consistent thermodynamic data set for phases of petrological interest. Journal of Metamorphic Geology, 16: 309–343. doi:10.1111/j.1525-1314.1998.00140.x.

Holtz, F., Johannes, W., Tamic, N., and Behrens, H. 2001. Maximum and minimum water contents of granitic melts generated in the crust: a reevaluation and implications. Lithos, 56: 1–14. doi:10.1016/S0024-4937(00)00056-6.

Huber, C., Townsend, M., Degruyter, W., and Bachmann, O. 2019. Optimal depth of subvolcanic magma chamber growth controlled by volatiles and crust rheology. Nature Geoscience, 12: 762–768. doi:10.1038/s41561-019-0415-6.

Ishii, T. 1991. Lava-flow and subvolcanic magma reservoir composition trends in the Ca-poor pyroxenes of Hakone Volcano, Japan. Journal of Petrology, 32: 429–450. doi:10.1093/petrology/32.2.429.

Kerr, A.C., Kempton, P.D., and Thompson, R.N. 1995. Crustal assimilation during turbulent magma ascent (ATA); new isotopic evidence from the Mull Tertiary lava succession, N. W. Scotland. : 142–154.

La Spina, G., Burton, M., De' Michieli Vitturi, M., and Arzilli, F. 2016. Role of syn-eruptive plagioclase disequilibrium crystallization in basaltic magma ascent dynamics. Nature Communications, 7: 13402. doi:10.1038/ncomms13402.

Linnen, R.L. 1998. Depth of emplacement, fluid provenance and metallogeny in granitic terranes: a comparison of western Thailand with other tin belts. Mineralium Deposita, 33: 461–476.

Lowenstern, J.B., Clynne, M.A., and Bullen, T.D. 1997. Comagmatic A-Type granophyre and rhyolite from the Alid Volcanic Center, Eritrea, Northeast Africa. Journal of Petrology, 38.

Mildren, S.D., and Sandiford, M. 1995. Heat refraction and low-pressure metamorphism in the northern flinders ranges, south australia. Australian Journal of Earth Sciences, 42: 241–247. doi:10.1080/08120099508728198.

Miller, J.S., Matzel, J.E.P., Miller, C.F., Burgess, S.D., and Miller, R.B. 2007. Zircon growth and recycling during the assembly of large, composite arc plutons. Journal of Volcanology and Geothermal Research, 167: 282–299. doi:10.1016/j.jvolgeores.2007.04.019.

Mo, J., Xia, X.-P., Li, P.-F., Spencer, C.J., Lai, C.-K., Xu, J., Yang, Q., Sun, M.-D., Yu, Y., and Milan, L. 2023. Water-in-zircon: a discriminant between S- and I-type granitoid. Contributions to Mineralogy and Petrology, 178: 5. doi:10.1007/s00410-022-01986-7.

Moyen, J.F., Janoušek, V., Laurent, O., Bachmann, O., Jacob, J.B., Farina, F., Fiannacca, P., and Villaros, A. 2021. Crustal melting vs. fractionation of basaltic magmas: Part 1, granites and paradigms. Lithos, 402–403. Elsevier B.V. doi:10.1016/j.lithos.2021.106291.

Olierook, H.K.H., Kirkland, C.L., Szilas, K., Hollis, J.A., Gardiner, N.J., Steenfelt, A., Jiang, Q., Yakymchuk, C., Evans, N.J., and McDonald, B.J. 2020. Differentiating between inherited and autocrystic zircon in granitoids. Journal of Petrology, 61: egaa081. doi:10.1093/petrology/egaa081.

Oliver, N.H.S., Rubenach, M.J., Fu, B., Baker, T., Blenkinsop, T.G., Cleverley, J.S., Marshall, L.J., and Ridd, P.J. 2006. Granite-related overpressure and volatile release in the mid crust: fluidized breccias from the Cloncurry District, Australia. Geofluids, 6: 346–358. doi:10.1111/j.1468-8123.2006.00155.x.

Perry, F.V., DePaolo, D.J., and Baldridge, W.S. 1993. Neodymium isotopic evidence for decreasing crustal contributions to Cenozoic ignimbrites of the western United States: Implications for the thermal evolution of the Cordilleran crust. Geological Society of America Bulletin, 105: 872–882. doi:10.1130/0016-7606(1993)105<0872:NIEFDC>2.3.CO;2.

Petford, N. 2003. Rheology of granitic magmas during ascent and emplacement. Annual Review of Earth and Planetary Sciences, 31: 399–427. doi:10.1146/annurev.earth.31.100901.141352.

Petford, N., Cruden, A.R., Mccaffrey, K.J.W., and Vigneresse, J.-L. 2000. Granite magma formation, transport and emplacement in the Earth's crust. Nature, 408. Available from www.nature.com.

Petford, N., Kerr, R.C., and Lister, J.R. 1993. Dike transport of granitoid magmas. Geology, 21: 845–848. doi:10.1130/0091-7613(1993)021<0845:DTOGM>2.3.CO;2.

Petford, N., Lister, J.R., and Kerr, R.C. 1994. The ascent of felsic magmas in dykes. Lithos, 32: 161–168. doi:10.1016/0024-4937(94)90028-0.

Petrelli, M., El Omari, K., Spina, L., Le Guer, Y., La Spina, G., and Perugini, D. 2018. Timescales of water accumulation in magmas and implications for short warning times of explosive eruptions. Nature Communications, 9: 770. doi:10.1038/s41467-018-02987-6.

Rutherford, M.J. 2008. Magma ascent rates. Reviews in Mineralogy and Geochemistry, 69: 241–271. doi:10.2138/rmg.2008.69.7.

Samsonov, G.V. 1973. The Oxide Handbook. Springer US, Boston, MA.

Scaillet, B., Pichavant, M., and Roux, J. 1995. Experimental crystallization of leucogranite magmas. Journal of Petrology, 36: 663–705. doi:10.1093/petrology/36.3.663.

Schaltegger, U., Brack, P., Ovtcharova, M., Peytcheva, I., Schoene, B., Stracke, A., Marocchi, M., and Bargossi, G.M. 2009. Zircon and titanite recording 1.5 million years of magma accretion, crystallization and initial cooling in a composite pluton (southern Adamello batholith, northern Italy). Earth and Planetary Science Letters, 286: 208–218. Elsevier B.V. doi:10.1016/j.epsl.2009.06.028.

Schorn, S., Diener, J.F.A., Powell, R., and Stüwe, K. 2018. Thermal buffering in the orogenic crust. Geology, 46: 643–646. doi:10.1130/G40246.1.

Siégel, C., Bryan, S.E., Allen, C.M., and Gust, D.A. 2018. Use and abuse of zircon-based thermometers: A critical review and a recommended approach to identify antecrystic zircons. Earth-Science Reviews, 176: 87–116. doi:10.1016/j.earscirev.2017.08.011.

Sizova, E., Gerya, T., Stüwe, K., and Brown, M. 2015. Generation of felsic crust in the Archean: A geodynamic modeling perspective. Precambrian Research, 271: 198–224. Elsevier. doi:10.1016/j.precamres.2015.10.005.

Teixeira, L.M.F., Troch, J., and Bachmann, O. 2024. The dynamic nature of aTiO_2: Implications for Ti-based thermometers in magmatic systems. Geology, 52: 92–96. doi:10.1130/G51587.1.

Thomas, J.B., and Watson, E.B. 2012. Application of the Ti-in-quartz thermobarometer to rutile-free systems. Reply to: a comment on: 'TitaniQ under pressure: the effect of pressure and temperature on the solubility of Ti in quartz'. Contributions to Mineralogy and Petrology, 164: 369–374. doi:10.1007/s00410-012-0761-5.

Thompson, A.B. 2002. Some thermal constraints on crustal assimilation during fractionation of hydrous, mantle-derived magmas with examples from Central Alpine Batholiths. Journal of Petrology, 43: 403–422. doi:10.1093/petrology/43.3.403.

Townsend, M., and Huber, C. 2020. A critical magma chamber size for volcanic eruptions. Geology, 48: 431–435. doi:10.1130/G47045.1.

Wadsworth, F.B., Llewellin, E.W., Vasseur, J., Gardner, J.E., and Tuffen, H. 2020. Explosive-effusive volcanic eruption transitions caused by sintering. Science Advances, 6: eaba7940. doi:10.1126/sciadv.aba7940.

Watson, E.B. 1979. Zircon saturation in felsic liquids: Experimental results and applications to trace element geochemistry. Contributions to Mineralogy and Petrology, 70: 407–419. doi:10.1007/BF00371047.

Watson, E.B., Wark, D.A., and Thomas, J.B. 2006. Crystallization thermometers for zircon and rutile. Contributions to Mineralogy and Petrology, 151: 413–433. doi:10.1007/s00410-006-0068-5.

Yan, L.L., He, Z.Y., Beier, C., and Klemd, R. 2018. Zircon trace element constrains on the link between volcanism and plutonism in SE China. Lithos, 320–321: 28–34. Elsevier B.V. doi:10.1016/j.lithos.2018.08.040.

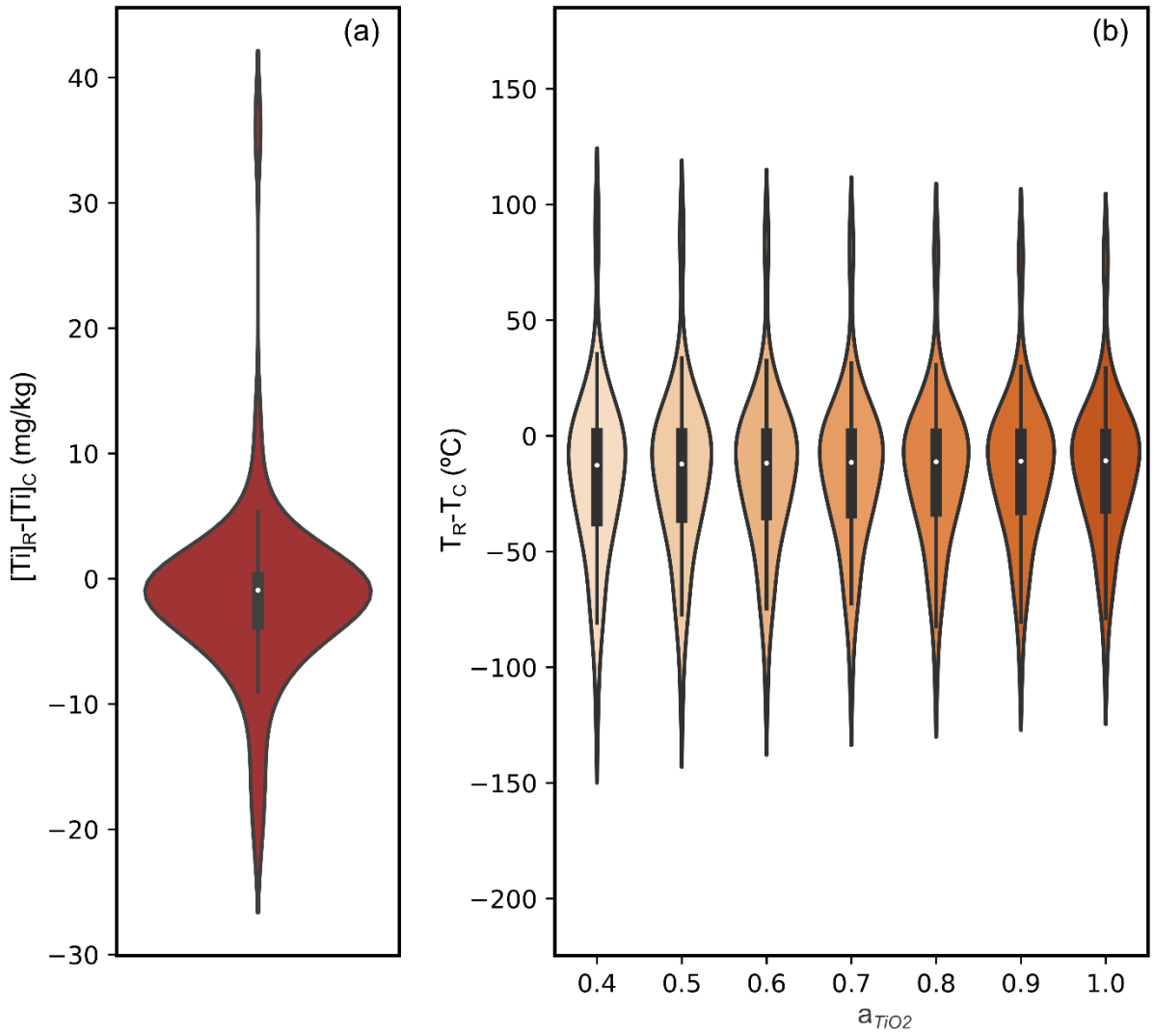


Figure 4.1: (a) Violin plots showing the difference of Ti concentration in the rim ($[Ti]_R$) to the core ($[Ti]_C$) of natural zircon samples. (b) The calculated apparent temperature difference between the rims (T_R) and cores (T_C) for a range of titania activities (a_{TiO2}). Boxes within violins extend from the first quartile (25%) to the third quartile (75%), whereas whiskers extend to 1.5x the interquartile range. Violin boundaries are kernel density lines representing the distribution of data. White dots show the median value.

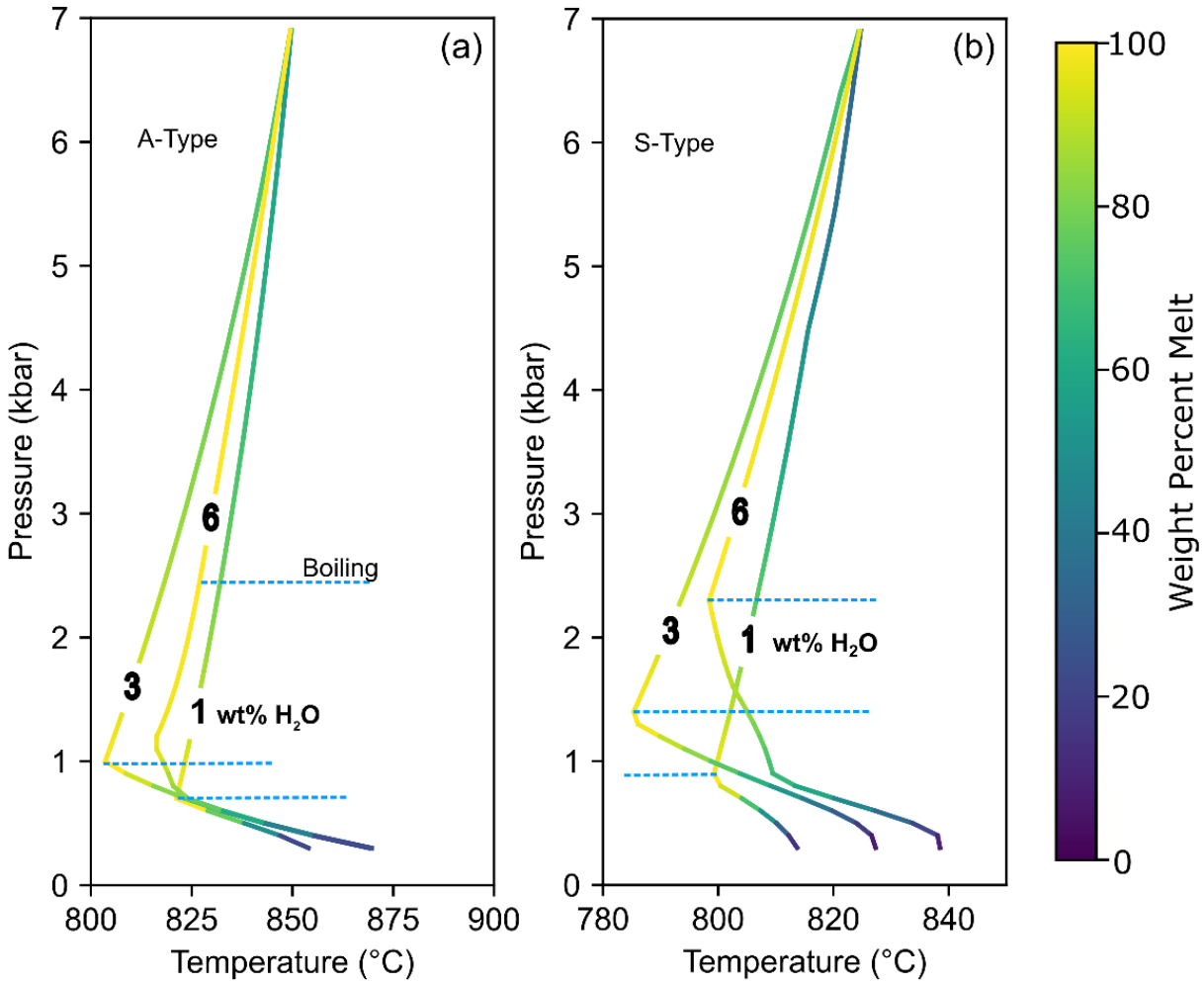


Figure 4.2: Pressure–temperature paths of A- and S-type magma ascending from 7 kbar to 0.3 kbar with 1 wt% H_2O, 3 wt% H_2O, and 6 wt% H_2O (bold numbers). The line colour corresponds to the proportion of melt in the system. The pressure of H_2O saturation is denoted by blue lines.

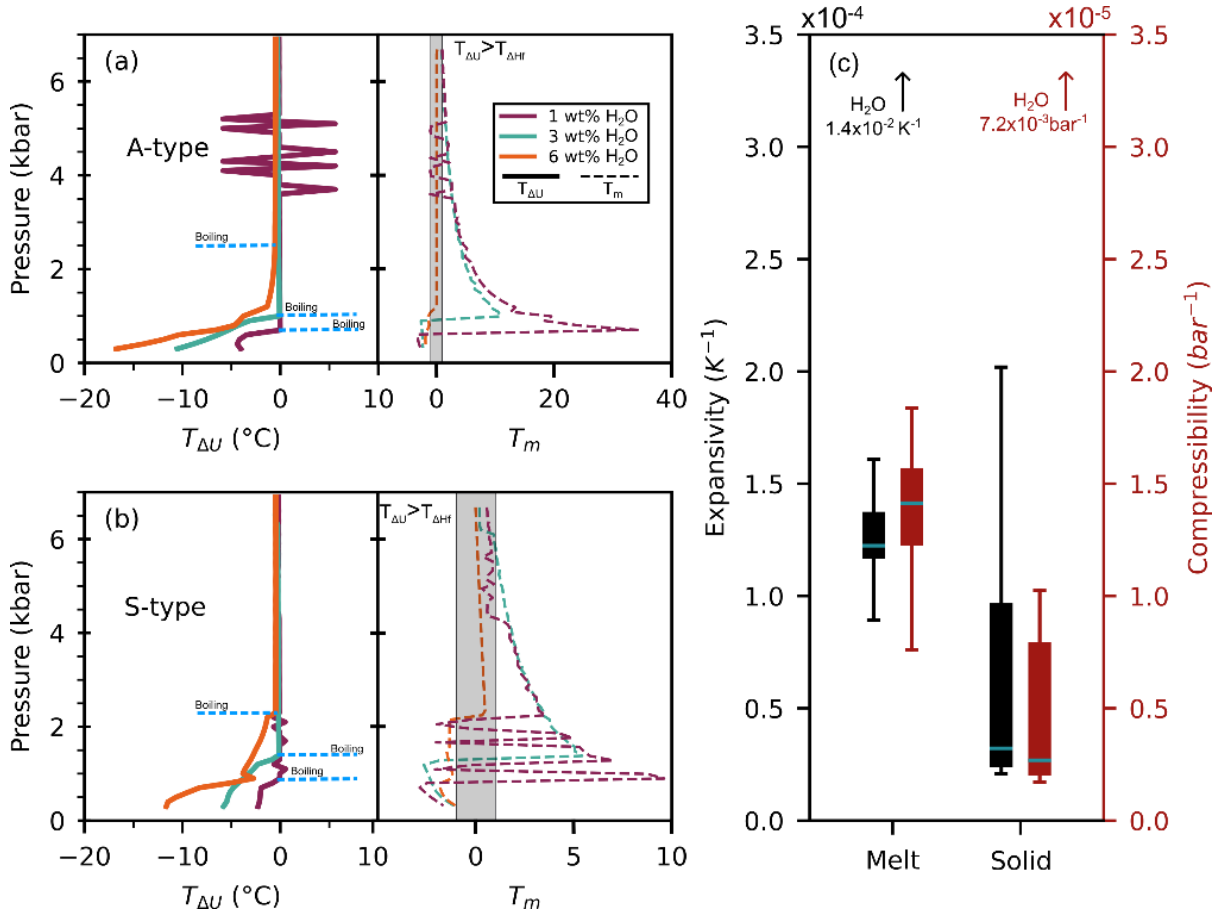


Figure 4.3: Predicted temperature change via pressure-volume work ($T_{\Delta U}$) during ascent (left-hand side) and the predicted temperature change from the heat of fusion ($T_{\Delta Hf}$) divided by $T_{\Delta U}$ (T_m; right-hand side) for (a) A-type and (b) S-type granitic magma during ascent (c) Expansivity and compressibility of melt and solid phases across all 6 model runs. Boxes extend from the first quartile (25%) to the third quartile (75%), whereas whiskers extend to 1.5x the interquartile range. Blue horizontal lines on (a) and (b) denote the pressure of H_2O saturation and boiling. The grey area on T_m plots indicates $-1<T_m<1$ where changes in internal energy are greater than those from the heat of fusion.

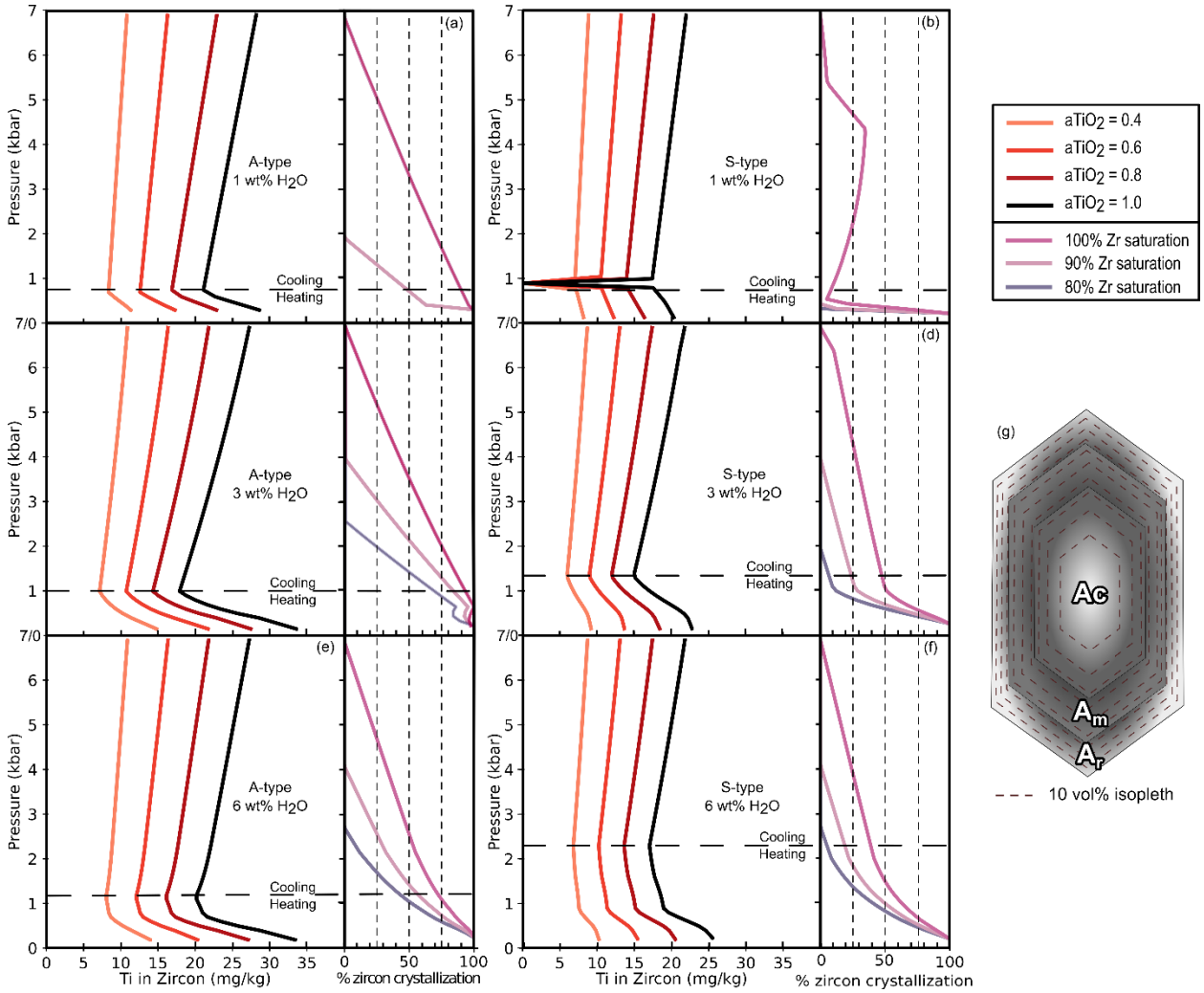


Figure 4.4: Predicted Ti-in-zircon for modelled magma ascent of A- and S-type magma with varying a_{TiO2}. The right-hand side plots show the percent of the maximum amount of zircon crystallized with varying initial Zr saturation at the source. (g) Representative schematic of titanium zoning in zircon. The volume of the three zones is equal (Ac=Am=Ar). Red dashed lines are 10 vol% contours. Due to a constant density, the area isopleths also represent weight percent isopleths.

Table 4.1: Modelled anhydrous compositions for A- and S-type granites (wt%). Compositions were reweighted to 1, 3, and 6 wt% H_2O.

	SiO_2	TiO_2	Al_2O_3	Fe_2O_3	FeO	MnO	MgO	CaO	Na_2O	K_2O
S-type (DK89)	73	0.13	15.32	0.17	0.7	0.01	0.2	0.85	3.85	4.96
A-type (GIG-1)	73.6	0.34	12.44	1.42	1.5	0.08	0.27	1.24	3.53	4.23

Table 4.2: Initial Zr concentrations (mg/kg) of the modelled melts.

	1 wt% H_2O	3 wt% H_2O	6 wt% H_2O
A-Type	512	460	434
S-Type	172	248	283

Chapter 5.0: The Frontenac Terrane— a record of advective ultra-high temperature metamorphism

Summary

Ultra-high temperature metamorphism is increasingly recognized as a common global process, though the source of sufficient heat for such extreme conditions is often enigmatic. The Frontenac Terrane records a unique tectonothermal history compared to other terranes in the southwestern Grenville Province. The Mesoproterozoic geology of the Frontenac Terrane includes the deposition of siliciclastic and carbonate sedimentary rocks intruded by several suites of mafic and felsic magmas, resulting in ultra-high temperature metamorphic conditions. Detrital zircon geochronology indicates that sedimentation was coeval in adjacent and distal terranes between ca 1390 and 1200 Ma. Geochemical discrimination of metasedimentary rocks in the Frontenac Terrane paired with lithological similarities with neighbouring terranes suggest sedimentation in a back-arc setting comparable to the modern Philippine Sea. The Frontenac Terrane experienced two-sided compression as a thrust belt formed between the Adirondack Lowlands and the Sharbot Lake Domain during the ca 1160 Ma Shawinigan orogeny. Magmatic activity—resulting from subduction and slab breakoff—before and during compression introduced significant heat-inducing (ultra-) high-temperature metamorphism at mid-crustal levels. Tectonic relaxation produced extensional folding followed by Ottawan (ca 1060 Ma) shortening and related plutonism. The Frontenac Terrane provides new insights into the evolution of the assembled terranes outboard Laurentia in the Mesoproterozoic and the mechanisms for ultra-high temperature metamorphism in compressional stress regimes.

5.1 Introduction

Ultra-high temperature metamorphism is increasingly recognized in a variety of tectonic settings as the thermal extreme of crustal conditions. However, ultra-high temperatures are generally associated with arc–backarc systems with either slab rollback, slab breakoff, slab window, or a subducting oceanic ridge as the responsible mechanism for the anomalously high temperatures (Jiao et al., 2023; Kelsey and Hand, 2015). Although thick highly radiogenic crust or lithospheric delamination and resulting upwelling asthenosphere are proposed to supply sufficient heat (Harley, 2016; Ueda et al., 2012). One mechanism commonly invoked to generate UHT

metamorphism, regardless of tectonic setting, is the intrusion of mafic magma (Giustina et al., 2011; Pownall et al., 2014). However, mafic magmatism coeval with UHT conditions is rarely observed (Kelsey and Hand, 2015). Some suggest that the hybridization of mantle-derived and crustal magmas can provide the necessary heat (Collins and Richards, 2008; Smithies et al., 2011)—although these are generally thought to occur in pre- or post-collisional environments. As mafic magmatism is uncommon in compression settings, a syn-collisional process to introduce sufficient heat to crustal levels remains enigmatic yet is required to explain the rock record in some hot orogenic systems.

The Grenville Province represents a transcontinental orogen formed through prolonged subduction-accretion processes along the Laurentian margin during the construction of Rodinia (Hynes and Rivers, 2010; Johnson et al., 2020; Rivers, 1997). Four orogenic events are recognized in the late Mesoproterozoic: Elzevirian (ca 1250–1190 Ma), Shawinigan (ca 1180–1140 Ma), Ottawan (ca 1090–1020 Ma), and Rigolet (ca 1010–980 Ma; Rivers 2008). However, the intensity and extent of these tectonic episodes vary spatially, with no single terrain recording all events (Chiarenzelli et al., 2011; McLelland et al., 2010; Rivers, 1997). The Frontenac Terrans is an undervalued region of the Grenville Province recording anomalous Shawinigan (ultra-) high-temperature metamorphism. Comparatively, neighbouring terranes of the Sharbot Lake Domain and Adirondack Lowlands record greenschist to upper amphibolite facies metamorphism. The Frontenac Terrane was thoroughly mapped in the mid-20th century (Currie and Ermanovics, 1971; Wynne-Edwards, 1967) with most subsequent work focused on the boundary sutures (Fig. 5.1) of the Maberly Mylonite (Hildebrand and Easton 1995, Corfu and Easton 1997) and Black Lake Shear zones (Russell 2009, Wong et al. 2011) as well as the petrogenesis of granitoid intrusions (Cutts, 2014; Dickin and Strong, 2021; Marcantonio et al., 1990; Peck et al., 2004). Consequently, there is a paucity of quantitative metamorphic data that is needed to link the evolution of the Frontenac Terrane with the causes of UHT metamorphism and the long-term evolution of the Laurentian margin before the Ottawan orogeny.

In this contribution, we present new regional field observations paired with petrographic and geochemical analyses that supplement historic work to provide a new interpretation of the evolution of the Frontenac Terrane. We use a combination of lithology, structural analysis, bulk-rock, mineral composition, and isotopic data to decipher the Proterozoic evolution of the

Frontenac Terrane and the Mesoproterozoic Laurentian margin and to assess the mechanisms for UHT metamorphism during crustal thickening.

5.2 Regional Geology

The Grenville Province exposed in Ontario and western Quebec can be broadly subdivided into 3 tectonic elements (inset Fig. 5.1): (1) Grenville Front Tectonic Zone, (2) Central Gneiss Belt, and (3) Central Metasedimentary Belt (Hynes and Rivers, 2010; Indares, 2024; Rivers, 2012). These broad divisions have been subdivided further on interpreted genetic relationships (e.g. Easton and Davidson 1994, Culshaw et al. 1997, Carr et al. 2000, Ketchum and Davidson 2000, Timmermann et al. 2002, Rivers 2008).

The Central Metasedimentary Belt is a patchwork of parallel, linear terranes—lithotectonic blocks denoted by unique tectono-lithologic relationships—composed of marbles and para- and ortho-gneisses metamorphosed at greenschist to granulite-facies conditions. Most terranes and domains of the Central Metasedimentary Belt have broadly synchronous metamorphism and deformation with the Central Gneiss Belt, resulting from the Ottawan orogeny (Cosca et al., 1992; Rivers, 1997; White et al., 2000). However, the Frontenac-Adirondack Belt is often discussed as being separated from the rest of the Central Metasedimentary Belt as it is dominated by Shawinigan-aged metamorphism with only a minor Ottawan overprint.

The Frontenac-Adirondack Belt is subdivided into the Frontenac Terrane, Adirondack Lowlands, and Adirondack Highlands—each bound by tectonic boundaries (Fig. 5.1 inset). The Sharbot Lake Domain, located north of the Frontenac Terrane, also shares a similar tectono-metamorphic history (Corfu and Easton, 1997). It is thus interpreted as the northwestern extent of the Frontenac-Adirondack Belt. The Sharbot Lake Domain primarily consists of carbonate sedimentary rocks, with lesser amounts of tholeiitic metavolcanic, clastic metasedimentary, and granitoid intrusive rocks (Corfu and Easton, 1997; Smith et al., 2001). Sedimentation and volcanism preceded magmatism and upper greenschist to granulite facies (increasing southward) metamorphism associated with the Shawinigan and Ottawan orogenic phases (Carr et al., 2000; Cosca et al., 1991; Peck and Lin, 2024; Rivers, 2008). The Sharbot Lake Domain is separated from the Mazinaw Domain (Fig. 1 inset) in the northwest by the ca 1000–900 Ma Robertson Lake mylonite zone, which exhibits both early compressional and late extensional features

(Busch and Van Der Pluijm, 1996; Carr et al., 2000; Rivers, 2012). The 10–20 km wide Maberly Mylonite Zone (Fig. 1), located between the Maberly Fault and the Rideau Lake Fault, separates the Sharbot Lake Domain from the Frontenac Terrane and records thrusting of the Frontenac onto the Sharbot Lake Domain (Corfu and Easton, 1997; Davidson and Ketchum, 1993; Hildebrand and Easton, 1995).

Southeast of the Black Lake Shear Zone lies the Adirondack Lowlands, which are composed of metacarbonate rocks, orthogneiss, clastic metasedimentary rocks, and metadacite intruded by A-type granitoids and metamorphosed to upper-amphibolite facies (Carl, 1988; Chiarenzelli et al., 2017; Peck et al., 2022). The A-type granitoids belong to the ca 1170–1154 Ma Frontenac Suite, which intrudes the Sharbot Lake Domain, Frontenac Terrane, and Adirondack Lowlands. A syn-to-post-Ottawan pulse of alkalic A-type magmatism, the Kensington-Skootamatta suite intruded greater portions of the Central Metasedimentary Belt (Cutts, 2014). The Carthage-Colton Shear Zone—separating the Adirondack Lowlands from the Adirondack Highlands—records Ottawan deformation (Baird and Shrady, 2011; Mezger et al., 1992; Streepey et al., 2001). However, the shear zone may represent a Shawinigan-aged suture between the Adirondack Lowlands and Highlands that was subsequently reactivated (Carr et al., 2000; Chiarenzelli et al., 2010; Peck et al., 2013). Meta-igneous and subordinate metasedimentary rocks of the Adirondack Highlands underwent significant metamorphism during the Ottawan Orogeny (Chiarenzelli and McLelland, 1991; Mezger et al., 1992; Streepey et al., 2004).

5.3 Methodology

We provide new structural, bulk rock and mineral geochemistry, and petrographic data to supplement previously reported data to develop a comprehensive understanding of the Frontenac Terrane. Field mapping was used to refine lithological boundaries and identify structures; new lithologic classifications, particularly of *granitic gneiss* (Wynne-Edwards, 1967) as quartzite and quartzofeldspathic schist (Fig. 1), further aid in reinterpreting the history of the Frontenac Terrane. Select metasedimentary and granitoid rocks were analyzed for whole-rock major and trace geochemical composition from Activation Laboratories (ActLabs) using lithium metaborate/tetraborate fusion and ICP-MS with FeO determined through titration. Petrographic analysis was used to identify metamorphic assemblages, microtextures, and alteration.

Thermodynamic modelling of bulk rock compositions (Appendix S4.2) was performed with the GeoPS program (Xiang and Connolly, 2022) to provide stable phase assemblage models in the MnNCKFMASHTO system. Activity-composition models for biotite, chlorite, cordierite, chloritoid, garnet, ilmenite, liquid, muscovite, orthopyroxene, and staurolite are from White et al. (2014), osumilite and sapphirine models are from Holland and Powell (1998), and feldspar models are from Holland and Powell (2003).

Garnet-biotite (Ferry and Spear, 1978), garnet-cordierite (Bhattacharya, 1993; Wells, 1979), and garnet-orthopyroxene (Aranovich and Berman, 1997) thermobarometry provide additional pressure-temperature estimates of metamorphism. Complete equilibrium phase diagrams (i.e. pseudosections) and thermobarometry estimates are presented in Appendix S4.3 with complete methods described in Appendix S4.4. Ternary feldspar solvus isotherms were calculated with Theriak-Domino (De Capitani and Brown, 1987) using the Fuhrman and Lindsley (1988) feldspar model. Integrated perthite compositions were calculated by coupling quantitative compositions of host and lamellae—from microprobe analyses—with proportions of host and lamellae estimated from backscatter-images were used to calculate crystallization compositions (e.g. Martignole and Wang, 2010). All new mineral compositions were attained using a JEOL JXA-8530F electron microprobe at the University of Toronto; operating conditions and standards are described in Appendix S4.4. Previously reported geochemical, isotopic, and geochronological data was collated and reinterpreted below.

5.4 Results

5.4.1 Rock types of the Frontenac Terrane

A revised geological map of the Frontenac Terrane is presented in Figure 5.1—a detailed version can be found in Appendix S4.1. In general, metasedimentary rocks intruded by monzonite-syenite-granite plutons with minor gabbro and anorthosite comprise the Proterozoic geology of the Frontenac Terrane. Eight mappable units—one being Paleozoic cover—have been identified; five of these are interpreted as sedimentary in origin as they are often interlayered and grade into another. However, most primary sedimentary structures are lost to recrystallization during ductile deformation and high-temperature metamorphism. Although not a mappable unit, two monomictic (quartzite clasts) conglomerates represent a new lithologic unit with implications discussed later. Decimetre- to metre-thick granitic dykes likely related to larger granitoid

intrusions are common. Minor alteration in the form of uralization, biotization, and chloritization of mafic minerals and seritization of feldspar shows post-peak metamorphic retrogression due to fluid infiltration. However, the interpreted peak metamorphic assemblages are preserved in most samples. In cordierite-bearing samples, variable pinitization suggests patchy retrogression of peak metamorphic assemblages across the Frontenac Terrane. Additional field images and microphotographs are available in Appendix S4.6.

Quartzite (Fig. 5.2a) dominates the southeastern Frontenac Terrane, forming white to grey outcrops. Two subgroups can be classified as clean quartzite or quartz arenite depending on the proportion of quartz being greater or less than 90 vol% respectively. Heavy mineral layers—1 to 5 mm thick—contain abundant zircon, apatite, and titanite in clean quartzite. Quartz arenite, formerly mapped as alaskite (Wynne-Edwards, 1967), contains fine-grained biotite and hornblende (10–15 vol%) with clinopyroxene, grandidierite, tourmaline, zircon, and titanite as accessory minerals. Ilmenite is the common Fe-oxide in both quartzite subunits, and sulfide minerals (pyrite and chalcopyrite) are rare.

Quartzofeldspathic schist (Fig. 5.2b) is the most common lithology of the Frontenac Terrane as grey to buff-coloured outcrops and can often be found to grade into quartzite or mafic schist. Quartzofeldspathic schist, mapped as granitic gneiss by Wynne-Edwards (1967), can include >50 vol% leucocratic sills and dykes when proximal to plutons and less (5–20 vol%) when distal. Although generally granoblastic and fine to medium-grained, alkali feldspar augen (1–5 cm) are common in quartzofeldspathic schist proximal to granitic injections. Quartz and feldspar comprise much of the rock with biotite or amphibole as the dominant ferromagnesian minerals; ilmenite and magnetite are common (1–5 vol%) oxide minerals. Titanite, calcite, apatite, zircon, monazite, pyrite, pyrrhotite, grandidierite, tourmaline, and, infrequently, garnet are accessory minerals. Undulose extinction and subgrains in quartz are common; myrmekite intergrowth of feldspar is rare.

Mafic schist (Fig. 5.2c) forms dark grey to black outcrops. It is often interlayered and gradational with quartzofeldspathic and aluminous units, suggesting a protolith genetically associated with sedimentary rocks, either as immature clastic sediments or hydrous and siliceous volcanogenic material. Mafic schist consists of quartz, feldspar, biotite, and amphibole with minor ilmenite, pyrite, pyrrhotite, magnetite, zircon, monazite, apatite, titanite, and occasional

pyrite, grandidierite, and tourmaline. Clinopyroxene, orthopyroxene and garnet are uncommon, though they can be up to 10 vol% of the assemblage when present. Mafic schist is fine to medium-grained and equigranular with an even distribution of minerals throughout samples. If proximal to granitoid magmatic rocks, 0.5–1 cm alkali feldspar augen are common (Fig. 5.2c).

Aluminous gneisses are the most mineralogically diverse unit of the Frontenac Terrane with three varieties based on the dominant aluminosilicate mineral: (1) garnet, (2) cordierite (Fig. 5.2d, e), and (3) clinopyroxene (Fig. 5.2f). Garnet-only aluminous gneisses are rare and appear coarse-grained and grey to purple in colour with white leucosome (if present), purple-red garnets, and white sillimanite. The garnet aluminous gneiss comprises porphyroblastic garnet, sillimanite, biotite, quartz, (often mesoperthitic) feldspar, intergrown Fe-Ti oxides (ilmenite and magnetite), and spinel with rare corundum, grandidierite, and tourmaline. The other two varieties of aluminous gneiss are often indistinguishable in the field as they are both fine-grained with a blueish-grey colour and pink or, less commonly, white leucosome (if present). It is possible to differentiate the two if large (>1 mm) blue cordierite, red garnet, or green clinopyroxene—often in leucosome (Fig. 5.2f)—are present. The cordierite aluminous gneiss contains porphyroblastic cordierite, mesoperthitic feldspar, biotite, quartz, magnetite, spinel, rutile, and ilmenite. Sillimanite, garnet, orthopyroxene, titanite, corundum, tourmaline, grandidierite, and sapphirine are occasionally present. Sillimanite and sapphirine are generally enveloped by cordierite; cordierite porphyroblasts commonly form discrete and discontinuous layers. Garnet and cordierite are commonly intergrown, with one enveloping the other. Clinopyroxene aluminous gneiss contains clinopyroxene, titanite, and feldspar with minor quartz and rare green amphibole, biotite, calcite, and scapolite. All three aluminous gneisses have zircon, monazite, and apatite as accessory minerals. Regardless of variety, aluminous gneiss is fine to medium-grained with quartz showing undulose extinction; grain boundary migration and polygonal recrystallization are sparse.

Marble and other calc-silicates are a significant lithology to the north-northwest of the Gananoque pluton (Fig. 5.1). Marble forms white to grey outcrops with heterogeneous but overall coarse grain sizes. Pure marbles are rare, with clinopyroxene, titanite, feldspar, and quartz being common, as well as occasional garnet, graphite, pyrite, pyrrhotite, chalcopyrite, and blue-

green apatite (occasionally >2 cm in length). Marble mélange with blocks of quartzofeldspathic material is common close to and within the Maberly Mylonite Zone (Fig. 5.2g).

Anorthosite, gabbro, and diorite (Fig. 5.2h) comprise ~5% of the exposed bedrock, often having little surficial weathering; anorthosite is light grey, whereas gabbro is dark grey to black, and diorite is light to dark grey. Gabbro contains clinopyroxene, orthopyroxene, and plagioclase. Ilmenite with magnetite lamellae and apatite are accessory minerals, comprising <2 vol% of a sample. Amphibole replacement of pyroxene and chloritization is common. Diorite is equigranular and composed of medium to coarse-grained brown amphibole (>60 vol%) and plagioclase feldspar (>30 vol%) with minor quartz; biotization of amphibole is common. Anorthosite is equigranular, coarse-grained, and comprised of mesoperthitic feldspar with green clinopyroxene, brown amphibole, and quartz. Titanite, calcite, apatite, and zircon are common accessory minerals.

Granitoids comprise <20% of the exposed bedrock and are present throughout the Frontenac Terrane forming generally elongate plutons 5–15 km across (Fig. 5.1). Plutons can be zoned from core to margin; the Perth Road Pluton (Fig. 5.1), gradually grades from gabbro in the centre to syenite, monzonite, and granite moving towards the perimeter (Ermanovics, 1970). Granitoids vary in colour from bright red (Fig. 5.2i) to purplish (Fig. 5.2j), often underlying flat-lying topographic lows. Granitoids are coarse-grained and contain ternary feldspar and quartz with green amphibole, brown and black biotite, and green clinopyroxene. Accessory ilmenite, magnetite, titanite, zircon, apatite, pyrite, pyrrhotite, and green-blue tourmaline are common with rare calcite. Quartz often displays undulose extinction and grain boundary migration; 1–2 mm clusters of polygonal crystals of quartz are common. Granitoids within the Frontenac Terrane are not- or weakly due to the alignment by biotite or amphibole, which is developed strongest near pluton margins.

5.4.2 Structural Geology

Multiple deformation events with variable styles are present in the Frontenac Terrane. Herein, we mainly focus on the ductile deformation relevant to its Proterozoic evolution. A singular foliation, defined by oriented mica or amphibole, is typical. Locally, it is also defined by 0.5–5 cm stromatic leucosome, which is common in most aluminous gneiss and transposed alkali feldspar augen. Lithologic contacts, including some granitic dykes related to the Frontenac Suite,

commonly are parallel to the foliation. Three generations of secondary structures (D_1, D_2, and D_3) are present based on overprinting relationships. The structures are represented by schistosity, commonly defined by amphibole- and mica, which is associated with folding events (F_1, F_2, and F_3) of the earlier foliation and/or compositional layering, at least in part thought to represent bedding (Fig. 5.1). Deformation predominately resulted in S > L tectonites with amphibole, recrystallized quartz ribbons and feldspar aggregates locally defining lineations.

Evidence for the oldest deformation event (D_1) is best preserved within regional fold hinges; particularly, the areas around the Crow Lake pluton (Fig. 5.1) are dominated by the S_1 foliation. Folding associated with D_1 resulted in open to closed folds (Fig. 5.3a) with an average axial plane orientation of 224º/77º and hinge line plunging 12º towards 042º (Fig. 5.3g). Leucosome is commonly aligned with S_1 axial planar foliation (Fig. 5.3d). Subsequent deformation resulted in a near-perpendicular foliation best preserved in the hinges of regional gentle F_2 folds or at the contact areas between quartzofeldspathic and carbonate lithologies overprinting F_1 axial planar foliation or bedding (see Fig. 5.3b, d). Folds proximal to the Lyndhurst pluton are predominantly F_2 structures (Fig. 5.1). However, F_2 folds at the outcrop scale (Fig. 5.3b, c, d) are generally rare. F_2 folds plunge on average ~23º towards ~132º with an approximate axial plane orientation of 125º/75º (Fig. 5.3h). Near the Devil Lake composite gabbro and anorthosite body (Fig. 5.1). F_3 axial planes have an average orientation of ~063º/84º with a hinge line plunging at ~18º towards ~065º (Fig. 5.3i). Schistosities are developed in all lithologies, whereas small and medium-scale folding is best preserved in siliceous metasedimentary units with abundant mica or amphibole.

Marble is a particularly helpful marker layer with folded lithologic contacts and can contain regionally mappable, discontinuous, folded metasedimentary layers. Granite bodies south of the Rideau Lake Fault have map patterns that elongate parallel to the axial traces of F_1 (e.g. Crow Lake and Gananoque plutons) or F_3 (Devil's Lake and Lyndhurst plutons). This relationship is less evident in the Maberly Mylonite Zone (Fig. 5.1) as the elongated shape of granite plutons is locally aligned parallel to the terrane boundaries (e.g. North Crosby or Wolfe Lake), indicating pre- and/or syn-tectonic to post-deformation emplacement.

The Maberly Mylonite Zone has a surface extent of 10–20 km between the Maberly and Rideau Lake faults, comprised of proto- and meso-mylonite, gneissic banding, and marble

mélange. The average foliation of these tectonites is 032/55. Marble tectonites of the Maberly Mylonite Zone contain milli- to decimeter-scale fragments of quartzofeldspathic, mafic schist, and aluminous gneiss (e.g. Fig. 5.2g). Although unequivocal shear indicators are rare, thrust indicators near Bob's Lake (Davidson and Ketchum, 1993) indicate northwestern thrusting though relative and absolute timing is unknown. The Black Lake Shear Zone separates the Frontenac Terrane and Adirondack Lowlands parallel to the south shore of the St. Lawrence River and strikes ~060º dipping ~70º with mineral lineation plunging 09º towards 065º (Wong et al., 2011).

5.4.3 Whole-rock geochemistry

5.4.3.1 Metasedimentary Rocks

All geochemical values are in Appendix S4.2, including 19 new and 212 previously published analyses. Whole-rock oxide concentrations are paired with mineral assemblages (when known) to differentiate the different units. Quartzite (n=4) have whole-rock SiO_2 concentrations >90 wt%. Quartzofeldspathic schist (n=59) have 75–90 wt% SiO_2, or 52–75 wt% SiO_2 with <10 wt% Al_2O_3. Garnet or cordierite aluminous gneiss (n=66)—chemically indistinguishable from each other—is 52–75 wt% SiO_2 with a chemical index of alteration >50. Clinopyroxene aluminous gneiss (n=35) is as siliceous as the other aluminous gneiss but with a chemical index of alteration below 50. Mafic schists (n=3) have silica contents below 52 wt% and less than 25 wt% CaO; samples with >25 wt% CaO are classified as (meta)carbonate rocks (n=147).

Major element compositions are used to approximate the nature of the metasedimentary rock protoliths using the classification scheme of Herron (1988). This is a crude approximation given the possibility of open system behaviour during metamorphism (e.g. Ague, 1991), particularly given anatectic conditions and possible melt loss (e.g. Hernández-Montenegro et al. 2019). Aluminous gneiss and mafic schist are chemically wacke or arkose with a few lith-arenites, Fe-sand, and shale (Fig. 5.4a). Quartzofeldspathic schist ranges from arkose to sublitharenite and subarkose, whereas all quartzite has major element compositions consistent with quartz arenite. Geochemical tectonic discrimination diagrams dominantly suggest a passive continental margin environment (Fig. 5.4b) with a few plotting in the continental arc field. Again, these diagrams should be used cautiously, considering that the clastic metasedimentary rocks may not represent the same composition as their sedimentary protoliths. The weathering

trends of different igneous sediment sources are presented in Figure 5.4d compared to the metasedimentary compositions. Notwithstanding the separation of aluminous gneiss using the chemical index of alteration, there is no discernible trend between lithology and the chemical index of alteration. However, metasedimentary rocks of the Frontenac Terrane generally lie on the weathering trend of granodiorite and granite (Fig. 5.4d).

Chondrite-normalized (McDonough and Sun, 1995) trace element concentrations are shown in Figure 5.4e; fields denote variability for rock types, whereas median values are solid lines. Trace element trends are similar regardless of lithology. The mafic schists have relatively elevated concentrations of trace elements, whereas quartzofeldspathic schists and clinopyroxene aluminous gneiss are relatively depleted. Most rock types exhibit a slight negative Eu anomaly with flat to gently negative HREE patterns. Metacarbonate rocks are enriched in LREE and depleted in HREE.

5.4.3.2 Magmatic Rocks

We have collated 11 new and 198 historical analyses of magmatic rocks from across the Frontenac Terrane that includes two suites, the Kensington-Skootamatta Suite (n=8; Cutts, 2014; Dickin and Strong, 2021; Marcantonio et al., 1990) and the Frontenac Suite (n=179; Currie and Ermanovics, 1971; Dickin and Strong, 2021; Easton, 2017; Grammatikopoulos et al., 2007; Marcantonio et al., 1990; Peck et al., 2013). Although the Kensington-Skootamatta Suite postdates the Frontenac Suite by ~100 Ma (Cutts, 2014; Dickin and Strong, 2021; Marcantonio et al., 1990), there is no distinct geochemical difference (Fig. 5.5), and therefore, we describe all granitoids together. However, we note that this lack of chemical difference may be an artefact of the low number of samples. Intrusive rocks of the Frontenac Terrane with SiO_2 concentrations <65 wt% are alkaline—more siliceous rocks are subalkaline (Fig. 5.5a). Using the Total Alkali Discrimination (Middlemost, 1994), the Frontenac Suite can range from foid-gabbro to granite, with most being syenite and quartz monzonite. The aluminium saturation index increases with silica content along a fractionation line of pargasite. Zirconium saturation temperatures increase with silica content from 775ºC to 1250ºC; however, the overall trend reaches a quasi-asymptote between 1000ºC and 1050ºC. The concentration of Al_2O_3, Na_2O, and K_2O increase with SiO_2 at relatively low SiO_2 concentrations (<65 wt%), decreasing with SiO_2 for samples with >65 wt% silica. The concentration of MgO, TiO_2, CaO, and $Fe_2O_{3(T)}$ decreases with increasing SiO_2. The

concentration of P_2O_5 increases with SiO_2<55 wt% and decreases if SiO_2>55 wt%. The Frontenac Suite can be classified as magnesian, metaluminous, and shoshonitic in composition.

Trace element compositions of the granitoids from the Frontenac Terrane are consistent with those from granitoids found in volcanic arc, within-plate, and post-collisional settings (Pearce et al. 1984; Fig. 5.5b). Further classification can be made as A-type (Whalen et al. 1987) and collisional or island arc (Eby 1992) in origin. A selection of trace elements is normalized against chondritic values (McDonough and Sun, 1995) in Figure 5.5c. Generally, most analyses are consistent with each other and the median; the most significant variability is Zr, which may reflect zircon fractionation. The Frontenac Suite has a high Ba relative to Th and Rb. Further, Nb and Ta are low compared to U and La; Eu anomalies, albeit rare, are negative.

5.4.3.3 Mineral Compositions

Previously published mineral compositions supplement new analyses presented in Figure 5.6 and reported in Appendix S4.6 with methods in Appendix S4.4—granitoid analyses are from the Frontenac Suite.

Seventy-one garnet compositions were measured from five garnet and cordierite aluminous gneiss samples; these data supplement 26 spot analyses of garnets from previous studies (Reinhardt, 1968; Russell, 2009; Wynne-Edwards, 1967; Wynne-Edwards and Hay, 1963). Generally, concentrations of major elements in garnet are consistent across individual grains (i.e. flat zoning) and between different grains in the same samples (Fig. 5.6a). However, there is variability between samples, with almandine proportions ranging from 55–75 mol% and pyrope proportions from 20–40 mol%, with minimal grossular (2–6 mol%) and spessartine (1–5 mol%).

Cordierite compositions (n=36) from 22 samples generally range from 0.625–0.75 X_{Mg} (molar Mg/Mg+Fe; Fig. 5.6b) though can be as low as 0.475 and as high as 0.85. Compositions from cordierite in the same sample are within 0.025 X_{Mg} of one another.

Biotite compositions (n=70) from seven granitoid (n=10) and 33 garnet/corderite aluminous gneisses (n=60) are presented in Fig. 5.6c. Biotite in granitoid samples range from 0.275 to 0.36 X_{Fe} (molar FeO/[FeO+MgO]), whereas X_{Fe} of biotite from the aluminous gneisses

vary from 0.215 to 0.6. Fluorine content ranges from 0.1–0.5 apfu and Cl from 0–0.125 apfu; Ti content ranges from 0.12–0.49 apfu.

Amphibole (n=12) from granitoid samples (10 analyses from 5 samples) is classified as pargasite or ferropargasite with iron content increasing with silica (Fig. 5.6d). A single analysis from the mafic schist is ferro-edenite in composition, whereas a clinopyroxene aluminous gneiss analysis is classified as pargasite.

Pyroxene analysed (n=10) from granitoid samples (n=3) are generally augite or diopside; however, 3 analyses are enstatite in composition (Fig. 5.6e). Diopside is found in the clinopyroxene aluminous gneiss (1 analysis), and enstatite is found in the garnet/cordierite aluminous (13 analyses from 5 samples). Enstatite from garnet/cordierite aluminous gneisses contain 5.2–9.5 wt% Al_2O_3.

Eighty-five feldspar analyses from 18 samples, including 40 analyses across 10 granitoid samples, 35 analyses from 7 garnet/cordierite samples, and 10 analyses from 1 quartzofeldspathic schist, typically lie along the albite–orthoclase or albite–anorthite mixing lines (Fig. 5.6f). Integrated feldspar compositions from granitoid and quartzofeldspathic rocks are ternary. Analyses from lamellae of antiperthite are generally orthoclase or sanidine, with host crystals being albite or oligoclase.

4.4 Stable and radiogenic isotopes

We have collated published stable and radiogenic isotope ratios for granitoids and metasedimentary rocks in the Frontenac Terrane (Fig. 5.7; Appendix S4.2). Isotopic values for the depleted mantle are from Bindeman et al. (2012; $\delta^{18}O$) and Goldstein and Jacobsen (1988; Nd and Sr), whereas mantle Nd and Sr concentrations are of DePaolo (1981). Radiogenic isotope (Nd, Sr) ratios are re-calculated to 1165 Ma, which is the approximate crystallization age of granitoids in the Frontenac Terrane (Davidson et al., 2000; Marcantonio et al., 1990; Shieh, 1985).

Whole-rock oxygen isotopes from granitoid samples have negligible $\delta^{18}O$ variation across the plutons—suggesting minimal post-crystallization alteration—as well as between coexisting feldspar and quartz (Marcantonio et al., 1990), further indicating primary ratios. Plutons are separated into two groups: the relatively low-$\delta^{18}O$ Kensington-Skootamatta suite

($\delta^{18}O$ = 9–10.7‰) and the high-^{18}O Frontenac Suite ($\delta^{18}O$ = 12.5–15.7‰; Marcantonio et al., 1990; Shieh, 1985); the Frontenac Suite is ~100 Ma older than the Kensington-Skootamatta suite. Clastic metasedimentary rocks in the Frontenac Terrane have $\delta^{18}O$ between 11.9–25.4‰, and carbonates have values of 18.3–26.8‰ (Fig. 5.7a, b; Shieh 1985, Peck et al. 2022).

The Frontenac Suite granitoids yield εNd values between -1 and +6, whereas the Kensington-Skootamatta suite ranges from +0.3 to +6.2 (Cutts, 2014; Dickin and Strong, 2021; Marcantonio et al., 1990). Clastic metasedimentary rocks have εNd ranging from -6 to 5.5 (Dickin and Strong, 2021; Marcantonio et al., 1990). $^{87}Sr/^{86}Sr_{(i)}$ values for the Frontenac suite are between 0.7043 and 0.7056 (Cutts, 2014; Krogh and Hurley, 1968; Marcantonio et al., 1990), which are more radiogenic than values from the Kensington-Skootamatta suite (0.7025–0.7028). Clastic metasedimentary rocks from the Frontenac Terrane have initial $^{87}Sr/^{86}Sr$ ratios between 0.7049 and 0.7337 (Marcantonio et al., 1990; Spooner, 1969).

The Frontenac Suite and Kensington-Skootamatta suite granitoids are isotopically distinct; the Kensington-Skootamatta suite has less radiogenic Nd and Sr ratios and lower $\delta^{18}O$ values (Fig. 5.7a, b). Together, they form a weak linear array between Nd, Sr and O isotope values (Fig. 5.7a–c). Carbonate $\delta^{13}C$ values range from -1.9 to 4.8‰ and generally increase with increasing $\delta^{18}O$ (Fig. 5.7d; Shieh 1985, Peck et al. 2022).

The association of gabbro and diorite with the Frontenac Suite (Figs 1, 5.5a) paired with pre-collisional and arc-like trace element signatures of the granitoids (Fig. 5.5b,c) indicate a mantle input. In contrast, high $\delta^{18}O$ values provide evidence for crustal contamination. Therefore, we consider mantle-derived magma interacted with regional (or similar) silicate and carbonate metasedimentary rocks. Note that there are no εNd or $^{87}Sr/^{86}Sr$ values for (meta)carbonate rocks from the Frontenac Terrane, so we use an εNd value of +1.6, which is a marble from the Bancroft Terrane to the northwest and interpreted to be representative of Grenvillian marbles in the region (Moecher et al., 1997). An $^{87}Sr/^{86}Sr$ value of 0.7056 and $\delta^{18}O$ value of 21.55 for marble in the Bancroft Terrane (Lentz, 1992) is used similarly. This $^{87}Sr/^{86}Sr_{(i)}$ lies within the bounds for carbonate rocks in the Adirondack Lowlands (Hauer 1995)—an association that we discuss later. These approximated εNd and $^{87}Sr/^{86}Sr_{(i)}$ values for Frontenac carbonate rocks are presented as a blue cross in Fig. 5.7c. Using these end members, the Kensington-Skootamatta represents a binary combination of 70/30 mantle with metasedimentary

rocks whereas the Frontenac Suite represents a possible binary between 15/85 of the mantle with carbonates or 50/50 mantle with clastic metasedimentary rocks.

5.4.4 Conditions of metamorphism and magma crystallization

Cordierite and garnet aluminous gneiss are amenable for thermobarometry estimates through exchange thermometry and thermodynamic modelling. Exchange thermobarometry calculations (Appendices S4.4 and S4.5) yield metamorphic condition estimates (Fig. 5.8a) of 770–1100ºC (median=945ºC) and 5.1–9.1 kbar (median=6.7 kbar). An estimated apparent thermal gradient of ~140ºC/kbar is calculated using these median estimate values. These temperature estimates are likely a minimum due to the relatively fast exchange of Fe-Mg under anatectic conditions. (Frost and Chacko 1989, Kelsey and Hand 2015) generally recording below-peak conditions (Harley 1998).

The assumed peak metamorphic assemblage of individual samples is used alongside pseudosections to infer sample-specific peak metamorphic conditions and is overlain to provide a regional estimate. This cumulative field provides estimates of 710–1150ºC and 3.2–7.1 kbar; median conditions of 900ºC, 6 kbar and overlapping fields at 800ºC and 5.2 kbar provide a calculated apparent thermal gradient of ~130ºC/kbar. These high-peak metamorphic conditions and apparent thermal gradients are further corroborated by high-Al (>8 wt%) orthopyroxene + sillimanite (Fig. 5.2d, Appendix S4.5) and sapphirine + quartz (Appendix S4.5), indicative of ultra-high temperature conditions (Harley, 1998; Kelsey and Hand, 2015). The integrated composition of ternary feldspar from granitoid rocks generally lies between the 900ºC and 1000ºC solvus isotherms (Fig. 5.8b). Similar to exchange thermometry, the minimum peak temperature is likely to be a minimum with the retrogression of peak minerals (e.g. Pattison 2003, Lei and Xu 2018) alongside assemblages predicted to be stable across wide temperatures, providing poor resolution.

5.4.5 Geochronology

Previously collected geochronology data is compiled and presented in Figure 5.9; analyses can be found in Appendix S4.2. Although most compiled detrital zircon data (Fig. 5.9a) is low in individual grains analyzed (n≤10), they are in general agreement with one another except for 21CK78A (Tan, 2024). Two dominant peaks in date frequency can be identified: 1900–1600 Ma and 1400–1180 Ma; a smaller 2800–2300 Ma peak indicates subordinate Archean sediment

sources. Another peak (<1180 Ma) coincides with the Shawinigan orogen and is interpreted as metamorphic resetting and not representative of deposition. However, the detrital zircon ages coincident with metamorphic ages associated with the Shawinigan orogeny (Fig. 5.9b; Heumann et al. 2006, Peck and Lin 2024) are taken to indicate that sedimentation ceased during the 1180–1160 Ma Shawinigan orogeny.

Sample 21CK78A (44.6057º N, -76.1663º E) provides a different story, with dates >100 Ma younger than any other sample analyzed. However, this sample is also unique in morphology as a monomictic conglomerate with quartzite matrix and quartzite clasts, comparable in lithology and age to some Flinton group metasediments of the Mazinaw Domain (Sager-Kinsman and Parrish, 1993). We interpret this data as the conglomerate forming through the erosion of proximal sedimentary units after the Shawinigan orogeny, agreeing with the Sager-Kinsman and Parrish (1993) interpretation of the Frontenac Terrane as the Flinton sediment source.

South of the Maberly Mylonite Zone, only ca 1177–1154 Ma Frontenac Suite granitoids intruded (Cutts, 2014; Davidson et al., 2000; Marcantonio et al., 1990; Peck et al., 2004; Shieh, 1985) with Nd depleted mantle model ages of ca 1600–1500 Ma (McNutt and Dickin 2012, Dickin and Strong 2021). Granitoids within the Maberly Mylonite Zone have U–Pb zircon dates ranging from 1177–1154 Ma (Frontenac Suite) and 1070–1020 Ma (Kensington-Skootamatta Suite; Marcantonio et al. 1990). The granitoids have Nd depleted mantle model ages of ~1600 Ma and ~1400 Ma, respectively (Davidson et al., 2000; Marcantonio et al., 1990). Comparatively, model mantle extraction ages of sediments found in the Frontenac Terrane span 2200–1400 Ma with a median age of 1600 Ma (Dickin and Strong, 2021; Marcantonio et al., 1990)—U-Pb zircon geochronology provides assumed metamorphic ages of ca 1180–1160 Ma (Easton, 2019).

U-Pb titanite analysis from granitoid samples provide dates of 1160–1100 Ma (Easton, 2017) which are 20–30 Ma younger than Shawinigan-aged (1169–1129 Ma) titanite from metasedimentary samples (Easton, 2019; Mezger et al., 1992); a titanite age of 1070 Ma is reported from a metasedimentary rock (Easton, 2019) seemingly between Shawinigan or Ottawan events. Other young dates include 1030–930 Ma rutile and 990 Ma apatite dates in metasedimentary rocks and 990 Ma apatite dates from a gabbro sample (Easton, 2019). These Ottawan ages are all reported from localities within the Maberly Mylonite Zone. Cosca et al.

(1992) report hornblende Ar-Ar cooling ages in metasedimentary rock from 1120–1100 Ma and a single 1000 Ma age.

Suturing of the Frontenac Terrane and Sharbot Lake domain predates an 1160 Ma Maberly Stock (Corfu and Easton, 1997), further evidenced by ca 1161 Ma crystallization ages from Frontenac granitoids in the Sharbot Lake Domain (Hildebrand and Easton, 1995; Ketchum and Davidson, 2000). Suturing of the Adirondack Lowlands and Frontenac Terrane was likely coeval with U-Pb titanite geochronology dates of 1150 ± 20 Ma and 1160 ± 26 Ma (Wong et al., 2011) from the Black Lake Shear Zone, which agrees with a U-Pb zircon upper intercept age of 1160 Ma (Baird and Shrady, 2011). Although exact ages of deformation are challenging to obtain, we suspect the Adirondack Lowland, Frontenac Terrane, and Sharbot Lake Domain were contemporaneously deformed ca 1160 Ma with collision-related deformation recorded in the Maberly and Black Lake Shear Zones. We make further interpretations regarding the suturing of the terranes within the Central Metasedimentary Belt later.

5.5 Discussion

A tectonic model of the Frontenac Terrane and SW Grenville Province is presented based on integrating the lithological, geochemical, structural, mineral, metamorphic, isotopic, and geochronological data discussed herein. The Frontenac Terrane is then incorporated into a model for the larger Grenville Province (Fig. 5.10). Rock types are discussed from oldest (e.g. metasedimentary rocks) to youngest. In addition, we explore advective heating as a mechanism for ultra-high metamorphic conditions in compressional stress regimes.

5.5.1 Deposition of Frontenac sediments

The metasedimentary rocks likely have protoliths ranging from quartz arenites, arkose sandstone, greywackes, and limestone/dolostone deposited in a marine environment (Fig. 5.4). The apparent interbedding, conformability of relict bedding, similar trace element patterns (Fig. 5.4e) of metasedimentary rocks, and linear geochemical pattern along a granite/granodiorite weathering trend (Fig. 5.4d) indicates these now deformed rocks were possibly deposited as a continuous sedimentary sequence. Mafic schists (SiO_2 ~50 wt%) are interbedded and interpreted to represent mafic volcanogenic material. Normalized trace element patterns of the metasedimentary rocks (Fig. 5.4e) and granitoids (Fig. 5.5c) are nearly identical to each other which, when paired with

sediments lying along a granite or granodiorite weathering trend (Fig. 5.4d), indicates a sediment source being an older granitoid terrane with similar composition to the Frontenac Suite.

Detrital zircon geochronology reveals the youngest frequency peak to be ca 1400–1180 Ma (Fig. 5.9a) with sedimentation directly preceding metamorphism and plutonism related to the Shawinigan orogeny at ca 1180 Ma (Fig. 5.9b). Sedimentation ended before 1177 Ma, which is the age of the oldest dated intrusive Frontenac Suite (Davidson and van Breemen 2000). To the northeast, the Mont-Laurier Terrane is considered the northwestern extension of the Frontenac Terrane (Rivers et al., 2012) and contains 1390–1330 arc-related basement rocks (Wodicka et al. 2004, Peck 2012), which is similar to the 1340–1330 Ma arc-related magmatism in the Adirondack Highlands (McLelland and Chiarenzelli 1990). We interpret these similarities, paired with their along-strike relationship to one another, to suggest the Mont-Laurier and Adirondack Terranes to be a part of the same arc system (discussed later) with the Frontenac Terrane within the associated backarc. Hence, we propose that sediment deposition in the Frontenac Terrane occurred between 1390 and 1180 Ma. This estimate extends to younger and older ages than previous suggestions in which deposition of sediments in the Frontenac-Adirondack basin occurred before 1200 Ma (Sager-Kinsman and Parrish 1993, Chiarenzelli et al. 2017, Peck and Lin 2024)—similar to >1200 Ma depositional estimates of other terranes within the Metasedimentary Belt (Corfu and Easton 1997, Carr et al. 2000).

Initial stratigraphic relationships are lost to deformation, but past studies have proposed possible lithostratigraphic relationships (from bottom to top): a two-time repeating sequence of granulitic gneiss-quartzite-marble (Wynne-Edwards, 1967) or a single succession of marble-granulitic gneiss-quartzite (Hildebrand and Easton, 1995). Considering that the detrital zircon ages in quartzite (Fig. 5.9, Appendix S4.2) record sedimentation (1390–1180 Ma) immediately preceding metamorphism (1180–1160 Ma), we consider quartzite to be the top of the preserved sedimentary package. Further, no difference between the zircon population is evident between samples (Fig. 5.9), except for the young conglomerate (21CK78A), which provides evidence for a single quartzite unit. Though not ubiquitous, quartzite is commonly in contact with quartzofeldspathic schist that is interleaved with marble (Fig. 5.1). Aluminous gneiss and mafic schist are often interleaved with quartzofeldspathic schist. Using these lithographic relationships,

we tentatively propose a single succession of marble-quartzofeldspathic schist (+aluminous gneiss and mafic schist)-quartzite similar to that of Hildebrand and Easton (1995).

The Frontenac Terranes shares a magmatic and metamorphic history with the Adirondack Lowlands (Marcantonio et al. 1990, McLelland and Chiarenzelli 1990, Davidson et al. 2000, Cutts 2014, Kamo and Hamilton 2017) and, paired with similar detrital zircon populations across the Frontenac-Adirondack Belt (Sager-Kinsman and Parrish 1993, Chiarenzelli et al. 2017, Peck and Lin 2024), indicates similar sources before thrusting at ca 1160 Ma along the Black Lake Shear Zone (Wong et al. 2011). The Adirondack Lowlands comprises siliclastic and carbonate metasedimentary rocks with subordinate pelitic and possible metavolcanic lithologies (Chiarenzelli et al. 2010); other than the absence of metavolcanic rocks in the Frontenac Terrane—which we now speculate the mafic schist to be—these two terrane are comprised of nearly identical lithologies (Figs 5.1, 5.2; Wynne-Edwards 1967). Proximity to ca 1300 Ma and 1200 Ma arc-related granitoids in the Adirondack Highlands (Ratcliffe et al. 1991) and Lowlands respectively (Chiarenzelli et al. 2010) coupled with the possible preservation of a pre-1200 Ma partial ophiolite (Pyrites Complex; Chiarenzelli et al. 2011b) in the Lowlands suggests the Frontenac-Adirondack Belt represents a former arc-backarc system. The evolving Mesoproterozoic geometry of Grenvillian terranes is discussed later. Still, we propose that the Adirondack Arc—preserved as plutonic rocks in the Adirondack Highlands and Lowlands—is the central source region for the Frontenac-Adirondack metasediments.

5.5.2 The Shawinigan orogen and Frontenac magmatism

Sedimentation in the Frontenac-Adirondack Belt between 1390 and 1180 Ma was coeval with a 1336–1300 Ma magmatic arc that is preserved in the Adirondacks Highlands and ca 1284 Ma, 1236–1230 Ma, and ca 1207 Ma magmatism in the Adirondack Lowlands (McLelland and Chiarenzelli 1990, McLelland et al. 1992; Fig. 5.10). Sm-Nd model ages indicate mantle extraction at ca 1440–1350 Ma for the calc-alkaline granitoids in the Adirondacks (Daly and McLelland 1991, McLelland et al. 1993); model mantle extraction ages of the Frontenac and Kensington-Skootamatta suite are generally 1540–1380 Ma (McNutt and Dickin 2012, Dickin and Strong 2021). Sedimentary rocks of the Frontenac-Adiriondack belt were subjected to tectonism and shortening before 1161 Ma—the minimum age of the thrusting-related Maberly Mylonite and Blake Lake Shear zones (Hildebrand and Easton 1995, Baird and Shrady 2011).

Shearing overlapped with crystallization of the Frontenac Suite (1177–1148 Ma; Marcantonio et al. 1990, Davidson et al. 2000), although magmatism may have started before thrusting. Coeval magmatism in the Adirondack Lowlands and Frontenac Terrane ca 1172 Ma (Peck et al. 2013) indicates an early relationship between these two terranes. A 1176 Ma U-Pb zircon date from a Frontenac aluminous gneiss (Easton 2019) suggests that metamorphism was contemporaneous with the earliest magmatism in the Frontenac Terrane. The ca 1161 Ma Silver Lake pluton in the Sharbot Lake Domain (Davidson et al. 2000) and 1164 Ma Edwardsville Syenite in the Adirondack Lowlands are coeval with intrusive rocks in the Frontenac Terrane (1177–1148 Ma; Marcantonio et al. 1990, Davidson et al. 2000, Peck and Lin 2024). They indicate the amalgamation of the *Adirondis* super terrane with Laurentia due to the closure of the intervening backarc basin (Fig. 5.10), which we infer started to spread and formed oceanic backarc basin lithosphere before 1200 Ma (Pyrites Complex; Chiarenzelli et al. 2011a). Hence, Adirondis is restricted to the Adirondack Lowlands and the Adirondack Highlands until ca1180 Ma, when the backarc closed and the arc was re-amalgamated with Laurentia during the Shawinigan orogeny (1190–1160 Ma).

The Frontenac Suite (ca 1177–1148 Ma; Marcantonio et al. 1990, Davidson et al. 2000, Peck et al. 2013) comprises shoshonitic, A-type granitoids that have trace element signatures such as negative Nb/Ta anomalies (Fig. 5.5c) that are consistent with magmatism formed during collision and/or in a magmatic arc setting (Fig. 5.5b). Isotopic signatures of Nd, Sr, and $\delta^{18}O$ provide evidence of a mixed source between a depleted mantle and evolved sedimentary material (Fig. 5.7). In addition, some plutons (e.g. Perth Road; Ermanovics 1970) are continuously zoned from granite at the margin to gabbro at the core, suggesting mantle melting produced mafic magmas, which underwent fractionation in the crust. Fractionation was mainly accommodated by pargasite, as implied by the chemical trend in Figs. 5.5a and 5.6d. Proposed sources for the Frontenac magmas are the Grenvillian metasediments (Shieh 1985), a mixture of Frontenac-Adirondack Belt metasedimentary rocks and underlying lower crust and/or upper mantle (Marcantonio et al. 1990, Davidson et al. 2000, Peck et al. 2013), and altered oceanic crust mixing with subducted sediments (Peck et al. 2004). We propose slab-breakoff (discussed later) and subsequent upwelling asthenosphere to induce melting of the lithospheric mantle beneath Adirondis, which has been enriched with fluids released by over 150 Ma of subduction with possible further mixing through the assimilation of metasediments during ascent.

Low- to medium-pressure granulite facies metamorphism is recorded across the Frontenac Terrane ca 1176–1157 Ma (Kamo and Hamilton 2017), coeval with the intrusion of the Frontenac Suite granitoids (ca 1177–1148 Ma; Fig 5.9); although overgrowths on zircon indicate metamorphism may have started locally before 1180 Ma (Peck and Lin 2024). Exchange thermometry (Fig. 5.8a) provides metamorphic estimates over 775ºC at 5–9 kbar with temperatures locally exceeding 1000ºC. Considering exchange thermometry often records lower than peak metamorphic conditions in high-temperature and anatectic systems (e.g. Pattison 2003), we consider 775ºC to represent the minimum temperature. These estimated metamorphic conditions from exchange thermobarometry are consistent with peak preserved temperatures of 710–1150ºC at 3.2–7.1 kbar predicted by thermodynamic modelling (GeoPS; Xiang and Connolly 2022). Such extreme temperature conditions are supported by high-Al (>8 wt%) orthopyroxene-garnet-sillimanite and sapphirine-quartz assemblages that are diagnostic of ultrahigh-temperature (>900 ºC) metamorphic conditions (Fig. 5.2d and e, Appendix S4.6; Harley 1998, Kelsey and Hand 2015). Conflicting garnet-cordierite growth relationships and the scarcity of garnet and/or other minerals indicative of higher pressures make it difficult to estimate the trajectory of the regional metamorphic pressure–temperature path. However, the lack of a clear pressure-temperature path, paired with most samples having peak metamorphic pressures of 5–6 kbar (Fig. 5.8a, Appendix S4.4), may suggest near isobaric metamorphic heating. Considering that high-temperature magmatism (Fig. 5.8b; Marcantonio et al. 1990, Davidson et al. 2000, Easton 2017) was coeval with metamorphism, which locally exceeded 950ºC (Figs 5.8a, 5.9b), we propose that the emplacement of the voluminous Frontenac Suite at mid-crustal (20–25 km) levels was the principal advective heat source responsible for Shawinigan-aged metamorphism in the Frontenac Terrane. We will discuss the role of siliceous magmas in ultra-high temperature metamorphic terranes where evidence of mafic underplating is sparse later on.

Deformation associated with D_1 overlapped with Frontenac suite crystallization and metamorphism evident by the parallel alignment of the long-axes of the plutons and leucosome veins with S_1 (Figs. 5.1, 5.3d), and aligned sillimanite in cordierite cores (Fig. 5.2e). Undulose extinction, subgrains, and recrystallization of quartz and feldspar recrystallization are common and indicate that deformation occurred at relatively high temperatures (>500ºC; Passchier and Trouw, 2005) whereas local evidence for late static recrystallization defined by aggregates of

quartz and feldspar with polygonal boundaries is inferred to indicate that high temperatures were maintained after deformation. Alternatively, this static recrystallization may result from reheating during subsequent tectonism where the Frontenac Terrane undergoes low strain—a possible scenario discussed with D_3 structures.

U-Pb zircon dates record metamorphism from 1180–1150 Ma (Kamo and Hamilton 2017) are consistent with ca 1160–1150 Ma U–Pb titanite dates from the Sharbot Lake Domain (Mezger et al. 1993), and ca 1170–1130 Ma garnet, titanite, and monazite dates from the Adirondack Lowlands (Mezger et al. 1991). Movement recorded before 1160 Ma along the Maberly Mylonite Zone and Black Lake Shear Zone, further constrain the magmatic-metamorphic-deformational connection between the Frontenac Terrane, Sharbot Lake Domain, and Adirondack Lowlands. We interpret D_1 as related to the NW-directed thrusting of the Adirondack Lowlands terrane onto the Frontenac Terrane, which was thrust upon the Sharbot Lake Domain. This tectonic scenario is consistent with the kinematics of the SE-dipping Maberly and Black Lake shear zones and the NW-overturning of F_1 folds. The F_1 folds are overprinted by commonly open WNW-ESE trending, upright F_2 folds, which have axial surfaces oriented at a high angle to those of the older F_1 folds. These D_2 structures are taken to indicate a constructional regime, possibly related to the uplift of the Frontenac Terrane between the Shawinigan and Ottawan orogenies (i.e. between ca 1160–1080 Ma), possibly in response to increased crustal buoyancy after ca 1160 Ma lithospheric foundering (e.g. McMillan et al. 2023, Carrapa et al. 2025).

Regional structures related to D_3 are broadly parallel to the NE-SW trending terrane boundaries (also at a low angle to D_1), and upright F_3 folds deform all older structures on outcrop and regional scale (Figs. 5.1, 5.3f). These overprinting relationships, combined with 1070 Ma U-Pb titanite, 1030–930 Ma rutile, and ~990 Ma apatite ages (Kamo and Hamilton 2017, Easton 2019) from the Maberly Mylonite Zone, suggest a tectonometamorphic overprint at ca 1070 Ma and subsequent slow-cooling during the Ottawan orogeny. The paucity of Ottawan metamorphic ages across the Frontenac-Adirondack Belt suggests this area occupied a relatively upper crustal level at this time, characterized by minor magmatism and reheating by the ca 1080-1060 Ma Kensington-Skootamatta suite (Corfu and Easton 1997, Cutts 2014) mainly ascending along the Maberly Shear Zone. Such a tectonic evolution is consistent with forming a regional-scale, bi-

vergent thrust block (i.e. orogenic lid of Rivers 2012), with the Frontenac Terrane in its hanging wall. This tectonic model is discussed further later.

5.5.3 Implications for Proterozoic Evolution of the Grenville Province

The Frontenac-Adirondack Belt is unique in the SW Grenville Province for preserving Shawinigan-aged metamorphism with minimal overprinting from later orogenic events. Ottawan-aged (1090–1020 Ma) metamorphism is recorded across the Metasedimentary and Orthogneiss belts (Figs. 5.1 and 5.10; Mezger et al. 1993, Timmermann et al. 2002, Hynes and Rivers 2010) whereas Rigolet-aged (1010–990 Ma) metamorphism is generally restricted to the Orthogneiss belt and the paleo-Laurentian margin (Grenville Front Tectonic Zone; Figs. 5.1 and 5.10, Lambert et al. 2023, Indares 2024). However, the amalgamation of the Elzevir, Sharbot Lake, and Frontenac terranes with Adirondis during the Shawinigan orogeny represents the construction of a central block in the proposed Ottawan orogenic architecture of the Grenville province (e.g. Rivers 2012). Hence, provides insights into the pre-Ottawan configuration of the Laurentian margin.

Sedimentation and arc-backarc magmatism is recorded across the Metasedimentary Belt at ca 1400–1200 Ma (Davis and Bartlett 1988, Corfu and Easton 1995, Wodicka et al. 1996, Smith et al. 2001, Peck and Lin 2024) with complex tectonometamorphic histories. Unpublished geochronology from the Elzevir terrane shows pre-1296 Ma mafic, interpreted as plume-related, magmatism in the Kaladar and Queensborough complexes of the Sharbot Lake Domain (Strong 2017) previously interpreted as a partial ophiolite complex (Smith and Harris 1996). The ages of these mafic complexes are unknown, but the intrusion of the 1296 Ma Elzevir tonalite (McNutt and Dickin 2012) provides a minimum age. Calc-alkaline magmatism preserved in the Adirondack Highlands (McLelland and Chiarenzelli 1990, Daly and McLelland 1991) and also as inliers within the Appalachian Orogen (Ratcliffe et al. 1991) at ca 1350–1300 Ma, is possibly overlapping with the onset of sedimentation within the Frontenac and Adirondack terranes (Sager-Kinsman and Parrish 1993, Peck and Lin 2024). If correct, this suggests the Adirondack Arc in the Adirondacks Highlands was positioned at the leading edge of the Laurentian margin at this time (Fig. 5.10).

Northwestern migration of calc-alkaline magmatism from the Adirondack Highlands with ca 1284 Ma, 1236–1230 Ma, and ca 1207 Ma magmatism in the Adirondack Lowlands

(McLelland and Chiarenzelli 1990, Wasteneys et al. 1999), 1280–1245 arc related tonalite-trondhjemite-granodiorite intrusions in the Mazinaw Domain (Duguet and Easton 2017), ca 1240 volcanic rocks in the Elzevir Terrane (Davis and Bartlett 1988), and ca 1250–1220 Ma tholeiitic mafic magmatism in the Bancroft, Mazinaw, and Sharbot Lake Domains (Fig. 5.10; Corfu and Easton 1995, 1997, Pehrsson et al. 1996), suggests a protracted and complex arc migration evolution across these terranes. Arc development was associated with intermittent rifting in its backarc region based on the extrusion of the ca 1250–1220 Ma tholeiitic basalts. We infer that the mafic schists interleaved with the quartzofeldspathic gneisses schists in the Frontenac Terrane formed part of this arc evolution. However, we presently have no geochronological constraints on the age of these rocks. Further, sedimentation during backarc inversion (~1200 Ma) may explain the significant facies change from carbonate sediments to shore-line sands in the Frontenac Terrane (e.g. Karig and Moore 1975). Rifting evolved into back-arc spreading within the Adirondack Lowlands before 1200 Ma, as suggested by the pre-1200 Ma Pyrites Complex in the Adirondack Lowlands (Chiarenzelli et al. 2011a). This back-arc basin is inferred to have started to close around 1200 Ma since calc-alkaline magmatism ceases between 1210 and 1200 Ma in all terranes (McLelland et al. 1992)—which we suggest was due to slab flattening. Further, the U-Pb zircon age from the Pyrites Complex was initially interpreted as metamorphic in origin (Chiarenzelli et al. 2011a) and, therefore, may further constrain the start of back-arc basin closure. We infer the inversion of the backarc basin during the Shawinigan orogeny ca 1200 Ma to form D_1 structures in the Frontenac Terrane (Figure 5.10). This, in turn, led to the assembly of Adirondis with the Frontenac, Sharbot Lake, and Elzevir terranes. Late syn-D_1 breakoff of the flat slab at ca 1180 Ma generated the Frontenac suite between 1177 and 1158 Ma (Davidson and van Breeman 2000). In contrast, the generation of the anorthosite-margarite-charnokite-granite (AMCG) suite between 1160 and 1130 Ma is attributed to partial foundering of the thickened and eclogitized (garnet pyroxenite) lithospheric mantle of the upper plate.

A combination of Shawinigan thrusting and isostatic rebounding following lithospheric delamination (e.g. Garzione et al. 2006, Wang and Currie 2015) between 1160 and 1100 Ma resulted in the uplift and erosion of greater Adirondis, which was followed by the deposition of the younger than 1150 Ma Flinton Group sediments (Sager-Kinsman and Parrish 1993). The Flinton Group deposition may have overlapped with the restarting of arc magmatism at ca 1103 Ma in the Adirondacks Highlands (McClelland et al., 2001), which, if correct, suggests the

Flinton Group represents retro-arc foreland basin deposits on top of the Elzevir terrane. The arc magmatism in the Adirondacks Highlands lasted until ca 1093 Ma, which is consistent with the proposed onset of collision between Amazonia and Laurentia at ca 1100 Ma (e.g. Bartholomew and Hatcher 2010) and hence the start of the Ottawan orogeny.

Structures associated with the oldest deformation (D_1) in the Frontenac Terrane include folded sedimentary layering (Fig. 5.1), stromatic leucosome (Figs. 5.2b-d, 5.2f, 5.3a,b,d), and aligned long-axis of plutons (Fig. 5.1), which are interpreted to have formed during the assembly of Adirondis. The structures were generated during the thrusting of the Adirondack Lowlands onto the Frontenac Terrane and the thrusting of the Frontenac Terrane onto the Sharbot Lake Domain along the Black Lake and Maberly shear zones, respectively. D_2 structures include gently plunging, steeply inclined open folds with axial planar dipping ca 75º to the SW and striking perpendicular to the trend of both F_2 and F_3 (Fig. 5.3) folds. F_2 folds are best illustrated by the regional scale open warping of the carbonate lithology, with the primary hinge closure situated between the Lyndhurst, Gananoque, and South Lake plutons of the Frontenac suite (Fig. 5.1). This type of deformation suggests of extension and shortening at high angles to the bounding shear zones, probably during uplift following the inferred lithospheric delamination (e.g. McMillan et al. 2023, Carrapa et al. 2025).

Tectonometamorphism and magmatism are continuously recorded across the Grenville Province from ca 1100–990 (McLelland and Chiarenzelli 1990, McEachern and van Breemen 1993, Corfu and Easton 1995, Wasteneys et al. 1999, Chiarenzelli et al. 2011b, Easton 2017, Kamo and Hamilton 2017, Indares 2024). However, any specific region may only record tectonometamorphic activity for a relatively narrow timespan (Fig. 5.10). Hence, whether this represent one continuous phase of tectonism or several separate events is difficult, which is further complicated by the intrusion of the late anorthosite-margarite-charnokite-granite suite between 1060 and 1020 Ma in the NE-part of the Quebec and Labrador Grenville province, which were interpreted to have formed during both extension and compression (Rivers et al. 2012) complicates establishing the period and extent of the tectonometamorphism (Emslie and Hunt 1990). In contrast, intrusion of leucogranite and burial metamorphism between ca 1090–1050 Ma in the Adirondacks Highlands and Lowlands suggest evidence for shortening during this period rather than extension (Chiarenzelli and McLelland 1991). We believe that the

intermittent shortening, metamorphism, and magmatism records progressive orogenesis from ca 1100–990 Ma and hence would represent a continuum between the Ottawan and Rigolet phases during Amazonia's protracted collision with Laurentia

Geochemically similar granitoids to the Frontenac Suite—the Kensington-Skootamatta suite—intrude Adirondis at ca 1060–1045 (McLelland et al. 2001, Cutts 2014). This later suite of alkaline granites appears undeformed in the Maberly Shear Zone (Fig. 5.1) and is interpreted to have intruded post-collisional. The source and tectonic environment where these granitoids were generated is likely slab break-off below the Adirondack Arc following the arrival and progressive underthrusting of Amazonia beneath Adirondis with a similar source as the Frontenac Suite—Adirondack Arc lithosphere and subducted sediments. Magmatic and metamorphic ages in the Frontenac Terrane younger than 1150 Ma are restricted to the Merly Shear Zone; this spatial restriction of young ages is taken to indicate reactivation of the bounding shear zones during post-Shawinigan deformation. In particular, the increased buoyancy after lithospheric foundering and Shawinigan thrusting is believed to have positioned the Frontenac Terrane and Adirondack Lowlands at a high elevation before the arrival of Amazonia— consistent with the 'orogenic lid' position proposed by Rivers (2012). Subsequent NE thrusting during the Ottawan-Rigolet orogeny produced D_3 structures in the Frontenac Terrane ca 1100–1060 Ma while protecting Shawinigan metamorphic assemblages. Progressive thrusting of the Central Gneiss Belt and Adirondis onto Laurentia ca 1020–980 Ma is recorded along the NW margin of the Grenville Province. Altogether, the SW Grenville Province is proposed to record rifting of an arc at ca. 1390 with subsequent inversion of the opened and long-lived backarc basin driven by a progressively flattening slab at ca 1280 to 1230 Ma, which led to basin closure at ca 1210–1160 Ma before continent-continent collision between Laurentia and Amazonia ca 1100–990 Ma.

5.5.4 Regional advective ultra-high temperature metamorphism

Subduction can induce tension in the upper plate and produce back-arc basins behind the volcanic arc during oceanward trench migration (Sdrolias and Müller, 2006; Shemenda, 1993). This process causes upwelling of the asthenosphere up to the crust-mantle boundary near the back-arc spreading ridge; resultant areas of high heat-flow are observable in modern-day systems such as the Tasman or Philippine Seas (Hamza and Vieira, 2012). The relationship between ultra-high temperature metamorphism and arc–backarc systems is well recognized (Clark et al., 2011;

Jiao et al., 2023; Zheng and Chen, 2017)—other accepted mechanisms to produce regional UHT metamorphism are ridge subduction, slab roll-back, slab breakoff, and removal of the lithospheric mantle (Jiao et al., 2023; Lei and Xu, 2018). However, these proposed mechanisms produce UHT conditions either before collision (slab roll-back, ridge subduction) or after collision (lithospheric removal, slab breakoff). In all of these scenarios, the advection of mantle heat to the crust through mafic magmatism is implied—though evidence of such (i.e. mafic magmatism) in ultra-high temperature terranes is commonly enigmatic (Kelsey and Hand, 2015). Alternatively, internal (radiogenic) heat can provide sufficient energy for high-temperature conditions (Clark et al., 2011; Lei and Xu, 2018). However, metasedimentary rocks of the Frontenac Terrane have an age-corrected (1180 Ma) median heat production of 0.7 $\mu W/m^3$ (0.2–1.2 $\mu W/m^3$ interquartile range), lower than modern and Proterozoic crustal average (Jaupart and Mareschal, 2014). Although heat-producing elements are generally incompatible during crustal anatexis, their mobility during the partial melting of metasedimentary rocks is uncertain (Alessio et al., 2018). Further, leucosome, injected and in-situ, is often <10 vol% of outcrops if present, and leucosome accumulations are less than a meter thick (Figs. 5.2 and 5.3). However, we acknowledge that melt extraction, ascent, and erosion like S-type granitoids of the Himalayas (Cao et al., 2022) would obscure the degree of melting. However, carbonate and quartzofeldspathic lithologies are dominant components of the Frontenac Terrane; these rock types generally have low heat production compared to granitic or pelitic compositions (Hasterok et al., 2018). This, coupled with the rapid transition from burial to metamorphism (Fig. 5.9), indicates that an external heat source is required to reach ultra-high temperatures in the Frontenac Terrane.

Granitoids of the Frontenac Terrane have trace element compositions consistent with those from modern arcs (Fig. 5.5), and the granitoids are deformed parallel to the axial plane of F_1 folds (Fig. 5.1), as are some leucosomes in the metasedimentary rocks (Fig. 5.3d). In addition, the deformation in the bounding shear zones is coeval with magmatism, indicating synchronous ultra-high temperature metamorphism, magmatism, and shortening. Metamorphic pressures are estimated to be ~5–7 kbar (Fig. 5.8a), suggesting a burial depth of 18–25 km, consistent with (ultra-) high-temperature metamorphism occurring at mid-crustal depths and not at the base of a large orogens (such as the Himalayas; Fan et al., 2024). However, zircon saturation temperatures (Fig. 5.5a) and feldspar thermometry (Fig. 5.8b) indicate crystallization temperature >950ºC,

possibly >1050ºC. Therefore, as metamorphism occurred at mid-crustal depths synchronous with regional shortening and hot, predominately felsic and alkalic magmatism, another mechanism for regional UHT conditions is the syn-collisional emplacement of voluminous, hot felsic magmas.

Advective heating describes the transfer of heat and mass from lower crustal or mantle depths to higher structural levels. The ascent of magma is primarily accomplished through dyking at rates greater than heat loss to the wall-rock (Clemens and Mawer, 1992; Glazner, 2019; Petford et al., 1994)—i.e. adiabatically—thus allowing for hot magmas to perturb the geothermal gradient higher in the crust. Further, crystallization releases significantly more heat than required to heat a crystalline solid; for example, the crystallization of an albite crystal can increase the heat of an equivalent mass of crystalline albite by ~200ºC (Glazner, 2019). However, as thermal conductivity in rocks is low (Vosteen and Schellschmidt, 2003), the transfer and diffusion of heat are pretty inefficient (Stüwe, 2007), resulting in short-length scales of heat dispersion. Hence, we argue that a magmatic heat source for ultra-high temperature metamorphism should be proximal (i.e. observable) to ultra-high temperature metamorphic rocks. The Frontenac Suite likely intruded syn-metamorphically at >950ºC (Figs 5.5a and 5.8b); the geothermal gradient of the intruded crustal section was likely already elevated due to the immediately preceding opening of a back-arc (Hamza and Vieira, 2012; Shemenda, 1993), providing a favourable environment for extreme thermal conditions. The vast extent of the Frontenac Suite (Fig. 5.1) suggests a scenario with large volumes—including those found in the Sharbot Lake Domain and Adirondack Lowlands—of magma percolating and ponding throughout the affected area. In support of advective felsic magmatism, the entirety of the Frontenac-Adirondack Belt, save for the north Sharbot Lake Domain, records upper-amphibole to ultra-high temperature metamorphic temperatures at mid-crustal pressures coeval with magmatism (Chiarenzelli et al., 2010; Chiarenzelli et al., 2011; Corfu and Easton, 1997; Russell, 2009). Although internal (radiogenic) and orogenic (burial) heating were sources of heat, the intrusion of the Frontenac Suite into the thermally conditioned crust provided the additional heat to reach ultra-high temperatures. It may represent an overlooked global mechanism for extreme thermal metamorphism in compressional settings.

5.6 Conclusions

The Frontenac Terrane records over 200 million years of basin opening, filling, and closure before the Ottawan orogenic phase. The oldest rocks are metasedimentary, consisting of quartzite, quartzofeldspathic schist, mafic schist, aluminous gneiss, and marble; these were intruded by voluminous monzonite-syenite-granite magmas with subordinate gabbro, diorite, and anorthosite. The inferred protoliths represent the deposition of sediments in a back-arc basin subjected to ultra-high temperature metamorphism via the intrusion of magma produced following slab breakoff—significant mixing between evolved sediments and mantle-derived material produced high $\delta^{18}O$ magmas. Deformation records multiple stages of thrusting and overall uplift to a high structural position following the 1200–1160 Ma Shawinigan orogeny. This tectonometamorphic history is shared with the Sharbot Lake Domain and Adirondack Lowlands, indicating a fundamental relationship between tectonic blocks. Further, similar timing of sedimentation elsewhere in the Central Metasedimentary Belt suggests the formation of an extensive back-arc system analogous to the Philippine or Tasman seas outboard of Laurentia before orogenesis. The advection of magma from lower crustal or upper mantle levels can produce ultra-high temperature metamorphism if a sufficient volume of hot magma intrudes thermally conditioned crust at mid-crustal depths.

5.7 References

Ague, J.J. 1991. Evidence for major mass transfer and volume strain during regional metamorphism of pelites. Geology, **19**: 855. doi:10.1130/0091-7613(1991)019<0855:EFMMTA>2.3.CO;2.

Alessio, K.L., Hand, M., Kelsey, D.E., Williams, M.A., Morrissey, L.J., and Barovich, K. 2018. Conservation of deep crustal heat production. Geology, **46**: 335–338. doi:10.1130/G39970.1.

Aranovich, L.Ya., and Berman, R.G. 1997. A new garnet-orthopyroxene thermometer based on reversed Al_2O_3 solubility in FeO-Al_2O_3-SiO_2 orthopyroxene. American Mineralogist, **82**: 345–353. doi:10.2138/am-1997-3-413.

Baird, G.B., and Shrady, C.H. 2011. Timing and kinematics of deformation in the northwest Adirondack Lowlands, New York State: Implications for terrane relationships in the southern Grenville Province. Geosphere, **7**: 1303–1323. doi:10.1130/GES00689.1.

Bartholomew, M.J., and Hatcher, R.D. 2010. The Grenville orogenic cycle of southern Laurentia: Unraveling sutures, rifts, and shear zones as potential piercing points for Amazonia. Journal of South American Earth Sciences, **29**: 4–20. doi:10.1016/j.jsames.2009.08.007.

Bhattacharya, S. 1993. Refinement of geothermobarometry for cordierite granulites. Journal of Earth System Science, **102**: 537–545. doi:10.1007/BF02871952.

Bindeman, I., Gurenko, A., Carley, T., Miller, C., Martin, E., and Sigmarsson, O. 2012. Silicic magma petrogenesis in Iceland by remelting of hydrothermally altered crust based on oxygen isotope diversity and disequilibria between zircon and magma with implications for MORB. Terra Nova, **24**: 227–232. doi:10.1111/j.1365-3121.2012.01058.x.

Boehnke, P., Watson, E.B., Trail, D., Harrison, T.M., and Schmitt, A.K. 2013. Zircon saturation re-revisited. Chemical Geology, **351**: 324–334. doi:10.1016/j.chemgeo.2013.05.028.

Busch, J.P., and Van Der Pluijm, B.A. 1996. Late orogenic, plastic to brittle extension along the Robertson Lake shear zone: implications for the style of deep-crustal extension in the Grenville orogen, Canada. Precambrian Research, **77**: 41–57. doi:10.1016/0301-9268(95)00044-5.

Cao, H.-W., Pei, Q.-M., Santosh, M., Li, G.-M., Zhang, L.-K., Zhang, X.-F., Zhang, Y.-H., Zou, H., Dai, Z.-W., Lin, B., Tang, L., and Yu, X. 2022. Himalayan leucogranites: A review of geochemical and isotopic characteristics, timing of formation, genesis, and rare metal mineralization. Earth-Science Reviews, **234**: 104229. doi:10.1016/j.earscirev.2022.104229.

Carl, J.D. 1988. Popple Hill Gneiss as dacite volcanics: A geochemical study of mesosome and leucosome, northwest Adirondacks, New York. Geological Society of America Bulletin, **100**: 841–849. doi:10.1130/0016-7606(1988)100<0841:PHGADV>2.3.CO;2.

Carr, S.D., Easton, R.M., Jamieson, R.A., and Culshaw, N.G. 2000. Geologic transect across the Grenville orogen of Ontario and New York. Canadian Journal of Earth Sciences, **37**: 193–216. doi:10.1139/e99-074.

Carrapa, B., Jepson, G., DeCelles, P.G., George, S.W.M., Ducea, M., Campbell, C., and Dawson (Née Canavan), R.R. 2025. Crustal bobbing in response to lithospheric foundering recorded by detrital proxy records from the central Andean Plateau. Geology, **53**: 29–33. doi:10.1130/G52455.1.

Chiarenzelli, J., Kratzmann, D., Selleck, B., deLorraine, W., and Lupulescu, M. 2017. Utility of detrital zircon grains from upper amphibolite facies rocks of the Grenville Supergroup, Adirondack Lowlands, Northeastern United States. *In* Sediment Provenance. Elsevier. pp. 371–401. doi:10.1016/B978-0-12-803386-9.00014-9.

Chiarenzelli, J., Lupulescu, M., Thern, E., and Cousens, B. 2011a. Tectonic implications of the discovery of a Shawinigan ophiolite (Pyrites Complex) in the Adirondack Lowlands. Geosphere, **7**: 333–356. doi:10.1130/GES00608.1.

Chiarenzelli, J., Regan, S., Peck, W.H., Selleck, B.W., Cousens, B., Baird, G.B., and Shrady, C.H. 2010. Shawinigan arc magmatism in the Adirondack Lowlands as a consequence of closure of the Trans-Adirondack backarc basin. Geosphere, **6**: 900–916. doi:10.1130/GES00576.1.

Chiarenzelli, J., Valentino, D., Lupulescu, M., Thern, E., and Johnston, S. 2011b. Differentiating Shawinigan and Ottawan orogenesis in the Central Adirondacks. Geosphere, **7**: 2–22. doi:10.1130/GES00583.1.

Chiarenzelli, J.R., and McLelland, J.M. 1991. Age and regional relationships of granitoid rocks of the Adirondack Highlands. The Journal of Geology, **99**: 571–590. doi:10.1086/629518.

Clark, C., Fitzsimons, I.C.W., Healy, D., and Harley, S.L. 2011. How does the continental crust get really hot? Elements, **7**: 235–240. doi:10.2113/gselements.7.4.235.

Clemens, J.D., and Mawer, C.K. 1992. Granitic magma transport by fracture propagation. Tectonophysics, **204**: 339–360. doi:10.1016/0040-1951(92)90316-X.

Collins, W.J., and Richards, S.W. 2008. Geodynamic significance of S-type granites in circum-Pacific orogens. Geology, **36**: 559. doi:10.1130/G24658A.1.

Corfu, F., and Easton, R. 1997. Sharbot Lake terrane and its relationships to Frontenac terrane, Central Metasedimentary Belt, Grenville Province: new insights from U-Pb geochronology. Canadian Journal of Earth Sciences, **34**: 1239–1257.

Corfu, F., and Easton, R.M. 1995. U–Pb geochronology of the Mazinaw terrane, an imbricate segment of the Central Metasedimentary Belt, Grenville Province, Ontario. Canadian Journal of Earth Sciences, **32**: 959–976. doi:10.1139/e95-081.

Corrigan, D., Culshaw, N.G., and Mortensen, J.K. 1994. Pre-Grenvillian evolution and Grenvillian overprinting of the Parautochthonous Belt in Key Harbour, Ontario: U–Pb

and field constraints. Canadian Journal of Earth Sciences, **31**: 583–596. doi:10.1139/e94-051.

Corriveau, L. 1990. Proterozoic subduction and terrane amalgamation in the southwestern Grenville province, Canada: Evidence from ultrapotassic to shoshonitic plutonism. Geology,.

Corriveau, L., and van Breemen, O. 2000. Docking of the Central Metasedimentary Belt to Laurentia in geon 12: evidence from the 1.17– 1.16 Ga Chevreuil intrusive suite and host gneisses, Quebec. **37**.

Cosca, M.A., Essene, E.J., Kunk, M.J., and Sutter, J.F. 1992. Differential unroofing within the Central Metasedimentary Belt of the Grenville Orogen: constraints from 40Ar/39Ar thermochronology. Contributions to Mineralogy and Petrology, **110**: 211–225. doi:10.1007/BF00310739.

Cosca, M.A., Sutter, J.F., and Essene, E.J. 1991. Cooling and inferred uplift/erosion history of the Grenville Orogen, Ontario: Constraints from 40Ar/39Ar thermochronology. Tectonics, **10**: 959–977. doi:10.1029/91TC00859.

Culshaw, N., Foster, J., Marsh, J., Slagstad, T., and Gerbi, C. 2016. Kiosk domain, Central Gneiss Belt, Grenville Province, Ontario: A Labradorian palimpsest preserved in the ductile deep crust. Precambrian Research, **280**: 249–278. doi:10.1016/j.precamres.2016.05.002.

Culshaw, N.G., Jamieson, R.A., Ketchum, J.W.F., Wodicka, N., Corrigan, D., and Reynolds, P.H. 1997. Transect across the northwestern Grenville orogen, Georgian Bay, Ontario: Polystage convergence and extension in the lower orogenic crust. Tectonics, **16**: 966–982. doi:10.1029/97TC02285.

Currie, K.L., and Ermanovics, I.F. 1971. Geology of the Loughborough Lake region, Ontario, with special emphasis on the origin of the granitoid rocks, a contribution to the syenite problem. doi:10.4095/102415.

Cutts, J. 2014. Age and geochemical character of granite and syenite plutons in the Grenville Province of Southeastern Ontario; Insights into magmatism during the Ottawan Orogeny and evidence of the Frontenac Intrusive Suite in the Sharbot Lake Domain. Master of Science, Carleton University, Ottawa, Ontario. doi:10.22215/etd/2014-10090.

Daly, J.S., and McLelland, J.M. 1991. Juvenile Middle Proterozoic crust in the Adirondack Highlands, Grenville province, northeastern North America. The Journal of Geology, **19**: 119–122. doi:10.1086/648198.

Davidson, A. (Anthony), Van Breemen, Otto., and Geological Survey of Canada. 2000. Age and extent of the Frontenac plutonic suite in the Central metasedimentary belt, Grenville Province, southeastern Ontario. Natural Resources Canada, Geological Survey of Canada.

Davidson, A., and van Breemen, O. 2000. Age and extent of the Frontenac plutonic suite in the Central metasedimentary belt, Grenville Province, southeastern Ontario. Current Research 2000-F4; Radiogenic Age and Isotopic Studies, Geological Survey of Canada.

Davidson, A., and Ketchum, J.W.F. 1993. Observations on the Maberly Shear Zone, a terrane boundary within the central metasedimentary belt, Grenville Province, Ontario. doi:10.4095/134253.

Davis, D.W., and Bartlett, J.R. 1988. Geochronology of the Belmont Lake Metavolcanic Complex and implications for crustal development in the Central Metasedimentary Belt, Grenville Province, Ontario. Canadian Journal of Earth Sciences, **25**: 1751–1759. doi:10.1139/e88-166.

Davis, D.W., and Sutcliffe, C.N. 2017. U-Pb Geochronology by LA-ICP-MS in samples from northern Ontario. Internal Report, Ontario Geological Survey.

De Capitani, C., and Brown, T.H. 1987. The computation of chemical equilibrium in complex systems containing non-ideal solutions. Geochimica et Cosmochimica Acta, **51**: 2639–2652. doi:10.1016/0016-7037(87)90145-1.

DePaolo, D.J. 1981. Neodymium isotopes in the Colorado Front Range and crust–mantle evolution in the Proterozoic. Nature, **291**: 193–196. doi:10.1038/291193a0.

Dickin, A., and Strong, J. 2021. Nd isotope mapping of the Frontenac Terrane in southwestern Grenville Province. Canadian Journal of Earth Sciences, **58**: 659–669. doi:10.1139/cjes-2020-0063.

Duguet, M., and Easton, R.M. 2017. Tectonic and metamorphic architecture of the northeastern Composite Arc Belt and the Central Metasedimentary Belt boundary tectonic zone, Grenville Orogen: A geological guidebook. Ontario Geological Survey.

Easton, R.M. 2017. Insights into the tectonic and metamorphic architecture of the Composite Arc Belt and the Frontenac-Adirondack Belt near Perth, Ontario, Grenville Orogen: A Geological Guidebook. Ontario Geological Survey.

Easton, R.M. 2019. Geological, geochemical, geophysical and petrographic data from the Perth Area, Grenville Province, Southeastern Ontario. Ontario Geological Survey, Sudbury Ontario.

Easton, R.M., and Davidson, A. 1994. Terranes, domains, and lithotectonic assemblages within the Grenville Province. Geoscience Canada,.

Eby, G.N. 1992. Chemical subdivision of the A-type granitoids: Petrogenetic and tectonic implications. Geology, **20**: 641. doi:10.1130/0091-7613(1992)020<0641:CSOTAT>2.3.CO;2.

Emslie, R.F., and Hunt, P.A. 1990. Ages and petrogenetic significance of igneous mangerite-charnockite suites associated with massif anorthosites, Grenville Province. The Journal of Geology, **98**: 213–231. doi:10.1086/629394.

Ermanovics, I.F. 1970. Zonal structure of the Perth Road monzonite, Grenville Province, Ontario. Canadian Journal of Earth Sciences, **7**: 414–434. doi:10.1139/e70-036.

Evelyne, T., Annelore, B., François, B., and Sébastien, P. 2018. Thermal model of successive dike injections and implications for the development of intraplate volcanoes. Lithos, **322**: 129–147. doi:10.1016/j.lithos.2018.10.007.

Fan, Y.-L., Zhang, L.-F., Wang, Y., and Li, Z.-H. 2024. Role of crustal radiogenic heating in ultra-high temperature metamorphism of the Greater Himalayan Crystalline complex: Phase equilibrium and numerical modelling. Gondwana Research, **125**: 301–316. Elsevier BV. doi:10.1016/j.gr.2023.09.002.

Ferry, J.M., and Spear, F.S. 1978. Experimental calibration of the partitioning of Fe and Mg between biotite and garnet. Contributions to Mineralogy and Petrology, **66**: 113–117. doi:10.1007/BF00372150.

Friedman, R.M., and Martignole, J. 1995. Mesoproterozoic sedimentation, magmatism, and metamorphism in the southern part of the Grenville Province (western Quebec): U–Pb geochronological constraints. Canadian Journal of Earth Sciences, **32**: 2103–2114. doi:10.1139/e95-164.

Frost, B.R., Barnes, C.G., Collins, W.J., Arculus, R.J., Ellis, D.J., and Frost, C.D. 2001. A geochemical classification for granitic rocks. Journal of Petrology, **42**: 2033–2048. doi:10.1093/petrology/42.11.2033.

Frost, B.R., and Chacko, T. 1989. The granulite uncertainty principle: Limitations on thermobarometry in granulites. The Journal of Geology, **97**: 435–450. doi:10.1086/629321.

Frost, B.R., and Frost, C.D. 2008. A geochemical classification for feldspathic igneous rocks. Journal of Petrology, **49**: 1955–1969. doi:10.1093/petrology/egn054.

Fuhrman, M., and Lindsley, D. 1988. Ternary-feldspar modeling and thermometry. American Mineralogist, **73**: 201–215.

Garzione, C.N., Molnar, P., Libarkin, J.C., and MacFadden, B.J. 2006. Rapid late Miocene rise of the Bolivian Altiplano: Evidence for removal of mantle lithosphere. Earth and Planetary Science Letters, **241**: 543–556. doi:10.1016/j.epsl.2005.11.026.

Giustina, M.E.S.D., Pimentel, M.M., Ferreira Filho, C.F., and De Hollanda, M.H.B.M. 2011. Dating coeval mafic magmatism and ultrahigh temperature metamorphism in the Anápolis–Itauçu Complex, Central Brazil. Lithos, **124**: 82–102. doi:10.1016/j.lithos.2010.11.004.

Glazner, A.F. 2019. The ascent of water-rich magma and decompression heating: A thermodynamic analysis. American Mineralogist, **104**: 890–896. doi:10.2138/am-2019-6925.

Goldstein, S.J., and Jacobsen, S.B. 1988. Nd and Sr isotopic systematics of river water suspended material: implications for crustal evolution. Earth and Planetary Science Letters, **87**: 249–265. doi:10.1016/0012-821X(88)90013-1.

Grammatikopoulos, T.A., Clark, A.H., and Archibald, D.A. 2007. Petrogenesis of the Leo Lake and Lyndhurst plutons, Frontenac terrane, Central Metasedimentary Belt, southeastern Ontario, Canada. Canadian Journal of Earth Sciences, **44**: 107–126. doi:10.1139/e06-072.

Hamza, V.M., and Vieira, F.P. 2012. Global distribution of the lithosphere-asthenosphere boundary: a new look. Solid Earth, **3**: 199–212. doi:10.5194/se-3-199-2012.

Harley, S. 1998. An appraisal of peak temperature and thermal histories in ultrahigh-temperature (UHT) crustal metamorphism: The significance of aluminous orthopyroxene. Memoirs of National Institute of Polar Resource,: 49–73.

Harley, S.L. 2016. A matter of time: The importance of the duration of UHT metamorphism. Journal of Mineralogical and Petrological Sciences, **111**: 50–72. doi:10.2465/jmps.160128.

Hasterok, D., Gard, M., and Webb, J. 2018. On the radiogenic heat production of metamorphic, igneous, and sedimentary rocks. Geoscience Frontiers, **9**: 1777–1794. doi:10.1016/j.gsf.2017.10.012.

Hauer, K. 1995. Protoliths, diagenesis, and depositional history of the Upper Marble, Adirondack Lowlands, New York. PhD, Miami University, Oxford, Ohio.

Hernández-Montenegro, D., Andronicos, C.L., Zuluaga, C.A., and Aronoff, R.F. 2019. Effects of melt loss, melt retention, and protolith composition on differentiation of anatectic metapelites: A case study of the Wet Mountains, Colorado. Lithos, **344–345**: 425–439. doi:10.1016/j.lithos.2019.06.032.

Herron, M.M. 1988. Geochemical classification of terrigenous sands and shales from core or Log data. SEPM Journal of Sedimentary Research, **58**: 820–829. doi:10.1306/212F8E77-2B24-11D7-8648000102C1865D.

Heumann, M.J., Bickford, M.E., Hill, B.M., McLelland, J.M., Selleck, B.W., and Jercinovic, M.J. 2006. Timing of anatexis in metapelites from the Adirondack lowlands and southern highlands: A manifestation of the Shawinigan orogeny and subsequent anorthosite-mangerite-charnockite-granite magmatism. Geological Society of America Bulletin, **118**: 1283–1298. doi:10.1130/B25927.1.

Hewitt, D.F., Jupe, D.F., and Jackson, B. 1961. Map of the Gananoque Area, Ontario. Ontario Department of Mines.

Hildebrand, R.S., and Easton, R.M. 1995. An 1161 Ma suture in the Frontenac terrane, Ontario segment of the Grenville orogen. Geology, **23**: 917. doi:10.1130/0091-7613(1995)023<0917:AMSITF>2.3.CO;2.

Holland, T., and Powell, R. 2003. Activity-composition relations for phases in petrological calculations: an asymmetric multicomponent formulation. Contributions to Mineralogy and Petrology, **145**: 492–501. doi:10.1007/s00410-003-0464-z.

Hynes, A., and Rivers, T. 2010. Protracted continental collision—evidence from the Grenville Orogen. Canadian Journal of Earth Sciences, **47**: 591–620. doi:10.1139/E10-003.

Indares, A. 2024. The Grenville Province: revisiting the orogenic framework and integrating recent findings. Canadian Journal of Earth Sciences,: cjes-2023-0143. doi:10.1139/cjes-2023-0143.

Jaupart, C., and Mareschal, J.-C. 2014. Constraints on crustal heat production from heat flow data. *In* Treatise on Geochemistry. Elsevier. pp. 53–73. doi:10.1016/B978-0-08-095975-7.00302-8.

Jiao, S., Brown, M., Mitchell, R.N., Chowdhury, P., Clark, C., Chen, L., Chen, Y., Korhonen, F., Huang, G., and Guo, J. 2023. Mechanisms to generate ultrahigh-temperature metamorphism. Nature Reviews Earth & Environment, **4**: 298–318. doi:10.1038/s43017-023-00403-2.

Johnson, T.A., Vervoort, J.D., Ramsey, M.J., Southworth, S., and Mulcahy, S.R. 2020. Tectonic evolution of the Grenville Orogen in the central Appalachians. Precambrian Research, **346**: 105740. doi:10.1016/j.precamres.2020.105740.

Kamo, S.L., and Hamilton, M.A. 2017. Part A: Report on U-Pb ID-TIMS geochronology for the Ontario Geological Survey: Bedrock mapping projects, Ontario, Year 2: 2016-207. Internal Report.

Karig, D., and Moore, G. 1975. Tectonically controlled sedimentation in marginal basins. Earth and Planetary Science Letters, **26**: 233–238.

Kelsey, D.E., and Hand, M. 2015. On ultrahigh temperature crustal metamorphism: Phase equilibria, trace element thermometry, bulk composition, heat sources, timescales and tectonic settings. Geoscience Frontiers, **6**: 311–356. doi:10.1016/j.gsf.2014.09.006.

Ketchum, J.W.F., and Davidson, A. 2000. Crustal architecture and tectonic assembly of the Central Gneiss Belt, southwestern Grenville Province, Canada: a new interpretation. **37**.

Kiessling, G.M. 2016. Provenance of the Flinton Group, Grenville Province, Southeastern Ontario. B.Sc, University of Waterloo, Waterloo, Ontario.

Krogh, T.E. 1993. High precision U-Pb ages for granulite metamorphism and deformation in the Archean Kapuskasing structural zone, Ontario: implications for structure and development of the lower crust. Earth and Planetary Science Letters, **119**: 1–18. doi:10.1016/0012-821X(93)90002-Q.

Krogh, T.E., and Hurley, P.M. 1968. Strontium isotope variation and whole-rock isochron studies, Grenville Province of Ontario. Journal of Geophysical Research, **73**: 7107–7125. doi:10.1029/JB073i022p07107.

Krogh, T.E., and Moser, D.E. 1994. U–Pb zircon and monazite ages from the Kapuskasing uplift: age constraints on deformation within the Ivanhoe Lake fault zone. Canadian Journal of Earth Sciences, **31**: 1096–1103. doi:10.1139/e94-098.

Lambert, C., Gervais, F., Crowley, J.L., Moukhsil, A., and Kavanagh-Lepage, C. 2023. Protracted melt-present deformation during the Rigolet phase of the Grenvillian Orogeny. Insights from geochronology along the highway 117 transect through the Grenville Province in western Quebec, Canada. Precambrian Research, **384**: 106939. doi:10.1016/j.precamres.2022.106939.

Lei, H., and Xu, H. 2018. A review of ultrahigh temperature metamorphism. Journal of Earth Science, **29**: 1167–1180. doi:10.1007/s12583-018-0846-9.

Lentz, D. 1992. U Ottawa. Petrogenesis of U-, Th-, Mo-, and REE-bearing pegmatites, skarns and veins in the central metasedimentary belt of the Grenville Province, ONtario and Quebec. PhD, University of Ottawa, Ottawa, ON, Canada.

Lumbers, S., Heaman, L.M., Vertolli, V.M., Wu, T.W., Gower, C.F., Rivers, T., and Ryan, A.B. 1990. Nature and timing of Middle Proterozoic magmatism in the Central metasedimentary belt, Grenville Province, Ontario. Geological Association of Canada, **38**: 243–276.

Marcantonio, F., Mcnutt, R.H., Dickin, A.P., and Heaman, L.M. 1990. Isotopic evidence for the crustal evolution of the Frontenac Arch in the Grenville Province of Ontario, Canada. Chemical Geology, **83**: 297–314.

Markley, M.J., Dunn, S.R., Jercinovic, M.J., Peck, W.H., and Williams, M.L. 2018. Monazite U–Th–Pb geochronology of the Central Metasedimentary Belt Boundary Zone (CMBbz), Grenville Province, Ontario Canada. Canadian Journal of Earth Sciences, **55**: 1063–1078. doi:10.1139/cjes-2018-0039.

Martignole, J., and Wang, Z. 2010. Feldspar thermometry of grenvillian-age UHT migmatites. Mollendo-Camana block, southern Peru. The Canadian Mineralogist, **48**: 1025–1039. doi:10.3749/canmin.48.4.1025.

McDonough, W.F., and Sun, S.-S. 1995. The composition of the Earth. Chemical Geology,: 223–253.

McEachern, S.J., and van Breemen, O. 1993. Age of deformation within the Central Metasedimentary Belt boundary thrust zone, southwest Grenville Orogen: constraints on the collision of the Mid-Proterozoic Elzevir terrane. Canadian Journal of Earth Sciences, **30**: 1155–1165. doi:10.1139/e93-098.

McLelland, J., Chiarenzelli, J., and Perham, A. 1992. Age, field, and petrological relationships of the Hyde School Gneiss, Adirondack Lowlands, New York: Criteria for an intrusive igneous origin. The Journal of Geology, **100**: 69–90. doi:10.1086/629572.

McLelland, J., Hamilton, M., Selleck, B., McLelland, J., Walker, D., and Orrell, S. 2001. Zircon U-Pb geochronology of the Ottawan Orogeny, Adirondack Highlands, New York: regional and tectonic implications. Precambrian Research, **109**: 39–72. doi:10.1016/S0301-9268(01)00141-3.

McLelland, J.M., and Chiarenzelli, J.R. 1990. Geochronological studies in the Adirondack Mountains and the implications of a Middle Proterozoic tonalitic suite. Geological Association of Canada,.

McLelland, J.M., Daly, J.S., and Chiarenzelli, J. 1993. Sm-Nd and U-Pb Isotopic evidence of juvenile crust in the Adirondack Lowlands and implications for the evolution of the Adirondack Mts. The Journal of Geology, **101**: 97–105. doi:10.1086/648198.

McLelland, J.M., Selleck, B.W., and Bickford, M.E. 2010. Review of the Proterozoic evolution of the Grenville Province, its Adirondack outlier, and the Mesoproterozoic inliers of the Appalachians. *In* From Rodinia to Pangea: The Lithotectonic Record of the Appalachian Region. Geological Society of America. doi:10.1130/2010.1206(02).

McMillan, M., Schoenbohm, L.M., and Tye, A.R. 2023. Plateau formation controlled by lithospheric foundering under a weak crust. Geophysical Research Letters, **50**: e2023GL103996. doi:10.1029/2023GL103996.

McNutt, R.H., and Dickin, A.P. 2012. A comparison of Nd model ages and U–Pb zircon ages of Grenville granitoids: constraints on the evolution of the Laurentian margin from 1.5 to 1.0 Ga. Terra Nova, **24**: 7–15. doi:10.1111/j.1365-3121.2011.01031.x.

Mezger, K., Essene, E.J., Van Der Pluijm, B.A., and Halliday, A.N. 1993. U-Pb geochronology of the Grenville Orogen of Ontario and New York: Constraints on ancient crustal

tectonics. Contributions to Mineralogy and Petrology, **114**: 13–26. doi:10.1007/BF00307862.

Mezger, K., Rawnsley, C.M., Bohlen, S.R., and Hanson, G.N. 1991. U-Pb garnet, sphene, monazite, and rutile ages: Implications for the duration of high-grade metamorphism and cooling histories, Adirondack Mts., New York. The Journal of Geology, **99**: 415–428. doi:10.1086/629503.

Mezger, K., Van Der Pluijm, B.A., Essene, E.J., and Halliday, A.N. 1992. The Carthage-Colton Mylonite Zone (Adirondack Mountains, New York): The site of a cryptic suture in the Grenville Orogen? The Journal of Geology, **100**: 630–638. doi:10.1086/629613.

Middlemost, E.A.K. 1994. Naming materials in the magma/igneous rock system. Earth-Science Reviews, **37**: 215–224. doi:10.1016/0012-8252(94)90029-9.

Moecher, D.P., Anderson, E.D., Cook, C.A., and Mezger, K. 1997. The petrogenesis of metamorphosed carbonatites in the Grenville Province, Ontario. Canadian Journal of Earth Sciences, **34**: 1185–1201. doi:10.1139/e17-095.

Nesbitt, H.W., and Young, G.M. 1984. Prediction of some weathering trends of plutonic and volcanic rocks based on thermodynamic and kinetic considerations. Geochimica et Cosmochimica Acta, **48**: 1523–1534. doi:10.1016/0016-7037(84)90408-3.

Passchier, C.W., and Trouw, R.A.J. 2005. Microtectonics. *In* 2nd, rev.enl. ed edition. Springer, Berlin ; New York.

Pattison, D.R.M. 2003. Temperatures of granulite-facies metamorphism: Constraints from experimental phase equilibria and thermobarometry corrected for retrograde exchange. Journal of Petrology, **44**: 867–900. doi:10.1093/petrology/44.5.867.

Pearce, J.A., Harris, N.B.W., and Tindle, A.G. 1984. Trace Element Discrimination Diagrams for the Tectonic Interpretation of Granitic Rocks. Journal of Petrology, **25**: 956–983. doi:10.1093/petrology/25.4.956.

Peck, W.H. 2012. Reconnaissance geochronology and geochemistry of the Mont-Tremblant gneiss of the Morin terrane, Grenville Province, Québec.

Peck, W.H., and Lin, H.Y. 2024. Provenance and depositional age of metasedimentary rocks in the Frontenac terrane (Grenville Province, Ontario). Canadian Journal of Earth Sciences,: cjes-2024-0029. doi:10.1139/cjes-2024-0029.

Peck, W.H., Rathkopf, C.A., Mathur, R.D., and Matt, P.D. 2022. Stable isotope (C, O, S, and Zn) geochemistry of marble-hosted exhalative zinc deposits in the Central Metasedimentary Belt, Grenville Province, Canada: Insights into ore deposition and tectonic setting. Ore Geology Reviews, **148**: 105057. doi:10.1016/j.oregeorev.2022.105057.

Peck, W.H., Selleck, B.W., Wong, M.S., Chiarenzelli, J.R., Harpp, K.S., Hollocher, K., Lackey, J.S., Catalano, J., Regan, S.P., and Stocker, A. 2013. Orogenic to postorogenic (1.20-1.15 Ga) magmatism in the Adirondack Lowlands and Frontenac terrane, southern Grenville Province, USA and Canada. Geosphere, **9**: 1637–1663. doi:10.1130/GES00879.1.

Peck, W.H., Valley, J.W., Corriveau, L., Davidson, A., McLelland, J., and Farber, D.A. 2004. Oxygen-isotope constraints on terrane boundaries and origin of 1.18-1.13 Ga granitoids in the southern Grenville Province. Geological Society of America Memior,: 163–182.

Pehrsson, S., Hanmer, S., and Van Breemen, O. 1996. U–Pb geochronology of the Raglan gabbro belt, Central Metasedimentary Belt, Ontario: implications for an ensialic marginal basin in the Grenville Orogen. Canadian Journal of Earth Sciences, **33**: 691–702. doi:10.1139/e96-052.

Petford, N., Lister, J.R., and Kerr, R.C. 1994. The ascent of felsic magmas in dykes. Lithos, **32**: 161–168. doi:10.1016/0024-4937(94)90028-0.

Powell, R., Holland, T., and Worley, B. 1998. Calculating phase diagrams involving solid solutions via non-linear equations, with examples using THERMOCALC. Journal of Metamorphic Geology, **16**: 577–588. doi:10.1111/j.1525-1314.1998.00157.x.

Pownall, J.M., Hall, R., Armstrong, R.A., and Forster, M.A. 2014. Earth's youngest known ultrahigh-temperature granulites discovered on Seram, eastern Indonesia. Geology, **42**: 279–282. doi:10.1130/G35230.1.

Ratcliffe, N.M., Aleinikoff, J.N., Burton, W.C., and Karabinos, P. 1991. Trondhjemitic, 1.35–1.31 Ga gneisses of the Mount Holly Complex of Vermont: evidence for an Elzevirian event in the Grenville Basement of the United States Appalachians. Canadian Journal of Earth Sciences, **28**: 77–93. doi:10.1139/e91-007.

Reinhardt, E.W. 1968. Phase relations in cordierite-bearing gneisses from the Gananoque area, Ontario. Canadian Journal of Earth Sciences, **5**: 455–482. doi:10.1139/e68-043.

Rivers, T. 1997. Lithotectonic elements of the Grenville Province: review and tectonic implications. Precambrian Research, **86**: 117–154. doi:10.1016/S0301-9268(97)00038-7.

Rivers, T. 2008. Assembly and preservation of lower, mid, and upper orogenic crust in the Grenville Province—Implications for the evolution of large hot long-duration orogens. Precambrian Research, **167**: 237–259. doi:10.1016/j.precamres.2008.08.005.

Rivers, T. 2012. Upper-crustal orogenic lid and mid-crustal core complexes: signature of a collapsed orogenic plateau in the hinterland of the Grenville Province. Canadian Journal of Earth Sciences, **49**: 1–42. doi:10.1139/e11-014.

Rivers, T., Culshaw, N., Hynes, A., Indares, A., Jamieson, R., and Martignole, J. 2012. The Grenville Orogen—a post-Lithprobe prospective. *In* Tectonic Styles in Canada: The Lithoprobe Perspective.

Roser, B.P., and Korsch, R.J. 1986. Determination of tectonic setting of sandstone-mudstone suites using SiO_2 content and K_2O/Na_2O ratio. Journal of Geology, **94**: 635–650.

Russell, A. 2009. Recent two-feldspar, Ti-in-biotite, and garnet-biotite geothermometry of the Frontenac terrane and Adirondack Lowlands, Grenville Province, Canada and the United States. Undergraduate Thesis, University of North Dakota, Grand Forks, North Dakota.

Sager-Kinsman, E.A., and Parrish, R.R. 1993. Geochronology of detrital zircons from the Elzevir and Frontenac terranes, Central Metasedimentary Belt, Grenville Province, Ontario. Canadian Journal of Earth Sciences, **30**: 465–473. doi:10.1139/e93-034.

Sdrolias, M., and Müller, R.D. 2006. Controls on back-arc basin formation. Geochemistry, Geophysics, Geosystems, **7**: 2005GC001090. doi:10.1029/2005GC001090.

Shemenda, A.I. 1993. Subduction of the lithosphere and back arc dynamics: Insights from physical modeling. Journal of Geophysical Research: Solid Earth, **98**: 16167–16185. doi:10.1029/93JB01094.

Shieh, Y.N. 1985. High-18O granitic plutons from the Frontenac Axis, Grenville province of Ontario, Canada. Geochimica et Cosmochimica Acta, **49**: 117–123. doi:10.1016/0016-7037(85)90195-4.

Smith, T.E., and Harris, M.J. 1996. The Queensborough mafic-ultramafic complex: a fragment of a Meso-Proterozoic ophiolite? Grenville Province, Canada. Tectonophysics, **265**: 53–82. doi:10.1016/S0040-1951(96)00146-1.

Smith, T.E., Harris, M.J., Huang, C.H., and Holm, P.E. 2001. The geochemical nature of the igneous rocks of the Sharbot Lake domain, Central Metasedimentary Belt, Ontario. Canadian Journal of Earth Sciences, **38**: 1037–1057. doi:10.1139/e01-001.

Smithies, R.H., Howard, H.M., Evins, P.M., Kirkland, C.L., Kelsey, D.E., Hand, M., Wingate, M.T.D., Collins, A.S., and Belousova, E. 2011. High-temperature granite magmatism, crust–mantle interaction and the Mesoproterozoic intracontinental evolution of the Musgrave Province, Central Australia. Journal of Petrology, **52**: 931–958. doi:10.1093/petrology/egr010.

Spooner, C.M. 1969. Sr^{87}/Sr^{86} ratios, K/Rb ratios,and rare-earth element abundances in pyroxene granulites. Doctor of Philosophy, Massachusetts Institite of Technology.

Storey, C.C., and Vos, M.A. 1981. Industrial minerals of the Pembroke-Renfrew Area. Ontario Geological Survey.

Streepey, M.M., Johnson, E.L., Mezger, K., and van der Pluijm, B.A. 2001. Early history of the Carthage-Colton Shear Zone, Grenville Province, Northwest Adirondacks, New York (U.S.A.). The Journal of Geology, **109**: 479–492. doi:10.1086/320792.

Streepey, M.M., Lithgow-Bertelloni, C., Van Der Pluijm, B.A., Essene, E.J., and Magloughlin, J.F. 2004. Exhumation of a collisional orogen: A perspective from the North American Grenville Province. *In* Memoir 197: Proterozoic Tectonic Evolution of the Grenville Orogen in North America. Geological Society of America. pp. 391–410. doi:10.1130/0-8137-1197-5.391.

Strong, J. 2017. Refining the tectonic and magmatic history of the SW Grenville Province. MSc, McMaster, Hamilton.

Stüwe, K. 2007. Geodynamics of the Lithosphere. *In* 2nd edition. Springer-Verlag.

Tan, S. 2024. Detrital zircon geochronology and provenance of quartzites in the Frontenac Terrane. Bachelor of Science, University of Waterloo, Waterloo, Ontario.

Timmermann, H., Jamieson, R.A., Parrish, R.R., and Culshaw, N.G. 2002. Coeval migmatites and granulites, Muskoka domain, southwestern Grenville Province, Ontario. Canadian Journal of Earth Sciences, **39**: 239–258. doi:10.1139/e01-076.

Tuccillo, M.E., Mezger, K., Essene, E.J., and Van Der Pluijm, B.A. 1992. Thermobarometry, Geochronology and the Interpretation of P-T-t Data in the Britt Domain, Ontario Grenville Orogen, Canada. Journal of Petrology, **33**: 1225–1259. doi:10.1093/petrology/33.6.1225.

Ueda, K., Jacobs, J., Thomas, R.J., Kosler, J., Jourdan, F., and Matola, R. 2012. Delamination-induced late-tectonic deformation and high-grade metamorphism of the Proterozoic

Nampula Complex, northern Mozambique. Precambrian Research, **196–197**: 275–294. doi:10.1016/j.precamres.2011.05.012.

Vosteen, H.-D., and Schellschmidt, R. 2003. Influence of temperature on thermal conductivity, thermal capacity and thermal diffusivity for different types of rock. Physics and Chemistry of the Earth, **28**: 499–509. doi:10.1016/S1474-7065(03)00069-X.

Wang, H., and Currie, C.A. 2015. Magmatic expressions of continental lithosphere removal. Journal of Geophysical Research: Solid Earth, **120**: 7239–7260. doi:10.1002/2015JB012112.

Wasteneys, H., McLelland, J., and Lumbers, S. 1999. Precise zircon geochronology in the Adirondack Lowlands and implications for revising plate- tectonic models of the Central Metasedimentary Belt and Adirondack Mountains, Grenville Province, Ontario and New York. **36**.

Wells, P.R.A. 1979. Chemical and thermal evolution of Archaean sialic crust, Southern West Greenland. Journal of Petrology, **20**: 187–226. doi:10.1093/petrology/20.2.187.

Whalen, J.B., Currie, K.L., and Chappell, B.W. 1987. A-type granites: geochemical characteristics, discrimination and petrogenesis. Contributions to Mineralogy and Petrology, **95**: 407–419. doi:10.1007/BF00402202.

White, D.J., Forsyth, D.A., Asudeh, I., Carr, S.D., Wu, H., Easton, R.M., and Mereu, R.F. 2000. A seismic-based cross-section of the Grenville Orogen in southern Ontario and western Quebec. Canadian Journal of Earth Sciences, **37**: 183–192. doi:10.1139/e99-094.

White, R.W., Powell, R., Holland, T.J.B., Johnson, T.E., and Green, E.C.R. 2014. New mineral activity–composition relations for thermodynamic calculations in metapelitic systems. Journal of Metamorphic Geology, **32**: 261–286. doi:10.1111/jmg.12071.

Wodicka, N., Corriveau, L., and Stern, R.A. 2004. SHRIMP U-Pb zircon geochronology of the Bondy gneiss complex: Evidence for circa 1.39 Ga arc magmatism and polyphase Grenvillian metamorphism in the Central Metasedimentary Belt, Grenville Province, Québec. *In* Memoir 197: Proterozoic Tectonic Evolution of the Grenville Orogen in North America. Geological Society of America. pp. 243–266. doi:10.1130/0-8137-1197-5.243.

Wodicka, N., Jamieson, R.A., and Parrish, R.R. 1996. The Parry Sound domain: a far-travelled allochthon? New evidence from U–Pb zicon geochronology. Canadian Journal of Earth Sciences, **33**: 1087–1104. doi:10.1139/e96-083.

Wong, M.S., Peck, W.H., Selleck, B.W., Catalano, J.P., Hochman, S.D., and Maurer, J.T. 2011. The Black Lake shear zone: A boundary between terranes in the Adirondack Lowlands, Grenville Province. Precambrian Research, **188**: 57–72. Elsevier B.V. doi:10.1016/j.precamres.2011.04.001.

Wynne-Edwards, H.R. 1967. Westport map area, Ontario, with special emphasis on the Precambrian rocks. doi:10.4095/100533.

Wynne-Edwards, H.R., and Hay, P.W. 1963. Coexisting cordierite and garnet in regionally metamorphosed rocks from the Westport area, Ontario. The Canadian Mineralogist, **7**: 453–478.

Xiang, H., and Connolly, J.A.D. 2022. GeoPS: An interactive visual computing tool for thermodynamic modelling of phase equilibria. Journal of Metamorphic Geology, **40**: 243–255. doi:10.1111/jmg.12626.

Zheng, Y.-F., and Chen, R.-X. 2017. Regional metamorphism at extreme conditions: Implications for orogeny at convergent plate margins. Journal of Asian Earth Sciences, **145**: 46–73. doi:10.1016/j.jseaes.2017.03.009.

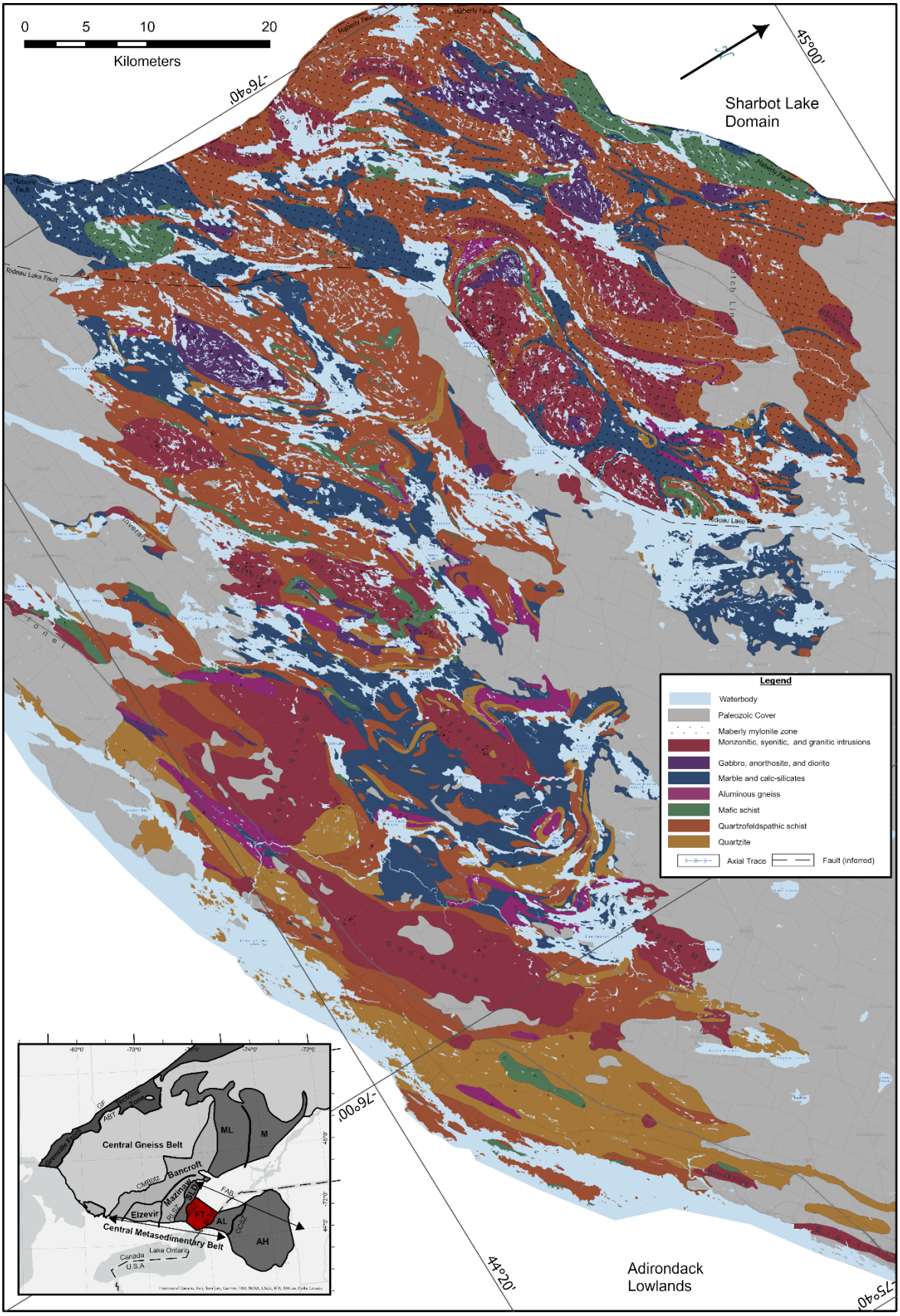

0 5 10 20
Kilometers
Sharbot Lake Domain
Adirondack Lowlands
Maberly Fault
Rideau Lake Fault
Robertson Lake Fault
Robertson Lake Shear Zone
Inverary
Tone
Ganaraska
Bancroft
Brockville
45°00'
76°40'
76°00'
44°20'
75°40'
Legend
Waterbody
Paleozoic Cover
Maberly mylonite zone
Monzonitic, syenitic, and granitic intrusions
Gabbro, anorthosite, and diorite
Marble and calc-silicates
Aluminous gneiss
Mafic schist
Quartzofeldspathic schist
Quartzite
Axial Trace
Fault (inferred)
Central Gneiss Belt
Central Metasedimentary Belt
Elzevir
Mazinaw
ML
M
FT
AL
AH
Lake Ontario
Canada
U.S.A

Figure 5.1: Geological map of the Frontenac Terrane. Data compiled from Hewitt et al. (1961), Wynne-Edwards (1967), Currie and Ermanovics (1971), and Davidson et al. (2000) were supplemented with new data and interpretations. Infrastructure and waterbody data are from the Government of Ontario (Ontario Road Network and Ontario Hydro Network, respectively) as of July 2024. A detailed version can be found in Appendix S4.1. Inset map of Grenville Province is modified from Carr et al. (2000). Abbreviations: SLB – Sharbot Lake Domain, FT – Frontenac Terrane, AL – Adirondack Lowlands, AH – Adirondack Highlands, ML – Mont Laurier Terrane, M – Morin Terrane, GF – Grenville Front, ABT – Allochthon Boundary Thrust, CMBbtz – Central Metasedimentary Belt boundary thrust zone, RLSZ – Robertson Lake Shear Zone, MSZ – Maberly Shear Zone, BLSZ – Black Lake Shear Zone, CCSZ – Carthage-Colton Shear Zone, FAB – Frontenac-Adirondack Belt.

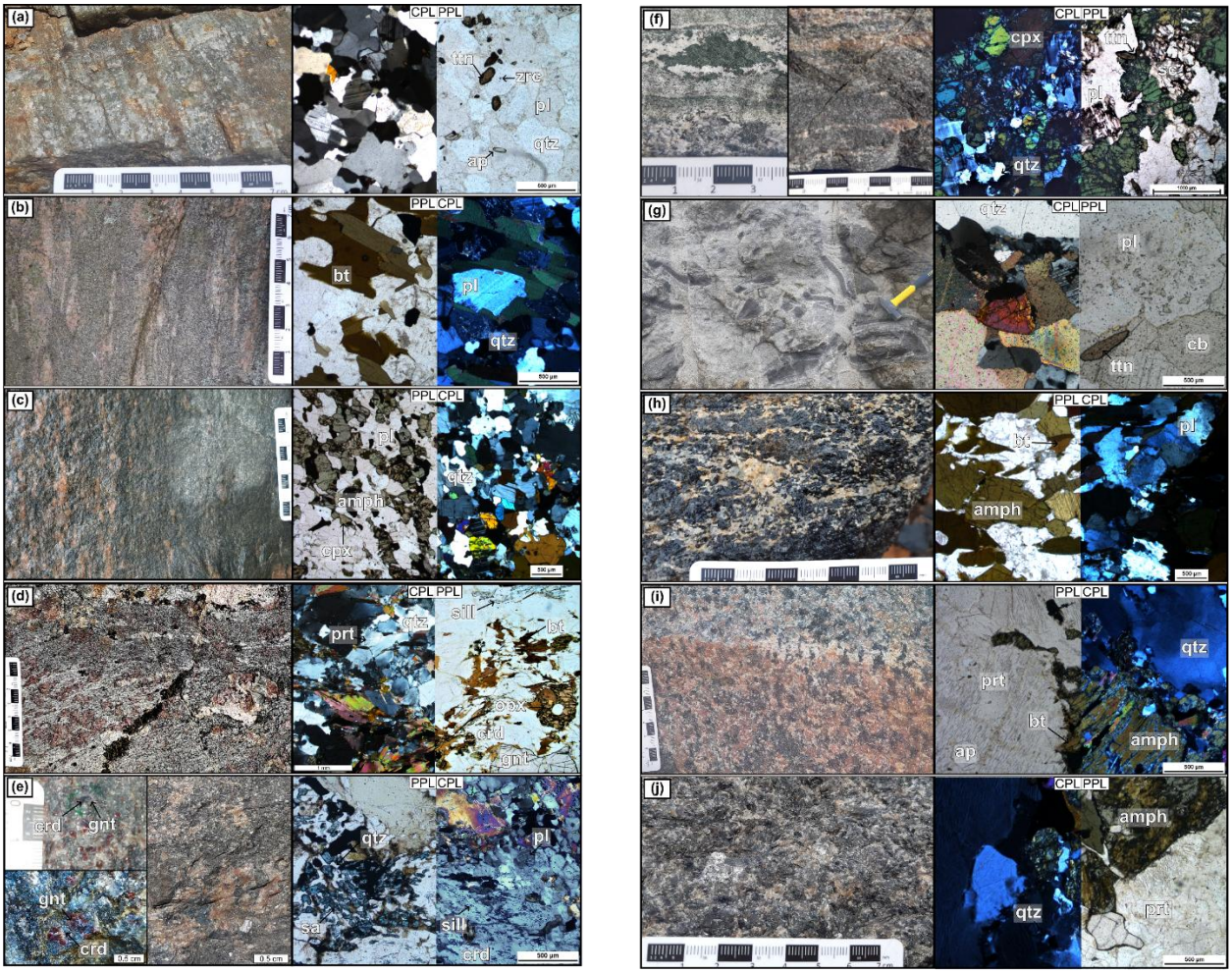


Figure 5.2: Outcrop (left) and microphotographs (right) of major rock types in the Frontenac Terrane. All split microphotographs are the same field of view in cross-polarized light (CPL) and plane-polarized light (PPL) (a) Clean quartzite with relict bedding and microphotograph of quartz arenite showing quartz, plagioclase, zircon, apatite, and titanite. (b) Blastomylonitic quartzofeldspathic schist with feldspar porphyroblasts and microphotograph of a different sample with plagioclase, quartz, and feldspar. (c) Mafic schist with mylonitic granitic dyke creating pink feldspar augen and microphotograph of representative mineralogy amphibole, clinopyroxene, plagioclase, and quartz. Ameboid grain boundaries—consistent with grain boundary migration—are visible in some quartz grains. (d) Cordierite aluminous gneiss with cm-scale light red garnet in patchy white leucosome. Microphotograph with sillimanite, orthopyroxene, cordierite, garnet, biotite, quartz, and ternary feldspar. Orthopyroxene is minorly replaced by biotite along fractures; cordierite is rimming garnet. Sillimanite is along grain boundaries and within cordierite. (e) Cordierite aluminous gneiss with patchy pink leucosome with photographs of

cordierite surrounded by garnet (top) and garnet surrounded by cordierite (bottom). Microphotograph with cordierite containing aligned sillimanite, sapphirine in apparent textural equilibrium with quartz, and plagioclase showing albite twinning. (f) Two photos of clinopyroxene aluminous gneiss, the left-hand side showing a clinopyroxene aggregate in stromatic white leucosome and the right-hand side showing pink layered leucosome in the grey groundmass. The microphotograph shows a representative mineral assemblage consisting of clinopyroxene, plagioclase, titanite, quartz, and scapolite. (g) Marble mélange enclosing blocks of dark grey clastic sedimentary rock and representative mineralogy of a dirty marble—quartz, plagioclase, titanite, and carbonate. (h) Amphibolized diorite with abundant leucosome and microphotograph showing amphibole, biotite, plagioclase, and quartz. (i) Syenite with foliation defined by amphibole and microphotograph showing ternary feldspar, biotite, amphibole, quartz, and apatite. (j) Monzonite with biotitzation of amphibole, ternary feldspar, and quartz. Mineral abbreviations: pl – plagioclase, qtz – quartz, cb – carbonate, ttn – titanite, bt – biotite, zrc – zircon, ap – apatite, amph – amphibole, cpx – clinopyroxene, sill – sillimanite, sa – sapphirine, prt – ternary feldspar, opx – orthopyroxene, crd – cordierite, gnt – garnet, sc – scapolite. Additional field images and microphotographs are available in Appendix S4.5.

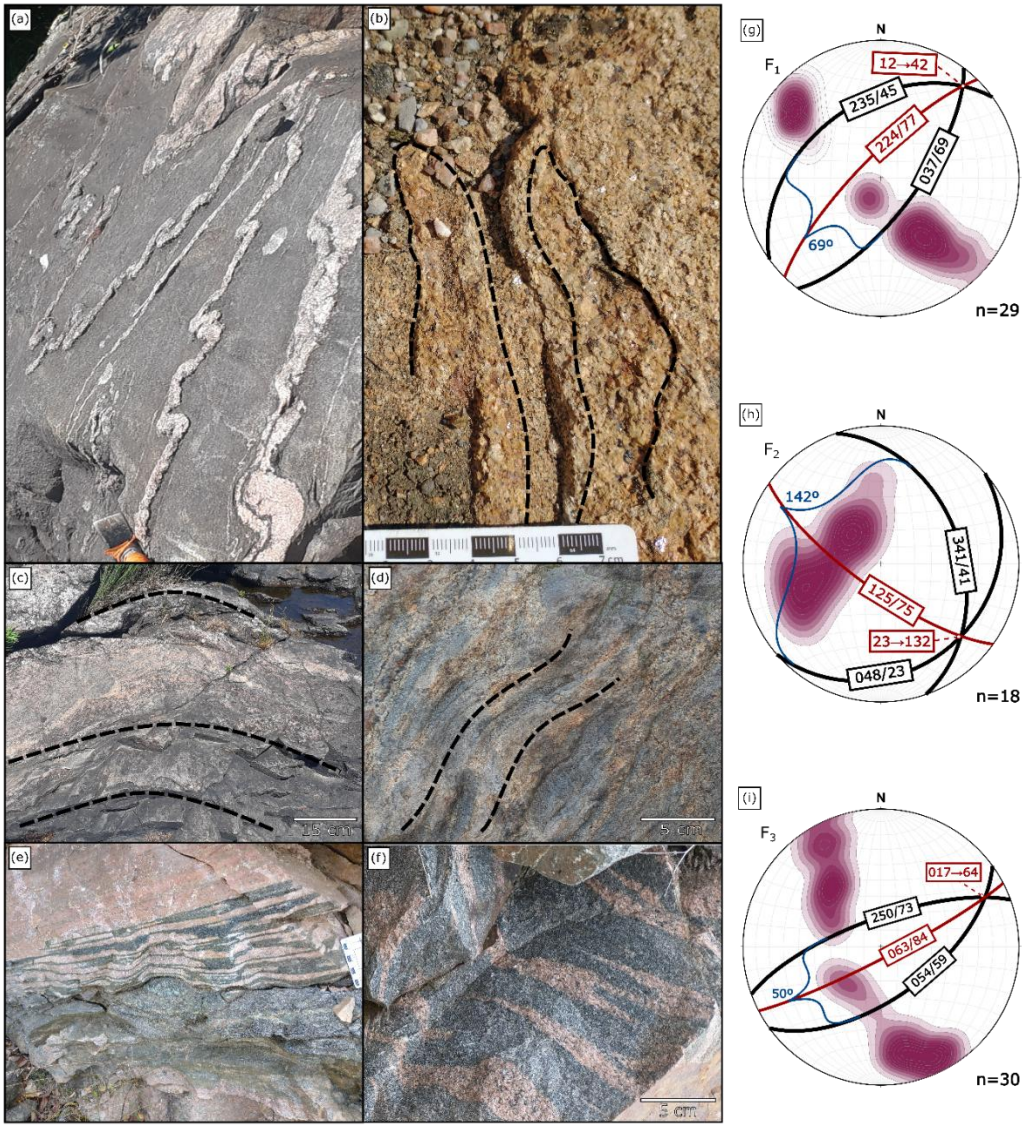


Figure 5.3: Photos of structures found in the Frontenac Terrane with steoronets for D_1, D_2, and D_3. (a) Stromatic leucosome folded by F_1. (b) Isoclinal fold parallel to F_1 refolded by broad F_2 folds. (c) Open F_2 fold on the top of an outcrop surface. (d) Stromatic leucosome parallel to F_1 stretching direction refolded by open F_2 folds. (e) Mylonitic monzogranite in contact with mafic schist. The contact and mylonite are folded by F_2 (f) Folded leucosome and boudinage parallel to F_2 refolded by F_3. (g-i) Steoronet summarizing F_1, F_2, and F_3 axial plane (red line), average limb (black lines), interlimb angle (blue line), and hinge (white dot with red border) orientations. Filled contours of foliation poles are spaced by 10% intervals.

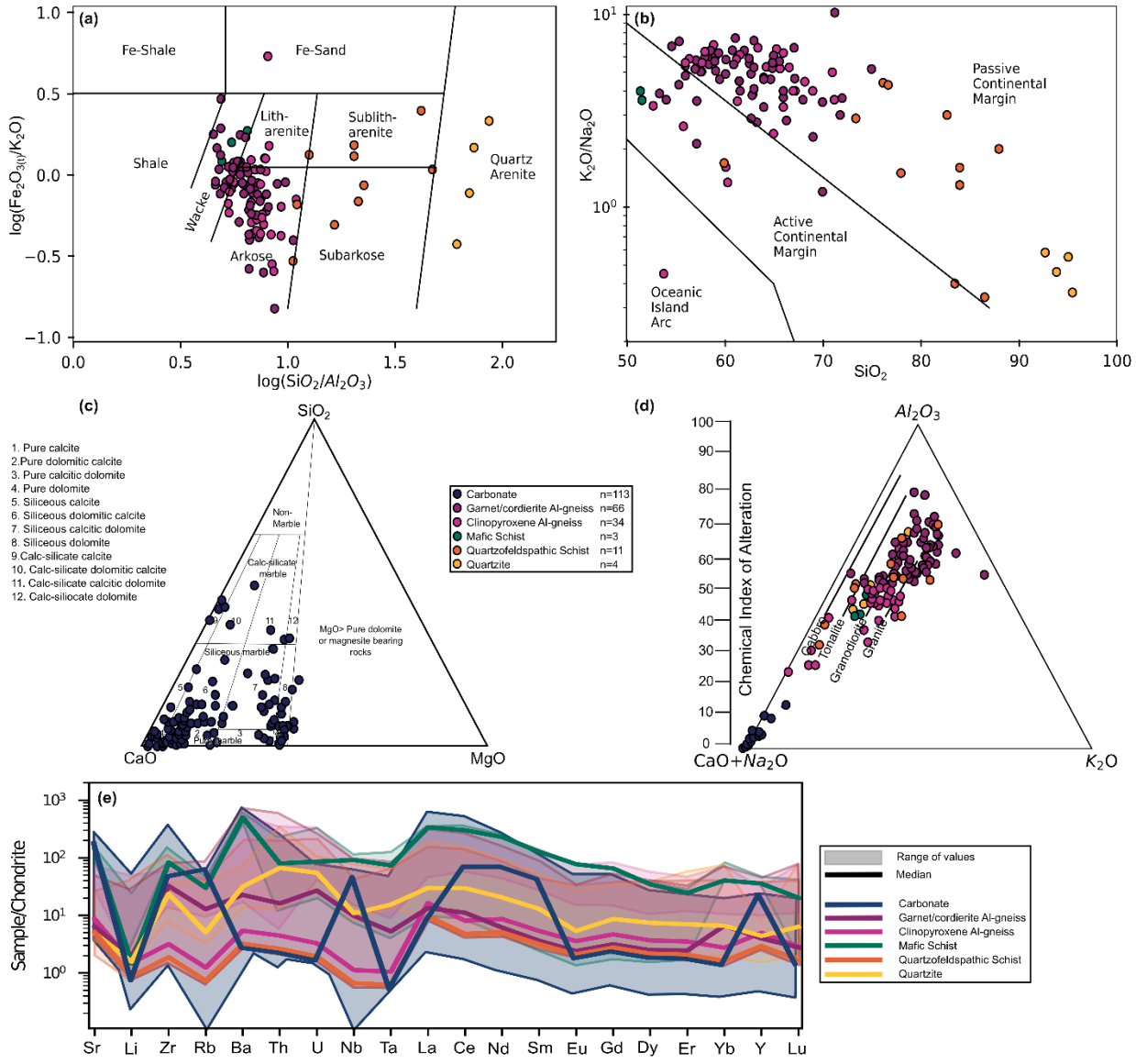


Figure 5.4: Geochemical plots of metasedimentary rocks from the Frontenac Terrane. (a) Geochemical-based lithology discrimination from Herron (1988). (b) Sedimentary source geochemical discrimination diagram (Roser and Korsch, 1986). (c) Marble classification ternary diagram (Storey and Vos, 1981) of Frontenac Terrane carbonates (d) ACNK ternary diagram with weathering trends of possible plutonic source (Nesbitt and Young, 1984). (e) Chondrite-normalized (McDonough and Sun, 1995) trace element diagram of metasedimentary rocks. Historic data from (Currie and Ermanovics, 1971; Easton, 2017; Marcantonio et al., 1990; Wynne-Edwards, 1967; Wynne-Edwards and Hay, 1963).

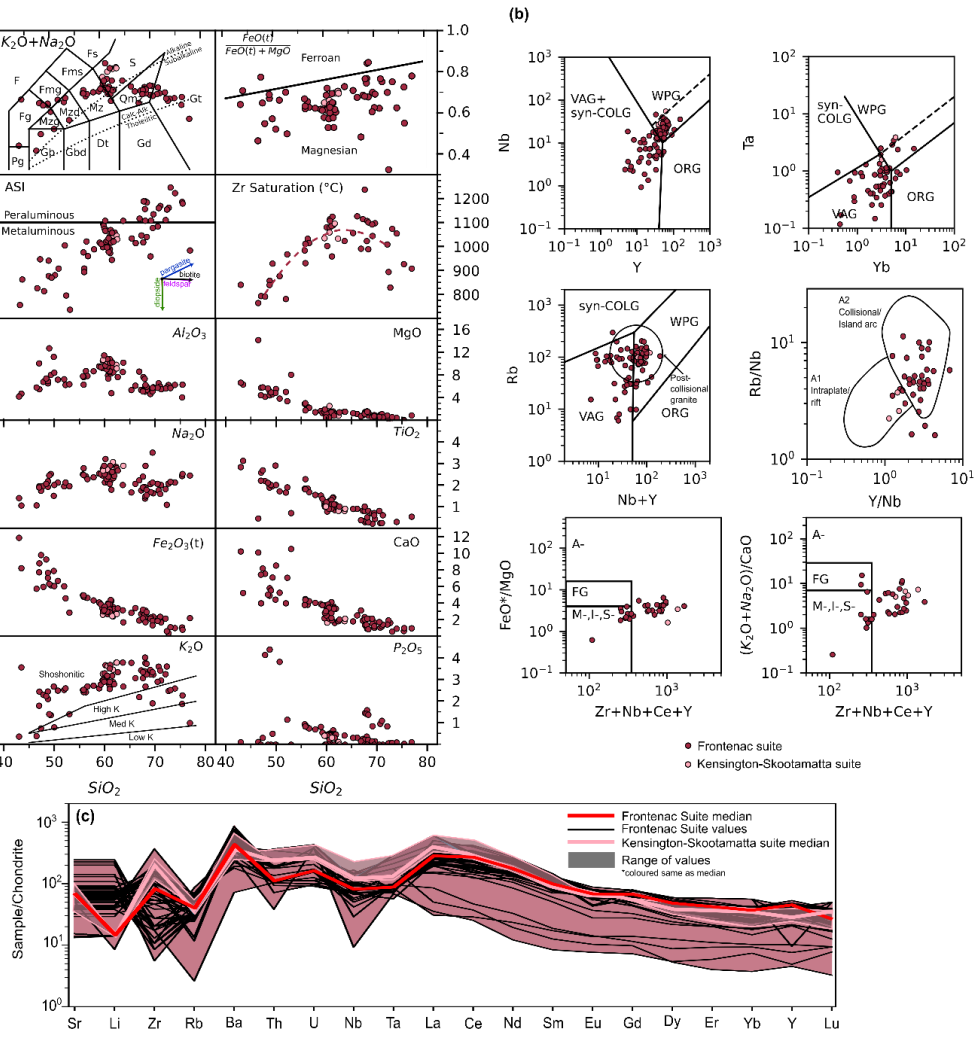


Figure 5.5: Geochemical plots of granitoid rocks from the Frontenac Terrane. (a) SiO_2 bivariate diagrams with geochemical naming scheme (upper leftmost) from Middlemost (1994), chemical classifications of Frost and Frost (2008) using FeO/(FeO+MgO) and K_2O, and zircon saturation temperature utilizing the expression of Boehnke et al. (2013) in the second from the top on the right side plot (b) Trace element classification diagrams (Eby, 1992; Pearce et al., 1984; Whalen et al., 1987). (c) Chondrite-normalized (McDonough and Sun, 1995) trace element diagram. The solid red line is the median value. Abbreviations: F - foidolite, Pg - peridot gabbro Fg - foid grabbro, Fmg - foid monzogabbro, Fms - foid monzosyenite, Fs - foid syenite, Gd - gabbro, Mg - monzograbbro, Md - monzodiorite, Mz - monzonite, S - syenite, Qmz - quartz monzonite, Gd - gabbroic diorite, Dt - diorite, Gd - granodiorite, G – granite. Historic data from (Currie and Ermanovics, 1971; Cutts, 2014; Dickin and Strong, 2021; Grammatikopoulos et al., 2007; Marcantonio et al., 1990; Peck et al., 2013; White et al., 2000).

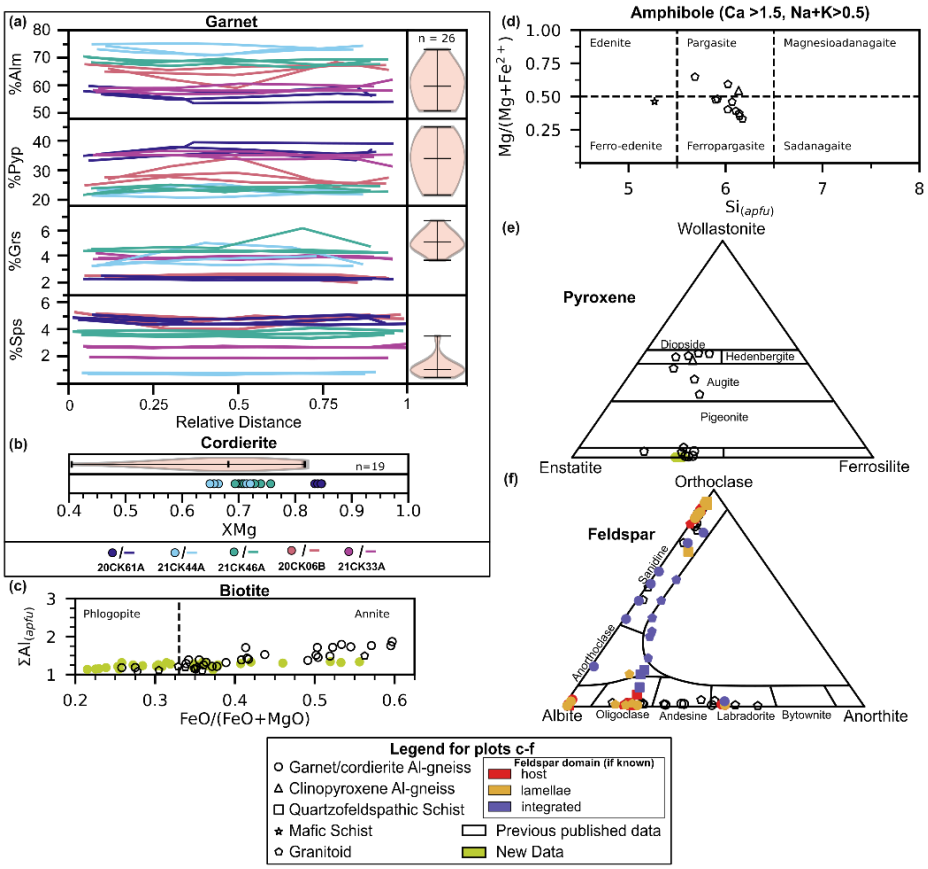


Figure 5.6: Compiled mineral compositions of metasedimentary and granitoid rocks in the Frontenac Terrane. (a) Garnet compositions from garnet-bearing aluminous gneisses show almandine (Alm), pyrope (Pyp), grossular (Grs), and spessartine (Sps) proportions. Line colours are for different samples to show garnet compositional variability within and between samples. Violin plots on the right-hand side are a compilation of spot analyses from historical data (n=26). (b) X_{Mg} (molar Mg/[Mg +Fe]) of cordierite from cordierite-bearing aluminous gneisses. The violin plot above the scatter plot shows values of spot analyses from historical data (n=19). (c) Biotite compositions of granitoid and aluminous gneiss samples. (d) Amphibole compositions for several granitoids and a single analysis each for mafic schist and clinopyroxene-bearing aluminous gneiss. (e) Pyroxene compositions for granitoids, quartzofeldspathic schists, and aluminous gneiss. (f) Feldspar compositions for granitoids, aluminous gneisses, and quartzofeldspathic schists. Historic data from Grammatikopoulos et al., 2007; Reinhardt, 1968; Russell, 2009; Wynne-Edwards, 1967; Wynne-Edwards and Hay, 1963.

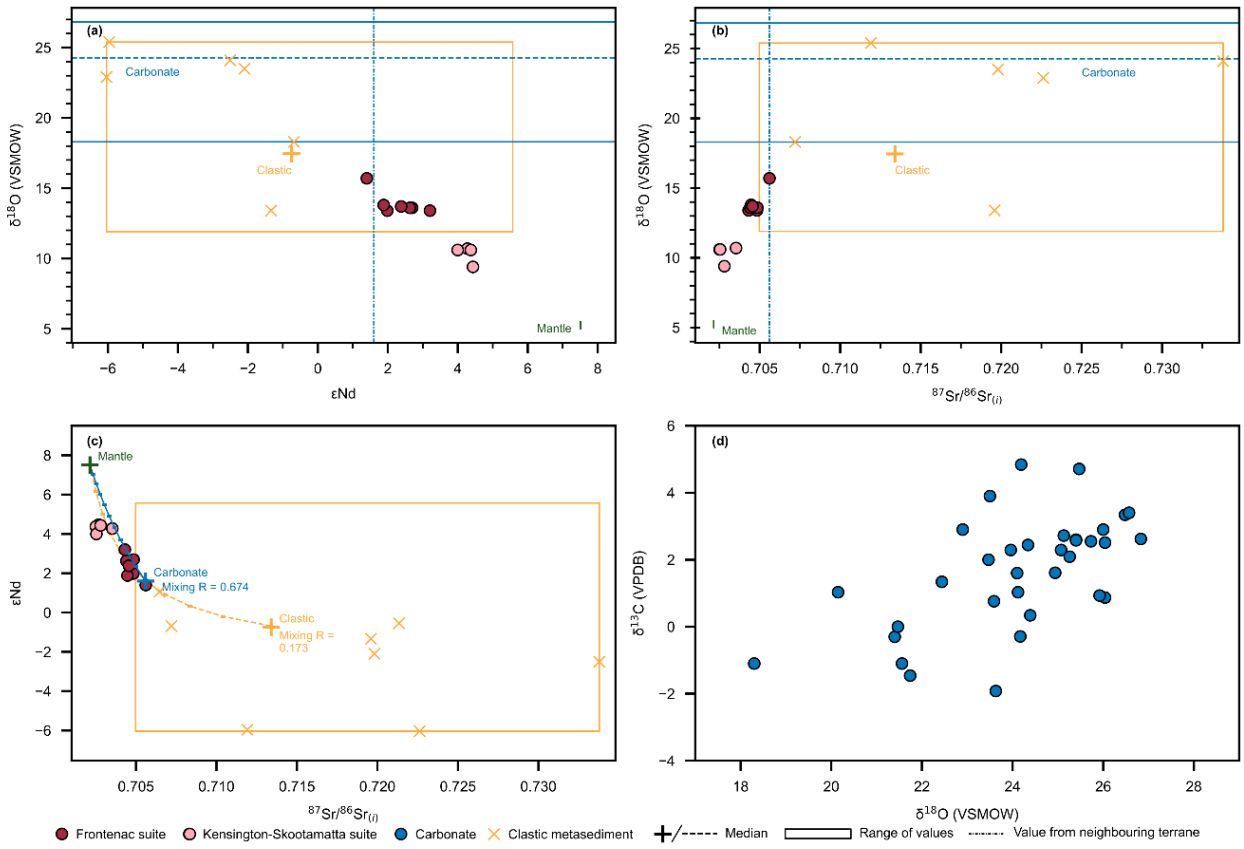


Figure 5.7: Isotopic composition of the granitoids and metasedimentary rocks of the Frontenac Terrane (a) $\delta^{18}O$ and εNd bivariate. (b) $\delta^{18}O$ and $^{87}Sr/^{86}Sr(i)$ bivariate, (c) εNd and $^{87}Sr/^{86}Sr(i)$ bivariate, (d) $\delta^{18}O$ and $\delta^{13}C$ bivariate of carbonate rocks. Samples with known values show regional variability in isotopic composition. All $\delta^{18}O$ is in reference to VSMOW, and all $\delta^{13}C$ is to VPDB. Dashed blue lines represent median values for carbonate rocks, and yellow and blue crosses denote median values for clastic and carbonate metasedimentary rocks, respectively. Dashed lines on subplot (c) are mixing lines between the mantle and different sedimentary end-members. Values for depleted mantle $\delta^{18}O$ from Bindeman et al. (2012), Nd and Sr isotopes from Goldstein and Jacobsen (1988), and mantle Nd and Sr concentrations of DePaolo (1981). Carbonate values for $^{87}Sr/^{86}Sr(i)$ and εNd on subplot (c) are from Lentz (1992) and Moecher et al. (1997), respectively. All epsilon notation is calculated to 1165 Ma. Data from (Cutts, 2014; Dickin and Strong, 2021; Marcantonio et al., 1990; Peck et al., 2022, 2004; Shieh, 1985).

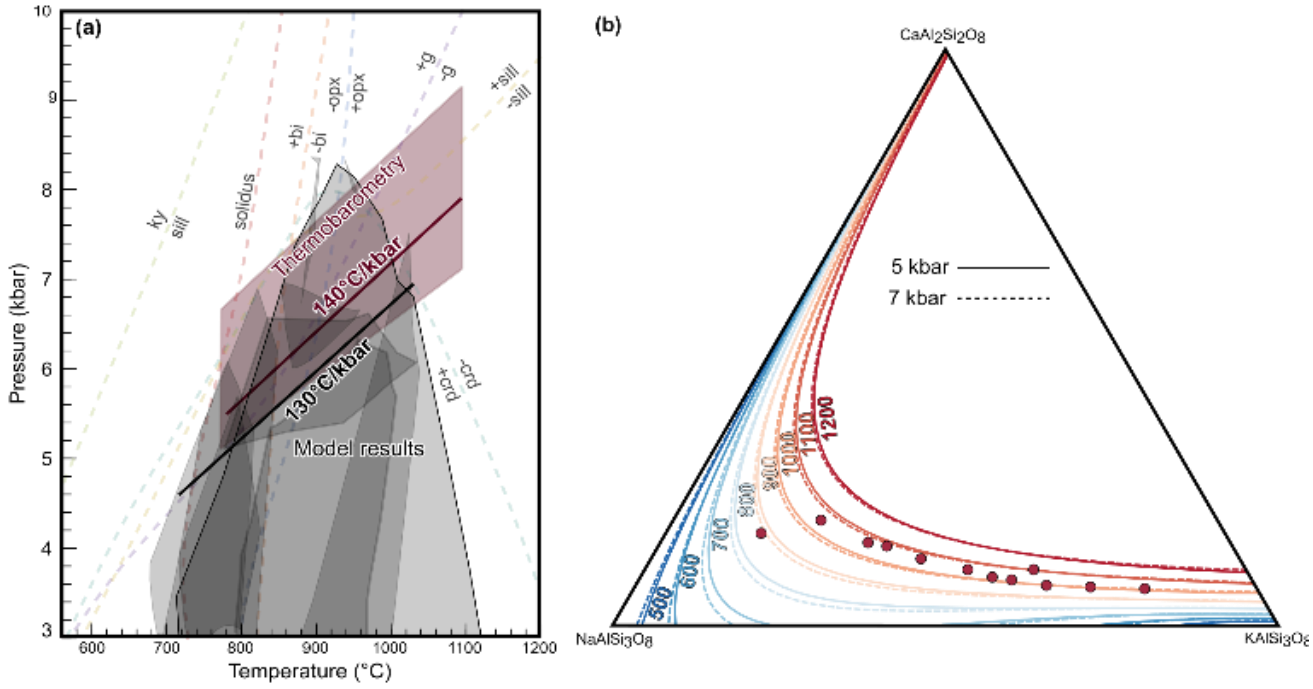


Figure 5.8: (a) Pressure-temperature estimates of metamorphism in the Frontenac Terrane. Shaded grey areas represent peak fields from pseudosection modelling, whereas the red field denotes estimates from thermobarometry (Appendix S4.3). Calculated regional geotherms (solid lines) of 130ºC/kbar from model results and 140ºC from thermobarometry are labelled. Dashed coloured lines are average mineral stability from pseudosection modelling. (b) Temperature estimates of Frontenac granitoids from ternary feldspar thermometry with an average temperature of ~950ºC

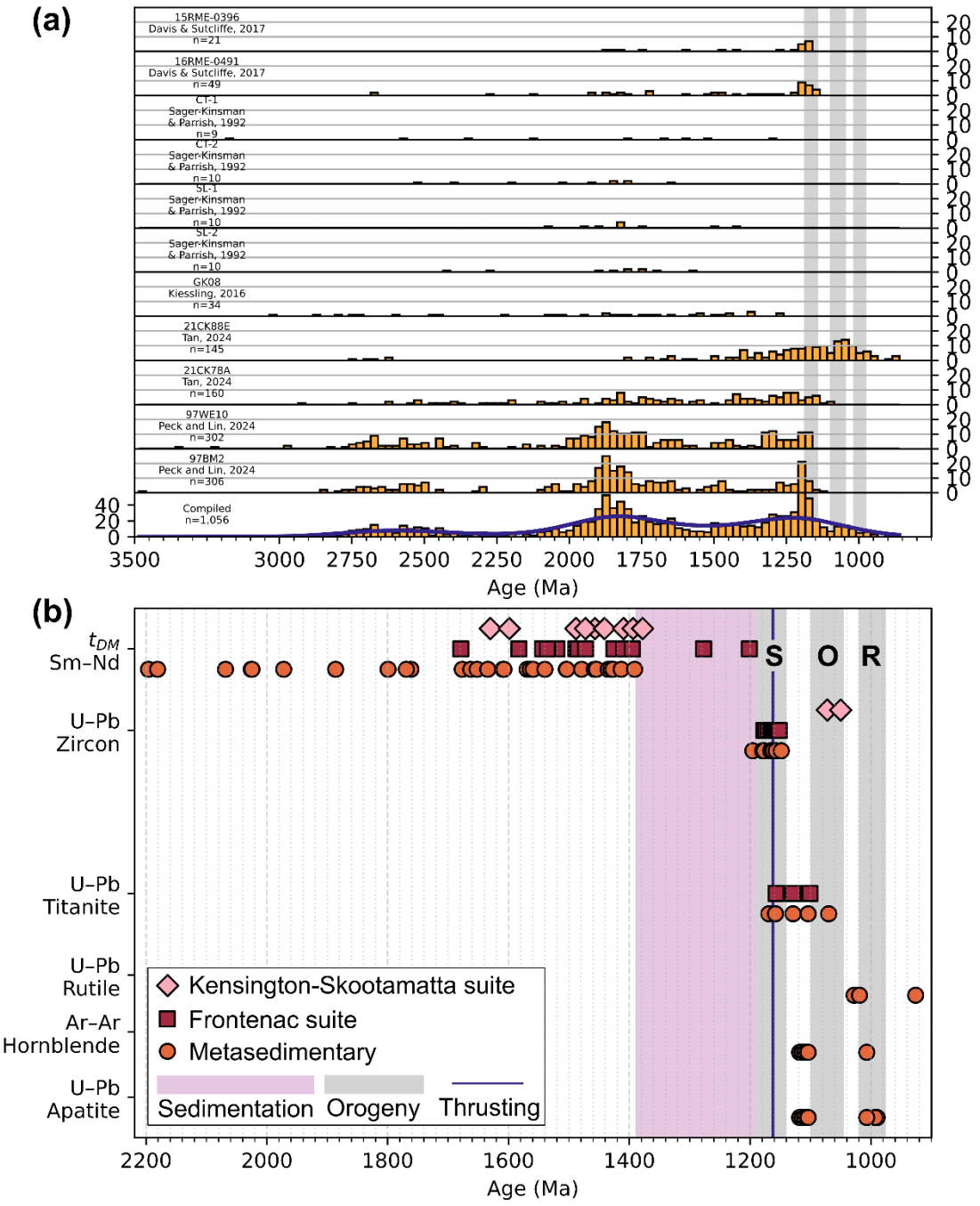


Figure 5.9: Summary of geochronology of the Frontenac Terrane. (a) Ages from detrital zircons. (b) Compiled geochronology, thermochronology, and depleted mantle model ages of the Frontenac Terrane from metasedimentary and granitoid samples. S – Shawinigan orogeny, O – Ottawan orogeny, R–Rigolet orogeny. Data from (Cosca et al., 1992, 1991; Davis and Sutcliffe, 2017; Dickin and Strong, 2021; Kamo and Hamilton, 2017; Kiessling, 2016; Marcantonio et al., 1990; Mezger et al., 1993; Peck and Lin, 2024; Sager-Kinsman and Parrish, 1993; Tan, 2024).

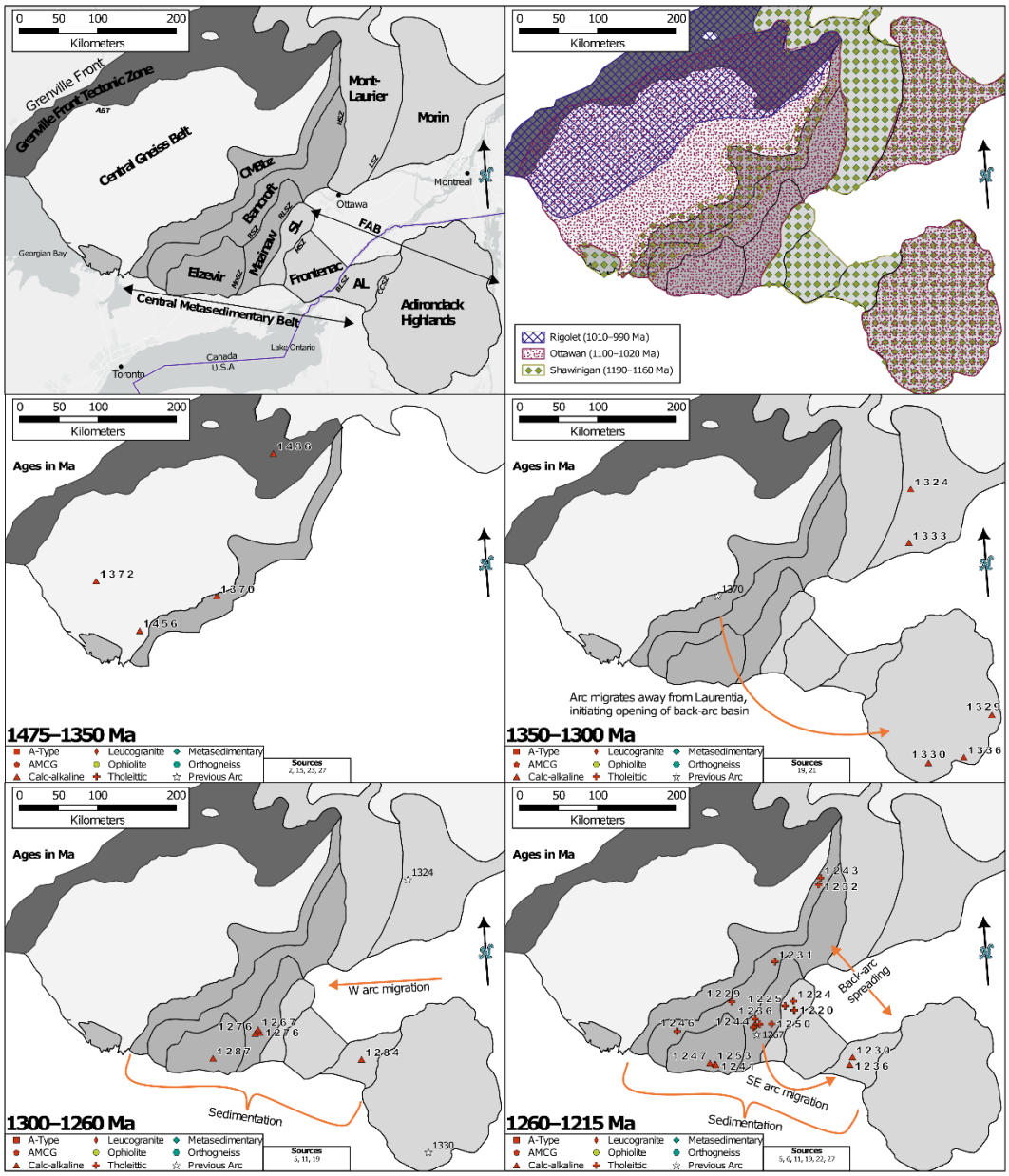


Figure 5.10: Current-day architecture of the SW Grenville Province (top left), approximation of the extensive metamorphic-deformation effects each orogeny (top right), and proposed Mesoproterozoic tectonic model for the SW Grenville (remaining panels). Domain/terrane labels are bolded: AL–Adirondack Lowlands, FAB–Frontenac Adirondack Belt, SL–Sharbot Lake. Shear zones are bolded abbreviations: ABT–Allochton Boundary Thrust, BSZ–Bancroft Shear Zone, BLSZ–Black Lake Shear Zone, CCSZ–Colton-Carthage Shear Zone, HSZ–Heney Shear Zone, LSZ–Labelle Shear Zone, MSZ–Maberly Shear Zone, MoSZ–Mooroton Shear Zone, RLSZ–Robertson Lake Shear Zone. Panels present compiled U-Pb geochronology from various sources (continued on next page).

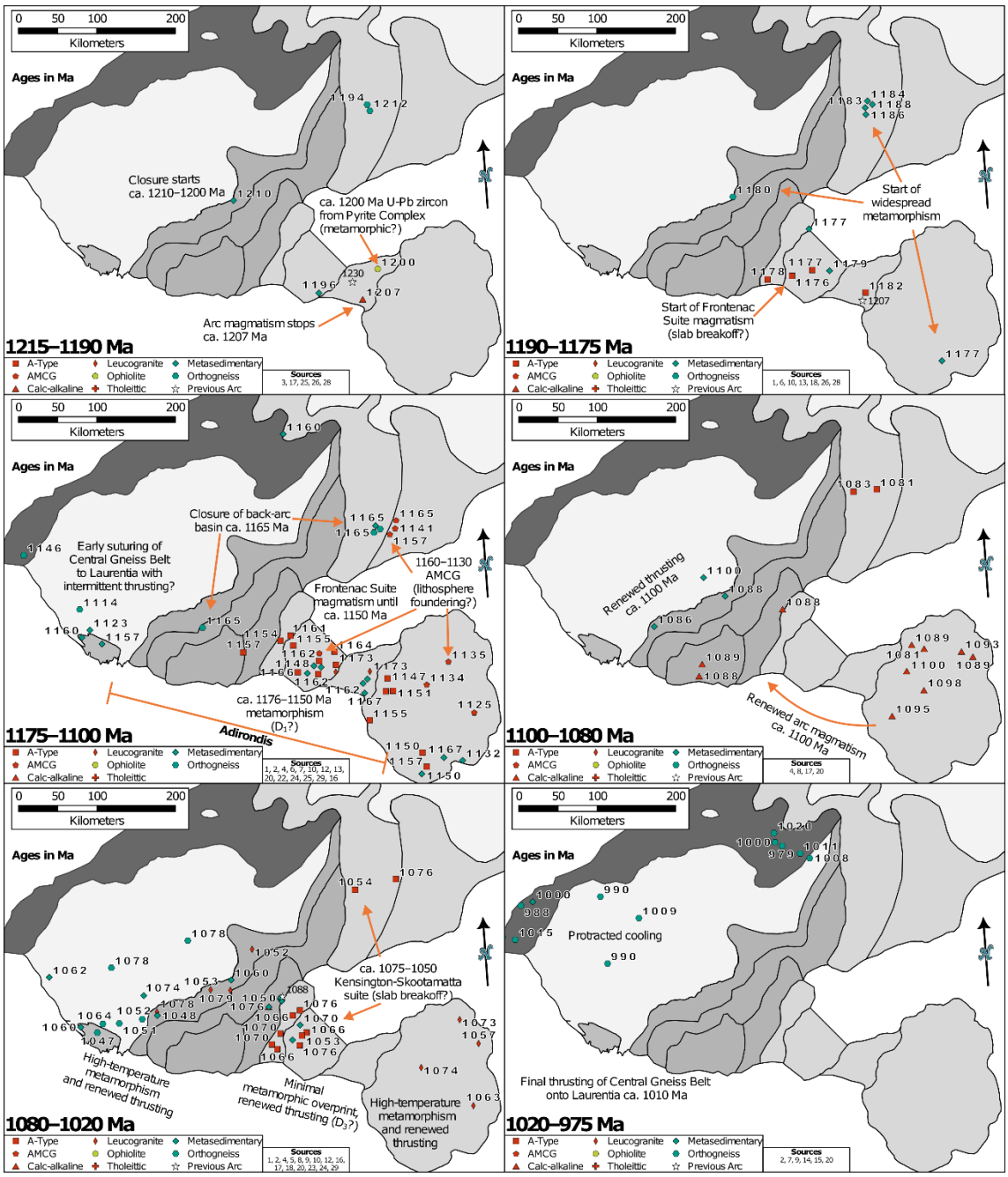


Figure 5.10 continued: numbers correspond to: 1–Cutts (2014), 2–Bussy and Krogh (1994), 3–Chiarenzelli et al. (2011),4–Chiarenzelli and McLelland (1991), 5–Corfu and Easton 1995, 6–Corfu and Easton 1997, 7–Corrigan et al. (1994),8–Corriveau et al. (1990), 9–Culshaw et al. (2016), 10–Davidson and van Breeman (2000), 11–Davis and Bartlett (1988),12–Friedman and Martignole (1995), 13–Heumann et al. (2006), 14–Krogh (1994), 15–Lambert et al. (2023), 16–Marcantonio et al. (1990),17–Markley et al. (2018), 18–McEachern and van Breeman (1993), 19–McLelland and Chiarenzelli (1990), 20–Mezger et al. (1993),21–Peck (2012), 22–Pehrsson et al. (1995), 23–Timmerman et al. (2002), 24–Tuccillo et al. (1992), 25–Wasteneys et al. (1999), 26–Wodicka et al. (2004), 27–Lumbers (1990), 28–Peck and Lin (2024), 29–Easton (2017).

Chapter 6.0: Conclusion

6.1 Summary of research

The research presented in this thesis focuses on the production and transfer of heat during crustal formation and differentiation. Emphasis is placed on the distribution of trace elements in partially molten systems and their behaviour under evolving system conditions. By employing a combination of traditional and innovative techniques, this work traces the journey of heat from its sources to sinks across geological time scales. Collectively, the chapters of this thesis underscore the intricate interplay of thermal processes that drive deep-crustal dynamics, offering new insights into the mechanisms of heat generation, transfer, and dissipation while unravelling their implications for crustal evolution and the redistribution of chemical elements.

Removing heat-producing elements from the deep crust is considered a critical aspect of crustal differentiation and cratonization. Yet, the distribution of heat-producing elements across the crustal section and the effectiveness of anatexis on their redistribution is uncertain. Natural observations are paired with forward phase equilibrium, accessory mineral, and trace element modelling to access the re-distribution of heat-producing elements during the anatexis of metabasites (Chapter 2). I investigate the effects of melting for a range of compositions from depleted, previously melted mafic granulite to relatively enriched greenstone on the retention of heat-producing elements during cratonization. Heat-producing elements are sub-equally partitioned between melt and solid phases at reasonable metamorphic conditions (850ºC, 10 kbar). Retaining heat-producing elements in the lower crust depends on the stability of apatite, feldspar, amphibole, and epidote—radiogenic and mantle heat are subequal contributors. The increased partitioning of heat production into the melt increases heating times in a negative feedback loop. These model results agree well with geochemical data collected across the Archean-aged Kapuskasing Uplift crustal cross-section. Further, comparable thermal latency modelling and previous U-Pb geochronology of mid-crustal tonalite-trondhjemite-granodiorite packages support the model results. Together, these data indicate that the lower crust may be more heat-producing than previously thought and that anatexis is a moderate mechanism for heat-producing element removal.

The timing, duration, and continuity of crustal growth remain contentious, with uncertainties arising from potential preservation biases in the crustal record. Therefore, we must try to verify

the crustal record before interpretation. By investigating a comprehensive crustal composition database (Chapter 3), we reveal that the heat production (at the time of formation) for mafic rocks decreases with increasing crystallization age; there is no temporal trend in the intermediate or siliceous crust. We are moderately successful in simulating these trends using phase equilibrium and trace element modelling—higher mantle temperatures and degrees of partial melting diluted heat-producing elements of primitive crust. Our analysis of the crust record reveals five pulses of marked crustal growth, evident by the significant contributions of low-silica, mantle-derived magmas possibly related to the episodic transfer of material between the lower and upper mantle. Historic heat loss during crustal formation and differentiation increases the duration of subdued magmatism between pulses of crustal growth. Altogether, we have determined crustal growth to be a dilating, episodic process driven by mantle cooling operatives since the Archean.

Trace element proxies—such as Ti-in-zircon—provide snapshots of their crystallization environments and can be used to trace deep-crustal processes. For example, high titanium rims in zircon are often used as evidence for subvolcanic magma recharge. However, the use of such thermometers predicates an understanding of the relative timing of mineral growth. As granite ascent occurs through dykes at rates greater than conductive heat loss (Petford et al. 1993), the growth of zircon during the adiabatic ascent of rhyolitic magma is considered (Chapter 4) with emphasis on the effects of pressure-volume work and latent heat of fusion on the zircon record. Decompression melting and system expansion decrease temperature and titanium concentration before boiling. After fluid separation, shallow crystallization releases considerable heat of fusion and increases the magma temperature—possibly hotter than the source region. Overall, our models highlight the importance of using multiple proxies in investigating the deep crust and exploring the effects of deep-crustal heat movement on magma temperatures.

Increased recognition of ultra-high temperature metamorphic terranes indicates that such extreme crustal conditions result from common crustal processes. However, the source of such heat is often obscure in ultra-high temperature terranes with enigmatic mafic underplating frequently suggested. The Frontenac Terrane in the southeastern Grenville Province provides a natural laboratory to investigate ultra-high temperature processes without widespread mafic magmatism or anomalous heat production (Chapter 5). 1390–1200 Ma sedimentation in a warm

back-arc basin thermally conditioned the crust before the ca 1190–1160 Ma Shawinigan orogeny. The advection of pre-syn-collisional granitic and subordinate mafic magma resulted in regional (ultra-) high-temperature metamorphism. Minor ca 1160 reworking in boundary shear zones protected ancient metamorphic assemblages in the central Frontenac. This work provides new insights into the Mesoproterozoic geometry offboard Laurentia and the mechanisms for syn-collisional ultra-high temperature metamorphism without widespread mafic magmatism.

6.2 Future work and recommendations

The work presented in this thesis highlights opportunities for continued research into the role of heat-producing elements in the crustal heat budget and the crustal thermal regime. This work accesses the heat production in the crustal record (Chapter 3) and the importance of accessory minerals on heat-producing element re-distribution (Chapter 2) during anatexis of mafic (primitive) crust. Together, they highlight the significance of enriched mafic material in creating intermediate middle crust during crustal building. However, the proportion of enriched primitive crustal material remains uncertain. Removing heat-producing elements from this enriched material and the reciprocal depleted material promotes crustal stability, as a more homogeneous crust may be too hot to be stable but too cold to melt. Therefore, initial heat-production heterogeneity in primitive continental crust may be critical in crustal differentiation and preservation. Targeted analysis of various crustal sections, including large igneous provinces and arc systems—areas of crustal formation—could provide some insights into the initial distribution of heat-producing elements. Further, the effects of variable lower crust composition on crustal heat regimes should be investigated, including sedimentary inliers (e.g. Downes et al. 1990) or granitic roots (e.g. Landenberger and Collins 1996).

Advective heat transfer is directly explored in Chapters 4 and 5 and indirectly in Chapter 3, linked to zircon titanium concentration, ultra-high temperature metamorphism, and dilating crustal growth. Mass and heat movement towards the surface is critical to crustal growth and stabilization. However, the investigations remain first-order and without numerical modelling; developing multi-scale advective heat flow models can provide new theories to test with field studies. These models could provide a numerical framework for understanding the thermal sources for metamorphism and could be applied to global and local processes. Further, understanding the heat loss associated with mass crustal building events such as those recorded

along the middle Mesoproterozoic Laurentian margin (Rivers 1997) could provide a greater perspective on changing tectonic regimes through time.

Heat production and transfer have not only contributed to the formation of buoyant continents and driven active tectonism on Earth, but their influence is also evident from Mercury to Venus. By appreciating the thermal dynamics underlying crustal differentiation and planetary evolution, we gain critical insights into the mechanisms shaping the structure and behaviour of terrestrial bodies over geological time. These insights have practical applications in fields ranging from geothermal energy and mineral resource exploration to extraplanetary habitability and interpreting the geologic histories of terrestrial worlds.

References

Abart, R., Petrishcheva, E., Käßner, S., and Milke, R. 2009. Perthite microstructure in magmatic alkali feldspar with oscillatory zoning; Weinsberg Granite, Upper Austria. Mineralogy and Petrology, 97: 251–263. doi:10.1007/s00710-009-0090-1.

Abbady, A.G.E., and Al-Ghamdi, A.H. 2018. Heat production rate from radioactive elements of granite rocks in north and southeastern Arabian shield Kingdom of Saudi Arabia. Journal of Radiation Research and Applied Sciences, 11: 281–290. doi:10.1016/j.jrras.2018.03.002.

Acosta-Vigil, A., Buick, I., Cesare, B., London, D., Morgan, G. (VI), The extent of Equilibration between melt and residuum during regional anatexis and its implications for differentiation of the continental crust: a study of partially melted metapelitic enclaves: Journal of Petrology, v. 53, p. 1319-1356, doi: 10.1093/petrology/egs018

Ague, J.J. 1991. Evidence for major mass transfer and volume strain during regional metamorphism of pelites. Geology, 19: 855. doi:10.1130/0091-7613(1991)019<0855:EFMMTA>2.3.CO;2.

Ahrens, L.H., 1965, Some observations on the uranium and thorium distributions in accessory zircon from granitic rocks: Geochimica et Cosmochimica Acta, v. 29, p. 711–716, doi:10.1016/0016-7037(65)90064-5.

Albarède, F. 1998. The growth of continental crust. Tectonophysics, 296: 1–14. doi:10.1016/S0040-1951(98)00133-4.

Alessio, K.L., Hand, M., Kelsey, D.E., Williams, M.A., Morrissey, L.J., and Barovich, K. 2018. Conservation of deep crustal heat production. Geology, 46: 335–338. doi:10.1130/G39970.1.

Allard, P. 1997. Endogenous magma degassing and storage at Mount Etna. Geophysical Research Letters, 24: 2219–2222. doi:10.1029/97GL02101.

Alvarez, L.W. 1938. The capture of orbital electrons by nuclei. Physical Review, 54: 486–497. doi:10.1103/PhysRev.54.486.

Anderson, J.L., Barth, A.P., Wooden, J.L., and Mazdab, F. 2008. Thermometers and Thermobarometers in Granitic Systems. Reviews in Mineralogy and Geochemistry, 69: 121–142.

Annen, C. 2011. Implications of incremental emplacement of magma bodies for magma differentiation, thermal aureole dimensions and plutonism–volcanism relationships. Tectonophysics, 500: 3–10. doi:10.1016/j.tecto.2009.04.010.

Apted, M., and Liou, J., 1983, Phase relationships among greenschist, epidote-amphibolite, and amphibolite in a basaltic system: American Journal of Science, v. 283, p. 328–354.

Aranovich, L.Ya., and Berman, R.G. 1997. A new garnet-orthopyroxene thermometer based on reversed Al 2 O 3 solubility in FeO-Al2O3-SiO2 orthopyroxene. American Mineralogist, 82: 345–353. doi:10.2138/am-1997-3-413.

Arevalo, R., McDonough, W.F., and Luong, M., 2009, The K/U ratio of the silicate Earth: Insights into mantle composition, structure and thermal evolution: Earth and Planetary Science Letters, v. 278, p. 361–369, doi:10.1016/j.epsl.2008.12.023.

Ashwal, L.D., Morgan, P., Kelley, S.A., and Percival, J.A. 1987. Heat production in an Archean crustal profile and implications for heat flow and mobilization of heat-producing elements. Earth and Planetary Science Letters, 85: 439–450. doi:10.1016/0012-821X(87)90139-7.

Bacon, C.R., and Druitt, T.H. 1988. Compositional evolution of the zoned calcalkaline magma chamber of Mount Mazama, Crater Lake, Oregon. Contributions to Mineralogy and Petrology, 98: 224–256. doi:10.1007/BF00402114.

Baird, G.B., and Shrady, C.H. 2011. Timing and kinematics of deformation in the northwest Adirondack Lowlands, New York State: Implications for terrane relationships in the southern Grenville Province. Geosphere, 7: 1303–1323. doi:10.1130/GES00689.1.

Barboni, M., Boehnke, P., Schmitt, A.K., Mark Harrison, T., Shane, P., Bouvier, A.S., and Baumgartner, L. 2016. Warm storage for arc magmas. Proceedings of the National Academy of Sciences of the United States of America, 113: 13959–13964. doi:10.1073/pnas.1616129113.

Bartholomew, M.J., and Hatcher, R.D. 2010. The Grenville orogenic cycle of southern Laurentia: Unraveling sutures, rifts, and shear zones as potential piercing points for Amazonia. Journal of South American Earth Sciences, 29: 4–20. doi:10.1016/j.jsames.2009.08.007.

Bartoli, O. 2019. Reintegrating nanogranitoid inclusion composition to reconstruct the prograde history of melt-depleted rocks. Geoscience Frontiers, 10: 517–525. doi:10.1016/j.gsf.2018.02.002.

Barton, M.D., and Hanson, R.B. 1989. Magmatism and the development of low-pressure metamorphic belts: Implications from the western United States and thermal modeling. Geological Society of America Bulletin, 101: 1051–1065. doi:10.1130/0016-7606(1989)101<1051:MATDOL>2.3.CO;2.

Bea, F. 1996. Residence of REE, Y, Th and U in granites and crustal protoliths; Implications for the chemistry of crustal melts. Journal of Petrology, 37: 521–552.

Bea, F. 2012. The sources of energy for crustal melting and the geochemistry of heat-producing elements. Lithos, 153: 278–291. doi:10.1016/j.lithos.2012.01.017.

Bea, F., and Montero, P. 1999. Behavior of accessory phases and redistribution of Zr, REE, Y, Th, and U during metamorphism and partial melting of metapelites in the lower crust: an example from the Kinzigite Formation of Ivrea-Verbano, NW Italy. Geochimica et Cosmochimica Acta, 63: 1133–1153. doi:10.1016/S0016-7037(98)00292-0.

Bea, F., Fershtater, G., Corretge, L.G., The geochemistry of phosphorus in granite rocks and the effect of aluminium: Lithos, v. 29, p. 43-56,

Bea, F., Montero, P., Ortega, M., 2006, A LA-ICP-MS evaluation of Zr reservoirs in common crustal rocks: Implications for Zr and Hf geochemistry, and zircon-forming processes: The Canadian Mineralogist, v. 44, p. 693-714, doi: 10.2113/gscanmin.44.3.693

Beard, J.S., and Lofgren, G.E. 1991. Dehydration Melting and Water-Saturated Melting of Basaltic and Andesitic Greenstones and Amphibolites at 1, 3, and 6. 9 kb. Journal of Petrology, 32: 365–401. doi:10.1093/petrology/32.2.365.

Benn, K., and Kamber, B.S. 2009. In Situ U/Pb Granulite-Hosted Zircon Dates, Kapuskasing Structural Zone, Ontario: A Late Archean Large Igneous Province (LIP) as a Substrate for Juvenile Crust. The Journal of Geology, 117: 519–541. doi:10.1086/600864.

Berman, R.G. 1988. Internally-consistent thermodynamic data for minerals in the system Na2O-K2O-CaO-MgO-FeO-Fe2O3-Al2O3-SiO2-TiO2-H2O-CO2. Journal of Petrology, 29: 445–522. doi:10.1093/petrology/29.2.445.

Bhattacharya, S. 1993. Refinement of geothermobarometry for cordierite granulites. Journal of Earth System Science, 102: 537–545. doi:10.1007/BF02871952.

Bindeman, I., Gurenko, A., Carley, T., Miller, C., Martin, E., and Sigmarsson, O. 2012. Silicic magma petrogenesis in Iceland by remelting of hydrothermally altered crust based on oxygen isotope diversity and disequilibria between zircon and magma with implications for MORB. Terra Nova, 24: 227–232. doi:10.1111/j.1365-3121.2012.01058.x.

Blundy, J., Cashman, K., and Humphreys, M. 2006. Magma heating by decompression-driven crystallization beneath andesite volcanoes. Nature, 443: 76–80. doi:10.1038/nature05100.

Bodri, L., and Čermák, V., 1993, Heat production in the continental lithosphere, part II: variational approach: Tectonophysics, v. 225, p. 29–34, doi:10.1016/0040-1951(93)90245-F.

Boehnke, P., Watson, E.B., Trail, D., Harrison, T.M., and Schmitt, A.K. 2013. Zircon saturation re-revisited. Chemical Geology, 351: 324–334. doi:10.1016/j.chemgeo.2013.05.028.

Bolhar, R., Weaver, S.D., Palin, J.M., Cole, J.W., and Paterson, L.A. 2008. Systematics of zircon crystallisation in the Cretaceous Separation Point Suite, New Zealand, using U/Pb isotopes, REE and Ti geothermometry. Contributions to Mineralogy and Petrology, 156: 133–160. doi:10.1007/s00410-007-0278-5.

Borisov, A., Aranovish, L., 2019, Zircon solubility in silicate melts: New experiments and probability of zircon crystallization in deeply evolved basic melts: Chemical Geology, v. 510, p. 103-112, doi: 10.1016/j.chemgeo.2019.02.019

Borisov, A., and Aranovich, L. 2020. Rutile solubility and TiO2 activity in silicate melts: An experimental study. Chemical Geology, 556: 119817. doi:10.1016/j.chemgeo.2020.119817.

Borisova, A.Y., Bohrson, W.A., and Grégoire, M. 2017. Origin of primitive ocean island basalts by crustal gabbro assimilation and multiple recharge of plume-derived melts. Geochemistry, Geophysics, Geosystems, 18: 2701–2716. doi:10.1002/2017GC006986.

Bowman, J.R., Moser, D.E., Valley, J.W., Wooden, J.L., Kita, N.T., and Mazdab, F.K., 2011, Zircon U-Pb isotope, δ18O and trace element response to 80 m.y. of high temperature metamorphism in the lower crust: Sluggish diffusion and new records of Archean craton formation: v. 311, 719–772 p., doi:10.2475/09.2011.01.

Brown, E.H., and Walker, N.W. 1993. A magma-loading model for Barrovian metamorphism in the southeast Coast Plutonic Complex,British Columbia and Washington. Geological Society of America Bulletin, 105: 479–500. doi:10.1130/0016-7606(1993)105<0479:AMLMFB>2.3.CO;2.

Brown, M. 1994. The generation, segregation, ascent and emplacement of granite magma: the migmatite-to-crustally-derived granite connection in thickened orogens. Earth Science Reviews, 36: 83–130. doi:10.1016/0012-8252(94)90009-4.

Brown, M. 2001. Orogeny, migmatites and leucogranites: A review. Journal of Earth System Science, 110: 313–336. doi:10.1007/BF02702898.

Brown, M. 2008. Geodynamic regimes and tectonic settings for metamorphism: Relationship to the supercontinent cycle. Indian Journal of Geology, 80: 3–21.

Brown, M. 2010. Melting of the continental crust during orogenesis: the thermal, rheological, and compositional consequences of melt transport from lower to upper continental crust. Canadian Journal of Earth Sciences, 47: 655–694. doi:10.1139/E09-057.

Brown, M., 2013, Granite: From genesis to emplacement: Bulletin of the Geological Society of America, v. 125, p. 1079–1113, doi:10.1130/B30877.1.

Brown, M., and Solar, G.S. 1999. The mechanism of ascent and emplacement of granite magma during transpression: a syntectonic granite paradigm. Tectonophysics, 312: 1–33. doi:10.1016/S0040-1951(99)00169-9.

Brugger, C.R., and Hammer, J.E. 2010. Crystallization kinetics in continuous decompression experiments: Implications for interpreting natural magma ascent processes. Journal of Petrology, 51: 1941–1965. doi:10.1093/petrology/egq044.

Busch, J.P., and Van Der Pluijm, B.A. 1996. Late orogenic, plastic to brittle extension along the Robertson Lake shear zone: implications for the style of deep-crustal extension in the Grenville orogen, Canada. Precambrian Research, 77: 41–57. doi:10.1016/0301-9268(95)00044-5.

Bushman, J.R. 1983. Hutton's Uniformitarianism. Bringham Young University Studies, 23: 41–48.

Bushmin, S.A., and Glebovitsky, V.A., 2008, Scheme of mineral facies of metamorphic rocks: Geology of Ore Deposits, v. 50, p. 659–669, doi:10.1134/S1075701508080011.

Bédard, J.H. 2006. A catalytic delamination-driven model for coupled genesis of Archaean crust and sub-continental lithospheric mantle. Geochimica et Cosmochimica Acta, 70: 1188–1214. doi:10.1016/j.gca.2005.11.008.

Bédard, J.H., Brouillette, P., Madore, L., and Berclaz, A. 2003. Archaean cratonization and deformation in the northern Superior Province, Canada: an evaluation of plate tectonic versus vertical tectonic models. Precambrian Research, 127: 61–87. doi:10.1016/S0301-9268(03)00181-5.

Cao, H.-W., Pei, Q.-M., Santosh, M., Li, G.-M., Zhang, L.-K., Zhang, X.-F., Zhang, Y.-H., Zou, H., Dai, Z.-W., Lin, B., Tang, L., and Yu, X. 2022. Himalayan leucogranites: A review of geochemical and isotopic characteristics, timing of formation, genesis, and rare metal mineralization. Earth-Science Reviews, 234: 104229. doi:10.1016/j.earscirev.2022.104229.

Caricchi, L., Townsend, M., Rivalta, E., and Namiki, A. 2021. The build-up and triggers of volcanic eruptions. Nature Reviews Earth & Environment, 2: 458–476. doi:10.1038/s43017-021-00174-8.

Carl, J.D. 1988. Popple Hill Gneiss as dacite volcanics: A geochemical study of mesosome and leucosome, northwest Adirondacks, New York. Geological Society of America Bulletin, 100: 841–849. doi:10.1130/0016-7606(1988)100<0841:PHGADV>2.3.CO;2.

Carr, S.D., Easton, R.M., Jamieson, R.A., and Culshaw, N.G. 2000. Geologic transect across the Grenville orogen of Ontario and New York. Canadian Journal of Earth Sciences, 37: 193–216. doi:10.1139/e99-074.

Carrapa, B., Jepson, G., DeCelles, P.G., George, S.W.M., Ducea, M., Campbell, C., and Dawson (Née Canavan), R.R. 2025. Crustal bobbing in response to lithospheric foundering recorded by detrital proxy records from the central Andean Plateau. Geology, 53: 29–33. doi:10.1130/G52455.1.

Carvalho, B.B., Bartoli, O. and Cesare, B., 2023, C–O–H fluid-melt-rock interaction in graphitic granulites and problems of quantifying carbon budget in the lower continental crust. Chemical Geology, v. 631, 121503. https://doi.org/10.1016/j.chemgeo.2023.121503

Cawood, P.A., Hawkesworth, C.J., and Dhuime, B. 2013. The continental record and the generation of continental crust. Geological Society of America Bulletin, 125: 14–32. doi:10.1130/B30722.1.

Chamberlain, C.P., and Sonder, L.J. 1990. Heat-Producing Elements and the Thermal and Baric Patterns of Metamorphic Belts. Science, New Series, 250: 763–769.

Chantel, J., Manthilake, G., Andrault, D., Novella, D., Yu, T., and Wang, Y. 2016. Experimental evidence supports mantle partial melting in the asthenosphere. Science Advances, 2: e1600246. doi:10.1126/sciadv.1600246.

Chen, S.R., Wang, Q., Zhu, D.C., Weinberg, R.F., Zhang, L.L., and Zhao, Z.D. 2021. Reheating and magma mixing recorded by zircon and quartz from high-silica rhyolite in the Coqen region, southern Tibet. American Mineralogist, 106: 112–122. doi:10.2138/am-2020-7426.

Chiarenzelli, J., Kratzmann, D., Selleck, B., deLorraine, W., and Lupulescu, M. 2017. Utility of detrital zircon grains from upper amphibolite facies rocks of the Grenville Supergroup,

Adirondack Lowlands, Northeastern United States. In Sediment Provenance. Elsevier. pp. 371–401. doi:10.1016/B978-0-12-803386-9.00014-9.

Chiarenzelli, J., Lupulescu, M., Thern, E., and Cousens, B. 2011a. Tectonic implications of the discovery of a Shawinigan ophiolite (Pyrites Complex) in the Adirondack Lowlands. Geosphere, 7: 333–356. doi:10.1130/GES00608.1.

Chiarenzelli, J.R., and McLelland, J.M. 1991. Age and regional relationships of granitoid rocks of the Adirondack Highlands. The Journal of Geology, 99: 571–590. doi:10.1086/629518.

Chiarenzelli, J., Regan, S., Peck, W.H., Selleck, B.W., Cousens, B., Baird, G.B., and Shrady, C.H. 2010. Shawinigan arc magmatism in the Adirondack Lowlands as a consequence of closure of the Trans-Adirondack backarc basin. Geosphere, 6: 900–916. doi:10.1130/GES00576.1.

Chiarenzelli, J., Valentino, D., Lupulescu, M., Thern, E., and Johnston, S. 2011b. Differentiating Shawinigan and Ottawan orogenesis in the Central Adirondacks. Geosphere, 7: 2–22. doi:10.1130/GES00583.1.

Ciufo, T.J., Jellicoe, K., Yakymchuk, C., Lin, S., Mercier-Langevin, P., and Wodicka, N., 2020, Gold through space and time in the Archean: Geology, structural evolution and hydrothermal alteration of the Island Gold deposit, Michipicoten greenstone belt, Ontario, in Targeted Geoscience Initiative 5: contributions to the understanding of Canadian gold systems, v. 8712, p. 328, doi:10.5382/econgeo.116.1.br01.

Claiborne, L.L., Miller, C.F., Flanagan, D.M., Clynne, M.A., and Wooden, J.L. 2010a. Zircon reveals protracted magma storage and recycling beneath Mount St. Helens. Geology, 38: 1011–1014. doi:10.1130/G31285.1.

Claiborne, L.L., Miller, C.F., and Wooden, J.L. 2010b. Trace element composition of igneous zircon: a thermal and compositional record of the accumulation and evolution of a large silicic batholith, Spirit Mountain, Nevada. Contributions to Mineralogy and Petrology, 160: 511–531. doi:10.1007/s00410-010-0491-5.

Clark, C., Fitzsimons, I.C.W., Healy, D., and Harley, S.L. 2011. How does the continental crust get really hot? Elements, 7: 235–240. doi:10.2113/gselements.7.4.235.

Clemens, J., Stevens, G., Bryan, S., 2020, Conditions during the formation of granitic magmas by crustal melting – Hot or cold; drenched, damp or dry?, Earth-Science Reviews, doi: 10.1016/j.earscirev.2019.102982

Clemens, J.D. 2005. Granites and granitic magmas: strange phenomena and new perspectives on some old problems. Proceedings of the Geologists' Association, 116: 9–16. doi:10.1016/S0016-7878(05)80013-6.

Clemens, J.D., and Mawer, C.K. 1992. Granitic magma transport by fracture propagation. Tectonophysics, 204: 339–360. doi:10.1016/0040-1951(92)90316-X.

Clemens, J.D., and Wall, V.J. 1981. Origin and crystallization of some peraluminous (S-Type) granitic magmas. Canadian Mineralogist, 19: 111–131.

Clemens, J.D., Holloway, J., and White, A.J.R. 1986. Origin of an A-type granite: Experimental constraints. American Mineralogist, 71: 317–324.

Clemens, J.D., Stevens, G., and Bryan, S.E. 2020. Conditions during the formation of granitic magmas by crustal melting – Hot or cold; drenched, damp or dry? Earth-Science Reviews, 200: 102982. doi:10.1016/j.earscirev.2019.102982.

Collins, W.J., and Richards, S.W. 2008. Geodynamic significance of S-type granites in circum-Pacific orogens. Geology, 36: 559. doi:10.1130/G24658A.1.

Coltice, N., Phillips, B.R., Bertrand, H., Ricard, Y., and Rey, P. 2007. Global warming of the mantle at the origin of flood basalts over supercontinents.

Condie, K. 1976. Trace-element geochemistry of Archean greenstone belts. Earth-Science Reviews, 12: 393–417. doi:10.1016/0012-8252(76)90012-X.

Condie, K.C. 1998. Episodic continental growth and supercontinents: a mantle avalanche connection? Earth and Planetary Science Letters, 163: 97–108. doi:10.1016/S0012-821X(98)00178-2.

Condie, K.C., and Aster, R.C. 2010. Episodic zircon age spectra of orogenic granitoids: The supercontinent connection and continental growth. Precambrian Research, 180: 227–236. doi:10.1016/j.precamres.2010.03.008.

Condie, K.C., Arndt, N., Davaille, A., and Puetz, S.J. 2017. Zircon age peaks: Production or preservation of continental crust? Geosphere, 13: 227–234. doi:10.1130/GES01361.1.

Cooper, A.F., and Lovering, J.F., 1970, Greenschist amphiboles from Haast river, New Zealand: Contributions to Mineralogy and Petrology, v. 27, p. 11–24, doi:10.1007/BF00539538.

Corfu, F., 1987, Inverse age stratification in the archaean crust of the superior province: Evidence for infra- and subcrustal accretion from high resolution U-Pb zircon and monazite ages: Precambrian Research, v. 36, p. 259–275, doi:10.1016/0301-9268(87)90024-6.

Corfu, F., and Easton, R. 1997. Sharbot Lake terrane and its relationships to Frontenac terrane, Central Metasedimentary Belt, Grenville Province: new insights from U-Pb geochronology. Canadian Journal of Earth Sciences, 34: 1239–1257.

Corfu, F., and Easton, R.M. 1995. U–Pb geochronology of the Mazinaw terrane, an imbricate segment of the Central Metasedimentary Belt, Grenville Province, Ontario. Canadian Journal of Earth Sciences, 32: 959–976. doi:10.1139/e95-081.

Corrigan, D., Culshaw, N.G., and Mortensen, J.K. 1994. Pre-Grenvillian evolution and Grenvillian overprinting of the Parautochthonous Belt in Key Harbour, Ontario: U–Pb and field constraints. Canadian Journal of Earth Sciences, 31: 583–596. doi:10.1139/e94-051.

Corriveau, L. 1990. Proterozoic subduction and terrane amalgamation in the southwestern Grenville province, Canada: Evidence from ultrapotassic to shoshonitic plutonism. Geology,.

Corriveau, L., and van Breemen, O. 2000. Docking of the Central Metasedimentary Belt to Laurentia in geon 12: evidence from the 1.17– 1.16 Ga Chevreuil intrusive suite and host gneisses, Quebec. 37.

Cosca, M.A., Essene, E.J., Kunk, M.J., and Sutter, J.F. 1992. Differential unroofing within the Central Metasedimentary Belt of the Grenville Orogen: constraints from 40Ar/39Ar thermochronology. Contributions to Mineralogy and Petrology, 110: 211–225. doi:10.1007/BF00310739.

Cosca, M.A., Sutter, J.F., and Essene, E.J. 1991. Cooling and inferred uplift/erosion history of the Grenville Orogen, Ontario: Constraints from 40Ar/39Ar thermochronology. Tectonics, 10: 959–977. doi:10.1029/91TC00859.

Coulson, I.M., Villeneuve, M.E., Dipple, G.M., Duncan, R.A., Russell, J.K., and Mortensen, J.K. 2002. Time-scales of assembly and thermal history of a composite felsic pluton: constraints from the Emerald Lake area, northern Canadian Cordillera, Yukon. Journal of Volcanology and Geothermal Research, 114: 331–356. doi:10.1016/S0377-0273(01)00294-3.

Culshaw, N., Foster, J., Marsh, J., Slagstad, T., and Gerbi, C. 2016. Kiosk domain, Central Gneiss Belt, Grenville Province, Ontario: A Labradorian palimpsest preserved in the ductile deep crust. Precambrian Research, 280: 249–278. doi:10.1016/j.precamres.2016.05.002.

Culshaw, N.G., Jamieson, R.A., Ketchum, J.W.F., Wodicka, N., Corrigan, D., and Reynolds, P.H. 1997. Transect across the northwestern Grenville orogen, Georgian Bay, Ontario: Polystage convergence and extension in the lower orogenic crust. Tectonics, 16: 966–982. doi:10.1029/97TC02285.

Currie, K.L., and Ermanovics, I.F. 1971. Geology of the Loughborough Lake region, Ontario, with special emphasis on the origin of the granitoid rocks, a contribution to the syenite problem. doi:10.4095/102415.

Cusack, R. 1896. On the Melting Points of Minerals. Proceedings of the Royal Irish Academy, 4: 399–413.

Cutts, J. 2014. Age and geochemical character of granite and syenite plutons in the Grenville Province of Southeastern Ontario; Insights into magmatism during the Ottawan Orogeny and evidence of the Frontenac Intrusive Suite in the Sharbot Lake Domain. Master of Science, Carleton University, Ottawa, Ontario. doi:10.22215/etd/2014-10090.

Daly, J.S., and McLelland, J.M. 1991. Juvenile Middle Proterozoic crust in the Adirondack Highlands, Grenville province, northeastern North America. The Journal of Geology, 19: 119–122. doi:10.1086/648198.

Davidson, A., and Ketchum, J.W.F. 1993. Observations on the Maberly Shear Zone, a terrane boundary within the central metasedimentary belt, Grenville Province, Ontario. doi:10.4095/134253.

Davidson, A., and van Breemen, O. 2000. Age and extent of the Frontenac plutonic suite in the Central metasedimentary belt, Grenville Province, southeastern Ontario. Current Research 2000-F4; Radiogenic Age and Isotopic Studies, Geological Survey of Canada.

Davies, G.F. 2001. Dynamic earth: plates, plumes and mantle convection. In Reprinted. Cambridge University Press, Cambridge.

Davis, D.W., and Bartlett, J.R. 1988. Geochronology of the Belmont Lake Metavolcanic Complex and implications for crustal development in the Central Metasedimentary Belt, Grenville Province, Ontario. Canadian Journal of Earth Sciences, 25: 1751–1759. doi:10.1139/e88-166.

Davis, D.W., and Sutcliffe, C.N. 2017. U-Pb Geochronology by LA-ICP-MS in samples from northern Ontario. Internal Report, Ontario Geological Survey.

De Capitani, C., and Brown, T.H. 1987. The computation of chemical equilibrium in complex systems containing non-ideal solutions. Geochimica et Cosmochimica Acta, 51: 2639–2652. doi:10.1016/0016-7037(87)90145-1.

De Capitani, C., and Petrakakis, K. 2010. The computation of equilibrium assemblage diagrams with Theriak/Domino software. American Mineralogist, 95: 1006–1016. doi:10.2138/am.2010.3354.

Deng, Z., Chaussidon, M., Guitreau, M., Puchtel, I.S., Dauphas, N., and Moynier, F. 2019. An oceanic subduction origin for Archaean granitoids revealed by silicon isotopes. Nature Geoscience, 12: 774–778. doi:10.1038/s41561-019-0407-6.

DePaolo, D.J. 1981. Neodymium isotopes in the Colorado Front Range and crust–mantle evolution in the Proterozoic. Nature, 291: 193–196. doi:10.1038/291193a0.

Dewey, J.F. 1986. Diversity in the lower continental crust. Geological Society, London, Special Publications, 24: 71–78. doi:10.1144/GSL.SP.1986.024.01.08.

Dhuime, B., Hawkesworth, C.J., Cawood, P.A., and Storey, C.D. 2012. A Change in the Geodynamics of Continental Growth 3 Billion Years Ago. Science, 335: 1334–1336. doi:10.1126/science.1216066.

Di Muro, A., Villemant, B., Montagnac, G., Scaillet, B., and Reynard, B. 2006. Quantification of water content and speciation in natural silicic glasses (phonolite, dacite, rhyolite) by confocal microRaman spectrometry. Geochimica et Cosmochimica Acta, 70: 2868–2884. doi:10.1016/j.gca.2006.02.016.

Dickin, A., and Strong, J. 2021. Nd isotope mapping of the Frontenac Terrane in southwestern Grenville Province. Canadian Journal of Earth Sciences, 58: 659–669. doi:10.1139/cjes-2020-0063.

Dickin, A.P. 2018. Radiogenic Isotope Geology. In 3rd edition. Cambridge University Press. doi:10.1017/9781316163009.

Diener, J.F.A., and Fagereng, Å. 2014. The influence of melting and melt drainage on crustal rheology during orogenesis. Journal of Geophysical Research: Solid Earth, 119: 6193–6210. doi:10.1002/2014JB011088.

Downes, H., Dupuy, C., and Leyreloup, A.F. 1990. Crustal evolution of the Hercynian belt of Western Europe: Evidence from lower-crustal granulitic xenoliths (French Massif Central). Chemical Geology, 83: 209–231. doi:10.1016/0009-2541(90)90281-B.

Duan, Z., Wei, C., and Rehman, H.U. 2017. Metamorphic evolution and zircon ages of pelitic granulites in eastern Hebei, North China Craton: Insights into the regional Archean P–T–t history. Precambrian Research, 292: 240–257. doi:10.1016/j.precamres.2017.02.008.

Duguet, M., and Easton, R.M. 2017. Tectonic and metamorphic architecture of the northeastern Composite Arc Belt and the Central Metasedimentary Belt boundary tectonic zone, Grenville Orogen: A geological guidebook. Ontario Geological Survey.

Dupuy, C., and Dostal, J., 1983, Uranium and thorium in paleozoic basalts of Nova Scotia (Canada): Bulletin Volcanologique, v. 46, p. 125–133, doi:10.1007/BF02597581.

Easton, R.M. 2017. Insights into the tectonic and metamorphic architecture of the Composite Arc Belt and the Frontenac-Adirondack Belt near Perth, Ontario, Grenville Orogen: A Geological Guidebook. Ontario Geological Survey.

Easton, R.M. 2019. Geological, geochemical, geophysical and petrographic data from the Perth Area, Grenville Province, Southeastern Ontario. Ontario Geological Survey, Sudbury Ontario.

Easton, R.M., and Davidson, A. 1994. Terranes, domains, and lithotectonic assemblages within the Grenville Province. Geoscience Canada,.

Eby, G.N. 1992. Chemical subdivision of the A-type granitoids: Petrogenetic and tectonic implications. Geology, 20: 641. doi:10.1130/0091-7613(1992)020<0641:CSOTAT>2.3.CO;2.

Einstein, A., 1905, Ist die trägheit eines körpers von seinem energieinhalt abhängig? Annalen der Physik, v. 18, p. 639–641.

Ekberg, C., Albinsson, Y., Comarmond, M.J., and Brown, P.L., 2000, Studies on the complexation behavior of thorium(IV). 1. Hydrolysis equilibria: Journal of Solution Chemistry, v. 29, p. 63–86, doi:10.1023/A:1005166517699.

Ellis, D.J., and Thompson, A.B. 1986. Subsolidus and Partial Melting Reactions in the Quartz-excess CaO+MgO+Al2O3+SiO2+H2O System under Water-excess and Water-deficient Conditions to 10 kb: Some Implications for the Origin of Peraluminous Melts from Mafic Rocks. Journal of Petrology, 27: 91–121. doi:10.1093/petrology/27.1.91.

Emslie, R.F., and Hunt, P.A. 1990. Ages and petrogenetic significance of igneous mangerite-charnockite suites associated with massif anorthosites, Grenville Province. The Journal of Geology, 98: 213–231. doi:10.1086/629394.

Ermanovics, I.F. 1970. Zonal structure of the Perth Road monzonite, Grenville Province, Ontario. Canadian Journal of Earth Sciences, 7: 414–434. doi:10.1139/e70-036.

Evelyne, T., Annelore, B., François, B., and Sébastien, P. 2018. Thermal model of successive dike injections and implications for the development of intraplate volcanoes. Lithos, 322: 129–147. doi:10.1016/j.lithos.2018.10.007.

Fan, Y.-L., Zhang, L.-F., Wang, Y., and Li, Z.-H. 2024. Role of crustal radiogenic heating in ultra-high temperature metamorphism of the Greater Himalayan Crystalline complex: Phase equilibrium and numerical modelling. Gondwana Research, 125: 301–316. Elsevier BV. doi:10.1016/j.gr.2023.09.002.

Fereidooni, D. 2022. Importance of the mineralogical and textural characteristics in the mechanical properties of rocks. Arabian Journal of Geosciences, 15: 637. doi:10.1007/s12517-022-09929-z.

Fernández, C., and Castro, A. 2018. Mechanical and structural consequences of magma differentiation at ascent conduits: A possible origin for some mafic microgranular enclaves in granites. Lithos, 320–321: 49–61. doi:10.1016/j.lithos.2018.09.004.

Ferry, J.M., and Spear, F.S. 1978. Experimental calibration of the partitioning of Fe and Mg between biotite and garnet. Contributions to Mineralogy and Petrology, 66: 113–117. doi:10.1007/BF00372150.

Ferry, J.M., and Watson, E.B. 2007. New thermodynamic models and revised calibrations for the Ti-in-zircon and Zr-in-rutile thermometers. Contributions to Mineralogy and Petrology, 154: 429–437. doi:10.1007/s00410-007-0201-0.

Frank, M.R., and Vaccaro, D.M., 2012, An experimental study of high temperature potassic alteration: Geochimica et Cosmochimica Acta, v. 83, p. 195–204, doi:10.1016/j.gca.2011.12.007.

Frank, M.R., Candela, P.A., and Piccoli, P.M., 1998, K-feldspar-muscovite-andalusite-quartz-brine phase equilibria: An experimental study at 25 to 60 MPa and 400 to 550°C: Geochimica et Cosmochimica Acta, v. 62, p. 3717–3727, doi:10.1016/S0016-7037(98)00261-0.

Frankel, H. 1988. From continental drift to plate tectonics.

Friedman, R.M., and Martignole, J. 1995. Mesoproterozoic sedimentation, magmatism, and metamorphism in the southern part of the Grenville Province (western Quebec): U–Pb geochronological constraints. Canadian Journal of Earth Sciences, 32: 2103–2114. doi:10.1139/e95-164.

Frost, B.R., and Chacko, T. 1989. The granulite uncertainty principle: Limitations on thermobarometry in granulites. The Journal of Geology, 97: 435–450. doi:10.1086/629321.

Frost, B.R., and Frost, C.D. 2008. A geochemical classification for feldspathic igneous rocks. Journal of Petrology, 49: 1955–1969. doi:10.1093/petrology/egn054.

Frost, B.R., Barnes, C.G., Collins, W.J., Arculus, R.J., Ellis, D.J., and Frost, C.D. 2001. A geochemical classification for granitic rocks. Journal of Petrology, 42: 2033–2048. doi:10.1093/petrology/42.11.2033.

Fuhrman, M., and Lindsley, D. 1988. Ternary-feldspar modeling and thermometry. American Mineralogist, 73: 201–215.

G. Pasqualon, N., Savian, J.F., F. Lima, E., R. Luz, F., R. Moncinhatto, T., and F. Trindade, R.I. 2020. Emplacement dynamics of alkaline volcanic and subvolcanic rocks in Trindade Island, Brazil. Journal of Volcanology and Geothermal Research, 406: 107078. doi:10.1016/j.jvolgeores.2020.107078.

Galer, S.J.G., Goldstein, S.L., and O'Nions, R.K. 1989. Limits on chemical and convective isolation in the Earth's interior. Chemical Geology, 75: 257–290. doi:10.1016/0009-2541(89)90001-6.

Gard, M., Hasterok, D., Hand, M., and Cox, G. 2019. Variations in continental heat production from 4 Ga to the present: Evidence from geochemical data. Lithos, 342–343: 391–406. doi:10.1016/j.lithos.2019.05.034.

Gardiner, N.J., Kirkland, C.L., Hollis, J., Szilas, K., Steenfelt, A., Yakymchuk, C., and Heide-Jørgensen, H., 2019, Building Mesoarchaean crust upon Eoarchaean roots: the Akia Terrane, West Greenland: Contributions to Mineralogy and Petrology, v. 174, p. 1–19, doi:10.1007/s00410-019-1554-x.

Garzione, C.N., Molnar, P., Libarkin, J.C., and MacFadden, B.J. 2006. Rapid late Miocene rise of the Bolivian Altiplano: Evidence for removal of mantle lithosphere. Earth and Planetary Science Letters, 241: 543–556. doi:10.1016/j.epsl.2005.11.026.

Garçon, M. 2021. Episodic growth of felsic continents in the past 3.7 Ga. Science Advances, 7: eabj1807. doi:10.1126/sciadv.abj1807.

Gerdes, A., Worner, G., Henk, A., 2000, Post-collisional granite generation and HT-LP metamorphism by radiogenic heating: the Variscan South Bohemian Batholith: Journal of the Geological Society. V. 157, p. 577–587, doi:10.1144/jgs.157.3.577

Ghiorso, M.S., and Gualda, G.A.R. 2013. A method for estimating the activity of titania in magmatic liquids from the compositions of coexisting rhombohedral and cubic iron–titanium oxides. Contributions to Mineralogy and Petrology, 165: 73–81. doi:10.1007/s00410-012-0792-y.

Ghiorso, M.S., and Gualda, G.A.R. 2015. An H2O–CO2 mixed fluid saturation model compatible with rhyolite-MELTS. Contributions to Mineralogy and Petrology, 169: 53. doi:10.1007/s00410-015-1141-8.

Giustina, M.E.S.D., Pimentel, M.M., Ferreira Filho, C.F., and De Hollanda, M.H.B.M. 2011. Dating coeval mafic magmatism and ultrahigh temperature metamorphism in the Anápolis–Itauçu Complex, Central Brazil. Lithos, 124: 82–102. doi:10.1016/j.lithos.2010.11.004.

Glazner, A.F. 2007. Thermal limitations on incorporation of wall rock into magma. Geology, 35: 319. doi:10.1130/G23134A.1.

Glazner, A.F. 2019. The ascent of water-rich magma and decompression heating: A thermodynamic analysis. American Mineralogist, 104: 890–896. De Gruyter Open Ltd. doi:10.2138/am-2019-6925.

Glazner, A.F. 2021. Thermal constraints on the longevity, depth, and vertical extent of magmatic systems. Geochemistry, Geophysics, Geosystems, 22: e2020GC009459. doi:10.1029/2020GC009459.

Goldstein, S.J., and Jacobsen, S.B. 1988. Nd and Sr isotopic systematics of river water suspended material: implications for crustal evolution. Earth and Planetary Science Letters, 87: 249–265. doi:10.1016/0012-821X(88)90013-1.

Graham, C.M., Maresch, W.V., Welch, M.D., and Pawley, A.R. 1989. Experimental studies on amphiboles: a review with thermodynamic perspectives. European Journal of Mineralogy, 1: 535–556. doi:10.1127/ejm/1/4/0535.

Grammatikopoulos, T.A., Clark, A.H., and Archibald, D.A. 2007. Petrogenesis of the Leo Lake and Lyndhurst plutons, Frontenac terrane, Central Metasedimentary Belt, southeastern Ontario, Canada. Canadian Journal of Earth Sciences, 44: 107–126. doi:10.1139/e06-072.

Graphchikov, A.A., Konilov, A.N., and Clemens, J.D. 1999. Biotite dehydration, partial melting, and fluid composition; experiments in the system KAlO2 -FeO-MgO-SiO2 -H2O-CO2. American Mineralogist, 84: 15–26. doi:10.2138/am-1999-1-202.

Green, D.H. 1975. Genesis of Archean peridotitic magmas and constraints on Archean geothermal gradients and tectonics. Geology, 3: 15–18.

Green, E.C.R., White, R.W., Diener, J.F.A., Powell, R., Holland, T.J.B., and Palin, R.M., 2016, Activity–composition relations for the calculation of partial melting equilibria in metabasic rocks: Journal of Metamorphic Geology, v. 34, p. 845–869, doi:10.1111/jmg.12211.

Gregory, C.J., Rubatto, D., Hermann, J., Berger, A., and Engi, M., 2012, Allanite behaviour during incipient melting in the southern Central Alps: Geochimica et Cosmochimica Acta, v. 84, p. 433–458, doi:10.1016/j.gca.2012.01.020.

Grove, T.L., and Parman, S.W. 2004. Thermal evolution of the Earth as recorded by komatiites. Earth and Planetary Science Letters, 219: 173–187. doi:10.1016/S0012-821X(04)00002-0.

Gualda, G.A.R., and Ghiorso, M.S. 2015. MELTS_Excel: A Microsoft Excel-based MELTS interface for research and teaching of magma properties and evolution. Geochemistry, Geophysics, Geosystems, 16: 315–324. doi:10.1002/2014GC005545.

Gualda, G.A.R., Ghiorso, M.S., Lemons, R. V., and Carley, T.L. 2012. Rhyolite-MELTS: A modified calibration of MELTS optimized for silica-rich, fluid-bearing magmatic systems. Journal of Petrology, 53: 875–890. doi:10.1093/petrology/egr080.

Hacker, B.R., Kelemen, P.B., and Behn, M.D., 2011, Differentiation of the continental crust by relamination: Earth and Planetary Science Letters, v. 307, p. 501–516, doi:10.1016/j.epsl.2011.05.024.

Halama, R., Bebout, G.E., John, T., and Scambelluri, M. 2014. Nitrogen recycling in subducted mantle rocks and implications for the global nitrogen cycle. International Journal of Earth Sciences, 103: 2081–2099. doi:10.1007/s00531-012-0782-3.

Hale, A.J., Wadge, G., and Mühlhaus, H.B. 2007. The influence of viscous and latent heating on crystal-rich magma flow in a conduit: Viscous and latent heating in crystal-rich magma. Geophysical Journal International, 171: 1406–1429. doi:10.1111/j.1365-246X.2007.03593.x.

Halliday, A.N. 2006. The Origin of the Earth - What's New? Elements, 2: 205–210. doi:10.2113/gselements.2.4.205.

Hamza, V.M., and Vieira, F.P. 2012. Global distribution of the lithosphere-asthenosphere boundary: a new look. Solid Earth, 3: 199–212. doi:10.5194/se-3-199-2012.

Hanson, G.N. 1980. Rare earth elements in petrogenetic studies of igneous systems. Annual Review of Earth and Planetary Sciences, 8: 371–406. doi:10.1146/annurev.ea.08.050180.002103.

Hanson, G.N., and Langmuir, C.H. 1978. Modelling of major elements in mantle-melt systems using trace element approaches. Geochimica et Cosmochimica Acta, 42: 725–741. doi:10.1016/0016-7037(78)90090-X.

Harley, S. 1998. An appraisal of peak temperature and thermal histories in ultrahigh-temperature (UHT) crustal metamorphism: The significance of aluminous orthopyroxene. Memoirs of National Institute of Polar Resource,: 49–73.

Harley, S.L. 2016. A matter of time: The importance of the duration of UHT metamorphism. Journal of Mineralogical and Petrological Sciences, 111: 50–72. doi:10.2465/jmps.160128.

Harrison, M., Watson, B., 1984, The behavior of apatite during crustal anatexis: Equilibrium and kinetic considerations: Geochemica et Cosmichimica Acta, v. 48, p/ 1467-1477

Harrison, T.M. 2024. We don't know when plate tectonics began. Journal of the Geological Society, 181: jgs2023-212. doi:10.1144/jgs2023-212.

Harrison, T.M., and Watson, E.B. 1983. Kinetics of zircon dissolution and zirconium diffusion in granitic melts of variable water content. Contributions to Mineralogy and Petrology, 84: 66–72. doi:10.1007/BF01132331.

Hartel, T.H.D., and Pattison, D.R.M., 1996, Genesis of the Kapuskasing (Ontario) migmatitic mafic granulites by dehydration melting of amphibolite: The importance of quartz to reaction progress: Journal of Metamorphic Geology, v. 14, p. 591–611, doi:10.1046/j.1525-1314.1996.00404.x.

Hasterok, D., Gard, M., and Webb, J. 2018. On the radiogenic heat production of metamorphic, igneous, and sedimentary rocks. Geoscience Frontiers, 9: 1777–1794. doi:10.1016/j.gsf.2017.10.012.

Hasterok, D., Gard, M., Cox, G., and Hand, M. 2019. A 4 Ga record of granitic heat production: Implications for geodynamic evolution and crustal composition of the early Earth. Precambrian Research, 331: 105375. doi:10.1016/j.precamres.2019.105375.

Hauer, K. 1995. Protoliths, diagenesis, and depositional history of the Upper Marble, Adirondack Lowlands, New York. PhD, Miami University, Oxford, Ohio.

Hawkesworth, C., and Jaupart, C. 2021. Heat flow constraints on the mafic character of Archean continental crust. Earth and Planetary Science Letters, 571: 117091. doi:10.1016/j.epsl.2021.117091.

Hawkesworth, C.J., and Kemp, A.I.S. 2006. Evolution of the continental crust. Nature, 443: 811–817. doi:10.1038/nature05191.

Hayes, B., Bédard, J.H., Hryciuk, M., Wing, B., Nabelek, P., MacDonald, W.D., and Lissenberg, C.J. 2015. Sulfide immiscibility induced by wall-rock assimilation in a fault-guided basaltic feeder system, Franklin Large Igneous Province, Victoria Island (Arctic Canada). Economic Geology, 110: 1697–1717. doi:10.2113/econgeo.110.7.1697.

Henry, D.J. 2005. The Ti-saturation surface for low-to-medium pressure metapelitic biotites: Implications for geothermometry and Ti-substitution mechanisms. American Mineralogist, 90: 316–328. doi:10.2138/am.2005.1498.

Hermann, J. 2002. Allanite: thorium and light rare earth element carrier in subducted crust. Chemical Geology, 192: 289–306. doi:10.1016/S0009-2541(02)00222-X.

Hernández-Montenegro, D., Andronicos, C.L., Zuluaga, C.A., and Aronoff, R.F. 2019. Effects of melt loss, melt retention, and protolith composition on differentiation of anatectic metapelites: A case study of the Wet Mountains, Colorado. Lithos, 344–345: 425–439. doi:10.1016/j.lithos.2019.06.032.

Herron, M.M. 1988. Geochemical classification of terrigenous sands and shales from core or Log data. SEPM Journal of Sedimentary Research, 58: 820–829. doi:10.1306/212F8E77-2B24-11D7-8648000102C1865D.

Hervig, R.L., Dunbar, N., Westrich, H.R., and Kyle, P.R. 1989. Pre-eruptive water content of rhyolitic magmas as determined by ion microprobe analyses of melt inclusions in phenocrysts. Journal of Volcanology and Geothermal Research, 36: 293–302. doi:10.1016/0377-0273(89)90075-9.

Herzberg, C. 1992. Depth and degree of melting of komatiites. Journal of Geophysical Research: Solid Earth, 97: 4521–4540. doi:10.1029/91JB03066.

Heumann, M.J., Bickford, M.E., Hill, B.M., McLelland, J.M., Selleck, B.W., and Jercinovic, M.J. 2006. Timing of anatexis in metapelites from the Adirondack lowlands and southern

highlands: A manifestation of the Shawinigan orogeny and subsequent anorthosite-mangerite-charnockite-granite magmatism. Geological Society of America Bulletin, 118: 1283–1298. doi:10.1130/B25927.1.

Hewitt, D.F., Jupe, D.F., and Jackson, B. 1961. Map of the Gananoque Area, Ontario. Ontario Department of Mines.

Hildebrand, R.S., and Easton, R.M. 1995. An 1161 Ma suture in the Frontenac terrane, Ontario segment of the Grenville orogen. Geology, 23: 917. doi:10.1130/0091-7613(1995)023<0917:AMSITF>2.3.CO;2.

Hinderer, M. 2012. From gullies to mountain belts: A review of sediment budgets at various scales. Sedimentary Geology, 280: 21–59. doi:10.1016/j.sedgeo.2012.03.009.

Holland, T., and Blundy, J. 1994. Non-ideal interactions in calcic amphiboles and their bearing on amphibole-plagioclase thermometry. Contributions to Mineralogy and Petrology, 116: 433–447. doi:10.1007/BF00310910.

Holland, T., and Powell, R. 2003. Activity-composition relations for phases in petrological calculations: an asymmetric multicomponent formulation. Contributions to Mineralogy and Petrology, 145: 492–501. doi:10.1007/s00410-003-0464-z.

Holland, T.J.B., and Powell, R. 1998. An internally consistent thermodynamic data set for phases of petrological interest. Journal of Metamorphic Geology, 16: 309–343. doi:10.1111/j.1525-1314.1998.00140.x.

Holland, T.J.B., and Powell, R. 2011. An improved and extended internally consistent thermodynamic dataset for phases of petrological interest, involving a new equation of state for solids: Thermodynamic dataset fopr phases of petrological interest. Journal of Metamorphic Geology, 29: 333–383. doi:10.1111/j.1525-1314.2010.00923.x.

Holland, T.J.B., and Powell, R., 1985, An internally consistent thermodynamic dataset with uncertainties and correlations: 2. Data and results: Journal of Metamorphic Geology, v. 3, p. 343–370, doi:10.1111/j.1525-1314.1985.tb00325.x.

Holland, T.J.B., and Powell, R., 1990, An enlarged and updated internally consistent thermodynamic dataset with uncertainties and correlations: the system K2O–Na2O–CaO–MgO–MnO–FeO–Fe2O3–Al2O3–TiO2–SiO2–C–H2–O2: Journal of Metamorphic Geology, v. 8, p. 89–124, doi:10.1111/j.1525-1314.1990.tb00458.x.

Holland, T.J.B., and Powell, R., 2011, An improved and extended internally consistent thermodynamic dataset for phases of petrological interest, involving a new equation of state for solids: Journal of Metamorphic Geology, p. 333–383, doi:10.1111/j.1525-1314.2010.00923.x.

Holtz, F., Johannes, W., Tamic, N., and Behrens, H. 2001. Maximum and minimum water contents of granitic melts generated in the crust: a reevaluation and implications. Lithos, 56: 1–14. doi:10.1016/S0024-4937(00)00056-6.

Horedt, G.P. 1980. Gravitational heating of planets. Physics of the Earth and Planetary Interiors, 21: 22–30. doi:10.1016/0031-9201(80)90016-3.

Huang, H., Fryer, B., and Polat, A., 2013, Origin of Archean tonalite–trondhjemite–granodiorite (TTG) suites and granites in the Fiskenæsset region, southern West Greenland: Implications for continental growth: Gondwana Research, v. 12, p. 85–93, doi:10.1016/j.gr.2011.12.001.

Huber, C., Townsend, M., Degruyter, W., and Bachmann, O. 2019. Optimal depth of subvolcanic magma chamber growth controlled by volatiles and crust rheology. Nature Geoscience, 12: 762–768. doi:10.1038/s41561-019-0415-6.

Hughes, L., Burgess, R., Chavrit, D., Pawley, A., Tartèse, R., Droop, G., Ballentine, C.J., and Lyon, I., 2018, Halogen behaviour in subduction zones: Eclogite facies rocks from the Western and Central Alps: Geochimica et Cosmochimica Acta, v. 243, p. 1–23, doi:10.1016/j.gca.2018.09.024.

Hurley, P.M., and Fairbairn, H.W., 1957, Abundance and distribution of uranium and thorium in zircon, sphene, apatite, epidote, and monazite in granitic rocks: Eos, Transactions American Geophysical Union, v. 38, p. 939–944, doi:10.1029/TR038i006p00939.

Hynes, A., and Rivers, T. 2010. Protracted continental collision—evidence from the Grenville Orogen. Canadian Journal of Earth Sciences, 47: 591–620. doi:10.1139/E10-003.

Indares, A. 2024. The Grenville Province: revisiting the orogenic framework and integrating recent findings. Canadian Journal of Earth Sciences,: cjes-2023-0143. doi:10.1139/cjes-2023-0143.

Ingamells, C.O. 1970. Lithium metaborate flux in silicate analysis. Analytica Chimica Acta,: 323–334.

Ishii, T. 1991. Lava-flow and subvolcanic magma reservoir composition trends in the Ca-poor pyroxenes of Hakone Volcano, Japan. Journal of Petrology, 32: 429–450. doi:10.1093/petrology/32.2.429.

Iyer, S.S., Choudhuri, A., Vasconcellos, M.B.A., and Cordani, U.G., 1984, Radioactive element distribution in the Archean granulite terrane of Jequié-Bahia, Brazil: Contributions to Mineralogy and Petrology, v. 85, p. 95–101, doi:10.1007/BF00380226.

Jacob, J.-B., Moyen, J.-F., Fiannacca, P., Laurent, O., Bachmann, O., Janoušek, V., Farina, F., and Villaros, A. 2021. Crustal melting vs. fractionation of basaltic magmas: Part 2, Attempting to quantify mantle and crustal contributions in granitoids. Lithos, 402–403: 106292. doi:10.1016/j.lithos.2021.106292.

Jamieson, R.A., and Beaumont, C., 2013, On the origin of orogens: Bulletin of the Geological Society of America, v. 125, p. 1671–1702, doi:10.1130/B30855.1.

Jaupart, C., and Mareschal, J.-C. 2014. Constraints on crustal heat production from heat flow data. In Treatise on Geochemistry. Elsevier. pp. 53–73. doi:10.1016/B978-0-08-095975-7.00302-8.

Javoy, M., and Kaminski, E. 2014. Earth's Uranium and Thorium content and geoneutrinos fluxes based on enstatite chondrites. Earth and Planetary Science Letters, 407: 1–8. doi:10.1016/j.epsl.2014.09.028.

Jiao, S., Brown, M., Mitchell, R.N., Chowdhury, P., Clark, C., Chen, L., Chen, Y., Korhonen, F., Huang, G., and Guo, J. 2023. Mechanisms to generate ultrahigh-temperature metamorphism. Nature Reviews Earth & Environment, 4: 298–318. doi:10.1038/s43017-023-00403-2.

Johnson, T., Yakymchuk, C., and Brown, M. 2021. Crustal melting and suprasolidus phase equilibria: From first principles to the state-of-the-art. Earth-Science Reviews, 221: 103778. doi:10.1016/j.earscirev.2021.103778.

Johnson, T.A., Vervoort, J.D., Ramsey, M.J., Southworth, S., and Mulcahy, S.R. 2020. Tectonic evolution of the Grenville Orogen in the central Appalachians. Precambrian Research, 346: 105740. doi:10.1016/j.precamres.2020.105740.

Johnson, T.E., Brown, M., Gardiner, N.J., Kirkland, C.L., and Smithies, R.H., 2017, Earth's first stable continents did not form by subduction: Nature Publishing Group, v. 543, p. 239–242, doi:10.1038/nature21383.

Kamo, S.L., and Hamilton, M.A. 2017. Part A: Report on U-Pb ID-TIMS geochronology for the Ontario Geological Survey: Bedrock mapping projects, Ontario, Year 2: 2016-207. Internal Report.

Kaneko, Y., and Miyano, T. 2004. Recalibration of mutually consistent garnet–biotite and garnet–cordierite geothermometers☆. Lithos, 73: 255–269. doi:10.1016/j.lithos.2003.12.009.

Karig, D., and Moore, G. 1975. Tectonically controlled sedimentation in marginal basins. Earth and Planetary Science Letters, 26: 233–238.

Karlstrom, K.E., and Williams, M.L. 1998. Heterogeneity of the middle crust: Implications for strength of continental lithosphere. Geology, 26: 815. doi:10.1130/0091-7613(1998)026<0815:HOTMCI>2.3.CO;2.

Keller, B., and Schoene, B. 2018. Plate tectonics and continental basaltic geochemistry throughout Earth history. Earth and Planetary Science Letters, 481: 290–304. doi:10.1016/j.epsl.2017.10.031.

Kelsey, D.E., and Hand, M. 2015. On ultrahigh temperature crustal metamorphism: Phase equilibria, trace element thermometry, bulk composition, heat sources, timescales and tectonic settings. Geoscience Frontiers, 6: 311–356. doi:10.1016/j.gsf.2014.09.006.

Kelsey, D.E., Clark, C., and Hand, M., 2008, Thermobarometric modelling of zircon and monazite growth in melt-bearing systems: Examples using model metapelitic and metapsammitic granulites: Journal of Metamorphic Geology, v. 26, p. 199–212, doi:10.1111/j.1525-1314.2007.00757.x.

Kemp, A.I.S., Hawkesworth, C.J., Foster, G.L., Paterson, B.A., Woodhead, J.D., Hergt, J.M., Gray, C.M., and Whitehouse, M.J. 2007. Magmatic and crustal differentiation history of granitic rocks from Hf-O Isotopes in zircon. Science, 315: 980–983. doi:10.1126/science.1136154.

Kendrick, J., Duguet, M., and Yakymchuk, C. 2022. Diversification of Archean tonalite-trondhjemite-granodiorite suites in a mushy middle crust. Geology, 50: 76–80. doi:10.1130/G49287.1.

Kendrick, J., Yakymchuk, C., 2020, Garnet fractionation, progressive melt loss and bulk composition variations in anatectic metabasites: Complications for interpreting the geodynamic significance of TTGs, Geoscience Frontiers, v. 11, p. 745-763, doi: 10.1016/j.gsf.2019.12.001

Kendrick, J., Yakymchuk, C., and Duguet, M., 2019, Tectonometamorphic history of the Wawa–Abitibi Terrane: Crustal differentiation and low-grade metamorphism in the Kapuskasing Uplift, in Summary of Field Work and Other Activities 2019, Sudbury, ON, Ontario Geologic Survey, p. 107–113.

Kerr, A.C., Kempton, P.D., and Thompson, R.N. 1995. Crustal assimilation during turbulent magma ascent (ATA); new isotopic evidence from the Mull Tertiary lava succession, N. W. Scotland. : 142–154.

Ketchum, J.W.F., and Davidson, A. 2000. Crustal architecture and tectonic assembly of the Central Gneiss Belt, southwestern Grenville Province, Canada: a new interpretation. 37.

Khitarov, N.I., Kadik, A.A., 1973, Water and carbon dioxide in magmatic melts and peculiarities of the melting process, Contributions to Mineralogy and Petrology, v. 41, p. 205-215, doi: 10.1007/BF00371031

Kiessling, G.M. 2016. Provenance of the Flinton Group, Grenville Province, Southeastern Ontario. B.Sc, University of Waterloo, Waterloo, Ontario.

Kinney, C., Kendrick, J., Duguet, M., and Yakymchuk, C. 2023. Redistribution of heat-producing elements during melting of Archean crust. Journal of Metamorphic Geology,: jmg.12751. doi:10.1111/jmg.12751.

Klein, M., Stosch, H.G., and Seek, H.A., 1997, Partitioning of high field-strength and rare-earth elements between amphibole and quartz-dioritic to tonalitic melts: An experimental study: Chemical Geology, v. 138, p. 257–271, doi:10.1016/S0009-2541(97)00019-3.

Kleine, T., Münker, C., Mezger, K., and Palme, H. 2002. Rapid accretion and early core formation on asteroids and the terrestrial planets from Hf–W chronometry. Nature, 418: 952–955. doi:10.1038/nature00982.

Kleine, T., Touboul, M., Bourdon, B., Nimmo, F., Mezger, K., Palme, H., Jacobsen, S.B., Yin, Q.-Z., and Halliday, A.N. 2009. Hf–W chronology of the accretion and early evolution of asteroids and terrestrial planets. Geochimica et Cosmochimica Acta, 73: 5150–5188. doi:10.1016/j.gca.2008.11.047.

Klimm, K., Blundy, J.D., and Green, T.H. 2008. Trace element partitioning and accessory phase saturation during H2O-saturated melting of basalt with implications for subduction zone chemical fluxes. Journal of Petrology, 49: 523–553. doi:10.1093/petrology/egn001.

Kol'tsov, A.B., and Bushmin, S.A. 2022. Metasomatism under Thermogradient Conditions: Models for the Coupled Heat Transfer and Fluid–Rock Interaction. Petrology, 30: 305–324. doi:10.1134/S0869591122030043.

Korenaga, J. 2008. Urey ratio and the structure and evolution of Earth's mantle. Reviews of Geophysics, 46: 2007RG000241. doi:10.1029/2007RG000241.

Krogh, T.E. 1993. High precision U-Pb ages for granulite metamorphism and deformation in the Archean Kapuskasing structural zone, Ontario: implications for structure and development of the lower crust. Earth and Planetary Science Letters, 119: 1–18. doi:10.1016/0012-821X(93)90002-Q.

Krogh, T.E., and Hurley, P.M. 1968. Strontium isotope variation and whole-rock isochron studies, Grenville Province of Ontario. Journal of Geophysical Research, 73: 7107–7125. doi:10.1029/JB073i022p07107.

Krogh, T.E., and Moser, D.E. 1994. U–Pb zircon and monazite ages from the Kapuskasing uplift: age constraints on deformation within the Ivanhoe Lake fault zone. Canadian Journal of Earth Sciences, 31: 1096–1103. doi:10.1139/e94-098.

Kröner, A., Hegner, E., Wendt, J.I., and Byerly, G.R., 1996, The oldest part of the Barberton granitoid-greenstone terrain, South Africa: Evidence for crust formation between 3.5 and 3.7 Ga: Precambrian Research, v. 78, p. 105–124, doi:10.1016/0301-9268(95)00072-0.

Kusky, T.M., Windley, B.F., and Polat, A. 2018. Geological Evidence for the Operation of Plate Tectonics throughout the Archean: Records from Archean Paleo-Plate Boundaries. Journal of Earth Science, 29: 1291–1303. doi:10.1007/s12583-018-0999-6.

La Spina, G., Burton, M., De' Michieli Vitturi, M., and Arzilli, F. 2016. Role of syn-eruptive plagioclase disequilibrium crystallization in basaltic magma ascent dynamics. Nature Communications, 7: 13402. doi:10.1038/ncomms13402.

Lambert, C., Gervais, F., Crowley, J.L., Moukhsil, A., and Kavanagh-Lepage, C. 2023. Protracted melt-present deformation during the Rigolet phase of the Grenvillian Orogeny. Insights from geochronology along the highway 117 transect through the Grenville Province in western Quebec, Canada. Precambrian Research, 384: 106939. doi:10.1016/j.precamres.2022.106939.

Lan, T.F., Sano, Y., Yang, T.F., Takahata, N., Shirai, K., and Pinti, D.L. 2010. Evaluating Earth degassing in subduction zones by measuring helium fluxes from the ocean floor. Earth and Planetary Science Letters, 298: 317–322. doi:10.1016/j.epsl.2010.07.049.

Landenberger, B., and Collins, W.J. 1996. Derivation of A-type Granites from a Dehydrated Charnockitic Lower Crust: Evidence from the Chaelundi Complex, Eastern Australia. Journal of Petrology, 37: 145–170. doi:10.1093/petrology/37.1.145.

Laurent, O., Guitreau, M., Bruand, E., and Moyen, J.-F. 2024. At the dawn of continents: Archean Tonalite-Trondhjemite-Granodiorite Suites. Elements, 20: 174–179. doi:10.2138/gselements.20.3.174.

Lei, H., and Xu, H. 2018. A review of ultrahigh temperature metamorphism. Journal of Earth Science, 29: 1167–1180. doi:10.1007/s12583-018-0846-9.

Lenardic, A., Moresi, L., Jellinek, A.M., O'Neill, C.J., Cooper, C.M., and Lee, C.T. 2011. Continents, supercontinents, mantle thermal mixing, and mantle thermal isolation: Theory, numerical simulations, and laboratory experiments: Continents and mantle thermal mixing. Geochemistry, Geophysics, Geosystems, 12. doi:10.1029/2011GC003663.

Lentz, D. 1992. U Ottawa. Petrogenesis of U-, Th-, Mo-, and REE-bearing pegmatites, skarns and veins in the central metasedimentary belt of the Grenville Province, ONtario and Quebec. PhD, University of Ottawa, Ottawa, ON, Canada.

Li, H., Schwarcz, H.P., and Shaw, D.M., 1991, Deep crustal oxygen isotope variations: The Wawa-Kapuskasing crustal transect, Ontario: Contributions to Mineralogy and Petrology, v. 107, p. 448–458, doi:10.1007/BF00310679.

Lin, S., and Beakhouse, G.P., 2013, Synchronous vertical and horizontal tectonism at late stages of Archean cratonization and genesis of Hemlo gold deposit, Superior craton, Ontario, Canada: Geology, v. 41, p. 359–362, doi:10.1130/G33887.1.

Linnen, R.L. 1998. Depth of emplacement, fluid provenance and metallogeny in granitic terranes: a comparison of western Thailand with other tin belts. Mineralium Deposita, 33: 461–476.

Liu, X., Zhang, C., Yuan, S., Fityus, S., Sloan, S.W., and Buzzi, O. 2016. Effect of High Temperature on Mineralogy, Microstructure, Shear Stiffness and Tensile Strength of Two Australian Mudstones. Rock Mechanics and Rock Engineering, 49: 3513–3524. doi:10.1007/s00603-016-1024-y.

London, D., 1992, Phosphorus in S-type magmas: the P2O5 content of feldspars from peraluminous granites, pegmatites, and rhyolites: American Mineralogist, v. 77, p. 126–145.

Loury, C., Rolland, Y., Cenki-Tok, B., Lanari, P., and Guillot, S., 2016, Late Paleozoic evolution of the South Tien Shan: Insights from P-T estimates and allanite geochronology on retrogressed eclogites (Chatkal range, Kyrgyzstan): Journal of Geodynamics, v. 96, p. 62–80, doi:10.1016/j.jog.2015.06.005.

Lowenstern, J.B., Clynne, M.A., and Bullen, T.D. 1997. Comagmatic A-Type granophyre and rhyolite from the Alid Volcanic Center, Eritrea, Northeast Africa. Journal of Petrology, 38.

Lumbers, S., Heaman, L.M., Vertolli, V.M., Wu, T.W., Gower, C.F., Rivers, T., and Ryan, A.B. 1990. Nature and timing of Middle Proterozoic magmatism in the Central metasedimentary belt, Grenville Province, Ontario. Geological Association of Canada, 38: 243–276.

Luo, Z., Mo, X., Lu, X., Chen, B., Ke, S., Hou, Z., and Jiang, W. 2007. Metallogeny by Trans-magmatic Fluids—Theoretical Analysis and Field Evidence. Earth Science Frontiers, 14: 165–183. doi:10.1016/S1872-5791(07)60025-6.

Mansard, N., Stünitz, H., Raimbourg, H., and Précigout, J. 2020. The role of deformation-reaction interactions to localize strain in polymineralic rocks: Insights from experimentally deformed plagioclase-pyroxene assemblages. Journal of Structural Geology, 134: 104008. doi:10.1016/j.jsg.2020.104008.

Manya, S., 2016, Petrogenesis and emplacement of the TTG and K-rich granites at the Buzwagi gold mine, northern Tanzania: Implications for the timing of gold mineralization: Lithos, v. 256–257, p. 26–40, doi:10.1016/j.lithos.2016.03.025.

Marcantonio, F., Mcnutt, R.H., Dickin, A.P., and Heaman, L.M. 1990. Isotopic evidence for the crustal evolution of the Frontenac Arch in the Grenville Province of Ontario, Canada. Chemical Geology, 83: 297–314.

Mareschal, J.-C., and Jaupart, C. 2006. Archean thermal regime and stabilization of the cratons. In Geophysical Monograph Series. American Geophysical Union, Washington, D. C. pp. 61–73. doi:10.1029/164GM06.

Mareschal, J.C., and Jaupart, C., 2006, Archean thermal regime and stabilization of the cratons: Archean Geodynamics and Environments, p. 61–73, doi:10.1029/164GM06.

Markley, M.J., Dunn, S.R., Jercinovic, M.J., Peck, W.H., and Williams, M.L. 2018. Monazite U–Th–Pb geochronology of the Central Metasedimentary Belt Boundary Zone (CMBbz), Grenville Province, Ontario Canada. Canadian Journal of Earth Sciences, 55: 1063–1078. doi:10.1139/cjes-2018-0039.

Martignole, J., and Wang, Z. 2010. Feldspar thermometry of grenvillian-age UHT migmatites. Mollendo-Camana block, southern Peru. The Canadian Mineralogist, 48: 1025–1039. doi:10.3749/canmin.48.4.1025.

Martin, H., Moyen, J.F., Guitreau, M., Blichert-Toft, J., and le Pennec, J.L., 2014, Why Archaean TTG cannot be generated by MORB melting in subduction zones: Lithos, v. 198–199, p. 1–13, doi:10.1016/j.lithos.2014.02.017.

Martin, H., Smithies, R.H., Rapp, R., Moyen, J.-F., and Champion, D. 2005. An overview of adakite, tonalite–trondhjemite–granodiorite (TTG), and sanukitoid: relationships and some implications for crustal evolution. Lithos, 79: 1–24. doi:10.1016/j.lithos.2004.04.048.

McDonough, W.F., and Sun, S.-S. 1995. The composition of the Earth. Chemical Geology,: 223–253.

McEachern, S.J., and van Breemen, O. 1993. Age of deformation within the Central Metasedimentary Belt boundary thrust zone, southwest Grenville Orogen: constraints on the collision of the Mid-Proterozoic Elzevir terrane. Canadian Journal of Earth Sciences, 30: 1155–1165. doi:10.1139/e93-098.

McKenzie, D., and O'Nions, R.K. 1991. Partial Melt Distributions from Inversion of Rare Earth Element Concentrations. Journal of Petrology, 32: 1021–1091. doi:10.1093/petrology/32.5.1021.

McLelland, J., Chiarenzelli, J., and Perham, A. 1992. Age, field, and petrological relationships of the Hyde School Gneiss, Adirondack Lowlands, New York: Criteria for an intrusive igneous origin. The Journal of Geology, 100: 69–90. doi:10.1086/629572.

McLelland, J., Hamilton, M., Selleck, B., McLelland, J., Walker, D., and Orrell, S. 2001. Zircon U-Pb geochronology of the Ottawan Orogeny, Adirondack Highlands, New York: regional and tectonic implications. Precambrian Research, 109: 39–72. doi:10.1016/S0301-9268(01)00141-3.

McLelland, J.M., and Chiarenzelli, J.R. 1990. Geochronological studies in the Adirondack Mountains and the implications of a Middle Proterozoic tonalitic suite. Geological Association of Canada,.

McLelland, J.M., Daly, J.S., and Chiarenzelli, J. 1993. Sm-Nd and U-Pb Isotopic evidence of juvenile crust in the Adirondack Lowlands and implications for the evolution of the Adirondack Mts. The Journal of Geology, 101: 97–105. doi:10.1086/648198.

McLelland, J.M., Selleck, B.W., and Bickford, M.E. 2010. Review of the Proterozoic evolution of the Grenville Province, its Adirondack outlier, and the Mesoproterozoic inliers of the Appalachians. In From Rodinia to Pangea: The Lithotectonic Record of the Appalachian Region. Geological Society of America. doi:10.1130/2010.1206(02).

McMillan, M., Schoenbohm, L.M., and Tye, A.R. 2023. Plateau formation controlled by lithospheric foundering under a weak crust. Geophysical Research Letters, 50: e2023GL103996. doi:10.1029/2023GL103996.

McNutt, R.H., and Dickin, A.P. 2012. A comparison of Nd model ages and U–Pb zircon ages of Grenville granitoids: constraints on the evolution of the Laurentian margin from 1.5 to 1.0 Ga. Terra Nova, 24: 7–15. doi:10.1111/j.1365-3121.2011.01031.x.

Menéndez, L.G., Azor, A., Ordóñez, A.R., and Sánchez-Almazo, I. 2011. The metamorphic aureole of the Nisa-Alburquerque batholith (SW Iberia): implications for deep structure and emplacement mode. International Journal of Earth Sciences, 100: 1533–1550. doi:10.1007/s00531-010-0568-4.

Mezger, K., Essene, E.J., Van Der Pluijm, B.A., and Halliday, A.N. 1993. U-Pb geochronology of the Grenville Orogen of Ontario and New York: Constraints on ancient crustal tectonics. Contributions to Mineralogy and Petrology, 114: 13–26. doi:10.1007/BF00307862.

Mezger, K., Rawnsley, C.M., Bohlen, S.R., and Hanson, G.N. 1991. U-Pb garnet, sphene, monazite, and rutile ages: Implications for the duration of high-grade metamorphism and cooling

histories, Adirondack Mts., New York. The Journal of Geology, 99: 415–428. doi:10.1086/629503.

Mezger, K., Van Der Pluijm, B.A., Essene, E.J., and Halliday, A.N. 1992. The Carthage-Colton Mylonite Zone (Adirondack Mountains, New York): The site of a cryptic suture in the Grenville Orogen? The Journal of Geology, 100: 630–638. doi:10.1086/629613.

Michaut, C., Jaupart, C., and Mareschal, J.-C. 2009. Thermal evolution of cratonic roots. Lithos, 109: 47–60. doi:10.1016/j.lithos.2008.05.008.

Middlemost, E.A.K. 1994. Naming materials in the magma/igneous rock system. Earth-Science Reviews, 37: 215–224. doi:10.1016/0012-8252(94)90029-9.

Mildren, S.D., and Sandiford, M. 1995. Heat refraction and low-pressure metamorphism in the northern flinders ranges, south australia. Australian Journal of Earth Sciences, 42: 241–247. doi:10.1080/08120099508728198.

Miller, J.S., Matzel, J.E.P., Miller, C.F., Burgess, S.D., and Miller, R.B. 2007. Zircon growth and recycling during the assembly of large, composite arc plutons. Journal of Volcanology and Geothermal Research, 167: 282–299. doi:10.1016/j.jvolgeores.2007.04.019.

Mo, J., Xia, X.-P., Li, P.-F., Spencer, C.J., Lai, C.-K., Xu, J., Yang, Q., Sun, M.-D., Yu, Y., and Milan, L. 2023. Water-in-zircon: a discriminant between S- and I-type granitoid. Contributions to Mineralogy and Petrology, 178: 5. doi:10.1007/s00410-022-01986-7.

Moecher, D.P., Anderson, E.D., Cook, C.A., and Mezger, K. 1997. The petrogenesis of metamorphosed carbonatites in the Grenville Province, Ontario. Canadian Journal of Earth Sciences, 34: 1185–1201. doi:10.1139/e17-095.

Montsion, R.M., Thurston, P., and Ayer, J., 2018, 1:2 000 000 Scale Geological Compilation of the Superior Craton:

Morgan, P. 1985. Crustal radiogenic heat production and the selective survival of ancient continental crust. Journal of Geophysical Research, 90: C561. American Geophysical Union (AGU). doi:10.1029/jb090is02p0c561.

Moser, D.E., 1994, The geology and structure of the mid-crustal Wawa gneiss domain: A key to understanding tectonic variation with depth and time in the late Archean Abitibi-Wawa Orogen: Canadian Journal of Earth Sciences, v. 31, p. 1064–1080, doi:10.1139/e94-096.

Moser, D.E., Heaman, L.M., Krogh, T.E., and Hanes, J.A., 1996, Intracrustal extension of an Archean orogen revealed using single-grain U-Pb zircon geochronology: Tectonics, v. 15, p. 1093–1109, doi:10.1029/96TC00130.

Mougeot, X. 2018. Improved calculations of electron capture transitions for decay data and radionuclide metrology. Applied Radiation and Isotopes, 134: 225–232. Elsevier Ltd. doi:10.1016/j.apradiso.2017.07.027.

Moyen, J., and Martin, H., 2012, Forty years of TTG research: Lithos, v. 148, p. 312–336, doi:10.1016/j.lithos.2012.06.010.

Moyen, J.-F. 2011. The composite Archaean grey gneisses: Petrological significance, and evidence for a non-unique tectonic setting for Archaean crustal growth. Lithos, 123: 21–36. doi:10.1016/j.lithos.2010.09.015.

Moyen, J.-F., Janoušek, V., Laurent, O., Bachmann, O., Jacob, J.-B., Farina, F., Fiannacca, P., and Villaros, A. 2021. Crustal melting vs. fractionation of basaltic magmas: Part 1, granites and paradigms. Lithos, 402–403: 106291. doi:10.1016/j.lithos.2021.106291.

Mulder, J.A., and Cawood, P.A. 2022. Evaluating preservation bias in the continental growth record against the monazite archive. Geology, 50: 243–247. doi:10.1130/G49416.1.

Nabelek, P.I., Liu, M., and Sirbescu, M.-L. 2001. Thermo-rheological, shear heating model for leucogranite generation, metamorphism, and deformation during the Proterozoic Trans-Hudson orogeny, Black Hills, South Dakota. Tectonophysics, 342: 371–388. doi:10.1016/S0040-1951(01)00171-8.

Nesbitt, H.W., and Young, G.M. 1984. Prediction of some weathering trends of plutonic and volcanic rocks based on thermodynamic and kinetic considerations. Geochimica et Cosmochimica Acta, 48: 1523–1534. doi:10.1016/0016-7037(84)90408-3.

Nisbet, H., Migdisov, A., Xu, H., Guo, X., van Hinsberg, V., Williams-Jones, A.E., Boukhalfa, H., and Roback, R., 2018, An experimental study of the solubility and speciation of thorium in chloride-bearing aqueous solutions at temperatures up to 250°C: Geochimica et Cosmochimica Acta, v. 239, p. 363–373, doi:10.1016/j.gca.2018.08.001.

Nisbet, H., Migdisov, A.A., Williams-Jones, A.E., Xu, H., van Hinsberg, V.J., and Roback, R., 2019, Challenging the thorium-immobility paradigm: Scientific Reports, v. 9, p. 8–13, doi:10.1038/s41598-019-53571-x.

Nitescu, B., and Halls, H.C., 2002, A gravity profile across southern Saganash Lake fault: Implications for the origin of the Kapuskasing Structural Zone: Canadian Journal of Earth Sciences, v. 39, p. 469–480, doi:10.1139/e01-100.

Olierook, H.K.H., Kirkland, C.L., Szilas, K., Hollis, J.A., Gardiner, N.J., Steenfelt, A., Jiang, Q., Yakymchuk, C., Evans, N.J., and McDonald, B.J. 2020. Differentiating between inherited and autocrystic zircon in granitoids. Journal of Petrology, 61: egaa081. doi:10.1093/petrology/egaa081.

Oliver, N.H.S., Rubenach, M.J., Fu, B., Baker, T., Blenkinsop, T.G., Cleverley, J.S., Marshall, L.J., and Ridd, P.J. 2006. Granite-related overpressure and volatile release in the mid crust: fluidized breccias from the Cloncurry District, Australia. Geofluids, 6: 346–358. doi:10.1111/j.1468-8123.2006.00155.x.

Ontario Geologic Survey, 2011, MRD 126 - 1:250 000 Scale Bedrock Geology of Ontario.:

O'Neill, C., Lenardic, A., Moresi, L., Torsvik, T.H., and Lee, C.-T.A. 2007. Episodic precambrian subduction. Earth and Planetary Science Letters, 262: 552–562. doi:10.1016/j.epsl.2007.04.056.

Palin, R.M., Weller, O.M., Waters, D.J., and Dyck, B., 2016, Quantifying geological uncertainty in metamorphic phase equilibria modelling; A Monte Carlo assessment and implications for tectonic interpretations: Geoscience Frontiers, v. 7, p. 591–607, doi:10.1016/j.gsf.2015.08.005.

Palin, R.M., White, R.W., and Green, E.C.R. 2016. Partial melting of metabasic rocks and the generation of tonalitic–trondhjemitic–granodioritic (TTG) crust in the Archaean: Constraints from phase equilibrium modelling. Precambrian Research, 287: 73–90. doi:10.1016/j.precamres.2016.11.001.

Palin, R.M., White, R.W., Green, E.C.R., Diener, J.F.A., Powell, R., and Holland, T.J.B., 2016c, High-grade metamorphism and partial melting of basic and intermediate rocks: Journal of Metamorphic Geology, v. 34, p. 871–892, doi:10.1111/jmg.12212.

Parman, S.W. 2007. Helium isotopic evidence for episodic mantle melting and crustal growth. Nature, 446: 900–903. doi:10.1038/nature05691.

Pasquale, V., Verdoya, M., Choizzi, P., 2015, Measurements of rock thermal conductivity with a transient divided bar: Geothermics, v. 53, p. 183-189, doi: 10.1016/j.geothermics.2014.05.008

Passchier, C.W., and Trouw, R.A.J. 2005. Microtectonics. In 2nd, rev.enl. ed edition. Springer, Berlin ; New York.

Pattison, D.R.M. 2003. Temperatures of granulite-facies metamorphism: Constraints from experimental phase equilibria and thermobarometry corrected for retrograde exchange. Journal of Petrology, 44: 867–900. doi:10.1093/petrology/44.5.867.

Pearce, J.A., Harris, N.B.W., and Tindle, A.G. 1984. Trace Element Discrimination Diagrams for the Tectonic Interpretation of Granitic Rocks. Journal of Petrology, 25: 956–983. doi:10.1093/petrology/25.4.956.

Pearson, D.G., Parman, S.W., and Nowell, G.M. 2007. A link between large mantle melting events and continent growth seen in osmium isotopes. Nature, 449: 202–205. doi:10.1038/nature06122.

Peck, W.H. 2012. Reconnaissance geochronology and geochemistry of the Mont-Tremblant gneiss of the Morin terrane, Grenville Province, Québec.

Peck, W.H., and Lin, H.Y. 2024. Provenance and depositional age of metasedimentary rocks in the Frontenac terrane (Grenville Province, Ontario). Canadian Journal of Earth Sciences,: cjes-2024-0029. doi:10.1139/cjes-2024-0029.

Peck, W.H., Rathkopf, C.A., Mathur, R.D., and Matt, P.D. 2022. Stable isotope (C, O, S, and Zn) geochemistry of marble-hosted exhalative zinc deposits in the Central Metasedimentary Belt, Grenville Province, Canada: Insights into ore deposition and tectonic setting. Ore Geology Reviews, 148: 105057. doi:10.1016/j.oregeorev.2022.105057.

Peck, W.H., Selleck, B.W., Wong, M.S., Chiarenzelli, J.R., Harpp, K.S., Hollocher, K., Lackey, J.S., Catalano, J., Regan, S.P., and Stocker, A. 2013. Orogenic to postorogenic (1.20-1.15 Ga) magmatism in the Adirondack Lowlands and Frontenac terrane, southern Grenville Province, USA and Canada. Geosphere, 9: 1637–1663. doi:10.1130/GES00879.1.

Peck, W.H., Valley, J.W., Corriveau, L., Davidson, A., McLelland, J., and Farber, D.A. 2004. Oxygen-isotope constraints on terrane boundaries and origin of 1.18-1.13 Ga granitoids in the southern Grenville Province. Geological Society of America Memior,: 163–182.

Pehrsson, S., Hanmer, S., and Van Breemen, O. 1996. U–Pb geochronology of the Raglan gabbro belt, Central Metasedimentary Belt, Ontario: implications for an ensialic marginal basin in the Grenville Orogen. Canadian Journal of Earth Sciences, 33: 691–702. doi:10.1139/e96-052.

Percival, J.A., 1983, High-grade metamorphism in the Chapleau-Foleyet Area, Ontario: American Mineralogist, v. 68, p. 667–686.

Percival, J.A., 1990, A field guide to the Kapuskasing Uplift, A cross section through the Archean Superior Province: Exposed Cross-Sections of the Continental Crust, p. 227–283.

Percival, J.A., and Card, K.D., 1983, Archean crust as revealed in the Kapuskasing uplift, Superior province, Canada: Geology, v. 11, p. 323, doi:10.1130/0091-7613.

Percival, J.A., and Krogh, T.E., 1983, U-Pb zircon geochronology of the Kapuskasing structural zone and vicinity in the Chapleau-Foleyet area, Ontario.: Canadian Journal of Earth Sciences, v. 20, p. 830–843, doi:10.1139/e83-073.

Percival, J.A., and Mcgrath, P.H., 1986, Deep crustal structure and tectonic history of the northern Kapuskasing Uplift of Ontario: An integrated petrological-geophysical study: Tectonics, v. 5, p. 553–572.

Percival, J.A., and West, G.F., 1994, The Kapuskasing uplift: a geological and geophysical synthesis: Canadian Journal of Earth Sciences, v. 31, p. 1256–1286, doi:10.1139/e94-110.

Perry, F.V., DePaolo, D.J., and Baldridge, W.S. 1993. Neodymium isotopic evidence for decreasing crustal contributions to Cenozoic ignimbrites of the western United States: Implications for the thermal evolution of the Cordilleran crust. Geological Society of America Bulletin, 105: 872–882. doi:10.1130/0016-7606(1993)105<0872:NIEFDC>2.3.CO;2.

Perry, H.K.C., Mareschal, J.-C., and Jaupart, C., 2006, Variations of strength and localized deformation in cratons: The 1.9 Ga Kapuskasing uplift, Superior Province, Canada: Earth and Planetary Science Letters, v. 249, p. 216–228, doi:10.1016/j.epsl.2006.07.013.

Petersson, A., Kemp, A.I.S., Gray, C.M., and Whitehouse, M.J., 2020, Formation of early Archean granite-greenstone terranes from a globally chondritic mantle: Insights from igneous rocks of the Pilbara Craton, Western Australia: Chemical Geology, v. 551, p. 119757, doi:10.1016/j.chemgeo.2020.119757.

Petford, N. 2003. Rheology of granitic magmas during ascent and emplacement. Annual Review of Earth and Planetary Sciences, 31: 399–427. doi:10.1146/annurev.earth.31.100901.141352.

Petford, N., Cruden, A.R., Mccaffrey, K.J.W., and Vigneresse, J.-L. 2000. Granite magma formation, transport and emplacement in the Earth's crust. Nature, 408. Available from www.nature.com.

Petford, N., Kerr, R.C., and Lister, J.R. 1993. Dike transport of granitoid magmas. Geology, 21: 845. doi:10.1130/0091-7613(1993)021<0845:DTOGM>2.3.CO;2.

Petford, N., Lister, J.R., and Kerr, R.C. 1994. The ascent of felsic magmas in dykes. Lithos, 32: 161–168. doi:10.1016/0024-4937(94)90028-0.

Petrelli, M., El Omari, K., Spina, L., Le Guer, Y., La Spina, G., and Perugini, D. 2018. Timescales of water accumulation in magmas and implications for short warning times of explosive eruptions. Nature Communications, 9: 770. doi:10.1038/s41467-018-02987-6.

Philpotts, J.A., and Schnetzler, C.C., 1970, Phenocryst-matrix partition coefficients for K, Rb, Sr and Ba, with applications to anorthosite and basalt genesis: Geochimica et Cosmochimica Acta, v. 34, p. 307–322, doi:10.1016/0016-7037(70)90108-0.

Powell, R., and Holland, T.J.B. 1988. An internally consistent dataset with uncertainties and correlations: 3. Applications to geobarometry, worked examples and a computer program. Journal of Metamorphic Geology, 6: 173–204. doi:10.1111/j.1525-1314.1988.tb00415.x.

Powell, R., and Holland, T.J.B., 1985, An internally consistent thermodynamic dataset with uncertainties and correlations: 1. Methods and a worked example: Journal of Metamorphic Geology, v. 3, p. 327–342, doi:10.1111/j.1525-1314.1985.tb00324.x.

Powell, R., Holland, T., and Worley, B. 1998. Calculating phase diagrams involving solid solutions via non-linear equations, with examples using THERMOCALC. Journal of Metamorphic Geology, 16: 577–588. doi:10.1111/j.1525-1314.1998.00157.x.

Pownall, J.M., Hall, R., Armstrong, R.A., and Forster, M.A. 2014. Earth's youngest known ultrahigh-temperature granulites discovered on Seram, eastern Indonesia. Geology, 42: 279–282. doi:10.1130/G35230.1.

Rampino, M.R., and Prokoph, A. 2013. Are mantle plumes periodic? Eos, Transactions American Geophysical Union, 94: 113–114. doi:10.1002/2013EO120001.

Ratcliffe, N.M., Aleinikoff, J.N., Burton, W.C., and Karabinos, P. 1991. Trondhjemitic, 1.35–1.31 Ga gneisses of the Mount Holly Complex of Vermont: evidence for an Elzevirian event in the Grenville Basement of the United States Appalachians. Canadian Journal of Earth Sciences, 28: 77–93. doi:10.1139/e91-007.

Reinhardt, E.W. 1968. Phase relations in cordierite-bearing gneisses from the Gananoque area, Ontario. Canadian Journal of Earth Sciences, 5: 455–482. doi:10.1139/e68-043.

Rey, P.F., Teyssier, C., and Whitney, D.L. 2009. Extension rates, crustal melting, and core complex dynamics. Geology, 37: 391–394. doi:10.1130/G25460A.1.

Rivers, T. 1997. Lithotectonic elements of the Grenville Province: review and tectonic implications. Precambrian Research, 86: 117–154. doi:10.1016/S0301-9268(97)00038-7.

Rivers, T. 2008. Assembly and preservation of lower, mid, and upper orogenic crust in the Grenville Province—Implications for the evolution of large hot long-duration orogens. Precambrian Research, 167: 237–259. doi:10.1016/j.precamres.2008.08.005.

Rivers, T. 2012. Upper-crustal orogenic lid and mid-crustal core complexes: signature of a collapsed orogenic plateau in the hinterland of the Grenville Province. Canadian Journal of Earth Sciences, 49: 1–42. doi:10.1139/e11-014.

Rivers, T., Culshaw, N., Hynes, A., Indares, A., Jamieson, R., and Martignole, J. 2012. The Grenville Orogen—a post-Lithprobe prospective. In Tectonic Styles in Canada: The Lithoprobe Perspective.

Roberts, N.M.W. 2012. Increased loss of continental crust during supercontinent amalgamation. Gondwana Research, 21: 994–1000. doi:10.1016/j.gr.2011.08.001.

Robin, C.M.I., and Bailey, R.C. 2009. Simultaneous generation of Archean crust and subcratonic roots by vertical tectonics. Geology, 37: 523–526. doi:10.1130/G25519A.1.

Rollinson, H. 2010. Coupled evolution of Archean continental crust and subcontinental lithospheric mantle. Geology, 38: 1083–1086. doi:10.1130/G31159.1.

Roser, B.P., and Korsch, R.J. 1986. Determination of tectonic setting of sandstone-mudstone suites using SiO2 content and K2O/Na2O ratio. Journal of Geology, 94: 635–650.

Rudnick, R.L., and Fountain, D., 1995, Nature and composition of the continental crust: A lower crustal perspective: Physics of the Earth and Planetary Interiors, v. 145, p. 267–309.

Rudnick, R.L., and Gao, S., 2003, Composition of the continental crust: Elsevier Ltd., v. 4, 1–51 p., doi:10.1016/B978-0-08-095975-7.00301-6.

Rudnick, R.L., McDonough, W.F., and O'Connell, R.J., 1998, Thermal structure, thickness and composition of continental lithosphere: Chemical Geology, v. 145, p. 395–411, doi:10.1016/S0009-2541(97)00151-4.

Ruedas, T. 2017. Radioactive heat production of six geologically important nuclides. Geochemistry, Geophysics, Geosystems,: 3530–3541. doi:10.1002/2017GC006997.Received.

Russell, A. 2009. Recent two-feldspar, Ti-in-biotite, and garnet-biotite geothermometry of the Frontenac terrane and Adirondack Lowlands, Grenville Province, Canada and the United States. Undergraduate Thesis, University of North Dakota, Grand Forks, North Dakota.

Rutherford, E., and Soddy, F., 1903, Radioactive Change: The London, Edinburgh, and Dublin Philosophical Magazine and Journal of Science, v. 5, p. 576–591, doi:10.1080/14786440309462960.

Rutherford, M.J. 2008. Magma ascent rates. Reviews in Mineralogy and Geochemistry, 69: 241–271. doi:10.2138/rmg.2008.69.7.

Sage, R.P., 1994, Geology of the Michipicoten Greenstone Belt: Ontario Geologic Survey, p. 671.

Sage, R.P., Lightfoot, P.C., and Doherty, W., 1996, Bimodal cyclical Archean basalts and rhyolites from the Michipicoten (Wawa) greenstone belt, Ontario: Geochemical evidence for magma contributions from the asthenospheric mantle and ancient continental lithosphere near the southern margin of the Superior: Precambrian Research, v. 76, p. 119–153, doi:10.1016/0301-9268(95)00020-8.

Sager-Kinsman, E.A., and Parrish, R.R. 1993. Geochronology of detrital zircons from the Elzevir and Frontenac terranes, Central Metasedimentary Belt, Grenville Province, Ontario. Canadian Journal of Earth Sciences, 30: 465–473. doi:10.1139/e93-034.

Samsonov, G.V. 1973. The Oxide Handbook. Springer US, Boston, MA.

Sawyer, E.W. 2008. Atlas of migmatites. NRC research press, Ottawa.

Sawyer, E.W., Cesare, B., and Brown, M. 2011. When the Continental Crust Melts. Elements, 7: 229–234. doi:10.2113/gselements.7.4.229.

Scaillet, B., Pichavant, M., and Roux, J. 1995. Experimental crystallization of leucogranite magmas. Journal of Petrology, 36: 663–705. doi:10.1093/petrology/36.3.663.

Schaltegger, U., Brack, P., Ovtcharova, M., Peytcheva, I., Schoene, B., Stracke, A., Marocchi, M., and Bargossi, G.M. 2009. Zircon and titanite recording 1.5 million years of magma accretion, crystallization and initial cooling in a composite pluton (southern Adamello batholith, northern Italy). Earth and Planetary Science Letters, 286: 208–218. Elsevier B.V. doi:10.1016/j.epsl.2009.06.028.

Schorn, S., Diener, J.F.A., Powell, R., and Stüwe, K. 2018. Thermal buffering in the orogenic crust. Geology, 46: 643–646. doi:10.1130/G40246.1.

Schwindinger, M., Weinberg, R.F., and White, R.W. 2020. The Fate of Accessory Minerals and Key Trace Elements During Anatexis and Magma Extraction. Journal of Petrology, 61: egaa031. doi:10.1093/petrology/egaa031.

Sdrolias, M., and Müller, R.D. 2006. Controls on back-arc basin formation. Geochemistry, Geophysics, Geosystems, 7: 2005GC001090. doi:10.1029/2005GC001090.

Shao, T., Xia, Y., Ding, X., Cai, Y., and Song, M., 2019, Zircon saturation in terrestrial basaltic melts and its geological implications: Solid Earth Sciences, v. 4, p. 27–42, doi:10.1016/j.sesci.2018.08.001.

Shemenda, A.I. 1993. Subduction of the lithosphere and back arc dynamics: Insights from physical modeling. Journal of Geophysical Research: Solid Earth, 98: 16167–16185. doi:10.1029/93JB01094.

Shieh, Y.N. 1985. High-18O granitic plutons from the Frontenac Axis, Grenville province of Ontario, Canada. Geochimica et Cosmochimica Acta, 49: 117–123. doi:10.1016/0016-7037(85)90195-4.

Sizova, E., Gerya, T., Stüwe, K., and Brown, M. 2015. Generation of felsic crust in the Archean: A geodynamic modeling perspective. Precambrian Research, 271: 198–224. Elsevier. doi:10.1016/j.precamres.2015.10.005.

Siégel, C., Bryan, S.E., Allen, C.M., and Gust, D.A. 2018. Use and abuse of zircon-based thermometers: A critical review and a recommended approach to identify antecrystic zircons. Earth-Science Reviews, 176: 87–116. doi:10.1016/j.earscirev.2017.08.011.

Smith, T.E., and Harris, M.J. 1996. The Queensborough mafic-ultramafic complex: a fragment of a Meso-Proterozoic ophiolite? Grenville Province, Canada. Tectonophysics, 265: 53–82. doi:10.1016/S0040-1951(96)00146-1.

Smith, T.E., Harris, M.J., Huang, C.H., and Holm, P.E. 2001. The geochemical nature of the igneous rocks of the Sharbot Lake domain, Central Metasedimentary Belt, Ontario. Canadian Journal of Earth Sciences, 38: 1037–1057. doi:10.1139/e01-001.

Smithies, R.H. 2000. The Archaean tonalite–trondhjemite–granodiorite (TTG) series is not an analogue of Cenozoic adakite. Earth and Planetary Science Letters, 182: 115–125. doi:10.1016/S0012-821X(00)00236-3.

Smithies, R.H., Howard, H.M., Evins, P.M., Kirkland, C.L., Kelsey, D.E., Hand, M., Wingate, M.T.D., Collins, A.S., and Belousova, E. 2011. High-temperature granite magmatism, crust–mantle interaction and the Mesoproterozoic intracontinental evolution of the Musgrave Province, Central Australia. Journal of Petrology, 52: 931–958. doi:10.1093/petrology/egr010.

Sorensen, S.S., 1991, Petrogenetic significance of zoned allanite in garnet amphibolites from a paleo-subduction zone: Catalina Schist, southern California: American Mineralogist, v. 76, p. 589–601.

Spooner, C.M. 1969. Sr87/Sr86 ratios, K/Rb ratios,and rare-earth element abundances in pyroxene granulites. Doctor of Philosophy, Massachusetts Institite of Technology.

Stein, M., and Hofmann, A.W. 1994. Mantle plumes and episodic crustal growth. Nature, 372: 63–68. doi:10.1038/372063a0.

Stepanov, A.S., Hermann, J., Rubatto, D., and Rapp, R.P. 2012. Experimental study of monazite/melt partitioning with implications for the REE, Th and U geochemistry of crustal rocks. Chemical Geology, 300–301: 200–220. doi:10.1016/j.chemgeo.2012.01.007.

Stevens, G., Clemens, J.D., and Droop, G.T.R. 1997. Melt production during granulite-facies anatexis: experimental data from “primitive” metasedimentary protoliths. Contributions to Mineralogy and Petrology, 128: 352–370. doi:10.1007/s004100050314.

Stix, J., and Gorton, M.P., 1990, Variations in trace element partition coefficients in sanidine in the Cerro Toledo Rhyolite, Jemez Mountains, New Mexico: Effects of composition, temperature,

and volatiles: Geochimica et Cosmochimica Acta, v. 54, p. 2697–2708, doi:10.1016/0016-7037(90)90005-6.

Storey, C.C., and Vos, M.A. 1981. Industrial minerals of the Pembroke-Renfrew Area. Ontario Geological Survey.

Storkey, A. C., Hermann, J., Hand, M., Buick, I. S., 2005, Using in situ trace-element determinations to monitor partial-melting processes in metabasites, Journal of Petrology, v. 46, p. 1283-1308, doi: 10.1093/petrology/egi017

Streepey, M.M., Johnson, E.L., Mezger, K., and van der Pluijm, B.A. 2001. Early history of the Carthage-Colton Shear Zone, Grenville Province, Northwest Adirondacks, New York (U.S.A.). The Journal of Geology, 109: 479–492. doi:10.1086/320792.

Streepey, M.M., Lithgow-Bertelloni, C., Van Der Pluijm, B.A., Essene, E.J., and Magloughlin, J.F. 2004. Exhumation of a collisional orogen: A perspective from the North American Grenville Province. In Memoir 197: Proterozoic Tectonic Evolution of the Grenville Orogen in North America. Geological Society of America. pp. 391–410. doi:10.1130/0-8137-1197-5.391.

Strong, J. 2017. Refining the tectonic and magmatic history of the SW Grenville Province. MSc, McMaster, Hamilton.

Stuck, T.J., and Diener, J.F.A., 2018, Mineral equilibria constraints on open-system melting in metamafic compositions: Journal of Metamorphic Geology, v. 36, p. 255–281, doi:10.1111/jmg.12292.

Stüwe, K. 2007. Geodynamics of the Lithosphere. In 2nd edition. Springer-Verlag.

Stüwe, K., 2007, Energetics: Heat and Temperature, in Geodynamics of the Lithosphere, Springer-Verlag, p. 51–137.

Sun, G., Lio, S., Cawood, P., Tang, M., van Hunen, J., Gao, L., Hu, Y., and Hu, F., 2021, Thermal state and evolving geodynamic regimes of the Meso- to Neoarchean North China Craton: Nature Communications, v. 12, doi: 10.1038/s41467-021-24139-z

Takahashi, E., Shimazaki, T., Tsuzaki, Y., and Yoshida, H. 1993. Melting study of a peridotite KLB-1 to 6.5 GPa, and the origin of basaltic magmas. Philosophical Transactions of the Royal Society of London. Series A: Physical and Engineering Sciences, 342: 105–120. doi:10.1098/rsta.1993.0008.

Tamblyn, R., Zack, T., Schmitt, A.K., Hand, M., Kelsey, D., Morrissey, L., Pabst, S., and Savov, I.P., 2019, Blueschist from the Mariana forearc records long-lived residence of material in the subduction channel: Earth and Planetary Science Letters, v. 519, p. 171–181, doi:10.1016/j.epsl.2019.05.013.

Tan, S. 2024. Detrital zircon geochronology and provenance of quartzites in the Frontenac Terrane. Bachelor of Science, University of Waterloo, Waterloo, Ontario.

Tang, M., Chen, K., and Rudnick, R.L. 2016. Archean upper crust transition from mafic to felsic marks the onset of plate tectonics. Science, 351: 372–375. doi:10.1126/science.aad5513.

Taylor, R.J.M., Harley, S.L., Hinton, R.W., Elphick, S., Clark, C., and Kelly, N.M. 2015. Experimental determination of REE partition coefficients between zircon, garnet and melt: a key to understanding high-T crustal processes. Journal of Metamorphic Geology, 33: 231–248. doi:10.1111/jmg.12118.

Taylor, S.R., and McLennan, S.M. 1986. The chemical composition of the Archaean crust. Geological Society, London, Special Publications, 24: 173–178. doi:10.1144/GSL.SP.1986.024.01.16.

Taylor, S.R., and McLennan, S.M. 1995. The geochemical evolution of the continental crust. Reviews of Geophysics, 33: 241–265. doi:10.1029/95RG00262.

Taylor, S.R., and Mclennan, S.M., 1981, The composition and evolution of the continental crust: rare earth element evidence from sedimentary rocks: Philosophical Transactions of the Royal Society of London. Series A, Mathematical and Physical Sciences, v. 301, p. 381–399, doi:10.1098/rsta.1981.0119.

Teixeira, L.M.F., Troch, J., and Bachmann, O. 2024. The dynamic nature of aTiO2: Implications for Ti-based thermometers in magmatic systems. Geology, 52: 92–96. doi:10.1130/G51587.1.

Thomas, J.B., and Watson, E.B. 2012. Application of the Ti-in-quartz thermobarometer to rutile-free systems. Reply to: a comment on: 'TitaniQ under pressure: the effect of pressure and temperature on the solubility of Ti in quartz'. Contributions to Mineralogy and Petrology, 164: 369–374. doi:10.1007/s00410-012-0761-5.

Thompson, A.B. 2002. Some thermal constraints on crustal assimilation during fractionation of hydrous, mantle-derived magmas with examples from Central Alpine Batholiths. Journal of Petrology, 43: 403–422. doi:10.1093/petrology/43.3.403.

Timmermann, H., Jamieson, R.A., Parrish, R.R., and Culshaw, N.G. 2002. Coeval migmatites and granulites, Muskoka domain, southwestern Grenville Province, Ontario. Canadian Journal of Earth Sciences, 39: 239–258. doi:10.1139/e01-076.

Timofeev, A., Migdisov, A.A., Williams-Jones, A.E., Roback, R., Nelson, A.T., and Xu, H., 2018, Uranium transport in acidic brines under reducing conditions: Nature Communications, v. 9, p. 2–8, doi:10.1038/s41467-018-03564-7.

Townsend, M., and Huber, C. 2020. A critical magma chamber size for volcanic eruptions. Geology, 48: 431–435. doi:10.1130/G47045.1.

Tuccillo, M.E., Mezger, K., Essene, E.J., and Van Der Pluijm, B.A. 1992. Thermobarometry, Geochronology and the Interpretation of P-T-t Data in the Britt Domain, Ontario Grenville Orogen, Canada. Journal of Petrology, 33: 1225–1259. doi:10.1093/petrology/33.6.1225.

Turek, A., Heather, K.B., Sage, R.P., and Van Schmus, W.R., 1996, U-Pb zircon ages for the Missanabie-Renabie area and their relation to the rest of the Michipicoten greenstone belt,

Superior Province, Ontario, Canada: Precambrian Research, v. 76, p. 191–211, doi:10.1016/0301-9268(95)00063-1.

Ueda, K., Jacobs, J., Thomas, R.J., Kosler, J., Jourdan, F., and Matola, R. 2012. Delamination-induced late-tectonic deformation and high-grade metamorphism of the Proterozoic Nampula Complex, northern Mozambique. Precambrian Research, 196–197: 275–294. doi:10.1016/j.precamres.2011.05.012.

Upadhyay, D., Chattopadhyay, S., Kooijman, E., Mezger, K., and Berndt, J., 2014, Magmatic and metamorphic history of Paleoarchean tonalite-trondhjemite-granodiorite (TTG) suite from the Singhbhum craton, eastern India: Precambrian Research, v. 252, p. 180, doi:10.1016/j.precamres.2014.07.011.

Vielzeuf, D., and Montel, J.M. 1994. Partial melting of metagreywackes. Part I. Fluid-absent experiments and phase relationships. Contributions to Mineralogy and Petrology, 117: 375–393. doi:10.1007/BF00307272.

Vigneresse, J.L., and Tikoff, B. 1999. Strain partitioning during partial melting and crystallizing felsic magmas. Tectonophysics, 312: 117–132. doi:10.1016/S0040-1951(99)00167-5.

Vitorello, I., and Pollack, H.N. 1980. On the variation of continental heat flow with age and the thermal evolution of continents. Journal of Geophysical Research, 85: 983. doi:10.1029/JB085iB02p00983.

Von Huene, R., and Scholl, D.W. 1991. Observations at convergent margins concerning sediment subduction, subduction erosion, and the growth of continental crust. Reviews of Geophysics, 29: 279–316. doi:10.1029/91RG00969.

Vosteen, H.-D., and Schellschmidt, R. 2003. Influence of temperature on thermal conductivity, thermal capacity and thermal diffusivity for different types of rock. Physics and Chemistry of the Earth, 28: 499–509. doi:10.1016/S1474-7065(03)00069-X.

Wadsworth, F.B., Llewellin, E.W., Vasseur, J., Gardner, J.E., and Tuffen, H. 2020. Explosive-effusive volcanic eruption transitions caused by sintering. Science Advances, 6: eaba7940. doi:10.1126/sciadv.aba7940.

Wang, H., and Currie, C.A. 2015. Magmatic expressions of continental lithosphere removal. Journal of Geophysical Research: Solid Earth, 120: 7239–7260. doi:10.1002/2015JB012112.

Wang, X., Griffin, W.L., Chen, J., Huang, P., and Li, X., 2011, U and Th contents and Th/U ratios of zircon in felsic and mafic magmatic rocks: Improved zircon-melt distribution coefficients: Acta Geologica Sinica, v. 84, p. 164–174.

Wang, X.-C., Wilde, S.A., Li, Z.-X., Li, S., and Li, L. 2020. Do supercontinent-superplume cycles control the growth and evolution of continental crust? Journal of Earth Science, 31: 1142–1169. doi:10.1007/s12583-020-1077-4.

Wasteneys, H., McLelland, J., and Lumbers, S. 1999. Precise zircon geochronology in the Adirondack Lowlands and implications for revising plate- tectonic models of the Central

Metasedimentary Belt and Adirondack Mountains, Grenville Province, Ontario and New York. 36.

Watson, E.B. 1979. Zircon saturation in felsic liquids: Experimental results and applications to trace element geochemistry. Contributions to Mineralogy and Petrology, 70: 407–419. doi:10.1007/BF00371047.

Watson, E.B., and Harrison, T.M., 1983, Zircon saturation revisited: temperature and composition effects in a variety of crustal magma types: Earth and Planetary Science Letters, v. 64, p. 295–304, doi:10.1016/0012-821X(83)90211-X.

Watson, E.B., Vicenzi, E.P., and Rapp, R.P., 1989, Inclusion/host relations involving accessory minerals in high-grade metamorphic and anatectic rocks: Contributions to Mineralogy and Petrology, v. 101, p. 220–231, doi:10.1007/BF00375308.

Watson, E.B., Wark, D.A., and Thomas, J.B. 2006. Crystallization thermometers for zircon and rutile. Contributions to Mineralogy and Petrology, 151: 413–433. doi:10.1007/s00410-006-0068-5.

Webster, J.D., and Piccoli, P.M., 2015, Magmatic apatite: A powerful, yet deceptive, mineral: Elements, v. 11, p. 177–182, doi:10.2113/gselements.11.3.177.

Wei, C., and Wang, W. 2007. Phase Equilibria in the Process of Anatexis in High-grade Metapelites. Earth Science Frontiers, 14: 125–134. doi:10.1016/S1872-5791(07)60006-2.

Wells, P.R.A. 1979. Chemical and thermal evolution of Archaean sialic crust, Southern West Greenland. Journal of Petrology, 20: 187–226. doi:10.1093/petrology/20.2.187.

Whalen, J.B., Currie, K.L., and Chappell, B.W. 1987. A-type granites: geochemical characteristics, discrimination and petrogenesis. Contributions to Mineralogy and Petrology, 95: 407–419. doi:10.1007/BF00402202.

White, D.J., Forsyth, D.A., Asudeh, I., Carr, S.D., Wu, H., Easton, R.M., and Mereu, R.F. 2000. A seismic-based cross-section of the Grenville Orogen in southern Ontario and western Quebec. Canadian Journal of Earth Sciences, 37: 183–192. doi:10.1139/e99-094.

White, Powell, Holland, and Worley, 2000, The effect of TiO2 and Fe2O3 on metapelitic assemblages at greenschist and amphibolite facies conditions: Mineral equilibria calculations in the system K2O-FeO-MgO-Al2O3-SiO2-H2O-TiO2-Fe2O3: Journal of Metamorphic Geology, v. 18, p. 497–511, doi:10.1046/j.1525-1314.2000.00269.x.

White, R.W., Powell, R., Holland, T.J.B., Johnson, T.E., and Green, E.C.R. 2014. New mineral activity–composition relations for thermodynamic calculations in metapelitic systems. Journal of Metamorphic Geology, 32: 261–286. doi:10.1111/jmg.12071.

Wilke, M., and Behrens, H., 1999, The dependence of the partitioning of iron and europium between plagioclase and hydrous tonalitic melt on oxygen fugacity: Contributions to Mineralogy and Petrology, v. 137, p. 102–114, doi:10.1007/s004100050585.

Williams, M.A., Kelsey, D.E., and Rubatto, D., 2022, Thorium zoning in monazite: a case study from the Ivrea–Verbano Zone, NW Italy: Journal of Metamorphic Geology, p. 0–2, doi:10.1111/jmg.12656.

Williams, M.A., Kelsey, D.E., Baggs, T., Hand, M., and Alessio, K.L. 2018. Thorium distribution in the crust: Outcrop and grain-scale perspectives. Lithos, 320–321: 222–235. doi:10.1016/j.lithos.2018.09.016.

Wodicka, N., Corriveau, L., and Stern, R.A. 2004. SHRIMP U-Pb zircon geochronology of the Bondy gneiss complex: Evidence for circa 1.39 Ga arc magmatism and polyphase Grenvillian metamorphism in the Central Metasedimentary Belt, Grenville Province, Québec. In Memoir 197: Proterozoic Tectonic Evolution of the Grenville Orogen in North America. Geological Society of America. pp. 243–266. doi:10.1130/0-8137-1197-5.243.

Wodicka, N., Jamieson, R.A., and Parrish, R.R. 1996. The Parry Sound domain: a far-travelled allochthon? New evidence from U–Pb zicon geochronology. Canadian Journal of Earth Sciences, 33: 1087–1104. doi:10.1139/e96-083.

Wong, M.S., Peck, W.H., Selleck, B.W., Catalano, J.P., Hochman, S.D., and Maurer, J.T. 2011. The Black Lake shear zone: A boundary between terranes in the Adirondack Lowlands, Grenville Province. Precambrian Research, 188: 57–72. Elsevier B.V. doi:10.1016/j.precamres.2011.04.001.

Wynne-Edwards, H.R. 1967. Westport map area, Ontario, with special emphasis on the Precambrian rocks. doi:10.4095/100533.

Wynne-Edwards, H.R., and Hay, P.W. 1963. Coexisting cordierite and garnet in regionally metamorphosed rocks from the Westport area, Ontario. The Canadian Mineralogist, 7: 453–478.

Xiang, H., and Connolly, J.A.D. 2022. GeoPS: An interactive visual computing tool for thermodynamic modelling of phase equilibria. Journal of Metamorphic Geology, 40: 243–255. doi:10.1111/jmg.12626.

Yakymchuk, C., 2016, Behaviour of apatite during partial melting of metapelites and consequences for prograde suprasolidus monazite growth: Lithos, v. 274-275, p. 412-426, doi: 10.1016/j.lithos.2017.01.009

Yakymchuk, C., and Acosta-Vigil, A. 2019. Geochemistry of phosphorus and the behavior of apatite during crustal anatexis: Insights from melt inclusions and nanogranitoids. American Mineralogist, 104: 1765–1780. doi:10.2138/am-2019-7054.

Yakymchuk, C., and Brown, M. 2019. Divergent behaviour of Th and U during anatexis: Implications for the thermal evolution of orogenic crust. Journal of Metamorphic Geology, 37: 899–916. doi:10.1111/jmg.12469.

Yakymchuk, C., and Brown, M., 2014, Consequences of open-system melting in tectonics: Journal of the Geological Society, v. 171, p. 21–40, doi:10.1144/jgs2013-039.

Yakymchuk, C., Brown, M., Ivanic, T.J., and Korhonen, F.J. 2013. Leucosome distribution in migmatitic paragneisses and orthogneisses: A record of self-organized melt migration and entrapment in a heterogeneous partially-molten crust. Tectonophysics, 603: 136–154. doi:10.1016/j.tecto.2013.05.022.

Yakymchuk, C., Kirkland, C.L., and Clark, C., 2018, Th/U ratios in metamorphic zircon: Journal of Metamorphic Geology, v. 36, p. 715–737, doi:10.1111/jmg.12307.

Yan, L.L., He, Z.Y., Beier, C., and Klemd, R. 2018. Zircon trace element constrains on the link between volcanism and plutonism in SE China. Lithos, 320–321: 28–34. Elsevier B.V. doi:10.1016/j.lithos.2018.08.040.

Yuguchi, T., Ishibashi, K., Sakata, S., Yokoyama, T., Itoh, D., Ogita, Y., Yagi, K., and Ohno, T. 2020. Simultaneous determination of zircon U–Pb age and titanium concentration using LA-ICP-MS for crystallization age and temperature. Lithos, 372–373: 105682. doi:10.1016/j.lithos.2020.105682.

Zhang, R.-X., Yang, S.-Y., Jiang, S.-Y., Fu, B., and Cui, J.-Q. 2024. Differentiation and convection in a magma chamber: Novel insights on the origin of mafic microgranular enclaves in the Tongkeng pluton, Xiaojiang area, SE China. Geological Society of America Bulletin, 136: 3027–3042. doi:10.1130/B37056.1.

Zheng, Y.-F., and Chen, R.-X. 2017. Regional metamorphism at extreme conditions: Implications for orogeny at convergent plate margins. Journal of Asian Earth Sciences, 145: 46–73. doi:10.1016/j.jseaes.2017.03.009.

Zhong, X., Li, Z.-H., and Wang, Y. 2024. Evaluation of plume-induced continental crust growth rate in early Earth: Insight from integrated petrological-thermo-mechanical modeling. Precambrian Research, 410: 107506. doi:10.1016/j.precamres.2024.107506.

Zhu, X.K., and O'Nions, R.K. 1999. Monazite chemical composition: some implications for monazite geochronology. Contributions to Mineralogy and Petrology, 137: 351–363. doi:10.1007/s004100050555.

Appendices

Appendix S1 (Chapter 2 Supplementary Material)

Appendix S1.1

Major element analyses (weight percent) for samples across the Kapuskasing Uplift

Name	Description	Latitude	Longitude	SG	Al_2O_3	BaO	CaO	Cr_2O_3	Fe_2O_3	K_2O	MgO	MnO
Greenstone												
18JK33	basalt (greenschist)	48.07	-84.55	2.94	11.77	0.029	8.021	0.008	18.43	2.49	4.97	0.246
18JK45	basalt (amphibolite)	48.05	-84.55	3.03	13.55	0.02	9.402	0.012	15.71	0.64	5.19	0.234
18JK46	basalt (greenschist)	48.02	-84.69	2.96	13.17	<0.004	10.855	0.016	11.99	0.1	6.24	0.221
18JK47	basalt (greenschist)	48.02	-84.69	3	13.4	0.005	8.678	0.016	13.52	0.07	7.97	0.201
18JK48	basalt (greenschist)	48.03	-84.68	2.85	11.68	<0.004	6.896	0.013	15.34	0.07	4.28	0.255
18JK49	basalt (greenschist)	48.03	-84.67	2.8	12.17	0.006	9.611	0.013	11.21	0.19	6.11	0.224
18JK50A	basalt (greenschist)	48.03	-84.65	2.93	11.32	0.004	8.312	0.011	16.6	0.05	5.02	0.191
18JK27G	phyllite	48.04	-84.54	2.99	14.13	0.022	9.844	0.035	13.79	1.02	6.71	0.216
19JK25	greenstone	48.16	-84.11		15.54	<0.004	17.278	0.022	10.4	0.04	2.9	0.135
19JK26	gabbro	48.17	-84.13		15.14	0.024	10.045	0.015	13.6	0.94	5.29	0.202
19JK28	greenstone	48.15	-84.21		14.78	0.004	10.218	0.039	13.19	0.08	7.66	0.208
19JK29A	greenstone	48.16	-84.19		14.31	0.023	13.564	0.018	7.8	0.53	5.56	0.193
19JK32B	porphyritic gabbro	48.20	-84.08		13.3	0.023	9.339	0.012	17.28	0.61	4.88	0.239
Tonalite-trondjhemite-granodiorite												
18JK60A	biotite-hornblende tonalite	48.09	-82.68	2.8	14.98	0.067	4.808	0.016	6.34	1.6	2.69	0.075
18JK57	intermediate gneiss	48.05	-82.72	2.75	15.46	0.051	4.808	0.007	4.96	1.67	1.73	0.064
18JK53	biotite-hornblende tonalite	47.70	-83.31	2.72	17.61	0.033	4.721	0.005	3.77	0.94	1.33	0.033
18JK52	biotite tonalite	47.68	-83.30	2.72	16.39	0.048	3.813	0.004	3.98	1.32	1.24	0.041
18JK38A	biotite tonalite	47.91	-83.79	2.64	14.62	0.072	2.06	0.005	1.06	2.04	0.27	0.016
18JK36A	biotite tonalite	47.97	-83.83	2.67	15.95	0.02	2.292	0.007	2.55	1.03	0.83	0.032
18JK35A	biotite tonalite	47.98	-83.87	2.69	15.87	0.033	1.729	0.007	2.42	1.96	1.24	0.043
18JK34A	biotite tonalite	48.06	-84.55	2.74	14.36	0.024	3.231	0.01	3.85	1.26	1.37	0.062
18JK32A	biotite tonalite	47.94	-84.50	2.66	15.09	0.062	2.164	0.01	1.79	2	0.45	0.028
18JK30A	biotite tonalite	47.96	-84.26	2.64	14.25	0.061	1.094	0.009	1.26	2.34	0.51	0.016
18JK29A	biotite tonalite	47.94	-84.15	2.67	15.62	0.053	2.305	0.008	1.8	1.71	0.49	0.021
18JK27A	biotite tonalite	48.04	-84.54	2.68	13.86	0.07	1.71	0.009	1.41	2.16	0.21	0.04
18JK25A	biotite-clinopyroxene tonalite	47.89	-84.04	2.66	15.9	0.026	2.706	0.008	1.79	1.21	0.65	0.021
18JK24A	biotite tonalite	47.87	-83.94	2.67	15.71	0.059	2.83	0.007	2	1.24	0.69	0.027
18JK23A	hornblende tonalite	47.86	-83.86	2.69	15.58	0.06	3.171	0.007	2.65	2.09	0.96	0.046
18JK19A	monzodiorite	48.16	-84.06	2.76	16.51	0.024	5.309	0.007	5	0.74	1.79	0.066
18JK13A	biotite tonalite	47.01	-84.12	2.68	14.67	0.095	2.786	0.008	2.45	2.07	0.73	0.037
18JK11-A	biotite-hornblende tonalite	47.95	-84.11		15.69		4.8		3.16	1.59	0.73	0.051
18JK09A	biotite-hornblende tonalite	47.87	-83.57	2.73	16.65	0.059	3.769	0.009	5.26	1.17	1.5	0.064
18JK08A	biotite tonalite	47.94	-83.65	2.67	15.67	0.041	2.889	0.01	2.83	1.6	1.14	0.04
18JK07A	biotite-hornblende tonalite	47.79	-83.53	2.73	16.23	0.047	4.421	0.008	1.75	1.13	0.58	0.024
18JK04A	biotite-hornblende tonalite	47.85	-83.74	2.71	15.69	0.031	4.369	0.012	3.92	1.26	1.46	0.05
18JK03A	biotite tonalite	47.85	-83.74	2.68	15.83	0.05	3.003	0.007	4.11	1.25	1.6	0.068
17JK26	Grt tonalite gneiss	48.08	-82.69	2.79	15.1	0.115	4.347	0.006	2.2	1.4	0.69	0.026
19JK01	biotite tonalite	47.77	-83.38		16.89	0.061	3.731	0.005	5.02	1.37	1.37	0.061
19JK02	biotite tonalite	47.89	-83.45		17.31	0.068	3.239	0.006	2.79	1.53	1.11	0.027
19JK03	biotite-hornblende tonalite	47.96	-83.43		16.25	0.053	4.649	0.009	1.89	2.24	0.74	0.027
19JK06A	biotite tonalite	47.80	-83.39		13.74	0.012	8.347	0.014	3.97	1.53	2.3	0.062
19JK07A	biotite tonalite	47.92	-83.14		15.26	0.067	4.338	0.007	17.12	0.86	5.33	0.236
19JK07B	hornblende tonalite	47.92	-83.14		15.51	0.043	4.262	0.004	4.71	1.27	1.65	0.056
19JK09A	biotite tonalite	47.94	-83.10		17.82	0.096	4.526	0.004	3.3	0.96	1.2	0.043
19JK10A	biotite-hornblende tonalite	47.97	-82.97		15.33	0.058	3.889	0.003	5.17	1.84	1.9	0.055
19JK11	biotite tonalite	48.09	-82.68		15.87	0.099	3.468	0.026	5.63	1.55	1.38	0.074

Name	Description	Latitude	Longitude	SG	Al_2O_3	BaO	CaO	Cr_2O_3	Fe_2O_3	K_2O	MgO	MnO
19JK12A	biotite tonalite	47.93	-83.12		15.77	0.074	3.957	0.007	8.68	2.17	3.38	0.136
19JK18	biotite tonalite	47.85	-83.33		14.9	0.02	3.275	0.005	3.67	1.41	1.44	0.045
19JK20	biotite-hornblende tonalite	47.99	-82.89		15.43	0.069	4.684	0.004	3.21	1.17	0.96	0.038
19JK21	biotite tonalite	48.06	-83.40		16.5	0.082	4.511	0.012	6.37	1.24	1.78	0.092
19JK23A	biotite tonalite	47.93	-83.49		16.31	0.078	3.467	0.017	4.04	1.64	2.21	0.047
19JK48A	biotite tonalite				14.05	0.194	1.39	0.003	4.48	2.08	2.37	0.046
Lower-crustal metabasites									1.85	5.37	0.35	0.018
17JK02	Garnet-clinopyroxene mafic gneiss	47.93	-83.11	3.03	16.1	0.024	12.485	0.073				
17JK03	Garnet mafic gneiss	47.93	-83.11	2.99	16.12	0.018	12.331	0.06	10.88	0.82	7.38	0.178
17JK05	Clinopyroxene mafic gneiss	47.93	-83.11	3.02	15.58	0.012	11.593	0.08	10.54	0.64	6.53	0.168
17JK09	Garnet-clinopyroxene mafic gneiss	48.01	-82.81	3.27	14.68	0.007	13.198	0.014	10.64	0.86	8.21	0.167
17JK10	Garnet-clinopyroxene mafic gneiss	48.01	-82.81	3.12	14.53	0.009	9.671	0.017	15.85	0.12	4.1	0.295
17JK12	Garnet-clinopyroxene mafic gneiss	48.06	-82.71	3.05	15.69	0.013	10.057	0.032	15.64	0.61	5.41	0.257
17JK14	Clinopyroxene mafic gneiss	47.77	-83.47	3.01	15.09	0.006	12.32	0.052	14.07	0.74	6.35	0.207
17JK15	Garnet-clinopyroxene mafic gneiss	47.78	-83.49	2.98	14.9	0.018	9.676	0.02	11.61	0.47	7.17	0.185
17JK17	Garnet Biotite Migmatite	48.01	-82.79	3.14	14.57	0.014	8.301	0.004	11.54	0.55	4.12	0.21
17JK18	Garnet-clinopyroxene mafic gneiss	48.01	-82.78	3.21	15.68	0.01	12.014	0.039	12.79	0.53	3.6	0.2
17JK19	Garnet felsic migmatite	48.01	-82.78	2.88	16.9	0.022	10.061	0.037	16.25	0.74	4.08	0.265
17JK20	Garnet mafic gneiss	48.01	-82.77	3.28	14.6	0.009	9.306	0.01	13.49	0.2	4.22	0.4
17JK21	Garnet-clinopyroxene mafic gneiss	48.03	-82.74	3.11	14.62	0.007	9.787	0.021	7.25	0.6	3.9	0.121
17JK24	Garnet-clinopyroxene mafic gneiss	48.03	-82.74	3.1	13.76	0.006	12.631	0.029	17.55	0.54	4.84	0.28
17JK27	Garnet mafic gneiss	48.09	-82.69	3.06	14.63	0.021	10.921	0.027	17.62	0.23	5.66	0.265
18JK54	mafic migmatite	47.81	-83.39	3.03	14.5	0.019	11.178	0.04	13.01	0.45	6.37	0.218
18JK55A	Garnet-clinopyroxene mafic gneiss	48.01	-82.81	3.26	13.41	0.008	12.756	0.019	13.01	0.9	5.64	0.213
18JK59A	mafic migmatite	48.10	-82.67	3.06	15.21	0.017	9.44	0.022	12.55	0.95	7.55	0.21
18JK59B	Garnet-clinopyroxene mafic gneiss	48.10	-82.67	3.22	14.54	0.01	12.203	0.022	16.43	0.16	4.59	0.253
18JK67A	mafic migmatite	48.07	-83.16	2.98	16.18	0.029	10.511	0.02	13.85	0.89	5.63	0.218
18JK69	mafic migmatite	48.10	-83.18	2.97	14.48	0.027	9.624	0.042	15.71	0.26	4.08	0.33
18JK70	mafic migmatite	48.10	-83.19	3.02	15.34	0.017	11.482	0.027	10.89	0.57	4.15	0.237
									11.54	1.06	6.52	0.199
									12.91	0.74	5.74	0.259

Name	Na_2O	P_2O_5	SiO_2	TiO_2	Total	LOI	Laboratory
Greenstone							
18JK33	1.27	0.12	42.59	2.32	99.59	7.33	Geolabs
18JK45	2.53	0.154	51.29	1.54	100.63	0.35	Geolabs
18JK46	1.84	0.075	49.14	0.89	99.75	5.2	Geolabs
18JK47	1.7	0.067	50.75	0.88	100.28	3.02	Geolabs
18JK48	2.6	0.119	49.22	1.46	99.72	7.79	Geolabs
18JK49	2.31	0.07	47.92	0.84	100.77	10.09	Geolabs
18JK50A	0.74	0.159	49.05	1.79	99.91	6.65	Geolabs
18JK27G	2.64	0.09	48.91	1.2	100.51	1.91	Geolabs
19JK25	0.2	0.063	51.32	0.77	100.22	1.56	Geolabs
19JK26	2.4	0.12	51.06	1.09	100.48	0.55	Geolabs
19JK28	2.45	0.068	48.36	0.9	100.08	2.12	Geolabs
19JK29A	3.94	0.188	51.55	0.63	100.59	2.28	Geolabs
19JK32B	2.47	0.273	50.06	1.95	100.41	-0.02	Geolabs
Tonalite-trondjhemite-granodiorite							
18JK60A	3.25	0.13	65.35	0.66	100.7	0.74	Geolabs
18JK57	3.47	0.153	67.2	0.63	100.76	0.57	Geolabs
18JK53	5.73	0.133	65.03	0.47	100.66	0.86	Geolabs
18JK52	4.9	0.156	68.18	0.46	101.1	0.56	Geolabs
18JK38A	4.82	0.014	75.74	0.1	101.14	0.32	Geolabs
18JK36A	5.78	0.091	71.55	0.28	101.3	0.89	Geolabs
18JK35A	5.11	0.068	70.99	0.26	101.02	1.3	ActLabs
18JK34A	3.93	0.098	71.42	0.39	100.99	0.99	ActLabs
18JK32A	5.24	0.056	73.14	0.21	100.59	0.35	Geolabs
18JK30A	5.38	0.053	74.84	0.17	100.63	0.65	Geolabs
18JK29A	5.4	0.064	72.48	0.22	100.73	0.56	Geolabs
18JK27A	4.76	0.019	75.52	0.1	100.64	0.77	Geolabs
18JK25A	5.63	0.079	71.76	0.27	100.75	0.7	Geolabs
18JK24A	5.3	0.084	71.95	0.3	100.97	0.78	Geolabs
18JK23A	4.75	0.079	70.34	0.28	100.69	0.69	Geolabs
18JK19A	4.42	0.164	64.24	0.63	100.07	1.18	Geolabs
18JK13A	4.19	0.087	72.78	0.27	100.84	0.66	Geolabs
18JK11-A	4.85	0.1	71.57	0.331	100.6		Geolabs
18JK09A	4.25	0.16	66.25	0.584	100.4		Geolabs
18JK08A	5.18	0.105	68.69	0.28	101.04	0.7	Geolabs
18JK07A	5.33	0.076	71.77	0.23	100.26	0.75	Geolabs
18JK04A	4.71	0.091	66.74	0.44	100.13	0.75	Geolabs
18JK03A	4.34	0.144	66.95	0.46	100.23	1.2	Geolabs
17JK26	5.17	0.076	71.01	0.26	100.35	0.62	Geolabs
19JK01	3.68	0.16	66.99	0.66	99.33	0.44	Geolabs
19JK02	5.25	0.116	67.5	0.41	100.22	0.8	Geolabs
19JK03	5.49	0.075	68.43	0.25	100.46	0.7	Geolabs
19JK06A	5.19	0.256	64.34	0.48	100.33	1.23	Geolabs
19JK07A	3.39	0.178	48.01	1.9	100.2	1.06	Geolabs
19JK07B	4.53	0.245	66.59	0.63	100.05	0.7	Geolabs
19JK09A	4.88	0.105	68.78	0.46	100.13	0.59	Geolabs
19JK10A	5.28	0.406	61.29	0.79	100.03	0.84	Geolabs
19JK11	4.26	0.172	66.69	0.69	100.08	0.37	Geolabs

Name	Na_2O	P_2O_5	SiO_2	TiO_2	Total	LOI	Laboratory
19JK12A	2.97	0.077	61.74	0.77	100.08	0.69	Geolabs
19JK18	4.72	0.155	68.05	0.44	100.27	0.53	Geolabs
19JK20	4.64	0.083	70.61	0.36	99.97	0.71	Geolabs
19JK21	4.25	0.211	64.65	0.85	100.06	0.42	Geolabs
19JK23A	4.56	0.238	65.19	0.56	100.26	0.68	Geolabs
19JK48A	4.26	0.124	65.31	0.55	99.86	0.77	Geolabs
Lower-crustal metabasites	3.24	0.06	73.14	0.13	100.17	0.39	Geolabs
17JK02							
17JK03	2.2	0.047	48.44	0.73	100.25	0.9	Geolabs
17JK05	2.48	0.05	49.65	0.76	100.23	0.89	Geolabs
17JK09	2.57	0.047	47.96	0.66	99.91	1.52	Geolabs
17JK10	2.31	0.127	47.72	1.49	99.76	-0.13	Geolabs
17JK12	2.47	0.113	49.67	1.39	100.19	0.42	Geolabs
17JK14	2.94	0.083	48.26	1.16	100.93	1.33	Geolabs
17JK15	2.63	0.058	47.74	0.8	98.86	0.74	Geolabs
17JK17	2.75	0.116	52.85	1.24	99.15	1.15	Geolabs
17JK18	4.13	0.58	50.1	2.13	100.01	0.45	Geolabs
17JK19	2.49	0.129	50.73	1.56	99.8	0.66	Geolabs
17JK20	1.84	0.077	50.72	1	100.18	0.5	Geolabs
17JK21	3.37	0.065	54.59	0.83	98.95	1.2	Geolabs
17JK24	1.97	0.199	48.44	1.69	99.44	-0.01	Geolabs
17JK27	2.37	0.126	47.03	1.63	99.35	0	Geolabs
18JK54	2.51	0.075	47.68	0.92	98.92	1.25	Geolabs
18JK55A	2.99	0.105	49.13	1.07	99.2	0.54	Geolabs
18JK59A	3.24	0.205	48.43	0.97	100.63	0.78	Geolabs
18JK59B	1.64	0.111	48.82	1.36	100.4	0.85	Geolabs
18JK67A	2.42	0.093	51.02	1.12	100.76	0.84	Geolabs
18JK69	1.91	0.113	50.13	1.49	100.84	0.05	Geolabs
18JK70	2.82	0.109	53.71	1.21	100.9	0.46	Geolabs
	3.57	0.074	52.1	0.74	100.52	0.54	Geolabs
	2.5	0.131	49.78	0.87	100.53	0.75	Geolabs

Appendix S1.2

Trace element analyses (mg/kg) for samples across the Kapuskasing Uplift

Name	Description	Latitude	Longitude	Ce	La	Nd	Pr	Sm	ΣLREE	Ba	Ce	Co
Detection Limit (Geolabs/Actlabs)				0.12/0.05	0.1/0.05	0.06/0.05	0.014/0.01	0.026/0.01		0.8/2	0.12/0.05	0.13/1
Greenstone												
18JK27G	phyllite	48.04	-84.54	9.92	3.7	8.29	1.572	2.761	26.243	176.9	9.92	50.15
18JK33	basalt (greenschist)	48.07	-84.55	20.89	8	15.77	3.184	4.213	52.057	267.2	20.89	63.64
18JK45	basalt (amphibolite)	48.05	-84.55	28.14	12.4	17.92	3.971	4.694	67.125	165.9	28.14	47.87
18JK46	basalt (greenschist)	48.02	-84.69	8.55	3.3	6.98	1.356	2.236	22.422	14.5	8.55	50.09
18JK47	basalt (greenschist)	48.02	-84.69	8.13	3.1	6.34	1.299	2.119	20.988	21.7	8.13	47.39
18JK48	basalt (greenschist)	48.03	-84.68	13.79	5.1	11.41	2.283	3.555	36.138	18.6	13.79	44.49
18JK49	basalt (greenschist)	48.03	-84.67	6.75	2.6	5.8	1.12	1.986	18.256	44.6	6.75	38.17
18JK50A	basalt (greenschist)	48.03	-84.65	18.73	7.1	15	3.032	4.556	48.418	10.5	18.73	42.24
19JK25	greenschist	48.16	-84.11	7.07	2.9	5.57	1.086	1.81	18.436	24.6	7.07	34.37
19JK26	gabbro	48.17	-84.13	23.82	10.7	13.43	3.14	3.491	54.581	216.3	23.82	52.19
19JK28	greenschist	48.15	-84.21	6.94	2.6	5.85	1.107	2.118	18.615	14.8	6.94	61.26
19JK29A	greenschist	48.16	-84.19	33.11	18.2	14.68	3.802	3.007	72.799	178.4	33.11	31.95
19JK32B	porphyritic gabbro	48.20	-84.08	35.36	15.8	21.79	4.841	5.841	83.632	197	35.36	52.97
Tonalite-trondjhemite-granodiorite									0			
17JK26	Grt tonalite gneiss	48.08	-82.69	152.48	88.9	48.19	14.71	6.116	310.396	1017.4	152.48	9
18JK03A	biotite tonalite	47.85	-83.74	35.99	21.5	11.38	3.585	1.409	73.864	452.6	35.99	4.43
18JK04A	biotite-hornblende tonalite	47.85	-83.74	58.97	31.6	23.67	6.556	3.956	124.752	268.6	58.97	11.26
18JK07A	biotite-hornblende tonalite	47.79	-83.53	27.85	15.7	10.95	3.076	1.898	59.474	421	27.85	10.62
18JK08A	biotite tonalite	47.94	-83.65	32.86	18.2	11.88	3.54	1.69	68.17	372.8	32.86	3.75
18JK09A	biotite-hornblende tonalite	47.87	-83.57	67.54	37.8	24.44	7.229	3.773	140.782	542.6	67.54	7.13
18JK11-A	biotite-hornblende tonalite	47.95	-84.11	49.1	26	19.7	5.37	3.77	103.94	387	49.1	11
18JK12-A	biotite tonalite	47.97	-84.11	37.1	19.2	14.9	4.09	2.92	78.21	499	37.1	5
18JK13A	biotite tonalite	47.01	-84.12	87.49	47.6	30.57	9.021	4.914	179.595	863.7	87.49	5.03
18JK19A	monzodiarite	48.16	-84.06	29.5	14.8	14.07	3.543	2.978	64.891	226.9	29.5	12.65
18JK23A	hornblende tonalite	47.86	-83.86	37.4	20.2	14.61	4.131	2.642	78.983	539.2	37.4	6.81
18JK24A	biotite tonalite	47.87	-83.94	37.79	22.5	12.13	3.835	1.412	77.667	544.9	37.79	4.77
18JK25A	biotite-clinopyroxene tonalite	47.89	-84.04	28	13.5	9.38	2.782	1.499	55.161	240.6	28	4.88
18JK27A	biotite tonalite	48.04	-84.54	29.24	16.6	10.95	3.084	2.14	62.014	638	29.24	1.42
18JK29A	biotite tonalite	47.94	-84.15	27.24	14.8	10.58	3.029	1.669	57.318	479.8	27.24	3.15
18JK30A	biotite tonalite	47.96	-84.26	78.63	44.3	27.04	8.403	3.813	162.186	557.2	78.63	2.47
18JK32A	biotite tonalite	47.94	-84.50	24.84	13.4	9.73	2.747	1.652	52.369	540	24.84	3.23
18JK34A	biotite tonalite	48.06	-84.55	57.78	32.5	22	6.277	4.059	122.616	221.7	57.78	9.73
18JK35A	biotite tonalite	47.98	-83.87	35.79	15.7	9.65	3.073	1.496	65.709	305.8	35.79	6.18
18JK36A	biotite tonalite	47.97	-83.83	28.38	13.7	10.15	2.992	1.512	56.734	180.8	28.38	5.4
18JK38A	biotite tonalite	47.91	-83.79	26.09	12.5	7.82	2.367	1.123	49.9	651.8	26.09	1.5
18JK52	biotite tonalite	47.68	-83.30	47.81	24.5	19.94	5.518	3.016	100.784	425.3	47.81	8.83
18JK53	hbl bt tonalite	47.70	-83.31	28.18	14.4	13.67	3.493	2.146	61.889	304.9	28.18	9.32
18JK57	intermediate gneiss	48.05	-82.72	62.52	33.9	26.52	7.177	4.87	134.987	451.9	62.52	12.34
18JK60A	biotite-hornblende tonalite	48.09	-82.68	55.59	30.5	22.88	6.287	4.357	119.614	642.5	55.59	20.47
19JK01	biotite tonalite	47.77	-83.38	84.65	51.5	22.2	7.787	1.986	168.123	507.8	84.65	8.55
19JK02	biotite tonalite	47.89	-83.45	52.16	28.9	18.03	5.507	2.441	107.038	559.9	52.16	5.65
19JK03	biotite-hornblende tonalite	47.96	-83.43	76.09	35.3	38.37	9.886	6.691	166.337	462.9	76.09	13.59
19JK06A	biotite tonalite	47.80	-83.39	22	8.8	16	3.315	4.553	54.668	105.7	22	52.88
19JK07A	biotite tonalite	47.92	-83.14	93.74	48.8	36.65	10.557	5.265	195.012	578.1	93.74	13.1
19JK07B	hornblende ton	47.92	-83.14	19.95	9	11.95	2.759	2.567	46.226	379.3	19.95	8.03
19JK09A	biotite tonalite	47.94	-83.10	134.39	67.5	54.89	15.531	7.753	280.064	809.7	134.39	15.83

Name	Description	Latitude	Longitude	Ce	La	Nd	Pr	Sm	ΣLREE	Ba	Ce	Co
Detection Limit (Geolabs/Actlabs)				0.12/0.05	0.1/0.05	0.06/0.05	0.014/0.01	0.026/0.01		0.8/2	0.12/0.05	0.13/1
19JK10A	biotite-hornblende tonalite	47.97	-82.97	59.83	31.6	22.1	6.309	4.03	123.869	503.3	59.83	11.26
19JK11	biotite tonalite	48.09	-82.68	26.11	15.2	9.2	2.632	1.807	54.949	890.2	26.11	29.33
19JK12A	biotite tonalite	47.93	-83.12	51.99	29.3	18.89	5.472	2.748	108.4	653.7	51.99	11.71
19JK18	biotite tonalite	47.85	-83.33	33.96	18.7	12.14	3.566	1.936	70.302	167.9	33.96	6.96
19JK20	biotite-hornblende tonalite	47.99	-82.89	78.5	42.2	30.81	8.593	5.398	165.501	631.3	78.5	13.76
19JK21	biotite tonalite	48.06	-83.40	67.83	33.7	28.28	7.7	4.027	141.537	683.2	67.83	14.5
19JK23A	biotite tonalite	47.93	-83.49	61.41	34.3	22.2	6.472	2.971	127.353	688.4	61.41	17.48
19JK48A	biotite tonalite			130.25	72.3	38.43	12.805	4.435	258.22	1669.4	130.25	2.5
Lower-crustal metabasites												
17JK02	Garnet-clinopyroxene mafic gneiss	47.93	-83.11	6.35	2.8	2.122	1.005	1.66	13.937	224.6	6.35	44.8
17JK03	Garnet mafic gneiss	47.93	-83.11	8.11	4	1.871	1.17	1.752	16.903	156.1	8.11	41.2
17JK05	Clinopyroxene mafic gneiss	47.93	-83.11	5.4	2.2	1.802	0.87	1.525	11.797	92.2	5.4	45.2
17JK09	Garnet-clinopyroxene mafic gneiss	48.01	-82.81	12.01	4.3	3.67	2.01	3.488	25.478	43.6	12.01	53.9
17JK10	Garnet-clinopyroxene mafic gneiss	48.01	-82.81	13.99	5.3	3.411	2.102	3.396	28.199	73	13.99	47.7
17JK12	Garnet-clinopyroxene mafic gneiss	48.06	-82.71	11.29	4.5	3.352	1.68	2.605	23.427	101.9	11.29	52.1
17JK14	Clinopyroxene mafic gneiss	47.77	-83.47	7.87	3.2	2.164	1.18	1.862	16.276	48.3	7.87	44.6
17JK15	Garnet-clinopyroxene mafic gneiss	47.78	-83.49	21.59	8.9	4.332	2.946	3.423	41.191	139.3	21.59	39.5
17JK16	Garnet mafic gneiss	47.78	-83.51	34.6	14.6	12.178	4.645	4.485	70.508	110.9	34.6	26.9
17JK17	Garnet Biotite Migmatite	48.01	-82.79	19.48	7.4	4.624	2.765	3.737	38.006	101.8	19.48	40.3
17JK18	Garnet-clinopyroxene mafic gneiss	48.01	-82.78	11.43	4.9	2.143	1.634	2.508	22.615	76.1	11.43	52.7
17JK19	Garnet felsic migmatite	48.01	-82.78	17.91	7.5	4.18	2.478	2.794	34.862	187.1	17.91	44.8
17JK20	Garnet mafic gneiss	48.01	-82.77	24.25	8.9	4.522	3.643	5.108	46.423	82.4	24.25	44.6
17JK21	Garnet-clinopyroxene mafic gneiss	48.03	-82.74	12.46	4.6	3.835	2.051	3.483	26.429	41.8	12.46	52.3
17JK24	Garnet-clinopyroxene mafic gneiss	48.03	-82.74	8.13	3.1	2.229	1.299	2.165	16.923	36.1	8.13	50.5
17JK27	Garnet mafic gneiss	48.09	-82.69	22.27	9.8	3.926	2.898	3.126	42.02	166.6	22.27	43.6
18JK54	mafic migmatite	47.81	-83.39	46.11	18.8	2.797	6.569	5.75	80.026	163.4	46.11	50.59
18JK55A	Garnet-clinopyroxene mafic gneiss	48.01	-82.81	11.6	4.6	3.235	1.886	3.244	24.565	50.4	11.6	51.5
18JK59A	mafic migmatite	48.10	-82.67	18.41	7.6	3.629	2.551	3.172	35.362	139	18.41	47.46
18JK59B	Garnet-clinopyroxene mafic gneiss	48.10	-82.67	13.88	4.9	3.608	2.267	3.612	28.267	64.4	13.88	55.74
18JK67A	mafic migmatite	48.07	-83.16	24.98	11.7	3.129	3.202	3.37	46.381	240.5	24.98	54.01
18JK69	mafic migmatite	48.10	-83.18	19.69	8.1	4.124	2.59	2.508	37.012	238.6	19.69	43.16
18JK70	mafic migmatite	48.10	-83.19	20.97	9	3.358	2.868	2.861	39.057	153.2	20.97	50.7

Name	Cr	Cs	Cu	Dy	Er	Eu	Ga	Gd	Hf	Ho	La	Lu	Mo	Nb
Detection Limit (Geolabs/Actlabs)	3/20	0.013/0.1	1.4/10	0.009/0.01	0.007/0.01	0.0031/0.005	0.04/1	0.009/0.01	0.14/0.1	0.0025/0.01	0.1/0.05	0.002/0.002	0.08/2	0.028/0.02
Greenstone														
18JK27G	250	0.926	106.3	4.31	2.683	0.9575	17.24	3.698	2.03	0.9547	3.7	0.408	0.8	2.918
18JK33	49	18.163	84.1	3.929	2.125	1.4988	21	4.364	2.64	0.7738	8	0.262	0.45	6.828
18JK45	88	0.998	180.2	6.16	3.899	1.4849	19.63	5.567	3.47	1.3235	12.4	0.547	1.12	6.696
18JK46	99	0.03	125.4	3.609	2.258	0.739	15.46	3.078	1.59	0.7824	3.3	0.329	0.44	2.23
18JK47	100	0.021	94.6	3.352	2.154	0.807	15.19	2.883	1.57	0.7087	3.1	0.323	0.47	2.231
18JK48	76	0.032	123.1	5.206	3.301	1.1967	17.96	4.565	2.75	1.0992	5.1	0.474	0.24	4.081
18JK49	84	0.365	93.4	3.203	2.075	0.6787	13.28	2.696	1.48	0.6996	2.6	0.304	0.15	2.085
18JK50A	54	0.055	140.3	6.572	4.226	1.5151	18.33	5.875	3.44	1.4145	7.1	0.624	0.31	5.446
19JK25	150	0.019	147.8	2.974	1.947	0.8721	26.95	2.509	1.23	0.6462	2.9	0.279	0.93	1.632
19JK26	110	1.036	172.3	4.394	2.779	1.1297	18.41	3.977	2.62	0.9389	10.7	0.407	0.77	4.583
19JK28	296	0.048	96.8	3.467	2.227	0.7806	16.86	2.903	1.48	0.753	2.6	0.344	0.32	1.755
19JK29A	139	0.528	36.9	2.657	1.522	0.9166	15.64	2.914	2.76	0.5364	18.2	0.219	2.62	10.925
19JK32B	81	0.618	162.6	7.425	4.816	1.7856	20.54	6.796	4.41	1.6032	15.8	0.701	1.03	8.252
Tonalite-trondjhemite-granodiorite														
17JK26	52	<7	<9	2.928	1.587	1.3445	17.1	3.928	6.84	0.5674	88.9	0.217	1.3	5.07
18JK03A	44	1.565	10	0.442	0.206	0.5542	19.48	0.753	3.94	0.0747	21.5	0.038	1.99	3.471
18JK04A	74	0.756	32.7	2.916	1.8	0.8951	19.51	3.164	4.23	0.5948	31.6	0.265	2.8	6.758
18JK07A	45	1.162	20.2	1.064	0.576	0.6797	19.33	1.494	3.04	0.2259	15.7	0.079	1.69	3.651
18JK08A	65	0.865	2.1	0.402	0.135	0.5276	19.93	0.97	3.63	0.0649	18.2	0.021	3.1	2.383
18JK09A	57	1.409	6.5	1.512	0.691	0.8047	21.19	2.454	3.4	0.2722	37.8	0.088	2.34	3.368
18JK11-A	110	1.7	< 10	2.26	1.13	0.978	22	2.87	4.2	0.42	26	0.157	< 2	5.6
18JK12-A	80	4.1	< 10	1.55	0.88	0.779	22	2.15	3	0.3	19.2	0.126	< 2	4.9
18JK13A	47	4.694	11.3	1.942	0.9	0.8775	17.26	3.2	5.45	0.3507	47.6	0.121	1.98	4.788
18JK19A	40	0.529	40	2.043	1.126	0.9002	20.25	2.55	3.86	0.4033	14.8	0.149	1.31	4.946
18JK23A	44	3.258	16.1	1.433	0.727	0.4778	19.48	2.027	2.92	0.2692	20.2	0.09	1.88	3.575
18JK24A	39	1.743	4.8	0.333	0.161	0.5612	19.64	0.75	3.41	0.0598	22.5	0.025	2.02	4.295
18JK25A	63	2.11	6.5	0.696	0.415	0.4695	20.03	0.965	3.29	0.1507	13.5	0.071	2.83	4.565
18JK27A	59	0.99	1.7	1.727	0.897	0.5041	20.03	1.964	2.97	0.3264	16.6	0.13	3	11.857
18JK29A	46	1.418	3	0.463	0.202	0.5684	22	1.016	3.35	0.0829	14.8	0.033	2.3	2.358
18JK30A	67	1.955	1.8	1.238	0.635	0.6101	16.79	2.233	4.57	0.2227	44.3	0.122	3.05	5.798
18JK32A	85	4.111	4.4	0.777	0.397	0.4854	22.34	1.253	3.61	0.154	13.4	0.062	4.07	3.815
18JK34A	74	0.687	15.2	3.328	1.98	0.8486	17.17	3.55	5.09	0.6743	32.5	0.312	2.46	8.277
18JK35A	52	1.515	6.1	0.689	0.326	0.4538	20.4	1.048	3.21	0.1225	15.7	0.043	2.14	4.583
18JK36A	36	1.723	8.2	0.486	0.256	0.5017	22.48	0.932	4.09	0.0862	13.7	0.051	1.73	3.509
18JK38A	25	0.989	<1.4	0.297	0.131	0.5054	18.04	0.637	2.22	0.0449	12.5	0.02	1.14	2.245
18JK52	22	1.067	27.7	1.14	0.489	0.8827	21.18	2.019	3.78	0.188	24.5	0.049	0.94	3.833
18JK53	29	0.674	27.9	1.108	0.545	0.7756	21.46	1.599	3.55	0.1996	14.4	0.071	1.09	2.418
18JK57	40	0.414	13.1	3.346	1.81	1.2154	18.81	4.075	5.34	0.6514	33.9	0.212	0.9	6.649
18JK60A	107	0.5	34.2	2.769	1.576	1.0186	18.67	3.483	3.34	0.556	30.5	0.225	1.76	6.577
19JK01	29	1.21	16.1	0.346	0.148	0.6252	19.74	0.822	3.84	0.053	51.5	0.025	0.96	2.399
19JK02	27	1.106	17.3	0.901	0.428	0.5948	21.8	1.611	2.57	0.1567	28.9	0.051	1.14	3.365
19JK03	63	1.146	3.3	2.598	1.227	1.6453	20.99	4.719	3.33	0.4546	35.3	0.131	0.85	4.649
19JK06A	91	0.596	194.1	6.736	4.441	1.4449	21.27	5.98	3.63	1.4718	8.8	0.645	1.54	5.868
19JK07A	45	0.654	24.9	2.242	1.104	1.3109	18.5	3.617	4.12	0.411	48.8	0.147	0.79	6.493
19JK07B	30	0.263	8.5	1.595	0.826	1.0071	17.09	2.095	2.85	0.3006	9	0.11	1.17	4.233
19JK09A	25	0.713	46.4	2.334	0.974	1.7332	20.9	4.624	5.15	0.3911	67.5	0.114	0.94	6.079

Name	Cr	Cs	Cu	Dy	Er	Eu	Ga	Gd	Hf	Ho	La	Lu	Mo	Nb
Detection Limit (Geolabs/Actlabs)	3/20	0.013/0.1	1.4/10	0.009/0.01	0.007/0.01	0.0031/0.005	0.04/1	0.009/0.01	0.14/0.1	0.0025/0.01	0.1/0.05	0.002/0.002	0.08/2	0.028/0.02
19JK10A	19	0.71	15.6	3.337	2.011	1.1055	18.62	3.589	8.83	0.6924	31.6	0.3	0.7	8.288
19JK11	190	0.81	55.5	3.703	2.551	0.7394	18.6	2.661	3.84	0.8235	15.2	0.379	1.39	6.714
19JK12A	42	0.401	28.1	1.261	0.639	0.7662	18.34	1.996	3.74	0.2424	29.3	0.084	0.95	3.286
19JK18	25	1.689	7.5	0.854	0.408	0.5751	19.51	1.398	3.92	0.1512	18.7	0.052	0.89	4.582
19JK20	22	0.475	16.1	4.284	2.729	1.2481	18.17	4.611	7.32	0.8815	42.2	0.42	0.76	6.989
19JK21	79	0.741	8.8	1.383	0.6	1.1087	19.13	2.535	3.54	0.2435	33.7	0.07	0.66	4.021
19JK23A	124	2.246	34.8	0.913	0.34	1.2185	21.06	1.923	6.44	0.142	34.3	0.045	2.03	5.915
19JK48A	16	1.312	1.7	0.771	0.338	0.6281	15.4	2.101	6.1	0.1263	72.3	0.069	0.76	1.63
Lower-crustal metabasites														
17JK02	529	<7	41	2.794	1.754	0.6228	16.5	2.252	1.07	0.6031	2.8	0.26	<0.8	2.122
17JK03	449	<7	72	2.847	1.799	0.668	15.3	2.295	1.14	0.6144	4	0.26	<0.8	1.871
17JK05	598	<7	32	2.668	1.675	0.619	15.7	2.112	0.96	0.574	2.2	0.244	<0.8	1.802
17JK09	127	<7	96	5.255	3.177	1.1868	21.8	4.53	1.56	1.0995	4.3	0.452	<0.8	3.67
17JK10	149	<7	83	5.332	3.442	1.1347	20.7	4.46	1.92	1.128	5.3	0.501	<0.8	3.411
17JK12	255	<7	36	3.863	2.414	0.9556	19.5	3.317	1.49	0.8385	4.5	0.354	<0.8	3.352
17JK14	384	<7	50	2.928	1.905	0.6915	16	2.48	1.18	0.632	3.2	0.283	<0.8	2.164
17JK15	153	<7	97	4.373	2.666	1.1226	18.6	4.007	2.42	0.9158	8.9	0.377	<0.8	4.332
17JK16	22	<7	73	3.71	2.058	1.6362	23.2	4.274	1.32	0.7354	14.6	0.267	0.9	12.178
17JK17	75	<7	88	5.839	3.839	1.2113	21	4.836	2.24	1.2577	7.4	0.566	1	4.624
17JK18	319	<7	86	4.086	2.65	0.9418	18.4	3.355	1.18	0.8775	4.9	0.386	<0.8	2.143
17JK19	262	<7	84	2.997	1.759	0.9373	20.1	2.968	1.27	0.6165	7.5	0.226	<0.8	4.18
17JK20	125	<7	87	6.761	4.216	1.5271	23	6.031	1.97	1.4371	8.9	0.614	0.9	4.522
17JK21	130	<7	361	5.822	3.826	1.1404	21.5	4.831	1.99	1.2708	4.6	0.577	2	3.835
17JK24	222	<7	76	3.503	2.329	0.8085	16.5	2.941	1.16	0.7743	3.1	0.349	<0.8	2.229
17JK27	210	<7	62	4.224	2.764	1.0334	18.4	3.738	1.92	0.9173	9.8	0.391	15.2	3.926
18JK54	288	0.084	105.5	4.162	2.389	1.5758	16.75	4.969	2.14	0.8124	18.8	0.348	0.64	2.797
18JK55A	141	0.052	86.8	5.315	3.334	1.1013	18.61	4.421	1.74	1.1472	4.6	0.509	1.18	3.235
18JK59A	150	0.162	71.2	4.219	2.744	0.9327	19.82	3.857	2.17	0.895	7.6	0.397	2.88	3.629
18JK59B	156	0.133	126.8	5.918	3.888	1.326	19.91	4.958	1.52	1.2858	4.9	0.579	1.26	3.608
18JK67A	139	0.139	50.7	4.644	3.007	1.1815	19.77	4.151	2.25	1.0056	11.7	0.45	0.91	3.129
18JK69	298	0.039	11.4	3.245	2.12	1.0426	15.3	2.928	1.88	0.6904	8.1	0.333	1.69	4.124
18JK70	196	0.057	95	3.577	2.25	0.9734	16.9	3.349	1.85	0.7539	9	0.339	3.8	3.358

Name	Nd	Ni	Pb	Pr	Rb	Sc	Sm	Sr	Ta	Tb	Th	U	Y	Yb	Zn
Detection Limit (Geolabs/Actlabs)	0.06/0.05	0.7/20	0.18/5	0.014/0.01	0.11/1	1.1/1	0.026/0.01	0.6/2	0007/0.01	0.0023/0.01	0.018/0.05	0.011/0.01	0.05/0.5	0.009/0.01	1.8/30
Greenstone															
18JK27G	8.29	88.1	1.82	1.572	26.97	43.6	2.761	95.3	0.186	0.6394	0.346	0.091	24.71	2.738	95.2
18JK33	15.77	64.7	3.89	3.184	106.56	30.3	4.213	173.5	0.429	0.6652	0.504	0.191	19.53	1.791	136
18JK45	17.92	49.3	4.64	3.971	21.28	42.2	4.694	175.6	0.453	0.9541	1.995	0.517	34.12	3.666	132.7
18JK46	6.98	83.4	1.76	1.356	1.17	41.1	2.236	133.3	0.142	0.539	0.258	0.067	20.94	2.23	78.5
18JK47	6.34	70.1	1.32	1.299	0.74	41.1	2.119	112.2	0.148	0.4853	0.265	0.067	18.54	2.083	86.8
18JK48	11.41	42.1	1.48	2.283	1.19	35.4	3.555	73.2	0.274	0.8031	0.437	0.111	28.03	3.227	110.9
18JK49	5.8	66.8	0.76	1.12	4.44	34.8	1.986	79.4	0.138	0.4601	0.24	0.055	18.09	1.999	77.6
18JK50A	15	25.5	1.1	3.032	1.3	40.4	4.556	116.8	0.344	1.0197	0.589	0.138	37.61	4.215	117.5
19JK25	5.57	56	2.06	1.086	0.28	39.6	1.81	291	0.107	0.4344	0.221	0.089	18.14	1.855	42.2
19JK26	13.43	61.5	3.62	3.14	31.59	42.9	3.491	188.9	0.286	0.6753	1.902	0.444	26.89	2.726	112.6
19JK28	5.85	156	2.7	1.107	0.46	45.1	2.118	114.5	0.111	0.5067	0.247	0.074	20.76	2.268	92.4
19JK29A	14.68	123	3.12	3.802	11.25	20.3	3.007	375	0.369	0.4497	1.685	0.554	15.26	1.454	71.2
19JK32B	21.79	53.1	3.77	4.841	17.41	43	5.841	138.5	0.536	1.1551	2.304	0.578	42.66	4.598	147.3
Tonalite-trondjhemite-granodiorite															
17JK26	48.19	8.9	11.3	14.71	41.18	10	6.116	293.3	0.138	0.5222	19.991	0.622	14.85	1.373	59
18JK03A	11.38	6	8.94	3.585	51.18	1.8	1.409	445.8	0.164	0.085	4.579	0.413	2.06	0.236	45.4
18JK04A	23.67	14.6	9.5	6.556	48.85	9	3.956	299.5	0.436	0.475	8.171	1.116	16.32	1.777	62.6
18JK07A	10.95	13.7	5.24	3.076	42.54	6.6	1.898	300.7	0.213	0.2047	2.372	0.269	5.71	0.545	56
18JK08A	11.88	2.1	10.12	3.54	42.14	1.5	1.69	430.7	0.102	0.1031	2.405	0.269	1.68	0.14	48.3
18JK09A	24.44	8.6	11.24	7.229	47.47	8.1	3.773	424.9	0.177	0.2992	11.569	0.536	7.29	0.601	55
18JK11-A	19.7	< 20	7	5.37	41	9	3.77	326	0.37	0.42	3.31	1.09	12.1	1.07	100
18JK12-A	14.9	< 20	12	4.09	71	4	2.92	276	0.8	0.3	4.02	1.34	9.5	0.85	70
18JK13A	30.57	5.1	14.33	9.021	104.06	3.3	4.914	332.4	0.35	0.4081	18.741	1.376	8.89	0.78	58.1
18JK19A	14.07	14.9	2.83	3.543	16.31	10.2	2.978	320	0.299	0.377	1.316	0.234	10.37	1.021	59.4
18JK23A	14.61	7.9	12.74	4.131	63.14	6.6	2.642	386.4	0.248	0.2727	6.193	2.429	7.17	0.618	56.2
18JK24A	12.13	5.2	9.14	3.835	58.17	<1.1	1.412	402.4	0.3	0.0746	6.506	5.345	1.6	0.163	43.2
18JK25A	9.38	5.4	10.96	2.782	52.41	<1.1	1.499	452.8	0.653	0.128	4.547	1.357	4.2	0.464	35.1
18JK27A	10.95	1	12.36	3.084	65.45	2.5	2.14	126.1	1.586	0.3	6.266	1.602	9.85	0.912	45.4
18JK29A	10.58	2.1	9.44	3.029	43.35	1.2	1.669	444.8	0.148	0.1035	2.951	0.809	2.32	0.189	49.9
18JK30A	27.04	3.5	13.33	8.403	75.13	1.7	3.813	218.4	0.593	0.258	26.501	3.096	6.53	0.741	19.4
18JK32A	9.73	2.3	9.74	2.747	63.86	2.7	1.652	337.8	0.485	0.1549	3.431	1.107	4.59	0.426	49.2
18JK34A	22	14.6	10.73	6.277	41.46	7.9	4.059	243.7	0.918	0.5347	13.067	2.876	19.8	2.043	41.2
18JK35A	9.65	10	6.65	3.073	88.53	3.5	1.496	235.7	0.25	0.1385	6.325	0.857	3.3	0.283	50.4
18JK36A	10.15	3.5	9.68	2.992	48.08	<1.1	1.512	263.4	0.314	0.1027	4.601	1.121	2.83	0.293	41.7
18JK38A	7.82	1.2	12.29	2.367	48.02	1.2	1.123	342	0.126	0.0634	6.504	0.382	1.25	0.145	27.5
18JK52	19.94	6	3.98	5.518	43.66	4.7	3.016	402.3	0.195	0.2455	3.52	0.37	4.98	0.373	75.2
18JK53	13.67	7.2	4.02	3.493	27.86	5.2	2.146	754	0.095	0.2077	2.121	0.255	5.27	0.508	72
18JK57	26.52	14.3	11.65	7.177	60.53	10.4	4.87	249.4	0.298	0.5866	8.234	0.488	16.98	1.514	58
18JK60A	22.88	41	9.25	6.287	53.57	13.8	4.357	256.3	0.446	0.487	8.89	0.449	14.52	1.474	72.8
19JK01	22.2	11.8	9.3	7.787	49.53	1.2	1.986	553.3	0.129	0.0705	9.049	0.225	1.56	0.165	49.2
19JK02	18.03	4.9	11.42	5.507	61.39	3.1	2.441	319.1	0.202	0.1804	9.044	0.31	4.12	0.325	37.5
19JK03	38.37	32.1	10.3	9.886	40.23	9	6.691	716.7	0.287	0.5396	4.489	0.627	12.52	0.951	67.3
19JK06A	16	54.6	4.2	3.315	17.42	46.7	4.553	143.9	0.406	1.0213	0.713	0.461	39.08	4.169	128.6
19JK07A	36.65	24.2	10.5	10.557	39.77	7.1	5.265	753.5	0.26	0.406	8.951	0.334	11.79	0.987	62.9
19JK07B	11.95	8.6	10.2	2.759	19.23	6.4	2.567	752.3	0.226	0.2856	1.33	0.188	8.21	0.743	41.2
19JK09A	54.89	20.8	12.88	15.531	51.99	6	7.753	937.9	0.275	0.4942	13.857	0.607	10.62	0.788	71.6

Name	Nd	Ni	Pb	Pr	Rb	Sc	Sm	Sr	Ta	Tb	Th	U	Y	Yb	Zn
Detection Limit (Geolabs/Actlabs)	0.06/0.05	0.7/20	0.18/5	0.014/0.01	0.11/1	1.1/1	0.026/0.01	0.6/2	0007/0.01	0.0023/0.01	0.018/0.05	0.011/0.01	0.05/0.5	0.009/0.01	1.8/30
19JK10A	22.1	11.3	9.53	6.309	52.51	10.8	4.03	259.1	0.449	0.5286	9.763	0.892	19.12	1.936	69.4
19JK11	9.2	81.3	7.63	2.632	74.66	20.7	1.807	250.6	0.283	0.5221	3.245	0.328	23.51	2.528	86.3
19JK12A	18.89	13.2	10.61	5.472	39.08	5.3	2.748	551.8	0.103	0.235	6.444	0.309	6.85	0.56	51.9
19JK18	12.14	6.5	7.96	3.566	53.87	5.4	1.936	235.6	0.177	0.1681	7.552	0.543	4.17	0.353	57.7
19JK20	30.81	10.3	10.1	8.593	34.97	13.8	5.398	345.9	0.353	0.6877	11.338	0.611	24.03	2.703	71.2
19JK21	28.28	42.7	7.57	7.7	53.43	5.5	4.027	664.6	0.15	0.2817	6.046	0.285	6.76	0.48	63.3
19JK23A	22.2	56.4	11.93	6.472	71.19	7.7	2.971	452	0.353	0.2036	9.594	0.712	3.93	0.312	74.3
19JK48A	38.43	2.8	17.75	12.805	124.01	<1.1	4.435	309.2	0.158	0.1924	25.098	0.778	3.6	0.391	28.8
Lower-crustal metabasites															
17JK02	5	120.2	3	1.005	15.15	43	1.66	221.5	0.195	0.4087	0.392	0.286	16.31	1.724	75
17JK03	5.62	98.1	2.9	1.17	9.12	41	1.752	128.8	0.159	0.4102	1.418	0.431	16.53	1.772	73
17JK05	4.66	145.2	2.8	0.87	14.97	39	1.525	105.7	0.089	0.3768	0.303	0.17	15.41	1.615	74
17JK09	10.48	79	<1.7	2.01	1.13	42	3.488	141.1	0.236	0.7754	0.704	0.215	29.32	3.108	116
17JK10	10.51	52.7	<1.7	2.102	5.74	44	3.396	106.5	0.216	0.7576	0.499	0.242	30.52	3.355	135
17JK12	8.38	121.7	1.7	1.68	11.75	39	2.605	121	0.204	0.5771	0.813	0.276	21.83	2.365	103
17JK14	5.89	147.2	<1.7	1.18	9.27	38	1.862	137.8	0.136	0.4301	0.426	0.2	17.23	1.839	85
17JK15	13.23	81.6	<1.7	2.946	9.15	36	3.423	145.9	0.307	0.6609	0.653	0.255	24.94	2.554	108
17JK16	20.62	5.6	3.4	4.645	11.96	26	4.485	419.4	1.091	0.6104	1.396	0.669	19.55	1.768	137
17JK17	12.98	23.8	<1.7	2.765	6.79	41	3.737	141.1	0.282	0.8521	0.742	0.227	34.08	3.694	116
17JK18	8.18	102.2	<1.7	1.634	2.97	41	2.508	107	0.129	0.5881	0.912	0.322	23.6	2.626	100
17JK19	10.81	99.7	3.5	2.478	7.86	33	2.794	201.9	0.146	0.4658	1.765	0.444	15.98	1.527	109
17JK20	17.62	30.4	<1.7	3.643	3.82	43	5.108	166.1	0.247	1.0101	0.176	0.059	38.09	4.055	132
17JK21	10.68	43.7	<1.7	2.051	1.78	51	3.483	119	0.232	0.8597	0.149	0.048	33.45	3.837	135
17JK24	6.47	128.3	2.4	1.299	4.11	38	2.165	101.1	0.142	0.5111	0.569	0.225	20.88	2.289	101
17JK27	12.53	89.6	4.4	2.898	7.11	39	3.126	170.1	0.31	0.633	2.168	0.71	24.41	2.617	114
18JK54	28.17	156	4.06	6.569	6.87	37.8	5.75	263.7	0.183	0.7083	1.936	0.32	21.47	2.235	108.1
18JK55A	9.74	62.2	2.45	1.886	1.3	46.9	3.244	135.5	0.203	0.7635	0.494	0.205	30.11	3.377	120
18JK59A	11.85	59.9	6.18	2.551	8.9	43	3.172	151.2	0.205	0.6467	0.625	0.241	23.82	2.617	128
18JK59B	11.5	65.4	2.07	2.267	3.1	51.5	3.612	131.7	0.227	0.8489	0.386	0.114	33.88	3.803	119
18JK67A	13.58	91.8	3.32	3.202	6.76	45.7	3.37	191.7	0.207	0.6857	1.139	0.2	27.12	2.857	126.7
18JK69	10.51	105.7	7.14	2.59	6.81	33.3	2.508	409.6	0.338	0.4876	2.534	0.624	18.95	2.144	110.3
18JK70	12.12	127.5	4.58	2.868	14.5	33.8	2.861	197	0.28	0.5294	1.308	0.339	20.03	2.206	98

Appendix S1.3

Quality Assurance and Control for chemical analyses of samples across the Kapuskasing Uplift

Major Element Duplicates

Sample Id	Sample	Analyte	Units	Measured Val	Value
Dup-18-45464	17JK13	Al2O3	wt%	16.13	15.94
Dup-18-45464	17JK13	CaO	wt%	5.686	5.643
Dup-18-45464	17JK13	Cr2O3	wt%	0.038	0.037
Dup-18-45464	17JK13	Fe2O3	wt%	10.06	9.97
Dup-18-45464	17JK13	K2O	wt%	2.11	2.08
Dup-18-45464	17JK13	MgO	wt%	4.68	4.61
Dup-18-45464	17JK13	Na2O	wt%	3.22	3.21
Dup-18-45464	17JK13	P2O5	wt%	0.21	0.209
Dup-18-45464	17JK13	SiO2	wt%	55.69	55.2
Dup-18-45464	17JK13	TiO2	wt%	1.16	1.14
Dup-18-45465	17JK26	Al2O3	wt%	15.22	15.1
Dup-18-45465	17JK26	CaO	wt%	4.359	4.347
Dup-18-45465	17JK26	Cr2O3	wt%	0.006	0.006
Dup-18-45465	17JK26	Fe2O3	wt%	5.04	5.02
Dup-18-45465	17JK26	K2O	wt%	1.36	1.37
Dup-18-45465	17JK26	MgO	wt%	1.38	1.37
Dup-18-45465	17JK26	MnO	wt%	0.061	0.061
Dup-18-45465	17JK26	Na2O	wt%	3.57	3.68
Dup-18-45465	17JK26	P2O5	wt%	0.16	0.16
Dup-18-45465	17JK26	SiO2	wt%	67.45	66.99
Dup-18-45465	17JK26	TiO2	wt%	0.67	0.66
Dup-18-47537	18JK53A	Al2O3	wt%	17.61	17.61
Dup-18-47537	18JK53A	CaO	wt%	4.727	4.721
Dup-18-47537	18JK53A	Fe2O3	wt%	3.78	3.77
Dup-18-47537	18JK53A	K2O	wt%	0.95	0.94
Dup-18-47537	18JK53A	MgO	wt%	1.34	1.33
Dup-18-47537	18JK53A	Na2O	wt%	5.71	5.73
Dup-18-47537	18JK53A	P2O5	wt%	0.133	0.133
Dup-18-47537	18JK53A	SiO2	wt%	64.97	65.03
Dup-18-47537	18JK53A	TiO2	wt%	0.47	0.47
Dup-18-47538	18JK67A	Al2O3	wt%	16.15	16.18
Dup-18-47538	18JK67A	CaO	wt%	10.51	10.511
Dup-18-47538	18JK67A	Fe2O3	wt%	10.87	10.89
Dup-18-47538	18JK67A	K2O	wt%	0.57	0.57
Dup-18-47538	18JK67A	MgO	wt%	4.16	4.15
Dup-18-47538	18JK67A	Na2O	wt%	2.82	2.82
Dup-18-47538	18JK67A	P2O5	wt%	0.111	0.109
Dup-18-47538	18JK67A	SiO2	wt%	53.66	53.71
Dup-18-47538	18JK67A	TiO2	wt%	1.22	1.21

Trace Element Duplicates

Sample Id	Sample	Analyte	Units	Measured Val	Value
Dup-18-45969	17JK02	Ce	mg/kg	6.66	6.35
Dup-18-45969	17JK02	La	mg/kg	2.9	2.8
Dup-18-45969	17JK02	Nd	mg/kg	5.27	5
Dup-18-45969	17JK02	Pr	mg/kg	1.012	1.005
Dup-18-45969	17JK02	Sm	mg/kg	1.689	1.66
Dup-18-45969	17JK02	Th	mg/kg	0.436	0.392
Dup-18-45969	17JK02	U	mg/kg	0.284	0.286
Dup-18-45969	17JK02	Zr	mg/kg	31	33
Dup-18-45970	17JK15	Ce	mg/kg	21.76	21.59
Dup-18-45970	17JK15	La	mg/kg	9	8.9
Dup-18-45970	17JK15	Nd	mg/kg	12.92	13.23
Dup-18-45970	17JK15	Pr	mg/kg	2.958	2.946
Dup-18-45970	17JK15	Th	mg/kg	0.622	0.653
Dup-18-45970	17JK15	U	mg/kg	0.25	0.255
Dup-18-45970	17JK15	Zr	mg/kg	91	91
Dup-18-45971	17JK02 SP	Ce	mg/kg	6.31	6.35
Dup-18-45971	17JK02 SP	La	mg/kg	2.7	2.8
Dup-18-45971	17JK02 SP	Nd	mg/kg	5.06	5
Dup-18-45971	17JK02 SP	Pr	mg/kg	0.999	1.005
Dup-18-45971	17JK02 SP	Sm	mg/kg	1.669	1.66
Dup-18-45971	17JK02 SP	Th	mg/kg	0.413	0.392
Dup-18-45971	17JK02 SP	U	mg/kg	0.279	0.286
Dup-18-45971	17JK02 SP	Zr	mg/kg	35	33
Dup-18-47929	18JK48A	Ce	mg/kg	13.37	13.79
Dup-18-47929	18JK48A	La	mg/kg	5	5.1
Dup-18-47929	18JK48A	Nd	mg/kg	10.65	11.41
Dup-18-47929	18JK48A	Pr	mg/kg	2.131	2.283
Dup-18-47929	18JK48A	Sm	mg/kg	3.353	3.555
Dup-18-47929	18JK48A	Th	mg/kg	0.448	0.437
Dup-18-47929	18JK48A	U	mg/kg	0.111	0.111
Dup-18-47929	18JK48A	Zr	mg/kg	96	94
Dup-18-47930	18JK59A	Ce	mg/kg	18.5	18.41
Dup-18-47930	18JK59A	La	mg/kg	7.6	7.6
Dup-18-47930	18JK59A	Nd	mg/kg	11.36	11.85
Dup-18-47930	18JK59A	Pr	mg/kg	2.6	2.551
Dup-18-47930	18JK59A	Sm	mg/kg	3.189	3.172
Dup-18-47930	18JK59A	Th	mg/kg	0.598	0.625
Dup-18-47930	18JK59A	U	mg/kg	0.231	0.241
Dup-18-47930	18JK59A	Zr	mg/kg	74	77
Dup-18-47931	18JK70A SP	Ce	mg/kg	20.99	20.97
Dup-18-47931	18JK70A SP	La	mg/kg	8.9	9
Dup-18-47931	18JK70A SP	Nd	mg/kg	12.57	12.12
Dup-18-47931	18JK70A SP	Pr	mg/kg	2.85	2.868
Dup-18-47931	18JK70A SP	Sm	mg/kg	2.978	2.861
Dup-18-47931	18JK70A SP	Th	mg/kg	1.295	1.308
Dup-18-47931	18JK70A SP	U	mg/kg	0.348	0.339
Dup-18-47931	18JK70A SP	Zr	mg/kg	69	68

Trace Element Blanks

Sample Id	Analyte	Units	Measured Value
BLANK-18-19581	Ce	mg/kg	0.03
BLANK-18-19581	La	mg/kg	0
BLANK-18-19581	Nd	mg/kg	0.01
BLANK-18-19581	Pr	mg/kg	0.004
BLANK-18-19581	Sm	mg/kg	0.003
BLANK-18-19581	Th	mg/kg	0.002
BLANK-18-19581	U	mg/kg	0.002
BLANK-18-19581	Zr	mg/kg	2
BLANK-18-20417	La	mg/kg	0
BLANK-18-20417	Ce	mg/kg	0.01
BLANK-18-20417	Nd	mg/kg	0
BLANK-18-20417	Pr	mg/kg	0.001
BLANK-18-20417	Sm	mg/kg	0.001
BLANK-18-20417	Th	mg/kg	0.004
BLANK-18-20417	U	mg/kg	0.002
BLANK-18-20417	Zr	mg/kg	2

Sample Id	Analyte	Units	Measured Value	Accepted Value
INTL-18-31721	Ce	mg/kg	433.93	410
INTL-18-31721	La	mg/kg	183	180
INTL-18-31721	Nd	mg/kg	208.6	200
INTL-18-31721	Pr	mg/kg	55.76	51
INTL-18-31721	Sm	mg/kg	26.397	27
INTL-18-31721	Th	mg/kg	108.715	105
INTL-18-31721	U	mg/kg	2.475	2.4
INTL-18-31721	Zr	mg/kg	467	550

Appendix S1.4

Model variables for Chapter 2 modelled samples

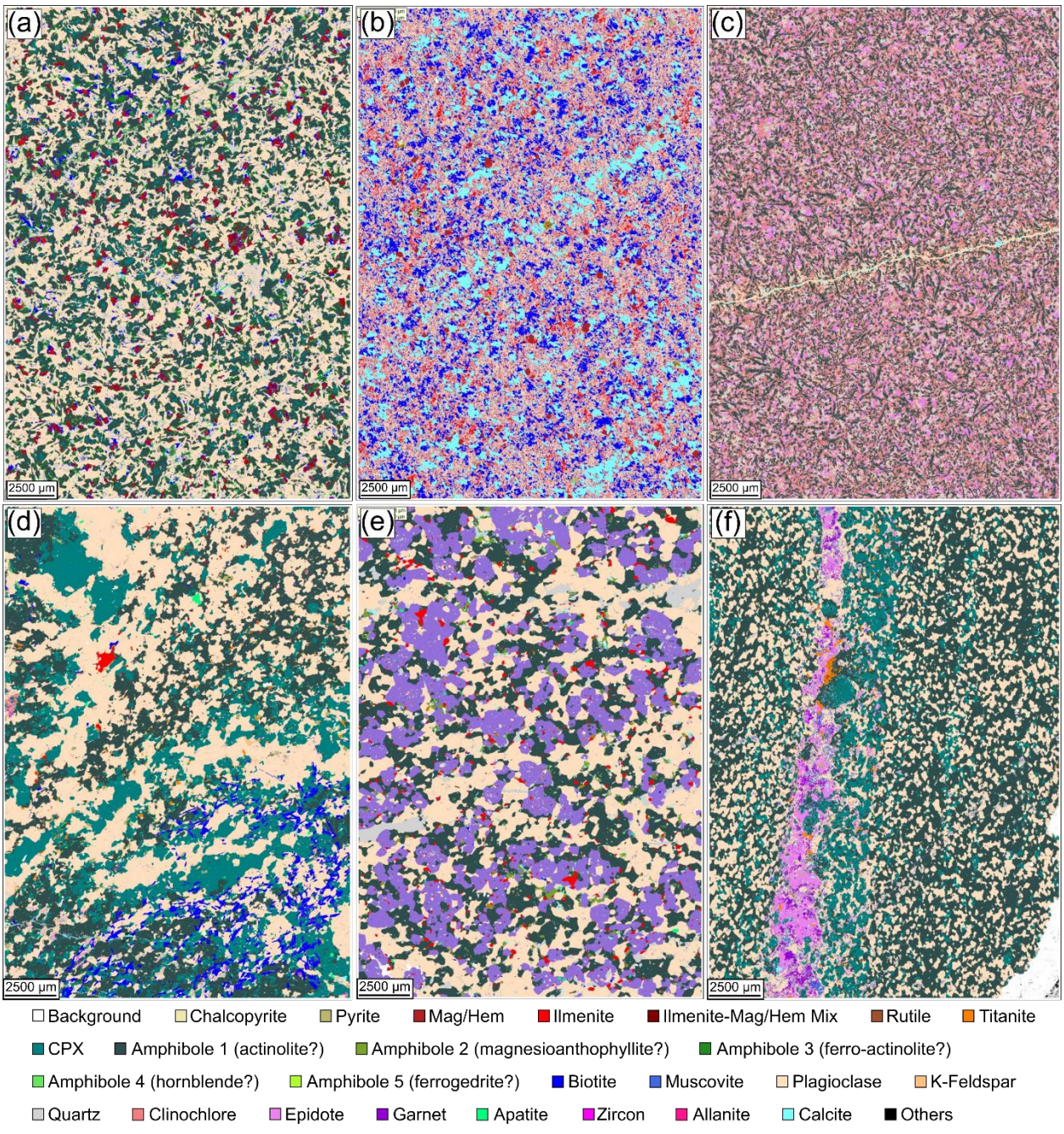
Sample	Specific Gravity (g/cm^3)	Molar weight (kg/mol)
Lower-crustal metabasites samples		
18JK54 (enriched)	3.03	0.06386
17JK09 (intermediate)	3.27	0.06398
17JK14 (depleted)	3.01	0.06300
Greenstone samples		
18JK45 (enrriched)	3.03	0.06560
18JK33 (intermediate)	2.94	0.06385
18JK47 (depleted)	3.00	0.06248

Mineral	Density
Apatite	3.19
Zircon	4.65
Allanite	3.85

Appendix S1.5

Weight percent of minerals and thinsection scans of modelled samples from Mineral Liberation Analysis for chapter 2.

MLA thinsection scans of 6 modelled samples. (a) 18JK45 (enriched greenstone) (b) 18JK33 (intermediate greenstone) (c) 18JK47 (depleted greenstone) (d) 18JK54 (enriched lower-crustal metabasite) (e) 17JK09 (intermediate lower-crustal metabasite) (f) 17JK14 (depleted lower-crustal metabasite)



Appendix S1.6

Chapter 2 accessory mineral modelling equations

Zircon

Temperature and melt composition are the salient variables responsible for zircon saturation with negligible effects from pressure and H_2O concentration (Watson and Harrison 1983). The Zr saturation expression of (Borisov and Aranovich 2019) fits new and previous experimental data well, providing the basis for assessing zircon stability during anatexis of metabasite. Melt composition is defined by the parameter *B:*

$$B = 0.14\left(\frac{X_{TiO_2}}{X_{SiO_2}}\right) + 1.3\left(\frac{X_{CaO}}{X_{SiO_2}}\right) + 1.5\left(\frac{X_{Na_2O}}{X_{SiO_2}}\right) - 4.5\left(\frac{X_{K_2O}}{X_{SiO_2}}\right) - 2.7\left(\frac{X_{Al_2O_3}}{SiO_2}\right)^2 + \left(\frac{X_{MgO}}{X_{SiO_2}}\right)^2 - 3.7\left(\frac{X_{CaO}}{X_{SiO_2}}\right)^2 + 75\left(\frac{X_{K_2O}}{X_{SiO_2}}\right)^2$$

where *X* are mole fractions ($\Sigma X = 1$). The compositional parameter of the melt is then used in the temperature-dependent zircon solubility expression:

$$Log\ Zr_{sat}(mg/kg) = 4.322 \cdot B - \frac{4338.8}{T(K)} + 6.456$$

Apatite

The solubility of apatite in the melt is dependent on temperature and melt composition in peralkaline and metaluminous compositions (Watson 1979a, Harrison and Watson 1984, Yakymchuk 2017). We use the solubility equation of (Harrison and Watson 1984)):

$$lnD_P^{ap/melt} = \left[\frac{\left(8400 + \left((SiO_2 - 0.5)2.64x10^4\right)\right)}{T(K)}\right] - \left[3.1 + \left(12.4(SiO_2 - 0.5)\right)\right]$$

Where SiO_2 is the weight proportion and D_p is the distribution coefficient of P_2O_5 between apatite and melt. The saturation concentration of P_2O_5 in the melt is then calculated using:

$$[P_2O_5]_{sat} = \frac{[P_2O_5]^{Ap}}{D_p}$$

This equation is valid if the aluminium saturation index (ASI; molar Al_2O_3 / [CaO + Na_2O + K_2O]) of the melt is less < 1. If the ASI of the melt is > 1, we use the e_{factor} correction (Bea et al. 1992) to account for the increase of P_2O_5 solubility with increasing ASI in peraluminous melt compositions:

$$e_{factor} = (ASI - 1) * \left(\frac{6429}{T(K)}\right)$$

Allanite

Allanite is modelled as a pure LREE/Ca endmember and is limited to reasonable metamorphic conditions by assuming similar thermodynamic stability as epidote (i.e., only present in epidote-present fields). However, the modelled modal proportions of allanite are determined based on the solubility equation (Equation 6) only and not the modelled proportions of epidote; the limitations of our approach are discussed later. We use the allanite solubility equation of (Klimm et al. 2008)which is sensitive to temperature, pressure and melt composition (CNKM; molar Ca / [Na + Mg + Ca + K]):

$$lnK_{sat}(\frac{mg}{kg}) = 12.13 \pm 0.13 - \left(\frac{12657 \pm 136}{T(K)}\right) - 0.155 \pm 0.010 \cdot P(GPa) + 4.41 \pm 0.12CNKM$$

Appendix S1.7

Chapter 2 Distribution coefficients of trace elements in major minerals from (Bédard, 2006)

	garnet	plagioclase	amphibole	clinopyroxene	epidote	sphene	orthopyroxene	rutile	ilmenite	zircon	allanite	apatite
La	0.028	0.358	0.319	0.028	2.05	4.73	0.0003	0.006	0.015	26.6	-	12
Ce	0.08	0.339	0.56	0.059	2.44	7.57	0.0007	0.007	0.012	23.5	-	15
Pr	0.15	0.316	0.898	0.116	2.86	9	0.0014	0.007	0.011	20	-	17
Nd	0.222	0.289	1.32	0.115	3.34	12.4	0.0028	0.008	0.01	21.7	-	19
Sm	1.43	0.237	2.09	0.259	4.22	14	0.0085	0.095	0.009	17.7	-	20
P	0.184	0.079	0.225	0.162	0.18	0.057	0.05	0.03	0.002	-	-	-
Zr	0.537	0.078	0.417	0.125	0.1	1.92	0.031	3.7	2.3	-	-	16
Th	0.008	0.095	0.055	0.104	156	0.16	0.13	0.2	0.09	62	2418	23
U	0.024	0.091	0.05	0.032	1.29	0.14	0.089	0.2	0.09	298	20	25

Appendix S1.8

Chapter 2 Accessory mineral model results

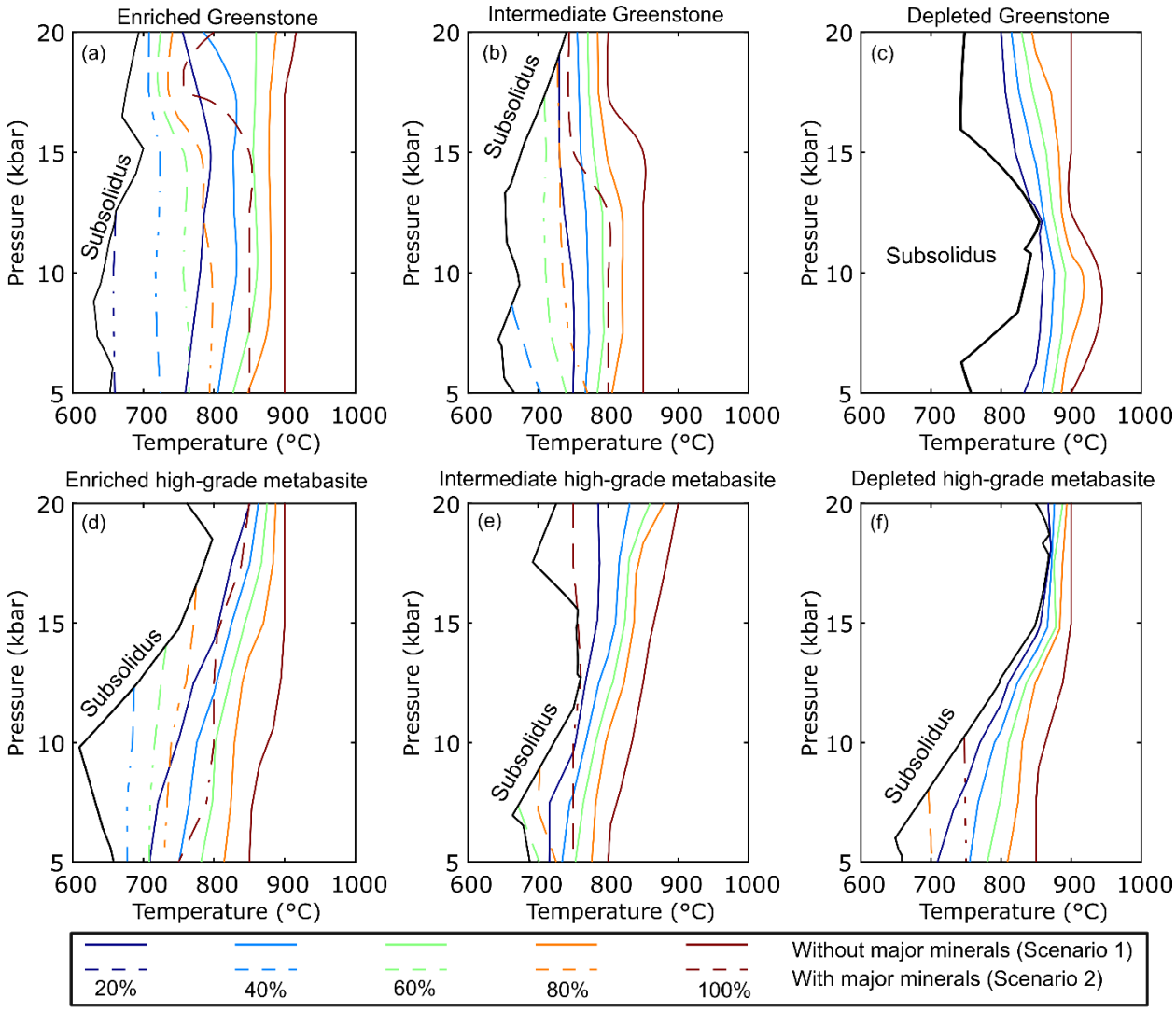
Each contour in S5-1–3 represents the percentage of the accessory mineral that has been dissolved normalized to the whole-rock concentration of the essential structural component (P_2O_5, Zr, LREE; Table 2) divided by the amount of that element in the accessory mineral (e.g. 0% $diss_{apatite}$ = whole rock P_2O_5/418,200; Kelsey et al., 2008). The 100% contours are equivalent to the mineral-out boundary, i.e. when the accessory mineral is no longer predicted to be part of the suprasolidus phase assemblage. Results for two scenarios are presented: (1) the trace element essential structural constituents of the accessory minerals are only found in that accessory mineral and melt (e.g. Zr found only in zircon and melt) and, (2) all investigated trace elements are partitioned between the major minerals, accessory minerals and melt based on equilibrium partitioning. We present both scenarios to assess the influence of major minerals sequestering P_2O_5, Zr, and LREE during anatexis on accessory mineral stability which in turn affects HPE distribution.

Apatite is predicted to be <20% dissolved at temperatures <800°C for all compositions and both modelled scenarios (S5-1). In general, the stability of apatite is decreased by 25–50°C for scenario 2 relative to scenario 1 for all six investigated compositions (S5-1). Apatite is expected to be completely dissolved in intermediate compositions at equal or lower temperatures than in depleted compositions with the apatite stability field predicted to extend to higher temperatures for enriched compositions. Apatite is expected to have increased stability for most high-grade metabasites compared to the greenstone counterparts (i.e. depleted, intermediate and enriched). This point is further discussed in section 5.2. In general, the sequestration of P_2O_5 in major minerals minimally affects the stability of apatite.

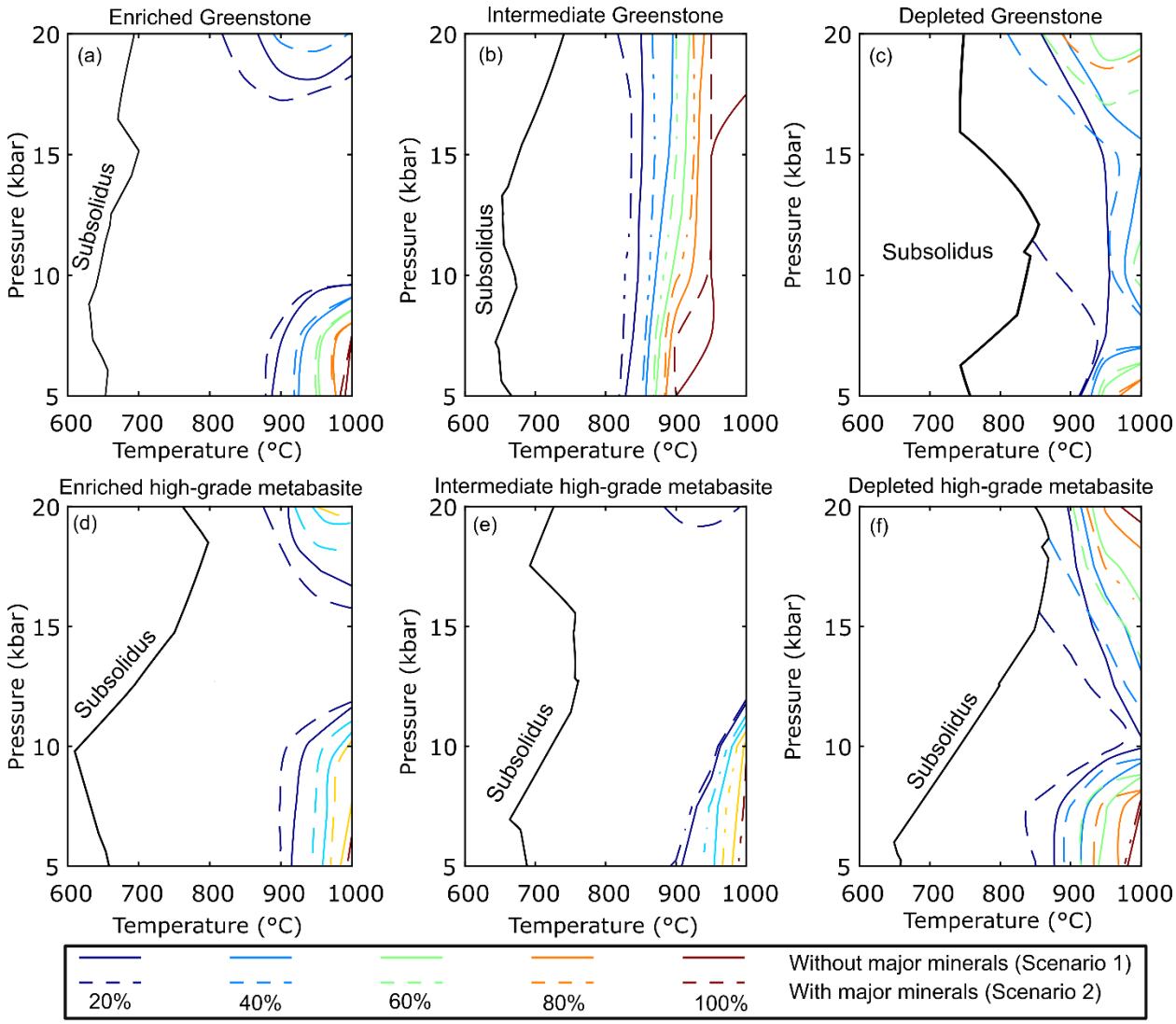
Zircon stability is temperature dependent, and zircon is expected to be completely dissolved at temperatures near 900°C for all modelled compositions and both scenarios (S5-2). For scenario 2 (i.e. Zr distributed in major minerals), zircon is not predicted to be stable for the depleted compositions (S5-2c,f) except at low temperature and pressure for the depleted high-grade metabasite (S5-2f). For intermediate and enriched compositions, the difference for modelled zircon-out contours between Scenario 1 and Scenario 2 can be greater than 200°C. The stability of zircon is comparable between greenstone and high-grade metabasite compositions. In general, the sequestration of Zr in major minerals affects the stability of zircon considerably.

In general, allanite is predicted to be stable at pressures greater than 5.5 kbar and temperatures between 650 and 950°C (S5-3) except for the intermediate greenstone composition

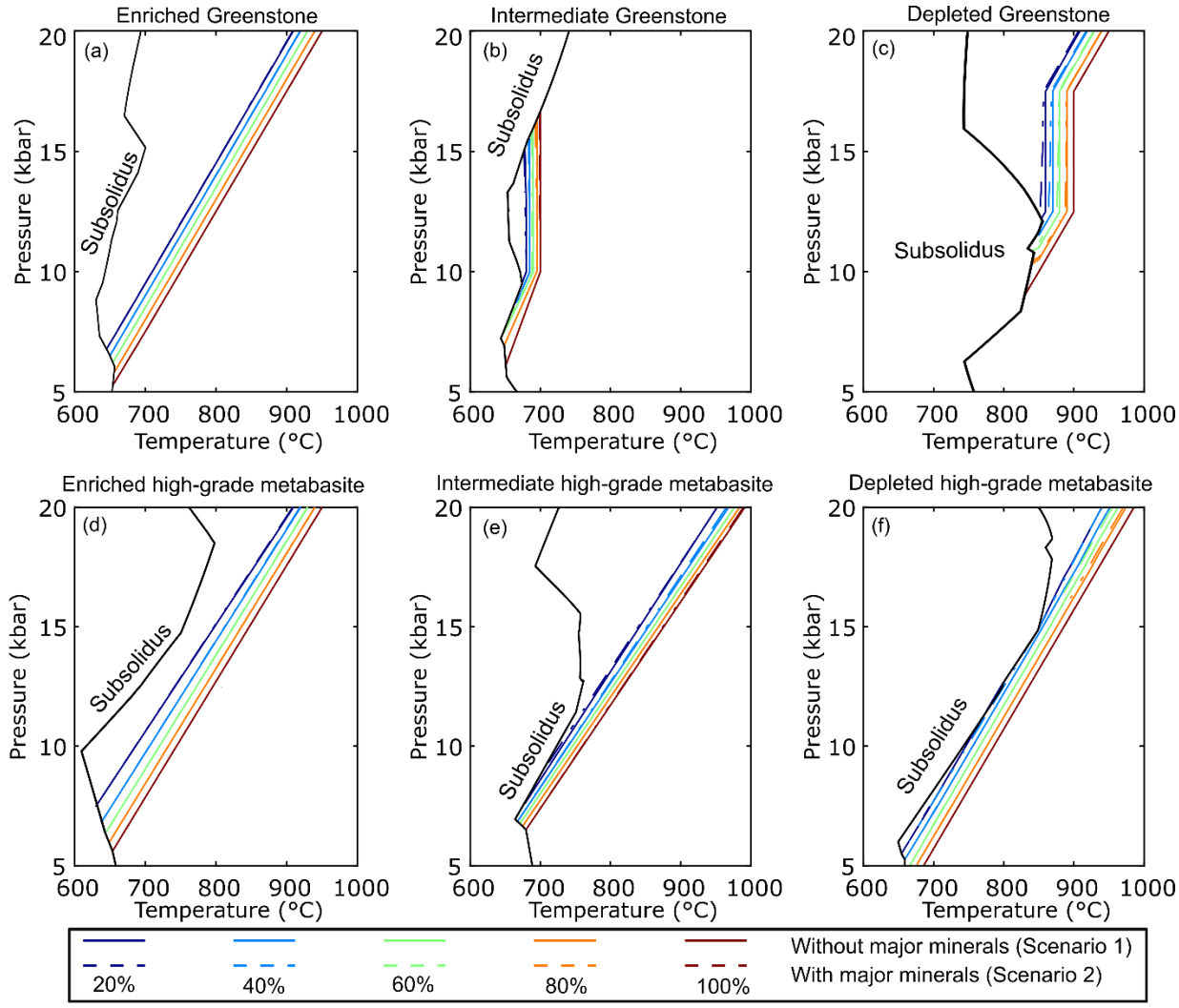
(700°C and 6.5–14 kbar) and is generally predicted to be stable at higher temperatures in the modelled high-grade metabasite compositions compared to the greenstone compositions. Percent dissolved contours are closely spaced and parallel to the allanite (epidote) stability boundary with a positive dP/dT slope for all modelled compositions and both scenarios. However, the melt is predicted to always be supersaturated with LREE; an explanation and implications of this are discussed later. The 100% allanite dissolved contour crosses the solidus at 5.5 kbar and ~650°C and crosses 20 kbar at 950°C (S5-3a). For the intermediate greenstone composition (S5-3b), allanite is restricted to temperatures between the solidus (650–675°C) and 700°C between 5 and 16.5 kbar. Allanite is predicted to be stable above 9.5 kbar at the solidus (~850°C) and temperatures <950°C at 20 kbar for the depleted greenstone composition (S5-3c). For the enriched high-grade metabasite composition, allanite is predicted to be stable above 5 kbar at the solidus (~650°C) and temperatures less than 950°C at 20 kbar (S5-3d). For the intermediate high-grade metabasite composition, the 100% dissolved contour crosses the solidus at 690°C and ~7 kbar with allanite predicted to be stable at greater pressures; at 20 kbar, allanite is predicted to be completely dissolved at temperatures above 985°C (S5-3e). Allanite is predicted to be stable at temperatures below 685°C at 5 kbar and temperatures below 985°C at 20 kbar for the depleted high-grade metabasite composition (S5-3f). The 100% dissolved contour is predicted at higher temperatures for depleted compositions compared to the modelled enriched compositions. However, allanite is predicted to be completely dissolved at lower temperatures for both intermediate greenstone and high-grade metabasite compared to depleted and enriched compositions. In general, the sequestration of LREE in major minerals minimally affects the stability of allanite.



Modelled percentage of zircon dissolved at suprasolidus conditions relative to the amount at the solidus for two scenarios. Percent dissolved contours for zircon with only melt and zircon as Zr reservoirs (solid lines) and when considering trace element partitioning into major minerals (dashed lines) for (a) enriched greenstone, (b) intermediate greenstone, (c) depleted greenstone, (d) enriched high-grade metabasite, (e) intermediate high-grade metabasite, and (f) depleted high-grade metabasite. All contour values are normalized to the amount of zircon in a sample if zircon is the only Zr reservoir. Solidus is marked by the solid black line.



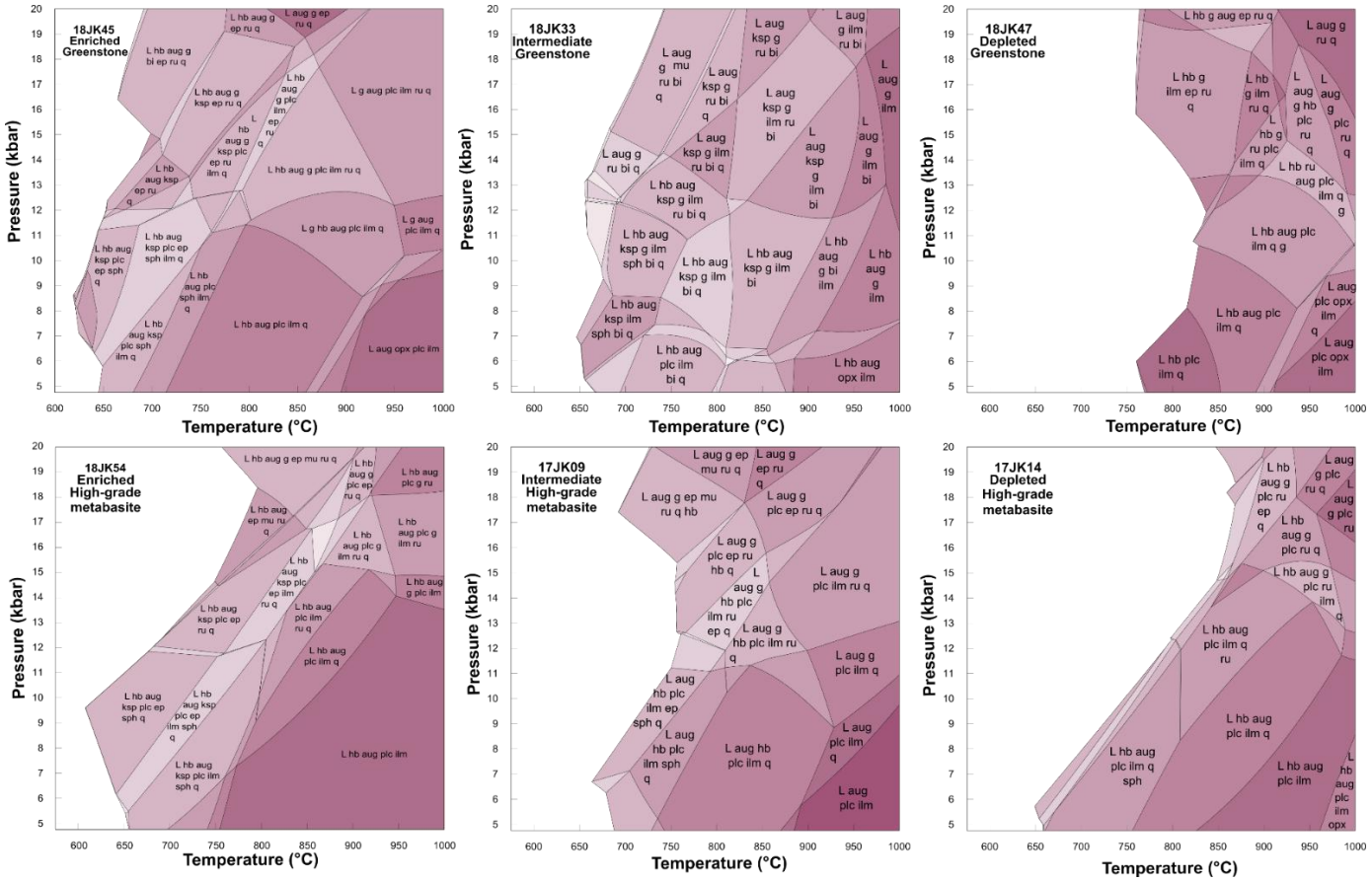
Modelled percentage of apatite dissolved at suprasolidus conditions relative to the amount at the solidus for two scenarios. Percent dissolved contours for apatite with only melt and apatite as P_2O_5 reservoirs (solid lines) and when considering trace element partitioning into major minerals (dashed lines) for (a) enriched greenstone, (b) intermediate greenstone, (c) depleted greenstone, (d) enriched high-grade metabasite, (e) intermediate high-grade metabasite, and (f) depleted high-grade metabasite. All contour values are normalized to the amount of apatite in a sample if apatite is the only P_2O_5 reservoir. The solidus is shown by the solid black line.



Modelled percentage of allanite dissolved at suprasolidus conditions relative to the amount at the solidus for two scenarios. Percent dissolved contours for allanite with only melt and allanite as LREE reservoirs (solid lines) and considering trace element partitioning into major minerals (dashed lines) for (a) enriched greenstone, (b) intermediate greenstone, (c) depleted greenstone, (d) enriched high-grade metabasite, (e) intermediate high-grade metabasite, and (f) depleted high -grade metabasite. All contour values are normalized to the amount of allanite in a sample if allanite is the only LREE reservoir. Solidus is marked by the solid black line. In most diagrams, there is a negligible difference between the results for scenarios 1 and 2.

Appendix S1.9

Non-simplified pseudosections for chapter 2 modelled metabasites



Phase equilibrium modelling results for metabasites from the Kapuskasing uplift. Mineral abbreviations are from Holland and Powell (2011) except for plagioclase (plc).

Appendix S2 (Chapter 3 Supplementary Material)

Appendix S2.1

Limitations and compositions for thermodynamic and trace element modelling

We made several assumptions to compare the natural geologic archive to model results. These relate to the composition and methods for modelling crustal building and the overall simplification of geologic systems. However, these assumptions were necessary to develop a first-order model of heat production of mantle-derived rocks through time.

The activity–composition models used to predict phase stability (Fig. 2) likely have an uncertainty of 50–100°C and 1–2 kbar (Green et al. 2016) which is of similar magnitude to the most uncertain thermodynamic parameter, enthalpy (Powell and Holland 1985, Powell et al. 1998). Furthermore, we use the compositions of KLB-1 (Davis et al. 2009) and Archean Pyrolite (Green 1974) as representative of the modern and ancient mantle. The mantle is heterogenous (Anderson 2006) and mantle composition estimates rely heavily on xenolith samples (Griffin et al. 2009). Nonetheless, as we are studying the effects of average mantle melting and only minor differences between compositions are predicted (Fig. 2), major element variations in mantle source composition probably play a minor role in the heat production in the crust. Crustal differentiation was simulated using the Enriched Archean Tholeiite composition of Condie (1976) which, although simplifies the diverse composition of Archean greenstones (Kendrick and Yakymchuk 2020), does replicate a potential source for tonalite-trondjhemite-granodiorite magmas (Palin et al. 2016).

Mineral–melt partitioning of Th and U is modelled to be constant though mineral and melt composition, pressure, and temperature will affect these distribution coefficients (Salters and Longhi 1999, Green et al. 2000). However, the mineral–melt distribution coefficients of Th and U are not expected to change significantly over the modelled conditions and compositions with experimental and observational data predicting K_d's to be of the order of $1x10^{-4}$ for basaltic magmas (McKenzie and O'Nions 1991b, Beattie 1993, Bédard 2006). Modelled equilibrium of trace elements between minerals and melts disregards compositional zoning in minerals and sluggish diffusion in minerals and melt (Chernoff and Carlson 1999). We also do not consider the complex processes that probably occur in natural systems, such as reactive transport (e.g. Oliveira et al. 2021), magma mixing (Zheng et al. 2020), and grain-scale disequilibrium (e.g. Grose and Afonso 2019). Nonetheless, our equilibrium-based models provide a first-order heat-producing element concentration in the derivatives of mantle melting and we compare these values with the long-term archive of mafic magmatism that represents an integrated product of all the mechanisms that affect melt composition from source to sink.

We use a simplistic scenario of mantle melting and rapid ascent to crustal levels without invoking MASH (melting, assimilation, storage, and homogenization) dynamics, heat loss during ascent, or polybaric melting. MASH processes result in ultramafic cumulates and intermediate to felsic melts (Moyen et al. 2021) and are therefore likely not a major process in the formation of basaltic crust (SiO_2 < 55 wt%). Magma ascent occurs in permeable pathways in the deep crust and through brittle fractures in the shallow crust. This process is rapid (1 to >100 m/year; Stracke et al. 2006), which coupled with the low conductivity of rocks, leads to a near-adiabatic process as long as the magma remains positively buoyant and a pathway is available (Clemens and Mawer 1992). Mantle melting occurs at a variety of depths with basaltic magmas often only

recording the final depth of melting due to quick equilibration during peridotite melting (Niu 2021). With this, we consider our pressure of melting to represent the final depth of melting.

References

Anderson, D.L. 2006. Speculations on the nature and cause of mantle heterogeneity. Tectonophysics, 416: 7–22. doi:10.1016/j.tecto.2005.07.011.

Beattie, P. 1993. The generation of uranium series disequilibria by partial melting of spinel peridotite: constraints from partitioning studies. Earth and Planetary Science Letters, 117: 379–391. doi:10.1016/0012-821X(93)90091-M.

Bédard, J.H. 2006. A catalytic delamination-driven model for coupled genesis of Archaean crust and sub-continental lithospheric mantle. Geochimica et Cosmochimica Acta, 70: 1188–1214. doi:10.1016/j.gca.2005.11.008.

Chernoff, C.B., and Carlson, W.D. 1999. Trace element zoning as a record of chemical disequilibrium during garnet growth. Geology, 27: 555. doi:10.1130/0091-7613(1999)027<0555:TEZAAR>2.3.CO;2.

Clemens, J.D., and Mawer, C.K. 1992. Granitic magma transport by fracture propagation. Tectonophysics, 204: 339–360. doi:10.1016/0040-1951(92)90316-X.

Condie, K. 1976. Trace-element geochemistry of archean greenstone belts. Earth-Science Reviews, 12: 393–417. doi:10.1016/0012-8252(76)90012-X.

Davis, F.A., Tangeman, J.A., Tenner, T.J., and Hirschmann, M.M. 2009. The composition of KLB-1 peridotite. American Mineralogist, 94: 176–180. Mineralogical Society of America. doi:10.2138/am.2009.2984.

Green, D.H. 1974. Genesis of Archean Peridotitic Magmas and Constraints on Archean Geothermal Gradients and Tectonics. Geology,.

Green, E.C.R., White, R.W., Diener, J.F.A., Powell, R., Holland, T.J.B., and Palin, R.M. 2016. Activity-composition relations for the calculation of partial melting equilibria in metabasic rocks. Journal of Metamorphic Geology, 34: 845–869. doi:10.1111/jmg.12211.

Green, T.H., Blundy, J.D., Adam, J., and Yaxley, G.M. 2000. SIMS determination of trace element partition coefficients between garnet, clinopyroxene and hydrous basaltic liquids at 2–7.5 GPa and 1080–1200°C. Lithos, 53: 165–187. doi:10.1016/S0024-4937(00)00023-2.

Griffin, W.L., O'Reilly, S.Y., Afonso, J.C., and Begg, G.C. 2009. The Composition and Evolution of Lithospheric Mantle: a Re-evaluation and its Tectonic Implications. Journal of Petrology, 50: 1185–1204. doi:10.1093/petrology/egn033.

Grose, C.J., and Afonso, J.C. 2019. Chemical Disequilibria, Lithospheric Thickness, and the Source of Ocean Island Basalts. Journal of Petrology, 60: 755–790. doi:10.1093/petrology/egz012.

Kendrick, J., and Yakymchuk, C. 2020. Garnet fractionation, progressive melt loss and bulk composition variations in anatectic metabasites: Complications for interpreting the geodynamic significance of TTGs. Geoscience Frontiers, 11: 745–763. doi:10.1016/j.gsf.2019.12.001.

McKenzie, D., and O'Nions, R.K. 1991. Partial Melt Distributions from Inversion of Rare Earth Element Concentrations. Journal of Petrology, 32: 1021–1091. doi:10.1093/petrology/32.5.1021.

Moyen, J.-F., Janoušek, V., Laurent, O., Bachmann, O., Jacob, J.-B., Farina, F., Fiannacca, P., and Villaros, A. 2021. Crustal melting vs. fractionation of basaltic magmas: Part 1, granites and paradigms. Lithos, 402–403: 106291. doi:10.1016/j.lithos.2021.106291.

Niu, Y. 2021. Lithosphere thickness controls the extent of mantle melting, depth of melt extraction and basalt compositions in all tectonic settings on Earth – A review and new perspectives. Earth-Science Reviews, 217: 103614. doi:10.1016/j.earscirev.2021.103614.

Oliveira, B., Afonso, J.C., and Tilhac, R. 2021. A Disequilibrium Reactive Transport Model for Mantle Magmatism. Journal of Petrology, 61: egaa067. doi:10.1093/petrology/egaa067.

Palin, R.M., White, R.W., and Green, E.C.R. 2016. Partial melting of metabasic rocks and the generation of tonalitic–trondhjemitic–granodioritic (TTG) crust in the Archaean: Constraints from phase equilibrium modelling. Precambrian Research, 287: 73–90. doi:10.1016/j.precamres.2016.11.001.

Powell, R., Holland, T., and Worley, B. 1998. Calculating phase diagrams involving solid solutions via non-linear equations, with examples using THERMOCALC. Journal of Metamorphic Geology, 16: 577–588.

Powell, R., and Holland, T.J.B. 1985. An internally consistent thermodynamic dataset with uncertainties and correlations: 1. Methods and a worked example. Journal of Metamorphic Geology, 3.

Salters, V.J.M., and Longhi, J. 1999. Trace element partitioning during the initial stages of melting beneath mid-ocean ridges. Earth and Planetary Science Letters, 166: 15–30.

Stracke, A., Bourdon, B., and Mckenzie, D. 2006. Melt extraction in the Earth's mantle: Constraints from U–Th–Pa–Ra studies in oceanic basalts. Earth and Planetary Science Letters, 244: 97–112. doi:10.1016/j.epsl.2006.01.057.

Zheng, Y.-F., Xu, Z., Chen, L., Dai, L.-Q., and Zhao, Z.-F. 2020. Chemical geodynamics of mafic magmatism above subduction zones. Journal of Asian Earth Sciences, 194: 104185. doi:10.1016/j.jseaes.2019.104185.

Appendix S2.2

Compositions for crustal formation and differentiation

Supplemental Table 2.2.1: Compositions for models presented in Figure 3.3. Values are mol% except for U and Th (mg/kg). KLB-1 (Davis et al., 2009) and Archean Pyrolite (Greens, 1975) are used as representative modern and ancient mantle compositions respectively whereas Enriched Archean Pyrolite (Condie, 1976) simulates source material for Archean tonalite-trondhjemite-granodiorite packages. Mantle trace elements are from (McDonough and Sun, 1995).

	H_2O	Na_2O	MgO	Al_2O_3	SiO_2	K_2O	CaO	FeO	TiO_2	O_2	Cr_2O_3	U	Th
KLB-1	-	0.25	50.80	1.78	38.67	0.01	2.84	5.32	0.07	0.15	0.11	0.02	0.08
Archean Pyrolite	-	0.30	48.65	2.01	38.92	0.07	3.46	6.13	0.13	0.17	0.17	0.02	0.08
Enriched Archean Tholeiite	5.67	2.31	10.66	9.96	56.39	0.23	11.43	7.59	0.85	0.54	-	0.18	0.6

Appendix S3 (Chapter 4 Supplementary Material)

Appendix S3.1

Compilation of natural A-type granite compositions for chapter 4

Source	Locality	Zr	Sample #	SiO_2	Al_2O_3	FeO(t)	MnO	MgO	CaO	Na_2O	K_2O	TiO2	P_2O_5	Total	M Value
	Unit	*mg/kg*		*wt%*	*wt%*	*wt%*	*wt%*	*wt%*	*wt%*	*wt%*	*wt%*	*wt%*	*wt%*	*wt%*	
Clemens et al. 1986	Watergums Granite	472	GIG-1	73.60	12.44	1.28	0.08	0.27	1.24	3.53	4.23	0.34	0.07	97.08	1.41
Yadav et al. 2020	Madanmahal Granite	994	IG-1	72.87	12.71	2.50	0.02	0.18	1.26	2.53	5.42	0.13	0.02	97.64	1.34
Yadav et al. 2020	Madanmahal Granite	281	IG-2	74.08	13.10	2.05	0.02	0.16	0.99	2.66	5.48	0.14	0.02	98.70	1.28
Yadav et al. 2020	Madanmahal Granite	500	IG-3	74.43	12.56	2.14	0.03	0.19	1.02	2.65	5.58	0.14	0.02	98.76	1.34
Yadav et al. 2020	Madanmahal Granite	360	IG-5	75.96	13.01	2.04	0.02	0.17	0.77	2.44	5.63	0.13	0.02	100.19	1.21
Yadav et al. 2020	Madanmahal Granite	334	IG-6	74.03	12.88	2.04	0.03	0.07	1.08	2.65	5.55	0.14	0.02	98.49	1.33
Yadav et al. 2020	Madanmahal Granite	654	IG-7	70.83	13.64	2.88	0.03	0.29	1.45	2.59	5.42	0.31	0.06	97.50	1.33
Yadav et al. 2020	Madanmahal Granite	540	IG-8	70.01	13.40	3.07	0.04	0.33	1.57	2.55	5.47	0.34	0.05	96.83	1.37
Yadav et al. 2020	Madanmahal Granite	435	IG-9	74.68	12.62	2.06	0.04	0.06	1.01	2.57	5.65	0.15	0.02	98.86	1.33
Yadav et al. 2020	Madanmahal Granite	500	IG-10	72.08	13.63	2.54	0.03	0.22	1.40	2.60	5.50	0.21	0.04	98.25	1.32
Yadav et al. 2020	Madanmahal Granite	339	IG-11	73.75	12.89	2.02	0.03	0.07	1.11	2.63	5.69	0.15	0.02	98.36	1.35
Yadav et al. 2020	Madanmahal Granite	353	IG-12	73.66	13.58	1.43	0.02	0.09	1.07	2.58	5.88	0.13	0.03	98.47	1.30
Yadav et al. 2020	Madanmahal Granite	393	IG-13	73.81	12.79	2.06	0.03	0.09	1.18	2.64	5.47	0.15	0.03	98.25	1.34
Yadav et al. 2020	Madanmahal Granite	519	IG-14	73.09	13.29	1.77	0.02	0.08	1.29	2.64	5.61	0.08	0.01	97.88	1.35
Yadav et al. 2020	Madanmahal Granite	751	IG-16	71.50	13.17	2.91	0.03	0.32	1.23	2.46	5.57	0.31	0.09	97.59	1.31
Yadav et al. 2020	Madanmahal Granite	722	IG-17	70.73	13.51	3.48	0.04	0.45	1.70	2.53	5.39	0.34	0.10	98.27	1.37
Yadav et al. 2020	Madanmahal Granite	492	IG-18	71.92	13.42	3.18	0.04	0.40	1.39	2.52	5.63	0.34	0.12	98.96	1.34
Yadav et al. 2020	Madanmahal Granite	356	IG-19	74.44	13.02	1.72	0.03	0.09	1.12	2.52	5.84	0.13	0.02	98.93	1.33
Yadav et al. 2020	Madanmahal Granite	485	IG-20	74.28	13.26	2.02	0.03	0.09	1.03	2.64	5.64	0.16	0.02	99.17	1.29
Yadav et al. 2020	Madanmahal Granite	795	IG-21	70.30	13.52	3.45	0.03	0.41	1.58	2.49	5.48	0.35	0.10	97.71	1.35
Yadav et al. 2020	Madanmahal Granite	680	IG-22	69.59	13.68	3.68	0.03	0.46	1.77	2.51	5.36	0.38	0.10	97.56	1.37
Yadav et al. 2020	Madanmahal Granite	971	IG-24	72.84	13.07	2.18	0.04	0.08	1.31	2.62	5.53	0.16	0.02	97.85	1.36
Yadav et al. 2020	Madanmahal Granite	496	IG-25	74.46	13.13	1.96	0.03	0.12	1.19	2.59	5.87	0.17	0.02	99.54	1.36
Yadav et al. 2020	Madanmahal Granite	385	IG-26	73.14	13.12	2.27	0.04	0.09	1.11	2.63	5.59	0.18	0.02	98.19	1.32
Yadav et al. 2020	Madanmahal Granite	408	IG-27	73.20	12.78	2.16	0.04	0.06	1.21	2.60	5.58	0.17	0.02	97.82	1.36
Yadav et al. 2020	Madanmahal Granite	548	IG-28	73.60	12.43	2.13	0.04	0.07	1.30	2.53	5.47	0.14	0.02	97.73	1.38
Yadav et al. 2020	Pink Sidhi Granites	499	BG-1	76.30	12.98	1.43	0.02	0.15	0.85	2.51	5.68	0.16	0.01	100.09	1.25
Yadav et al. 2020	Pink Sidhi Granites	594	BG-2	74.17	13.65	1.76	0.02	0.28	1.09	2.61	5.53	0.26	0.04	99.41	1.25
Yadav et al. 2020	Pink Sidhi Granites	489	BG-3	74.94	13.53	1.63	0.02	0.25	1.09	2.62	5.49	0.23	0.04	99.84	1.26
Yadav et al. 2020	Pink Sidhi Granites	433	BG-4	74.31	13.30	1.73	0.03	0.27	1.13	2.63	5.50	0.20	0.03	99.13	1.29
Yadav et al. 2020	Pink Sidhi Granites	459	BG-5	75.13	13.35	1.56	0.02	0.23	1.07	2.65	5.51	0.21	0.03	99.76	1.27
Yadav et al. 2020	Pink Sidhi Granites	435	BG-6	74.73	13.42	1.39	0.04	0.21	1.08	2.68	5.67	0.23	0.01	99.46	1.30
Yadav et al. 2020	Pink Sidhi Granites	475	BG-7	77.23	13.00	1.25	0.01	0.11	0.83	2.55	5.72	0.07	0.01	100.78	1.25
Yadav et al. 2020	Pink Sidhi Granites	310	BG-8	77.87	13.04	1.19	0.01	0.09	0.82	2.61	5.74	0.05	0.01	101.43	1.26
Yadav et al. 2020	Pink Sidhi Granites	393	BG-9	76.91	12.90	1.35	0.01	0.13	0.84	2.59	5.81	0.08	0.01	100.63	1.28
Yadav et al. 2020	Pink Sidhi Granites	381	BG-10	76.90	12.79	1.30	0.01	0.14	0.88	2.52	5.65	0.16	0.01	100.36	1.27
Yadav et al. 2020	Grey Sidhi Granites	539	BG-14	67.38	13.72	4.64	0.07	0.63	2.00	2.66	5.59	0.43	0.16	97.28	1.49
Yadav et al. 2020	Grey Sidhi Granites	483	BG-15	70.15	13.18	3.96	0.04	0.39	1.42	2.67	5.63	0.25	0.06	97.75	1.41
Yadav et al. 2020	Grey Sidhi Granites	597	BG-16	67.03	13.86	4.45	0.07	0.59	2.13	2.51	5.57	0.42	0.16	96.79	1.47
Yadav et al. 2020	Grey Sidhi Granites	617	BG-17	68.18	13.67	4.51	0.07	0.58	1.98	2.46	5.56	0.44	0.16	97.61	1.44
Yadav et al. 2020	Grey Sidhi Granites	690	BG-18	66.07	13.94	4.64	0.08	0.64	1.93	2.64	5.58	0.45	0.16	96.13	1.46
Yadav et al. 2020	Grey Sidhi Granites	630	BG-19	66.64	13.70	4.45	0.07	0.56	1.87	2.58	5.62	0.44	0.17	96.10	1.46
Yadav et al. 2020	Grey Sidhi Granites	629	BG-20	68.22	13.62	4.74	0.08	0.58	1.96	2.49	5.67	0.45	0.17	97.98	1.46
Yadav et al. 2020	Grey Sidhi Granites	764	BG-21	69.62	13.23	3.46	0.06	0.61	1.80	2.64	5.55	0.40	0.17	97.54	1.47
Yadav et al. 2020	Grey Sidhi Granites	613	BG-22	68.68	13.43	3.08	0.06	0.54	1.78	2.61	5.67	0.34	0.14	96.33	1.46
Yadav et al. 2020	Grey Sidhi Granites	563	BG-23	68.51	13.69	2.70	0.05	0.45	1.64	2.73	5.59	0.30	0.14	95.80	1.42
Yadav et al. 2020	Grey Sidhi Granites	639	BG-24	68.11	13.68	3.10	0.05	0.51	1.88	2.58	5.62	0.36	0.14	96.03	1.45

	Unit	*mg/kg*		*wt%*	*wt%*	*wt%*	*wt%*	*wt%*	*wt%*	*wt%*	*wt%*	*wt%*	*wt%*	*wt%*	
Source	**Locality**	**Zr**	**Sample #**	**SiO_2**	**Al_2O_3**	**FeO(t)**	**MnO**	**MgO**	**CaO**	**Na_2O**	**K_2O**	**TiO2**	**P_2O_5**	**Total**	**M Value**
Yadav et al. 2020	Grey Sidhi Granites	577	BG-25	69.97	13.72	3.19	0.06	0.54	1.95	2.70	5.53	0.37	0.14	98.17	1.46
Yadav et al. 2020	Grey Sidhi Granites	616	BG-26	66.14	13.86	4.52	0.08	0.87	2.25	2.46	5.74	0.59	0.21	96.72	1.52
Yadav et al. 2020	Grey Sidhi Granites	974	BG-27	68.91	13.16	4.01	0.08	0.73	1.89	2.42	5.71	0.59	0.21	97.71	1.48
Yadav et al. 2020	Grey Sidhi Granites	538	BG-28	70.89	13.01	2.40	0.05	0.33	1.72	2.43	5.58	0.32	0.09	96.82	1.43
Yadav et al. 2020	Grey Sidhi Granites	611	BG-29	65.30	13.95	5.18	0.08	0.72	2.35	2.56	5.44	0.61	0.20	96.39	1.52
Yadav et al. 2020	Grey Sidhi Granites	805	BG-31	65.63	13.78	5.09	0.09	0.73	2.33	2.50	5.43	0.58	0.22	96.38	1.51
Yadav et al. 2020	Grey Sidhi Granites	814	BG-32	64.47	13.88	5.58	0.08	0.91	2.19	2.55	5.39	0.70	0.16	95.91	1.49
Yadav et al. 2020	Grey Sidhi Granites	397	MSB/G/28	72.87	12.80	2.02	0.03	0.29	1.24	2.77	5.60	0.24	0.06	97.92	1.40
Yadav et al. 2020	Grey Sidhi Granites	344	MSB/G/29	72.88	12.68	1.93	0.03	0.29	1.21	2.62	5.67	0.26	0.05	97.62	1.39
Yadav et al. 2020	Grey Sidhi Granites	568	MSB/G/30	70.59	13.22	2.95	0.04	0.39	1.44	2.55	5.85	0.34	0.08	97.45	1.41
Teixeira et al 2017	Gongo da Onca Granite	577	PFA-22	64.20	15.60	5.54	0.09	0.66	4.01	3.60	3.22	0.76	0.27	97.95	1.63
Teixeira et al 2017	Gongo da Onca Granite	510	PFR-18B	64.22	15.81	5.20	0.08	0.59	4.19	3.76	3.14	0.68	0.26	97.93	1.67
Teixeira et al 2017	Gongo da Onca Granite	559	PFA-21A	64.59	15.33	5.51	0.08	0.65	4.29	3.55	3.29	0.72	0.27	98.28	1.71
Teixeira et al 2017	Gongo da Onca Granite	752	PFR-19A	64.85	14.68	5.69	0.09	0.61	3.73	3.37	3.64	0.69	0.26	97.61	1.66
Teixeira et al 2017	Gongo da Onca Granite	766	PFR-18A	67.04	14.14	5.20	0.08	0.52	3.34	3.49	3.90	0.69	0.23	98.63	1.68
Teixeira et al 2017	Gongo da Onca Granite	563	PFR-22	68.06	14.06	4.34	0.07	0.43	3.10	3.27	3.81	0.51	0.16	97.81	1.57
Teixeira et al 2017	Gongo da Onca Granite	658	PFR-20	68.93	13.63	4.49	0.06	0.38	2.70	3.14	4.26	0.51	0.15	98.25	1.55
Teixeira et al 2017	Gongo da Onca Granite	437	PFA-21B	71.57	12.34	3.93	0.06	0.13	1.46	2.78	5.20	0.23	0.03	97.73	1.45
Teixeira et al 2017	Gongo da Onca Granite	496	PFR-19B	72.75	12.18	3.55	0.05	0.19	1.43	2.73	5.03	0.27	0.05	98.23	1.42
Teixeira et al 2017	Gongo da Onca Granite	350	PFR-21	73.50	12.14	3.08	0.04	0.09	1.20	2.74	5.08	0.17	0.02	98.06	1.38
Xu et al. 2020	Songnen Block	158	BQH-1	61.69	16.53	4.08	0.09	2.80	3.94	4.51	2.68	0.56	0.24	97.11	1.67
Xu et al. 2020	Songnen Block	149	BQH-10	77.13	12.22	0.51	0.01	0.09	0.18	4.10	4.72	0.09	0.02	99.07	1.37
Xu et al. 2020	Songnen Block	152	BQH-11	77.05	12.67	0.72	0.00	0.20	0.11	3.67	4.65	0.10	0.02	99.18	1.21
Xu et al. 2020	Songnen Block	143	BQH-12	76.85	12.87	0.70	0.01	0.10	0.25	4.27	4.09	0.09	0.02	99.24	1.27
Xu et al. 2020	Songnen Block	145	BQH-13	77.05	12.55	0.70	0.01	0.13	0.22	4.08	4.56	0.09	0.02	99.41	1.32
Xu et al. 2020	Songnen Block	149	BQH-14	77.23	12.21	1.04	0.01	0.08	0.12	3.89	4.55	0.09	0.01	99.24	1.29
Xu et al. 2020	Songnen Block	120	BQH-15	77.12	12.21	0.65	0.01	0.06	0.12	4.05	4.38	0.07	0.02	98.68	1.30
Xu et al. 2020	Songnen Block	161	BQH-16	76.77	12.16	0.94	0.01	0.10	0.11	4.11	4.31	0.10	0.02	98.61	1.30
Xu et al. 2020	Songnen Block	128	BQH-17	76.07	12.40	1.07	0.01	0.17	0.16	3.68	4.15	0.09	0.01	97.81	1.19
Xu et al. 2020	Songnen Block	154	BQH-19	62.28	16.50	3.04	0.06	1.89	1.84	4.72	3.51	0.46	0.20	94.50	1.41
Xu et al. 2020	Songnen Block	148	BQH-2	62.22	16.31	4.08	0.10	2.92	3.45	4.60	2.75	0.58	0.24	97.25	1.62
Xu et al. 2020	Songnen Block	208	BQH-20	60.02	16.21	4.35	0.08	2.92	3.59	3.82	3.22	0.57	0.21	94.99	1.58
Xu et al. 2020	Songnen Block	154	BQH-21	62.06	16.71	4.00	0.08	2.99	2.57	5.61	1.60	0.58	0.25	96.43	1.47
Xu et al. 2020	Songnen Block	156	BQH-22	60.67	16.30	4.80	0.07	2.85	2.30	5.29	2.32	0.55	0.24	95.37	1.49
Xu et al. 2020	Songnen Block	150	BQH-3	61.43	16.64	3.85	0.09	2.46	3.90	4.21	2.82	0.60	0.25	96.25	1.62
Xu et al. 2020	Songnen Block	136	BQH-4	62.56	16.42	3.65	0.06	2.58	2.45	5.12	2.29	0.50	0.18	95.81	1.45
Xu et al. 2020	Songnen Block	139	BQH-5	62.25	16.48	3.95	0.06	2.59	2.40	4.93	2.07	0.50	0.19	95.41	1.38
Xu et al. 2020	Songnen Block	150	BQH-6	62.74	16.46	3.16	0.07	2.86	2.11	4.12	3.03	0.51	0.14	95.19	1.30
Xu et al. 2020	Songnen Block	158	BQH-9	77.22	11.75	0.94	0.01	0.15	0.08	3.71	4.79	0.10	0.02	98.76	1.32
Li et al 2018	Wagone granite	71	W1	79.84	10.96	0.57	0.02	0.06	0.25	2.39	5.11	0.03	0.00	99.23	1.18
Li et al 2018	Wagone granite	178	W2	82.53	7.81	3.45	0.19	0.16	0.60	1.05	2.66	0.10	0.00	98.55	0.86
Li et al 2018	Wagone granite	72	W3	75.62	12.92	0.79	0.05	0.07	0.58	2.91	5.76	0.05	0.01	98.76	1.29
Li et al 2018	Wagone granite	93	W4	75.51	12.78	1.25	0.08	0.08	0.86	3.33	4.76	0.06	0.01	98.72	1.31
Li et al 2018	Wagone granite	75	W5	77.20	12.46	0.87	0.06	0.08	0.86	3.19	4.79	0.05	0.00	99.56	1.31
Li et al 2018	Wagone granite	78	W6	76.12	12.77	1.16	0.10	0.06	0.72	3.53	4.57	0.05	0.00	99.08	1.30
Li et al 2018	Wagone granite	35	W7	75.15	13.10	0.66	0.38	0.05	0.47	2.63	6.45	0.02	0.00	98.91	1.29
Li et al 2018	Wagone granite	80	W8	76.91	12.33	1.05	0.09	0.06	0.68	3.15	4.67	0.05	0.01	99.00	1.26

	Unit	*mg/kg*		*wt%*	*wt%*	*wt%*	*wt%*	*wt%*	*wt%*	*wt%*	*wt%*	*wt%*	*wt%*	*wt%*	
Source	**Locality**	**Zr**	**Sample #**	**SiO_2**	**Al_2O_3**	**FeO(t)**	**MnO**	**MgO**	**CaO**	**Na_2O**	**K_2O**	**TiO2**	**P_2O_5**	**Total**	**M Value**
Li et al 2018	Hermyingyi Granite	80	H1	76.50	12.54	0.99	0.31	0.03	0.56	4.24	4.35	0.02	0.01	99.55	1.40
Li et al 2018	Hermyingyi Granite	70	H2	77.15	11.25	1.21	0.27	0.02	0.43	3.16	3.87	0.02	0.01	97.39	1.19
Mesquita et al. 2017	Southern Ribeira Belt	871	506A	71.40	11.69	4.25	0.09	0.44	1.52	2.03	5.30	0.61	0.12	97.46	1.38
Mesquita et al. 2017	Southern Ribeira Belt	707	506C	66.23	14.88	4.04	0.08	0.37	1.65	2.99	6.76	0.42	0.11	97.53	1.55
Mesquita et al. 2017	Southern Ribeira Belt	879	506D	66.76	12.95	6.35	0.07	0.55	2.18	2.78	5.23	0.72	0.23	97.82	1.58
Mesquita et al. 2017	Southern Ribeira Belt	865	506F	66.69	12.76	6.39	0.07	0.56	2.27	2.83	5.08	0.71	0.22	97.59	1.61
Zhao et al. 2013	Caijiang granite	263	08TS-46A	61.46	18.41	3.30	0.06	0.67	1.20	5.69	6.46	0.62	0.28	98.15	1.70
Zhao et al. 2013	Caijiang granite	263	08TS-47A	65.90	15.22	3.39	0.06	0.79	1.49	3.43	6.34	0.60	0.26	97.48	1.52
Zhao et al. 2013	Caijiang granite	259	08TS-47B	67.34	13.98	3.67	0.07	0.79	1.90	4.45	3.95	0.70	0.27	97.12	1.59
Zhao et al. 2013	Caijiang granite	458	08TS-48	59.11	17.04	4.61	0.08	1.09	2.52	6.30	4.07	0.88	0.35	96.05	1.91
Zhao et al. 2013	Caijiang granite	215	09TS-18	69.72	14.97	2.28	0.08	0.49	1.14	2.86	6.80	0.39	0.17	98.90	1.39
Zhao et al. 2013	Caijiang granite	293	09TS-20	69.62	14.04	3.25	0.06	0.74	1.16	3.13	5.41	0.50	0.25	98.16	1.35
Zhao et al. 2013	Gaoxi granite	250	08GX-20	68.55	14.43	2.47	0.04	0.79	1.18	3.34	5.64	0.50	0.14	97.08	1.40
Zhao et al. 2013	Gaoxi granite	250	08GX-25	70.90	14.13	2.56	0.04	0.58	0.30	3.32	5.40	0.49	0.13	97.85	1.20
Zhao et al. 2013	Gaoxi granite	314	1*	69.90	13.90	3.35	0.64	0.63	0.84	3.28	5.51	0.27	0.11	98.43	1.33
Zhao et al. 2013	Gaoxi granite	240	2*	68.50	14.90	3.87	0.09	1.22	2.24	2.49	5.32	0.66	0.16	99.45	1.37
Yang et al 2012	Yangmeiwan granite	260	XL-5	75.89	12.57	1.17	0.04	0.07	0.89	3.44	5.02	0.09	0.05	99.23	1.40
Yang et al 2012	Yangmeiwan granite	175	XL-6	76.66	12.34	1.02	0.03	0.09	0.69	3.69	4.40	0.07	0.04	99.03	1.34
Yang et al 2012	Yangmeiwan granite	191	XL-7	77.21	12.94	0.76	0.02	0.13	0.16	3.51	4.42	0.08	0.05	99.28	1.14
Yang et al 2012	Yangmeiwan granite	174	XL-8	76.50	12.08	1.22	0.05	0.11	0.86	3.57	4.33	0.07	0.05	98.84	1.37
Yang et al 2012	Yangmeiwan granite	220	XL-11	75.24	13.23	1.29	0.05	0.12	0.47	3.42	5.61	0.11	0.07	99.61	1.33
Yang et al 2012	Yangmeiwan granite	224	XL-12	74.93	12.84	1.30	0.06	0.07	0.81	3.48	5.11	0.09	0.06	98.75	1.38
Yang et al 2012	Yangmeiwan granite	175	XL-13	76.23	12.58	1.14	0.04	0.06	0.73	3.46	4.91	0.07	0.06	99.28	1.35
Yang et al 2012	Yangmeiwan granite	196	XL-15	75.43	12.84	1.23	0.04	0.06	0.83	3.31	5.31	0.10	0.07	99.22	1.37
Yang et al 2012	Yangmeiwan granite	378	XL 16-16	70.14	12.66	3.86	0.22	0.31	1.69	0.23	7.68	0.27	0.09	97.15	1.29
Yang et al 2012	Yangmeiwan granite	362	XL-16-17	72.79	12.91	2.47	0.09	0.23	1.49	0.95	6.64	0.25	0.09	97.91	1.22
Yang et al 2012	Yangmeiwan granite	423	XL-16-18	70.83	12.75	2.68	0.09	0.24	1.88	2.57	5.94	0.29	0.10	97.37	1.57
Yang et al 2012	Yangmeiwan granite	413	XL-16-19	70.81	13.45	2.46	0.07	0.26	1.48	2.62	6.26	0.25	0.09	97.75	1.47
Yang et al 2012	Yangmeiwan granite	441	XK-16-20	70.24	13.18	2.59	0.08	0.20	2.15	2.71	5.45	0.27	0.10	96.97	1.55
Yang et al 2012	Yangmeiwan granite	512	XL-16-21	70.41	12.87	2.53	0.08	0.21	1.96	2.42	5.97	0.33	0.10	96.88	1.55
Yang et al 2012	Yangmeiwan granite	271	XL-17-1	74.78	12.09	1.92	0.22	0.22	1.05	0.66	6.60	0.18	0.08	97.80	1.12
Yang et al 2012	Yangmeiwan granite	270	XL-17-2	74.52	11.17	1.70	0.08	0.20	1.89	1.16	6.18	0.14	0.07	97.11	1.44
Yang et al 2012	Yangmeiwan granite	298	XL-17-3	73.49	12.76	1.94	0.10	0.21	1.44	1.49	5.97	0.19	0.07	97.66	1.24
Yang et al 2012	Yangmeiwan granite	340	XL-17-4	71.74	12.23	2.42	0.15	0.27	2.08	1.49	6.30	0.22	0.08	96.98	1.48
Yang et al 2012	Yangmeiwan granite	347	XL-17-8	72.01	13.32	2.25	0.10	0.28	1.76	2.33	5.59	0.24	0.10	97.98	1.38
Yang et al 2012	Daqiaowu Granite	368	DQW-1-1	69.15	13.82	2.78	0.06	0.50	1.68	3.46	6.04	0.36	0.05	97.90	1.63
Yang et al 2012	Daqiaowu Granite	351	DQW-1-2	69.18	13.84	2.75	0.07	0.52	1.74	3.38	5.99	0.36	0.05	97.88	1.61
Yang et al 2012	Daqiaowu Granite	255	DQW-2-1	71.00	13.18	2.00	0.08	0.40	1.67	1.61	7.21	0.22	0.01	97.38	1.45
Yang et al 2012	Daqiaowu Granite	250	DQW-2-2	71.76	12.85	2.04	0.07	0.44	1.41	1.49	7.11	0.22	0.01	97.40	1.38
Yang et al 2012	Daqiaowu Granite	204	DQW-3-1	74.50	11.88	1.47	0.07	0.43	0.97	0.42	7.15	0.16	0.00	97.05	1.15
Yang et al 2012	Daqiaowu Granite	194	DQW3-2	72.84	11.87	1.72	0.10	0.45	1.71	0.40	7.10	0.14	0.00	96.33	1.30
Yang et al 2012	Daqiaowu Granite	203	DQW-3-3	73.19	11.75	1.83	0.11	0.44	1.65	0.39	6.94	0.15	0.00	96.45	1.28
Rao and Reddy 2007	Kanigiri granite	350	1	72.85	12.80	2.47	0.06	0.11	0.97	4.01	4.79	0.14	0.00	98.20	1.49
Rao and Reddy 2007	Kanigiri granite	290	2	72.17	13.00	2.31	0.04	0.01	0.92	3.63	5.58	0.16	0.01	97.83	1.50
Rao and Reddy 2007	Kanigiri granite	330	3	72.20	13.09	2.61	0.05	0.05	0.96	3.82	5.04	0.13	0.00	97.95	1.46
Rao and Reddy 2007	Kanigiri granite	220	4	74.46	12.44	2.25	0.05	0.00	0.68	3.39	5.14	0.13	0.00	98.54	1.38
Rao and Reddy 2007	Kanigiri granite	225	5	73.19	12.68	2.16	0.04	0.00	0.85	3.68	5.08	0.13	0.00	97.81	1.45

	Unit	*mg/kg*		*wt%*	*wt%*	*wt%*	*wt%*	*wt%*	*wt%*	*wt%*	*wt%*	*wt%*	*wt%*	*wt%*	
Source	**Locality**	**Zr**	**Sample #**	**SiO_2**	**Al_2O_3**	**FeO(t)**	**MnO**	**MgO**	**CaO**	**Na_2O**	**K_2O**	**TiO2**	**P_2O_5**	**Total**	**M Value**
Rao and Reddy 2007	Kanigiri granite	220	6	73.52	12.22	2.03	0.04	0.01	0.88	3.46	5.12	0.13	0.00	97.41	1.46
Rao and Reddy 2007	Kanigiri granite	280	7	74.17	12.71	1.55	0.04	0.00	0.63	4.12	4.60	0.40	0.05	98.27	1.42
Rao and Reddy 2007	Kanigiri granite	130	8	71.66	13.77	2.53	0.07	0.03	0.91	3.88	5.57	0.16	0.00	98.58	1.48
Rao and Reddy 2007	Kanigiri granite	325	9	74.05	12.60	2.17	0.05	0.00	0.90	4.28	4.20	0.15	0.00	98.40	1.47
Rao and Reddy 2007	Kanigiri granite	275	10	68.95	14.31	3.10	0.08	0.04	1.07	4.50	5.73	0.19	0.02	97.99	1.62
Rao and Reddy 2007	Kanigiri granite	445	11												
Rao and Reddy 2007	Kanigiri granite	425	12												
Rao and Reddy 2007	Kanigiri granite	450	13												
Rao and Reddy 2007	Kanigiri granite	535	14												
Rao and Reddy 2007	Kanigiri granite	530	15												
Rao and Reddy 2007	Kanigiri granite	370	16	71.29	13.80	2.56	0.06	0.04	0.99	4.16	5.33	0.16	0.08	98.47	1.52
Rao and Reddy 2007	Kanigiri granite	270	17												
Rao and Reddy 2007	Kanigiri granite	220	18	72.78	12.46	1.92	0.03	0.00	0.75	3.49	5.28	0.11	0.01	96.83	1.44
Rao and Reddy 2007	Kanigiri granite	330	19	70.60	13.48	3.37	0.08	0.02	1.42	4.13	4.84	0.21	0.01	98.16	1.57
Rao and Reddy 2007	Kanigiri granite	245	20	73.14	12.50	2.66	0.04	0.02	0.84	3.42	5.18	0.16	0.00	97.96	1.42
Rao and Reddy 2007	Kanigiri granite	430	21	68.79	13.61	2.82	0.06	0.00	1.03	4.23	5.59	0.16	0.05	96.34	1.61
Rao and Reddy 2007	Kanigiri granite	395	22	71.41	13.92	3.41	0.07	0.00	0.88	4.16	5.70	0.16	0.03	99.74	1.53
Rao and Reddy 2007	Kanigiri granite	530	23	72.76	14.62	2.22	0.10	0.00	1.27	4.51	4.57	0.23	0.02	100.30	1.46
Rao and Reddy 2007	Kanigiri granite	350	24	70.92	14.11	3.01	0.06	0.00	0.86	4.43	5.10	0.13	0.00	98.62	1.49
Rao and Reddy 2007	Kanigiri granite	660	25	68.32	13.68	3.01	0.08	0.00	1.11	3.82	5.82	0.18	0.00	96.02	1.57
Rao and Reddy 2007	Kanigiri granite	545	26	69.28	13.36	3.26	0.10	0.02	1.11	4.26	5.24	0.20	0.00	96.83	1.61
Rao and Reddy 2007	Kanigiri granite	185	27	73.87	12.98	1.59	0.03	0.01	0.48	4.40	4.42	0.05	0.00	97.83	1.40
Rao and Reddy 2007	Kanigiri granite	430	28	69.79	13.56	2.83	0.07	0.04	1.02	4.16	5.31	0.17	0.00	96.95	1.55
Rao and Reddy 2007	Kanigiri granite	355	29	70.38	13.35	2.75	0.07	0.10	0.98	4.08	5.01	0.18	0.01	96.91	1.50
Rao and Reddy 2007	Kanigiri granite	150	30												
Rao and Reddy 2007	Kanigiri granite	255	31	74.31	11.78	2.13	0.04	0.00	0.76	3.33	4.94	0.12	0.02	97.43	1.42
Rao and Reddy 2007	Kanigiri granite	305	32	73.29	12.59	2.49	0.05	0.00	0.89	3.62	5.00	0.17	0.02	98.12	1.44
Rao and Reddy 2007	Kanigiri granite	270	33	72.66	11.79	2.34	0.05	0.04	0.85	3.52	5.22	0.15	0.04	96.66	1.53
Rao and Reddy 2007	Kanigiri granite	160	34	76.00	13.13	2.13	0.05	0.00	0.73	3.04	5.25	0.14	0.01	100.48	1.26
Rao and Reddy 2007	Kanigiri granite	310	35	73.47	13.13	2.68	0.06	0.00	0.86	3.58	5.54	0.16	0.00	99.48	1.45
Rao and Reddy 2007	Kanigiri granite	240	36	71.99	13.24	2.06	0.04	0.21	0.77	3.50	5.56	0.15	0.04	97.56	1.41
Rao and Reddy 2007	Kanigiri granite	210	37	72.82	12.77	2.15	0.04	0.00	0.81	3.58	5.33	0.13	0.01	97.64	1.45
Rao and Reddy 2007	Kanigiri granite	235	38	70.98	13.05	2.55	0.06	0.03	0.93	4.01	5.15	0.16	0.01	96.93	1.52
Rao and Reddy 2007	Kanigiri granite	315	41	74.07	12.95	2.09	0.03	0.02	0.38	4.36	4.84	0.09	0.01	98.84	1.43
Rao and Reddy 2007	Kanigiri granite	380	42	71.14	13.56	2.44	0.06	0.01	0.76	3.35	5.46	0.14	0.15	97.07	1.35
Rao and Reddy 2007	Kanigiri granite	340	43	71.51	13.68	2.33	0.04	0.01	0.93	4.24	5.36	0.13	0.00	98.23	1.53
Rao and Reddy 2007	Kanigiri granite	145	44												
Rao and Reddy 2007	Kanigiri granite	100	45	75.75	13.50	1.05	0.03	0.00	0.24	4.76	4.53	0.02	0.00	99.88	1.38
Rao and Reddy 2007	Kanigiri granite	180	46												
Rao and Reddy 2007	Kanigiri granite	165	47												
Rao and Reddy 2007	Kanigiri granite	345	48												
Rao and Reddy 2007	Kanigiri granite	290	49												
Rao and Reddy 2007	Kanigiri granite	290	50												
Rao and Reddy 2007	Kanigiri granite	485	51	71.80	12.86	2.22	0.05	0.00	0.88	4.55	4.91	0.11	0.00	97.38	1.61
Rao and Reddy 2007	Kanigiri granite	460	52												
Rao and Reddy 2007	Kanigiri granite	390	53												
Rao and Reddy 2007	Kanigiri granite	255	54	73.51	13.43	1.95	0.04	0.08	0.66	4.11	4.98	0.11	0.00	98.87	1.41

Source	Locality	Zr	Sample #	SiO_2	Al_2O_3	FeO(t)	MnO	MgO	CaO	Na_2O	K_2O	TiO2	P_2O_5	Total	M Value
	Unit	*mg/kg*		*wt%*	*wt%*	*wt%*	*wt%*	*wt%*	*wt%*	*wt%*	*wt%*	*wt%*	*wt%*	*wt%*	
Rao and Reddy 2007	Kanigiri granite	530	55	70.00	13.41	2.76	0.06	0.09	1.41	3.96	5.23	0.20	0.07	97.19	1.60
Rao and Reddy 2007	Kanigiri granite	325	56	70.23	13.80	2.23	0.05	0.02	1.02	4.36	5.36	0.15	0.00	97.22	1.57
Rao and Reddy 2007	Kanigiri granite	395	57												
Rao and Reddy 2007	Kanigiri granite	305	58												
Rao and Reddy 2007	Kanigiri granite	330	59												
Rao and Reddy 2007	Kanigiri granite	340	60												
Rao and Reddy 2007	Kanigiri granite	745	61												
Rao and Reddy 2007	Kanigiri granite	355	62												
Rao and Reddy 2007	Kanigiri granite	205	63												
Rao and Reddy 2007	Kanigiri granite	260	64	73.73	13.15	2.17	0.05	0.00	0.93	3.55	5.38	0.14	0.00	99.10	1.43
Rao and Reddy 2007	Kanigiri granite	290	65	71.96	13.38	1.93	0.03	0.01	0.84	4.27	5.15	0.13	0.00	97.70	1.52
Rao and Reddy 2007	Kanigiri granite	325	66	71.28	13.31	2.38	0.05	0.01	0.83	3.97	5.31	0.16	0.00	97.30	1.49
Rao and Reddy 2007	Kanigiri granite	325	67	69.71	13.32	2.62	0.06	0.02	0.89	3.97	5.49	0.17	0.01	96.26	1.53
Rao and Reddy 2007	Kanigiri granite	335	68												
Rao and Reddy 2007	Kanigiri granite	365	69	71.39	14.44	2.47	0.06	0.02	0.99	4.05	5.66	0.16	0.01	99.25	1.48
Rao and Reddy 2007	Kanigiri granite	380	70												
Rao and Reddy 2007	Kanigiri granite	490	71												
Rao and Reddy 2007	Kanigiri granite	375	72												
Rao and Reddy 2007	Kanigiri granite	375	73												
Rao and Reddy 2007	Kanigiri granite	470	74												
Rao and Reddy 2007	Kanigiri granite	380	75												
Rao and Reddy 2007	Kanigiri granite	315	76												
Rao and Reddy 2007	Kanigiri granite	280	77												
Rao and Reddy 2007	Kanigiri granite	235	78												
Rao and Reddy 2007	Kanigiri granite	260	79												
Rao and Reddy 2007	Kanigiri granite	420	80												
Xiong Lei et al. 2013	Hongliujing granite	859	XJ400	68.26	15.56	2.42	0.08	0.19	1.36	4.97	5.31	0.23	0.03	98.41	1.61
Xiong Lei et al. 2013	Hongliujing granite	379	XJ404	72.69	14.06	1.47	0.05	0.01	0.59	4.44	5.44	0.15	0.02	98.92	1.47
Xiong Lei et al. 2013	Hongliujing granite	391	XJ405	72.20	14.20	1.75	0.04	0.02	0.61	4.52	5.47	0.16	0.02	98.99	1.49
Xiong Lei et al. 2013	Hongliujing granite	556	XJ406	71.91	14.65	1.83	0.05	0.01	0.87	4.79	4.68	0.17	0.02	98.98	1.45
Wang et al 2018	Jiuhuashan	222	14JHS09-1	77.65	12.09	0.69	0.05	0.05	0.27	4.17	4.41	0.08	0.00	99.46	1.37
Wang et al 2018	Jiuhuashan	190	14JHS11-1	77.87	11.72	0.83	0.02	0.05	0.28	3.94	4.41	0.14	0.00	99.26	1.36
Wang et al 2018	Jiuhuashan	159	14JHS15-1	76.86	12.67	0.52	0.06	0.04	0.25	4.58	4.33	0.04	0.00	99.35	1.39
Wang et al 2018	Jiuhuashan	128	14JHS28-5	76.38	12.34	0.67	0.07	0.07	0.32	4.39	4.32	0.06	0.00	98.62	1.39
Wang et al 2018	Jiuhuashan	176	14JHS23-1	76.47	12.48	0.80	0.05	0.09	0.25	3.55	5.33	0.14	0.01	99.17	1.33
Wang et al 2018	Jiuhuashan	186	14JHS18-1	75.79	12.38	0.83	0.04	0.07	0.05	3.78	4.81	0.12	0.00	97.87	1.28
Wang et al 2018	Huayuangong	823	14JHS31-1	76.98	11.05	1.85	0.10	0.14	0.18	3.09	4.58	0.21	0.00	98.18	1.24
Wang et al 2018	Huayuangong	233	14JHS33-1	74.93	13.17	1.08	0.03	0.12	0.28	4.50	4.80	0.20	0.01	99.12	1.40
Wang et al 2018	Huayuangong	245	14JHS34-1	73.79	13.36	0.99	0.07	0.10	0.32	4.54	4.93	0.18	0.01	98.29	1.43
Wang et al 2018	Huayuangong	508	14JHS36-1	67.12	16.55	1.48	0.09	0.21	0.63	5.44	6.56	0.33	0.03	98.44	1.64
Salih et al 2020	El Dair Complex	563	15MD01	75.37	11.02	2.86	0.06	0.01	0.32	4.03	4.99	0.21	0.01	98.88	1.56
Salih et al 2020	El Dair Complex	740	15MD02	75.54	11.18	2.63	0.08	0.04	0.28	3.93	4.99	0.21	0.01	98.89	1.51
Salih et al 2020	El Dair Complex	764	15MD03	76.21	10.76	2.65	0.06	0.04	0.26	3.70	4.67	0.23	0.01	98.59	1.45
Salih et al 2020	El Dair Complex	800	15MD04	77.25	10.92	1.94	0.03	0.11	0.12	3.17	4.72	0.20	0.01	98.47	1.28
Salih et al 2020	El Dair Complex	1165	15MD07a	76.36	9.72	4.37	0.07	0.04	0.07	4.27	3.97	0.09	0.01	98.97	1.56
Salih et al 2020	El Dair Complex	834	15MD07b	75.83	9.80	4.04	0.07	0.03	0.07	4.40	4.01	0.07	0.01	98.33	1.59
Salih et al 2020	El Dair Complex	929	17MD02	75.68	10.93	2.82	0.04	0.02	0.33	4.09	4.87	0.15	0.01	98.94	1.57

Source	Locality	Zr	Sample #	SiO_2	Al_2O_3	FeO(t)	MnO	MgO	CaO	Na_2O	K_2O	TiO2	P_2O_5	Total	M Value
	Unit	*mg/kg*		*wt%*	*wt%*	*wt%*	*wt%*	*wt%*	*wt%*	*wt%*	*wt%*	*wt%*	*wt%*	*wt%*	
Hong Chen et al 2017	Wuyishan terrane	208	WY-13	70.11	13.91	2.90	0.05	0.50	1.32	2.27	6.53	0.38	0.14	98.11	1.36
Hong Chen et al 2017	Wuyishan terrane	208	WY-14	68.11	14.21	3.82	0.06	0.68	1.81	2.05	6.21	0.42	0.16	97.53	1.36
Hong Chen et al 2017	Wuyishan terrane	197	WY-15	70.51	13.77	2.46	0.04	0.75	1.12	2.83	6.67	0.36	0.11	98.62	1.46
Hong Chen et al 2017	Wuyishan terrane	183	WY-16	72.43	13.17	2.29	0.03	0.56	0.41	2.21	7.26	0.25	0.09	98.70	1.31
Zhou et al 2006	Qiaqihai intrusion	488	QQH-13	67.87	15.83	2.37	0.08	0.53	1.06	5.02	5.69	0.55	0.13	99.13	1.59
Zhou et al 2006	Qiaqihai intrusion	429	QQH-14	67.77	15.88	2.37	0.10	0.53	1.21	5.20	5.89	0.62	0.13	99.70	1.68
Zhou et al 2006	Qiaqihai intrusion	221	QQH-17	67.10	16.29	2.37	0.08	0.42	0.75	4.78	6.55	0.70	0.22	99.26	1.56
Zhou et al 2006	Qiaqihai intrusion	1334	QQH-9	68.77	15.76	2.21	0.10	0.44	1.04	4.84	5.66	0.53	0.10	99.45	1.55
Zhou et al 2006	Qiaqihai intrusion	861	QQH-19	68.12	15.98	2.07	0.05	0.40	1.03	4.98	5.70	0.56	0.12	99.01	1.57
Zhou et al 2006	Qiaqihai intrusion	607	QQH-20	67.51	16.58	2.10	0.09	0.48	1.29	5.02	5.77	0.67	0.16	99.67	1.59
Zhou et al 2006	Kuoyitasi intrusion	354	YQ-56*	73.54	12.34	2.66	0.04	0.34	0.60	4.42	4.66	0.24	0.14	98.98	1.53
Zhou et al 2006	Kuoyitasi intrusion	674	YQ-55*	74.26	11.71	3.05	0.05	0.35	0.28	4.00	4.82	0.25	0.13	98.90	1.45
Zhou et al 2006	Kuoyitasi intrusion	420	YQ-9*	76.57	11.14	2.29	0.04	0.15	0.28	4.00	4.84	0.16	0.09	99.56	1.50
Zhou et al 2006	Kuoyitasi intrusion	298	YQ-10*	77.09	11.43	4.04	0.04	0.15	0.12	4.08	4.48	0.13	0.07	101.63	1.39
Zhou et al 2006	Kuoyitasi intrusion	490	YQ-54*	74.89	11.63	2.73	0.04	0.16	0.20	4.40	4.68	0.21	0.12	99.06	1.50
Zhou et al 2006	Kuoyitasi intrusion	322	KY-5	74.46	12.66	1.96	0.06	0.30	0.49	4.58	4.84	0.20	0.02	99.57	1.52
Zhou et al 2006	Kuoyitasi intrusion	1096	KY-9	75.16	12.52	1.89	0.06	0.18	0.43	4.18	4.74	0.20	0.04	99.40	1.42

Sample #	°C T_{Zr}^{FW}	°C $T_{Zr}^{B\ et\ al}$	°C Difference
GIG-1	889	862	27
IG-1	979	976	3
IG-2	847	816	31
IG-3	900	878	22
IG-5	878	856	22
IG-6	860	830	30
IG-7	932	917	14
IG-8	906	884	22
IG-9	887	863	25
IG-10	902	882	21
IG-11	860	829	31
IG-12	868	841	27
IG-13	875	848	28
IG-14	904	883	21
IG-16	949	940	9
IG-17	938	924	14
IG-18	899	877	22
IG-19	866	837	29
IG-20	902	882	20
IG-21	951	941	10
IG-22	932	916	16
IG-24	975	970	4
IG-25	898	875	23
IG-26	875	849	27
IG-27	878	850	28
IG-28	907	885	22
BG-1	909	893	16
BG-2	928	916	12
BG-3	906	889	17
BG-4	890	868	22
BG-5	898	878	20
BG-6	890	867	23
BG-7	903	885	18
BG-8	859	831	28
BG-9	880	856	24
BG-10	879	855	24
BG-14	895	866	29
BG-15	891	864	27
BG-16	908	882	26
BG-17	914	891	23
BG-18	925	903	21
BG-19	915	891	24
BG-20	914	891	24
BG-21	935	916	19
BG-22	912	887	24
BG-23	906	882	24
BG-24	917	894	23

Sample #	°C T_{Zr}^{FW}	°C $T_{Zr}^{B\ et\ al}$	°C Difference
BG-25	905	879	26
BG-26	907	879	28
BG-27	963	950	13
BG-28	901	875	25
BG-29	906	878	28
BG-31	937	916	21
BG-32	941	922	19
MSB/G/28	871	840	31
MSB/G/29	858	825	33
MSB/G/30	908	885	23
PFA-22	890	854	36
PFR-18B	873	833	41
PFA-21A	880	839	41
PFR-19A	915	883	32
PFR-18A	916	884	32
PFR-22	893	860	33
PFR-20	911	882	28
PFA-21B	877	845	32
PFR-19B	893	866	27
PFR-21	861	829	32
BQH-1	765	707	58
BQH-10	782	736	46
BQH-11	795	756	39
BQH-12	786	743	43
BQH-13	784	739	45
BQH-14	788	745	43
BQH-15	769	722	46
BQH-16	794	752	42
BQH-17	782	742	41
BQH-19	782	734	48
BQH-2	764	707	57
BQH-20	796	745	51
BQH-21	778	728	50
BQH-22	778	727	51
BQH-3	765	708	57
BQH-4	768	717	51
BQH-5	775	727	48
BQH-6	788	745	43
BQH-9	791	748	43
W1	734	686	49
W2	837	819	18
W3	728	675	53
W4	747	696	50
W5	730	677	53
W6	734	682	52
W7	675	615	60
W8	738	688	50

Sample #	°C T_{Zr}^{FW}	°C $T_{Zr}^{B\ et\ al}$	°C Difference
H1	729	674	55
H2	732	683	49
506A	959	949	10
506C	919	893	26
506D	940	917	23
506F	936	910	25
08TS-46A	808	755	53
08TS-47A	822	777	45
08TS-47B	815	766	48
08TS-48	843	789	54
09TS-18	813	771	42
09TS-20	846	812	34
08GX-20	827	787	39
08GX-25	843	814	29
1*	854	822	32
2*	825	787	39
XL-5	830	792	39
XL-6	799	756	43
XL-7	822	790	32
XL-8	796	752	44
XL-11	820	782	38
XL-12	818	777	40
XL-13	798	755	43
XL-15	806	764	42
XL 16-16	876	851	25
XL-16-17	878	855	22
XL-16-18	864	825	38
XL-16-19	870	836	34
XK-16-20	870	833	37
XL-16-21	885	851	34
XL-17-1	857	834	23
XL-17-2	830	790	40
XL-17-3	857	829	28
XL-17-4	849	811	38
XL-17-8	860	827	32
DQW-1-1	845	801	44
DQW-1-2	841	797	44
DQW-2-1	824	782	42
DQW-2-2	828	789	39
DQW-3-1	828	797	31
DQW3-2	810	771	39
DQW-3-3	817	780	37
1	851	813	38
2	833	791	42
3	848	810	38
4	816	776	41
5	813	769	44

Sample #	°C T_{Zr}^{FW}	°C $T_{Zr}^{B\ et\ al}$	°C Difference
6	810	765	45
7	836	797	39
8	763	710	53
9	846	808	38
10	818	769	49
11			
12			
13			
14			
15			
16	855	816	38
17			
18	811	768	44
19	839	796	43
20	823	781	41
21	862	821	40
22	860	822	38
23	896	868	28
24	851	814	38
25	910	880	29
26	886	850	36
27	799	755	44
28	866	829	37
29	852	813	38
30			
31	827	786	40
32	842	804	38
33	823	779	45
34	796	756	40
35	843	805	38
36	821	780	41
37	807	762	45
38	811	765	46
41	846	810	37
42	872	843	29
43	845	804	41
44			
45	748	696	52
46			
47			
48			
49			
50			
51	874	836	38
52			
53			
54	827	787	40

Sample #	°C T_{Zr}^{FW}	°C $T_{Zr}^{B\ et\ al}$	°C Difference
55	884	848	36
56	837	793	44
57			
58			
59			
60			
61			
62			
63			
64	827	787	40
65	831	788	43
66	844	805	39
67	840	799	42
68			
69	856	820	37
70			
71			
72			
73			
74			
75			
76			
77			
78			
79			
80			
XJ400	935	909	26
XJ404	861	825	36
XJ405	862	827	36
XJ406	902	876	26
14JHS09-1	818	778	40
14JHS11-1	804	762	42
14JHS15-1	787	740	46
14JHS28-5	767	718	50
14JHS23-1	800	758	42
14JHS18-1	809	770	39
14JHS31-1	966	965	1
14JHS33-1	820	779	41
14JHS34-1	822	781	41
14JHS36-1	875	836	39
15MD01	893	861	32
15MD02	928	905	23
15MD03	937	919	18
15MD04	959	954	5
15MD07a	975	962	14
15MD07b	933	908	25
17MD02	948	927	21

Sample #	°C T_{Zr}^{FW}	°C $T_{Zr}^{B\ et\ al}$	°C Difference
WY-13	812	771	41
WY-14	812	771	41
WY-15	800	754	46
WY-16	805	764	40
QQH-13	876	839	37
QQH-14	856	812	44
QQH-17	802	753	49
QQH-9	993	985	9
QQH-19	940	917	23
QQH-20	899	867	32
YQ-56*	849	810	40
YQ-55*	923	902	21
YQ-9*	868	833	35
YQ-10*	843	807	36
YQ-54*	884	852	32
KY-5	840	799	41
KY-9	983	977	5

Appendix S3.2

Compilation of natural S-type granite compositions for chapter 4

	Unit	*mg/kg*		*wt%*	*wt%*	*wt%*	*wt%*	*wt%*	*wt%*	*wt%*	*wt%*
Source	**Locality**	**Zr**	**Sample #**	**SiO_2**	**Al_2O_3**	**FeO(t)**	**MnO**	**MgO**	**CaO**	**Na_2O**	**K_2O**
He et al 2016	Bokalike gneissic granite	83	NLG-142C	78.01	11.79	0.92	0.01	0.11	0.81	2.21	4.52
He et al 2016	Bokalike gneissic granite	105	NLG-143	76.97	12.33	0.87	0.01	0.10	0.63	2.26	5.68
He et al 2016	Bokalike gneissic granite	97	NLG-144	76.74	12.30	0.85	0.01	0.10	0.67	2.21	5.58
He et al 2016	Bokalike gneissic granite	92	NLG-145	76.73	12.27	0.85	0.01	0.12	0.70	2.09	5.59
He et al 2016	Bokalike gneissic granite	80	NGL-146	76.38	12.21	1.63	0.01	0.11	1.01	2.04	5.42
He et al 2016	Bokalike gneissic granite	84	NLG-147A	77.10	11.65	1.22	0.01	0.11	0.96	2.13	5.25
He et al 2016	Bokalike gneissic granite	100	NLG-148	76.51	12.15	1.50	0.01	0.10	0.64	2.09	5.49
He et al 2016	Bokalike gneissic granite	78	NLG-149	75.95	12.42	1.42	0.01	0.09	0.63	2.19	5.68
He et al 2016	Bokalike gneissic granite	80	NLG-151A	76.14	12.41	1.34	0.01	0.11	0.90	2.03	5.47
Jung et al 2000	Oetmoed Granite complx	133	89.6	71.72	15.53	1.54	0.04	0.47	0.98	2.80	5.15
Jung et al 2000	Oetmoed Granite complx	150	89.7	72.30	15.21	1.50	0.04	0.55	0.97	2.70	5.20
Jung et al 2000	Oetmoed Granite complx	174	89.66	71.49	15.59	1.77	0.03	0.53	1.05	2.74	5.27
Jung et al 2000	Oetmoed Granite complx	143	7.2	73.04	14.60	1.24	0.03	0.28	0.89	2.69	5.21
Jung et al 2000	Oetmoed Granite complx	88	89.76	72.91	14.47	1.11	0.02	0.32	0.77	3.39	5.90
Jung et al 2000	Oetmoed Granite complx	75	89.8	73.22	14.83	0.94	0.02	0.27	1.13	2.85	5.66
Jung et al 2000	Oetmoed Granite complx	116	89.16	73.01	15.25	0.76	0.01	0.17	1.12	3.50	5.09
Jung et al 2000	Oetmoed Granite complx	178	89.17	72.70	14.87	0.76	0.01	0.21	1.05	3.23	5.38
Jung et al 2000	Oetmoed Granite complx	82	89.19	71.74	15.33	1.14	0.03	0.32	1.20	2.91	5.90
Jung et al 2000	Oetmoed Granite complx	46	89.2	72.59	15.25	0.83	0.02	0.21	1.09	3.41	5.03
Jung et al 2000	Oetmoed Granite complx	88	89.71	71.40	16.24	2.01	0.03	0.74	1.47	4.31	3.20
Jung et al 2000	Oetmoed Granite complx	38	89.75	74.34	14.72	2.21	0.06	1.30	0.33	1.60	5.05
Jung et al 2000	Oetmoed Granite complx	33	79.57	75.78	13.75	0.63	0.02	1.30	0.28	2.10	5.36
Jung et al 2000	Oetmoed Granite complx	25	89.52	73.10	15.22	0.73	0.07	0.20	0.89	3.10	5.73
Jung et al 2000	Oetmoed Granite complx	26	26.5	73.60	14.85	0.54	0.04	0.13	0.80	3.11	5.83
Jung et al 2000	Oetmoed Granite complx	3	9.1	73.34	14.41	0.29	0.01	0.03	0.49	2.34	8.81
Jung et al 2000	Oetmoed Granite complx	3	13	73.13	14.85	0.35	0.01	0.03	0.57	2.32	8.97
Jung et al 2000	Oetmoed Granite complx	30	89.5	73.97	14.89	1.54	0.22	0.16	0.60	3.18	4.69
Tulloch et al 2009	Maruia Pluton	354	P52247	65.32	15.87	5.04	0.05	1.44	2.83	3.04	3.98
Tulloch et al 2009	Horatio Pluton	256	OU49111	66.87	16.27	4.11	0.06	1.02	3.46	4.17	2.01
Tulloch et al 2009	Ridge Pluton	358	P57323	67.73	15.72	4.16	0.06	1.17	4.56	2.87	1.85
Tulloch et al 2009	Big Pluton	87	P70787	72.93	14.36	1.30	0.04	0.32	1.11	3.12	5.11
Tulloch et al 2009	RS Dike	114	P71266	73.52	14.45	1.11	0.01	0.35	0.89	2.62	5.33
Tulloch et al 2009	Table Pluton	172	P60678	76.10	13.19	0.78	0.02	0.14	1.01	3.13	5.04
Tulloch et al 2009	Tarn Summit	220	OU45087	66.95	14.91	5.04	0.09	1.88	2.80	3.17	2.71
Tulloch et al 2009	Barrytown	259	P45613	68.24	14.43	4.18	0.05	1.28	1.50	2.62	4.31
Tulloch et al 2009	Falls Ck	196	P45594	68.33	14.76	3.82	0.06	1.47	2.54	2.86	3.88
Tulloch et al 2009	Oparara	225	P45397	69.45	14.16	3.46	0.05	1.09	1.98	2.71	4.37
Tulloch et al 2009	Evans	173	OU49226	69.92	14.61	0.49	0.06	1.10	1.98	3.04	3.51
Tulloch et al 2009	Barrytown	178	P45608	70.60	13.99	3.05	0.05	0.92	1.28	2.72	4.80
Tulloch et al 2009	Newton	191	P64999	70.73	14.76	2.92	0.04	0.89	0.85	3.17	4.55
Tulloch et al 2009	Crosscut	204	P52240	70.87	14.12	3.33	0.03	1.29	1.66	2.73	4.10
Tulloch et al 2009	Rangitoto	98	P52355	71.61	14.46	1.95	0.05	0.85	1.91	2.94	4.20
Tulloch et al 2009	Barrytown	171	P66549	71.81	13.98	2.70	0.07	0.77	0.85	2.90	4.91
Tulloch et al 2009	Kakpotahi	58	P52283	75.46	13.59	1.25	0.04	0.18	0.74	3.38	4.93
Wang et al 2018	Baitoushain Mu Granite	138	XIMZ135	72.80	13.80	1.51	0.03	0.46	1.00	2.81	5.48
Wang et al 2018	Baitoushain Mu Granite	140	XIMZ136	72.80	14.10	1.57	0.03	0.47	1.01	2.77	5.15
Wang et al 2018	Baitoushain Mu Granite	125	XIMZ137	72.60	13.90	1.46	0.03	0.43	0.99	2.98	5.44

	Unit	*mg/kg*		*wt%*	*wt%*	*wt%*	*wt%*	*wt%*	*wt%*	*wt%*	*wt%*
Source	**Locality**	**Zr**	**Sample #**	**SiO_2**	**Al_2O_3**	**FeO(t)**	**MnO**	**MgO**	**CaO**	**Na_2O**	**K_2O**
Wang et al 2018	Baitoushain Mu Granite	50	XIMZ138	75.70	13.40	0.72	0.02	0.25	0.61	2.92	4.78
Wang et al 2018	Baitoushain Mu Granite	214	XIMZ139	72.50	14.10	1.54	0.03	0.45	0.96	2.90	5.39
Wang et al 2018	Baitoushain Mu Granite	76	XIMZ140	74.20	14.00	1.03	0.03	0.34	0.93	3.20	4.34
Wang et al 2018	Baitoushain Mu Granite	144	XIMZ142	73.70	13.90	1.31	0.06	0.32	0.55	3.08	4.98
Wang et al 2018	Baitoushain Mu Granite	151	XIMZ143	73.20	13.90	1.38	0.05	0.33	0.62	3.34	4.99
Wang et al 2018	Baitoushain Mu Granite	146	XIMZ144	72.80	13.80	1.44	0.03	0.38	1.21	2.92	4.94
Wang et al 2018	Haergen 2 mica granite	156	XIMZ145	72.70	13.90	1.44	0.03	0.37	1.15	2.93	5.15
Wang et al 2018	Haergen 2 mica granite	153	XIMZ146	72.80	13.90	1.45	0.03	0.37	1.20	3.02	4.92
Wang et al 2018	Haergen 2 mica granite	207	XIMZ159	72.20	13.40	2.44	0.05	0.71	0.82	2.90	4.68
Wang et al 2018	Haergen 2 mica granite	209	XIMZ160	70.80	13.90	2.49	0.05	0.70	0.91	2.95	5.32
Wang et al 2018	Haergen 2 mica granite	219	XIMZ161	71.70	13.40	2.70	0.05	0.79	0.88	3.04	4.55
Wang et al 2018	Haergen 2 mica granite	232	XIMZ162	70.00	14.00	2.80	0.06	0.82	1.04	2.98	5.14
Wang et al 2018	Haergen 2 mica granite	244	XIMZ163	71.70	13.20	2.93	0.06	0.81	1.01	2.87	4.27
Kalsbeek et al 2001	East Greenland Caledonides	101	427402	74.30	14.02	1.35	0.02	0.41	0.80	3.70	4.61
Kalsbeek et al 2001	East Greenland Caledonides	15	427443	75.72	14.34	0.52	0.03	0.04	0.26	5.08	3.72
Kalsbeek et al 2001	East Greenland Caledonides	80	427472	73.56	14.48	1.08	0.02	0.37	1.02	3.69	4.58
Kalsbeek et al 2001	East Greenland Caledonides	128	427487	73.45	14.74	1.52	0.03	0.43	1.01	4.39	3.52
Kalsbeek et al 2001	East Greenland Caledonides	34	427491	72.37	14.70	0.87	0.01	0.38	0.71	3.16	7.00
Kalsbeek et al 2001	East Greenland Caledonides	90	427495	73.92	14.25	1.12	0.02	0.26	0.78	3.35	5.42
Kalsbeek et al 2001	East Greenland Caledonides	31	427410	76.59	12.99	0.67	0.02	0.21	0.71	3.00	4.89
Kalsbeek et al 2001	East Greenland Caledonides	80	427433	76.09	12.90	1.51	0.03	0.30	0.49	2.68	5.23
Song et al 2021	Taggula granitoids	162	10TG03	67.36	14.26	3.59	0.09	1.84	3.38	2.57	3.45
Song et al 2021	Taggula granitoids	190	10TG05	67.97	14.84	3.33	0.08	1.25	1.95	2.97	4.78
Song et al 2021	Taggula granitoids	177	10TG06	66.92	14.55	4.03	0.10	2.57	2.00	2.78	2.98
Song et al 2021	Taggula granitoids	193	10TG09	68.12	14.86	3.51	0.08	1.69	0.78	4.08	3.67
Song et al 2021	Taggula granitoids	167	10TG11	69.24	14.65	3.52	0.07	1.70	1.38	2.79	3.28
Song et al 2021	Taggula granitoids	145	10TG12	68.79	13.97	3.87	0.07	2.22	0.93	2.90	3.27
Song et al 2021	Taggula granitoids	195	10TG14	65.40	14.75	3.73	0.05	1.60	2.29	3.23	3.78
Song et al 2021	Taggula granitoids	186	10TG15	66.42	14.87	3.67	0.10	1.39	2.29	2.68	4.68
Song et al 2021	Taggula granitoids	175	10TG17	67.91	14.84	3.14	0.04	2.10	3.38	3.78	1.47
Song et al 2021	Taggula granitoids	156	10TG19	68.30	14.67	3.92	0.09	2.02	0.70	3.61	3.53
Song et al 2021	Taggula granitoids	149	10TG21	69.42	14.38	3.39	0.05	2.11	2.74	3.77	0.94
Song et al 2021	Taggula granitoids	220	10TG22	64.76	15.49	3.97	0.08	1.60	2.45	2.97	4.80
Song et al 2021	Taggula granitoids	117	10TG23	79.18	10.77	1.35	0.02	0.83	1.00	2.77	1.84
Song et al 2021	Taggula granitoids	140	10TG24	75.52	12.21	1.60	0.02	0.90	1.02	2.98	2.26
Liu et al 2020	Bandi Sn mine	181	CR-1	69.44	14.50	3.63	0.05	1.07	2.83	2.41	3.58
Liu et al 2020	Bandi Sn mine	212	CR-2	67.90	14.88	3.48	0.05	0.91	3.02	2.86	3.84
Liu et al 2020	Machang Setahun granite	162	KT-1(1)	71.65	13.85	2.75	0.06	0.66	2.28	2.39	4.68
Liu et al 2020	Machang Setahun granite	144	KT-1(2)	71.31	13.87	2.62	0.04	0.66	1.70	2.46	4.86
Liu et al 2020	Kajang Kemaman granite	186	KT-2(1)	70.56	14.02	3.41	0.06	0.89	2.75	2.26	3.73
Liu et al 2020	Kajang Kemaman granite	181	KT-2(2)	74.13	12.19	3.46	0.13	0.94	1.89	3.21	1.43
Liu et al 2020	Kuantan area	151	KT-3(2)	78.52	12.41	0.31	0.03	0.15	0.45	3.18	4.36
Liu et al 2020	Kuantan area	111	KT-4	76.38	13.30	0.67	0.01	0.10	0.40	3.43	5.20
Liu et al 2020	Berkelah granite	220	LB-1	72.42	13.95	2.02	0.05	0.40	1.43	3.32	4.82
Liu et al 2020	Gambang granite	128	LM-8	75.45	12.63	1.65	0.04	0.32	0.93	3.26	4.32
Liu et al 2020	Kulim granite	142	PK-4	72.81	14.44	1.68	0.04	0.54	0.73	2.77	5.26
Liu et al 2020	Sintok Sn mine	66	SK-10(1)	76.35	13.34	0.67	0.04	0.15	0.59	3.73	4.56

	Unit	*mg/kg*		*wt%*	*wt%*	*wt%*	*wt%*	*wt%*	*wt%*	*wt%*	*wt%*
Source	**Locality**	**Zr**	**Sample #**	**SiO_2**	**Al_2O_3**	**FeO(t)**	**MnO**	**MgO**	**CaO**	**Na_2O**	**K_2O**
Liu et al 2020	Genting Highland	160	YD-1	73.48	13.44	1.84	0.04	0.94	1.71	2.30	4.87
Liu et al 2020	Rahman Perak	187	PK-1	73.91	13.76	1.22	0.02	0.47	0.70	2.31	5.89
Liu et al 2020	Rahman Perak	280	PK-2	68.23	13.80	3.02	0.04	2.34	2.76	1.93	5.39
Liu et al 2020	Rahman Perak	440	PK-3	55.82	12.04	6.43	0.14	7.09	5.13	0.39	7.67
Dan et al 2020	Duguer	173	15ZB96-1	72.65	14.17	2.70	0.02	0.63	0.36	1.37	6.84
Dan et al 2020	Duguer	173	15ZB97-1	73.68	13.92	1.98	0.03	0.72	0.47	1.49	6.92
Dan et al 2020	Duguer	159	DG0701	73.12	13.78	2.88	0.06	0.75	0.70	2.47	4.74
Dan et al 2020	Duguer	144	GE08191	73.85	14.45	1.97	0.01	0.54	0.45	1.49	6.48
Dan et al 2020	Duguer	181	GE08192	78.22	11.37	1.30	0.02	0.43	0.39	1.70	4.97
Dan et al 2020	Duguer	98	GE08193	77.17	11.46	2.25	0.02	0.48	0.57	1.37	5.07
Dan et al 2020	Duguer	137	GE08195	74.32	13.06	2.80	0.04	0.52	0.43	1.26	6.30
Dan et al 2020	Duguer	173	GE08196	72.83	14.03	2.23	0.02	0.46	0.45	1.81	6.74
Dan et al 2020	Duguer	112	GE08197	76.30	12.72	1.46	0.02	0.29	0.37	0.94	6.80
Dan et al 2020	Bensong Co	147	15ZB130-1	72.01	14.38	2.69	0.06	0.81	0.84	2.64	5.19
Dan et al 2020	Bensong Co	129	15ZB135-1	75.05	12.43	3.07	0.06	1.07	0.25	1.57	5.18
Dan et al 2020	Bensong Co	358	15ZB139-1	71.06	12.12	4.73	0.08	1.94	1.28	1.55	5.58
Dan et al 2020	Bensong Co	190	BS0715	73.59	13.99	2.44	0.02	0.56	0.52	1.68	6.05
Dan et al 2020	Bensong Co	125	BS08031	73.40	13.88	2.64	0.05	0.78	0.95	2.23	5.07
Dan et al 2020	Bensong Co	120	BS08032	74.28	13.63	2.29	0.05	0.62	0.74	2.63	5.03
Dan et al 2020	Bensong Co	131	BS08033	72.47	13.82	2.69	0.06	0.74	0.89	2.83	4.98
Dan et al 2020	Bensong Co	161	BS08035	72.25	14.40	2.89	0.06	0.78	0.71	2.56	5.45
Dan et al 2020	Bensong Co	170	BS08036	73.01	13.42	2.80	0.11	1.14	0.65	1.90	6.32
Dan et al 2020	Bensong Co	42	BS08038	78.82	11.87	0.66	0.01	0.20	0.41	2.47	4.16
Dan et al 2020	Bensong Co	77	BS1001	76.82	12.52	1.27	0.04	0.32	0.40	2.88	5.30
Dan et al 2020	Bensong Co	142	BS1002	74.20	13.33	2.36	0.04	0.77	0.69	3.05	4.75
Dan et al 2020	Bensong Co	189	BS1003	72.72	14.42	3.02	0.04	1.46	0.38	1.43	4.73
Dan et al 2020	Bensong Co	182	BS1004	75.19	13.06	2.78	0.05	1.67	0.30	1.35	4.57
Dan et al 2020	Bensong Co	204	BS1005	74.40	13.25	2.99	0.05	1.17	0.67	2.71	3.66
Dan et al 2020	Bensong Co	184	BS1006	74.51	13.09	2.93	0.05	1.56	0.41	1.45	5.03
Dan et al 2020	Bensong Co	126	BS1007	73.94	14.23	2.26	0.04	1.89	0.28	2.50	4.05
Dan et al 2020	Bensong Co	168	BS1008	75.23	12.98	2.69	0.04	1.21	0.37	1.94	4.60
Dan et al 2020	Bensong Co	43	BS1009	79.57	9.36	2.47	0.04	1.00	0.36	1.83	4.60
Dan et al 2020	Bensong Co	112	BS1010	73.93	12.60	3.36	0.05	2.71	0.31	2.25	3.87
Zhang et al 2017	Helanshan region	185	B2068	72.69	13.75	1.89	0.01	0.53	0.81	2.55	5.67
Zhang et al 2017	Helanshan region	58	B2125[a]	73.69	13.96	1.21	0.01	0.38	0.49	2.72	5.86
Zhang et al 2017	Helanshan region	131	B2127[a]	72.28	14.43	2.37	0.04	0.58	0.66	2.78	5.25
Zhang et al 2017	Helanshan region	161	B2128[a]	75.97	12.26	1.95	0.02	0.40	0.48	2.35	5.21
Zhang et al 2017	Helanshan region	92	B2138[a]	74.00	13.81	1.10	0.01	0.46	0.59	2.96	5.09
Zhang et al 2017	Helanshan region	88	B2160[a]	74.48	13.54	1.80	0.01	0.41	0.50	2.45	5.14
Gou et al 2015	Southwest Tianshan	34	W8011	83.24	9.73	0.55	0.00	0.00	0.61	2.26	3.09
Gou et al 2015	Southwest Tianshan	106	W8015	75.68	13.84	1.07	0.02	0.05	0.82	2.26	5.45
Gou et al 2015	Southwest Tianshan	15	W8017	73.77	15.00	0.99	0.04	0.49	0.87	2.69	5.05
Gou et al 2015	Southwest Tianshan	124	W8020	72.41	14.85	1.19	0.19	0.20	0.71	1.54	8.47
Gou et al 2015	Southwest Tianshan	100	W8053	75.64	13.78	0.67	0.08	0.29	0.80	2.61	5.69
Gou et al 2015	Southwest Tianshan	68	W1033	75.04	14.98	0.86	0.03	0.39	1.18	3.47	2.96
Gou et al 2015	Southwest Tianshan	222	W1013	74.33	13.87	1.97	0.39	0.07	1.51	2.55	4.20

	Unit	*mg/kg*		*wt%*	*wt%*	*wt%*	*wt%*	*wt%*	*wt%*	*wt%*	*wt%*
Source	**Locality**	**Zr**	**Sample #**	**SiO_2**	**Al_2O_3**	**FeO(t)**	**MnO**	**MgO**	**CaO**	**Na_2O**	**K_2O**
Potratz et al 2021	Sana Granite	235	SANA 04	73.84	13.45	1.54	0.02	0.34	1.16	2.76	5.57
Potratz et al 2021	Sana Granite	364	SANA 05	67.45	14.89	3.13	0.04	0.75	0.95	2.72	6.08
Potratz et al 2021	Sana Granite	603	SANA 06A	67.60	13.86	3.19	0.05	0.68	1.86	2.56	5.88
Potratz et al 2021	Sana Granite	667	SANA 06B	68.21	14.61	3.32	0.05	0.80	1.98	2.91	5.08
Potratz et al 2021	Sana Granite	457	SANA 07	69.38	14.38	2.20	0.03	0.57	1.89	2.79	5.77
Potratz et al 2021	Sana Granite	378	SANA 08A	70.55	13.85	2.36	0.04	0.49	1.43	3.08	4.81
Potratz et al 2021	Sana Granite	458	SANA 08B	70.60	13.99	2.85	0.05	0.59	1.48	3.15	4.80
Potratz et al 2021	Sana Granite	627	SANA 09	68.77	13.99	3.84	0.05	0.66	1.83	2.54	5.90
Potratz et al 2021	Sana Granite	783	SANA 10	66.81	13.91	3.70	0.06	0.75	2.20	2.55	5.62
Potratz et al 2021	Sana Granite	192	SANA 15	73.31	13.71	1.35	0.04	0.22	0.60	2.84	5.72
Potratz et al 2021	Sana Granite	180	SANA 16	73.77	13.90	1.84	0.02	0.36	0.59	2.51	5.65
Potratz et al 2021	Sana Granite	239	SANA 17A	71.11	13.52	1.81	0.02	0.38	1.06	2.69	5.85
Potratz et al 2021	Sana Granite	219	SANA 17B	71.17	13.83	1.63	0.02	0.35	1.09	2.76	6.13
Potratz et al 2021	Sana Granite	212	SANA 41	72.84	14.32	1.61	0.01	0.34	1.03	3.02	5.74
Potratz et al 2021	Sana Granite	168	SANA 43	74.75	13.46	1.75	0.02	0.34	0.68	2.18	5.71
Potratz et al 2021	Sana Granite	402	SANA 20	69.43	13.98	2.54	0.05	0.58	1.64	2.61	5.38
Potratz et al 2021	Sana Granite	374	SANA 21	70.52	13.85	2.12	0.04	0.46	1.41	2.60	5.82
Potratz et al 2021	Sana Granite	188	Sana 4'	71.62	14.34	2.14	0.04	0.35	0.83	2.75	6.03
Potratz et al 2021	Sana Granite	202	Sana 5'	73.22	13.75	2.12	0.03	0.41	0.88	2.77	5.66
Potratz et al 2021	Sana Granite	607	Sana 12'	70.30	13.85	3.11	0.05	0.68	1.71	2.62	5.80
Potratz et al 2021	Sana Granite	194	Sana 14'	72.88	14.28	1.97	0.03	0.32	1.05	2.82	5.75
Potratz et al 2021	Sana Granite	763	Sana 17'	68.50	14.22	3.83	0.06	0.70	2.15	2.61	5.84
Healy et al 2004	Cooma Suite	180	23A	70.24	15.07	4.18	0.07	2.02	0.96	0.38	3.66
Healy et al 2004	Cooma Suite	201	20A	7.67	14.36	3.95	0.08	1.88	0.93	1.26	3.83
Healy et al 2004	Cooma Suite	201	66	70.43	14.15	4.20	0.06	2.16	1.33	1.52	3.25
Healy et al 2004	Cooma Suite	201	CC1	72.00	13.72	3.66	0.06	1.76	1.00	1.49	3.73
Healy et al 2004	Clear Range Suite	190	20562	62.19	15.56	6.41	0.12	3.84	5.09	1.12	2.53
Healy et al 2004	Clear Range Suite	125	20563	64.34	14.88	5.08	0.09	3.88	5.36	1.85	2.20
Healy et al 2004	Clear Range Suite	154	8	64.84	15.61	4.72	0.07	2.88	4.24	1.97	2.58
Healy et al 2004	Clear Range Suite	150	20532	66.43	14.96	4.90	0.09	3.20	4.21	1.96	2.74
Healy et al 2004	Clear Range Suite	181	34	67.83	14.62	4.16	0.06	2.30	2.72	1.98	3.28
Healy et al 2004	Clear Range Suite	155	20359	69.12	14.20	3.60	0.07	1.86	2.87	2.29	3.52
Healy et al 2004	Shannons Flat Suite	160	20501	70.66	14.34	2.35	0.05	1.06	2.40	2.65	4.55
Healy et al 2004	Shannons Flat Suite	155	20506	71.65	14.16	2.38	0.05	0.92	2.75	2.62	4.11
Healy et al 2004	Shannons Flat Suite	130	20518	72.51	14.30	1.91	0.04	0.68	2.73	2.72	4.22
Healy et al 2004	Shannons Flat Suite	165	20523	73.34	13.60	2.11	0.04	0.83	2.15	2.73	4.67
Healy et al 2004	Shannons Flat Suite	105	50225	74.89	13.32	1.51	0.04	0.52	1.32	2.80	4.75
Antunes et al 2008	Castelo Branco pluton	91	GCL7	72.09	14.89	1.30	0.02	0.45	0.53	4.03	4.88
Antunes et al 2008	Castelo Branco pluton	78	GEB2	73.10	15.12	1.07	0.02	0.32	0.46	4.06	5.03
Antunes et al 2008	Castelo Branco pluton	238	GIN	68.78	15.83	3.37	0.05	1.21	1.52	3.90	4.06
Antunes et al 2008	Castelo Branco pluton	207	INFX2	69.37	15.42	2.91	0.04	1.03	1.33	3.88	4.28
Antunes et al 2008	Castelo Branco pluton	168	PC	70.36	15.42	2.59	0.03	0.72	1.01	3.90	4.49
Antunes et al 2008	Castelo Branco pluton	148	BCAL	71.52	14.85	2.27	0.04	0.63	0.87	4.07	4.45
Antunes et al 2008	Castelo Branco pluton	156	ER	71.56	15.17	1.93	0.02	0.57	0.98	4.00	4.99
Antunes et al 2008	Castelo Branco pluton	94	NAC	72.99	14.75	1.74	0.04	0.44	0.65	4.14	4.30
Antunes et al 2008	Castelo Branco pluton	81	LARDO	72.90	14.82	1.25	0.02	0.29	0.56	3.56	4.79
Antunes et al 2008	Castelo Branco pluton	70	LC1	74.27	14.24	1.13	0.01	0.22	0.36	3.50	4.47

	wt%	*wt%*	*wt%*		*°C*	*°C*	*°C*
Sample #	**TiO2**	**P_2O_5**	**Total**	**M Value**	**T_{Zr}^{FW}**	**$T_{Zr}^{B\ et\ al}$**	**Difference**
NLG-142C	0.11	0.16	98.65	1.12	751	707	44
NLG-143	0.11	0.17	99.13	1.20	764	720	44
NLG-144	0.10	0.15	98.71	1.19	758	713	45
NLG-145	0.11	0.16	98.63	1.18	755	710	45
NGL-146	0.12	0.16	99.09	1.22	741	693	48
NLG-147A	0.12	0.16	98.71	1.25	743	694	49
NLG-148	0.12	0.16	98.77	1.16	763	720	43
NLG-149	0.10	0.15	98.64	1.19	741	694	48
NLG-151A	0.12	0.16	98.69	1.18	743	696	47
89.6	0.27	0.24	98.74	1.11	792	755	36
89.7	0.29	0.28	99.04	1.11	802	768	34
89.66	0.30	0.18	98.95	1.12	815	783	32
7.2	0.28	0.13	98.39	1.13	796	760	36
89.76	0.16	0.30	99.35	1.33	741	690	52
89.8	0.10	0.14	99.16	1.24	735	684	50
89.16	0.15	0.12	99.18	1.26	769	723	45
89.17	0.25	0.19	98.65	1.26	806	767	39
89.19	0.22	0.31	99.10	1.27	740	690	50
89.2	0.15	0.19	98.77	1.23	698	643	55
89.71	0.26	0.15	99.81	1.19	751	704	46
89.75	0.09	0.10	99.80	0.81	711	669	42
79.57	0.20	0.25	99.67	0.97	690	641	49
89.52	0.01	0.19	99.24	1.22	656	596	60
26.5	0.02	0.23	99.15	1.24	657	597	61
9.1	0.01	0.26	99.99	1.44	524	449	75
13	0.01	0.24	100.48	1.44	524	449	75
89.5	0.01	0.22	99.48	1.08	677	623	54
P52247	0.75	0.30	98.62	1.37	863	831	31
OU49111	0.55	0.19	98.71	1.41	827	788	40
P57323	0.72	0.19	99.03	1.40	861	829	33
P70787	0.15	0.04	98.48	1.25	745	697	49
P71266	0.18	0.06	98.52	1.14	776	736	40
P60678	0.11	0.01	99.53	1.30	800	758	41
OU45087	0.83	0.27	98.65	1.29	823	787	36
P45613	0.74	0.25	97.60	1.16	849	823	26
P45594	0.62	0.16	98.50	1.33	810	769	40
P45397	0.57	0.21	98.05	1.29	825	789	36
OU49226	0.48	0.23	95.42	1.21	807	771	37
P45608	0.48	0.18	98.07	1.21	810	773	36
P64999	0.38	0.15	98.44	1.13	823	792	31
P52240	0.53	0.19	98.85	1.19	824	791	33
P52355	0.27	0.08	98.32	1.26	754	707	48
P66549	0.39	0.14	98.52	1.17	809	774	35
P52283	0.06	0.02	99.65	1.25	714	660	54
XIMZ135	0.23	0.06	98.18	1.26	783	740	43
XIMZ136	0.25	0.06	98.21	1.19	790	750	40
XIMZ137	0.22	0.06	98.11	1.28	773	728	45

	wt%	*wt%*	*wt%*		*°C*	*°C*	*°C*
Sample #	**TiO2**	**P_2O_5**	**Total**	**M Value**	**T_{Zr}^{FW}**	**$T_{Zr}^{B\ et\ al}$**	**Difference**
XIMZ138	0.11	0.07	98.58	1.14	710	659	51
XIMZ139	0.24	0.06	98.17	1.24	824	790	34
XIMZ140	0.14	0.07	98.28	1.16	741	694	47
XIMZ142	0.21	0.08	98.19	1.15	795	758	37
XIMZ143	0.23	0.10	98.14	1.22	795	755	39
XIMZ144	0.25	0.08	97.85	1.26	789	747	42
XIMZ145	0.23	0.07	97.97	1.27	794	753	41
XIMZ146	0.24	0.07	98.00	1.26	792	751	41
XIMZ159	0.31	0.16	97.67	1.18	826	795	32
XIMZ160	0.32	0.16	97.60	1.25	821	786	36
XIMZ161	0.32	0.16	97.59	1.20	830	798	32
XIMZ162	0.33	0.17	97.17	1.26	830	797	34
XIMZ163	0.34	0.16	97.19	1.17	842	814	28
427402	0.30	0.15	99.51	1.26	757	710	47
427443	0.04	0.10	99.75	1.27	620	555	65
427472	0.28	0.15	99.08	1.27	738	688	50
427487	0.29	0.23	99.38	1.25	778	735	43
427491	0.27	0.18	99.47	1.40	667	604	63
427495	0.24	0.18	99.36	1.28	747	698	49
427410	0.10	0.21	99.18	1.21	671	613	58
427433	0.21	0.20	99.44	1.16	745	699	46
10TG03	0.46	0.10	97.00	1.43	785	737	48
10TG05	0.53	0.11	97.70	1.34	806	764	41
10TG06	0.57	0.12	96.50	1.12	817	785	32
10TG09	0.55	0.10	97.34	1.18	820	786	33
10TG11	0.55	0.12	97.18	1.02	819	791	28
10TG12	0.56	0.11	96.58	1.00	808	778	30
10TG14	0.61	0.15	95.44	1.35	807	765	42
10TG15	0.57	0.12	96.67	1.35	803	761	42
10TG17	0.52	0.10	97.18	1.36	797	754	44
10TG19	0.51	0.10	97.35	1.08	808	776	32
10TG21	0.49	0.08	97.29	1.20	795	757	39
10TG22	0.60	0.15	96.72	1.41	814	771	42
10TG23	0.26	0.06	98.02	0.99	789	757	33
10TG24	0.32	0.09	96.83	0.99	805	775	30
CR-1	0.56	0.14	98.06	1.27	806	767	39
CR-2	0.49	0.20	97.44	1.41	810	768	43
KT-1(1)	0.35	0.10	98.68	1.34	792	748	44
KT-1(2)	0.43	0.09	97.95	1.26	787	745	42
KT-2(1)	0.47	0.12	98.27	1.28	809	770	39
KT-2(2)	0.45	0.11	97.93	1.12	818	787	31
KT-3(2)	0.22	0.03	99.66	1.16	799	762	37
KT-4	0.16	0.03	99.69	1.25	766	720	45
LB-1	0.23	0.06	98.70	1.35	818	779	40
LM-8	0.24	0.06	98.90	1.27	776	732	44
PK-4	0.34	0.19	98.81	1.13	796	759	36
SK-10(1)	0.14	0.05	99.61	1.26	723	670	52

Sample #	wt% TiO2	wt% P_2O_5	wt% Total	M Value	°C T_{Zr}^{FW}	°C $T_{Zr}^{B\ et\ al}$	°C Difference
YD-1	0.44	0.11	99.16	1.25	797	757	40
PK-1	0.35	0.15	98.77	1.16	818	786	33
PK-2	0.70	0.24	98.46	1.46	832	791	41
PK-3	1.08	0.43	96.22	2.34	805	732	73
15ZB96-1	0.35	0.18	99.27	1.01	822	795	27
15ZB97-1	0.37	0.17	99.76	1.08	817	787	30
DG0701	0.39	0.18	99.07	1.05	812	782	30
GE08191	0.37	0.17	99.78	0.99	808	779	29
GE08192	0.28	0.14	98.82	1.02	827	801	26
GE08193	0.26	0.13	98.76	0.99	774	737	36
GE08195	0.34	0.19	99.26	1.00	802	771	31
GE08196	0.33	0.17	99.07	1.11	815	784	32
GE08197	0.19	0.19	99.29	1.01	784	749	35
15ZB130-1	0.35	0.27	99.24	1.13	799	763	36
15ZB135-1	0.35	0.15	99.18	0.92	803	775	28
15ZB139-1	0.62	0.09	99.06	1.23	876	853	23
BS0715	0.35	0.17	99.36	1.01	831	806	25
BS08031	0.36	0.11	99.48	1.09	788	751	36
BS08032	0.30	0.16	99.73	1.13	781	742	39
BS08033	0.37	0.31	99.16	1.18	785	745	40
BS08035	0.40	0.15	99.65	1.12	808	775	33
BS08036	0.38	0.15	99.87	1.15	810	776	34
BS08038	0.07	0.16	98.83	1.03	703	654	49
BS1001	0.11	0.14	99.80	1.22	738	689	49
BS1002	0.32	0.16	99.66	1.18	792	753	39
BS1003	0.49	0.14	98.84	0.77	851	839	12
BS1004	0.45	0.17	99.60	0.78	846	833	13
BS1005	0.49	0.20	99.60	0.98	841	819	22
BS1006	0.41	0.15	99.59	0.88	839	821	18
BS1007	0.32	0.16	99.68	0.86	805	780	26
BS1008	0.40	0.15	99.62	0.91	828	806	22
BS1009	0.33	0.06	99.64	1.17	697	644	54
BS1010	0.28	0.16	99.54	0.89	792	763	29
B2068	0.33	0.23	98.46	1.20	814	779	35
B2125[a]	0.12	0.17	98.61	1.18	719	668	51
B2127[a]	0.24	0.17	98.80	1.12	789	752	37
B2128[a]	0.20	0.15	98.99	1.14	806	772	35
B2138[a]	0.23	0.16	98.41	1.16	757	713	44
B2160[a]	0.20	0.22	98.75	1.07	760	719	41
W8011	0.03	0.03	99.54	1.05	688	637	52
W8015	0.09	0.03	99.31	1.11	772	732	40
W8017	0.11	0.07	99.08	1.08	630	570	60
W8020	0.01	0.01	99.58	1.26	774	729	44
W8053	0.01	0.03	99.60	1.20	760	715	45
W1033	0.05	0.05	99.01	1.03	741	698	43
W1013	0.01	0.00	98.90	1.14	836	807	29

Sample #	wt% TiO2	wt% P_2O_5	wt% Total	M Value	°C T_{Zr}^{FW}	°C $T_{Zr}^{B\ et\ al}$	°C Difference
SANA 04	0.38	0.08	99.14	1.32	827	790	37
SANA 05	0.76	0.27	97.04	1.26	875	850	25
SANA 06A	0.74	0.22	96.64	1.47	909	884	25
SANA 06B	0.90	0.26	98.12	1.39	928	910	18
SANA 07	0.59	0.17	97.77	1.45	882	852	30
SANA 08A	0.50	0.18	97.11	1.32	873	846	27
SANA 08B	0.64	0.18	98.15	1.34	892	868	24
SANA 09	0.73	0.19	98.31	1.44	916	894	22
SANA 10	0.87	0.24	96.47	1.50	935	914	21
SANA 15	0.32	0.10	98.11	1.22	816	780	36
SANA 16	0.34	0.18	98.98	1.14	817	784	32
SANA 17A	0.40	0.14	96.84	1.33	828	791	37
SANA 17B	0.34	0.14	97.32	1.36	817	777	40
SANA 41	0.35	0.11	99.26	1.30	819	781	38
SANA 43	0.33	0.20	99.22	1.12	811	778	33
SANA 20	0.54	0.17	96.75	1.34	878	850	27
SANA 21	0.48	0.14	97.30	1.36	869	840	30
Sana 4'	0.33	0.20	98.43	1.25	812	774	37
Sana 5'	0.36	0.17	99.20	1.26	818	782	36
Sana 12'	0.65	0.19	98.77	1.42	914	892	22
Sana 14'	0.30	0.16	99.40	1.27	813	775	38
Sana 17'	0.80	0.20	98.71	1.49	933	912	21
23A	0.60	0.14	97.18	0.56	863	863	0
20A	0.56	0.07	34.52	2.36	737	656	81
66	0.67	0.08	97.77	0.81	854	841	12
CC1	0.54	0.10	97.96	0.81	853	841	13
20562	0.80	17.00	97.66	1.31	808	769	40
20563	0.58	0.11	98.26	1.49	759	705	54
8	0.65	0.13	97.56	1.29	791	749	42
20532	0.67	0.13	99.16	1.34	785	740	45
34	0.67	0.14	97.62	1.14	817	785	32
20359	0.55	0.12	98.08	1.28	792	751	42
20501	0.39	0.09	98.45	1.36	789	744	45
20506	0.41	0.09	99.05	1.38	785	739	46
20518	0.30	0.07	99.41	1.39	769	720	49
20523	0.36	0.09	99.83	1.39	790	744	46
50225	0.23	0.06	99.38	1.26	760	714	47
GCL7	0.19	0.34	98.38	1.25	749	701	48
GEB2	0.16	0.38	99.34	1.24	738	688	50
GIN	0.58	0.31	99.61	1.27	832	798	34
INFX2	0.49	0.31	99.06	1.28	818	781	37
PC	0.39	0.36	99.27	1.24	802	763	39
BCAL	0.34	0.36	99.40	1.28	788	746	42
ER	0.31	0.32	99.85	1.33	789	745	44
NAC	0.22	0.39	99.66	1.23	753	707	47
LARDO	0.17	0.45	98.81	1.16	746	700	46
LC1	0.14	0.36	98.70	1.11	738	692	46

Appendix S3.3

Statistical summary of zircon compilation from A-type granites for Chapter 4

of analyses
400
Sumproduct (Zr)
177630
of unique granites
21
Sumproduct (unique)
9135

mean Zr (mg/kg)
395
Weighted Mean Zr (mg/kg)
444
Mode Zr (mg/kg)
220
Median Zr (mg/kg)
351
S.D Zr (mg/kg)
226
2S.D Zr (mg/kg)
453

Max Zr (mg/kg)
1334
Min Zr (mg/kg)
35

of T
220
Unique T
20
Sumproduct (T)^{FW}
186504
Unique SumProduct (T)^{FW}
17563
Sumproduct (T)^{B}
179084
Unique Sumproduct (T)^{B}
16861

Mean [T_{Zr}(°C)]^{FW}
856
Weighted Mean [T_{Zr}(°C)] ^{FW}
848
Unique Weighted Mean [T_{Zr}(°C)] ^{FW}
878.16
Mean [T_{Zr}(°C)]^{B}
821
Weighted Mean [T_{Zr}(°C)]^{B}
814
Unique Weighted Mean [T_{Zr}(°C)]^{B}
843
S.D^{FW} (°C)
28
S.D^{B} (°C)
69
Max^{FW} (°C)
993
Min^{FW} (°C)
675
Max^{B} (°C)
985
Min^{B} (°C)
615

Appendix S3.4

Statistical summary of zircon from S-type granites for Chapter 4

of analyses
187

Sumproduct (Zr)
32059

of unique granites
43

Sumproduct (unique)
7024

mean Zr (mg/kg)
171.44

Weighted Mean Zr (mg/kg)
171

Mode Zr (mg/kg)
181

Median Zr (mg/kg)
155

S.D Zr (mg/kg)
72

2S.D Zr (mg/kg)
144

Max Zr (mg/kg)
783

Min Zr (mg/kg)
3

of T
187

Unique T
43

Sumproduct (T)^{FW}
147656

Unique SumProduct (T)^{FW}
33174

Sumproduct (T)^{B}
140325

Unique Sumproduct (T)^{B}
31474

Mean [T_{Zr}(°C)]^{FW}
790

Weighted Mean [T_{Zr}(°C)]^{FW}
790

Unique Weighted Mean [T_{Zr}(°C)]^{FW}
771

Mean [T_{Zr}(°C)]^{B}
750

Weighted Mean [T_{Zr}(°C)]^{B}
750

Unique Weighted Mean [T_{Zr}(°C)]^{B}
732

S.D^{FW} (°C)
60

S.D^{B} (°C)
70

Max^{FW} (°C)
935

Min^{FW} (°C)
524

Max^{B} (°C)
914

Min^{B} (°C)
449

Appendix S3.5

Compiled Ti-in-zircon concentrations of rim and core for Chapter 4

	unit	*mg/kg*	*mg/kg*	*mg/kg*	*Calculated temperature difference between core and rim using ºC*								
Author	**Sample**	**Core [Ti]**	**Rim [Ti]**	**Difference [Ti]**	**Description**	**aTiO2 = 0.1**	**aTiO2 = 0.2**	**aTiO2 = 0.3**	**aTiO2 = 0.4**	**aTiO2 = 0.5**	**aTiO2 = 0.6**	**aTiO2 = 0.7**	**aTiO2 = 0.8**
Andersen et al 2010	Ar-49c	12.12	11.05	-1.07	Rhyolite	-14.49	-12.37	-11.34	-10.68	-10.21	-9.85	-9.55	-9.31
Andersen et al 2010	LdM-12-06	12.95	8.71	-4.24	Rhyolite	-60.95	-52.09	-47.77	-45.03	-43.06	-41.54	-40.33	-39.31
Andersen et al 2010	LdM-12-20	13.36	9.33	-4.03	Rhyolite	-55.75	-47.60	-43.63	-41.11	-39.31	-37.92	-36.80	-35.87
Andersen et al 2010	LdM-12-23	5.63	4.66	-0.96	Rhyolite	-24.40	-21.10	-19.48	-18.43	-17.68	-17.10	-16.63	-16.24
Andersen et al 2010	LdM-12-30	11.38	6.18	-5.20	Rhyolite	-88.75	-76.15	-69.99	-66.06	-63.23	-61.05	-59.30	-57.84
Bolhar et al 2008	NF3	3.19	3.27	0.09	Granite	3.11	2.71	2.51	2.38	2.29	2.21	2.16	2.11
Bolhar et al 2008	RNZ20	4.48	3.52	-0.96	Granite	-29.59	-25.69	-23.76	-22.52	-21.62	-20.92	-20.36	-19.90
Bolhar et al 2008	RNZ49	5.10	3.46	-1.64	Granite	-48.42	-42.01	-38.83	-36.78	-35.31	-34.17	-33.25	-32.48
Bolhar et al 2008	RNZ83	9.76	9.41	-0.35	Granodiorite	-5.47	-4.69	-4.30	-4.06	-3.88	-3.75	-3.64	-3.55
Bolhar et al 2008	RNZ87	10.11	5.63	-4.48	Granodiorite	-83.18	-71.50	-65.77	-62.12	-59.49	-57.46	-55.83	-54.47
Bolhar et al 2008	SF2a	3.68	3.96	0.28	Granodiorite	8.97	7.79	7.20	6.83	6.56	6.35	6.18	6.04
Bolhar et al 2008	TT6	3.89	9.23	5.34	Granite	116.60	100.58	92.70	87.65	84.02	81.21	78.95	77.07
Chen et al	13MD03-1	2.97	3.77	0.80	Rhyolite	28.44	24.75	22.92	21.74	20.88	20.22	19.69	19.24
Chen et al	13MD04-1	3.01	3.91	0.89	Rhyolite	31.00	26.97	24.97	23.68	22.75	22.03	21.44	20.96
Chen et al	13MD06-2	3.25	3.38	0.12	Rhyolite	4.46	3.88	3.59	3.41	3.27	3.17	3.09	3.02
Chen et al	13MD07-1	2.49	3.15	0.66	Rhyolite	26.99	23.55	21.83	20.72	19.92	19.30	18.80	18.38
Claiborne et al 2010	BC101	8.15	8.20	0.05	Cumulate	0.88	0.76	0.70	0.66	0.63	0.61	0.59	0.58
Claiborne et al 2010	DSCG	10.80	9.75	-1.05	Cumulate	-15.58	-13.32	-12.22	-11.52	-11.02	-10.63	-10.32	-10.06
Claiborne et al 2010	SML49Z	7.50	5.55	-1.95	Leucogranite	-41.25	-35.55	-32.75	-30.96	-29.67	-28.67	-27.87	-27.20
Claiborne et al 2010	SML54Z	14.30	7.30	-7.00	Transitional/Leucogranite	-102.45	-87.60	-80.37	-75.76	-72.46	-69.92	-67.87	-66.17
Johnson 2014	428	5.61	5.57	-0.04	Trachyandesite	-0.95	-0.82	-0.76	-0.72	-0.69	-0.66	-0.65	-0.63
Johnson 2014	505	4.97	5.96	0.99	Trachyandesite	23.97	20.71	19.10	18.08	17.33	16.76	16.30	15.91
Johnson 2014	DSL-22	15.20	11.70	-3.50	Quartz Monzonite	-42.44	-36.12	-33.05	-31.11	-29.72	-28.65	-27.79	-27.08
Johnson 2014	DSL-24	28.05	11.05	-17.00	Granite	-162.26	-137.29	-125.27	-117.67	-112.25	-108.09	-104.75	-101.98
Johnson 2014	HR1	5.25	5.30	0.05	Trachyandesite	1.24	1.07	0.99	0.94	0.90	0.87	0.85	0.83
Johnson 2014	HR15	28.73	13.77	-14.96	Trachyandesite	-131.95	-111.39	-101.51	-95.28	-90.84	-87.43	-84.70	-82.44
Johnson 2014	HR61	25.88	14.07	-11.81	Trachyandesite	-108.12	-91.36	-83.30	-78.21	-74.58	-71.80	-69.57	-67.71
Johnson 2014	HRLB27	16.88	17.10	0.22	Trachyandesite	2.23	1.89	1.72	1.62	1.55	1.49	1.44	1.40
Johnson 2014	KD4Z	16.56	9.82	-6.74	Felsic Dyke	-83.91	-71.46	-65.43	-61.60	-58.85	-56.74	-55.05	-53.64
Johnson 2014	KD5Z	7.90	7.70	-0.20	Trachyandesite	-3.67	-3.15	-2.90	-2.73	-2.62	-2.53	-2.46	-2.40
Johnson 2014	KS1532	22.25	18.63	-3.62	Felsic Dyke	-31.97	-26.98	-24.59	-23.08	-22.00	-21.17	-20.51	-19.96
Johnson 2014	NM8	14.19	18.86	4.67	Monzonite	48.51	41.12	37.56	35.30	33.69	32.45	31.46	30.64
Johnson 2014	NM18	35.10	27.71	-7.39	Trachyandesite	-47.64	-39.83	-36.12	-33.80	-32.15	-30.88	-29.87	-29.04
Johnson 2014	NSL1	4.06	9.95	5.89	Felsic Dyke	122.67	105.71	97.38	92.05	88.21	85.25	82.86	80.87
Johnson 2014	RM14	5.69	5.57	-0.13	Quartz Monzonite	-2.95	-2.55	-2.35	-2.22	-2.13	-2.06	-2.00	-1.96
Johnson 2014	SL3	30.13	30.26	0.14	Monzonite	0.89	0.75	0.68	0.63	0.60	0.58	0.56	0.55
Johnson 2014	SL200	16.00	12.18	-3.82	Felsic Dyke	-44.73	-38.03	-34.79	-32.74	-31.27	-30.14	-29.23	-28.48
Johnson 2014	SLRMZ	8.86	5.87	-2.99	Felsic Dyke	-57.87	-49.79	-45.82	-43.28	-41.46	-40.05	-38.92	-37.98
Johnson 2014	SM02	14.20	6.90	-7.30	Granite	-109.18	-93.40	-85.71	-80.82	-77.30	-74.60	-72.42	-70.61
Stelten et al. 2015	12-GP-1	6.46	4.06	-2.40	Rhyolite	-60.56	-52.38	-48.34	-45.75	-43.88	-42.44	-41.28	-40.31
Stelten et al. 2015	12-PPF-1	5.29	4.52	-0.77	Rhyolite	-20.38	-17.64	-16.28	-15.42	-14.79	-14.31	-13.91	-13.59
Stelten et al. 2015	12-PPF-2	5.45	4.04	-1.41	Rhyolite	-38.24	-33.12	-30.59	-28.96	-27.79	-26.88	-26.15	-25.54
Stelten et al. 2015	12-WY-2	6.00	4.19	-1.81	Rhyolite	-46.45	-40.19	-37.10	-35.11	-33.68	-32.58	-31.69	-30.94
Stelten et al. 2015	YCV-06	6.49	4.24	-2.25	Rhyolite	-55.74	-48.19	-44.47	-42.08	-40.36	-39.03	-37.96	-37.06
Stelten et al. 2015	YCV-09	5.16	4.53	-0.63	Rhyolite	-16.78	-14.53	-13.41	-12.70	-12.18	-11.79	-11.46	-11.20
Stelten et al. 2015	YCV-12	4.52	3.61	-0.91	Rhyolite	-27.95	-24.26	-22.43	-21.26	-20.41	-19.75	-19.22	-18.78
Troch et al 2018	12001	9.88	5.15	-4.73	Rhyolite	-91.33	-78.57	-72.31	-68.31	-65.44	-63.22	-61.43	-59.94

	unit	*mg/kg*	*mg/kg*	*mg/kg*	*Calculated temperature difference between core and rim using ºC*							
Author	**Sample**	**Core [Ti]**	**Rim [Ti]**	**Difference [Ti]**	**Description**	**aTiO2 = 0.1**	**aTiO2 = 0.2**	**aTiO2 = 0.3**	**aTiO2 = 0.4**	**aTiO2 = 0.5**	**aTiO2 = 0.6**	**aTiO2 = 0.7**	**aTiO2 = 0.8**
Troch et al 2018	12018	7.50	5.13	-2.37	Rhyolite	-51.57	-44.47	-40.98	-38.74	-37.13	-35.89	-34.89	-34.06
Troch et al 2018	12020	5.36	4.94	-0.43	Rhyolite	-10.83	-9.37	-8.65	-8.18	-7.85	-7.59	-7.38	-7.21
Troch et al 2018	12036	4.70	3.99	-0.71	Rhyolite	-20.61	-17.87	-16.51	-15.64	-15.01	-14.53	-14.14	-13.81
Troch et al 2018	12043	7.36	5.82	-1.54	Rhyolite	-32.26	-27.80	-25.60	-24.20	-23.19	-22.41	-21.78	-21.26
Weber et al. 2020	BAF	3.97	3.18	-0.78	Pryoclastic Flow	-26.52	-23.06	-21.34	-20.23	-19.44	-18.82	-18.32	-17.90
Weber et al. 2020	LTP	3.80	3.76	-0.04	Pumice	-1.24	-1.08	-1.00	-0.95	-0.91	-0.88	-0.86	-0.84
Weber et al. 2020	MTP	3.30	3.37	0.07	Pumice	2.40	2.09	1.94	1.84	1.76	1.71	1.66	1.62
Weber et al. 2020	UTP	3.92	4.00	0.08	Pumice	2.50	2.17	2.01	1.90	1.83	1.77	1.72	1.68
Weber et al. 2020	WQ	4.16	3.99	-0.17	Pryoclastic Flow	-5.16	-4.48	-4.14	-3.93	-3.77	-3.65	-3.55	-3.47
Cooper et al 2014	P1842	9.71	8.08	-1.62		-26.92	-23.08	-21.20	-20.01	-19.15	-18.49	-17.95	-17.51
Cooper et al 2014	P2243A	8.67	5.98	-2.69		-52.17	-44.88	-41.30	-39.02	-37.38	-36.11	-35.09	-34.24
Cooper et al 2014	P2243B	10.52	6.35	-4.17		-72.98	-62.65	-57.59	-54.36	-52.04	-50.26	-48.82	-47.62
Cooper et al 2014	P2006A	13.03	12.88	-0.16		-1.96	-1.66	-1.52	-1.43	-1.37	-1.32	-1.28	-1.25
Cooper et al 2014	P2006B	13.52	13.76	0.24		2.82	2.40	2.19	2.06	1.97	1.90	1.84	1.80
Cooper et al 2014	P2006C	13.73	13.16	-0.57		-6.84	-5.82	-5.33	-5.02	-4.79	-4.62	-4.48	-4.37
Cooper et al 2014	P2006D	13.18	13.62	0.44		5.37	4.57	4.18	3.94	3.76	3.63	3.52	3.43
Cooper et al 2014	P2008A	13.36	13.36	0.00		-0.02	-0.02	-0.02	-0.02	-0.02	-0.02	-0.02	-0.02
Cooper et al 2014	P2008B	12.64	13.35	0.72		8.88	7.56	6.92	6.52	6.23	6.00	5.82	5.67
Cooper et al 2014	P2008C	13.69	13.47	-0.21		-2.57	-2.18	-2.00	-1.88	-1.80	-1.73	-1.68	-1.64
Cooper et al 2014	P1993B	7.27	5.21	-2.06		-45.21	-38.99	-35.93	-33.97	-32.56	-31.47	-30.59	-29.86
Cooper et al 2014	P1993A	7.02	7.03	0.01		0.15	0.13	0.12	0.12	0.11	0.11	0.10	0.10
Cooper et al 2014	P2027A	9.00	9.43	0.43		6.90	5.91	5.43	5.12	4.90	4.73	4.59	4.48

unit		
Sample	**aTiO2 = 0.9**	**aTiO2 = 1**
Ar-49c	-9.11	-8.93
LdM-12-06	-38.45	-37.70
LdM-12-20	-35.08	-34.39
LdM-12-23	-15.91	-15.62
LdM-12-30	-56.60	-55.52
NF3	2.06	2.03
RNZ20	-19.50	-19.15
RNZ49	-31.82	-31.25
RNZ83	-3.47	-3.40
RNZ87	-53.31	-52.30
SF2a	5.92	5.81
TT6	75.46	74.06
13MD03-1	18.86	18.53
13MD04-1	20.54	20.18
13MD06-2	2.96	2.90
13MD07-1	18.02	17.71
BC101	0.56	0.55
DSCG	-9.84	-9.65
SML49Z	-26.63	-26.13
SML54Z	-64.72	-63.47
428	-0.62	-0.61
505	15.58	15.30
DSL-22	-26.47	-25.94
DSL-24	-99.63	-97.59
HR1	0.81	0.79
HR15	-80.51	-78.85
HR61	-66.14	-64.78
HRLB27	1.37	1.34
KD4Z	-52.44	-51.41
KD5Z	-2.35	-2.30
KS1532	-19.50	-19.09
NM8	29.94	29.33
NM18	-28.33	-27.72
NSL1	79.17	77.70
RM14	-1.92	-1.88
SL3	0.53	0.52
SL200	-27.83	-27.28
SLRMZ	-37.17	-36.47
SM02	-69.07	-67.74
12-GP-1	-39.48	-38.76
12-PPF-1	-13.31	-13.07
12-PPF-2	-25.02	-24.57
12-WY-2	-30.31	-29.76
YCV-06	-36.30	-35.64
YCV-09	-10.97	-10.77
YCV-12	-18.40	-18.07
12001	-58.67	-57.57

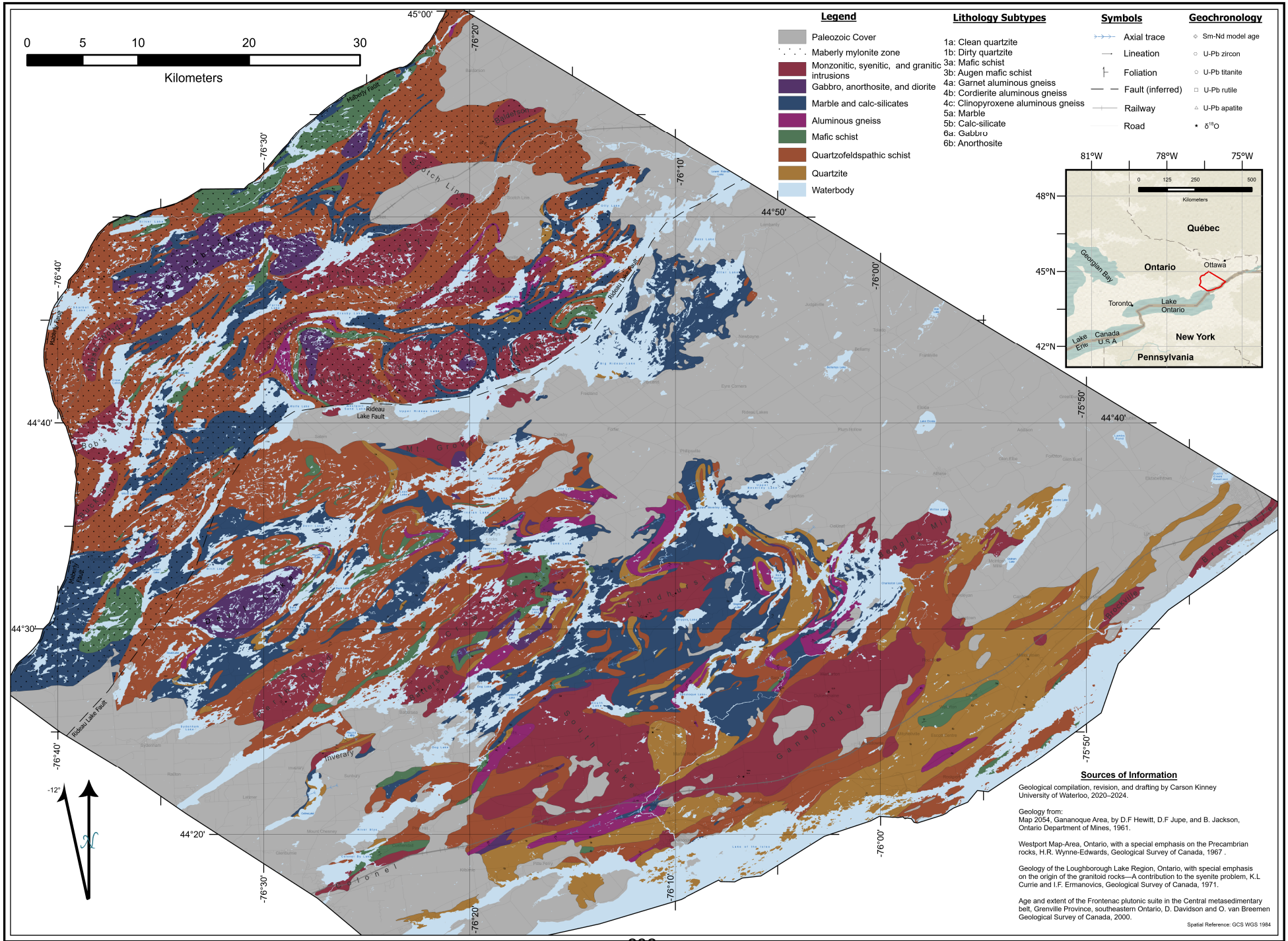
unit		
Sample	**aTiO2 = 0.9**	**aTiO2 = 1**
12018	-33.34	-32.73
12020	-7.06	-6.93
12036	-13.53	-13.29
12043	-20.81	-20.43
BAF	-17.54	-17.23
LTP	-0.82	-0.81
MTP	1.59	1.56
UTP	1.65	1.62
WQ	-3.40	-3.34
P1842	-17.13	-16.80
P2243A	-33.51	-32.88
P2243B	-46.60	-45.72
P2006A	-1.22	-1.20
P2006B	1.76	1.72
P2006C	-4.27	-4.18
P2006D	3.35	3.28
P2008A	-0.02	-0.02
P2008B	5.55	5.44
P2008C	-1.60	-1.57
P1993B	-29.24	-28.70
P1993A	0.10	0.10
P2027A	4.38	4.30

Appendix S4 (Chapter 5 Supplementary Material

Appendix S4.1

Map of Frontenac Terrane for Chapter 5

FRONTENAC TERRANE



Appendix S4.2

Compiled geochemical and geochronological data from Frontenac Terrane granitoids for Chapter 5

Sample	Paper	Terrane	Pluton	Suite	Lat(°N)	Long(°E)	wt% SiO2	wt% Al2O3	wt% Fe2O3(t)	wt% MgO	wt% CaO	wt% Na2O	wt% K2O	wt% TiO2	wt% P2O5
109	Currie & Ermanovics 1971	FT	FT-UN	Frontenac	44.5382	-76.2585	47.00	15.20	17.74	5.30	6.50	2.00	4.10	3.00	0.00
154	Currie & Ermanovics 1971	FT	Crow Lake	Frontenac	44.5140	-76.2926	47.00	17.90	13.01	4.40	7.40	3.40	3.20	2.20	0.00
199	Currie & Ermanovics 1971	FT	Crow Lake	Frontenac	44.5308	-76.3234	48.40	15.80	15.62	5.60	5.00	3.70	4.00	2.10	0.00
145	Currie & Ermanovics 1971	FT	Crow Lake	Frontenac	44.5204	-76.2618	49.00	20.00	10.66	4.90	5.50	4.40	2.50	2.00	0.00
108	Currie & Ermanovics 1971	FT	Crow Lake	Frontenac	44.5359	-76.2555	49.90	18.80	13.29	4.80	4.40	2.70	4.80	2.90	0.00
64-35	Currie & Ermanovics 1971	FT	Perth Road	Frontenac	44.4458	-76.4867	50.00	16.60	10.20	5.50	8.50	3.60	1.40	2.00	0.00
183	Currie & Ermanovics 1971	FT	FT-UN	Frontenac	44.4785	-76.3471	53.00	16.90	9.09	3.80	4.00	4.10	5.40	2.50	0.00
64-34	Currie & Ermanovics 1971	FT	Perth Road	Frontenac	44.4500	-76.4868	53.00	15.00	4.80	8.00	10.50	3.50	2.50	0.70	0.00
64-60	Currie & Ermanovics 1971	FT	Perth Road	Frontenac	44.4677	-76.4514	59.70	18.40	5.06	1.90	2.80	4.80	5.30	1.00	0.00
64-61	Currie & Ermanovics 1971	FT	Perth Road	Frontenac	44.4718	-76.4513	59.90	19.00	5.30	0.50	3.00	5.20	5.20	1.00	0.00
64-58	Currie & Ermanovics 1971	FT	Perth Road	Frontenac	44.4636	-76.4515	60.00	18.50	6.00	1.10	2.50	4.50	5.90	1.20	0.00
64-59	Currie & Ermanovics 1971	FT	Perth Road	Frontenac	44.4655	-76.4513	60.50	18.50	5.00	0.50	3.40	4.90	5.70	0.90	0.00
104	Currie & Ermanovics 1971	FT	FT-UN	Frontenac	44.5293	-76.2469	60.80	18.40	5.73	1.20	2.80	4.50	5.40	0.80	0.00
113	Currie & Ermanovics 1971	FT	Crow Lake	Frontenac	44.5456	-76.2680	61.00	18.50	5.46	1.30	2.20	3.70	5.20	0.90	0.00
139	Currie & Ermanovics 1971	FT	Crow Lake	Frontenac	44.5324	-76.2768	61.00	18.00	4.87	1.40	2.80	3.70	6.30	0.90	0.00
64-57	Currie & Ermanovics 1971	FT	Perth Road	Frontenac	44.4638	-76.4477	61.50	18.00	4.10	0.80	3.30	4.70	5.70	1.10	0.00
170	Currie & Ermanovics 1971	FT	Crow Lake	Frontenac	44.5270	-76.3091	62.60	16.00	5.67	1.40	2.00	4.80	6.00	1.00	0.00
216	Currie & Ermanovics 1971	FT	Battersea	Frontenac	44.4639	-76.3645	63.70	18.00	2.82	1.50	2.10	5.20	4.80	0.90	0.00
506	Currie & Ermanovics 1971	FT		Frontenac			66.20	19.30	0.30	0.00	2.70	3.60	7.50	0.20	0.00
180	Currie & Ermanovics 1971	FT	Crow Lake	Frontenac	44.4775	-76.3563	67.60	14.00	3.63	1.10	2.00	4.30	6.00	1.00	0.00
152	Currie & Ermanovics 1971	FT	FT-UN	Frontenac	44.5088	-76.2468	67.70	14.00	3.58	0.80	1.90	4.60	6.00	1.00	0.00
213	Currie & Ermanovics 1971	FT	Battersea	Frontenac	44.4670	-76.3732	68.10	14.90	2.84	1.50	2.10	5.20	4.80	0.50	0.00
130	Currie & Ermanovics 1971	FT	Crow Lake	Frontenac	44.5469	-76.2939	69.50	14.00	3.11	0.90	1.00	6.30	3.40	0.70	0.00
64-44a	Currie & Ermanovics 1971	FT	Perth Road	Frontenac	44.4264	-76.4810	69.50	14.50	2.21	0.70	1.20	3.80	6.00	0.60	0.00
516	Currie & Ermanovics 1971	FT		Frontenac			70.30	18.60	0.40	0.20	1.80	1.30	6.10	0.70	0.00
FJ97	Currie & Ermanovics 1971	FT	MMZ-UN	Frontenac	44.5329	-76.6922	70.36	13.60	4.35	1.26	2.16	2.79	4.87	0.64	0.16
64-43	Currie & Ermanovics 1971	FT	Perth Road	Frontenac	44.4280	-76.4821	70.50	14.50	3.09	0.60	1.70	3.70	5.20	0.80	0.00
151	Currie & Ermanovics 1971	FT	FT-UN	Frontenac	44.5105	-76.2491	71.00	14.00	2.71	0.20	1.40	3.00	6.00	0.80	0.00
105	Currie & Ermanovics 1971	FT	Crow Lake	Frontenac	44.5311	-76.2492	71.20	14.30	2.81	0.50	1.40	3.60	5.30	0.60	0.00
513	Currie & Ermanovics 1971	FT		Frontenac			72.00	16.90	0.10	0.20	21.00	2.70	6.00	0.30	0.00
501	Currie & Ermanovics 1971	FT		Frontenac			64..4	21.00	0.30	0.30	1.10	1.50	10.90	0.50	0.00
JC-050	Cutts, 2014	FT-MSZ	Wolfe Lake	Kensington-Skootamatta	44.6991	-76.4274	60.16	17.61	4.60	1.33	1.63	5.77	6.58	0.77	0.39
JC-070	Cutts, 2014	FT-MSZ	Rideau Lake	Kensington-Skootamatta	44.7103	-76.2993	59.63	18.25	4.38	1.40	2.15	4.96	5.86	1.06	0.39
JC-014	Cutts, 2014	FT-MSZ	Wolfe Lake	Kensington-Skootamatta	44.7066	-76.4288									
JC-043	Cutts, 2014	FT-MSZ	Westport	Kensington-Skootamatta	44.6931	-76.3925									
JC-067	Cutts, 2014	FT-MSZ	Rideau Lake	Kensington-Skootamatta	44.7198	-76.3102									
JC-045	Cutts, 2014	FT-MSZ	Westport	Kensington-Skootamatta	44.7241	-76.3386									
JC-081	Cutts, 2014	FT-MSZ	Westport	Kensington-Skootamatta	44.7168	-76.3746	61.64	17.41	4.02	1.06	1.60	5.51	6.21	0.84	0.29
91DM14b	Davidson & van Breemen, 2000	FT-MSZ	Pike Lake	Frontenac	44.7814	-76.3067									
93DM18b	Davidson & van Breemen, 2000	FT	Bennett Bay	Frontenac	44.8435	-76.4969									
93DM19	Davidson & van Breemen, 2000	FT-MSZ	Fall River	Frontenac	44.7853	-76.6313									
94DM53	Davidson & van Breemen, 2000	FT	Beagles Mills	Frontenac	44.5753	-75.9695									
96DM1	Davidson & van Breemen, 2000	FT	Mountain Grove	Frontenac	44.6862	-76.8159									
91DM131a	Davidson & van Breemen, 2000	FT-MSZ	North Crosby	Frontenac	44.7782	-76.4216									
15RME-0179	Davis et al., 2018	FT		Frontenac	44.9498	-76.4364									
FJ50	Dickin & Strong 2021	FT	FT-UN	Frontenac	44.4656	-76.5701	72.94	15.00	0.82	0.30	1.30	3.59	5.72	0.07	0.04
FJ24	Dickin & Strong 2021	FT-MSZ	MMZ-UN	Frontenac	44.8683	-76.4121	52.67	16.03	9.55	4.30	7.85	4.51	1.90	1.60	0.75

Sample	Paper	Terrane	Pluton	Suite	Lat(°N)	Long(°E)	*wt%* SiO2	*wt%* Al2O3	*wt%* Fe2O3(t)	*wt%* MgO	*wt%* CaO	*wt%* Na2O	*wt%* K2O	*wt%* TiO2	*wt%* P2O5
FJ27	Dickin & Strong 2021	FT	FT-UN	Frontenac	44.6454	-76.5018	66.94	17.12	1.26	0.47	0.91	2.55	9.77	0.19	0.41
FJ40	Dickin & Strong 2021	FT	FT-UN	Frontenac	44.6277	-76.3362	60.76	16.01	6.07	1.42	2.94	3.74	5.71	1.39	0.59
FJ51	Dickin & Strong 2021	FT-MSZ	MMZ-UN	Frontenac	44.5192	-76.5804	60.65	17.78	4.13	0.73	3.59	5.35	5.76	0.91	0.26
FJ93	Dickin & Strong 2021	FT	FT-UN	Frontenac	44.6337	-76.5226	68.22	14.54	2.33	0.71	1.49	3.30	6.80	1.12	0.19
FJ20	Dickin & Strong 2021	FT-MSZ	MMZ-UN	Frontenac	44.9514	-76.3785	60.31	17.98	4.21	1.14	2.21	4.99	6.39	0.83	0.28
FJ46	Dickin & Strong 2021	FT-MSZ	MMZ-UN	Frontenac	44.8457	-76.4861	56.39	17.81	6.59	1.84	4.22	4.81	5.24	1.24	0.44
FJ18	Dickin & Strong 2021	FT-MSZ	MMZ-UN	Frontenac	44.8862	-76.2500	74.28	13.91	1.30	0.18	1.26	4.48	3.87	0.09	0.03
FJ22	Dickin & Strong 2021	FT-MSZ	MMZ-UN	Frontenac	44.8063	-76.4073	47.80	18.06	11.20	4.90	8.95	4.39	1.44	1.56	0.34
FJ44	Dickin & Strong 2021	FT-MSZ	MMZ-UN	Frontenac	44.6564	-76.6545	53.86	15.65	9.99	2.86	5.36	4.93	3.32	2.14	1.04
FJ45	Dickin & Strong 2021	FT-MSZ	MMZ-UN	Frontenac	44.7219	-76.6761	55.17	17.50	8.63	2.12	5.50	4.97	3.16	1.81	0.79
FJ2	Dickin & Strong 2021	FT-MSZ	MMZ-UN	Frontenac	44.5202	-76.6456	57.67	13.11	11.62	2.08	4.08	5.31	1.66	1.89	0.78
FJ25	Dickin & Strong 2021	FT-MSZ	MMZ-UN	Frontenac	44.7886	-76.6296	59.17	16.50	7.14	1.57	4.06	5.20	4.35	1.27	0.39
FJ67	Dickin & Strong 2021	FT-MSZ	MMZ-UN	Frontenac	44.6056	-76.6423	61.92	14.71	8.23	1.58	3.72	4.63	3.22	1.16	0.43
FJ16	Dickin & Strong 2021	FT	FT-UN	Frontenac	44.6914	-76.2909	62.85	17.65	2.79	0.39	1.75	5.18	7.10	0.80	0.04
FJ12	Dickin & Strong 2021	FT-MSZ	MMZ-UN	Frontenac	44.7280	-76.4829	63.04	17.57	5.24	1.86	3.67	5.26	1.37	0.99	0.34
FJ60	Dickin & Strong 2021	FT-MSZ	MMZ-UN	Frontenac	44.5099	-76.6671	66.25	13.22	6.22	1.40	2.43	5.87	1.58	1.08	0.30
JS46	Dickin & Strong 2021	FT-MSZ	MMZ-UN	Frontenac	45.0771	-76.2454	68.38	13.18	4.22	0.51	2.29	3.42	5.27	0.61	0.09
FJ8	Dickin & Strong 2021	FT-MSZ	MMZ-UN	Frontenac	44.7298	-76.6459	69.29	13.27	4.88	0.67	2.54	2.66	4.27	0.70	0.17
FJ7	Dickin & Strong 2021	FT-MSZ	MMZ-UN	Frontenac	44.6816	-76.6723	69.67	13.51	4.82	1.06	2.16	3.60	3.79	0.62	0.15
FJ4	Dickin & Strong 2021	FT-MSZ	MMZ-UN	Frontenac	44.5676	-76.6684	69.69	13.30	4.39	0.90	1.73	3.37	4.67	0.54	0.14
FJ63	Dickin & Strong 2021	FT-MSZ	MMZ-UN	Frontenac	44.5828	-76.6706	69.70	14.12	3.41	1.71	2.62	3.87	3.05	0.42	0.05
FJ26	Dickin & Strong 2021	FT-MSZ	MMZ-UN	Frontenac	44.7628	-76.6140	70.32	13.09	4.55	1.41	3.55	3.35	1.01	1.34	0.22
FJ64	Dickin & Strong 2021	FT-MSZ	MMZ-UN	Frontenac	44.5858	-76.6494	70.33	13.84	4.63	0.95	1.73	3.31	4.56	0.61	0.14
FJ3	Dickin & Strong 2021	FT-MSZ	MMZ-UN	Frontenac	44.5644	-76.6684	70.40	14.35	2.86	0.86	3.72	4.25	1.51	0.60	0.16
FJ72	Dickin & Strong 2021	FT-MSZ	MMZ-UN	Frontenac	44.6430	-76.6486	71.00	13.97	3.74	0.71	1.35	3.03	5.24	0.47	0.12
FJ78	Dickin & Strong 2021	FT-MSZ	MMZ-UN	Frontenac	44.7331	-76.6258	72.66	13.09	3.40	0.75	1.68	2.67	4.97	0.51	0.09
FJ9	Dickin & Strong 2021	FT-MSZ	MMZ-UN	Frontenac	44.7394	-76.5683	72.89	13.55	2.41	0.97	1.75	6.18	0.32	0.49	0.13
FJ43	Dickin & Strong 2021	FT-MSZ	MMZ-UN	Frontenac	44.6406	-76.6700	74.63	13.53	1.51	0.21	0.60	3.94	4.83	0.16	0.44
FJ73	Dickin & Strong 2021	FT-MSZ	MMZ-UN	Frontenac	44.6863	-76.6854	74.72	13.09	1.86	0.12	0.75	4.08	4.84	0.11	0.02
JS44	Dickin & Strong 2021	FT-MSZ	MMZ-UN	Frontenac	45.0593	-76.2326	75.61	12.94	1.70	0.22	0.60	2.50	6.73	0.16	0.03
15RME-0409	Easton 2016 (MRD351)	FT-MSZ	MMZ-UN	Frontenac	44.7663	-76.2861	49.79	15.76	9.27	5.31	7.76	4.31	2.81	2.36	1.03
16RME-0573	Easton 2016 (MRD351)	FT-MSZ	MMZ-UN	Frontenac	44.7954	-76.2276	50.97	16.17	9.21	3.07	5.11	3.93	5.58	2.06	1.29
16RME-0290	Easton 2016 (MRD351)	FT-MSZ	MMZ-UN	Frontenac	44.7572	-76.4759	52.76	13.11	13.09	3.28	5.77	3.89	2.68	2.55	1.30
16RME-0519	Easton 2016 (MRD351)	FT-MSZ	MMZ-UN	Frontenac	44.7676	-76.2291	54.02	14.59	6.40	7.47	7.53	4.34	3.20	0.69	0.37
15RME-0220	Easton 2016 (MRD351)	FT-MSZ	MMZ-UN	Frontenac	44.8855	-76.4277	54.76	17.44	6.85	2.04	4.87	5.10	3.87	1.91	0.95
15RME-0221	Easton 2016 (MRD351)	FT-MSZ	MMZ-UN	Frontenac	44.8666	-76.4539	58.27	18.18	4.54	1.54	2.93	4.69	5.54	1.19	0.49
15RME-0358	Easton 2016 (MRD351)	FT-MSZ	MMZ-UN	Frontenac	44.8505	-76.4230	58.92	17.97	4.70	1.89	3.55	4.68	5.83	1.15	0.40
16RME-0517	Easton 2016 (MRD351)	FT-MSZ	MMZ-UN	Frontenac	44.7622	-76.2268	58.96	17.52	2.61	2.99	6.93	6.98	1.14	0.51	0.39
15RME-0219	Easton 2016 (MRD351)	FT-MSZ	MMZ-UN	Frontenac	44.9514	-76.3786	60.19	18.50	3.55	1.24	2.07	4.78	6.58	0.90	0.28
16RME-0194	Easton 2016 (MRD351)	FT-MSZ	FT-UN	Frontenac	44.7534	-76.2058	60.75	19.92	2.26	2.52	5.29	5.10	1.21	0.82	0.21
15RME-0370	Easton 2016 (MRD351)	FT-MSZ	MMZ-UN	Frontenac	44.8381	-76.3301	61.56	17.39	4.94	1.42	1.63	4.52	6.61	0.85	0.26
15RME-0357	Easton 2016 (MRD351)	FT-MSZ	MMZ-UN	Frontenac	44.8483	-76.4204	62.98	17.33	2.14	1.35	2.97	3.68	8.20	0.69	0.33
16RME-0392	Easton 2016 (MRD351)	FT-MSZ	MMZ-UN	Frontenac	44.7535	-76.3899	64.85	17.16	0.59	0.76	1.96	2.54	10.91	0.16	0.06
16RME-0202	Easton 2016 (MRD351)	FT-MSZ	MMZ-UN	Frontenac	44.7941	-76.2694	68.70	12.71	5.42	0.47	2.12	2.86	5.69	0.88	0.06
15RME-0431	Easton 2016 (MRD351)	FT-MSZ	MMZ-UN	Frontenac	44.8469	-76.4805	68.87	14.60	2.70	1.17	1.62	3.89	4.78	1.29	0.17
15RME-0466	Easton 2016 (MRD351)	FT-MSZ	MMZ-UN	Frontenac	44.9034	-76.4015	68.92	17.32	0.56	0.88	2.49	7.62	1.88	0.13	0.03
16RME-0594	Easton 2016 (MRD351)	FT-MSZ	FT-UN	Frontenac	44.7807	-76.1090	69.68	15.91	2.04	0.45	2.51	3.32	4.63	0.16	0.06

Sample	Paper	Terrane	Pluton	Suite	Lat(°N)	Long(°E)	*wt%* SiO2	*wt%* Al2O3	*wt%* Fe2O3(t)	*wt%* MgO	*wt%* CaO	*wt%* Na2O	*wt%* K2O	*wt%* TiO2	*wt%* P2O5
16RME-0555	Easton 2016 (MRD351)	FT-MSZ	MMZ-UN	Frontenac	44.7844	-76.2363	70.88	16.08	0.17	0.50	1.34	4.19	6.08	0.07	0.08
15RME-0250	Easton 2016 (MRD351)	FT-MSZ	MMZ-UN	Frontenac	44.8996	-76.3294	72.69	15.45	1.08	0.44	1.39	3.35	5.09	0.17	0.04
15RME-0259	Easton 2016 (MRD351)	FT-MSZ	MMZ-UN	Frontenac	44.8849	-76.3577	73.00	15.58	0.72	0.21	1.23	3.89	5.31	0.12	0.02
16RME-0466	Easton 2016 (MRD351)	FT-MSZ	MMZ-UN	Frontenac	44.8861	-76.2500	73.34	15.11	0.77	0.15	1.33	4.74	3.71	0.09	0.02
15RME-0254	Easton 2016 (MRD351)	FT-MSZ	MMZ-UN	Frontenac	44.8906	-76.3475	73.38	14.67	1.09	0.19	0.98	3.32	5.84	0.19	0.10
16RME-0305	Easton 2016 (MRD351)	FT-MSZ	MMZ-UN	Frontenac	44.7798	-76.4657	74.20	14.56	0.26	0.15	1.73	4.36	3.83	0.04	0.01
16RME-0465	Easton 2016 (MRD351)	FT-MSZ	MMZ-UN	Frontenac	44.8862	-76.2502	74.32	14.61	0.69	0.12	1.12	4.58	4.00	0.06	0.01
16RME-0318	Easton 2016 (MRD351)	FT-MSZ	MMZ-UN	Frontenac	44.9361	-76.4249	75.40	14.26	0.86	0.13	0.62	5.40	3.88	0.06	0.00
16RME-0572	Easton 2016 (MRD351)	FT-MSZ	MMZ-UN	Frontenac	44.7965	-76.2277	83.27	6.44	1.66	1.22	1.90	2.40	0.96	0.45	0.05
LL138	Grammatikopoulos et al 2007	FT	Leo Lake	Frontenac	44.4461	-76.2650	43.01	13.29	20.03	6.60	10.20	2.51	0.63	2.83	0.09
LL53	Grammatikopoulos et al 2007	FT	Leo Lake	Frontenac	44.4506	-76.2481	46.48	14.55	9.66	14.11	10.07	1.90	0.67	0.45	0.10
LL120	Grammatikopoulos et al 2007	FT	Leo Lake	Frontenac	44.4572	-76.2567	47.37	######	16.53	5.79	8.15	3.12	1.31	2.68	0.29
LL56	Grammatikopoulos et al 2007	FT	Leo Lake	Frontenac	44.4464	-76.2492	49.32	16.29	10.38	4.59	7.06	4.52	2.41	1.95	0.48
LN25	Grammatikopoulos et al 2007	FT	Lyndhurst	Frontenac	44.5336	-76.1464	52.24	14.90	7.71	3.35	7.03	3.81	4.65	1.89	1.13
LL157	Grammatikopoulos et al 2007	FT	Leo Lake	Frontenac	44.4564	-76.2189	55.69	16.11	8.34	2.87	3.76	4.48	4.51	1.83	0.92
LN24	Grammatikopoulos et al 2007	FT	Lyndhurst	Frontenac	44.5264	-76.1967	55.82	14.94	8.31	3.00	4.38	4.43	4.53	1.80	0.82
LL137	Grammatikopoulos et al 2007	FT	Leo Lake	Frontenac	44.4464	-76.2569	55.83	15.99	8.04	1.73	4.47	5.00	4.34	2.27	0.88
LL04	Grammatikopoulos et al 2007	FT	Leo Lake	Frontenac	44.4542	-76.2350	56.28	16.83	7.89	2.34	3.78	4.33	4.33	1.84	0.77
LL23	Grammatikopoulos et al 2007	FT	Leo Lake	Frontenac	44.4561	-76.2347	56.58	16.15	7.81	2.20	4.21	4.09	4.81	1.67	0.73
LN23	Grammatikopoulos et al 2007	FT	Lyndhurst	Frontenac	44.5264	-76.1967	65.30	14.19	4.76	1.24	1.78	2.98	6.78	0.89	0.29
LN10	Grammatikopoulos et al 2007	FT	Lyndhurst	Frontenac	44.5472	-76.1472	66.86	16.76	3.19	0.70	3.09	3.99	3.92	0.37	0.13
LN06	Grammatikopoulos et al 2007	FT	Lyndhurst	Frontenac	44.5472	-76.1472	69.06	13.64	3.57	0.50	2.11	3.67	6.19	0.69	0.13
15RME-0247	Kamo & Hamilton, 2017	FT		Frontenac	44.8950	-76.3240									
15RME-0320	Kamo & Hamilton, 2017	FT		Frontenac	44.7293	-76.4959									
15RME-0420	Kamo & Hamilton, 2017	FT		Frontenac	44.7724	-76.2865									
21CK47A	Kinney	FT	Gananoque	Frontenac	44.4492	-76.0440	60.04	17.27	5.50	1.14	3.14	3.82	5.60	0.99	0.38
21CK48A	Kinney	FT	Gananoque	Frontenac	44.4168	-76.0533	60.65	16.21	6.65	1.03	3.38	4.17	5.16	1.23	0.49
21CK70A	Kinney	FT	Gananoque	Frontenac	44.3800	-76.1130	60.71	15.78	6.22	1.13	3.76	3.79	5.14	1.28	0.46
21CK76A	Kinney	FT	Lyndhurst	Frontenac	44.5418	-76.1368	61.34	13.76	7.21	1.54	3.56	3.21	4.94	1.43	0.64
20CK88A	Kinney	FT	Lyndhurst	Frontenac	44.5100	-76.1923	67.24	14.21	4.49	0.86	1.87	3.15	6.15	0.81	0.24
20CK36B	Kinney	FT	Crow Lake	Frontenac	44.4955	-76.3784	68.01	13.97	3.90	1.03	1.08	2.47	7.22	0.41	0.35
20CK06A	Kinney	FT	Crow Lake	Frontenac	44.5416	-76.2586	69.64	14.58	3.96	0.84	1.61	2.91	5.79	0.43	0.13
20CK86A	Kinney	FT	South Lake	Frontenac	44.4790	-76.2210	72.33	14.59	1.01	0.27	1.90	1.95	6.47	0.09	0.05
20CK18A	Kinney	FT	Crow Lake	Frontenac	44.5592	-76.3007	72.67	14.89	0.61	0.19	1.60	3.72	4.43	0.02	0.05
20CK52B	Kinney	FT	Battersea	Frontenac	44.4508	-76.3740	75.37	13.17	1.77	0.13	0.61	4.35	3.35	0.07	0.02
20CK100A	Kinney	FT	Crow Lake	Frontenac	44.5886	-76.2692	76.92	9.27	3.67	0.84	0.95	4.39	1.76	0.53	0.09
5207W	Krogh & Hurley 1968	FT	Westport	Kensington-Skootamatta	44.7178	-76.3508									
R5179G	Krogh & Hurley 1968	FT	Gananoque	Frontenac											
R5180G	Krogh & Hurley 1968	FT	Gananoque	Frontenac											
R5181G	Krogh & Hurley 1968	FT	Gananoque	Frontenac											
R5182G	Krogh & Hurley 1968	FT	Gananoque	Frontenac											
R5183W	Krogh & Hurley 1968	FT	Westport	Kensington-Skootamatta											
R5184W	Krogh & Hurley 1968	FT	Westport	Kensington-Skootamatta											
R5185W	Krogh & Hurley 1968	FT	Westport	Kensington-Skootamatta											
R5186L	Krogh & Hurley 1968	FT	Gananoque	Frontenac											
R5208W	Krogh & Hurley 1968	FT	Westport	Kensington-Skootamatta	44.6842	-76.4000									
R5209W	Krogh & Hurley 1968	FT	Westport	Kensington-Skootamatta	44.6842	-76.4000									

Sample	Paper	Terrane	Pluton	Suite	Lat(°N)	Long(°E)	*wt%* SiO2	*wt%* Al2O3	*wt%* Fe2O3(t)	*wt%* MgO	*wt%* CaO	*wt%* Na2O	*wt%* K2O	*wt%* TiO2	*wt%* P2O5
LH87-30	Marcantonio et al, 1990	FT	Crow Lake	Frontenac											
LH86-64	Marcantonio et al, 1990	FT	Perth Road	Frontenac	44.9034	-76.4014	61.00	16.80	6.49	1.40	4.10	4.60	4.60	1.30	0.40
LH87-31	Marcantonio et al, 1990	FT	Lyndhurst	Frontenac											
LH86-63	Marcantonio et al, 1990	FT	Battersea	Frontenac	44.4508	-76.3740	67.60	14.10	5.39	1.20	2.30	3.40	5.50	0.80	0.20
WP1	Marcantonio et al, 1990	FT-MSZ	Westport	Kensington-Skootamatta	44.6931	-76.3925	62.40	17.20	4.51	0.80	1.80	5.00	6.80	0.80	0.10
LH86-7	Marcantonio et al, 1990	FT-MSZ	Westport	Kensington-Skootamatta	44.6931	-76.3925	62.30	17.70	4.73	0.90	1.80	5.10	6.80	0.90	0.10
CL3	Marcantonio et al, 1990	FT	Crow Lake	Frontenac	44.5374	-76.2630	63.60	16.70	5.28	1.50	1.80	3.60	6.80	0.80	0.40
RLI	Marcantonio et al, 1990	FT-MSZ	Rideau Lake	Kensington-Skootamatta	44.7103	-76.2993	60.60	18.10	4.51	2.50	2.10	4.90	6.50	0.90	0.20
LY3	Marcantonio et al, 1990	FT	Lyndhurst	Frontenac	44.5100	-76.1923	68.30	14.20	4.85	0.80	2.10	3.20	5.80	0.80	0.20
GQ1	Marcantonio et al, 1990	FT	Gananoque	Frontenac	44.3800	-76.1130									
SL2	Marcantonio et al, 1990	FT	South Lake	Frontenac	44.4002	-76.2106	60.70	17.50	6.49	1.40	3.50	4.30	5.20	1.10	0.40
BS1	Marcantonio et al, 1990	FT	Battersea	Frontenac	44.4508	-76.3740									
WL1	Marcantonio et al, 1990	FT-MSZ	Wolfe Lake	Kensington-Skootamatta	44.6991	-76.4274	61.10	18.40	4.73	1.00	1.90	5.20	6.60	1.10	0.30
GQI	Marcantonio et al, 1990	FT	Gananoque	Frontenac	44.3800	-76.1130	61.20	16.50	7.37	1.30	3.60	4.00	4.90	1.40	0.40
BSI	Marcantonio et al, 1990	FT	Battersea	Frontenac	44.4508	-76.3740	66.10	14.80	5.72	1.10	2.50	3.70	5.50	0.90	0.30
CL3	Marcantonio et al, 1990	FT	Crow Lake	Frontenac	44.5374	-76.2630									
LY3	Marcantonio et al, 1990	FT	Lyndhurst	Frontenac	44.5100	-76.1923									
16RME-0280	MRD351	FT-MSZ	MMZ-UN	Frontenac	44.7039	-76.4301	40.89	10.42	18.33	5.97	9.91	2.64	2.31	4.30	2.94
16RME-0557A	MRD351	FT-MSZ	MMZ-UN	Frontenac	44.7855	-76.2358	45.78	17.94	4.42	11.36	2.13	0.39	9.65	1.07	1.21
16RME-0366	MRD351	FT-MSZ	MMZ-UN	Frontenac	44.7720	-76.3640	46.78	14.57	13.28	8.75	9.32	3.33	1.23	1.09	0.08
16RME-0376	MRD351	FT-MSZ	MMZ-UN	Frontenac	44.7661	-76.3704	47.24	15.71	12.22	6.21	7.38	4.25	2.12	2.07	0.61
16RME-0253	MRD351	FT-MSZ	MMZ-UN	Frontenac	44.7977	-76.3393	47.42	16.21	10.09	5.82	8.88	3.95	0.92	2.28	0.60
16RME-0389	MRD351	FT-MSZ	MMZ-UN	Frontenac	44.7538	-76.3897	47.47	16.89	11.13	6.40	7.80	3.87	2.02	1.44	0.44
16RME-0535	MRD351	FT-MSZ	MMZ-UN	Frontenac	44.8944	-76.2896	47.75	17.35	10.48	4.22	7.10	3.37	3.93	1.88	1.00
16RME-0237	MRD351	FT-MSZ	MMZ-UN	Frontenac	44.8212	-76.3178	48.33	15.94	9.95	4.72	7.05	2.87	5.59	1.79	1.76
15RME-0090	MRD351	FT-MSZ	MMZ-UN	Frontenac	44.8917	-76.3200	48.61	14.99	12.51	5.38	8.18	3.50	2.33	2.15	1.00
16RME-0529	MRD351	FT-MSZ	MMZ-UN	Frontenac	44.8786	-76.2965	52.62	15.06	6.96	6.88	6.86	3.34	4.88	0.86	0.57
16RME-0211	MRD351	FT-MSZ	MMZ-UN	Frontenac	44.7956	-76.2524	54.12	15.78	11.01	4.23	7.31	4.15	0.84	1.80	0.26
15RME-0359	MRD351	FT-MSZ	MMZ-UN	Frontenac	44.8516	-76.4243	57.17	14.11	11.20	4.32	7.00	3.38	1.30	1.37	0.16
MEW1	Peck et al 2013	FT	Crow Lake	Frontenac	44.5123	-76.2918	43.47	13.69	13.85	6.27	5.20	1.89	6.40	3.12	6.27
JJF1	Peck et al 2013	FT	Crow Lake	Frontenac	44.5127	-76.2920	47.04	14.30	14.84	5.71	3.96	3.50	4.38	2.57	5.71
JK02	Peck et al 2013	FT	Crow Lake	Frontenac	44.5135	-76.2927	47.83	15.33	10.04	4.13	7.51	3.52	4.12	2.18	4.13
MEW2	Peck et al 2013	FT	Crow Lake	Frontenac	44.5135	-76.2927	48.73	15.44	11.87	5.13	4.87	3.45	4.39	1.88	5.13
JT2	Peck et al 2013	FT	Crow Lake	Frontenac	44.5353	-76.2792	48.75	15.12	12.90	4.38	5.77	3.91	3.76	1.94	4.38
MP2	Peck et al 2013	FT	Crow Lake	Frontenac	44.5353	-76.2794	50.72	15.63	11.26	3.81	5.23	3.80	4.46	1.71	3.81
JK01	Peck et al 2013	FT	Crow Lake	Frontenac	44.5123	-76.2918	51.96	15.70	10.17	4.98	3.96	3.49	4.52	1.65	4.98
KC03	Peck et al 2013	FT	South Lake	Frontenac	44.3888	-76.2323	57.80	16.80	7.29	1.41	4.01	4.24	4.87	1.54	0.68
KC02	Peck et al 2013	FT	South Lake	Frontenac	44.3888	-76.2323	58.91	17.48	6.87	1.64	3.86	4.55	4.65	1.51	0.80
MP3	Peck et al 2013	FT	South Lake	Frontenac	44.4002	-76.2106	59.22	17.38	6.50	1.27	3.73	4.52	4.96	1.36	0.53
JT3	Peck et al 2013	FT	South Lake	Frontenac	44.4002	-76.2106	59.57	17.25	5.65	1.19	3.74	4.40	5.32	1.19	0.46
MP4	Peck et al 2013	FT	South Lake	Frontenac	44.4002	-76.2106	60.37	17.08	4.72	1.22	3.81	4.10	5.50	1.10	0.43
JT4	Peck et al 2013	FT	South Lake	Frontenac	44.4002	-76.2106	60.92	17.77	5.67	1.50	3.27	4.76	4.98	1.12	0.45
JK03	Peck et al 2013	FT	South Lake	Frontenac	44.3727	-76.1994	60.95	16.72	6.21	1.25	3.46	4.74	4.93	1.19	0.47
JJF2	Peck et al 2013	FT	South Lake	Frontenac	44.3731	-76.1990	61.38	18.10	5.37	1.20	3.58	4.32	5.10	1.10	0.45
JJF3	Peck et al 2013	FT	South Lake	Frontenac	44.3727	-76.1994	61.69	16.67	5.92	1.18	3.34	4.17	5.16	1.11	0.46
MEW3	Peck et al 2013	FT	South Lake	Frontenac	44.3727	-76.1994	61.89	17.64	5.55	1.03	3.31	4.37	4.99	1.07	0.44
EHW02	Peck et al 2013	FT	Crow Lake	Frontenac	44.5581	-76.2739	67.68	16.00	4.75	1.44	1.33	3.32	6.03	0.28	1.44

Sample	Paper	Terrane	Pluton	Suite	Lat(°N)	Long(°E)	*wt%* SiO2	*wt%* Al2O3	*wt%* Fe2O3(t)	*wt%* MgO	*wt%* CaO	*wt%* Na2O	*wt%* K2O	*wt%* TiO2	*wt%* P2O5
KC01	Peck et al 2013	FT	Crow Lake	Frontenac	44.5581	-76.2739	67.94	15.75	4.38	1.40	1.37	3.43	6.08	0.32	1.40
JT1	Peck et al 2013	FT	Crow Lake	Frontenac	44.5353	-76.2794	68.07	14.80	5.23	1.57	0.91	2.65	6.76	0.31	1.57
MP1	Peck et al 2013	FT	Crow Lake	Frontenac	44.5353	-76.2794	68.32	14.66	4.92	1.36	0.83	2.74	6.70	0.28	1.36
LJT1	Peck et al 2013	FT	Crow Lake	Frontenac	44.5123	-76.2918	69.15	14.06	3.80	0.83	1.48	3.01	5.80	0.21	0.83
DH2	Peck et al 2013	FT	Crow Lake	Frontenac	44.5427	-76.2646	70.70	15.14	3.68	0.94	1.03	3.17	6.46	0.23	0.94
EHW01	Peck et al 2013	FT	Crow Lake	Frontenac	44.5581	-76.2739	71.02	14.67	3.94	1.08	1.19	2.86	6.13	0.24	1.08
DH1	Peck et al 2013	FT	Crow Lake	Frontenac	44.5374	-76.2630	72.08	14.40	3.58	0.82	1.40	3.26	5.83	0.16	0.82
LJT3	Peck et al 2013	FT	South Lake	Frontenac	44.3985	-76.1862	73.05	14.47	1.82	0.55	0.55	3.86	4.51	0.17	0.06
DH3	Peck et al 2013	FT	South Lake	Frontenac	44.4166	-76.1865	73.94	14.91	1.65	0.42	0.90	3.81	4.64	0.29	0.08
LJT2	Peck et al 2013	FT	South Lake	Frontenac	44.4164	-76.1870	75.45	14.94	1.31	0.01	0.97	4.52	4.06	0.16	0.03
86DM96	Peck et al. 2004	FT	South Lake	Frontenac											
93DM131	Peck et al. 2004	FT-MSZ	North Crosby	Frontenac											
89S3	Shieh 1985	FT-MSZ	Westport	Frontenac	44.6931	-76.3925									
89S4	Shieh 1985	FT	Battersea	Frontenac	44.4508	-76.3740									
89S1	Shieh 1985	FT-MSZ	Rideau Lake	Frontenac	44.7103	-76.2993									
89S2	Shieh 1985	FT-MSZ	Wolfe Lake	Frontenac	44.6991	-76.4274									
89S5	Shieh 1985	FT	Perth Road	Frontenac	44.9034	-76.4014									
89S6	Shieh 1985	FT	Lyndhurst	Frontenac	44.5100	-76.1923									
89S7	Shieh 1985	FT	Gananoque	Frontenac	44.4492	-76.0440									
89S8	Shieh 1985	FT	South Lake	Frontenac	44.4164	-76.1870									
89S9	Shieh 1985	FT	Crow Lake	Frontenac	44.5353	-76.2794									

	wt%	*wt%*	*wt%*	*wt%*	*wt%*	*wt%*	*dry mol%*	*dry mol%*	*dry mol%*	*dry mol%*	*dry mol%*	*dry mol%*	*dry mol%*	*dry mol%*	*dry mol%*	*dry mol%*
Sample	**MnO**	**Cr2O3**	**LOI**	**Total**	**FeO**	**Fe2O3**	**SiO2**	**Al2O3**	**Fe2O3(t)**	**MgO**	**CaO**	**Na2O**	**K2O**	**TiO2**	**P2O5**	**MnO**
109	0.07	0.00	1.30		11.20	5.30	55.71	10.62	7.91	9.37	8.25	2.30	3.10	2.67	0.00	0.07
154	0.06	0.00	2.10		8.20	3.90	55.97	12.56	5.83	7.81	9.44	3.92	2.43	1.97	0.00	0.06
199	0.10	0.00	1.80		10.10	4.40	56.88	10.94	6.91	9.81	6.29	4.21	3.00	1.86	0.00	0.10
145	0.06	0.00	1.50		5.90	4.10	57.37	13.80	4.69	8.55	6.90	4.99	1.87	1.76	0.00	0.06
108	0.06	0.00	1.10		8.00	4.40	58.19	12.92	5.83	8.34	5.50	3.05	3.57	2.54	0.00	0.06
64-35	0.16	0.00	1.60				57.51	11.25	4.41	9.43	10.47	4.01	1.03	1.73	0.00	0.16
183	0.04	0.00	1.80		5.30	3.20	61.87	11.63	3.99	6.61	5.00	4.64	4.02	2.20	0.00	0.04
64-34	0.08	0.00	1.80				57.36	9.57	1.95	12.91	12.17	3.67	1.73	0.57	0.00	0.07
64-60	0.04	0.00	0.90		2.30	2.50	68.55	12.45	2.18	3.25	3.44	5.34	3.88	0.86	0.00	0.04
64-61	0.03	0.00	0.60		1.80	3.30	69.50	12.99	2.31	0.86	3.73	5.85	3.85	0.87	0.00	0.03
64-58	0.03	0.00	0.70				69.34	12.60	2.61	1.90	3.10	5.04	4.35	1.04	0.00	0.03
64-59	0.05	0.00	1.00		1.80	3.00	69.72	12.56	2.17	0.86	4.20	5.47	4.19	0.78	0.00	0.05
104	0.02	0.00	0.70		3.00	2.40	69.87	12.46	2.48	2.06	3.45	5.01	3.96	0.69	0.00	0.02
113	0.04	0.00	1.20		2.30	2.90	71.04	12.70	2.39	2.26	2.74	4.18	3.86	0.79	0.00	0.04
139	0.02	0.00	1.20		2.40	2.20	70.26	12.22	2.11	2.40	3.45	4.13	4.63	0.78	0.00	0.02
64-57	0.03	0.00	0.50				70.35	12.13	1.76	1.36	4.04	5.21	4.16	0.95	0.00	0.03
170	0.04	0.00	0.90		2.40	3.00	71.42	10.76	2.43	2.38	2.44	5.31	4.37	0.86	0.00	0.04
216	0.02	0.00	1.10		1.10	1.60	71.86	11.96	1.20	2.52	2.54	5.69	3.45	0.76	0.00	0.02
506	0.00	0.00	0.20				74.38	12.78	0.13	0.00	3.25	3.92	5.37	0.17	0.00	0.00
180	0.04	0.00	0.80		2.10	1.30	75.30	9.19	1.52	1.83	2.39	4.64	4.26	0.84	0.00	0.04
152	0.03	0.00	1.10		1.60	1.80	75.57	9.21	1.50	1.33	2.27	4.98	4.27	0.84	0.00	0.03
213	0.01	0.00	1.00		1.30	1.40	74.90	9.66	1.18	2.46	2.47	5.54	3.37	0.41	0.00	0.01
130	0.03	0.00	1.00		1.90	1.00	77.08	9.15	1.30	1.49	1.19	6.77	2.41	0.58	0.00	0.03
64-44a	0.02	0.00	1.20		1.00	1.10	77.93	9.58	0.93	1.17	1.44	4.13	4.29	0.51	0.00	0.02
516	0.00	0.00	0.20				78.71	12.27	0.17	0.33	2.16	1.41	4.36	0.59	0.00	0.00
FJ97	0.05	0.00	0.51				77.68	8.85	1.81	2.07	2.55	2.99	3.43	0.53	0.04	0.05
64-43	0.03	0.00	0.80		1.70	1.20	77.94	9.45	1.28	0.99	2.01	3.97	3.67	0.67	0.00	0.03
151	0.01	0.00	1.00		1.00	1.60	79.41	9.23	1.14	0.33	1.68	3.25	4.28	0.67	0.00	0.01
105	0.01	0.00	0.60		1.00	1.70	78.88	9.34	1.17	0.83	1.66	3.87	3.75	0.50	0.00	0.01
513	0.01	0.00	0.10				64.59	8.93	0.03	0.27	20.18	2.35	3.43	0.20	0.00	0.01
501	0.00	0.00	0.30				0.00	0.00	34.51	1.95	1.40	4.66	4.18	35.81	0.46	0.00
JC-050	0.12	0.00	0.71	99.65			69.51	11.99	2.00	2.29	2.02	6.46	4.85	0.67	0.10	0.12
JC-070	0.09	0.00	0.86	99.17			69.40	12.52	1.92	2.43	2.68	5.60	4.35	0.93	0.10	0.08
JC-014																
JC-043																
JC-067																
JC-045																
JC-081	0.07	0.00	0.95	99.59			71.05	11.82	1.74	1.82	1.97	6.16	4.57	0.73	0.07	0.07
91DM14b																
93DM18b																
93DM19																
94DM53																
96DM1																
91DM131a																
15RME-0179																
FJ50	0.01		0.78				80.04	9.70	0.34	0.49	1.53	3.82	4.00	0.06	0.01	0.01
FJ24	0.11	0.00	1.43				60.15	10.79	4.10	7.32	9.60	4.99	1.38	1.37	0.18	0.11

	wt%	*wt%*	*wt%*	*wt%*	*wt%*	*wt%*	*dry mol%*	*dry mol%*	*dry mol%*	*dry mol%*	*dry mol%*	*dry mol%*	*dry mol%*	*dry mol%*	*dry mol%*	*dry mol%*
Sample	**MnO**	**Cr2O3**	**LOI**	**Total**	**FeO**	**Fe2O3**	**SiO2**	**Al2O3**	**Fe2O3(t)**	**MgO**	**CaO**	**Na2O**	**K2O**	**TiO2**	**P2O5**	**MnO**
FJ27	0.01		0.83				75.97	11.45	0.54	0.80	1.11	2.81	7.07	0.16	0.10	0.01
FJ40	0.03		1.79				70.48	10.94	2.65	2.46	3.65	4.21	4.22	1.21	0.14	0.03
FJ51	0.05	0.00	1.20				69.51	12.01	1.78	1.25	4.41	5.94	4.21	0.78	0.06	0.05
FJ93	0.02		1.15				76.86	9.65	0.99	1.19	1.80	3.60	4.89	0.95	0.05	0.02
FJ20	0.04	0.00	1.13				69.98	12.29	1.84	1.97	2.75	5.61	4.73	0.72	0.07	0.04
FJ46	0.08	0.00	1.30				65.78	12.24	2.89	3.20	5.27	5.44	3.90	1.09	0.11	0.08
FJ18	0.01	0.00	0.44				81.20	8.96	0.53	0.29	1.48	4.75	2.70	0.07	0.01	0.01
FJ22	0.10	0.00	1.49				55.55	12.37	4.90	8.49	11.14	4.95	1.07	1.36	0.08	0.10
FJ44	0.15	0.00	1.27				62.85	10.76	4.39	4.98	6.70	5.58	2.47	1.88	0.26	0.15
FJ45	0.16	0.00	0.78				63.94	11.95	3.76	3.66	6.83	5.58	2.34	1.58	0.19	0.16
FJ2	0.15	0.00	0.89				67.72	9.07	5.13	3.64	5.13	6.04	1.24	1.67	0.19	0.15
FJ25	0.11	0.00	0.83				67.84	11.15	3.08	2.68	4.99	5.78	3.18	1.10	0.09	0.11
FJ67	0.15	0.00	0.82				70.64	9.89	3.53	2.69	4.55	5.12	2.34	1.00	0.10	0.14
FJ16	0.03		1.96				72.29	11.96	1.21	0.67	2.16	5.78	5.21	0.69	0.01	0.03
FJ12	0.04	0.00	1.35				70.92	11.65	2.22	3.12	4.42	5.74	0.98	0.84	0.08	0.04
FJ60	0.03	0.00	2.14				74.72	8.79	2.64	2.35	2.94	6.42	1.14	0.92	0.07	0.03
JS46	0.03	0.00	0.92				77.59	8.81	1.80	0.86	2.78	3.76	3.81	0.52	0.02	0.03
FJ8	0.07	0.00	0.73				78.22	8.83	2.07	1.13	3.07	2.91	3.07	0.59	0.04	0.07
FJ7	0.06	0.00	0.43				77.59	8.87	2.02	1.76	2.58	3.89	2.69	0.52	0.04	0.06
FJ4	0.04	0.00	0.76				78.23	8.80	1.85	1.51	2.08	3.67	3.34	0.46	0.03	0.04
FJ63	0.04	0.00	1.15				76.83	9.17	1.41	2.81	3.09	4.14	2.14	0.35	0.01	0.04
FJ26	0.05	0.00	0.87				77.58	8.51	1.89	2.32	4.20	3.58	0.71	1.11	0.05	0.05
FJ64	0.05	0.00	0.46				78.02	9.05	1.93	1.57	2.06	3.56	3.23	0.51	0.03	0.05
FJ3	0.03	0.00	0.53				77.54	9.31	1.19	1.41	4.39	4.54	1.06	0.50	0.04	0.03
FJ72	0.04	0.00	0.51				79.03	9.16	1.57	1.18	1.61	3.27	3.72	0.39	0.03	0.04
FJ78	0.03	0.00	0.62				80.06	8.50	1.41	1.23	1.98	2.85	3.49	0.42	0.02	0.03
FJ9	0.03	0.00	0.46				79.47	8.71	0.99	1.58	2.04	6.53	0.22	0.40	0.03	0.03
FJ43	0.02	0.00	0.32				81.78	8.74	0.62	0.34	0.70	4.19	3.38	0.13	0.10	0.02
FJ73	0.03	0.00	0.46				81.87	8.45	0.77	0.20	0.88	4.33	3.38	0.09	0.00	0.03
JS44	0.01	0.00	0.37				82.46	8.32	0.70	0.36	0.70	2.64	4.68	0.13	0.01	0.01
15RME-0409	0.12	0.01	2.07	100.71	6.53	2.01	57.33	10.69	4.02	9.11	9.57	4.81	2.06	2.04	0.25	0.11
16RME-0573	0.07	0.00	1.42	99.00	4.51	4.20	61.21	11.44	4.16	5.50	6.58	4.57	4.27	1.86	0.33	0.08
16RME-0290	0.18	0.00	0.78	99.47	6.93	5.39	62.58	9.16	5.84	5.80	7.34	4.47	2.03	2.28	0.33	0.18
16RME-0519	0.08	0.05	1.22	100.08	3.92	2.04	59.27	9.43	2.64	12.22	8.86	4.62	2.24	0.57	0.08	0.07
15RME-0220	0.09	0.00	0.85	99.01	3.27	3.22	64.42	12.09	3.03	3.58	6.14	5.82	2.90	1.69	0.24	0.09
15RME-0221	0.06	0.00	1.42	99.26	2.26	2.03	68.35	12.57	2.00	2.69	3.68	5.33	4.14	1.05	0.12	0.06
15RME-0358	0.06	0.00	1.24	100.63	2.30	2.14	67.60	12.15	2.03	3.23	4.37	5.20	4.27	0.99	0.10	0.06
16RME-0517	0.04	0.01	1.63	99.73	1.36	1.10	65.41	11.45	1.09	4.95	8.23	7.51	0.81	0.43	0.09	0.03
15RME-0219	0.02	0.00	1.26	99.54	1.17	2.25	69.93	12.66	1.55	2.15	2.57	5.38	4.88	0.79	0.07	0.02
16RME-0194	0.01	0.00	2.19	100.32	1.40	0.70	68.15	13.17	0.95	4.21	6.36	5.55	0.87	0.69	0.05	0.01
15RME-0370	0.04	0.00	1.01	100.42	2.19	2.51	70.88	11.80	2.14	2.44	2.00	5.05	4.85	0.74	0.06	0.04
15RME-0357	0.06	0.00	0.83	100.69	1.13	0.88	71.06	11.52	0.91	2.27	3.59	4.02	5.90	0.59	0.08	0.05
16RME-0392	0.02	0.00	1.01	100.14	0.35	0.20	73.71	11.49	0.25	1.29	2.38	2.80	7.91	0.14	0.02	0.02
16RME-0202	0.03	0.00	0.87	99.98	1.67	3.56	77.80	8.48	2.31	0.79	2.57	3.14	4.11	0.75	0.02	0.02
15RME-0431	0.02	0.00	1.54	100.89	1.40	1.14	76.68	9.58	1.13	1.94	1.93	4.20	3.39	1.08	0.04	0.02
15RME-0466	0.02	0.01	1.56	101.45	0.40	0.12	74.90	11.09	0.23	1.43	2.89	8.03	1.30	0.11	0.01	0.02
16RME-0594	0.04	0.00	0.66	99.55	1.13	0.78	77.83	10.47	0.86	0.75	3.00	3.59	3.30	0.13	0.01	0.04

	wt%	*wt%*	*wt%*	*wt%*	*wt%*	*wt%*	*dry mol%*	*dry mol%*	*dry mol%*	*dry mol%*	*dry mol%*	*dry mol%*	*dry mol%*	*dry mol%*	*dry mol%*	*dry mol%*
Sample	**MnO**	**Cr2O3**	**LOI**	**Total**	**FeO**	**Fe2O3**	**SiO2**	**Al2O3**	**Fe2O3(t)**	**MgO**	**CaO**	**Na2O**	**K2O**	**TiO2**	**P2O5**	**MnO**
16RME-0555	0.00	0.01	0.85	100.32	0.16	-0.01	78.23	10.46	0.07	0.82	1.58	4.48	4.28	0.06	0.02	0.00
15RME-0250	0.02	0.01	1.14	100.90	0.65	0.36	79.89	10.01	0.45	0.72	1.64	3.57	3.57	0.14	0.01	0.01
15RME-0259	0.01	0.00	0.95	101.11	0.35	0.33	79.91	10.05	0.30	0.34	1.45	4.13	3.71	0.10	0.00	0.01
16RME-0466	0.01	0.00	0.51	99.84	0.25	0.49	80.40	9.76	0.32	0.25	1.56	5.04	2.59	0.07	0.00	0.01
15RME-0254	0.01	0.01	1.14	100.96	0.27	0.79	80.75	9.51	0.45	0.31	1.15	3.54	4.10	0.16	0.02	0.00
16RME-0305	0.00	0.00	0.94	100.12	0.17	0.07	80.95	9.36	0.11	0.24	2.02	4.61	2.66	0.03	0.00	0.00
16RME-0465	0.01	0.00	0.64	100.21	0.26	0.40	81.12	9.40	0.28	0.20	1.31	4.85	2.78	0.05	0.00	0.01
16RME-0318	0.02	0.00	0.25	100.89	0.18	0.66	81.29	9.06	0.35	0.21	0.72	5.64	2.67	0.05	0.00	0.02
16RME-0572	0.02	0.01	0.99	99.39	1.20	0.33	87.79	4.00	0.66	1.92	2.15	2.45	0.65	0.36	0.01	0.02
LL138	0.17		0.58				51.04	9.29	8.94	11.68	12.97	2.89	0.48	2.53	0.02	0.17
LL53	0.22		1.81				49.80	9.19	3.89	22.54	11.56	1.97	0.46	0.36	0.02	0.20
LL120	0.23		0.18				4.94	91.97	0.65	0.90	0.91	0.32	0.09	0.21	0.01	0.02
LL56	0.43		1.37				57.97	11.28	4.59	8.04	8.89	5.15	1.81	1.72	0.12	0.43
LN25	0.09		3.08				61.57	10.35	3.42	5.89	8.88	4.35	3.50	1.68	0.28	0.09
LL157	0.08		1.84				65.15	11.10	3.67	5.01	4.71	5.08	3.36	1.61	0.23	0.08
LN24	0.14		0.33				65.10	10.27	3.65	5.22	5.47	5.01	3.37	1.58	0.20	0.14
LL137	0.05		1.84				65.53	11.06	3.55	3.03	5.62	5.69	3.25	2.00	0.22	0.05
LL04	0.27		0.81				65.87	11.61	3.47	4.08	4.74	4.91	3.23	1.62	0.19	0.27
LL23	0.10		0.65				66.29	11.15	3.44	3.84	5.28	4.64	3.59	1.47	0.18	0.10
LN23	0.06		0.54				74.88	9.59	2.05	2.12	2.19	3.31	4.96	0.77	0.07	0.06
LN10	0.06		0.70				75.11	11.09	1.35	1.17	3.72	4.35	2.81	0.31	0.03	0.06
LN06	0.07		1.15				77.11	8.97	1.50	0.83	2.52	3.97	4.41	0.58	0.03	0.07
15RME-0247																
15RME-0320																
15RME-0420																
21CK47A	0.03					2.83	70.24	11.91	2.42	1.99	3.94	4.33	4.18	0.87	0.09	0.03
21CK48A	0.06					4.42	70.30	11.07	2.90	1.78	4.20	4.69	3.81	1.07	0.12	0.06
21CK70A	0.08					2.89	70.48	10.79	2.72	1.96	4.68	4.26	3.81	1.11	0.11	0.08
21CK76A	0.11					3.66	71.46	9.45	3.16	2.67	4.44	3.63	3.67	1.25	0.16	0.11
20CK88A	0.05					1.93	76.18	9.49	1.91	1.45	2.27	3.46	4.44	0.69	0.06	0.05
20CK36B	0.02					1.79	77.46	9.38	1.67	1.75	1.32	2.73	5.24	0.35	0.08	0.02
20CK06A	0.02					1.62	77.74	9.59	1.66	1.40	1.93	3.15	4.12	0.36	0.03	0.02
20CK86A	0.01					0.12	80.50	9.57	0.42	0.45	2.27	2.10	4.59	0.08	0.01	0.01
20CK18A	0.01					0.01	80.62	9.73	0.25	0.31	1.90	4.00	3.13	0.02	0.01	0.01
20CK52B	0.01					1.11	82.77	8.52	0.73	0.21	0.72	4.63	2.35	0.06	0.00	0.01
20CK100A	0.05					2.78	83.73	5.95	1.50	1.36	1.11	4.63	1.22	0.43	0.02	0.05
5207W																
R5179G																
R5180G																
R5181G																
R5182G																
R5183W																
R5184W																
R5185W																
R5186L																
R5208W																
R5209W																

Sample	wt% MnO	wt% Cr2O3	wt% LOI	wt% Total	wt% FeO	wt% Fe2O3	dry mol% SiO2	dry mol% Al2O3	dry mol% Fe2O3(t)	dry mol% MgO	dry mol% CaO	dry mol% Na2O	dry mol% K2O	dry mol% TiO2	dry mol% P2O5	dry mol% MnO
LH87-30																
LH86-64	0.00			100.10		0.60	69.10	11.21	2.77	2.36	4.98	5.05	3.32	1.11	0.10	0.00
LH87-31																
LH86-63	0.10			100.10		0.50	75.34	9.26	2.26	1.99	2.75	3.67	3.91	0.67	0.05	0.09
WP1	0.10	0.00	0.00	99.10		0.40	71.52	11.62	1.95	1.37	2.21	5.56	4.97	0.69	0.02	0.10
LH86-7	0.10	0.00	0.00	100.00		0.40	70.92	11.87	2.03	1.53	2.20	5.63	4.94	0.77	0.02	0.10
CL3	0.00			100.00		0.50	72.19	11.17	2.25	2.54	2.19	3.96	4.92	0.68	0.10	0.00
RLI	0.10	0.00	0.00	100.00		0.40	68.37	12.03	1.92	4.20	2.54	5.36	4.68	0.76	0.05	0.10
LY3	0.10			99.90		0.40	76.34	9.35	2.04	1.33	2.51	3.47	4.13	0.67	0.05	0.09
GQ1																
SL2	0.10			100.10		0.60	69.16	11.75	2.78	2.38	4.27	4.75	3.78	0.94	0.10	0.10
BS1																
WL1	0.10	0.00	0.00	100.00		0.40	69.85	12.39	2.04	1.70	2.33	5.76	4.81	0.95	0.07	0.10
GQI	0.10			100.10		0.70	69.77	11.08	3.16	2.21	4.40	4.42	3.56	1.20	0.10	0.10
BSI	0.00			100.10		0.50	74.16	9.78	2.42	1.84	3.01	4.02	3.94	0.76	0.07	0.00
CL3																
LY3																
16RME-0280	0.23	0.00	1.43	99.50	9.09	8.23	50.16	7.53	8.46	10.92	13.02	3.14	1.81	3.97	0.76	0.24
16RME-0557A	0.01	0.00	4.42	98.71	2.68	1.44	53.96	12.46	1.96	19.96	2.69	0.45	7.25	0.95	0.30	0.01
16RME-0366	0.18	0.04	0.97	99.62	9.78	2.41	52.93	9.71	5.65	14.76	11.29	3.65	0.89	0.93	0.02	0.17
16RME-0376	0.14	0.00	2.06	100.11	9.23	1.96	55.23	10.82	5.38	10.82	9.24	4.82	1.58	1.82	0.15	0.13
16RME-0253	0.11	0.01	2.75	99.08	7.75	1.48	55.59	11.20	4.45	10.17	11.15	4.49	0.69	2.01	0.15	0.11
16RME-0389	0.14	0.00	1.43	99.13	6.54	3.86	55.30	11.59	4.88	11.11	9.74	4.37	1.50	1.26	0.11	0.14
16RME-0535	0.10	0.00	1.52	98.88	5.67	4.18	57.32	12.27	4.73	7.55	9.13	3.92	3.01	1.70	0.25	0.10
16RME-0237	0.14	0.02	1.21	99.61	7.33	1.80	57.37	11.15	4.44	8.35	8.97	3.30	4.23	1.60	0.44	0.14
15RME-0090	0.17	0.00	0.93	99.85	7.98	3.64	56.67	10.30	5.49	9.35	10.22	3.96	1.73	1.89	0.25	0.16
16RME-0529	0.10	0.04	1.21	99.56	4.36	2.11	59.18	9.98	2.95	11.54	8.26	3.64	3.50	0.73	0.13	0.09
16RME-0211	0.13	0.01	0.67	100.32	6.88	3.36	61.66	10.59	4.72	7.18	8.92	4.58	0.61	1.54	0.06	0.12
15RME-0359	0.14	0.01	0.78	100.98	6.97	3.45	64.29	9.35	4.74	7.24	8.43	3.68	0.93	1.16	0.04	0.13
MEW1	0.05		2.68	102.89			53.47	9.92	6.41	11.50	6.85	2.25	5.02	2.89	1.63	0.05
JJF1	0.05		1.26	103.32			56.56	10.13	6.71	10.23	5.10	4.08	3.36	2.32	1.45	0.05
JK02	0.05		2.95	101.79			57.32	10.83	4.53	7.38	9.64	4.09	3.15	1.97	1.05	0.05
MEW2	0.04		1.66	102.59			58.12	10.85	5.33	9.12	6.22	3.99	3.34	1.69	1.29	0.04
JT2	0.22		0.24	101.37			58.05	10.61	5.78	7.77	7.36	4.51	2.86	1.74	1.10	0.22
MP2	0.06		1.30	101.79			60.29	10.95	5.04	6.75	6.66	4.38	3.38	1.53	0.96	0.06
JK01	0.03		1.97	103.41			60.92	10.85	4.49	8.70	4.97	3.97	3.38	1.46	1.24	0.03
KC03	0.11		0.57	99.32			67.64	11.58	3.21	2.46	5.03	4.81	3.63	1.36	0.17	0.11
KC02	0.09		0.65	101.01			67.61	11.82	2.97	2.81	4.75	5.06	3.40	1.30	0.19	0.09
MP3	0.09		0.69	100.25			68.42	11.83	2.83	2.19	4.62	5.06	3.65	1.18	0.13	0.09
JT3	0.09		0.49	99.35			68.97	11.77	2.46	2.05	4.64	4.94	3.93	1.04	0.11	0.09
MP4	0.05		1.66	100.04			69.75	11.63	2.05	2.10	4.72	4.59	4.05	0.96	0.11	0.05
JT4	0.09		0.57	101.10			69.17	11.89	2.42	2.54	3.98	5.24	3.61	0.96	0.11	0.09
JK03	0.12		0.84	100.88			69.62	11.25	2.67	2.13	4.23	5.25	3.59	1.02	0.11	0.12
JJF2	0.06			100.66			69.67	12.11	2.29	2.03	4.35	4.75	3.69	0.94	0.11	0.06
JJF3	0.10		0.64	100.44			70.56	11.24	2.55	2.01	4.09	4.62	3.76	0.96	0.11	0.10
MEW3	0.09		0.63	101.01			70.45	11.83	2.38	1.75	4.04	4.82	3.62	0.92	0.11	0.09
EHW02	0.02		0.83	103.12			75.15	10.47	1.98	2.38	1.58	3.57	4.27	0.23	0.34	0.02

	wt%	*wt%*	*wt%*	*wt%*	*wt%*	*wt%*	*dry mol%*	*dry mol%*	*dry mol%*	*dry mol%*	*dry mol%*	*dry mol%*	*dry mol%*	*dry mol%*	*dry mol%*	*dry mol%*
Sample	**MnO**	**Cr2O3**	**LOI**	**Total**	**FeO**	**Fe2O3**	**SiO2**	**Al2O3**	**Fe2O3(t)**	**MgO**	**CaO**	**Na2O**	**K2O**	**TiO2**	**P2O5**	**MnO**
KC01	0.03		0.81	102.91			75.33	10.29	1.83	2.31	1.63	3.69	4.30	0.27	0.33	0.03
JT1	0.02		1.18	103.07			76.02	9.74	2.20	2.61	1.09	2.87	4.82	0.26	0.37	0.02
MP1	0.02		0.00	101.19			76.62	9.69	2.08	2.27	1.00	2.98	4.79	0.24	0.32	0.02
LJT1	0.02		0.99	100.18			78.00	9.35	1.61	1.40	1.79	3.29	4.17	0.18	0.20	0.02
DH2	0.01		1.23	103.53			77.62	9.79	1.52	1.54	1.21	3.37	4.52	0.19	0.22	0.01
EHW01	0.02		0.83	103.06			77.92	9.48	1.63	1.77	1.40	3.04	4.29	0.20	0.25	0.02
DH1	0.02		1.07	103.44			78.50	9.24	1.47	1.33	1.63	3.44	4.05	0.13	0.19	0.02
LJT3	0.00		0.96	100.00			80.78	9.43	0.76	0.91	0.65	4.14	3.18	0.14	0.01	0.00
DH3	0.00		1.20	101.84			80.52	9.57	0.68	0.68	1.05	4.02	3.22	0.24	0.02	0.00
LJT2	0.00		0.53	101.98			81.22	9.48	0.53	0.02	1.12	4.72	2.79	0.13	0.01	0.00
86DM96																
93DM131																
89S3																
89S4																
89S1																
89S2																
89S5																
89S6																
89S7																
89S8																
89S9																

Sample	mg/kg Ba	mg/kg Be	mg/kg Bi	mg/kg Cd	mg/kg Ce	mg/kg Co	mg/kg Cr	mg/kg Cs	mg/kg Cu	mg/kg Dy	mg/kg Er	mg/kg Eu	mg/kg Ga	mg/kg Gd	mg/kg Hf	mg/kg Ho	mg/kg In	mg/kg La	mg/kg Li	mg/kg Lu	mg/kg Mo
109																					
154																					
199																					
145																					
108																					
64-35																					
183																					
64-34																					
64-60																					
64-61																					
64-58																					
64-59																					
104																					
113																					
139																					
64-57																					
170																					
216																					
506																					
180																					
152																					
213																					
130																					
64-44a																					
516																					
FJ97																					
64-43																					
151																					
105																					
513																					
501																					
JC-050	531.0	1.8	0.1	0.1	162.9	2.6	13.0	0.6	6.0	6.8	3.4	3.1	19.1	8.6	5.7	1.3	0.0	73.4	12.8	0.4	1.3
JC-070	1576.2	3.2	0.1	0.1	177.8	4.6	3.0	0.8	0.7	7.9	3.9	4.1	23.4	10.4	5.9	1.4	0.0	80.1	21.0	0.5	1.7
JC-014																					
JC-043																					
JC-067																					
JC-045																					
JC-081	640.3	3.6	0.1	0.1	307.7	4.0	8.0	0.5	1.6	11.6	6.5	3.3	23.6	13.4	15.2	2.2	0.0	142.8	21.0	0.9	1.5
91DM14b																					
93DM18b																					
93DM19																					
94DM53																					
96DM1																					
91DM131a																					
15RME-0179																					
FJ50																					
FJ24																					

Sample	mg/kg Ba	mg/kg Be	mg/kg Bi	mg/kg Cd	mg/kg Ce	mg/kg Co	mg/kg Cr	mg/kg Cs	mg/kg Cu	mg/kg Dy	mg/kg Er	mg/kg Eu	mg/kg Ga	mg/kg Gd	mg/kg Hf	mg/kg Ho	mg/kg In	mg/kg La	mg/kg Li	mg/kg Lu	mg/kg Mo
FJ27																					
FJ40																					
FJ51																					
FJ93																					
FJ20																					
FJ46																					
FJ18																					
FJ22																					
FJ44																					
FJ45																					
FJ2																					
FJ25																					
FJ67																					
FJ16																					
FJ12																					
FJ60																					
JS46																					
FJ8																					
FJ7																					
FJ4																					
FJ63																					
FJ26																					
FJ64																					
FJ3																					
FJ72																					
FJ78																					
FJ9																					
FJ43																					
FJ73																					
JS44																					
15RME-0409	935.2	1.3	0.2	0.1	76.4	27.2	57.0	0.7	4.8	6.5	3.5	2.6	20.0	8.1	4.2	1.2	0.1	31.4	25.5	0.4	1.3
16RME-0573	988.8	1.2	0.2	0.1	191.1	18.2	17.0	0.4	8.0	7.7	3.8	3.7	19.0	11.0	3.5	1.4	0.1	83.1	23.5	0.4	0.7
16RME-0290	711.1	3.0	0.2	0.2	146.1	28.3	13.0	0.2	29.1	18.9	11.1	4.6	22.7	19.6	11.2	3.8	0.1	59.0	13.0	1.5	1.9
16RME-0519	1099.6	2.9	0.2	0.0	76.1	25.9	376.0	2.0	0.7	4.3	2.3	1.6	19.3	5.7	5.7	0.8	0.0	34.6	29.4	0.3	0.3
15RME-0220	1740.0	0.3	0.2	0.1	53.9	9.1	12.0	0.6	0.7	6.3	3.1	4.7	18.6	8.2	1.3	1.2	0.0	23.9	12.7	0.3	0.9
15RME-0221	1740.0	1.2	0.2	0.0	97.2	3.3	10.0	0.8	4.9	7.3	3.8	4.5	20.6	9.1	2.6	1.4	0.0	44.3	12.9	0.5	1.5
15RME-0358	1740.0	1.7	0.2	0.0	92.9	3.3	10.0	0.9	3.6	5.4	2.8	3.0	20.5	7.0	4.1	1.0	0.1	39.5	17.9	0.3	1.5
16RME-0517	294.6	3.0	0.2	0.0	123.1	7.3	44.0	0.1	0.7	6.0	3.2	2.6	20.2	7.8	6.8	1.1	0.1	47.7	16.6	0.4	0.7
15RME-0219	1703.2	1.4	0.2	0.1	54.4	4.8	13.0	0.3	4.1	6.5	3.8	2.1	22.1	7.0	10.6	1.3	0.1	26.1	10.6	0.5	1.2
16RME-0194	287.0	1.7	0.2	0.0	35.6	5.6	22.0	0.3	23.0	3.3	1.9	1.5	25.5	3.9	9.7	0.6	0.0	16.7	34.3	0.3	0.6
15RME-0370	1740.0	1.3	0.2	0.0	85.2	3.2	14.0	0.2	3.8	9.7	5.8	4.2	21.4	10.6	11.2	1.9	0.1	35.0	10.1	0.8	1.3
15RME-0357	1283.6	1.9	0.2	0.0	111.2	1.4	9.0	1.0	0.7	5.9	3.3	1.6	19.6	6.9	9.8	1.1	0.1	38.2	10.3	0.5	1.0
16RME-0392	1187.8	1.0	0.2	0.1	27.7	1.2	19.0	3.0	2.5	1.4	0.9	0.5	24.4	1.5	3.4	0.3	0.0	13.4	4.8	0.1	1.5
16RME-0202	1555.4	1.4	0.2	0.1	150.4	3.5	30.0	0.2	1.6	26.5	16.9	3.6	19.1	22.9	9.4	5.6	0.0	47.4	8.9	1.9	2.7
15RME-0431	1740.0	1.1	0.2	0.1	36.1	2.3	26.0	0.3	0.7	3.4	2.4	1.7	16.6	3.3	25.2	0.7	0.0	16.5	10.5	0.5	3.0
15RME-0466	361.2	0.6	0.2	0.0	13.8	0.8	27.0	0.1	0.7	0.8	0.5	0.4	15.2	0.9	1.9	0.2	0.0	5.6	6.1	0.1	1.1
16RME-0594	760.5	2.1	0.2	0.0	34.8	1.8	32.0	0.4	0.7	2.0	1.3	0.8	16.8	2.2	3.9	0.4	0.0	18.3	21.0	0.2	1.6

	mg/kg	*mg/kg*	*mg/kg*	*mg/kg*	*mg/kg*	*mg/kg*	*mg/kg*	*mg/kg*	*mg/kg*	*mg/kg*	*mg/kg*	*mg/kg*	*mg/kg*	*mg/kg*	*mg/kg*	*mg/kg*	*mg/kg*	*mg/kg*	*mg/kg*	*mg/kg*	*mg/kg*
Sample	**Ba**	**Be**	**Bi**	**Cd**	**Ce**	**Co**	**Cr**	**Cs**	**Cu**	**Dy**	**Er**	**Eu**	**Ga**	**Gd**	**Hf**	**Ho**	**In**	**La**	**Li**	**Lu**	**Mo**
16RME-0555	561.9	3.3	0.2	0.0	21.4	0.3	23.0	0.4	0.7	2.6	1.0	1.2	16.0	3.1	0.9	0.4	0.0	9.2	3.8	0.1	1.1
15RME-0250	324.4	2.2	0.2	0.0	57.0	1.7	33.0	0.4	6.7	1.5	0.6	1.0	17.8	2.7	3.6	0.2	0.0	29.1	18.3	0.1	2.0
15RME-0259	556.3	1.6	0.2	0.0	44.8	0.9	32.0	0.2	1.7	3.4	2.1	1.0	23.0	3.5	3.5	0.7	0.0	21.7	4.8	0.3	2.0
16RME-0466	465.4	1.9	0.2	0.0	13.5	0.6	17.0	1.3	4.3	1.0	0.7	0.4	24.0	1.2	3.4	0.2	0.0	6.6	5.9	0.1	0.9
15RME-0254	560.7	0.8	0.2	0.0	113.2	1.4	39.0	0.3	6.1	3.2	1.4	1.0	17.6	4.5	5.3	0.6	0.0	55.3	3.4	0.1	2.3
16RME-0305	304.0	2.6	0.2	0.0	9.4	0.3	20.0	0.3	2.6	2.0	1.2	0.5	20.3	1.4	1.3	0.4	0.0	5.5	5.1	0.1	1.1
16RME-0465	482.6	1.9	0.2	0.0	11.9	0.5	24.0	1.0	1.7	1.1	0.7	0.4	22.1	1.2	2.8	0.2	0.0	5.8	7.2	0.1	1.3
16RME-0318	92.2	2.8	0.2	0.0	22.6	0.4	22.0	0.2	0.7	3.1	3.7	0.2	24.4	1.7	2.8	0.9	0.0	12.0	1.4	1.1	1.1
16RME-0572	60.6	0.7	0.2	0.0	33.0	7.7	63.0	0.3	17.8	2.2	1.3	0.6	6.8	2.5	6.0	0.5	0.0	15.6	13.4	0.2	3.6
LL138	234.0						61.0		22.0				29.0								
LL53	173.0				17.5		1086.0		45.0	3.1	1.8	0.8	10.0	2.8		0.6		7.3		0.2	
LL120	239.0						78.0		5.0				28.0								
LL56	955.0				17.5		10.0		8.0	11.2	6.6	3.9	17.0	12.0		2.3		37.3		0.8	
LN25	573.0						42.0		5.0				21.0								
LL157	994.0						44.0		5.0				34.0								
LN24	865.0				183.4		54.0		5.0	13.0	7.5	3.8	19.0	15.5		2.6		79.3		1.0	
LL137	895.0						48.0		5.0				29.0								
LL04	1152.0				146.0		10.0		10.0	12.5	6.9	4.3	16.0	13.8		2.4		63.0		0.9	
LL23	1308.0				145.6		10.0		12.0	11.3	6.4	4.4	15.0	12.7		2.3		63.4		0.8	
LN23	902.0						39.0		5.0				16.0								
LN10	687.0						37.0		5.0				27.0								
LN06	432.0				203.5		29.0		5.0	14.6	9.3	2.5	20.0	15.0		3.1		75.0		1.2	
15RME-0247																					
15RME-0320																					
15RME-0420																					
21CK47A	1683.0	2.0	0.1		101.0	5.0	10.0	0.8	5.0	7.4	4.2	3.9	21.0	8.9	13.2	1.4	0.1	50.2		0.6	2.0
21CK48A	1562.0	2.0																			
21CK70A	1618.0	2.0																			
21CK76A	1005.0	3.0	0.2		194.0	9.0	10.0	0.5	5.0	13.9	7.4	3.7	21.0	15.8	13.9	2.6	0.1	84.4		1.0	8.0
20CK88A	862.0	3.0																			
20CK36B	1042.0	1.0																			
20CK06A	689.0	1.0																			
20CK86A	235.0	8.0																			
20CK18A	601.0	2.0																			
20CK52B	429.0	2.0																			
20CK100A	106.0	2.0																			
5207W																					
R5179G																					
R5180G																					
R5181G																					
R5182G																					
R5183W																					
R5184W																					
R5185W																					
R5186L																					
R5208W																					
R5209W																					

Sample	mg/kg Ba	mg/kg Be	mg/kg Bi	mg/kg Cd	mg/kg Ce	mg/kg Co	mg/kg Cr	mg/kg Cs	mg/kg Cu	mg/kg Dy	mg/kg Er	mg/kg Eu	mg/kg Ga	mg/kg Gd	mg/kg Hf	mg/kg Ho	mg/kg In	mg/kg La	mg/kg Li	mg/kg Lu	mg/kg Mo
LH87-30																					
LH86-64					118.9																
LH87-31																					
LH86-63					181.0																
WP1					180.3																
LH86-7					174.0																
CL3					134.7																
RLI					156.0																
LY3					188.9																
GQ1																					
SL2					122.7																
BS1																					
WL1					190.8																
GQI					141.8																
BSI					173.1																
CL3																					
LY3																					
16RME-0280	1257.8	0.8	0.2	0.2	210.1	28.9	6.0	0.5	16.0	18.3	9.5	5.6	18.5	24.1	3.9	3.5	0.1	85.7	23.8	1.1	1.1
16RME-0557A	1740.0	2.5	0.2	0.0	35.1	9.5	5.0	3.7	6.3	1.1	0.5	0.6	13.5	1.8	1.2	0.2	0.0	15.3	138.4	0.1	0.6
16RME-0366	85.5	0.7	0.2	0.2	14.0	53.4	312.0	3.1	12.0	3.7	2.1	1.0	18.3	3.4	1.5	0.8	0.1	6.9	30.7	0.3	0.6
16RME-0376	908.5	1.3	0.2	0.2	73.7	36.2	33.0	0.7	17.2	7.3	4.1	2.5	20.8	8.2	4.3	1.4	0.1	28.9	21.6	0.6	1.5
16RME-0253	337.1	1.4	0.2	0.1	55.7	42.6	65.0	0.4	23.0	10.3	5.7	3.0	20.7	11.0	5.3	2.0	0.1	19.2	24.8	0.7	1.3
16RME-0389	857.4	1.0	0.2	0.1	61.0	38.1	29.0	3.1	43.6	6.0	3.4	2.1	19.3	6.8	2.5	1.2	0.1	24.5	64.9	0.5	0.9
16RME-0535	1740.0	1.1	0.2	0.1	121.3	23.6	15.0	0.7	14.6	7.2	3.4	3.4	20.2	10.4	1.9	1.3	0.1	51.5	44.3	0.3	1.0
16RME-0237	1740.0	2.2	0.2	0.3	242.2	21.3	8.0	1.7	10.6	8.8	4.1	5.4	18.1	15.0	6.2	1.5	0.1	100.7	38.7	0.5	1.6
15RME-0090	971.9	1.6	0.2	0.1	100.1	35.3	44.0	0.3	23.9	9.6	5.3	3.2	20.2	11.3	4.7	1.9	0.1	42.1	21.7	0.7	1.3
16RME-0529	1736.9	2.6	0.2	0.0	57.9	27.3	291.0	4.9	0.7	4.2	2.1	1.7	17.5	5.6	3.5	0.8	0.0	28.4	36.8	0.3	0.5
16RME-0211	214.3	1.1	0.2	0.1	23.4	35.6	97.0	1.7	52.2	6.0	3.0	1.9	22.2	6.7	3.8	1.1	0.1	9.6	11.9	0.4	2.0
15RME-0359	308.6	1.7	0.2	0.0	38.9	29.9	111.0	1.0	15.6	8.1	4.9	1.6	22.1	7.0	4.1	1.7	0.1	16.2	23.2	0.7	1.2
MEW1	1254.0				205.0	48.0	6.2		3.6	10.0	5.1	4.2		13.8	1.1	2.0		91.6		0.6	
JJF1	816.0				242.0	46.8	2.2		0.0	10.4	5.7	3.3		13.6	1.0	2.1		119.0		0.7	
JK02	1475.0				187.0	38.0	2.3		4.1	10.5	5.2	4.6		13.9	0.8	2.0		85.7		0.6	
MEW2	2038.0				163.0	45.2	2.6		7.3	7.9	4.0	3.7		10.8	1.8	1.6		73.9		0.5	
JT2	1262.0				167.0	47.3	4.1		9.3	9.3	4.8	3.9		12.1	1.7	1.8		75.7		0.6	
MP2	1367.0				172.0	37.0	1.8		7.1	9.5	4.9	3.9		12.3	2.3	1.9		78.2		0.6	
JK01	1482.0				165.0	31.4	12.5		7.9	8.9	4.6	3.8		11.7	0.6	1.8		74.9		0.5	
KC03	1855.0				134.0	25.8	0.1		0.0	12.9	7.3	4.5		13.8		2.7		61.0		0.9	
KC02	1675.0				138.0	31.0	0.0		0.0	14.7	8.2	5.0		15.6		3.1		66.2		1.0	
MP3	1558.0				91.7	18.7	0.0		0.0	10.3	5.8	3.9		10.7		2.2		45.3		0.7	
JT3	2069.0				114.0	18.8	0.0		0.0	10.5	6.0	4.3		11.1		2.2		53.4		0.7	
MP4	1600.0				74.9	25.4	0.0		0.0	9.1	5.2	3.6		9.7		1.9		46.7		0.6	
JT4	1544.0				110.0	30.1	0.6		0.0	10.4	5.9	4.1		10.8		2.2		51.3		0.7	
JK03	1551.0				94.7	31.3	0.8		0.0	10.0	5.6	4.1		10.7		2.1		55.1		0.7	
JJF2	1619.0				107.0	20.8	0.0		0.0	9.5	5.4	4.1		10.1		2.0		49.6		0.7	
JJF3	1632.0				124.0	28.5	0.8		0.4	10.9	6.1	4.4		11.6		2.3		58.7		0.7	
MEW3	1634.0				110.0	34.7	0.0		0.0	10.7	6.1	4.4		11.0		2.2		47.7		0.7	
EHW02	1035.0				168.0	55.9	7.5		6.9	12.3	7.1	3.1		12.8		2.6		59.9		0.9	

	mg/kg	*mg/kg*	*mg/kg*	*mg/kg*	*mg/kg*	*mg/kg*	*mg/kg*	*mg/kg*	*mg/kg*	*mg/kg*	*mg/kg*	*mg/kg*	*mg/kg*	*mg/kg*	*mg/kg*	*mg/kg*	*mg/kg*	*mg/kg*	*mg/kg*	*mg/kg*	*mg/kg*
Sample	**Ba**	**Be**	**Bi**	**Cd**	**Ce**	**Co**	**Cr**	**Cs**	**Cu**	**Dy**	**Er**	**Eu**	**Ga**	**Gd**	**Hf**	**Ho**	**In**	**La**	**Li**	**Lu**	**Mo**
KC01	819.0				204.0	36.1	6.0		3.9	13.0	7.4	3.2		13.7		2.7		83.0		1.0	
JT1	1064.0				209.0	40.3	0.0		0.0	9.9	5.4	3.2		11.7	13.2	2.0		84.8		0.7	
MP1	975.0				255.0	53.7	0.0		0.0	11.5	6.3	3.5		13.7	12.1	2.3		103.0		0.8	
LJT1	646.0				164.0	42.2	3.4		1.5	11.4	7.2	2.4		11.2	6.3	2.5		66.3		0.9	
DH2	795.0				86.5	67.7	4.9		1.2	5.9	3.2	2.1		6.5		1.2		36.7		0.3	
EHW01	931.0				135.0	60.0	7.3		14.4	9.9	5.7	2.6		10.9		2.1		54.0		0.7	
DH1	463.0				77.9	61.3	3.0		1.2	5.3	3.2	1.6		5.5	4.4	1.1		35.0		0.4	
LJT3	644.0				15.4	71.9	0.0		0.0	1.3	0.9	0.4		1.4	6.8	0.3		8.4		0.2	
DH3	979.0				28.6	103.0	0.1		1.7	2.2	1.5	0.8		2.3	5.4	0.5		20.2		0.2	
LJT2	815.0				22.7	86.2	0.0		0.0	1.3	0.6	0.6		2.0		0.2		11.9		0.1	
86DM96																					
93DM131																					
89S3																					
89S4																					
89S1																					
89S2																					
89S5																					
89S6																					
89S7																					
89S8																					
89S9																					

Sample	mg/kg Nb	mg/kg Nd	mg/kg Ni	mg/kg Pb	mg/kg Pr	mg/kg Rb	mg/kg Sb	mg/kg Sc	mg/kg Sm	mg/kg Sn	mg/kg Sr	mg/kg Ta	mg/kg Tb	mg/kg Th	mg/kg Ti	mg/kg Tl	mg/kg Tm	mg/kg U	mg/kg V	mg/kg W	mg/kg Y
109																					
154																					
199																					
145																					
108																					
64-35																					
183																					
64-34																					
64-60																					
64-61																					
64-58																					
64-59																					
104																					
113																					
139																					
64-57																					
170																					
216																					
506																					
180																					
152																					
213																					
130																					
64-44a																					
516																					
FJ97											111.0										47.0
64-43																					
151																					
105																					
513																					
501																					
JC-050	19.0	77.3	3.0	13.8	20.6	97.1	0.1	5.5	12.6	1.8	363.0	1.3	1.2	3.9		0.6	0.5	1.3	30.0	0.3	33.9
JC-070	26.6	89.5	0.8	10.5	23.0	99.0	0.1	5.0	15.0	2.6	698.2	1.6	1.4	6.5		0.6	0.5	1.8	33.0	0.4	38.5
JC-014																					
JC-043																					
JC-067																					
JC-045																					
JC-081	54.4	127.1	0.8	7.0	36.1	121.4	0.1	5.6	19.9	4.0	266.4	3.9	2.0	10.6		0.6	0.9	3.2	37.0	0.2	61.5
91DM14b																					
93DM18b																					
93DM19																					
94DM53																					
96DM1																					
91DM131a																					
15RME-0179																					
FJ50											209.0										0.5
FJ24											808.0										30.0

Sample	mg/kg Nb	mg/kg Nd	mg/kg Ni	mg/kg Pb	mg/kg Pr	mg/kg Rb	mg/kg Sb	mg/kg Sc	mg/kg Sm	mg/kg Sn	mg/kg Sr	mg/kg Ta	mg/kg Tb	mg/kg Th	mg/kg Ti	mg/kg Tl	mg/kg Tm	mg/kg U	mg/kg V	mg/kg W	mg/kg Y
FJ27											439.0										18.0
FJ40											482.0										54.0
FJ51											1314.0										25.0
FJ93											349.0										63.0
FJ20											453.0										29.0
FJ46											860.0										49.0
FJ18											208.0										10.0
FJ22											1021.0										14.0
FJ44											609.0										66.0
FJ45											680.0										53.0
FJ2											229.0										174.0
FJ25											336.0										59.0
FJ67											293.0										82.0
FJ16											182.0										49.0
FJ12											450.0										20.0
FJ60											212.0										84.0
JS46											490.0										90.0
FJ8											128.0										79.0
FJ7											194.0										33.0
FJ4											139.0										47.0
FJ63											276.0										11.0
FJ26											489.0										9.0
FJ64											135.0										50.0
FJ3											346.0										71.0
FJ72											135.0										46.0
FJ78											142.0										48.0
FJ9											61.0										79.0
FJ43											161.0										26.0
FJ73											19.0										41.0
JS44											99.0										29.0
15RME-0409	7.7	46.7	20.0	13.3	10.5	40.3	0.1	19.1	9.1	1.8	1126.9	0.5	1.1	1.4	14520.0	0.4	0.5	0.6	207.5	0.7	35.1
16RME-0573	24.2	93.6	8.9	12.7	24.3	88.7	0.1	7.6	15.3	2.5	890.9	1.0	1.4	2.3	12364.0	0.4	0.5	0.4	101.4	0.1	39.9
16RME-0290	20.2	89.8	8.6	6.7	20.7	41.5	0.1	17.8	20.0	3.8	370.9	1.0	3.0	3.4	14982.0	0.2	1.6	1.1	172.7	0.2	105.5
16RME-0519	7.4	39.5	104.4	2.5	9.7	93.0	0.0	18.5	7.4	1.7	917.0	0.4	0.8	3.4	4308.0	0.4	0.3	0.5	135.1	0.0	23.4
15RME-0220	2.3	38.1	1.4	5.3	7.9	21.2	0.1	7.3	8.3	0.7	847.9	0.1	1.1	0.5	11484.0	0.1	0.4	0.2	69.3	0.2	32.9
15RME-0221	11.8	56.7	1.6	7.5	13.2	62.2	0.1	8.8	10.8	1.9	846.8	0.6	1.3	0.7	6996.0	0.3	0.5	0.3	34.1	0.5	38.2
15RME-0358	17.8	46.4	2.0	6.3	11.5	97.3	0.1	7.7	8.8	2.5	964.6	0.9	0.9	4.0	7062.0	0.5	0.4	1.3	42.8	0.2	27.5
16RME-0517	12.5	61.9	16.0	3.3	16.0	9.9	0.0	9.4	11.0	1.8	1235.8	0.8	1.1	16.0	3209.0	0.0	0.5	3.3	76.4	0.0	33.6
15RME-0219	15.6	34.4	3.8	15.2	7.7	90.8	0.1	10.3	7.7	5.5	514.5	0.6	1.1	0.7	5225.0	0.5	0.5	0.8	38.8	0.4	34.4
16RME-0194	7.2	19.9	5.7	5.4	4.8	6.8	0.0	8.6	4.2	1.0	898.7	0.5	0.6	0.3	4924.0	0.1	0.3	0.4	69.0	0.0	17.1
15RME-0370	12.1	52.9	1.2	3.7	11.8	72.2	0.0	8.4	11.4	2.6	188.9	0.4	1.6	1.8	5103.0	0.3	0.8	0.5	22.2	0.1	55.1
15RME-0357	45.7	56.5	0.8	8.1	14.6	204.8	0.1	2.8	9.6	4.2	567.2	2.5	1.0	13.0	4184.0	0.8	0.5	2.4	20.6	0.1	32.9
16RME-0392	11.7	11.8	1.7	15.3	3.3	297.6	0.1	0.6	2.0	1.5	732.4	0.9	0.2	10.3	1038.0	1.6	0.1	1.4	7.6	0.6	8.2
16RME-0202	35.3	103.3	2.0	4.2	23.8	104.5	0.0	2.3	23.8	5.1	535.0	2.5	4.0	6.1	5442.0	0.6	2.4	1.5	70.1	0.2	152.8
15RME-0431	14.5	17.6	1.2	7.7	4.4	69.1	0.0	4.3	3.5	1.7	428.4	0.5	0.5	1.8	7929.0	0.3	0.4	1.1	48.3	0.4	21.5
15RME-0466	2.4	6.7	1.6	0.9	1.8	15.3	0.0	3.8	1.2	0.5	197.9	0.2	0.1	1.2	818.0	0.1	0.1	0.4	10.0	0.1	4.7
16RME-0594	4.5	13.8	1.3	11.3	3.9	86.4	0.0	1.8	2.6	1.1	503.4	0.1	0.3	3.8	981.0	0.5	0.2	0.3	10.5	0.0	12.9

	mg/kg	*mg/kg*	*mg/kg*	*mg/kg*	*mg/kg*	*mg/kg*	*mg/kg*	*mg/kg*	*mg/kg*	*mg/kg*	*mg/kg*	*mg/kg*	*mg/kg*	*mg/kg*	*mg/kg*	*mg/kg*	*mg/kg*	*mg/kg*	*mg/kg*	*mg/kg*	*mg/kg*
Sample	**Nb**	**Nd**	**Ni**	**Pb**	**Pr**	**Rb**	**Sb**	**Sc**	**Sm**	**Sn**	**Sr**	**Ta**	**Tb**	**Th**	**Ti**	**Tl**	**Tm**	**U**	**V**	**W**	**Y**
16RME-0555	3.6	12.2	0.9	2.2	2.8	104.1	0.0	2.5	3.2	0.5	204.8	0.7	0.5	2.5	475.0	0.4	0.1	1.1	5.9	0.1	11.3
15RME-0250	2.4	20.8	1.1	14.0	5.9	117.6	0.1	2.3	3.7	0.4	307.3	0.1	0.3	18.9	898.0	0.6	0.1	1.9	12.2	0.1	6.4
15RME-0259	3.5	19.1	1.1	7.1	5.1	100.1	0.0	1.7	3.9	0.7	170.0	0.3	0.5	5.4	664.0	0.4	0.3	1.3	4.9	0.1	20.8
16RME-0466	3.6	6.6	0.7	15.1	1.6	88.4	0.1	1.6	1.4	2.7	201.5	0.4	0.2	7.4	576.0	0.7	0.1	3.7	3.8	0.1	5.6
15RME-0254	1.8	43.4	1.1	8.7	12.1	106.6	0.0	2.3	7.1	0.8	135.4	0.1	0.6	26.0	1026.0	0.5	0.2	1.6	10.6	0.1	16.0
16RME-0305	0.9	3.7	0.7	19.1	1.0	81.9	0.0	0.6	0.9	0.5	141.2	0.1	0.3	4.0	239.0	0.5	0.2	8.2	1.8	0.2	12.9
16RME-0465	2.8	5.4	0.4	12.1	1.4	89.0	0.3	1.3	1.4	0.6	198.6	0.3	0.2	5.2	379.0	0.6	0.1	1.6	4.9	0.1	6.8
16RME-0318	9.1	7.1	0.4	4.1	2.3	146.0	0.0	0.6	1.4	1.7	107.0	0.7	0.4	11.7	298.0	0.8	0.7	2.9	1.8	0.0	30.7
16RME-0572	10.2	15.5	7.3	3.5	3.9	15.3	0.0	3.6	3.0	1.1	71.2	0.8	0.4	0.8	2602.0	0.1	0.2	0.6	14.9	1.0	12.5
LL138	5.0		38.0	10.0		8.0		35.0			435.0								430.0		22.0
LL53	10.0	10.7	36.0	2.6	2.4	6.0			2.5		275.0		0.4				0.3		116.0		16.0
LL120	5.0		40.0	11.0		29.0		18.0			248.0								276.0		34.0
LL56		58.2	131.0	7.5	12.5	13.0			12.7		492.0		1.9				0.9		183.0		39.0
LN25	27.0		20.0	10.0		119.0		27.0			529.0								110.0		56.0
LL157	13.0		26.0	10.0		74.0		16.0			781.0								93.0		55.0
LN24	23.0	99.3	28.0	20.0	24.4	82.0		7.0	18.3		449.0		2.2				1.0		129.0		53.0
LL137	22.0		25.0	10.0		56.0		26.0			501.0								147.0		60.0
LL04	14.0	81.8	28.0	12.0	19.3	27.0			16.6		519.0		2.1				1.0		64.0		46.0
LL23	19.0	77.4	28.0	12.5	19.1	31.0			14.9		590.0		1.9				0.9		75.0		42.0
LN23	16.0		15.0	16.0		160.0		13.0			306.0								67.0		44.0
LN10	12.0		10.0	12.0		92.0		6.0			537.0								12.0		15.0
LN06	32.0	108.9	26.0	13.0	28.2	155.0			19.1		212.0		2.3				1.4		39.0		66.0
15RME-0247																					
15RME-0320																					
15RME-0420																					
21CK47A	16.3	52.6	30.0	13.0	12.7	84.0	0.1	10.0	10.4	3.0	482.0	0.8	1.3	2.1		0.4	0.6	0.7	33.0	0.3	39.3
21CK48A								10.0											42.0		53.0
21CK70A																			29.0		57.0
21CK76A	25.3	105.0	40.0	16.0	25.5	102.0	0.1		19.7	3.0	391.0	1.0	2.4	3.0		0.4	1.0	0.7	84.0	0.3	71.9
20CK88A								7.0			215.0								31.0		70.0
20CK36B								3.0			227.0								60.0		31.0
20CK06A								4.0			230.0								43.0		38.0
20CK86A								2.0			200.0								2.5		4.0
20CK18A								0.1			318.0								2.5		2.0
20CK52B								0.1			223.0								21.0		2.0
20CK100A											107.0								51.0		18.0
5207W																					
R5179G																					
R5180G																					
R5181G																					
R5182G																					
R5183W																					
R5184W																					
R5185W																					
R5186L																					
R5208W																					
R5209W																					

Sample	mg/kg Nb	mg/kg Nd	mg/kg Ni	mg/kg Pb	mg/kg Pr	mg/kg Rb	mg/kg Sb	mg/kg Sc	mg/kg Sm	mg/kg Sn	mg/kg Sr	mg/kg Ta	mg/kg Tb	mg/kg Th	mg/kg Ti	mg/kg Tl	mg/kg Tm	mg/kg U	mg/kg V	mg/kg W	mg/kg Y
LH87-30																					
LH86-64	24.0	65.4				77.0			12.7		626.0										69.0
LH87-31																					
LH86-63	40.0	91.6				140.0			17.3		299.0										50.0
WP1		76.2				114.0			11.6		100.0										
LH86-7	26.0	72.2				115.0			11.0		96.0										72.0
CL3	17.0	65.7				149.0			12.7		405.0										61.0
RLI	29.0	74.2				75.0			12.5		469.0										44.0
LY3	14.0	103.4				141.0			19.5		219.0										52.0
GQ1																					
SL2	16.0	69.5				76.0			13.9		499.0										57.0
BS1																					
WL1	28.0	118.5				84.0			21.5		256.0										51.0
GQI	20.0	80.3				81.0			15.6		468.0										63.0
BSI	26.0	91.2				120.0			17.4		319.0										73.0
CL3																					
LY3																					
16RME-0280	15.3	135.6	6.3	6.1	30.8	32.4	0.1	22.1	26.8	3.6	728.9	0.9	3.2	2.9	24477.0	0.3	1.3	0.9	231.7	0.3	89.8
16RME-0557A	18.3	17.1	3.2	5.7	4.5	198.9	0.1	0.6	2.7	0.8	823.3	1.0	0.2	1.9	6535.0	0.9	0.1	0.6	55.4	0.1	5.6
16RME-0366	1.3	9.0	177.7	5.3	1.9	31.1	0.1	28.8	2.7	1.4	223.6	0.1	0.6	1.9	6476.0	0.3	0.3	0.4	218.3	0.5	20.2
16RME-0376	6.2	46.3	18.3	10.3	10.7	30.5	0.3	22.0	9.4	1.7	813.6	0.4	1.2	1.2	12643.0	0.3	0.6	0.4	228.5	0.5	39.3
16RME-0253	6.2	41.8	56.5	10.2	8.8	9.8	0.1	23.0	10.5	2.1	676.4	0.4	1.7	1.3	13472.0	0.2	0.8	0.4	210.5	0.2	54.2
16RME-0389	4.3	38.4	20.5	11.7	8.9	36.1	0.5	22.0	7.7	1.3	881.1	0.3	1.0	1.2	8812.0	0.5	0.5	0.4	188.8	1.5	33.5
16RME-0535	13.1	69.7	11.0	5.6	16.3	62.1	0.0	12.3	12.9	1.9	1560.0	0.5	1.3	1.5	11448.0	0.3	0.4	0.4	155.4	0.1	35.2
16RME-0237	12.7	135.8	5.5	23.7	33.2	107.7	0.0	9.7	22.6	2.2	1560.0	0.5	1.8	9.2	10598.0	0.7	0.6	1.8	164.5	0.6	43.6
15RME-0090	11.8	62.8	26.4	6.4	14.4	34.3	0.0	22.9	12.6	2.1	866.8	0.6	1.6	1.0	13192.0	0.2	0.7	0.3	219.9	0.1	52.3
16RME-0529	7.2	31.8	94.4	6.5	7.5	137.7	0.1	18.0	6.8	2.0	1203.1	0.4	0.8	5.1	5150.0	0.4	0.3	1.6	151.3	0.2	22.1
16RME-0211	4.9	19.0	73.1	6.8	3.7	27.4	0.1	17.6	5.9	1.8	342.4	0.3	1.0	3.1	10774.0	0.3	0.4	1.3	144.9	0.6	30.1
15RME-0359	5.2	21.3	52.6	2.9	5.0	30.2	0.1	21.3	5.6	1.6	276.0	0.4	1.2	6.2	8310.0	0.2	0.7	2.3	169.0	0.3	47.1
MEW1	17.1	114.0	10.7	8.5	31.1	100.0		10.8	20.4		505.0	1.0	2.0	5.7			0.7	1.8	244.0		59.3
JJF1	22.1	115.0	10.9	4.0	33.5	198.0		9.9	19.8		510.0	1.1	2.0	5.3			0.7	1.9	241.0		65.7
JK02	17.1	106.0	8.9	10.0	28.4	75.5		13.1	19.6		1575.0	1.0	2.1	3.1			0.7	0.9	187.0		62.4
MEW2	16.1	87.9	6.5	10.3	24.3	122.0		11.8	15.7		1772.0	1.1	1.6	5.2			0.5	2.2	178.0		48.0
JT2	16.5	94.6	11.5	11.1	25.5	73.3		11.8	17.5		1661.0	1.1	1.8	3.3			0.6	0.8	202.0		52.8
MP2	18.5	95.5	7.9	10.1	26.0	96.0		11.4	17.5		1449.0	1.1	1.8	3.0			0.6	1.1	171.0		55.3
JK01	16.6	91.0	11.8	9.5	24.8	75.6		12.1	16.6		1024.0	1.0	1.7	2.7			0.6	0.7	141.0		51.2
KC03		80.7	2.6	10.4	20.9	67.9		10.4	17.4		621.0		2.4				1.0		39.1		75.8
KC02		88.9	2.7	8.4	22.8	56.6		10.7	19.5		597.0		2.7				1.1		35.0		83.4
MP3		59.5	2.7	8.3	15.2	60.4		8.3	13.1		467.0		1.8				0.8		35.1		58.2
JT3		64.7	2.4	9.0	17.1	77.1		8.6	13.7		643.0		1.9				0.8		32.2		62.2
MP4		55.5	2.7	8.4	14.4	66.3		7.0	11.9		448.0		1.6				0.7		30.0		49.9
JT4		62.8	2.7	9.4	16.6	73.5		8.0	13.4		556.0		1.8				0.8		30.5		61.0
JK03		66.4	3.5	13.0	17.6	66.4		8.6	13.7		485.0		1.8				0.8		30.7		55.8
JJF2		61.5	2.2	14.0	16.2	78.1		7.1	12.9		668.0		1.7				0.7		21.6		54.2
JJF3		70.4	3.5	14.4	18.5	87.9		8.9	14.8		526.0		2.0				0.8		26.4		63.7
MEW3		63.3	2.5	13.3	16.3	75.6		7.9	13.9		638.0		1.9				0.8		19.0		62.4
EHW02		96.6	6.8	5.8	27.4	126.0		4.9	18.4		366.0		2.2				1.1		46.9		73.9

	mg/kg	*mg/kg*	*mg/kg*	*mg/kg*	*mg/kg*	*mg/kg*	*mg/kg*	*mg/kg*	*mg/kg*	*mg/kg*	*mg/kg*	*mg/kg*	*mg/kg*	*mg/kg*	*mg/kg*	*mg/kg*	*mg/kg*	*mg/kg*	*mg/kg*	*mg/kg*	*mg/kg*
Sample	**Nb**	**Nd**	**Ni**	**Pb**	**Pr**	**Rb**	**Sb**	**Sc**	**Sm**	**Sn**	**Sr**	**Ta**	**Tb**	**Th**	**Ti**	**Tl**	**Tm**	**U**	**V**	**W**	**Y**
KC01		105.0	7.4	7.0	30.8	150.0		5.2	19.6		359.0		2.3				1.0		41.7		75.7
JT1	34.0	105.0	2.9	11.2	31.2	135.0		4.8	18.2		464.0	2.9	1.9	7.3			0.8	2.2	45.0		52.9
MP1	35.5	126.0	2.5	10.6	38.1	137.0		4.2	21.4		436.0	3.4	2.2	10.0			0.9	2.2	38.8		60.1
LJT1	30.2	84.2	4.6	7.9	24.3	138.0		6.9	15.7		285.0	2.4	2.0	7.0			1.0	2.1	40.9		70.4
DH2		48.1	5.3	7.9	13.2	153.0		2.0	8.9		412.0		1.0				0.4		42.7		32.3
EHW01		78.5	8.3	6.5	21.6	116.0		5.3	15.2		599.0		1.8				0.8		50.7		58.2
DH1	17.2	38.6	4.6	9.3	11.0	127.0		3.9	7.5		235.0	2.0	0.9	5.1			0.5	1.5	28.8		32.8
LJT3	2.2	5.6	2.3	5.8	1.3	67.3		0.0	1.2		463.0	0.9	0.2	1.1			0.2	2.9	11.5		7.7
DH3	6.9	15.0	3.2	10.4	4.6	78.5		2.0	2.8		304.0	1.3	0.3	5.3			0.3	2.8	20.6		11.9
LJT2		8.9	2.7	18.9	2.2	71.8		0.4	1.9		943.0		0.2				0.1		9.2		7.1
86DM96																					
93DM131																					
89S3																					
89S4																					
89S1																					
89S2																					
89S5																					
89S6																					
89S7																					
89S8																					
89S9																					

Sample	mg/kg Yb	mg/kg Zn	mg/kg Zr	calc ΣLREE	calc ΣREE	calc Mg#	calc A/NK	calc ASI	calc N+K-C	calc XFe2+	calc FeO(t)/FeO(t)+MgO	U-Pb Preffered Age	reported [Sm]	reported [Nd]	reported 143Nd/144Nd
109						0.29	1.97	0.78	-0.40		0.71				
154						0.39	1.98	0.80	-0.80		0.61				
199						0.26	1.52	0.81	2.70		0.74				
145						0.36	2.01	1.00	1.40		0.64				
108						0.27	1.95	1.07	3.10		0.73				
64-35						0.48	2.23	0.73	-3.50		0.52				
183						0.33	1.34	0.85	5.50		0.67				
64-34						0.71	1.77	0.54	-4.50		0.29				
64-60						0.38	1.35	0.98	7.30		0.62				
64-61						0.39	1.34	0.97	7.40		0.61				
64-58						0.32	1.34	1.01	7.90		0.68				
64-59						0.43	1.30	0.91	7.20		0.57				
104						0.35	1.39	1.00	7.10		0.65				
113						0.31	1.58	1.18	6.70		0.69				
139						0.39	1.39	1.00	7.20		0.61				
64-57						0.47	1.29	0.90	7.10		0.53				
170						0.28	1.11	0.89	8.80		0.72				
216						0.45	1.31	1.02	7.90		0.55				
506						0.91	1.37	1.02	8.40		0.09				
180						0.38	1.03	0.81	8.30		0.62				
152						0.37	1.00	0.80	8.70		0.63				
213						0.45	1.08	0.85	7.90		0.55				
130						0.26	1.00	0.88	8.70		0.74				
64-44a						0.38	1.14	0.97	8.60		0.62				
516						0.83	2.13	1.55	5.60		0.17				
FJ97			388.0			0.36	1.38	0.99	5.50		0.64				
64-43						0.38	1.24	0.98	7.20		0.62				
151						0.36	1.22	1.00	7.60		0.64				
105						0.36	1.23	1.01	7.50		0.64				
513						1.00	1.55	0.34	-12.30		0.00				
501						0.80	0.00	0.00	11.30		0.20				
JC-050	2.9	97.0	582.0	346.6	374.8	0.28	1.06	0.90	10.72		0.72	1072.3	12.572	77.26	0.51218
JC-070	3.2	102.0	467.0	385.4	418.8	0.35	1.26	0.99	8.67		0.65	1050.1	15.029	89.52	0.51215
JC-014													13.247	81.33	0.51214
JC-043													29.165	170.38	0.51216
JC-067													41.172	234.48	0.51218
JC-045													15.638	88.68	0.51219
JC-081	6.2	62.0	956.0	633.5	680.4	0.31	1.10	0.93	10.12		0.69				
91DM14b												1177			
93DM18b												1174.1			
93DM19												1166			
94DM53												1163.4			
96DM1												1156			
91DM131a												1155.3			
15RME-0179															
FJ50			59.0			0.64	1.24	1.04	8.01		0.36		0.64	6.8	0.51152
FJ24			169.0			0.48	1.69	0.68	-1.44		0.52		10.36	60	0.51201

Sample	mg/kg Yb	mg/kg Zn	mg/kg Zr	calc ΣLREE	calc ΣREE	calc Mg#	calc A/NK	calc ASI	calc N+K-C	calc XFe2+	calc FeO(t)/FeO(t)+MgO	U-Pb Preffered Age	reported [Sm]	reported [Nd]	reported 143Nd/144Nd
FJ27			59.0			0.45	1.16	1.04	11.41		0.55		4.82	24.8	0.51207
FJ40			457.0			0.35	1.30	0.91	6.51		0.65		16.91	90.8	0.51210
FJ51			81.0			0.49	1.18	0.82	7.52		0.51		6.44	33.2	0.51213
FJ93			822.0			0.42	1.14	0.94	8.61		0.58		16.98	80	0.51219
FJ20			570.0			0.37	1.19	0.94	9.17		0.63		8	37.7	0.51226
FJ46			537.0			0.42	1.31	0.84	5.83		0.58		16.79	79.5	0.51231
FJ18			75.0			0.52	1.20	1.00	7.09		0.48		1.49	6	0.51250
FJ22			29.0			0.47	2.06	0.72	-3.12		0.53				
FJ44			339.0			0.37	1.34	0.73	2.89		0.63				
FJ45			237.0			0.41	1.51	0.81	2.63		0.59				
FJ2			1012.0			0.28	1.24	0.73	2.89		0.72				
FJ25			619.0			0.39	1.24	0.80	5.49		0.61				
FJ67			611.0			0.33	1.33	0.82	4.13		0.67				
FJ16			1117.0			0.41	1.09	0.91	10.53		0.59				
FJ12			261.0			0.44	1.73	1.05	2.96		0.56				
FJ60			1383.0			0.30	1.16	0.84	5.02		0.70				
JS46			668.0			0.38	1.16	0.85	6.40		0.62				
FJ8			409.0			0.37	1.47	0.97	4.39		0.63				
FJ7			275.0			0.33	1.35	0.97	5.23		0.67				
FJ4			323.0			0.30	1.25	0.97	6.31		0.70				
FJ63			324.0			0.46	1.46	0.98	4.30		0.54				
FJ26			877.0			0.46	1.98	1.00	0.81		0.54				
FJ64			390.0			0.29	1.33	1.02	6.14		0.71				
FJ3			371.0			0.59	1.66	0.93	2.04		0.41				
FJ72			272.0			0.29	1.31	1.07	6.92		0.71				
FJ78			312.0			0.35	1.34	1.02	5.96		0.65				
FJ9			439.0			0.45	1.29	0.99	4.75		0.55				
FJ43			216.0			0.31	1.16	1.06	8.17		0.69				
FJ73			329.0			0.31	1.10	0.98	8.17		0.69				
JS44			120.0			0.28	1.14	1.04	8.63		0.72				
15RME-0409	3.0	104.0	155.0	174.0	200.9	0.48	1.56	0.65	-0.64		0.52				
16RME-0573	3.0	79.0	144.0	407.3	440.2	0.38	1.29	0.74	4.40		0.62				
16RME-0290	10.3	133.0	453.0	335.5	409.8	0.33	1.41	0.66	0.80		0.67				
16RME-0519	2.1	35.0	246.0	167.3	185.6	0.57	1.38	0.60	0.01		0.43				
15RME-0220	2.3	66.0	47.0	132.0	159.7	0.44	1.39	0.81	4.10		0.56				
15RME-0221	3.2	50.0	115.0	222.2	253.8	0.42	1.33	0.96	7.31		0.58				
15RME-0358	2.3	53.0	179.0	199.0	222.0	0.46	1.28	0.88	6.96		0.54				
16RME-0517	3.0	15.0	306.0	259.7	285.4	0.75	1.38	0.69	1.19		0.25				
15RME-0219	3.5	34.0	470.0	130.3	156.8	0.39	1.23	0.99	9.30		0.61				
16RME-0194	1.7	11.0	406.0	81.1	95.0	0.72	2.05	1.03	1.02		0.28				
15RME-0370	5.2	42.0	522.0	196.4	236.9	0.27	1.19	0.99	9.51		0.73				
15RME-0357	3.1	41.0	420.0	230.2	253.9	0.61	1.16	0.85	8.91		0.39				
16RME-0392	0.9	16.0	129.0	58.2	64.1	0.79	1.07	0.88	11.50		0.21				
16RME-0202	14.7	38.0	392.0	348.7	447.1	0.30	1.17	0.86	6.43		0.70				
15RME-0431	2.7	12.0	1138.0	78.0	93.7	0.40	1.26	1.01	7.05		0.60				
15RME-0466	0.5	7.0	71.0	29.1	32.6	0.83	1.19	0.91	7.01		0.17				
16RME-0594	1.6	28.0	138.0	73.3	82.4	0.58	1.52	1.06	5.44		0.42				

	mg/kg	*mg/kg*	*mg/kg*	*calc*	*calc*	*calc*	*calc*	*calc*	*calc*		*calc*	*U-Pb*	*reported*	*reported*	*reported*
Sample	**Yb**	**Zn**	**Zr**	**ΣLREE**	**ΣREE**	**Mg#**	**A/NK**	**ASI**	**N+K-C**	**XFe2+**	**FeO(t)/FeO(t)+MgO**	**Preffered Age**	**[Sm]**	**[Nd]**	**143Nd/144Nd**
16RME-0555	0.7	2.0	28.0	48.8	58.6	0.90	1.19	1.01	8.93		0.10				
15RME-0250	0.4	10.0	106.0	116.5	123.4	0.59	1.40	1.14	7.05		0.41				
15RME-0259	2.0	5.0	107.0	94.5	108.5	0.66	1.28	1.08	7.97		0.34				
16RME-0466	0.9	15.0	99.0	29.7	34.5	0.66	1.28	1.06	7.12		0.34				
15RME-0254	1.0	4.0	165.0	231.0	243.6	0.50	1.25	1.08	8.18		0.50				
16RME-0305	0.9	3.0	32.0	20.5	27.5	0.88	1.29	1.01	6.46		0.12				
16RME-0465	0.9	10.0	76.0	25.9	30.9	0.64	1.23	1.05	7.46		0.36				
16RME-0318	6.1	7.0	80.0	45.4	63.2	0.45	1.09	1.00	8.66		0.55				
16RME-0572	1.3	9.0	235.0	71.0	80.2	0.56	1.29	0.76	1.46		0.44				
LL138		122.0	59.0			0.36	2.76	0.57	-7.06		0.64				
LL53	1.7	83.0	66.0	40.5	52.1	0.54	3.78	0.66	-7.50		0.46				
LL120		115.0	132.0			0.35	228.69	70.10	-3.72		0.65				
LL56	5.7	202.0	164.0	138.3	183.4	0.43	1.62	0.71	-0.13		0.57				
LN25		134.0	376.0			0.50	1.32	0.62	1.43		0.50				
LL157		52.0	273.0			0.33	1.31	0.84	5.23		0.67				
LN24	6.6	196.0	435.0	404.6	457.9	0.37	1.23	0.74	4.58		0.63				
LL137		40.0	178.0			0.38	1.24	0.76	4.87		0.62				
LL04	5.9	63.0	360.0	326.8	376.6	0.35	1.43	0.90	4.88		0.65				
LL23	5.4	72.0	380.0	320.5	366.6	0.37	1.35	0.82	4.69		0.63				
LN23		65.0	549.0			0.29	1.16	0.92	7.98		0.71				
LN10		43.0	147.0			0.52	1.55	1.02	4.82		0.48				
LN06	9.0	97.0	603.0	434.8	493.1	0.40	1.07	0.82	7.75		0.60				
15RME-0247															
15RME-0320															
15RME-0420															
21CK47A	3.8	40.0	591.0	226.9	259.0	0.39	1.40	0.96	6.28		0.61				
21CK48A			592.0			0.36	1.30	0.87	5.95		0.64				
21CK70A			781.0			0.40	1.34	0.85	5.17		0.60				
21CK76A	6.6	160.0	573.0	428.6	483.0	0.35	1.29	0.80	4.59		0.65				
20CK88A			640.0			0.32	1.20	0.93	7.43		0.68				
20CK36B			345.0			0.24	1.18	1.01	8.61		0.76				
20CK06A			401.0			0.31	1.32	1.04	7.09		0.69				
20CK86A			50.0			0.68	1.43	1.07	6.52		0.32				
20CK18A			17.0			0.74	1.36	1.08	6.55		0.26				
20CK52B			59.0			0.28	1.22	1.11	7.09		0.72				
20CK100A			69.0			0.22	1.02	0.85	5.20		0.78				
5207W															
R5179G															
R5180G															
R5181G															
R5182G															
R5183W															
R5184W															
R5185W															
R5186L															
R5208W															
R5209W															

Sample	mg/kg Yb	mg/kg Zn	mg/kg Zr	calc ΣLREE	calc ΣREE	calc Mg#	calc A/NK	calc ASI	calc N+K-C	XFe2+	calc FeO(t)/FeO(t)+MgO	U-Pb Preffered Age	reported [Sm]	reported [Nd]	reported 143Nd/144Nd
LH87-30												1170.1			
LH86-64			600.0	197.0	197.0	0.41	1.34	0.84	5.10		0.59	1165.5			0.51213
LH87-31												1158.1			
LH86-63			1404.0	289.9	289.9	0.32	1.22	0.90	6.60		0.68	1152			0.51211
WP1				268.1	268.1	0.31	1.10	0.91	10.00		0.69				0.51204
LH86-7			674.0	257.2	257.2	0.30	1.12	0.93	10.10		0.70				0.51206
CL3			438.0	213.1	213.1	0.28	1.26	1.01	8.60		0.72				0.51210
RLI			801.0	242.7	242.7	0.34	1.20	0.96	9.30		0.66				0.51213
LY3			182.0	311.8	311.8	0.33	1.23	0.92	6.90		0.67				0.51214
GQ1															0.51217
SL2			709.0	206.1	206.1	0.37	1.38	0.92	6.00		0.63				0.51218
BS1															0.51218
WL1			301.0	330.8	330.8	0.31	1.17	0.96	9.90		0.69				0.51220
GQI			747.0	237.7	237.7	0.35	1.39	0.90	5.30		0.65				
BSI			700.0	281.7	281.7	0.33	1.23	0.89	6.70		0.67				
CL3															
LY3															
16RME-0280	7.6	221.0	184.0	488.9	563.0	0.38	1.52	0.42	-4.96		0.62				
16RME-0557A	0.4	50.0	55.0	74.5	79.4	0.35	1.62	1.20	7.91		0.65				
16RME-0366	1.9	201.0	50.0	34.5	48.6	0.44	2.14	0.61	-4.76		0.56				
16RME-0376	3.7	142.0	169.0	168.9	198.4	0.40	1.69	0.69	-1.01		0.60				
16RME-0253	5.0	85.0	230.0	135.9	176.1	0.49	2.16	0.69	-4.01		0.51				
16RME-0389	3.1	119.0	113.0	140.6	165.1	0.44	1.97	0.74	-1.91		0.56				
16RME-0535	2.4	85.0	114.0	271.7	301.9	0.43	1.77	0.76	0.20		0.57				
16RME-0237	3.4	172.0	228.0	534.5	575.5	0.44	1.48	0.68	1.41		0.56				
15RME-0090	4.7	142.0	215.0	232.0	271.0	0.42	1.81	0.65	-2.35		0.58				
16RME-0529	1.9	67.0	124.0	132.4	150.1	0.52	1.40	0.65	1.36		0.48				
16RME-0211	2.5	118.0	134.0	61.6	84.7	0.42	2.04	0.75	-2.32		0.58				
15RME-0359	4.4	95.0	149.0	86.9	117.2	0.41	2.03	0.72	-2.32		0.59				
MEW1	4.1	82.6	49.3	462.1	504.4	0.29	1.36	0.70	3.09		0.71				
JJF1	4.6	121.0	40.9	529.3	572.4	0.23	1.36	0.81	3.92		0.77				
JK02	4.0	77.1	32.5	426.7	470.1	0.45	1.50	0.64	0.13		0.55				
MEW2	3.2	89.6	66.2	364.8	398.5	0.31	1.48	0.80	2.97		0.69				
JT2	3.8	113.0	77.2	380.3	419.0	0.33	1.44	0.72	1.90		0.67				
MP2	4.0	86.5	104.0	389.2	428.6	0.34	1.41	0.76	3.03		0.66				
JK01	3.7	60.2	21.2	372.3	409.6	0.30	1.48	0.88	4.05		0.70				
KC03	6.0	64.1		314.0	365.4	0.38	1.37	0.86	5.10		0.62				
KC02	6.7	54.8		335.4	393.2	0.38	1.40	0.89	5.34		0.62				
MP3	4.9	42.9		224.8	265.8	0.39	1.36	0.89	5.75		0.61				
JT3	5.1	44.3		262.9	305.5	0.42	1.33	0.87	5.98		0.58				
MP4	4.3	39.7		203.4	240.2	0.47	1.35	0.87	5.79		0.53				
JT4	5.0	71.3		254.1	295.8	0.39	1.34	0.93	6.47		0.61				
JK03	4.7	114.0		247.5	287.8	0.38	1.27	0.86	6.21		0.62				
JJF2	4.7	50.1		247.2	286.0	0.43	1.43	0.95	5.84		0.57				
JJF3	5.0	49.5		286.4	330.2	0.39	1.34	0.90	5.99		0.61				
MEW3	5.1	76.3		251.2	294.1	0.40	1.40	0.95	6.05		0.60				
EHW02	6.7	57.1		370.3	419.0	0.24	1.33	1.11	8.02		0.76				

	mg/kg	*mg/kg*	*mg/kg*	*calc*	*calc*	*calc*	*calc*	*calc*	*calc*	*calc*	*U-Pb*	*reported*	*reported*	*reported*
Sample	**Yb**	**Zn**	**Zr**	**ΣLREE**	**ΣREE**	**Mg#**	**A/NK**	**ASI**	**N+K-C**	**XFe2+**	**FeO(t)/FeO(t)+MgO**	**Preffered Age**	**[Sm]**	**[Nd]**	**143Nd/144Nd**
KC01	6.8	65.1		442.4	493.5	0.26	1.29	1.07	8.14		0.74				
JT1	5.2	41.7	554.0	448.2	488.9	0.16	1.27	1.11	8.50		0.84				
MP1	5.7	38.1	512.0	543.5	590.3	0.16	1.25	1.10	8.61		0.84				
LJT1	6.9	27.6	262.0	354.5	400.0	0.30	1.25	1.01	7.33		0.70				
DH2	2.4	36.7		193.4	216.3	0.24	1.24	1.08	8.60		0.76				
EHW01	5.0	38.9		304.3	343.7	0.25	1.29	1.09	7.80		0.75				
DH1	3.0	36.1	178.0	170.0	191.5	0.30	1.23	1.01	7.69		0.70				
LJT3	1.2	0.0	236.0	31.9	38.1	0.25	1.29	1.18	7.82		0.75				
DH3	1.5	0.0	207.0	71.2	80.7	0.38	1.32	1.15	7.55		0.62				
LJT2	0.6	0.0		47.5	53.3	0.45	1.26	1.10	7.61		0.55				
86DM96															
93DM131															
89S3												1175.55			
89S4												1164.85			
89S1												1162			
89S2												1161.2			
89S5												1157			
89S6															
89S7															
89S8															
89S9															

Sample	*reported* 147Sm/144Nd	*calc* 147/144 (i)	*calc* tDM (Sm-Nd)	*calc* tCHUR (Sm-Nd)	*calc* εNd	*reported* RbSr method	*reported* [Rb]	*reported* [Sr]	*reported* 87Rb/86Sr	*reported* 87Sr/86Sr	*calc* 87/86 (i)	*calc* tDM (Rb-Sr)	*calc* tCHUR (Rb-Sr)
109													
154													
199													
145													
108													
64-35													
183													
64-34													
64-60													
64-61													
64-58													
64-59													
104													
113													
139													
64-57													
170													
216													
506													
180													
152													
213													
130													
64-44a													
516													
FJ97													
64-43													
151													
105													
513													
501													
JC-050	0.10770	0.51136	1409.57	840.91	4.36		87.1	355.5	0.77400	0.70748	0.69478	19.72	-2685.30
JC-070	0.10300	0.51136	1456.85	896.81	4.47		98.98	698.2	0.41000	0.70941	0.70268	230.86	-2465.41
JC-014	0.11230	0.51128	1472.61	915.43	2.89								
JC-043	0.09250	0.51145	1441.09	878.18	6.24								
JC-067	0.10660	0.51136	1409.57	840.91	4.52	TIMS							
JC-045	0.13590	0.51115	1393.80	822.27	0.33								
JC-081						TIMS							
91DM14b													
93DM18b													
93DM19													
94DM53													
96DM1													
91DM131a													
15RME-0179													
FJ50	0.05760	0.51108	2441.84	2060.39	-1.00								
FJ24	0.10440	0.51121	1678.91	1159.25	1.51								

	reported	*calc*	*calc*	*calc*	*calc*	*reported*	*reported*	*reported*	*reported*	*reported*	*calc*	*calc*	*calc*
Sample	**147Sm/144Nd**	**147/144 (i)**	**tDM (Sm-Nd)**	**tCHUR (Sm-Nd)**	**εNd**	**RbSr method**	**[Rb]**	**[Sr]**	**87Rb/86Sr**	**87Sr/86Sr**	**87/86 (i)**	**tDM (Rb-Sr)**	**tCHUR (Rb-Sr)**
FJ27	0.11740	0.51117	1582.88	1045.77	0.75								
FJ40	0.11260	0.51123	1543.51	999.23	1.96								
FJ51	0.11720	0.51124	1485.22	930.34	2.00								
FJ93	0.12820	0.51121	1395.38	824.14	1.47								
FJ20	0.12840	0.51128	1277.08	684.29	2.90								
FJ46	0.12770	0.51134	1201.33	594.72	3.95								
FJ18	0.14920	0.51136	907.41	247.15	4.37								
FJ22													
FJ44													
FJ45													
FJ2													
FJ25													
FJ67													
FJ16													
FJ12													
FJ60													
JS46													
FJ8													
FJ7													
FJ4													
FJ63													
FJ26													
FJ64													
FJ3													
FJ72													
FJ78													
FJ9													
FJ43													
FJ73													
JS44													
15RME-0409													
16RME-0573													
16RME-0290													
16RME-0519													
15RME-0220													
15RME-0221													
15RME-0358													
16RME-0517													
15RME-0219													
16RME-0194													
15RME-0370													
15RME-0357													
16RME-0392													
16RME-0202													
15RME-0431													
15RME-0466													
16RME-0594													

	reported	*calc*	*calc*	*calc*	*calc*	*reported*	*reported*	*reported*	*reported*	*reported*	*calc*	*calc*	*calc*
Sample	**147Sm/144Nd**	**147/144 (i)**	**tDM (Sm-Nd)**	**tCHUR (Sm-Nd)**	**εNd**	**RbSr method**	**[Rb]**	**[Sr]**	**87Rb/86Sr**	**87Sr/86Sr**	**87/86 (i)**	**tDM (Rb-Sr)**	**tCHUR (Rb-Sr)**
16RME-0555													
15RME-0250													
15RME-0259													
16RME-0466													
15RME-0254													
16RME-0305													
16RME-0465													
16RME-0318													
16RME-0572													
LL138													
LL53													
LL120													
LL56													
LN25													
LL157													
LN24													
LL137													
LL04													
LL23													
LN23													
LN10													
LN06													
15RME-0247													
15RME-0320													
15RME-0420													
21CK47A													
21CK48A													
21CK70A													
21CK76A													
20CK88A													
20CK36B													
20CK06A													
20CK86A													
20CK18A													
20CK52B													
20CK100A													
5207W													
R5179G													
R5180G													
R5181G													
R5182G													
R5183W													
R5184W													
R5185W													
R5186L													
R5208W													
R5209W													

Sample	*reported* 147Sm/144Nd	*calc* 147/144 (i)	*calc* tDM (Sm-Nd)	*calc* tCHUR (Sm-Nd)	*calc* εNd	*reported* RbSr method	*reported* [Rb]	*reported* [Sr]	*reported* 87Rb/86Sr	*reported* 87Sr/86Sr	*calc* 87/86 (i)	*calc* tDM (Rb-Sr)	*calc* tCHUR (Rb-Sr)
LH87-30						TIMS							
LH86-64	0.11770	0.51123	1488.37	934.06	1.88	TIMS	77	626	0.35780	0.71034	0.70447	332.37	-2359.69
LH87-31													
LH86-63	0.11440	0.51124	1519.88	971.30	1.98		140	299	1.35580	0.72708	0.70483	2135.45	-483.02
WP1	0.09180	0.51134	1630.12	1101.59	4.00	TIMS	114	100	3.30310	0.75674	0.70254	5222.71	2725.86
LH86-7	0.09190	0.51136	1598.63	1064.37	4.37	TIMS	115	96	3.46490	0.75936	0.70251	5489.13	3002.52
CL3	0.11700	0.51121	1535.63	989.92	1.40		149	405	1.06910	0.72315	0.70561	1716.21	-919.20
RLI	0.10170	0.51135	1488.37	934.06	4.28		75	469	0.46500	0.71116	0.70353	421.76	-2266.61
LY3	0.11400	0.51127	1472.61	915.43	2.63		141	219	1.85840	0.73490	0.70441	2962.43	377.08
GQ1	0.11750	0.51127	1425.33	859.55	2.69		81	468	0.50140	0.71308	0.70485	630.62	-2049.13
SL2	0.12090	0.51126	1409.57	840.91	2.38	TIMS	76	499	0.44370	0.71184	0.70456	495.80	-2189.51
BS1	0.11540	0.51130	1409.57	840.91	3.20		120	319	1.09330	0.72225	0.70431	1619.85	-1019.46
WL1	0.10980	0.51136	1378.03	803.63	4.43	TIMS	84	256	0.95460	0.71847	0.70281	1213.73	-1442.11
GQI						TIMS							
BSI						TIMS							
CL3													
LY3													
16RME-0280													
16RME-0557A													
16RME-0366													
16RME-0376													
16RME-0253													
16RME-0389													
16RME-0535													
16RME-0237													
15RME-0090													
16RME-0529													
16RME-0211													
15RME-0359													
MEW1						TIMS							
JJF1													
JK02													
MEW2													
JT2													
MP2													
JK01													
KC03													
KC02													
MP3													
JT3													
MP4													
JT4													
JK03													
JJF2													
JJF3													
MEW3													
EHW02													

	reported	*calc*	*calc*	*calc*	*calc*	*reported*	*reported*	*reported*	*reported*	*reported*	*calc*	*calc*	*calc*
Sample	**147Sm/144Nd**	**147/144 (i)**	**tDM (Sm-Nd)**	**tCHUR (Sm-Nd)**	**εNd**	**RbSr method**	**[Rb]**	**[Sr]**	**87Rb/86Sr**	**87Sr/86Sr**	**87/86 (i)**	**tDM (Rb-Sr)**	**tCHUR (Rb-Sr)**
KC01													
JT1													
MP1													
LJT1													
DH2													
EHW01													
DH1													
LJT3													
DH3													
LJT2													
86DM96													
93DM131													
89S3													
89S4													
89S1													
89S2													
89S5													
89S6													
89S7													
89S8													
89S9													

Sample	*reported* 147Sm/144Nd	*calc* 147/144 (i)	*calc* tDM (Sm-Nd)	*calc* tCHUR (Sm-Nd)	*calc* εNd	*reported* RbSr method	*reported* [Rb]	*reported* [Sr]	*reported* 87Rb/86Sr	*reported* 87Sr/86Sr	*calc* 87/86 (i)	*calc* tDM (Rb-Sr)	*calc* tCHUR (Rb-Sr)

Sample	*calc* **εSr**	*reported* **δO18**	*Borisov&Aranovish 2019* **T (Zr)**	*uW/m3* **HP**	*cl(N)* **Sr**	*cl(N)* **Li**	*cl(N)* **Zr**	*cl(N)* **Rb**	*cl(N)* **Ba**	*cl(N)* **Th**	*cl(N)* **U**	*cl(N)* **Nb**	*cl(N)* **Ta**
109													
154													
199													
145													
108													
64-35													
183													
64-34													
64-60													
64-61													
64-58													
64-59													
104													
113													
139													
64-57													
170													
216													
506													
180													
152													
213													
130													
64-44a													
516													
FJ97			1109		15.31		101.57						
64-43													
151													
105													
513													
501													
JC-050	-119.52		1003	1.30	50.07	8.53	152.36	42.22	220.33	135.72	172.03	79.25	99.04
JC-070	-7.14		1035	1.56	96.30	14.00	122.25	43.03	654.02	225.59	246.76	110.67	117.28
JC-014													
JC-043													
JC-067													
JC-045													
JC-081			1097	2.26	36.74	14.00	250.26	52.80	265.68	366.69	429.86	226.76	288.53
91DM14b													
93DM18b													
93DM19		10.01											
94DM53													
96DM1													
91DM131a													
15RME-0179													
FJ50			911		28.83		15.45						
FJ24			927		111.45		44.24						

Sample	*calc* εSr	*reported* δO18	*Borisov&Aranovish 2019* T (Zr)	*uW/m3* HP	*cl(N)* Sr	*cl(N)* Li	*cl(N)* Zr	*cl(N)* Rb	*cl(N)* Ba	*cl(N)* Th	*cl(N)* U	*cl(N)* Nb	*cl(N)* Ta
FJ27			756		60.55		15.45						
FJ40			1042		66.48		119.63						
FJ51			857		181.24		21.20						
FJ93			1122		48.14		215.18						
FJ20			1025		62.48		149.21						
FJ46			1030		118.62		140.58						
FJ18			938		28.69		19.63						
FJ22			813		140.83		7.59						
FJ44			996		84.00		88.74						
FJ45			984		93.79		62.04						
FJ2			1103		31.59		264.92						
FJ25			1073		46.34		162.04						
FJ67			1103		40.41		159.95						
FJ16			1072		25.10		292.41						
FJ12			998		62.07		68.32						
FJ60			1173		29.24		362.04						
JS46			1139		67.59		174.87						
FJ8			1120		17.66		107.07						
FJ7			1064		26.76		71.99						
FJ4			1083		19.17		84.55						
FJ63			1072		38.07		84.82						
FJ26			1145		67.45		229.58						
FJ64			1114		18.62		102.09						
FJ3			1042		47.72		97.12						
FJ72			1072		18.62		71.20						
FJ78			1095		19.59		81.68						
FJ9			1011		8.41		114.92						
FJ43			1054		22.21		56.54						
FJ73			1094		2.62		86.13						
JS44			974		13.66		31.41						
15RME-0409			914	0.56	155.43	17.00	40.58	17.51	388.05	48.38	85.41	32.23	33.75
16RME-0573			856	0.84	122.88	15.67	37.70	38.57	410.29	79.48	52.43	100.90	74.04
16RME-0290			1028	0.83	51.16	8.67	118.59	18.05	295.06	118.31	153.24	84.28	76.76
16RME-0519			928	0.71	126.48	19.60	64.40	40.42	456.27	116.03	70.14	30.68	29.85
15RME-0220			841	0.48	116.95	8.47	12.30	9.22	721.99	17.72	24.59	9.78	10.88
15RME-0221			906	0.69	116.80	8.60	30.10	27.04	721.99	24.41	39.46	49.21	40.88
15RME-0358			922	1.22	133.05	11.93	46.86	42.30	721.99	137.83	169.32	73.97	63.60
16RME-0517			933	2.17	170.46	11.07	80.10	4.30	122.24	553.31	440.81	51.92	61.99
15RME-0219			1005	0.93	70.97	7.07	123.04	39.49	706.72	24.69	104.59	65.09	43.82
16RME-0194			1045	0.25	123.96	22.87	106.28	2.94	119.09	10.17	52.30	30.11	33.46
15RME-0370			1028	0.93	26.06	6.73	136.65	31.40	721.99	60.52	66.89	50.25	32.13
15RME-0357			910	2.43	78.23	6.87	109.95	89.03	532.61	447.17	330.00	190.34	184.49
16RME-0392			709	2.23	101.02	3.20	33.77	129.41	492.86	355.17	187.03	48.78	68.46
16RME-0202			1075	1.43	73.79	5.93	102.62	45.43	645.39	211.03	202.97	147.17	182.21
15RME-0431			1243	0.91	59.09	7.00	297.91	30.04	721.99	62.97	147.97	60.27	40.07
15RME-0466			868	0.39	27.30	4.07	18.59	6.64	149.88	42.52	54.32	9.94	12.57
16RME-0594			996	0.84	69.43	14.00	36.13	37.57	315.56	132.69	45.14	18.63	5.74

	calc	*reported*	*Borisov&Aranovish 2019*	*uW/m3*	*cl(N)*	*cl(N)*	*cl(N)*	*cl(N)*	*cl(N)*	*cl(N)*	*cl(N)*	*cl(N)*	*cl(N)*
Sample	**εSr**	**δO18**	**T (Zr)**	**HP**	**Sr**	**Li**	**Zr**	**Rb**	**Ba**	**Th**	**U**	**Nb**	**Ta**
16RME-0555			837	1.08	28.25	2.53	7.33	45.27	233.15	86.07	143.51	15.01	49.63
15RME-0250			981	2.40	42.39	12.20	27.75	51.11	134.61	653.00	254.32	9.87	8.68
15RME-0259			971	1.27	23.45	3.20	28.01	43.50	230.83	185.86	169.59	14.44	18.90
16RME-0466			962	1.91	27.79	3.93	25.92	38.43	193.11	255.31	494.46	15.18	25.88
15RME-0254			1012	2.92	18.68	2.27	43.19	46.35	232.66	898.07	215.54	7.68	5.51
16RME-0305			867	2.91	19.48	3.40	8.38	35.63	126.14	136.24	1111.49	3.85	4.71
16RME-0465			942	1.23	27.39	4.80	19.90	38.70	200.25	180.17	220.27	11.70	21.76
16RME-0318			940	2.02	14.76	0.93	20.94	63.46	38.26	404.76	386.49	37.82	54.78
16RME-0572			1021	0.33	9.82	8.93	61.52	6.66	25.15	28.10	85.27	42.37	59.41
LL138			840		60.00		15.45	3.48	97.10			20.83	
LL53			764		37.93		17.28	2.61	71.78			41.67	
LL120			-1		34.21		34.55	12.61	99.17			20.83	
LL56			929		67.86		42.93	5.65	396.27				
LN25			968		72.97		98.43	51.74	237.76			112.50	
LL157			984		107.72		71.47	32.17	412.45			54.17	
LN24			1012		61.93		113.87	35.65	358.92			95.83	
LL137			931		69.10		46.60	24.35	371.37			91.67	
LL04			1033		71.59		94.24	11.74	478.01			58.33	
LL23			1015		81.38		99.48	13.48	542.74			79.17	
LN23			1057		42.21		143.72	69.57	374.27			66.67	
LN10			991		74.07		38.48	40.00	285.06			50.00	
LN06			1093		29.24		157.85	67.39	179.25			133.33	
15RME-0247													
15RME-0320													
15RME-0420													
21CK47A			1081	0.91	66.48		154.71	36.52	698.34	71.38	95.95	67.92	56.62
21CK48A			1080										
21CK70A			1115										
21CK76A			1089	0.91	53.93		150.00	44.35	417.01	103.45	98.65	105.42	71.32
20CK88A			1115										
20CK36B			1023										
20CK06A			1098										
20CK86A			894										
20CK18A			829										
20CK52B			927										
20CK100A			908										
5207W													
R5179G													
R5180G													
R5181G													
R5182G													
R5183W													
R5184W													
R5185W													
R5186L													
R5208W													
R5209W													

Sample	*calc* εSr	*reported* δO18	*Borisov&Aranovish 2019* T (Zr)	*uW/m3* HP	*cl(N)* Sr	*cl(N)* Li	*cl(N)* Zr	*cl(N)* Rb	*cl(N)* Ba	*cl(N)* Th	*cl(N)* U	*cl(N)* Nb	*cl(N)* Ta
LH87-30		15.7											
LH86-64	18.27	13.8	1086		86.34		157.07	33.48				100.00	
LH87-31		13.6											
LH86-63	23.45	13.4	1238		41.24		367.54	60.87				166.67	
WP1	-9.14	10.6			13.79			49.57					
LH86-7	-9.64	10.6	1033		13.24		176.44	50.00				108.33	
CL3	34.46	15.7	1024		55.86		114.66	64.78				70.83	
RLI	4.91	10.7	1059		64.69		209.69	32.61				120.83	
LY3	17.38	13.6	989		30.21		47.64	61.30				58.33	
GQ1	23.72	13.6											
SL2	19.55	13.7	1107		68.83		185.60	33.04				66.67	
BS1	16.02	13.4											
WL1	-5.38	9.4	959		35.31		78.80	36.52				116.67	
GQI			1125		64.55		195.55	35.22				83.33	
BSI			1127		44.00		183.25	52.17				108.33	
CL3													
LY3													
16RME-0280			926	0.68	100.54	15.87	48.17	14.07	521.91	99.69	119.19	63.92	64.71
16RME-0557A			527	1.28	113.56	92.27	14.40	86.49	721.99	66.90	84.05	76.41	70.22
16RME-0366			804	0.37	30.84	20.47	13.09	13.50	35.48	65.17	52.03	5.59	5.81
16RME-0376			917	0.41	112.22	14.40	44.24	13.26	376.97	41.41	55.54	26.03	27.28
16RME-0253			943	0.30	93.30	16.53	60.21	4.26	139.88	46.38	52.57	25.94	32.13
16RME-0389			905	0.40	121.53	43.27	29.58	15.68	355.77	41.07	56.35	18.03	18.82
16RME-0535			911	0.61	215.17	29.53	29.84	27.01	721.99	51.34	51.22	54.52	39.34
16RME-0237			876	1.73	215.17	25.80	59.69	46.80	721.99	317.86	248.65	52.79	39.85
15RME-0090			958	0.40	119.56	14.47	56.28	14.92	403.28	35.00	45.41	49.32	46.10
16RME-0529			858	1.30	165.94	24.53	32.46	59.88	720.71	176.10	214.86	29.95	29.93
16RME-0211			893	0.67	47.23	7.93	35.08	11.93	88.92	108.52	175.27	20.21	25.37
15RME-0359			919	1.20	38.07	15.47	39.01	13.13	128.05	213.14	305.95	21.74	29.34
MEW1			683	1.56	69.66		12.91	43.48	520.33	195.52	248.65	71.25	70.59
JJF1			793	1.33	70.34		10.71	86.09	338.59	183.45	250.00	92.08	83.09
JK02			791	0.89	217.24		8.51	32.83	612.03	105.52	125.68	71.25	75.74
MEW2			840	1.41	244.41		17.33	53.04	845.64	177.59	293.24	67.08	80.88
JT2			857	0.84	229.10		20.21	31.87	523.65	112.41	112.16	68.75	80.88
MP2			877	0.98	199.86		27.23	41.74	567.22	103.79	154.05	77.08	83.82
JK01			781	0.83	141.24		5.55	32.87	614.94	93.45	90.54	69.17	72.79
KC03					85.66			29.52	769.71				
KC02					82.34			24.61	695.02				
MP3					64.41			26.26	646.47				
JT3					88.69			33.52	858.51				
MP4					61.79			28.83	663.90				
JT4					76.69			31.96	640.66				
JK03					66.90			28.87	643.57				
JJF2					92.14			33.96	671.78				
JJF3					72.55			38.22	677.18				
MEW3					88.00			32.87	678.01				
EHW02					50.48			54.78	429.46				

Sample	*calc* **εSr**	*reported* **δO18**	*Borisov&Aranovish 2019* **T (Zr)**	*uW/m3* **HP**	*cl(N)* **Sr**	*cl(N)* **Li**	*cl(N)* **Zr**	*cl(N)* **Rb**	*cl(N)* **Ba**	*cl(N)* **Th**	*cl(N)* **U**	*cl(N)* **Nb**	*cl(N)* **Ta**
KC01					49.52			65.22	339.83				
JT1			1107	1.79	64.00		145.03	58.70	441.49	250.69	290.54	141.67	211.76
MP1			1101	2.00	60.14		134.03	59.57	404.56	343.10	300.00	147.92	252.94
LJT1			1044	1.68	39.31		68.59	60.00	268.05	241.38	289.19	125.83	175.00
DH2					56.83			66.52	329.88				
EHW01					82.62			50.43	386.31				
DH1			1009	1.37	32.41		46.60	55.22	192.12	177.24	205.41	71.67	143.38
LJT3			1074	1.31	63.86		61.78	29.26	267.22	38.28	386.49	9.21	68.38
DH3			1055	1.61	41.93		54.19	34.13	406.22	181.03	377.03	28.92	95.59
LJT2					130.07			31.22	338.17				
86DM96		12.48											
93DM131		9.13											
89S3		10.1											
89S4		13.4											
89S1		9.9											
89S2		9.6											
89S5		14.6											
89S6		14.1											
89S7		13.9											
89S8		14.4											
89S9		14.6											

Sample	*cl(N)* La	*cl(N)* Ce	*cl(N)* Nd	*cl(N)* Sm	*cl(N)* Eu	*cl(N)* Gd	*cl(N)* Dy	*cl(N)* Er	*cl(N)* Yb	*cl(N)* Y	*cl(N)* Lu
109											
154											
199											
145											
108											
64-35											
183											
64-34											
64-60											
64-61											
64-58											
64-59											
104											
113											
139											
64-57											
170											
216											
506											
180											
152											
213											
130											
64-44a											
516											
FJ97										29.94	
64-43											
151											
105											
513											
501											
JC-050	309.54	267.00	169.06	84.95	55.11	43.36	27.73	21.30	17.91	21.57	16.58
JC-070	338.14	291.46	195.89	101.55	73.47	52.49	32.11	24.11	19.84	24.52	18.33
JC-014											
JC-043											
JC-067											
JC-045											
JC-081	602.41	504.38	278.18	134.20	59.10	67.38	47.01	40.34	38.29	39.15	35.72
91DM14b											
93DM18b											
93DM19											
94DM53											
96DM1											
91DM131a											
15RME-0179											
FJ50										0.64	
FJ24										19.11	

Sample	*cl(N)* La	*cl(N)* Ce	*cl(N)* Nd	*cl(N)* Sm	*cl(N)* Eu	*cl(N)* Gd	*cl(N)* Dy	*cl(N)* Er	*cl(N)* Yb	*cl(N)* Y	*cl(N)* Lu
FJ27										11.46	
FJ40										34.39	
FJ51										15.92	
FJ93										40.13	
FJ20										18.47	
FJ46										31.21	
FJ18										6.37	
FJ22										8.92	
FJ44										42.04	
FJ45										33.76	
FJ2										110.83	
FJ25										37.58	
FJ67										52.23	
FJ16										31.21	
FJ12										12.74	
FJ60										53.50	
JS46										57.32	
FJ8										50.32	
FJ7										21.02	
FJ4										29.94	
FJ63										7.01	
FJ26										5.73	
FJ64										31.85	
FJ3										45.22	
FJ72										29.30	
FJ78										30.57	
FJ9										50.32	
FJ43										16.56	
FJ73										26.11	
JS44										18.47	
15RME-0409	132.28	125.30	102.12	61.62	45.70	40.49	26.55	21.78	18.57	22.34	17.84
16RME-0573	350.51	313.26	204.77	103.45	66.33	55.22	31.18	23.76	18.39	25.40	16.71
16RME-0290	248.82	239.43	196.39	135.28	81.59	98.30	76.80	69.20	64.15	67.21	61.67
16RME-0519	146.03	124.69	86.50	49.99	28.91	28.84	17.48	14.36	13.02	14.92	12.72
15RME-0220	100.72	88.28	83.35	55.75	83.95	41.23	25.75	19.38	14.40	20.98	13.83
15RME-0221	187.09	159.26	124.09	73.02	80.79	45.97	29.56	23.69	19.66	24.34	18.78
15RME-0358	166.46	152.26	101.55	59.23	52.97	34.96	21.78	17.39	14.24	17.53	13.55
16RME-0517	201.43	201.79	135.49	74.15	45.91	39.37	24.46	20.09	18.47	21.38	17.65
15RME-0219	110.08	89.20	75.34	51.83	38.03	35.07	26.59	23.86	21.97	21.89	21.23
16RME-0194	70.30	58.36	43.44	28.24	26.23	19.39	13.58	11.58	10.35	10.89	10.40
15RME-0370	147.85	139.74	115.78	77.22	74.59	53.31	39.24	35.95	32.04	35.06	30.65
15RME-0357	161.31	182.28	123.72	64.75	27.94	34.58	23.79	20.87	18.97	20.94	18.64
16RME-0392	56.58	45.44	25.71	13.34	8.04	7.63	5.80	5.38	5.58	5.20	5.28
16RME-0202	200.00	246.56	225.93	161.10	64.63	115.19	107.52	105.44	91.60	97.32	75.53
15RME-0431	69.75	59.10	38.40	23.64	30.40	16.71	13.78	14.98	16.98	13.71	19.00
15RME-0466	23.80	22.67	14.70	7.91	7.97	4.70	3.18	2.82	2.87	2.97	3.08
16RME-0594	77.13	57.10	30.11	17.39	14.00	10.90	8.22	8.10	9.93	8.23	10.15

Sample	*cl(N)* La	*cl(N)* Ce	*cl(N)* Nd	*cl(N)* Sm	*cl(N)* Eu	*cl(N)* Gd	*cl(N)* Dy	*cl(N)* Er	*cl(N)* Yb	*cl(N)* Y	*cl(N)* Lu
16RME-0555	38.65	35.15	26.63	21.72	22.13	15.70	10.66	6.49	4.35	7.20	3.37
15RME-0250	122.78	93.46	45.51	24.91	17.65	13.43	6.11	3.56	2.73	4.10	2.72
15RME-0259	91.35	73.41	41.84	26.39	18.54	17.57	14.02	13.34	12.48	13.25	11.40
16RME-0466	27.97	22.10	14.33	9.74	7.71	5.89	4.17	4.20	5.33	3.59	5.19
15RME-0254	233.16	185.61	94.88	47.78	17.92	22.82	13.04	8.83	6.05	10.21	5.61
16RME-0305	23.25	15.36	8.01	6.12	8.19	7.11	8.24	7.80	5.71	8.23	5.09
16RME-0465	24.56	19.57	11.73	9.15	7.38	5.96	4.67	4.64	5.42	4.34	5.76
16RME-0318	50.46	37.03	15.51	9.53	3.64	8.71	12.54	23.01	37.92	19.55	43.73
16RME-0572	65.78	54.15	33.83	20.18	11.49	12.81	9.10	8.30	7.93	7.93	8.06
LL138										14.01	
LL53	30.78	28.72	23.39	17.18	13.73	13.88	12.43	11.03	10.26	10.19	9.43
LL120										21.66	
LL56	157.46	28.72	127.43	86.07	68.61	60.31	45.35	41.14	35.29	24.84	32.52
LN25										35.67	
LL157										35.03	
LN24	334.43	300.72	217.25	123.65	67.39	77.90	52.83	46.99	41.10	33.76	38.66
LL137										38.22	
LL04	265.94	239.40	179.02	112.00	76.43	69.16	50.88	43.31	36.85	29.30	35.73
LL23	267.33	238.72	169.37	100.89	78.40	63.83	46.07	40.20	33.76	26.75	32.48
LN23										28.03	
LN10										9.55	
LN06	316.58	333.67	238.26	129.09	43.59	75.21	59.33	57.83	55.94	42.04	49.76
15RME-0247											
15RME-0320											
15RME-0420											
21CK47A	211.81	165.57	115.10	70.27	69.27	44.67	30.12	26.25	23.66	25.03	24.15
21CK48A											
21CK70A											
21CK76A	356.12	318.03	229.76	133.11	64.83	79.40	56.50	46.50	40.87	45.80	39.51
20CK88A											
20CK36B											
20CK06A											
20CK86A											
20CK18A											
20CK52B											
20CK100A											
5207W											
R5179G											
R5180G											
R5181G											
R5182G											
R5183W											
R5184W											
R5185W											
R5186L											
R5208W											
R5209W											

Sample	*cl(N)* La	*cl(N)* Ce	*cl(N)* Nd	*cl(N)* Sm	*cl(N)* Eu	*cl(N)* Gd	*cl(N)* Dy	*cl(N)* Er	*cl(N)* Yb	*cl(N)* Y	*cl(N)* Lu
LH87-30											
LH86-64		194.92	143.11	85.81						43.95	
LH87-31											
LH86-63		296.72	200.44	116.89						31.85	
WP1		295.57	166.74	78.38							
LH86-7		285.25	157.99	74.32						45.86	
CL3		220.82	143.76	85.81						38.85	
RLI		255.74	162.36	84.46						28.03	
LY3		309.67	226.26	131.76						33.12	
GQ1											
SL2		201.15	152.08	93.92						36.31	
BS1											
WL1		312.79	259.30	145.27						32.48	
GQI		232.46	175.71	105.41						40.13	
BSI		283.77	199.56	117.57						46.50	
CL3											
LY3											
16RME-0280	361.39	344.41	296.76	180.98	99.34	121.08	74.44	59.46	46.98	57.17	43.64
16RME-0557A	64.43	57.46	37.35	18.03	11.03	8.95	4.43	2.94	2.45	3.54	2.13
16RME-0366	29.07	22.98	19.63	18.05	18.59	17.08	14.98	13.08	11.98	12.85	11.55
16RME-0376	122.03	120.75	101.23	63.25	44.19	41.30	29.48	25.51	23.23	25.01	22.59
16RME-0253	80.80	91.33	91.42	71.08	53.83	55.36	41.80	35.86	30.85	34.52	29.89
16RME-0389	103.50	100.03	83.98	52.34	37.40	34.39	24.20	21.33	19.44	21.33	18.51
16RME-0535	217.38	198.84	152.43	87.32	59.65	52.48	29.27	20.94	15.20	22.40	13.57
16RME-0237	424.85	397.08	297.13	152.60	95.80	75.45	35.61	25.69	21.17	27.75	20.19
15RME-0090	177.59	164.02	137.35	85.41	56.41	56.64	39.02	33.21	29.34	33.31	28.43
16RME-0529	119.79	94.97	69.67	45.77	30.06	28.27	17.24	13.33	11.59	14.10	10.37
16RME-0211	40.42	38.43	41.60	39.95	34.63	33.44	24.38	18.75	15.48	19.18	14.76
15RME-0359	68.19	63.80	46.59	37.70	28.17	35.14	33.00	30.31	27.57	29.98	26.78
MEW1	386.50	336.07	249.45	137.84	73.89	69.35	40.65	31.56	25.47	37.77	23.58
JJF1	502.11	396.72	251.64	133.78	58.61	68.34	42.28	35.38	28.82	41.85	27.24
JK02	361.60	306.56	231.95	132.43	80.82	69.85	42.68	32.44	24.78	39.75	22.76
MEW2	311.81	267.21	192.34	106.08	64.83	54.27	32.24	25.19	19.94	30.57	18.70
JT2	319.41	273.77	207.00	118.24	68.92	60.80	37.72	29.69	23.79	33.63	22.36
MP2	329.96	281.97	208.97	118.24	68.38	61.81	38.41	30.63	24.60	35.22	23.58
JK01	316.03	270.49	199.12	112.16	68.21	58.79	36.18	28.69	22.73	32.61	21.14
KC03	257.38	219.67	176.59	117.57	80.11	69.35	52.44	45.38	37.52	48.28	35.37
KC02	279.32	226.23	194.53	131.76	87.92	78.39	59.76	51.00	41.30	53.12	38.62
MP3	191.14	150.33	130.20	88.51	68.56	53.77	41.87	36.38	30.19	37.07	28.86
JT3	225.32	186.89	141.58	92.57	75.84	55.78	42.68	37.63	31.61	39.62	30.08
MP4	197.05	122.79	121.44	80.41	63.94	48.79	36.99	32.44	26.71	31.78	26.02
JT4	216.46	180.33	137.42	90.54	72.65	54.27	42.28	37.00	30.87	38.85	29.27
JK03	232.49	155.25	145.30	92.57	72.11	53.77	40.65	34.88	29.25	35.54	27.64
JJF2	209.28	175.41	134.57	87.16	71.94	50.75	38.70	33.50	29.13	34.52	27.24
JJF3	247.68	203.28	154.05	100.00	78.86	58.29	44.31	38.13	31.30	40.57	28.86
MEW3	201.27	180.33	138.51	93.92	77.62	55.28	43.50	37.88	31.68	39.75	29.27
EHW02	252.74	275.41	211.38	124.32	54.17	64.32	50.00	44.56	41.55	47.07	37.40

	cl(N)	*cl(N)*	*cl(N)*	*cl(N)*	*cl(N)*	*cl(N)*	*cl(N)*	*cl(N)*	*cl(N)*	*cl(N)*	*cl(N)*
Sample	**La**	**Ce**	**Nd**	**Sm**	**Eu**	**Gd**	**Dy**	**Er**	**Yb**	**Y**	**Lu**
KC01	350.21	334.43	229.76	132.43	57.55	68.84	52.85	46.13	42.36	48.22	38.62
JT1	357.81	342.62	229.76	122.97	56.84	58.79	40.08	33.63	32.55	33.69	29.67
MP1	434.60	418.03	275.71	144.59	62.17	68.84	46.75	39.19	35.09	38.28	32.52
LJT1	279.75	268.85	184.25	106.08	42.98	56.28	46.34	45.06	42.55	44.84	38.21
DH2	154.85	141.80	105.25	59.86	36.77	32.56	23.98	20.13	14.72	20.57	12.60
EHW01	227.85	221.31	171.77	102.70	45.47	54.77	40.24	35.56	31.18	37.07	27.64
DH1	147.68	127.70	84.46	50.41	27.71	27.69	21.67	20.00	18.82	20.89	17.48
LJT3	35.49	25.25	12.14	8.38	7.64	7.24	5.41	5.88	7.39	4.88	7.72
DH3	85.23	46.89	32.82	18.72	14.21	11.51	8.74	9.25	9.32	7.58	9.35
LJT2	50.21	37.21	19.37	12.57	10.30	9.80	5.28	4.00	3.73	4.52	3.25
86DM96											
93DM131											
89S3											
89S4											
89S1											
89S2											
89S5											
89S6											
89S7											
89S8											
89S9											

Appendix S4.3

Compiled geochemical and geochronological data from Frontenac Terrane metasedimentary rocks for Chapter 5

reported Sample Number	*reported* Source	*reported* Rock Name	*reported* UTM Zone	*reported* Lat(°N)	*reported* Long(°E)	*calc* Sample Details	*wt%* SiO_2	*wt%* TiO2	*wt%* Al_2O_3	*wt%* FeO	*wt%* Fe2O3
FA86-3	Cosca et al. 1991										
FA86-10	Cosca et al. 1991										
FA86-1	Cosca et al. 1992										
FA86-4	Cosca et al. 1992										
FA86-5	Cosca et al. 1992										
FA86-6	Cosca et al. 1992										
105	Currie & Ermanovics 1971	paragneiss	18	44.53107	-76.24918	Quartzofeldspathic	82.70	0.50	6.20	1.80	2.20
114	Currie & Ermanovics 1971	paragneiss	18	44.54744	-76.27036	Gnt/Crd Aluminious	64.70	1.00	15.20		6.70
125	Currie & Ermanovics 1971	paragneiss	18	44.55580	-76.30344	Cpx Aluminious	63.40	1.20	15.00	1.00	4.10
127	Currie & Ermanovics 1971	paragneiss	18	44.55191	-76.29926	Cpx Aluminious	65.00	1.20	14.00	3.70	1.20
128	Currie & Ermanovics 1971	paragneiss	18	44.55013	-76.29737	Gnt/Crd Aluminious	58.40	1.50	19.60	6.30	0.40
129	Currie & Ermanovics 1971	paragneiss	18	44.54859	-76.29571	Gnt/Crd Aluminious	58.00	1.00	18.00	5.00	2.30
131	Currie & Ermanovics 1971	paragneiss	18	44.54452	-76.29136	Gnt/Crd Aluminious	67.10	0.70	15.50	3.00	0.50
132	Currie & Ermanovics 1971	paragneiss	18	44.54309	-76.28976	Cpx Aluminious	57.70	1.10	18.30	4.70	1.80
133	Currie & Ermanovics 1971	paragneiss	18	44.54149	-76.28787	Cpx Aluminious	65.30	0.50	15.50	3.00	0.90
135	Currie & Ermanovics 1971	paragneiss	18	44.53840	-76.28421	Cpx Aluminious	56.00	2.50	17.00	5.50	1.90
137	Currie & Ermanovics 1971	paragneiss	18	44.53605	-76.28117	Cpx Aluminious	71.20	0.10	14.30		1.30
144	Currie & Ermanovics 1971	paragneiss	18	44.52495	-76.26784	Gnt/Crd Aluminious	63.00	1.20	16.40		7.10
148	Currie & Ermanovics 1971	paragneiss	18	44.51562	-76.25565	Quartzofeldspathic	84.00	0.60	7.00	1.70	1.80
155	Currie & Ermanovics 1971	paragneiss	18	44.51253	-76.29079	Gnt/Crd Aluminious	60.80	1.20	16.80	7.00	1.70
156	Currie & Ermanovics 1971	paragneiss	18	44.51018	-76.28884	Gnt/Crd Aluminious	59.40	1.20	16.80	7.00	2.80
161	Currie & Ermanovics 1971	paragneiss	18	44.50286	-76.28003	Quartzofeldspathic	88.00	0.60	7.00	1.10	0.90
173	Currie & Ermanovics 1971	paragneiss	18	44.52142	-76.30248	Gnt/Crd Aluminious	60.10	1.20	18.40	5.90	2.10
182	Currie & Ermanovics 1971	paragneiss	18	44.47853	-76.35054	Gnt/Crd Aluminious	62.50	1.20	17.00	4.00	2.70
183	Currie & Ermanovics 1971	paragneiss	18	44.47853	-76.34705	Cpx Aluminious	56.00	2.50	18.00	3.80	1.50
185	Currie & Ermanovics 1971	paragneiss	18	44.47864	-76.33978	Gnt/Crd Aluminious	64.00	1.20	15.00	3.70	1.50
186	Currie & Ermanovics 1971	paragneiss	18	44.47847	-76.33709	Gnt/Crd Aluminious	56.00	2.00	18.00	6.60	1.90
189	Currie & Ermanovics 1971	paragneiss	18	44.47653	-76.32559	Cpx Aluminious	58.00	1.20	18.50	3.50	1.70
190	Currie & Ermanovics 1971	paragneiss	18	44.47887	-76.32736	Quartzofeldspathic	83.50		3.00	0.30	0.40
194	Currie & Ermanovics 1971	paragneiss	18	44.54436	-76.32788	Gnt/Crd Aluminious	68.00	0.60	17.30	2.30	1.00
211	Currie & Ermanovics 1971	paragneiss	18	44.46772	-76.38129	Gnt/Crd Aluminious	70.00	0.10	18.00		0.40
212	Currie & Ermanovics 1971	paragneiss	18	44.46790	-76.37673	Cpx Aluminious	66.00	0.70	15.00	2.70	1.70
229	Currie & Ermanovics 1971	paragneiss	18	44.45422	-76.33803	Gnt/Crd Aluminious	61.50	1.30	17.90	7.00	1.70
61-021	Currie & Ermanovics 1971	paragneiss	18	44.49663	-76.43040	Gnt/Crd Aluminious	59.00	1.70	18.00	7.40	2.60
64-025	Currie & Ermanovics 1971	paragneiss	18	44.46136	-76.49265	Quartzofeldspathic	84.00	0.70	7.00	2.00	1.40
64-002	Currie & Ermanovics 1971	paragneiss	18	44.48981	-76.40241	Cpx Aluminious	66.00	0.60	15.00	3.00	0.50
64-003	Currie & Ermanovics 1971	paragneiss	18	44.48904	-76.39933	Cpx Aluminious	67.20	1.00	15.00		3.40
64-004	Currie & Ermanovics 1971	paragneiss	18	44.48831	-76.39640	Cpx Aluminious	71.00	0.20	14.00		1.60
64-007	Currie & Ermanovics 1971	paragneiss	18	44.48688	-76.39061	Cpx Aluminious	8.00	0.90	20.00	5.00	1.80
64-008	Currie & Ermanovics 1971	paragneiss	18	44.48798	-76.38768	Gnt/Crd Aluminious	63.00	0.70	18.00	4.00	1.00
64-010	Currie & Ermanovics 1971	paragneiss	18	44.48567	-76.38556	Gnt/Crd Aluminious	64.00	0.80	16.90	3.90	2.00
64-011	Currie & Ermanovics 1971	paragneiss	18	44.48520	-76.38332	Gnt/Crd Aluminious	65.60	0.80	14.00	4.00	2.40
64-012	Currie & Ermanovics 1971	paragneiss	18	44.48468	-76.38138	Gnt/Crd Aluminious	63.00	1.10	16.00	4.20	2.30
64-015	Currie & Ermanovics 1971	paragneiss	18	44.49146	-76.40919	Gnt/Crd Aluminious	75.00	0.30	12.00	2.10	0.50
64-020	Currie & Ermanovics 1971	paragneiss	18	44.49582	-76.42743	Gnt/Crd Aluminious	66.00	1.00	15.00	5.10	1.10
64-026	Currie & Ermanovics 1971	paragneiss	18	44.45990	-76.49279	Gnt/Crd Aluminious	65.00	0.70	15.50	2.90	1.90
64-027	Currie & Ermanovics 1971	paragneiss	18	44.45880	-76.49311	Gnt/Crd Aluminious	64.00	1.10	16.00	4.30	2.20

reported	*reported*	*reported*	*reported*	*reported*	*reported*	*calc*	*wt%*	*wt%*	*wt%*	*wt%*	*wt%*
Sample Number	**Source**	**Rock Name**	**UTM Zone**	**Lat(°N)**	**Long(°E)**	**Sample Details**	**SiO_2**	**TiO2**	**Al_2O_3**	**FeO**	**Fe2O3**
64-028	Currie & Ermanovics 1971	paragneiss	18	44.45896	-76.49225	Gnt/Crd Aluminious	66.00	1.50	17.00		2.40
64-029	Currie & Ermanovics 1971	paragneiss	18	44.45850	-76.49183	Cpx Aluminious	67.00	0.40	15.00	1.90	1.10
64-49	Currie & Ermanovics 1971	paragneiss	18	44.45386	-76.41505	Gnt/Crd Aluminious	70.00	0.70	16.00	3.00	0.40
64-53	Currie & Ermanovics 1971	paragneiss	18	44.45884	-76.43411	Cpx Aluminious	69.00	0.50	14.00		2.40
64-54	Currie & Ermanovics 1971	paragneiss	18	44.45993	-76.43823	Gnt/Crd Aluminious	71.80	0.80	12.50	2.90	1.20
64-55	Currie & Ermanovics 1971	paragneiss	18	44.45821	-76.44332	Gnt/Crd Aluminious	57.00	0.80	21.00	6.00	1.10
64-56	Currie & Ermanovics 1971	paragneiss	18	44.46061	-76.44338	Quartzofeldspathic	78.00	0.30	12.00	1.00	0.40
64-57	Currie & Ermanovics 1971	paragneiss	18	44.46382	-76.44767	Gnt/Crd Aluminious	59.50	1.30	18.80	5.50	1.00
64-65	Currie & Ermanovics 1971	paragneiss	18	44.48299	-76.45105	Gnt/Crd Aluminious	64.90	0.80	16.30		4.80
FJ46	Dickin & Strong 2021	Quartzo-felspathic gneiss		44.84574	-76.48610	Quartzofeldspathic					
FJ45	Dickin & Strong 2021	Quartzo-felspathic gneiss		44.72193	-76.67606	Quartzofeldspathic					
FJ25	Dickin & Strong 2021	Quartzo-felspathic gneiss		44.78862	-76.62956	Quartzofeldspathic					
FJ26	Dickin & Strong 2021	Quartzo-felspathic gneiss		44.76284	-76.61399	Quartzofeldspathic					
FJ9	Dickin & Strong 2021	Quartzo-felspathic gneiss		44.73938	-76.56832	Quartzofeldspathic					
FJ12	Dickin & Strong 2021	Quartzo-felspathic gneiss		44.72797	-76.48289	Quartzofeldspathic					
FJ44	Dickin & Strong 2021	Quartzo-felspathic gneiss		44.65644	-76.65446	Quartzofeldspathic					
FJ67	Dickin & Strong 2021	Quartzo-felspathic gneiss		44.60557	-76.64225	Quartzofeldspathic					
FJ2	Dickin & Strong 2021	Quartzo-felspathic gneiss		44.52017	-76.64555	Quartzofeldspathic					
FJ60	Dickin & Strong 2021	Quartzo-felspathic gneiss		44.50994	-76.66706	Quartzofeldspathic					
FJ22	Dickin & Strong 2021	Quartzo-felspathic gneiss		44.80629	-76.40725	Quartzofeldspathic					
FJ8	Dickin & Strong 2021	Quartzo-felspathic gneiss		44.72979	-76.64589	Quartzofeldspathic					
FJ78	Dickin & Strong 2021	Quartzo-felspathic gneiss		44.73311	-76.62579	Quartzofeldspathic					
FJ7	Dickin & Strong 2021	Quartzo-felspathic gneiss		44.68159	-76.67231	Quartzofeldspathic					
FJ63	Dickin & Strong 2021	Quartzo-felspathic gneiss		44.58278	-76.67059	Quartzofeldspathic					
FJ64	Dickin & Strong 2021	Quartzo-felspathic gneiss		44.58577	-76.64943	Quartzofeldspathic					
FJ4	Dickin & Strong 2021	Quartzo-felspathic gneiss		44.56761	-76.66844	Quartzofeldspathic					
FJ3	Dickin & Strong 2021	Quartzo-felspathic gneiss		44.56438	-76.66840	Quartzofeldspathic					
FJ97	Dickin & Strong 2021	Quartzo-felspathic gneiss		44.53293	-76.69223	Quartzofeldspathic					
FJ21	Dickin & Strong 2021	Quartzo-felspathic gneiss		44.89649	-76.29102	Quartzofeldspathic					
R7085	Dickin & Strong 2021	Quartzo-felspathic gneiss		44.89649	-76.29102	Quartzofeldspathic					
R7083	Dickin & Strong 2021	Quartzo-felspathic gneiss		44.89649	-76.29102	Quartzofeldspathic					
R7070	Dickin & Strong 2021	Quartzo-felspathic gneiss		44.89649	-76.29102	Quartzofeldspathic					
R7090	Dickin & Strong 2021	Quartzo-felspathic gneiss		44.89649	-76.29102	Quartzofeldspathic					
R7113	Dickin & Strong 2021	Quartzo-felspathic gneiss		44.89649	-76.29102	Quartzofeldspathic					
R7062	Dickin & Strong 2021	Quartzo-felspathic gneiss		44.89649	-76.29102	Quartzofeldspathic					
R7061	Dickin & Strong 2021	Quartzo-felspathic gneiss		44.89649	-76.29102	Quartzofeldspathic					
R7112	Dickin & Strong 2021	Quartzo-felspathic gneiss		44.89649	-76.29102	Quartzofeldspathic					
R7071	Dickin & Strong 2021	Quartzo-felspathic gneiss		44.89649	-76.29102	Quartzofeldspathic					
FA1	Marcantonio et al. 1990		18			Gnt/Crd Aluminious	62.10	1.10	15.50	8.10	0.90
FA2	Marcantonio et al. 1990		18			Cpx Aluminious	66.50	0.70	13.40	5.60	0.60
FA3	Marcantonio et al. 1990		18			Cpx Aluminious	74.90	0.50	11.30	2.20	0.20
.1-3	Marcantonio et al. 1990		18			Cpx Aluminious	57.50	1.00	17.00	9.50	1.10
.1-5	Marcantonio et al. 1990		18			Gnt/Crd Aluminious	59.30	1.50	20.10	9.50	1.10
.1-7	Marcantonio et al. 1990		18			Gnt/Crd Aluminious	60.10	1.40	18.90	8.70	1.00
.2-0	Marcantonio et al. 1990		18			Gnt/Crd Aluminious	58.00	1.00	16.40	3.90	0.40
.2-1	Marcantonio et al. 1990		18			Cpx Aluminious	59.70	0.70	10.40	3.90	0.40
WP2	Marcantonio et al. 1990		18			Gnt/Crd Aluminious	62.20	0.70	15.30	7.10	0.80

reported	*reported*	*reported*	*reported*	*reported*	*reported*	*calc*	*wt%*	*wt%*	*wt%*	*wt%*	*wt%*
Sample Number	**Source**	**Rock Name**	**UTM Zone**	**Lat(°N)**	**Long(°E)**	**Sample Details**	**SiO_2**	**TiO2**	**Al_2O_3**	**FeO**	**Fe2O3**
WP3	Marcantonio et al. 1990		18			Cpx Aluminious	73.90	0.40	11.40	2.50	0.30
89-20	Mezger et al., 1993			44.78339	76.15386						
1157	MRD251	paragneiss	18	44.74751	-76.28031	Carbonate	0.26	0.02	0.11		0.15
1170	MRD251	paragneiss	18	44.74416	-76.41223	Carbonate	4.54	0.03	0.73		0.81
1171	MRD251	paragneiss	18	44.74489	-76.42552	Carbonate	2.48	0.02	0.64		0.60
1173	MRD251	paragneiss	18	44.75387	-76.19163	Carbonate	4.60	0.01	1.15		0.80
1174	MRD251	paragneiss	18	44.76822	-76.19736	Carbonate	7.67	0.22	3.04		1.96
1175	MRD251	paragneiss	18	44.76783	-76.18231	Carbonate	16.20	0.36	5.00		2.83
1176	MRD251	paragneiss	18	44.76109	-76.17270	Carbonate	0.60	0.01	0.25		0.09
1177	MRD251	paragneiss	18	44.77691	-76.18351	Carbonate	9.76	0.02	2.96		0.95
1178	MRD251	paragneiss	18	44.77518	-76.20281	Carbonate	12.20	0.10	1.25		1.37
1179	MRD251	paragneiss	18	44.78214	-76.19992	Carbonate	5.13	0.21	1.67		2.65
1180	MRD251	paragneiss	18	44.79601	-76.18188	Carbonate	3.87	0.01	0.45		0.24
1181	MRD251	paragneiss	18	44.79376	-76.16464	Carbonate	12.80	0.01	0.48		1.45
1182	MRD251	paragneiss	18	44.77788	-76.16786	Carbonate	0.86	0.01	0.51		0.56
1183	MRD251	paragneiss	18	44.78517	-76.15031	Carbonate	0.22	0.01	0.24		0.77
1184	MRD251	paragneiss	18	44.78862	-76.13900	Carbonate	0.69	0.01	0.21		0.02
1185	MRD251	paragneiss	18	44.78249	-76.14014	Carbonate	2.22	0.01	0.43		0.22
1186	MRD251	paragneiss	18	44.77067	-76.11463	Carbonate	20.00	0.08	1.38		0.83
1187	MRD251	paragneiss	18	44.76055	-76.11937	Carbonate	20.00	0.08	0.58		1.14
1188	MRD251	paragneiss	18	44.75572	-76.13393	Carbonate	2.69	0.02	1.00		0.83
1189	MRD251	paragneiss	18	44.75804	-76.14471	Carbonate	11.10	0.15	2.43		1.55
1190	MRD251	paragneiss	18	44.76533	-76.15396	Carbonate	20.00	0.02	1.07		0.17
1191	MRD251	paragneiss	18	44.76774	-76.13871	Carbonate	16.00	0.12	2.37		1.77
1192	MRD251	paragneiss	18	44.77338	-76.13238	Carbonate	20.00	0.01	0.51		0.10
1193	MRD251	paragneiss	18	44.88574	-76.31566	Carbonate	20.00	0.16	5.00		2.65
1194	MRD251	paragneiss	18	44.81327	-76.32425	Carbonate	5.70	0.11	1.38		2.45
1195	MRD251	paragneiss	18	44.80618	-76.33004	Carbonate	7.38	0.02	1.11		1.57
1196	MRD251	paragneiss	18	44.86303	-76.24628	Carbonate	1.81	0.03	1.35		2.20
1197	MRD251	paragneiss	18	44.87430	-76.20272	Carbonate	20.00	0.13	2.43		0.43
1198	MRD251	paragneiss	18	44.87282	-76.20649	Carbonate	4.48	0.04	0.70		0.90
1199	MRD251	paragneiss	18	44.86096	-76.19548	Carbonate	3.41	0.01	1.13		1.57
1200	MRD251	paragneiss	18	44.76526	-76.18782	Carbonate	4.38	0.01	1.46		2.04
1201	MRD251	paragneiss	18	44.85486	-76.17637	Carbonate	3.90	0.08	1.50		0.45
1202	MRD251	paragneiss	18	44.85457	-76.16029	Carbonate	4.55	0.03	0.73		0.60
1203	MRD251	paragneiss	18	44.83415	-76.20201	Carbonate	3.08	0.01	1.40		1.95
1204	MRD251	paragneiss	18	44.81370	-76.19514	Carbonate	6.76	0.09	0.85		1.15
1205	MRD251	paragneiss	18	44.82220	-76.20037	Carbonate	8.62	0.01	0.13		1.21
1206	MRD251	paragneiss	18	44.83444	-76.22593	Carbonate	0.14	0.01	0.18		0.01
1207	MRD251	paragneiss	18	44.82932	-76.21684	Carbonate	3.90	0.01	0.27		0.07
1208	MRD251	paragneiss	18	44.82300	-76.22683	Carbonate	1.77	0.01	0.40		0.07
1209	MRD251	paragneiss	18	44.81239	-76.23419	Carbonate	3.21	0.02	0.73		0.46
1210	MRD251	paragneiss	18	44.85075	-76.24108	Carbonate	0.91	0.01	0.17		0.01
1211	MRD251	paragneiss	18	44.85810	-76.22770	Carbonate	0.01	0.01	0.10		0.02
1212	MRD251	paragneiss	18	44.85046	-76.22640	Carbonate	0.61	0.01	0.13		0.01
1213	MRD251	paragneiss	18	44.84329	-76.23207	Carbonate	4.07	0.01	0.39		0.29
1214	MRD251	paragneiss	18	44.82280	-76.26110	Carbonate	12.70	0.04	1.95		2.10

reported	*reported*	*reported*	*reported*	*reported*	*reported*	*calc*	*wt%*	*wt%*	*wt%*	*wt%*	*wt%*
Sample Number	**Source**	**Rock Name**	**UTM Zone**	**Lat(°N)**	**Long(°E)**	**Sample Details**	**SiO_2**	**TiO2**	**Al_2O_3**	**FeO**	**Fe2O3**
1215	MRD251	paragneiss	18	44.82665	-76.27130	Carbonate	20.00	0.25	5.00		4.48
1216	MRD251	paragneiss	18	44.77895	-76.28669	Carbonate	13.80	0.02	0.57		0.91
1217	MRD251	paragneiss	18	44.77008	-76.29066	Carbonate	2.28	0.05	0.69		0.83
1218	MRD251	paragneiss	18	44.75048	-76.28884	Carbonate	6.79	0.10	1.53		1.65
1219	MRD251	paragneiss	18	44.75877	-76.28814	Carbonate	0.37	0.01	0.11		0.01
1220	MRD251	paragneiss	18	44.76539	-76.28361	Carbonate	2.17	0.01	0.35		0.18
1221	MRD251	paragneiss	18	44.76469	-76.27386	Carbonate	7.98	0.03	1.58		1.39
1222	MRD251	paragneiss	18	44.76535	-76.25492	Carbonate	8.20	0.01	0.89		0.17
1223	MRD251	paragneiss	18	44.76861	-76.24438	Carbonate	6.45	0.03	1.36		1.79
1224	MRD251	paragneiss	18	44.77984	-76.23880	Carbonate	7.53	0.10	1.42		0.96
1225	MRD251	paragneiss	18	44.77848	-76.22247	Carbonate	3.15	0.04	0.52		0.86
1226	MRD251	paragneiss	18	44.78507	-76.22109	Carbonate	3.24	0.07	0.85		0.99
1227	MRD251	paragneiss	18	44.75017	-76.32382	Carbonate	5.17	0.01	0.28		0.25
1228	MRD251	paragneiss	18	44.80287	-76.32010	Carbonate	20.00	0.90	5.00		3.69
1229	MRD251	paragneiss	18	44.74871	-76.40767	Carbonate	10.60	0.06	0.91		1.32
1230	MRD251	paragneiss	18	44.74901	-76.42701	Carbonate	0.19	0.01	0.12		0.40
1231	MRD251	paragneiss	18	44.75167	-76.41646	Carbonate	20.00	0.07	2.25		0.14
1232	MRD251	paragneiss	18	44.75700	-76.38551	Carbonate	0.73	0.01	0.19		0.97
1233	MRD251	paragneiss	18	44.76126	-76.37538	Carbonate	1.31	0.02	0.51		1.10
1234	MRD251	paragneiss	18	44.76775	-76.36732	Carbonate	1.98	0.02	0.43		0.44
1235	MRD251	paragneiss	18	44.77633	-76.35766	Carbonate	20.00	0.21	3.06		3.68
1236	MRD251	paragneiss	18	44.78583	-76.34562	Carbonate	4.78	0.01	0.49		1.36
1237	MRD251	paragneiss	18	44.79725	-76.33868	Carbonate	2.89	0.01	0.63		1.21
1238	MRD251	paragneiss	18	44.81643	-76.42804	Carbonate	1.51	0.01	0.24		0.11
1239	MRD251	paragneiss	18	44.81602	-76.43928	Carbonate	2.53	0.03	0.55		0.26
1240	MRD251	paragneiss	18	44.85119	-76.44864	Carbonate	7.39	0.08	1.13		1.21
1241	MRD251	paragneiss	18	44.84866	-76.46313	Carbonate	0.53	0.01	0.17		0.11
1242	MRD251	paragneiss	18	44.84726	-76.47435	Carbonate	9.27	0.09	1.98		1.22
1243	MRD251	paragneiss	18	44.83591	-76.47444	Carbonate	6.99	0.06	0.69		1.02
1244	MRD251	paragneiss	18	44.84062	-76.46520	Carbonate	11.60	0.14	2.52		2.56
1246	MRD251	paragneiss	18	44.78328	-76.44416	Carbonate	1.37	0.01	0.35		0.10
1247	MRD251	paragneiss	18	44.79058	-76.43574	Carbonate	1.97	0.01	0.27		0.18
1248	MRD251	paragneiss	18	44.83734	-76.41843	Carbonate	1.10	0.02	0.38		0.14
1249	MRD251	paragneiss	18	44.83934	-76.43164	Carbonate	0.29	0.01	0.14		0.01
1250	MRD251	paragneiss	18	44.83153	-76.44397	Carbonate	0.52	0.01	0.15		0.12
1251	MRD251	paragneiss	18	44.84365	-76.45389	Carbonate	5.59	0.09	1.24		1.12
1252	MRD251	paragneiss	18	44.84729	-76.44348	Carbonate	0.68	0.01	0.16		0.09
1257	MRD251	paragneiss	18	44.77538	-76.49780	Carbonate	3.12	0.05	0.67		0.61
1258	MRD251	paragneiss	18	44.77814	-76.48688	Carbonate	3.14	0.05	0.60		0.79
1259	MRD251	paragneiss	18	44.77394	-76.47742	Carbonate	0.83	0.00	0.18		0.13
1276	MRD251	paragneiss	18	44.76381	-76.49485	Carbonate	2.70	0.00	0.19		0.13
1277	MRD251	paragneiss	18	44.76817	-76.49875	Carbonate	0.80	0.00	0.14		0.04
1278	MRD251	paragneiss	18	44.77019	-76.48869	Carbonate	0.60	0.00	0.14		0.07
1279	MRD251	paragneiss	18	44.76994	-76.50764	Carbonate	0.70	0.00	0.34		0.06
1284	MRD251	paragneiss	18	44.75410	-76.51418	Carbonate	1.73	0.01	0.26		0.13
1285	MRD251	paragneiss	18	44.75786	-76.50227	Carbonate	2.23	0.00	0.28		0.16
15RME-0247	MRD351	gneiss	18	44.89503	-76.32403	Gnt/Crd Aluminious	62.01	0.95	15.60	4.21	2.12

reported	*reported*	*reported*	*reported*	*reported*	*reported*	*calc*	*wt%*	*wt%*	*wt%*	*wt%*	*wt%*
Sample Number	**Source**	**Rock Name**	**UTM Zone**	**Lat(°N)**	**Long(°E)**	**Sample Details**	**SiO_2**	**TiO2**	**Al_2O_3**	**FeO**	**Fe2O3**
15RME-0403	MRD351	paragneiss	18	44.75486	-76.28705	Mafic Schist	51.41	2.03	17.71	5.38	2.47
15RME-0411	MRD351	paragneiss	18	44.76724	-76.27042	Cpx Aluminious	65.67	0.63	11.99	2.73	0.05
15RME-0420	MRD351	paragneiss	18	44.77235	-76.28654	Gnt/Crd Aluminious	57.17	1.49	20.76	7.12	1.50
15RME-0452	MRD351	paragneiss	18	44.83570	-76.32901	Cpx Aluminious	60.32	0.73	15.17	2.08	0.58
16RME-0208	MRD351	paragneiss	18	44.79717	-76.25971	Cpx Aluminious	66.60	1.04	10.33	2.77	2.73
16RME-0214	MRD351	paragneiss	18	44.79571	-76.25140	Gnt/Crd Aluminious	57.09	1.57	21.07	6.46	0.97
16RME-0222	MRD351	paragneiss	18	44.79717	-76.23429	Quartzofeldspathic	73.40	0.98	9.90	3.61	2.79
16RME-0225	MRD351	paragneiss	18	44.77692	-76.28477	Cpx Aluminious	61.57	1.16	13.17	3.65	1.46
16RME-0227	MRD351	paragneiss	18	44.77733	-76.28453	Cpx Aluminious	64.26	0.36	16.25	1.97	1.04
16RME-0230	MRD351	paragneiss	18	44.77975	-76.28388	Cpx Aluminious	61.21	0.90	15.02	2.49	0.82
16RME-0231	MRD351	paragneiss	18	44.77975	-76.28388	Gnt/Crd Aluminious	55.38	1.04	17.56	6.97	1.28
16RME-0236	MRD351	paragneiss	18	44.79172	-76.27539	Gnt/Crd Aluminious	71.25	0.08	13.93	0.34	1.34
16RME-0265	MRD351	paragneiss	18	44.78904	-76.44018	Cpx Aluminious	52.72	0.68	11.30	3.93	1.59
16RME-0358	MRD351	paragneiss	18	44.77867	-76.35708	Gnt/Crd Aluminious	66.32	1.25	16.97	0.83	0.62
16RME-0360	MRD351	paragneiss	18	44.77828	-76.35754	Gnt/Crd Aluminious	69.03	1.11	14.43	1.47	0.60
16RME-0362	MRD351	paragneiss	18	44.77810	-76.35745	Quartzofeldspathic	86.55	0.22	3.51	1.00	0.60
16RME-0371	MRD351	paragneiss	18	44.76820	-76.36825	Gnt/Crd Aluminious	61.10	1.37	15.76	5.25	1.05
16RME-0390	MRD351	paragneiss	18	44.75388	-76.38970	Quartzofeldspathic	76.18	0.51	7.83	1.54	1.42
16RME-0391	MRD351	paragneiss	18	44.75352	-76.38982	Cpx Aluminious	68.19	0.48	12.42	2.47	1.59
16RME-0396	MRD351	paragneiss	18	44.75032	-76.39019	Cpx Aluminious	56.40	0.84	14.14	3.51	0.45
16RME-0456	MRD351	paragneiss	18	44.83574	-76.25363	Gnt/Crd Aluminious	57.66	1.55	20.46	7.38	1.09
16RME-0558	MRD351	paragneiss	18	44.78617	-76.23555	Gnt/Crd Aluminious	62.71	1.55	17.09	5.63	0.72
16RME-0571	MRD351	paragneiss	18	44.79676	-76.22788	Gnt/Crd Aluminious	60.94	1.19	16.97	7.90	0.65
15RME-0092	MRD351	paragneiss	18	44.98970	-76.34450	Quartzofeldspathic	76.70	0.21	12.31	0.33	1.27
94RME-0016	MRD351	paragneiss	18	44.71688	-76.22009	Quartzite	95.08	0.07	2.63	0.19	0.07
15RME-0396	MRD351	paragneiss	18	44.80759	-76.22369	Quartzite	92.72	0.17	2.24	0.43	0.23
16RME-0394	MRD351	paragneiss	18	44.75406	-76.38936	Gnt/Crd Aluminious	72.00	0.14	15.85	0.55	0.54
16RME-0491	MRD351	paragneiss	18	44.83824	-76.24741	Quartzite	95.50	0.30	1.87	0.45	1.02
15RME-0233	MRD351	paragneiss	18	44.76399	-76.11852	Carbonate	3.75	0.04	0.91	0.68	0.02
15RME-0234	MRD351	paragneiss	18	44.76131	-76.12017	Carbonate	0.60	0.01	0.30	0.28	nc
15RME-0331	MRD351	paragneiss	18	44.85062	-76.46201	Carbonate	4.84	0.07	1.05	0.70	0.01
15RME-0335	MRD351	paragneiss	18	44.85157	-76.45437	Carbonate	1.54	0.02	0.44	0.20	0.01
15RME-0350	MRD351	paragneiss	18	44.83729	-76.43805	Carbonate	1.57	0.01	0.28	0.19	nc
15RME-0351	MRD351	paragneiss	18	44.83828	-76.43591	Carbonate	1.73	0.02	0.38	0.30	nc
15RME-0366	MRD351	paragneiss	18	44.84238	-76.42596	Carbonate	1.64	0.01	0.24	0.14	nc
15RME-0402	MRD351	paragneiss	18	44.75503	-76.28712	Carbonate	3.25	0.02	0.30	0.16	nc
15RME-0410	MRD351	paragneiss	18	44.76755	-76.26893	Carbonate	6.96	0.07	1.06	0.86	nc
16RME-0108	MRD351	paragneiss	18	44.79993	-76.17427	Carbonate	0.04	0.01	0.09	0.18	0.05
16RME-0115	MRD351	paragneiss	18	44.79707	-76.18535	Carbonate	1.33	0.01	0.43	0.52	nc
16RME-0153	MRD351	paragneiss	18	44.75991	-76.13787	Carbonate	0.50	0.01	0.59	0.36	nc
16RME-0212	MRD351	paragneiss	18	44.79566	-76.25242	Carbonate	14.23	0.08	2.81	0.78	0.25
16RME-0264	MRD351	paragneiss	18	44.78907	-76.44018	Carbonate	1.99	0.01	0.46	0.24	nc
16RME-0297	MRD351	paragneiss	18	44.77947	-76.48557	Carbonate	0.95	0.01	0.31	0.34	nc
16RME-0298	MRD351	paragneiss	18	44.77963	-76.48584	Carbonate	1.37	0.01	0.34	0.23	nc
16RME-0335	MRD351	paragneiss	18	44.81801	-76.43928	Carbonate	0.75	0.01	0.35	0.17	nc
16RME-0433	MRD351	paragneiss	18	44.87364	-76.20758	Carbonate	6.70	0.01	0.58	0.30	0.00
16RME-0557B	MRD351	paragneiss	18	44.78553	-76.23580	Carbonate	4.69	0.01	0.47	0.30	nc

reported	*reported*	*reported*	*reported*	*reported*	*reported*	*calc*	*wt%*	*wt%*	*wt%*	*wt%*	*wt%*
Sample Number	**Source**	**Rock Name**	**UTM Zone**	**Lat(°N)**	**Long(°E)**	**Sample Details**	**SiO_2**	**TiO2**	**Al_2O_3**	**FeO**	**Fe2O3**
16RME-0560	MRD351	paragneiss	18	44.78895	-76.23179	Carbonate	4.18	0.02	0.47	0.41	0.03
16RME-0573A	MRD351	paragneiss	18	44.79523	-76.22769	Carbonate	2.75	0.01	0.46	0.39	0.03
16RME-0591	MRD351	paragneiss	18	44.76072	-76.14086	Carbonate	0.59	0.01	0.23	0.28	nc
AKR21	Peck and Lin, 2024	Pelite		44.31700	-76.19520	Gnt/Crd Aluminious					
MP6A	Peck and Lin, 2024	Pelite		44.49370	-76.06200	Gnt/Crd Aluminious					
96TE17	Peck and Lin, 2024	Marble		44.54510	-76.65570	Carbonate					
09PH01B	Peck et al. 2022	Marble		44.77620	-76.49500	Carbonate					
09PH04	Peck et al. 2022	Marble		44.78480	-76.44340	Carbonate					
09PH05	Peck et al. 2022	Marble		44.84240	-76.42560	Carbonate					
09PH10	Peck et al. 2022	Marble		44.79690	-76.16400	Carbonate					
09PH18	Peck et al. 2022	Marble		44.77620	-76.49500	Carbonate					
09TE09	Peck et al. 2022	Marble		44.84760	-76.47290	Carbonate					
09TE21	Peck et al. 2022	Marble		44.53530	-76.58100	Carbonate					
09WE12	Peck et al. 2022	Marble		44.54840	-76.22060	Carbonate					
09WE17	Peck et al. 2022	Marble		44.50740	-76.40300	Carbonate					
96GE02	Peck et al. 2022	Marble		44.45960	-76.32360	Carbonate					
96GE09	Peck et al. 2022	Marble		44.46940	-76.19180	Carbonate					
96GE20	Peck et al. 2022	Marble		44.38440	-76.45700	Carbonate					
96GE22	Peck et al. 2022	Marble		44.37500	-76.39580	Carbonate					
96GE24	Peck et al. 2022	Marble		44.46200	-76.29350	Carbonate					
96GE27	Peck et al. 2022	Marble		44.57350	-76.33750	Carbonate					
96GE30	Peck et al. 2022	Marble		44.55450	-76.35000	Carbonate					
96PH04	Peck et al. 2022	Marble		44.79040	-76.43940	Carbonate					
96PH06	Peck et al. 2022	Marble		44.85650	-76.16090	Carbonate					
96PH07	Peck et al. 2022	Marble		44.81510	-76.32340	Carbonate					
96TE15	Peck et al. 2022	Marble		44.53890	-76.68170	Carbonate					
96TE23	Peck et al. 2022	Marble		44.63880	-76.55120	Carbonate					
96TE25	Peck et al. 2022	Marble		44.65670	-76.54220	Carbonate					
96TE26	Peck et al. 2022	Marble		44.65620	-76.56080	Carbonate					
96WT03	Peck et al. 2022	Marble		44.50410	-76.11520	Carbonate					
96WT04	Peck et al. 2022	Marble		44.50410	-76.11520	Carbonate					
96WT15	Peck et al. 2022	Marble		44.71650	-76.17390	Carbonate					
96WT27	Peck et al. 2022	Marble		44.57360	-76.33710	Carbonate					
809-2A	Shieh 1985	Marble				Quartzofeldspathic					
809-2B	Shieh 1985	Marble				Quartzofeldspathic					
809-3	Shieh 1985	Marble				Quartzofeldspathic					
809-8	Shieh 1985	Marble				Quartzofeldspathic					
809-9	Shieh 1985	Marble				Quartzofeldspathic					
809-12	Shieh 1985	Marble				Quartzofeldspathic					
809-15A	Shieh 1985	Marble				Quartzofeldspathic					
809-15B	Shieh 1985	Marble				Quartzofeldspathic					
809-20	Shieh 1985	Marble				Quartzofeldspathic					
811-7	Shieh 1985	Marble				Quartzofeldspathic					
811-11	Shieh 1985	Marble				Quartzofeldspathic					
811-12	Shieh 1985	Marble				Quartzofeldspathic					
811-14A	Shieh 1985	Marble				Quartzofeldspathic					
811-14B	Shieh 1985	Marble				Quartzofeldspathic					

reported Sample Number	*reported* Source	*reported* Rock Name	*reported* UTM Zone	*reported* Lat(°N)	*reported* Long(°E)	*calc* Sample Details	*wt%* SiO_2	*wt%* TiO2	*wt%* Al_2O_3	*wt%* FeO	*wt%* Fe2O3
811-23	Shieh 1985	Marble				Quartzofeldspathic					
811-2	Shieh 1985	Marble				Quartzofeldspathic					
812-11	Shieh 1985	Marble				Quartzofeldspathic					
812-12	Shieh 1985	Marble				Quartzofeldspathic					
FA6	Shieh 1985	Marble				Quartzofeldspathic					
FA7	Shieh 1985	Diopside Gneiss				Cpx Aluminious					
802-7	Shieh 1985	Marble				Carbonate					
808-5	Shieh 1985	Marble				Carbonate					
811-13	Shieh 1985	Marble				Carbonate					
811-16	Shieh 1985	Marble				Carbonate					
811-21	Shieh 1985	Marble				Carbonate					
303	Shieh 1985	Marble				Carbonate					
3011	Shieh 1985	Marble				Carbonate					
20CK06B	This Study	paragneiss	18	44.54161	-76.25864	Gnt/Crd Aluminious	57.56	1.00	16.46	6.70	2.81
20CK46A	This Study	paragneiss	18	44.47804	-76.34762	Mafic Schist	48.20	2.59	14.94	5.80	5.94
21CK76B	This Study	paragneiss	18	44.54183	-76.13683	Mafic Schist	51.58	2.54	13.51	6.90	5.06
20CK14A	This Study	paragneiss	18	44.54864	-76.32831	Cpx Aluminious	58.88	0.69	12.94	3.10	1.51
20CK52A	This Study	paragneiss	18	44.45083	-76.37399	Cpx Aluminious	60.13	0.84	12.47	2.70	1.43
20CK25A1	This Study	paragneiss	18	44.52208	-76.28885	Cpx Aluminious	61.31	0.89	14.79	3.30	2.81
21CK43C	This Study	paragneiss	18	44.49996	-76.06688	Quartzofeldspathic	59.96	0.86	9.83		
21CK43B	This Study	paragneiss	18	44.49996	-76.06688	Gnt/Crd Aluminious	62.55	0.97	15.51	1.70	4.91
20CK61A	This Study	paragneiss	18	44.58514	-76.30745	Gnt/Crd Aluminious	54.61	1.04	17.93	7.70	1.55
20CK85B	This Study	paragneiss	18	44.45295	-76.26697	Gnt/Crd Aluminious	58.57	1.35	17.70	1.70	7.47
20CK16A	This Study	paragneiss	18	44.55904	-76.30444	Gnt/Crd Aluminious	67.17	1.00	12.75	2.20	4.21
21CK44A	This Study	paragneiss	18	44.49367	-76.06210	Gnt/Crd Aluminious	55.34	1.39	19.31	8.00	1.24
21CK46A	This Study	paragneiss	18	44.48121	-76.04582	Gnt/Crd Aluminious	54.05	1.45	18.82	8.30	4.18
21CK45A	This Study	paragneiss	18	44.48925	-76.05468	Gnt/Crd Aluminious	62.72	1.36	16.72	5.90	2.60
20CK92B	This Study	paragneiss	18	44.55275	-76.23819	Cpx Aluminious	53.79	0.54	11.31	4.20	1.09
20CK28A1	This Study	paragneiss	18	44.42385	-76.47179	Cpx Aluminious	55.80	0.78	12.13	2.10	3.49
20CK68B	This Study	paragneiss	18	44.49610	-76.41757	Quartzite	93.88	0.15	2.16	0.80	0.34
21CK36A	This Study	paragneiss	18	44.46737	-76.08256	Gnt/Crd Aluminious	60.14	0.93	16.38	4.70	3.07
21CK33A	This Study	paragneiss	18	44.45131	-76.08068	Gnt/Crd Aluminious	57.15	1.59	19.86	8.20	3.98
H-29	Wynne-Edwards, 1960	paragneiss	18			Gnt/Crd Aluminious	62.88	1.15	17.57	6.14	0.59
H-60	Wynne-Edwards, 1960	paragneiss	18			Gnt/Crd Aluminious	58.36	1.11	20.43	4.17	2.50
H-66	Wynne-Edwards, 1960	paragneiss	18			Gnt/Crd Aluminious	59.09	1.20	19.10	6.29	0.43
H-70	Wynne-Edwards, 1960	paragneiss	18			Gnt/Crd Aluminious	61.59	1.32	18.70	4.92	2.78
H-90	Wynne-Edwards, 1960	paragneiss	18			Gnt/Crd Aluminious	59.05	1.05	18.63	5.15	2.64
H-105	Wynne-Edwards, 1960	paragneiss	18			Gnt/Crd Aluminious	64.89	0.91	15.70	4.40	2.01
H-126	Wynne-Edwards, 1960	paragneiss	18			Gnt/Crd Aluminious	62.82	1.00	17.70	6.67	0.55
WE-4-58	Wynne-Edwards, 1960	paragneiss	18			Gnt/Crd Aluminious	63.29	1.18	17.90	6.94	1.41
WE-10-57	Wynne-Edwards, 1960	paragneiss	18			Gnt/Crd Aluminious	53.36	1.25	20.10	8.00	4.12
WE-17-57	Wynne-Edwards, 1960	paragneiss	18			Gnt/Crd Aluminious	65.01	0.98	14.70	2.28	3.94

reported	*wt%*	*wt%*	*wt%*	*wt%*	*wt%*	*wt%*	*wt%*	*wt%*	*wt%*	*wt%*	*wt%*	*wt%*	*wt%*	*wt%*	*mol%*	*mol%*	*mol%*
Sample Number	**MnO**	**MgO**	**CaO**	**Na_2O**	**K_2O**	**P_2O_5**	**CO_2**	**S**	**BaO**	**Cr_2O_3**	**Nitrogen 105°C**	**LOI**	**Total**	**$Fe_2O_{3(t)}$**	**SiO_2**	**TiO2**	**Al_2O_3**
FA86-3																	
FA86-10																	
FA86-1																	
FA86-4																	
FA86-5																	
FA86-6																	
105	0.01	0.90	0.50	0.90	3.00							1.10	99.80		88.2	0.4	3.9
114	0.04	1.40	2.60	2.60	4.60							1.20	100.00		74.1	0.9	10.3
125	0.04	1.80	2.70	3.50	6.70							1.00	100.40		71.4	1.0	10.0
127	0.02	3.60	4.40	3.60	2.40							0.90	100.00		70.0	1.0	8.9
128	0.06	3.20	1.40	1.30	5.50							1.20	98.90		66.7	1.3	13.2
129	0.17	3.20	2.00	2.40	6.00							1.20	99.30		66.2	0.9	12.1
131	0.06	2.10	1.30	2.10	6.70							0.90	100.00		74.3	0.6	10.1
132	0.04	3.20	2.60	4.70	5.60							1.10	100.80		64.4	0.9	12.0
133	0.01	1.00	1.20	4.90	6.60							1.20	100.10		73.0	0.4	10.2
135	0.04	3.80	4.00	4.10	5.40							0.90	101.10		61.8	2.1	11.1
137	0.01	1.30	1.40	5.60	3.60							0.90	99.70		77.9	0.1	9.2
144	0.05	2.40	0.50	4.20	4.10							2.00	100.90		72.3	1.0	11.1
148	0.01	0.70	0.80	1.30	1.60							0.90	100.40		88.5	0.5	4.3
155	0.02	2.20	1.00	2.00	6.50							1.00	100.20		68.7	1.0	11.2
156	0.04	2.70	1.00	1.90	6.30							0.90	100.00		67.4	1.0	11.2
161		0.20		0.60	2.00							0.60	101.00		91.7	0.5	4.3
173	0.07	2.40	0.80	1.60	4.90							2.20	99.70		69.3	1.0	12.5
182	0.07	3.20	0.80	2.20	5.90							0.80	100.40		69.9	1.0	11.2
183	0.04	3.30	5.00	4.00	5.60							0.80	100.50		62.2	2.1	11.8
185	0.03	3.40	2.10	3.50	4.70							0.80	99.90		70.2	1.0	9.7
186	0.03	3.40	3.40	3.70	4.80							1.10	100.90		62.4	1.7	11.8
189	0.04	2.40	3.30	4.00	6.40							1.10	100.10		65.6	1.0	12.3
190	0.01	0.40	1.00	0.50	0.40							0.70	100.20		94.8	0.0	2.0
194	0.01	2.80	0.90	2.60	3.60							1.40	100.50		74.8	0.5	11.2
211	0.01	0.80	1.90	6.50	1.20							1.00	99.90		76.8	0.1	11.6
212	0.02	2.60	2.90	4.00	3.30							1.20	100.10		72.3	0.6	9.7
229	0.05	2.60	0.50	0.90	4.50							2.00	99.90		70.1	1.1	12.0
61-021	0.03	1.70	0.20	1.60	5.70							1.30	99.20		68.6	1.5	12.3
64-025	0.01	0.80	0.50	0.90	1.30							1.00	99.60		89.1	0.6	4.4
64-002	0.03	2.30	3.30	3.10	6.30							0.60	100.70		71.7	0.5	9.6
64-003	0.03	1.80	1.90	4.60	4.00							1.30	100.20		74.8	0.8	9.8
64-004	0.01	0.50	1.40	6.00	5.00							1.10	100.80		77.8	0.2	9.0
64-007	0.05	2.90	0.80	3.90	4.20							1.90	99.40		21.6	1.8	31.9
64-008	0.05	1.50	1.60	2.30	7.30							1.00	100.40		71.0	0.6	12.0
64-010	0.03	2.30	1.30	3.20	3.30							1.80	99.50		72.2	0.7	11.2
64-011	0.04	2.30	0.70	2.10	5.70							2.10	99.70		74.1	0.7	9.3
64-012	0.02	2.70	1.60	2.90	5.30							1.30	100.40		70.3	0.9	10.5
64-015	0.02	2.30	0.50	1.50	5.20							1.30	100.70		80.7	0.2	7.6
64-020	0.03	2.70	1.50	2.90	3.70							1.30	100.30		72.5	0.8	9.7
64-026	0.02	3.20	1.50	2.40	6.10							1.40	100.60		71.9	0.6	10.1
64-027	0.05	2.20	1.70	3.50	4.60							1.20	100.80		71.0	0.9	10.5

reported	*wt%*	*wt%*	*wt%*	*wt%*	*wt%*	*wt%*	*wt%*	*wt%*	*wt%*	*wt%*	*wt%*	*wt%*	*wt%*	*wt%*	*mol%*	*mol%*	*mol%*
Sample Number	**MnO**	**MgO**	**CaO**	**Na_2O**	**K_2O**	**P_2O_5**	**CO_2**	**S**	**BaO**	**Cr_2O_3**	**Nitrogen 105°C**	**LOI**	**Total**	**$Fe_2O_{3(t)}$**	**SiO_2**	**TiO2**	**Al_2O_3**
64-028	0.01	1.80	3.60	2.50	4.00							1.10	99.90		73.7	1.3	11.2
64-029	0.02	2.30	3.50	4.00	4.00							1.00	100.20		73.0	0.3	9.6
64-49	0.02	1.40	0.80	1.70	3.50							2.10	99.60		78.3	0.6	10.5
64-53	0.07	1.10	2.60	4.80	4.00							1.40	99.90		76.5	0.4	9.1
64-54	0.01	0.80	0.70	4.30	3.00							1.10	99.10		79.2	0.7	8.1
64-55	0.02	2.10	2.40	3.80	5.20							0.80	100.20		64.7	0.7	14.0
64-56	0.00	0.30	0.80	5.20	1.50							0.80	100.30		83.3	0.2	7.6
64-57	0.08	3.00	2.40	2.00	4.60							1.20	99.40		67.2	1.1	12.5
64-65	0.03	1.60	2.60	1.50	5.60							1.30	99.40		74.5	0.7	11.0
FJ46																	
FJ45																	
FJ25																	
FJ26																	
FJ9																	
FJ12																	
FJ44																	
FJ67																	
FJ2																	
FJ60																	
FJ22																	
FJ8																	
FJ78																	
FJ7																	
FJ63																	
FJ64																	
FJ4																	
FJ3																	
FJ97																	
FJ21																	
R7085																	
R7083																	
R7070																	
R7090																	
R7113																	
R7062																	
R7061																	
R7112																	
R7071																	
FA1	0.10	3.30	2.40	3.60	2.80	0.20									67.5	0.9	9.9
FA2	0.10	3.90	3.20	3.40	2.60	0.20									70.6	0.6	8.4
FA3	0.00	1.20	2.60	5.40	1.50	0.10									79.1	0.4	7.0
.1-3	0.10	4.10	1.20	3.60	48.00	0.20									48.6	0.6	8.5
.1-5	0.10	3.40	0.80	0.80	3.30	0.10									66.2	1.3	13.2
.1-7	0.10	2.50	1.00	1.50	4.70	0.10									67.3	1.2	12.5
.2-0	0.10	4.50	1.80	2.40	6.80	0.10									66.5	0.9	11.1
.2-1	0.10	5.30	13.60	3.40	2.20	0.20									61.5	0.5	6.3
WP2	0.10	3.40	1.40	2.60	6.20	0.10									68.3	0.6	9.9

reported	*wt%*	*wt%*	*wt%*	*wt%*	*wt%*	*wt%*	*wt%*	*wt%*	*wt%*	*wt%*	*wt%*	*wt%*	*wt%*	*wt%*	*mol%*	*mol%*	*mol%*
Sample Number	**MnO**	**MgO**	**CaO**	**Na_2O**	**K_2O**	**P_2O_5**	**CO_2**	**S**	**BaO**	**Cr_2O_3**	**Nitrogen 105°C**	**LOI**	**Total**	**$Fe_2O_{3(t)}$**	**SiO_2**	**TiO2**	**Al_2O_3**
WP3	0.10	1.70	2.40	2.40	4.70	0.10									78.9	0.3	7.2
89-20																	
1157	0.03	10.70	44.20	0.01	0.01	0.01							99.60		0.4	0.0	0.1
1170	0.04	8.27	45.60	0.01	0.29	0.01							100.73		6.8	0.0	0.6
1171	0.02	1.14	55.60	0.01	0.10	0.05							101.86		3.8	0.0	0.6
1173	0.02	3.41	51.50	0.01	0.06	0.05							103.11		7.0	0.0	1.0
1174	0.16	17.40	29.80	0.01	0.94	0.01							97.91		11.1	0.2	2.6
1175	0.17	12.30	25.80	0.01	1.74	0.06							96.97		23.9	0.4	4.3
1176	0.01	4.50	54.50	0.01	0.01	0.01							103.89		0.9	0.0	0.2
1177	0.02	2.46	42.10	0.13	0.89	0.01							94.10		15.9	0.0	2.8
1178	0.12	16.70	29.70	0.01	0.54	0.18							100.87		17.2	0.1	1.0
1179	0.15	18.30	28.30	0.01	0.49	0.01							99.22		7.9	0.2	1.5
1180	0.03	11.20	42.10	0.01	0.18	0.01							100.10		5.8	0.0	0.4
1181	0.11	22.10	27.60	0.01	0.01	0.01							105.18		16.8	0.0	0.4
1182	0.06	20.30	29.90	0.01	0.03	0.01							98.55		1.3	0.0	0.5
1183	0.09	20.30	30.30	0.01	0.01	0.01							99.86		0.3	0.0	0.2
1184	0.02	1.07	59.90	0.01	0.01	0.01							105.25		1.0	0.0	0.2
1185	0.19	1.57	55.90	0.01	0.08	0.01							102.74		3.4	0.0	0.4
1186	0.16	3.83	30.50	0.01	0.31	0.01							82.01		33.4	0.1	1.4
1187	0.10	22.90	26.00	0.01	0.29	0.01							108.31		24.1	0.1	0.4
1188	0.08	20.70	29.30	0.01	0.01	0.01							100.35		4.1	0.0	0.9
1189	0.20	14.30	29.10	0.01	1.13	0.13							98.40		16.7	0.2	2.1
1190	0.16	0.50	24.50	0.01	0.17	0.01							58.41		41.7	0.0	1.3
1191	0.05	6.51	37.70	0.01	0.04	0.09							97.86		23.4	0.1	2.0
1192	0.16	0.20	31.70	0.01	0.05	0.01							73.05		36.5	0.0	0.5
1193	0.02	1.33	25.50	0.28	0.78	0.03							59.15		36.9	0.2	5.4
1194	0.22	16.10	31.50	0.01	0.40	0.05							98.02		8.7	0.1	1.2
1195	0.09	11.70	40.50	0.01	0.01	0.01							106.10		10.6	0.0	0.9
1196	0.22	16.20	32.70	0.01	0.01	0.01							100.14		2.9	0.0	1.3
1197	0.14	11.20	25.60	0.01	1.17	0.01							88.12		30.0	0.1	2.1
1198	0.03	9.72	44.20	0.01	0.28	0.01							99.27		6.7	0.0	0.6
1199	0.14	18.40	31.30	0.01	0.02	0.01							103.30		5.2	0.0	1.0
1200	0.17	18.40	31.10	0.01	0.01	0.01							101.49		6.5	0.0	1.3
1201	0.21	7.14	45.00	0.01	0.84	0.01							93.44		6.0	0.1	1.4
1202	0.02	4.98	49.10	0.01	0.05	0.01							98.18		7.0	0.0	0.7
1203	0.14	20.80	28.80	0.01	0.01	0.01							104.11		4.6	0.0	1.2
1204	0.25	8.45	40.30	0.01	0.32	0.02							93.90		10.6	0.1	0.8
1205	0.29	15.30	32.50	0.01	0.01	0.01							98.89		12.9	0.0	0.1
1206	0.01	3.67	56.30	0.01	0.02	0.01							91.76		0.2	0.0	0.2
1207	0.01	5.52	50.90	0.01	0.01	0.04							95.24		5.8	0.0	0.2
1208	0.01	1.39	57.60	0.01	0.07	0.01							97.44		2.7	0.0	0.4
1209	0.02	3.27	54.40	0.01	0.10	0.01							100.23		4.8	0.0	0.6
1210	0.01	5.52	52.60	0.01	0.01	0.01							94.16		1.4	0.0	0.2
1211	0.01	2.91	57.10	0.01	0.01	0.01							98.19		0.0	0.0	0.1
1212	0.01	6.70	51.20	0.01	0.01	0.01							92.60		0.9	0.0	0.1
1213	0.02	6.80	47.40	0.01	0.19	0.01							94.29		6.2	0.0	0.4
1214	0.18	14.20	30.90	0.01	0.05	0.01							98.94		18.4	0.0	1.7

reported	*wt%*	*wt%*	*wt%*	*wt%*	*wt%*	*wt%*	*wt%*	*wt%*	*wt%*	*wt%*	*wt%*	*wt%*	*wt%*	*wt%*	*mol%*	*mol%*	*mol%*
Sample Number	**MnO**	**MgO**	**CaO**	**Na_2O**	**K_2O**	**P_2O_5**	**CO_2**	**S**	**BaO**	**Cr_2O_3**	**Nitrogen 105°C**	**LOI**	**Total**	**$Fe_2O_{3(t)}$**	**SiO_2**	**TiO2**	**Al_2O_3**
1215	0.15	15.70	24.50	0.01	0.03	0.14							95.06		26.8	0.3	3.9
1216	0.21	11.90	36.10	0.01	0.01	0.28							99.51		19.4	0.0	0.5
1217	0.24	10.40	43.40	0.01	0.01	0.01							99.02		3.5	0.1	0.6
1218	0.20	16.80	31.20	0.01	0.30	0.01							98.69		10.1	0.1	1.3
1219	0.01	5.73	52.40	0.01	0.01	0.01							101.97		0.6	0.0	0.1
1220	0.01	5.60	51.50	0.01	0.16	0.01							98.40		3.3	0.0	0.3
1221	0.04	3.94	45.80	0.01	0.24	0.07							97.58		12.4	0.0	1.4
1222	0.01	6.98	48.40	0.01	0.07	0.03							98.57		11.5	0.0	0.7
1223	0.13	15.80	32.50	0.01	0.05	0.01							99.23		9.7	0.0	1.2
1224	0.11	19.00	28.60	0.01	0.70	0.13							95.66		11.0	0.1	1.2
1225	0.13	20.60	29.70	0.01	0.18	0.01							100.90		4.7	0.0	0.5
1226	0.13	19.40	30.90	0.01	0.01	0.01							100.91		4.9	0.1	0.8
1227	0.03	7.86	46.40	0.01	0.01	0.05							96.37		7.7	0.0	0.2
1228	0.10	3.30	17.40	0.01	1.75	0.12							64.37		40.2	1.4	5.9
1229	0.05	21.20	29.20	0.01	0.08	0.01							100.24		14.2	0.1	0.7
1230	0.02	5.37	53.10	0.01	0.01	0.01							97.94		0.3	0.0	0.1
1231	0.10	0.69	27.20	0.01	1.06	0.03							66.85		38.2	0.1	2.5
1232	0.12	18.70	32.50	0.01	0.01	0.01							100.75		1.1	0.0	0.2
1233	0.17	17.70	33.50	0.01	0.01	0.01							98.94		2.0	0.0	0.5
1234	0.01	1.36	56.70	0.01	0.01	0.02							100.98		3.0	0.0	0.4
1235	0.08	15.40	26.20	0.01	0.01	0.07							83.32		26.9	0.2	2.4
1236	0.22	10.50	40.00	0.01	0.01	0.01							95.79		7.4	0.0	0.4
1237	0.10	22.00	28.70	0.01	0.01	0.01							102.37		4.3	0.0	0.6
1238	0.01	0.90	58.90	0.01	0.01	0.01							98.81		2.3	0.0	0.2
1239	0.02	5.10	51.40	0.01	0.27	0.01							96.68		3.8	0.0	0.5
1240	0.02	5.64	46.00	0.01	0.13	0.01							99.52		11.1	0.1	1.0
1241	0.03	5.05	54.20	0.01	0.03	0.01							99.15		0.8	0.0	0.2
1242	0.03	7.59	40.80	0.01	0.85	0.01							92.85		13.9	0.1	1.8
1243	0.05	20.30	31.10	0.01	0.02	0.01							100.45		9.8	0.1	0.6
1244	0.05	6.18	40.20	0.01	0.25	0.01							98.52		17.4	0.2	2.2
1246	0.02	5.47	52.30	0.01	0.13	0.07							96.63		2.1	0.0	0.3
1247	0.02	10.00	46.20	0.01	0.01	0.01							97.38		3.0	0.0	0.2
1248	0.04	4.24	55.00	0.01	0.02	0.01							100.46		1.6	0.0	0.3
1249	0.02	3.74	56.70	0.01	0.01	0.01							92.74		0.4	0.0	0.1
1250	0.02	4.06	56.00	0.01	0.01	0.01							98.91		0.8	0.0	0.1
1251	0.03	4.71	48.10	0.01	0.07	0.01							96.47		8.5	0.1	1.1
1252	0.02	4.37	55.20	0.01	0.01	0.01							95.86		1.0	0.0	0.1
1257	0.13	18.00	31.00	0.00	0.28	0.12							104.68		4.9	0.1	0.6
1258	0.02	5.70	48.00	0.00	0.04	0.08							97.92		4.9	0.1	0.6
1259	0.03	3.56	56.00	0.00	0.01	0.09							103.53		1.3	0.0	0.2
1276	0.02	6.00	51.10	0.00	0.02	0.09							103.35		4.1	0.0	0.2
1277	0.04	11.60	42.50	0.00	0.00	0.08							99.70		1.3	0.0	0.1
1278	0.01	5.77	52.70	0.00	0.00	0.08							102.77		0.9	0.0	0.1
1279	0.02	5.99	52.60	0.00	0.06	0.09							103.66		1.1	0.0	0.3
1284	0.02	5.96	52.10	0.00	0.02	0.09							102.92		2.6	0.0	0.2
1285	0.02	5.41	51.30	0.00	0.04	0.09							101.63		3.4	0.0	0.3
15RME-0247	0.04	2.76	1.76	2.75	6.49	0.13				0.01		1.54	100.93	6.8	69.6	0.8	10.3

reported	*wt%*	*wt%*	*wt%*	*wt%*	*wt%*	*wt%*	*wt%*	*wt%*	*wt%*	*wt%*	*wt%*	*wt%*	*wt%*	*wt%*	*mol%*	*mol%*	*mol%*
Sample Number	**MnO**	**MgO**	**CaO**	**Na_2O**	**K_2O**	**P_2O_5**	**CO_2**	**S**	**BaO**	**Cr_2O_3**	**Nitrogen 105°C**	**LOI**	**Total**	**$Fe_2O_{3(t)}$**	**SiO_2**	**TiO2**	**Al_2O_3**
15RME-0403	0.11	4.00	3.39	5.30	3.99	1.81				0.00		1.73	100.02	8.45	59.4	1.8	12.1
15RME-0411	0.03	4.88	4.64	2.43	5.23	0.08				0.01		1.85	100.62	3.08	70.2	0.5	7.6
15RME-0420	0.08	3.69	1.05	3.69	3.55	0.06				0.02		0.35	101.32	9.41	63.8	1.3	13.7
15RME-0452	0.05	6.69	6.22	5.84	1.34	0.21				0.01		1.18	100.68	2.89	63.5	0.6	9.4
16RME-0208	0.04	2.07	3.20	1.95	5.30	0.13				0.01		2.60	99.18	5.81	75.1	0.9	6.9
16RME-0214	0.05	3.80	1.02	0.87	5.78	0.07				0.02		1.10	100.63	8.15	65.0	1.3	14.1
16RME-0222	0.09	1.82	2.56	0.62	2.88	0.07				0.01		1.42	100.60	6.8	79.8	0.8	6.3
16RME-0225	0.07	3.71	3.01	3.16	6.17	0.12				0.01		1.54	99.31	5.52	68.7	1.0	8.7
16RME-0227	0.02	1.83	2.68	3.69	5.33	0.06				0.00		1.92	99.73	3.23	72.4	0.3	10.8
16RME-0230	0.05	1.68	4.21	2.82	5.84	0.09				0.01		2.78	98.51	3.59	70.6	0.8	10.2
16RME-0231	0.09	4.68	0.75	2.36	7.23	0.07				0.01		1.14	99.45	9.03	63.2	0.9	11.8
16RME-0236	0.01	0.64	0.05	0.55	10.20	0.01				0.00		0.86	99.49	1.72	80.6	0.1	9.3
16RME-0265	0.10	6.83	13.71	2.73	3.35	0.14				0.01		1.59	99.25	5.96	56.4	0.5	7.1
16RME-0358	0.01	1.99	1.51	6.27	2.81	0.16				0.01		1.32	100.16	1.54	73.1	1.0	11.0
16RME-0360	0.01	2.20	0.80	5.71	2.31	0.12				0.01		1.91	99.88	2.23	75.9	0.9	9.3
16RME-0362	0.01	1.99	2.10	0.92	0.34	0.03				0.01		2.56	99.96	1.71	90.0	0.2	2.2
16RME-0371	0.06	3.07	0.53	0.78	7.52	0.07				0.01		2.52	99.75	6.88	70.3	1.2	10.7
16RME-0390	0.05	1.88	2.61	1.07	4.41	0.08				0.01		2.02	99.84	3.13	82.3	0.4	5.0
16RME-0391	0.06	2.17	2.28	3.11	4.47	0.36				0.01		2.05	100.01	4.33	75.6	0.4	8.1
16RME-0396	0.09	4.85	7.45	2.66	5.87	0.12				0.01		1.87	98.78	4.35	62.6	0.7	9.2
16RME-0456	0.08	2.76	0.77	1.25	5.04	0.11				0.02		0.31	99.37	9.29	66.3	1.3	13.9
16RME-0558	0.05	3.31	1.21	1.48	4.91	0.04				0.02		0.67	100.10	6.98	69.9	1.3	11.2
16RME-0571	0.09	3.32	1.40	1.17	5.49	0.10				0.01		0.11	100.31	9.43	67.8	1.0	11.1
15RME-0092	0.01	0.10	0.82	3.04	4.30	0.01				0.00		0.29	99.52	1.64	83.7	0.2	7.9
94RME-0016	0.01	0.35	0.53	0.63	0.55	0.01				0.01		0.51	100.66	0.28	96.1	0.1	1.6
15RME-0396	0.01	0.41	0.87	0.34	0.58	0.01				0.01		0.68	98.76	0.71	95.7	0.1	1.4
16RME-0394	0.02	0.28	1.25	4.75	3.67	0.03				0.00		0.52	99.77	1.15	79.3	0.1	10.3
16RME-0491	0.01	0.17	0.16	0.15	0.36	0.01				0.01		0.32	100.40	1.52	97.1	0.2	1.1
15RME-0233	0.05	21.64	28.32	0.01	0.08	0.00				0.00		44.35	99.92	0.78	5.5	0.0	0.8
15RME-0234	0.03	20.63	30.31	0.01	0.04	0.00				0.00		46.98	99.14	0.25	0.9	0.0	0.3
15RME-0331	0.02	3.75	49.92	0.09	0.20	0.02				0.00		39.94	100.70	0.79	7.4	0.1	0.9
15RME-0335	0.05	20.42	30.61	0.01	0.01	0.00				0.00		45.95	99.25	0.23	2.4	0.0	0.4
15RME-0350	0.03	9.75	44.53	0.01	0.05	0.01				0.00		43.91	100.36	0.2	2.4	0.0	0.3
15RME-0351	0.02	3.66	51.63	0.01	0.15	0.01				0.00		42.89	100.78	0.31	2.7	0.0	0.4
15RME-0366	0.00	1.93	53.82	0.01	0.09	0.01				0.00		42.88	100.69	0.06	2.6	0.0	0.2
15RME-0402	0.00	5.21	49.64	0.01	0.10	0.03				0.00		41.86	100.51	0.1	5.0	0.0	0.3
15RME-0410	0.02	1.48	50.85	0.12	0.38	0.05				0.00		38.40	100.28	0.88	10.6	0.1	1.0
16RME-0108	0.03	1.00	54.12	0.01	0.01	0.02				0.00		43.85	99.39	0.25	0.1	0.0	0.1
16RME-0115	0.07	20.09	29.72	0.01	0.05	0.00				0.00		46.90	99.13	0.56	2.1	0.0	0.4
16RME-0153	0.04	20.14	30.20	0.01	0.01	0.00				0.00		46.97	98.78	0.38	0.8	0.0	0.5
16RME-0212	0.03	2.58	44.12	0.31	1.05	0.17				0.00		32.68	99.24	1.12	20.7	0.1	2.4
16RME-0264	0.02	6.33	47.73	0.02	0.07	0.00				0.00		42.73	99.61	0.24	3.2	0.0	0.4
16RME-0297	0.02	3.72	50.60	0.01	0.10	0.01				0.00		43.41	99.47	0.33	1.6	0.0	0.3
16RME-0298	0.02	5.83	48.15	0.02	0.09	0.03				0.00		43.66	99.69	0.19	2.2	0.0	0.3
16RME-0335	0.01	4.52	49.18	0.01	0.12	0.02				0.00		44.03	99.10	0.11	1.2	0.0	0.3
16RME-0433	0.04	4.98	47.38	0.03	0.24	0.01				0.00		39.18	99.61	0.33	10.2	0.0	0.5
16RME-0557B	0.02	1.42	51.27	0.03	0.18	0.03				0.00		41.30	99.72	0.32	7.5	0.0	0.4

reported	*wt%*	*wt%*	*wt%*	*wt%*	*wt%*	*wt%*	*wt%*	*wt%*	*wt%*	*wt%*	*wt%*	*wt%*	*wt%*	*wt%*	*mol%*	*mol%*	*mol%*
Sample Number	**MnO**	**MgO**	**CaO**	**Na_2O**	**K_2O**	**P_2O_5**	**CO_2**	**S**	**BaO**	**Cr_2O_3**	**Nitrogen 105°C**	**LOI**	**Total**	**$Fe_2O_{3(t)}$**	**SiO_2**	**TiO2**	**Al_2O_3**
16RME-0560	0.04	2.08	50.59	0.02	0.09	0.22				0.00		41.16	99.37	0.49	6.7	0.0	0.4
16RME-0573A	0.03	3.36	50.28	0.02	0.13	0.01				0.00		42.05	99.55	0.46	4.4	0.0	0.4
16RME-0591	0.03	20.17	30.23	0.01	0.06	0.00				0.00		47.02	98.54	0.24	0.9	0.0	0.2
AKR21																	
MP6A																	
96TE17																	
09PH01B																	
09PH04																	
09PH05																	
09PH10																	
09PH18																	
09TE09																	
09TE21																	
09WE12																	
09WE17																	
96GE02																	
96GE09																	
96GE20																	
96GE22																	
96GE24																	
96GE27																	
96GE30																	
96PH04																	
96PH06																	
96PH07																	
96TE15																	
96TE23																	
96TE25																	
96TE26																	
96WT03																	
96WT04																	
96WT15																	
96WT27																	
809-2A																	
809-2B																	
809-3																	
809-8																	
809-9																	
809-12																	
809-15A																	
809-15B																	
809-20																	
811-7																	
811-11																	
811-12																	
811-14A																	
811-14B																	

reported	*wt%*	*wt%*	*wt%*	*wt%*	*wt%*	*wt%*	*wt%*	*wt%*	*wt%*	*wt%*	*wt%*	*wt%*	*wt%*	*wt%*	*mol%*	*mol%*	*mol%*
Sample Number	**MnO**	**MgO**	**CaO**	**Na_2O**	**K_2O**	**P_2O_5**	**CO_2**	**S**	**BaO**	**Cr_2O_3**	**Nitrogen 105°C**	**LOI**	**Total**	**$Fe_2O_{3(t)}$**	**SiO_2**	**TiO2**	**Al_2O_3**
811-23																	
811-2																	
812-11																	
812-12																	
FA6																	
FA7																	
802-7																	
808-5																	
811-13																	
811-16																	
811-21																	
303																	
3011																	
20CK06B	0.16	4.45	1.06	2.88	5.03	0.07						2.38	99.80		65.0	0.8	10.9
20CK46A	0.18	4.15	5.70	3.72	4.24	2.03						1.38	98.22		56.6	2.3	10.3
21CK76B	0.17	3.24	5.63	3.19	3.58	1.58						1.37	97.60		60.1	2.2	9.3
20CK14A	0.11	2.84	7.73	2.98	6.94	0.19						1.55	99.12		65.3	0.6	8.5
20CK52A	0.06	5.23	9.63	5.60	1.61	0.15						0.78	100.30		62.9	0.7	7.7
20CK25A1	0.02	2.56	2.60	4.09	3.54	0.22						2.27	98.02		70.2	0.8	10.0
21CK43C	0.16	6.79	8.39	2.47	1.69	0.14								1.216012746	67.3	0.7	6.5
21CK43B	0.03	1.58	0.31	4.13	5.55	0.10						1.06	98.19		72.8	0.8	10.6
20CK61A	0.17	5.24	0.61	1.81	6.82	0.09						1.94	98.64		62.3	0.9	12.0
20CK85B	0.04	2.81	0.50	1.62	6.48	0.11						1.55	99.72		69.1	1.2	12.3
20CK16A	0.05	2.63	1.17	2.48	4.64	0.10						1.01	99.16		75.1	0.8	8.4
21CK44A	0.05	2.89	3.12	2.47	4.31	0.08						1.74	99.04		63.1	1.2	13.0
21CK46A	0.13	4.29	1.76	0.54	3.60	0.11						2.05	98.35		62.9	1.3	12.9
21CK45A	0.11	3.62	1.68	0.19	2.88	0.07						1.66	98.85		70.6	1.2	11.1
20CK92B	0.14	6.56	18.05	1.91	0.45	0.04						1.42	99.05		55.9	0.4	6.9
20CK28A1	0.21	4.27	14.69	3.06	2.62	0.11						1.38	100.40		59.6	0.6	7.6
20CK68B	0.01	0.43	0.75	0.61	0.46	0.04						0.85	100.40		95.4	0.1	1.3
21CK36A	0.05	4.06	0.71	1.39	5.82	0.09						1.74	98.57		68.7	0.8	11.0
21CK33A	0.10	3.34	1.05	0.58	2.13	0.03						1.36	98.46		66.1	1.4	13.5
H-29	0.06	3.40	1.88	1.48	3.84	0.09									69.5	1.0	11.4
H-60	0.07	4.10	0.31	1.46	5.89	0.12									66.8	1.0	13.8
H-66	0.06	3.15	1.34	1.06	5.09	0.12									67.8	1.0	12.9
H-70	0.06	3.35	1.63	0.95	4.00	0.35									69.1	1.1	12.4
H-90	0.04	3.70	0.36	1.46	6.02	0.18									67.6	0.9	12.6
H-105	0.04	2.80	0.55	1.60	5.25	0.15									72.9	0.8	10.4
H-126	0.12	2.50	2.11	1.86	3.80	0.12									69.7	0.8	11.6
WE-4-58	0.12	2.80	0.74	0.45	2.75	0.20									71.6	1.0	11.9
WE-10-57	0.10	4.50	1.60	0.85	3.88	0.00									61.9	1.1	13.7
WE-17-57	0.05	2.25	0.37	2.75	5.78	0.00									73.9	0.8	9.8

reported	*mol%*	*mol%*	*mol%*	*mol%*	*mol%*	*mol%*	*mol%*	*mol%*	*mol%*	*mol%*	*mg/kg*	*mg/kg*	*mg/kg*	*mg/kg*	*mg/kg*	*mg/kg*
Sample Number	**FeO**	**Fe2O3**	**MnO**	**MgO**	**CaO**	**Na_2O**	**K_2O**	**P_2O_5**	**Cr_2O_3**	**LOI**	**Ag**	**As**	**Au**	**Ba**	**Be**	**Bi**
FA86-3																
FA86-10																
FA86-1																
FA86-4																
FA86-5																
FA86-6																
105	1.6	0.9	0.0	1.4	0.6	0.9	2.0	0.0	0.0							
114	0.0	2.9	0.0	2.4	3.2	2.9	3.4	0.0	0.0							
125	0.9	1.7	0.0	3.0	3.3	3.8	4.8	0.0	0.0							
127	3.3	0.5	0.0	5.8	5.1	3.8	1.6	0.0	0.0							
128	6.0	0.2	0.1	5.4	1.7	1.4	4.0	0.0	0.0							
129	4.8	1.0	0.2	5.4	2.4	2.7	4.4	0.0	0.0							
131	2.8	0.2	0.1	3.5	1.5	2.3	4.7	0.0	0.0							
132	4.4	0.8	0.0	5.3	3.1	5.1	4.0	0.0	0.0							
133	2.8	0.4	0.0	1.7	1.4	5.3	4.7	0.0	0.0							
135	5.1	0.8	0.0	6.3	4.7	4.4	3.8	0.0	0.0							
137	0.0	0.5	0.0	2.1	1.6	5.9	2.5	0.0	0.0							
144	0.0	3.1	0.0	4.1	0.6	4.7	3.0	0.0	0.0							
148	1.5	0.7	0.0	1.1	0.9	1.3	1.1	0.0	0.0							
155	6.6	0.7	0.0	3.7	1.2	2.2	4.7	0.0	0.0							
156	6.6	1.2	0.0	4.6	1.2	2.1	4.6	0.0	0.0							
161	1.0	0.4	0.0	0.3	0.0	0.6	1.3	0.0	0.0							
173	5.7	0.9	0.1	4.1	1.0	1.8	3.6	0.0	0.0							
182	3.7	1.1	0.1	5.3	1.0	2.4	4.2	0.0	0.0							
183	3.5	0.6	0.0	5.5	6.0	4.3	4.0	0.0	0.0							
185	3.4	0.6	0.0	5.6	2.5	3.7	3.3	0.0	0.0							
186	6.1	0.8	0.0	5.6	4.1	4.0	3.4	0.0	0.0							
189	3.3	0.7	0.0	4.0	4.0	4.4	4.6	0.0	0.0							
190	0.3	0.2	0.0	0.7	1.2	0.6	0.3	0.0	0.0							
194	2.1	0.4	0.0	4.6	1.1	2.8	2.5	0.0	0.0							
211	0.0	0.2	0.0	1.3	2.2	6.9	0.8	0.0	0.0							
212	2.5	0.7	0.0	4.2	3.4	4.2	2.3	0.0	0.0							
229	6.7	0.7	0.0	4.4	0.6	1.0	3.3	0.0	0.0							
61-021	7.2	1.1	0.0	2.9	0.2	1.8	4.2	0.0	0.0							
64-025	1.8	0.6	0.0	1.3	0.6	0.9	0.9	0.0	0.0							
64-002	2.7	0.2	0.0	3.7	3.8	3.3	4.4	0.0	0.0							
64-003	0.0	1.4	0.0	3.0	2.3	5.0	2.8	0.0	0.0							
64-004	0.0	0.7	0.0	0.8	1.6	6.4	3.5	0.0	0.0							
64-007	11.3	1.8	0.1	11.7	2.3	10.2	7.2	0.0	0.0							
64-008	3.8	0.4	0.0	2.5	1.9	2.5	5.2	0.0	0.0							
64-010	3.7	0.8	0.0	3.9	1.6	3.5	2.4	0.0	0.0							
64-011	3.8	1.0	0.0	3.9	0.8	2.3	4.1	0.0	0.0							
64-012	3.9	1.0	0.0	4.5	1.9	3.1	3.8	0.0	0.0							
64-015	1.9	0.2	0.0	3.7	0.6	1.6	3.6	0.0	0.0							
64-020	4.7	0.5	0.0	4.4	1.8	3.1	2.6	0.0	0.0							
64-026	2.7	0.8	0.0	5.3	1.8	2.6	4.3	0.0	0.0							
64-027	4.0	0.9	0.0	3.6	2.0	3.8	3.3	0.0	0.0							

reported	*mol%*	*mol%*	*mol%*	*mol%*	*mol%*	*mol%*	*mol%*	*mol%*	*mol%*	*mol%*	*mg/kg*	*mg/kg*	*mg/kg*	*mg/kg*	*mg/kg*	*mg/kg*
Sample Number	**FeO**	**Fe2O3**	**MnO**	**MgO**	**CaO**	**Na_2O**	**K_2O**	**P_2O_5**	**Cr_2O_3**	**LOI**	**Ag**	**As**	**Au**	**Ba**	**Be**	**Bi**
64-028	0.0	1.0	0.0	3.0	4.3	2.7	2.8	0.0	0.0							
64-029	1.7	0.5	0.0	3.7	4.1	4.2	2.8	0.0	0.0							
64-49	2.8	0.2	0.0	2.3	1.0	1.8	2.5	0.0	0.0							
64-53	0.0	1.0	0.1	1.8	3.1	5.2	2.8	0.0	0.0							
64-54	2.7	0.5	0.0	1.3	0.8	4.6	2.1	0.0	0.0							
64-55	5.7	0.5	0.0	3.6	2.9	4.2	3.8	0.0	0.0							
64-56	0.9	0.2	0.0	0.5	0.9	5.4	1.0	0.0	0.0							
64-57	5.2	0.4	0.1	5.1	2.9	2.2	3.3	0.0	0.0							
64-65	0.0	2.1	0.0	2.7	3.2	1.7	4.1	0.0	0.0							
FJ46																
FJ45																
FJ25																
FJ26																
FJ9																
FJ12																
FJ44																
FJ67																
FJ2																
FJ60																
FJ22																
FJ8																
FJ78																
FJ7																
FJ63																
FJ64																
FJ4																
FJ3																
FJ97																
FJ21																
R7085																
R7083																
R7070																
R7090																
R7113																
R7062																
R7061																
R7112																
R7071																
FA1	7.4	0.4	0.1	5.3	2.8	3.8	1.9	0.0	0.0							
FA2	5.0	0.2	0.1	6.2	3.6	3.5	1.8	0.0	0.0							
FA3	1.9	0.1	0.0	1.9	2.9	5.5	1.0	0.0	0.0							
.1-3	6.7	0.3	0.1	5.2	1.1	3.0	25.9	0.0	0.0							
.1-5	8.9	0.5	0.1	5.7	1.0	0.9	2.4	0.0	0.0							
.1-7	8.1	0.4	0.1	4.2	1.2	1.6	3.4	0.0	0.0							
.2-0	3.7	0.2	0.1	7.7	2.2	2.7	5.0	0.0	0.0							
.2-1	3.4	0.2	0.1	8.1	15.0	3.4	1.4	0.0	0.0							
WP2	6.5	0.3	0.1	5.6	1.6	2.8	4.3	0.0	0.0							

reported	*mol%*	*mol%*	*mol%*	*mol%*	*mol%*	*mol%*	*mol%*	*mol%*	*mol%*	*mol%*	*mg/kg*	*mg/kg*	*mg/kg*	*mg/kg*	*mg/kg*	*mg/kg*
Sample Number	**FeO**	**Fe2O3**	**MnO**	**MgO**	**CaO**	**Na_2O**	**K_2O**	**P_2O_5**	**Cr_2O_3**	**LOI**	**Ag**	**As**	**Au**	**Ba**	**Be**	**Bi**
WP3	2.2	0.1	0.1	2.7	2.7	2.5	3.2	0.0	0.0							
89-20																
1157	0.0	0.1	0.0	25.0	74.3	0.0	0.0	0.0	0.0					80.0		
1170	0.0	0.5	0.1	18.5	73.2	0.0	0.3	0.0	0.0					150.0		
1171	0.0	0.4	0.0	2.6	92.4	0.0	0.1	0.0	0.0					150.0		
1173	0.0	0.5	0.0	7.7	83.7	0.0	0.1	0.0	0.0					130.0		
1174	0.0	1.1	0.2	37.6	46.3	0.0	0.9	0.0	0.0					230.0		
1175	0.0	1.6	0.2	27.1	40.8	0.0	1.6	0.0	0.0					320.0		
1176	0.0	0.1	0.0	10.2	88.6	0.0	0.0	0.0	0.0					120.0		
1177	0.0	0.6	0.0	6.0	73.5	0.2	0.9	0.0	0.0					410.0		
1178	0.0	0.7	0.1	35.2	45.0	0.0	0.5	0.1	0.0					130.0		
1179	0.0	1.5	0.2	41.8	46.4	0.0	0.5	0.0	0.0					150.0		
1180	0.0	0.1	0.0	25.2	68.1	0.0	0.2	0.0	0.0					100.0		
1181	0.0	0.7	0.1	43.2	38.8	0.0	0.0	0.0	0.0					70.0		
1182	0.0	0.3	0.1	47.5	50.2	0.0	0.0	0.0	0.0					50.0		
1183	0.0	0.5	0.1	47.7	51.1	0.0	0.0	0.0	0.0					60.0		
1184	0.0	0.0	0.0	2.4	96.3	0.0	0.0	0.0	0.0					130.0		
1185	0.0	0.1	0.2	3.6	92.1	0.0	0.1	0.0	0.0					130.0		
1186	0.0	0.5	0.2	9.5	54.5	0.0	0.3	0.0	0.0					180.0		
1187	0.0	0.5	0.1	41.1	33.5	0.0	0.2	0.0	0.0					60.0		
1188	0.0	0.5	0.1	46.8	47.6	0.0	0.0	0.0	0.0					50.0		
1189	0.0	0.9	0.3	32.0	46.8	0.0	1.1	0.0	0.0					190.0		
1190	0.0	0.1	0.3	1.6	54.7	0.0	0.2	0.0	0.0					120.0		
1191	0.0	1.0	0.1	14.2	59.1	0.0	0.0	0.0	0.0					130.0		
1192	0.0	0.1	0.2	0.5	62.0	0.0	0.1	0.0	0.0					50.0		
1193	0.0	1.8	0.0	3.7	50.4	0.5	0.9	0.0	0.0					820.0		
1194	0.0	1.4	0.3	36.5	51.3	0.0	0.4	0.0	0.0					150.0		
1195	0.0	0.8	0.1	25.1	62.4	0.0	0.0	0.0	0.0					130.0		
1196	0.0	1.3	0.3	38.4	55.7	0.0	0.0	0.0	0.0					70.0		
1197	0.0	0.2	0.2	25.0	41.1	0.0	1.1	0.0	0.0					220.0		
1198	0.0	0.5	0.0	21.5	70.3	0.0	0.3	0.0	0.0					150.0		
1199	0.0	0.9	0.2	41.7	51.0	0.0	0.0	0.0	0.0					70.0		
1200	0.0	1.1	0.2	41.0	49.8	0.0	0.0	0.0	0.0					60.0		
1201	0.0	0.3	0.3	16.5	74.6	0.0	0.8	0.0	0.0					200.0		
1202	0.0	0.3	0.0	11.4	80.5	0.0	0.0	0.0	0.0					100.0		
1203	0.0	1.1	0.2	46.5	46.3	0.0	0.0	0.0	0.0					50.0		
1204	0.0	0.7	0.3	19.7	67.5	0.0	0.3	0.0	0.0					260.0		
1205	0.0	0.7	0.4	34.0	51.9	0.0	0.0	0.0	0.0					140.0		
1206	0.0	0.0	0.0	8.3	91.3	0.0	0.0	0.0	0.0					80.0		
1207	0.0	0.0	0.0	12.3	81.5	0.0	0.0	0.0	0.0					100.0		
1208	0.0	0.0	0.0	3.1	93.7	0.0	0.1	0.0	0.0					220.0		
1209	0.0	0.3	0.0	7.3	86.9	0.0	0.1	0.0	0.0					130.0		
1210	0.0	0.0	0.0	12.5	85.9	0.0	0.0	0.0	0.0					120.0		
1211	0.0	0.0	0.0	6.6	93.2	0.0	0.0	0.0	0.0					80.0		
1212	0.0	0.0	0.0	15.2	83.7	0.0	0.0	0.0	0.0					80.0		
1213	0.0	0.2	0.0	15.5	77.5	0.0	0.2	0.0	0.0					130.0		
1214	0.0	1.1	0.2	30.6	47.9	0.0	0.0	0.0	0.0					140.0		

reported	*mol%*	*mol%*	*mol%*	*mol%*	*mol%*	*mol%*	*mol%*	*mol%*	*mol%*	*mol%*	*mg/kg*	*mg/kg*	*mg/kg*	*mg/kg*	*mg/kg*	*mg/kg*
Sample Number	**FeO**	**Fe2O3**	**MnO**	**MgO**	**CaO**	**Na_2O**	**K_2O**	**P_2O_5**	**Cr_2O_3**	**LOI**	**Ag**	**As**	**Au**	**Ba**	**Be**	**Bi**
1215	0.0	2.3	0.2	31.4	35.2	0.0	0.0	0.0	0.0					70.0		
1216	0.0	0.5	0.2	24.9	54.3	0.0	0.0	0.1	0.0					70.0		
1217	0.0	0.5	0.3	23.8	71.2	0.0	0.0	0.0	0.0					140.0		
1218	0.0	0.9	0.3	37.3	49.7	0.0	0.3	0.0	0.0					290.0		
1219	0.0	0.0	0.0	13.1	86.2	0.0	0.0	0.0	0.0					110.0		
1220	0.0	0.1	0.0	12.6	83.5	0.0	0.2	0.0	0.0					150.0		
1221	0.0	0.8	0.1	9.1	75.9	0.0	0.2	0.0	0.0					200.0		
1222	0.0	0.1	0.0	14.6	72.9	0.0	0.1	0.0	0.0					230.0		
1223	0.0	1.0	0.2	35.4	52.4	0.0	0.0	0.0	0.0					220.0		
1224	0.0	0.5	0.1	41.4	44.8	0.0	0.7	0.0	0.0					280.0		
1225	0.0	0.5	0.2	46.1	47.8	0.0	0.2	0.0	0.0					80.0		
1226	0.0	0.6	0.2	43.6	49.9	0.0	0.0	0.0	0.0					120.0		
1227	0.0	0.1	0.0	17.5	74.3	0.0	0.0	0.0	0.0					170.0		
1228	0.0	2.8	0.2	9.9	37.4	0.0	2.2	0.1	0.0					2000.0		
1229	0.0	0.7	0.1	42.3	41.9	0.0	0.1	0.0	0.0					140.0		
1230	0.0	0.2	0.0	12.3	87.1	0.0	0.0	0.0	0.0					100.0		
1231	0.0	0.1	0.2	2.0	55.6	0.0	1.3	0.0	0.0					190.0		
1232	0.0	0.6	0.2	43.5	54.4	0.0	0.0	0.0	0.0					80.0		
1233	0.0	0.6	0.2	40.9	55.7	0.0	0.0	0.0	0.0					90.0		
1234	0.0	0.3	0.0	3.1	93.1	0.0	0.0	0.0	0.0					130.0		
1235	0.0	1.9	0.1	30.8	37.7	0.0	0.0	0.0	0.0					80.0		
1236	0.0	0.8	0.3	24.3	66.6	0.0	0.0	0.0	0.0					160.0		
1237	0.0	0.7	0.1	48.7	45.6	0.0	0.0	0.0	0.0					50.0		
1238	0.0	0.1	0.0	2.0	95.4	0.0	0.0	0.0	0.0					120.0		
1239	0.0	0.1	0.0	11.5	83.6	0.0	0.3	0.0	0.0					170.0		
1240	0.0	0.7	0.0	12.7	74.2	0.0	0.1	0.0	0.0					250.0		
1241	0.0	0.1	0.0	11.4	87.5	0.0	0.0	0.0	0.0					190.0		
1242	0.0	0.7	0.0	17.0	65.7	0.0	0.8	0.0	0.0					250.0		
1243	0.0	0.5	0.1	42.3	46.6	0.0	0.0	0.0	0.0					80.0		
1244	0.0	1.4	0.1	13.8	64.6	0.0	0.2	0.0	0.0					180.0		
1246	0.0	0.1	0.0	12.4	85.0	0.0	0.1	0.0	0.0					210.0		
1247	0.0	0.1	0.0	22.4	74.3	0.0	0.0	0.0	0.0					130.0		
1248	0.0	0.1	0.1	9.5	88.3	0.0	0.0	0.0	0.0					90.0		
1249	0.0	0.0	0.0	8.4	91.0	0.0	0.0	0.0	0.0					160.0		
1250	0.0	0.1	0.0	9.1	89.9	0.0	0.0	0.0	0.0					150.0		
1251	0.0	0.6	0.0	10.7	78.7	0.0	0.1	0.0	0.0					220.0		
1252	0.0	0.1	0.0	9.8	88.9	0.0	0.0	0.0	0.0					130.0		
1257	0.0	0.4	0.2	41.8	51.8	0.0	0.3	0.0	0.0					130.0		
1258	0.0	0.5	0.0	13.3	80.6	0.0	0.0	0.0	0.0					140.0		
1259	0.0	0.1	0.0	8.0	90.4	0.0	0.0	0.0	0.0					120.0		
1276	0.0	0.1	0.0	13.4	82.2	0.0	0.0	0.0	0.0					220.0		
1277	0.0	0.0	0.1	27.1	71.4	0.0	0.0	0.0	0.0					110.0		
1278	0.0	0.0	0.0	13.1	85.8	0.0	0.0	0.0	0.0					110.0		
1279	0.0	0.0	0.0	13.5	85.0	0.0	0.1	0.0	0.0					140.0		
1284	0.0	0.1	0.0	13.3	83.7	0.0	0.0	0.0	0.0					160.0		
1285	0.0	0.1	0.0	12.3	83.9	0.0	0.0	0.0	0.0					150.0		
15RME-0247	3.9	0.9	0.0	4.6	2.1	3.0	4.6	0.0	0.0		2.0	3.0	4.0	722.0	1.2	0.2

reported	*mol%*	*mol%*	*mol%*	*mol%*	*mol%*	*mol%*	*mol%*	*mol%*	*mol%*	*mol%*	*mg/kg*	*mg/kg*	*mg/kg*	*mg/kg*	*mg/kg*	*mg/kg*
Sample Number	**FeO**	**Fe2O3**	**MnO**	**MgO**	**CaO**	**Na_2O**	**K_2O**	**P_2O_5**	**Cr_2O_3**	**LOI**	**Ag**	**As**	**Au**	**Ba**	**Be**	**Bi**
15RME-0403	5.2	1.1	0.1	6.9	4.2	5.9	2.9	0.4	0.0		2.0	3.0	4.0	641.0	3.9	0.2
15RME-0411	2.4	0.0	0.0	7.8	5.3	2.5	3.6	0.0	0.0		2.0	3.0	4.0	998.0	1.4	0.2
15RME-0420	6.6	0.6	0.1	6.1	1.3	4.0	2.5	0.0	0.0		2.0	3.0	4.0	178.0	0.2	0.2
15RME-0452	1.8	0.2	0.0	10.5	7.0	6.0	0.9	0.0	0.0		2.0	3.0	4.0	118.0	1.5	0.2
16RME-0208	2.6	1.2	0.0	3.5	3.9	2.1	3.8	0.0	0.0		2.0	3.0	0.8	788.0	0.6	0.2
16RME-0214	6.1	0.4	0.1	6.5	1.2	1.0	4.2	0.0	0.0		2.0	3.0	0.8	551.0	0.2	0.2
16RME-0222	3.3	1.1	0.1	2.9	3.0	0.7	2.0	0.0	0.0		2.0	3.0	0.8	469.0	0.9	0.2
16RME-0225	3.4	0.6	0.1	6.2	3.6	3.4	4.4	0.0	0.0		2.0	3.0	0.8	902.0	0.6	0.2
16RME-0227	1.9	0.4	0.0	3.1	3.2	4.0	3.8	0.0	0.0		3.0	3.0	0.8	678.0	1.0	0.2
16RME-0230	2.4	0.4	0.0	2.9	5.2	3.2	4.3	0.0	0.0		3.0	3.0	0.8	2935.0	0.4	0.2
16RME-0231	6.7	0.6	0.1	8.0	0.9	2.6	5.3	0.0	0.0		3.0	3.0	0.8	977.0	0.2	0.2
16RME-0236	0.3	0.6	0.0	1.1	0.1	0.6	7.4	0.0	0.0		2.0	3.0	0.8	1729.0	0.5	0.2
16RME-0265	3.5	0.6	0.1	10.9	15.7	2.8	2.3	0.0	0.0		4.0	3.0	2.0	1366.0	2.4	0.2
16RME-0358	0.8	0.3	0.0	3.3	1.8	6.7	2.0	0.0	0.0		3.0	3.0	0.8	41.0	1.4	0.2
16RME-0360	1.4	0.2	0.0	3.6	0.9	6.1	1.6	0.0	0.0		1.0	3.0	0.8	50.0	1.4	0.2
16RME-0362	0.9	0.2	0.0	3.1	2.3	0.9	0.2	0.0	0.0		3.0	3.0	0.8	4.0	0.4	0.2
16RME-0371	5.0	0.5	0.1	5.3	0.7	0.9	5.5	0.0	0.0		2.0	3.0	0.8	697.0	0.4	0.2
16RME-0390	1.4	0.6	0.0	3.0	3.0	1.1	3.0	0.0	0.0		1.0	3.0	0.8	561.0	0.9	0.2
16RME-0391	2.3	0.7	0.1	3.6	2.7	3.3	3.2	0.1	0.0		1.0	3.0	0.8	793.0	1.2	0.2
16RME-0396	3.3	0.2	0.1	8.0	8.9	2.9	4.2	0.0	0.0		3.0	3.0	0.8	1215.0	1.6	0.2
16RME-0456	7.1	0.5	0.1	4.7	0.9	1.4	3.7	0.0	0.0		1.0	3.0	0.8	852.0	0.2	0.2
16RME-0558	5.2	0.3	0.0	5.5	1.4	1.6	3.5	0.0	0.0		2.0	3.0	0.8	776.0	0.3	0.2
16RME-0571	7.3	0.3	0.1	5.5	1.7	1.3	3.9	0.0	0.0		1.0	3.0	0.8	744.0	0.7	0.2
15RME-0092	0.3	0.5	0.0	0.2	1.0	3.2	3.0	0.0	0.0		2.0	3.0	4.0	801.1	1.0	0.2
94RME-0016	0.2	0.0	0.0	0.5	0.6	0.6	0.4	0.0	0.0		1.0	3.0	2.0	86.9	0.5	0.2
15RME-0396	0.4	0.1	0.0	0.6	1.0	0.3	0.4	0.0	0.0		2.0	3.0	0.8	166.2	0.4	0.2
16RME-0394	0.5	0.2	0.0	0.5	1.5	5.1	2.6	0.0	0.0		2.0	3.0	0.8	996.9	1.7	0.2
16RME-0491	0.4	0.4	0.0	0.3	0.2	0.1	0.2	0.0	0.0		3.0	3.0	0.8	62.6	0.2	0.2
15RME-0233	0.8	0.0	0.1	47.7	44.9	0.0	0.1	0.0	0.0		2.0	3.0	8.0	14.3	0.1	0.2
15RME-0234	0.4	0.0	0.0	47.8	50.5	0.0	0.0	0.0	0.0		2.0	3.0	4.0	5.7	0.1	0.2
15RME-0331	0.9	0.0	0.0	8.5	81.8	0.1	0.2	0.0	0.0		4.0	3.0	4.0	300.3	0.2	0.2
15RME-0335	0.3	0.0	0.1	46.7	50.2	0.0	0.0	0.0	0.0		2.0	3.0	4.0	95.0	0.0	0.2
15RME-0350	0.2	0.0	0.0	22.6	74.3	0.0	0.0	0.0	0.0		3.0	3.0	4.0	34.2	0.1	0.2
15RME-0351	0.4	0.0	0.0	8.6	87.6	0.0	0.2	0.0	0.0		5.0	3.0	10.0	42.9	0.1	0.2
15RME-0366	0.2	0.0	0.0	4.6	92.3	0.0	0.1	0.0	0.0		4.0	3.0	4.0	46.4	0.1	0.2
15RME-0402	0.2	0.0	0.0	12.0	82.3	0.0	0.1	0.0	0.0		4.0	3.0	4.0	31.0	0.1	0.2
15RME-0410	1.1	0.0	0.0	3.4	83.3	0.2	0.4	0.0	0.0		4.0	3.0	4.0	168.8	0.3	0.2
16RME-0108	0.3	0.0	0.0	2.5	97.0	0.0	0.0	0.0	0.0		4.0	3.0	0.8	76.2	0.1	0.2
16RME-0115	0.7	0.0	0.1	46.9	49.8	0.0	0.0	0.0	0.0		3.0	3.0	0.8	7.9	0.2	0.2
16RME-0153	0.5	0.0	0.1	47.2	50.9	0.0	0.0	0.0	0.0		3.0	3.0	0.8	3.9	0.0	0.2
16RME-0212	0.9	0.1	0.0	5.6	68.7	0.4	1.0	0.1	0.0		4.0	3.0	0.8	510.2	0.5	0.2
16RME-0264	0.3	0.0	0.0	15.0	81.0	0.0	0.1	0.0	0.0		4.0	3.0	0.8	176.5	0.0	0.2
16RME-0297	0.5	0.0	0.0	9.1	88.5	0.0	0.1	0.0	0.0		5.0	3.0	0.8	105.2	0.1	0.2
16RME-0298	0.3	0.0	0.0	14.0	83.0	0.0	0.1	0.0	0.0		4.0	3.0	0.8	21.8	0.1	0.2
16RME-0335	0.2	0.0	0.0	11.1	86.9	0.0	0.1	0.0	0.0		5.0	3.0	0.8	48.4	0.1	0.2
16RME-0433	0.4	0.0	0.1	11.3	77.3	0.0	0.2	0.0	0.0		4.0	3.0	0.8	1137.3	0.1	0.2
16RME-0557B	0.4	0.0	0.0	3.4	88.0	0.0	0.2	0.0	0.0		4.0	3.0	0.8	205.7	0.1	0.2

reported	*mol%*	*mol%*	*mol%*	*mol%*	*mol%*	*mol%*	*mol%*	*mol%*	*mol%*	*mol%*	*mg/kg*	*mg/kg*	*mg/kg*	*mg/kg*	*mg/kg*	*mg/kg*
Sample Number	**FeO**	**Fe2O3**	**MnO**	**MgO**	**CaO**	**Na_2O**	**K_2O**	**P_2O_5**	**Cr_2O_3**	**LOI**	**Ag**	**As**	**Au**	**Ba**	**Be**	**Bi**
16RME-0560	0.6	0.0	0.1	5.0	87.0	0.0	0.1	0.1	0.0		4.0	3.0	0.8	142.0	0.2	0.2
16RME-0573A	0.5	0.0	0.0	8.0	86.4	0.0	0.1	0.0	0.0		4.0	3.0	0.8	59.2	0.1	0.2
16RME-0591	0.4	0.0	0.0	47.4	51.0	0.0	0.1	0.0	0.0		2.0	3.0	0.8	6.5	0.0	0.2
AKR21																
MP6A																
96TE17																
09PH01B																
09PH04																
09PH05																
09PH10																
09PH18																
09TE09																
09TE21																
09WE12																
09WE17																
96GE02																
96GE09																
96GE20																
96GE22																
96GE24																
96GE27																
96GE30																
96PH04																
96PH06																
96PH07																
96TE15																
96TE23																
96TE25																
96TE26																
96WT03																
96WT04																
96WT15																
96WT27																
809-2A																
809-2B																
809-3																
809-8																
809-9																
809-12																
809-15A																
809-15B																
809-20																
811-7																
811-11																
811-12																
811-14A																
811-14B																

reported	*mol%*	*mol%*	*mol%*	*mol%*	*mol%*	*mol%*	*mol%*	*mol%*	*mol%*	*mol%*	*mg/kg*	*mg/kg*	*mg/kg*	*mg/kg*	*mg/kg*	*mg/kg*
Sample Number	**FeO**	**Fe2O3**	**MnO**	**MgO**	**CaO**	**Na_2O**	**K_2O**	**P_2O_5**	**Cr_2O_3**	**LOI**	**Ag**	**As**	**Au**	**Ba**	**Be**	**Bi**
811-23																
811-2																
812-11																
812-12																
FA6																
FA7																
802-7																
808-5																
811-13																
811-16																
811-21																
303																
3011																
20CK06B	6.3	1.2	0.2	7.5	1.3	3.2	3.6	0.0	0.0					602.0	5.0	
20CK46A	5.7	2.6	0.2	7.3	7.2	4.2	3.2	0.5	0.0					1471.0	2.0	
21CK76B	6.7	2.2	0.2	5.6	7.0	3.6	2.7	0.4	0.0		0.8	2.5		1216.0	2.0	0.1
20CK14A	2.9	0.6	0.1	4.7	9.2	3.2	4.9	0.0	0.0					736.0	3.0	
20CK52A	2.4	0.6	0.1	8.2	10.8	5.7	1.1	0.0	0.0					214.0	3.0	
20CK25A1	3.2	1.2	0.0	4.4	3.2	4.5	2.6	0.1	0.0					714.0	2.0	
21CK43C	0.0	0.0	0.2	11.4	10.1	2.7	1.2	0.0	0.0		0.3	3.0	29.0	389.0	4.0	0.1
21CK43B	1.7	2.1	0.0	2.7	0.4	4.7	4.1	0.0	0.0		0.5	2.5		714.0	2.0	0.1
20CK61A	7.3	0.7	0.2	8.9	0.7	2.0	5.0	0.0	0.0					703.0	4.0	
20CK85B	1.7	3.3	0.0	4.9	0.6	1.9	4.9	0.0	0.0					1142.0	2.0	
20CK16A	2.1	1.8	0.0	4.4	1.4	2.7	3.3	0.0	0.0					562.0	0.5	
21CK44A	7.6	0.5	0.0	4.9	3.8	2.7	3.1	0.0	0.0		0.3	2.5		617.0	1.0	0.1
21CK46A	8.1	1.8	0.1	7.4	2.2	0.6	2.7	0.0	0.0		0.3	2.5		475.0	2.0	0.1
21CK45A	5.6	1.1	0.1	6.1	2.0	0.2	2.1	0.0	0.0		0.3	2.5		499.0	2.0	0.1
20CK92B	3.7	0.4	0.1	10.2	20.1	1.9	0.3	0.0	0.0					40.0	3.0	
20CK28A1	1.9	1.4	0.2	6.8	16.8	3.2	1.8	0.0	0.0					883.0	1.0	
20CK68B	0.7	0.1	0.0	0.7	0.8	0.6	0.3	0.0	0.0					31.0	0.5	
21CK36A	4.5	1.3	0.0	6.9	0.9	1.5	4.2	0.0	0.0		0.3	2.5		507.0	2.0	0.1
21CK33A	7.9	1.7	0.1	5.8	1.3	0.6	1.6	0.0	0.0		0.3	2.5		611.0	2.0	0.1
H-29	5.7	0.2	0.1	5.6	2.2	1.6	2.7	0.0	0.0					245.0		
H-60	4.0	1.1	0.1	7.0	0.4	1.6	4.3	0.0	0.0					330.0		
H-66	6.0	0.2	0.1	5.4	1.6	1.2	3.7	0.0	0.0					380.0		
H-70	4.6	1.2	0.1	5.6	2.0	1.0	2.9	0.1	0.0					127.0		
H-90	4.9	1.1	0.0	6.3	0.4	1.6	4.4	0.0	0.0					17.0		
H-105	4.1	0.8	0.0	4.7	0.7	1.7	3.8	0.0	0.0					103.0		
H-126	6.2	0.2	0.1	4.1	2.5	2.0	2.7	0.0	0.0					110.0		
WE-4-58	6.6	0.6	0.1	4.7	0.9	0.5	2.0	0.0	0.0					119.0		
WE-10-57	7.8	1.8	0.1	7.8	2.0	1.0	2.9	0.0	0.0							
WE-17-57	2.2	1.7	0.0	3.8	0.5	3.0	4.2	0.0	0.0							

reported	*mg/kg*	*mg/kg*	*mg/kg*	*mg/kg*	*mg/kg*	*mg/kg*	*mg/kg*	*mg/kg*	*mg/kg*	*mg/kg*	*mg/kg*	*mg/kg*	*mg/kg*	*mg/kg*	*mg/kg*
Sample Number	**Cd**	**Ce**	**Co**	**Cr**	**Cs**	**Cu**	**Dy**	**Er**	**Eu**	**Ga**	**Gd**	**Hf**	**Ho**	**In**	**La**
FA86-3															
FA86-10															
FA86-1															
FA86-4															
FA86-5															
FA86-6															
105															
114															
125															
127															
128															
129															
131															
132															
133															
135															
137															
144															
148															
155															
156															
161															
173															
182															
183															
185															
186															
189															
190															
194															
211															
212															
229															
61-021															
64-025															
64-002															
64-003															
64-004															
64-007															
64-008															
64-010															
64-011															
64-012															
64-015															
64-020															
64-026															
64-027															

reported	*mg/kg*	*mg/kg*	*mg/kg*	*mg/kg*	*mg/kg*	*mg/kg*	*mg/kg*	*mg/kg*	*mg/kg*	*mg/kg*	*mg/kg*	*mg/kg*	*mg/kg*	*mg/kg*	*mg/kg*
Sample Number	**Cd**	**Ce**	**Co**	**Cr**	**Cs**	**Cu**	**Dy**	**Er**	**Eu**	**Ga**	**Gd**	**Hf**	**Ho**	**In**	**La**
64-028															
64-029															
64-49															
64-53															
64-54															
64-55															
64-56															
64-57															
64-65															
FJ46															
FJ45															
FJ25															
FJ26															
FJ9															
FJ12															
FJ44															
FJ67															
FJ2															
FJ60															
FJ22															
FJ8															
FJ78															
FJ7															
FJ63															
FJ64															
FJ4															
FJ3															
FJ97															
FJ21															
R7085															
R7083															
R7070															
R7090															
R7113															
R7062															
R7061															
R7112															
R7071															
FA1		87.6													
FA2		65.8													
FA3		57.1													
.1-3		84.2													
.1-5		113.6													
.1-7		99.7													
.2-0															
.2-1		42.6													
WP2															

reported	*mg/kg*	*mg/kg*	*mg/kg*	*mg/kg*	*mg/kg*	*mg/kg*	*mg/kg*	*mg/kg*	*mg/kg*	*mg/kg*	*mg/kg*	*mg/kg*	*mg/kg*	*mg/kg*	*mg/kg*
Sample Number	**Cd**	**Ce**	**Co**	**Cr**	**Cs**	**Cu**	**Dy**	**Er**	**Eu**	**Ga**	**Gd**	**Hf**	**Ho**	**In**	**La**
WP3															
89-20															
1157			3.0	3.0		8.0									
1170			8.0	37.0		10.0									
1171			7.0	8.0		12.0									
1173			7.0	8.0		12.0									
1174			8.0	7.0		10.0									
1175			9.0	26.0		8.0									
1176			6.0	3.0		8.0									
1177			8.0	3.0		8.0									
1178			12.0	10.0		22.0									
1179			12.0	12.0		68.0									
1180			8.0	6.0		13.0									
1181			9.0	3.0		8.0									
1182			7.0	3.0		6.0									
1183			8.0	3.0		10.0									
1184			6.0	3.0		10.0									
1185			9.0	12.0		16.0									
1186			9.0	13.0		8.0									
1187			7.0	6.0		3.0									
1188			3.0	3.0		6.0									
1189			6.0	14.0		16.0									
1190			3.0	3.0		3.0									
1191			6.0	12.0		14.0									
1192			3.0	3.0		3.0									
1193			11.0	32.0		24.0									
1194			12.0	14.0		22.0									
1195			11.0	45.0		21.0									
1196			6.0	17.0		10.0									
1197			3.0	19.0		6.0									
1198			3.0	16.0		6.0									
1199			6.0	13.0		20.0									
1200			3.0	8.0		8.0									
1201			3.0	7.0		9.0									
1202			3.0	9.0		10.0									
1203			6.0	22.0		7.0									
1204			10.0	7.0		22.0									
1205			3.0	3.0		24.0									
1206			3.0	3.0		8.0									
1207			3.0	3.0		8.0									
1208			3.0	6.0		10.0									
1209			3.0	7.0		10.0									
1210			3.0	6.0		8.0									
1211			3.0	3.0		9.0									
1212			3.0	3.0		8.0									
1213			3.0	7.0		7.0									
1214			8.0	10.0		12.0									

reported	*mg/kg*	*mg/kg*	*mg/kg*	*mg/kg*	*mg/kg*	*mg/kg*	*mg/kg*	*mg/kg*	*mg/kg*	*mg/kg*	*mg/kg*	*mg/kg*	*mg/kg*	*mg/kg*	*mg/kg*
Sample Number	**Cd**	**Ce**	**Co**	**Cr**	**Cs**	**Cu**	**Dy**	**Er**	**Eu**	**Ga**	**Gd**	**Hf**	**Ho**	**In**	**La**
1215			15.0	27.0		13.0									
1216			3.0	3.0		18.0									
1217			3.0	6.0		10.0									
1218			6.0	44.0		12.0									
1219			3.0	3.0		8.0									
1220			3.0	6.0		7.0									
1221			3.0	10.0		9.0									
1222			3.0	6.0		8.0									
1223			3.0	7.0		8.0									
1224			3.0	6.0		8.0									
1225			6.0	9.0		8.0									
1226			3.0	3.0		8.0									
1227			3.0	6.0		6.0									
1228			8.0	50.0		9.0									
1229			3.0	55.0		11.0									
1230			3.0	3.0		7.0									
1231			3.0	15.0		6.0									
1232			3.0	3.0		6.0									
1233			3.0	3.0		9.0									
1234			3.0	8.0		12.0									
1235			8.0	30.0		8.0									
1236			3.0	6.0		10.0									
1237			3.0	3.0		6.0									
1238			3.0	6.0		8.0									
1239			3.0	3.0		10.0									
1240			3.0	9.0		14.0									
1241			3.0	3.0		7.0									
1242			6.0	14.0		18.0									
1243			3.0	9.0		14.0									
1244			6.0	10.0		9.0									
1246			3.0	3.0		7.0									
1247			3.0	7.0		6.0									
1248			3.0	6.0		12.0									
1249			3.0	3.0		8.0									
1250			3.0	3.0		6.0									
1251			9.0	16.0		14.0									
1252			3.0	6.0		8.0									
1257			3.0	6.0		10.0									
1258			3.0	5.0		5.0									
1259			3.0	3.0		8.0									
1276			3.0	3.0		5.0									
1277			3.0	3.0		6.0									
1278			3.0	3.0		5.0									
1279			3.0	3.0		6.0									
1284			3.0	3.0		5.0									
1285			3.0	3.0		5.0									
15RME-0247	0.0	52.9	22.9	84.0	1.7	43.8	3.2	1.9	1.5	19.4	3.6	6.4	0.7	0.0	25.2

reported	*mg/kg*	*mg/kg*	*mg/kg*	*mg/kg*	*mg/kg*	*mg/kg*	*mg/kg*	*mg/kg*	*mg/kg*	*mg/kg*	*mg/kg*	*mg/kg*	*mg/kg*	*mg/kg*	*mg/kg*
Sample Number	**Cd**	**Ce**	**Co**	**Cr**	**Cs**	**Cu**	**Dy**	**Er**	**Eu**	**Ga**	**Gd**	**Hf**	**Ho**	**In**	**La**
15RME-0403	0.1	210.8	14.4	5.0	1.2	0.7	8.4	3.8	4.5	22.4	12.8	12.6	1.5	0.1	85.4
15RME-0411	0.0	66.0	13.8	48.0	0.7	7.7	3.3	2.0	0.8	15.7	4.3	3.6	0.7	0.0	29.0
15RME-0420	0.0	163.1	24.8	119.0	0.2	3.4	9.5	5.1	1.4	25.1	10.4	5.3	1.8	0.1	75.2
15RME-0452	0.0	30.8	9.2	52.0	0.2	1.9	6.9	4.2	1.1	18.9	7.0	4.1	1.4	0.0	9.7
16RME-0208	0.1	67.9	18.2	76.0	0.6	18.5	3.5	1.9	1.4	11.9	4.4	7.0	0.7	0.1	35.5
16RME-0214	0.0	30.5	25.1	130.0	0.6	13.4	2.5	1.8	0.7	27.0	2.2	4.8	0.6	0.1	14.9
16RME-0222	0.1	48.0	12.1	89.0	0.6	28.9	4.6	2.9	1.0	10.5	4.3	7.1	1.0	0.0	22.5
16RME-0225	0.1	61.5	13.5	75.0	0.4	14.6	5.5	4.1	1.7	16.6	4.4	8.4	1.3	0.1	34.0
16RME-0227	0.0	53.1	7.0	35.0	0.4	12.7	2.6	1.9	1.7	17.7	2.9	4.9	0.6	0.0	31.1
16RME-0230	0.0	99.0	16.6	75.0	0.4	53.9	8.5	4.8	2.0	17.5	8.8	7.2	1.7	0.1	48.1
16RME-0231	0.1	74.1	31.3	84.0	0.6	43.9	4.9	3.1	1.0	21.2	5.5	6.0	1.0	0.1	35.1
16RME-0236	0.0	5.6	2.5	22.0	0.4	0.7	0.8	0.7	0.2	15.7	0.7	2.2	0.2	0.0	2.5
16RME-0265	0.1	53.4	17.1	52.0	0.8	122.3	5.4	3.2	1.3	14.9	5.5	3.8	1.1	0.1	20.8
16RME-0358	0.0	101.1	13.2	83.0	0.2	14.7	6.8	4.0	1.5	22.0	7.2	6.0	1.4	0.0	48.3
16RME-0360	0.0	93.2	7.8	78.0	0.2	0.7	6.5	3.7	1.5	19.4	7.0	5.0	1.3	0.0	44.4
16RME-0362	0.1	12.5	7.5	76.0	0.1	23.4	2.5	1.5	0.3	2.4	2.1	3.2	0.5	0.0	6.6
16RME-0371	0.0	32.0	14.1	104.0	4.8	7.8	3.9	2.5	1.0	16.3	3.5	5.3	0.8	0.1	15.9
16RME-0390	0.1	45.6	4.5	81.0	1.3	2.0	4.6	2.8	1.0	8.5	4.5	6.4	0.9	0.0	22.0
16RME-0391	0.2	40.4	13.7	75.0	2.8	39.5	3.9	2.4	1.2	14.3	3.8	1.3	0.8	0.0	19.4
16RME-0396	0.3	56.2	11.5	72.0	2.5	10.2	5.2	3.1	1.4	18.7	5.3	3.8	1.1	0.1	25.8
16RME-0456	0.0	120.6	44.4	136.0	0.4	62.0	6.6	4.8	1.3	24.9	6.9	4.6	1.5	0.1	52.5
16RME-0558	0.1	80.3	22.4	125.0	0.6	11.3	6.4	3.9	1.7	22.7	6.2	6.3	1.3	0.1	39.6
16RME-0571	0.0	106.9	34.8	97.0	1.3	5.2	6.6	4.0	1.6	21.5	6.9	5.0	1.3	0.1	49.0
15RME-0092	0.0	61.9	0.7	17.0	0.1	0.7	9.3	6.5	1.5	19.2	7.5	9.4	2.0	0.0	31.1
94RME-0016	0.0	17.1	0.5	56.0	0.1	0.7	1.5	0.9	0.2	3.0	1.4	2.1	0.3	0.0	7.3
15RME-0396	0.0	18.4	1.3	64.0	0.1	9.7	2.1	1.3	0.4	2.3	2.0	3.9	0.4	0.0	6.6
16RME-0394	0.0	16.2	1.4	22.0	0.9	1.4	0.8	0.4	0.4	23.7	1.1	3.0	0.2	0.0	8.1
16RME-0491	0.0	5.1	2.9	63.0	0.1	5.0	0.4	0.3	0.1	2.4	0.3	2.3	0.1	0.0	2.4
15RME-0233	0.0	5.2	1.7	7.0	0.1	6.5	0.7	0.4	0.2	1.3	0.7	0.2	0.1	0.0	3.2
15RME-0234	0.0	3.6	0.8	5.0	0.0	0.7	0.5	0.3	0.1	0.3	0.5	0.2	0.1	0.0	2.5
15RME-0331	0.1	8.3	2.6	4.0	0.7	0.7	0.7	0.5	0.2	1.3	0.8	0.3	0.2	0.0	5.6
15RME-0335	0.2	2.2	1.5	3.0	0.0	2.4	0.3	0.2	0.1	0.4	0.4	0.2	0.1	0.0	1.9
15RME-0350	0.0	33.4	1.0	3.0	0.0	1.4	1.2	0.7	0.4	0.5	1.4	0.2	0.2	0.0	17.9
15RME-0351	0.0	6.1	2.2	1.5	0.2	2.2	0.5	0.3	0.1	0.4	0.5	0.2	0.1	0.0	4.4
15RME-0366	0.0	1.2	0.7	3.0	0.0	0.7	0.1	0.1	0.0	0.3	0.1	0.1	0.0	0.0	0.6
15RME-0402	0.0	2.7	0.7	3.0	0.1	0.7	0.1	0.1	0.1	0.3	0.1	0.1	0.0	0.0	1.5
15RME-0410	0.0	20.0	2.7	8.0	0.2	3.5	1.2	0.7	0.5	1.5	1.5	0.3	0.2	0.0	10.1
16RME-0108	0.0	348.3	1.3	3.0	0.0	1.8	7.5	4.0	3.3	0.6	11.4	0.1	1.4	0.0	172.1
16RME-0115	0.1	4.5	1.4	5.0	0.0	1.4	0.5	0.3	0.1	0.5	0.6	0.1	0.1	0.0	3.1
16RME-0153	0.0	2.6	1.1	3.0	0.0	1.5	0.4	0.3	0.1	0.5	0.5	0.1	0.1	0.0	2.0
16RME-0212	0.1	77.2	3.4	10.0	0.3	4.9	1.8	1.0	0.8	3.1	2.7	0.8	0.3	0.0	41.7
16RME-0264	0.0	16.4	0.9	5.0	0.1	1.8	0.3	0.2	0.3	0.5	0.5	0.1	0.1	0.0	9.3
16RME-0297	0.0	24.7	1.6	23.0	0.1	12.0	1.1	0.6	0.4	0.3	1.5	0.1	0.2	0.0	12.2
16RME-0298	0.0	3.1	1.3	4.0	0.1	2.3	0.5	0.3	0.1	0.4	0.6	0.3	0.1	0.0	2.4
16RME-0335	0.0	2.1	1.2	4.0	0.1	2.4	0.5	0.3	0.1	0.3	0.5	0.1	0.1	0.0	2.1
16RME-0433	0.1	10.7	1.0	7.0	0.3	0.7	0.5	0.3	0.2	0.8	0.6	0.2	0.1	0.0	5.7
16RME-0557B	0.0	6.7	0.9	4.0	0.1	0.7	0.3	0.2	0.1	0.5	0.3	0.2	0.1	0.0	3.6

reported	*mg/kg*	*mg/kg*	*mg/kg*	*mg/kg*	*mg/kg*	*mg/kg*	*mg/kg*	*mg/kg*	*mg/kg*	*mg/kg*	*mg/kg*	*mg/kg*	*mg/kg*	*mg/kg*	*mg/kg*
Sample Number	**Cd**	**Ce**	**Co**	**Cr**	**Cs**	**Cu**	**Dy**	**Er**	**Eu**	**Ga**	**Gd**	**Hf**	**Ho**	**In**	**La**
16RME-0560	0.1	110.9	1.2	4.0	0.1	0.7	2.1	1.2	1.1	0.9	3.0	0.3	0.4	0.0	60.4
16RME-0573A	0.0	87.2	1.0	3.0	0.2	0.7	1.6	0.8	0.8	0.9	2.3	0.2	0.3	0.0	45.7
16RME-0591	0.0	2.5	1.0	3.0	0.0	0.7	0.4	0.3	0.1	0.2	0.5	0.1	0.1	0.0	2.0
AKR21															
MP6A															
96TE17															
09PH01B															
09PH04															
09PH05															
09PH10															
09PH18															
09TE09															
09TE21															
09WE12															
09WE17															
96GE02															
96GE09															
96GE20															
96GE22															
96GE24															
96GE27															
96GE30															
96PH04															
96PH06															
96PH07															
96TE15															
96TE23															
96TE25															
96TE26															
96WT03															
96WT04															
96WT15															
96WT27															
809-2A															
809-2B															
809-3															
809-8															
809-9															
809-12															
809-15A															
809-15B															
809-20															
811-7															
811-11															
811-12															
811-14A															
811-14B															

reported	*mg/kg*	*mg/kg*	*mg/kg*	*mg/kg*	*mg/kg*	*mg/kg*	*mg/kg*	*mg/kg*	*mg/kg*	*mg/kg*	*mg/kg*	*mg/kg*	*mg/kg*	*mg/kg*	*mg/kg*
Sample Number	**Cd**	**Ce**	**Co**	**Cr**	**Cs**	**Cu**	**Dy**	**Er**	**Eu**	**Ga**	**Gd**	**Hf**	**Ho**	**In**	**La**
811-23															
811-2															
812-11															
812-12															
FA6															
FA7															
802-7															
808-5															
811-13															
811-16															
811-21															
303															
3011															
20CK06B															
20CK46A															
21CK76B		184.0	20.0	10.0	0.3	5.0	14.0	7.3	4.3	20.0	16.6	7.5	2.7	0.1	80.8
20CK14A															
20CK52A															
20CK25A1															
21CK43C	0.3	88.4	17.4	51.2	1.0	0.5	6.9	4.5	1.8	14.0	7.1	10.6	1.4	0.1	34.8
21CK43B		105.0	12.0	60.0	1.3	5.0	5.5	2.9	1.5	19.0	6.6	5.9	1.0	0.1	51.3
20CK61A															
20CK85B															
20CK16A															
21CK44A		84.6	44.0	100.0	1.7	50.0	5.2	2.9	1.9	21.0	5.7	4.6	1.0	0.1	42.2
21CK46A		72.6	37.0	90.0	2.1	70.0	6.4	3.7	1.7	23.0	6.1	5.4	1.3	0.1	34.5
21CK45A		95.6	24.0	90.0	1.3	70.0	9.3	9.1	1.5	18.0	6.4	4.4	2.5	0.1	45.6
20CK92B															
20CK28A1															
20CK68B															
21CK36A		99.6	19.0	70.0	2.5	40.0	6.3	3.3	1.7	20.0	7.3	5.6	1.2	0.1	49.4
21CK33A		53.2	42.0	120.0	0.6	40.0	2.2	1.6	1.4	28.0	2.5	4.8	0.5	0.1	28.7
H-29			36.0	96.0		46.0									
H-60			47.0	76.0		8.0									
H-66			33.0	107.0		10.0									
H-70			49.0	106.0		52.0									
H-90			43.0	84.0		48.0									
H-105			35.0	68.0		78.0									
H-126			44.0	79.0		67.0									
WE-4-58			44.0	98.0		86.0									
WE-10-57															
WE-17-57															

reported	*mg/kg*	*mg/kg*	*mg/kg*	*mg/kg*	*mg/kg*	*mg/kg*	*mg/kg*	*mg/kg*	*mg/kg*	*mg/kg*	*mg/kg*	*mg/kg*	*mg/kg*	*mg/kg*	*mg/kg*
Sample Number	**Li**	**Lu**	**Mn**	**Mo**	**Nb**	**Nd**	**Ni**	**Pb**	**Pr**	**Rb**	**Sb**	**Sc**	**Sm**	**Sn**	**Sr**
FA86-3															
FA86-10															
FA86-1															
FA86-4															
FA86-5															
FA86-6															
105															
114															
125															
127															
128															
129															
131															
132															
133															
135															
137															
144															
148															
155															
156															
161															
173															
182															
183															
185															
186															
189															
190															
194															
211															
212															
229															
61-021															
64-025															
64-002															
64-003															
64-004															
64-007															
64-008															
64-010															
64-011															
64-012															
64-015															
64-020															
64-026															
64-027															

reported	*mg/kg*	*mg/kg*	*mg/kg*	*mg/kg*	*mg/kg*	*mg/kg*	*mg/kg*	*mg/kg*	*mg/kg*	*mg/kg*	*mg/kg*	*mg/kg*	*mg/kg*	*mg/kg*	*mg/kg*
Sample Number	**Li**	**Lu**	**Mn**	**Mo**	**Nb**	**Nd**	**Ni**	**Pb**	**Pr**	**Rb**	**Sb**	**Sc**	**Sm**	**Sn**	**Sr**
64-028															
64-029															
64-49															
64-53															
64-54															
64-55															
64-56															
64-57															
64-65															
FJ46															
FJ45															
FJ25															
FJ26															
FJ9															
FJ12															
FJ44															
FJ67															
FJ2															
FJ60															
FJ22															
FJ8															
FJ78															
FJ7															
FJ63															
FJ64															
FJ4															
FJ3															
FJ97															
FJ21															
R7085										15.0					530.0
R7083										85.0					359.0
R7070										140.0					466.0
R7090										57.0					417.0
R7113										125.0					121.0
R7062										24.0					454.0
R7061										28.0					99.0
R7112										88.0					142.0
R7071										63.0					180.0
FA1					15.0	42.8				143.0			9.0		82.0
FA2					13.0	40.4				103.0			9.2		90.0
FA3					17.0	28.5				12.0			5.9		37.0
.1-3					15.0	39.7				251.0			8.1		76.0
.1-5					14.0	50.2				113.0			9.2		73.0
.1-7					17.0	44.9				140.0			8.4		98.0
.2-0					12.0	42.9				133.0			7.8		112.0
.2-1					11.0	24.2				59.0			5.2		288.0
WP2						29.2							5.7		

reported	*mg/kg*	*mg/kg*	*mg/kg*	*mg/kg*	*mg/kg*	*mg/kg*	*mg/kg*	*mg/kg*	*mg/kg*	*mg/kg*	*mg/kg*	*mg/kg*	*mg/kg*	*mg/kg*	*mg/kg*
Sample Number	**Li**	**Lu**	**Mn**	**Mo**	**Nb**	**Nd**	**Ni**	**Pb**	**Pr**	**Rb**	**Sb**	**Sc**	**Sm**	**Sn**	**Sr**
WP3						32.0							6.3		
89-20															
1157	2.0						3.0	5.0							100.0
1170	4.0						12.0	5.0							210.0
1171	6.0						3.0	5.0							1120.0
1173	17.0						3.0	5.0							2170.0
1174	12.0						7.0	5.0							90.0
1175	14.0						3.0	5.0							200.0
1176	7.0						3.0	5.0							250.0
1177	16.0						3.0	5.0							1960.0
1178	18.0						8.0	5.0							150.0
1179	16.0						6.0	5.0							80.0
1180	13.0						3.0	28.0							140.0
1181	13.0						3.0	5.0							70.0
1182	5.0						3.0	5.0							40.0
1183	2.0						3.0	5.0							90.0
1184	2.0						3.0	5.0							750.0
1185	4.0						3.0	5.0							100.0
1186	8.0						3.0	5.0							120.0
1187	15.0						3.0	5.0							60.0
1188	6.0						3.0	5.0							40.0
1189	10.0						3.0	5.0							160.0
1190	2.0						3.0	5.0							50.0
1191	30.0						9.0	78.0							340.0
1192	2.0						3.0	5.0							60.0
1193	14.0						19.0	5.0							820.0
1194	15.0						10.0	5.0							130.0
1195	10.0						13.0	5.0							140.0
1196	10.0						9.0	5.0							100.0
1197	4.0						3.0	5.0							90.0
1198	4.0						3.0	5.0							180.0
1199	15.0						8.0	5.0							90.0
1200	20.0						7.0	5.0							90.0
1201	4.0						3.0	5.0							110.0
1202	6.0						3.0	5.0							1100.0
1203	12.0						11.0	5.0							80.0
1204	8.0						3.0	5.0							120.0
1205	8.0						3.0	5.0							110.0
1206	4.0						3.0	5.0							140.0
1207	6.0						3.0	5.0							730.0
1208	8.0						3.0	5.0							1490.0
1209	8.0						3.0	5.0							290.0
1210	5.0						3.0	5.0							210.0
1211	4.0						3.0	5.0							1450.0
1212	4.0						3.0	5.0							1020.0
1213	5.0						3.0	5.0							780.0
1214	28.0						3.0	5.0							120.0

reported	*mg/kg*	*mg/kg*	*mg/kg*	*mg/kg*	*mg/kg*	*mg/kg*	*mg/kg*	*mg/kg*	*mg/kg*	*mg/kg*	*mg/kg*	*mg/kg*	*mg/kg*	*mg/kg*	*mg/kg*
Sample Number	**Li**	**Lu**	**Mn**	**Mo**	**Nb**	**Nd**	**Ni**	**Pb**	**Pr**	**Rb**	**Sb**	**Sc**	**Sm**	**Sn**	**Sr**
1215	91.0						13.0	5.0							90.0
1216	18.0						3.0	17.0							140.0
1217	7.0						3.0	5.0							90.0
1218	18.0						8.0	5.0							150.0
1219	2.0						3.0	5.0							900.0
1220	2.0						3.0	5.0							800.0
1221	18.0						3.0	11.0							980.0
1222	8.0						3.0	5.0							880.0
1223	27.0						3.0	5.0							190.0
1224	14.0						3.0	5.0							100.0
1225	8.0						3.0	5.0							80.0
1226	11.0						3.0	5.0							110.0
1227	6.0						3.0	5.0							910.0
1228	18.0						12.0	5.0							230.0
1229	9.0						15.0	20.0							130.0
1230	2.0						3.0	5.0							110.0
1231	2.0						3.0	5.0							100.0
1232	4.0						3.0	5.0							70.0
1233	8.0						3.0	5.0							90.0
1234	10.0						3.0	60.0							2020.0
1235	26.0						10.0	5.0							400.0
1236	10.0						3.0	14.0							80.0
1237	8.0						3.0	5.0							80.0
1238	4.0						3.0	5.0							1470.0
1239	4.0						3.0	5.0							340.0
1240	12.0						3.0	5.0							600.0
1241	2.0						3.0	5.0							290.0
1242	18.0						7.0	12.0							760.0
1243	4.0						3.0	5.0							110.0
1244	28.0						3.0	5.0							540.0
1246	2.0						3.0	5.0							800.0
1247	2.0						3.0	5.0							650.0
1248	4.0						3.0	5.0							100.0
1249	6.0						3.0	5.0							460.0
1250	2.0						3.0	5.0							320.0
1251	12.0						8.0	5.0							580.0
1252	4.0						3.0	10.0							390.0
1257	7.0						3.0	5.0							70.0
1258	4.0						3.0	5.0							380.0
1259	2.0						3.0	5.0							320.0
1276	4.0						3.0	5.0							420.0
1277	2.0						3.0	5.0							110.0
1278	2.0						3.0	5.0							180.0
1279	2.0						3.0	5.0							200.0
1284	2.0						3.0	5.0							600.0
1285	3.0						3.0	5.0							260.0
15RME-0247	20.0	0.3	245.0	1.7	14.7	22.7	41.2	9.9	5.8	192.5	0.1	14.1	4.3	3.9	168.0

reported	*mg/kg*	*mg/kg*	*mg/kg*	*mg/kg*	*mg/kg*	*mg/kg*	*mg/kg*	*mg/kg*	*mg/kg*	*mg/kg*	*mg/kg*	*mg/kg*	*mg/kg*	*mg/kg*	*mg/kg*
Sample Number	**Li**	**Lu**	**Mn**	**Mo**	**Nb**	**Nd**	**Ni**	**Pb**	**Pr**	**Rb**	**Sb**	**Sc**	**Sm**	**Sn**	**Sr**
15RME-0403	35.3	0.5	934.0	0.5	26.2	113.2	1.4	11.5	28.0	89.1	0.0	7.4	18.8	2.5	967.8
15RME-0411	72.0	0.3	163.0	2.0	9.2	31.6	15.1	3.3	8.3	86.6	0.0	12.5	5.6	0.8	70.0
15RME-0420	25.3	0.7	566.0	2.9	18.0	71.7	37.2	3.9	18.9	37.1	0.0	24.9	13.1	1.4	11.6
15RME-0452	8.9	0.6	388.0	1.1	8.9	25.5	29.2	2.0	5.2	18.2	0.1	18.0	6.8	1.5	199.6
16RME-0208	18.3	0.3	308.0	2.5	9.9	29.5	36.9	11.1	7.9	78.1	0.1	11.2	5.3	2.2	481.5
16RME-0214	44.0	0.3	386.0	1.0	17.4	12.9	40.7	5.2	3.5	67.8	0.0	13.9	2.3	3.2	45.3
16RME-0222	62.3	0.5	618.0	2.5	8.6	21.9	14.5	5.2	5.7	49.5	0.0	10.5	4.4	1.8	181.1
16RME-0225	18.3	0.7	512.0	1.6	10.8	24.9	25.9	16.7	6.9	92.2	0.0	15.8	4.3	2.5	284.4
16RME-0227	20.9	0.4	171.0	1.8	3.7	20.9	7.3	14.1	5.8	67.5	0.0	7.5	3.6	1.3	423.1
16RME-0230	16.8	0.7	341.0	1.2	10.0	47.2	40.5	22.2	12.2	104.8	0.0	16.3	9.3	2.9	267.0
16RME-0231	8.3	0.5	667.0	1.0	12.6	34.7	50.8	26.3	9.0	76.5	0.0	10.6	6.3	3.1	109.7
16RME-0236	5.2	0.1	55.0	1.2	4.8	3.4	5.3	2.5	0.8	95.8	0.1	0.6	0.7	1.6	228.7
16RME-0265	11.2	0.5	755.0	1.3	11.1	28.7	26.1	4.5	7.2	66.2	0.1	12.9	6.0	2.8	327.0
16RME-0358	25.1	0.5	54.0	2.0	16.1	46.2	31.5	8.9	12.2	32.7	0.1	18.6	8.8	1.0	79.4
16RME-0360	14.5	0.5	41.0	1.9	14.5	43.0	26.5	1.9	11.1	13.1	0.0	11.6	8.3	1.0	43.6
16RME-0362	19.9	0.3	99.0	4.7	4.4	6.3	11.9	10.6	1.6	3.1	0.1	3.9	1.6	0.4	16.9
16RME-0371	32.5	0.4	390.0	1.8	16.9	15.0	23.5	15.9	3.8	72.4	0.1	13.4	3.2	0.9	78.3
16RME-0390	24.5	0.4	409.0	3.2	6.8	23.2	11.0	6.1	5.8	70.7	0.1	7.7	4.9	1.4	91.8
16RME-0391	21.2	0.3	458.0	2.1	5.8	20.1	23.8	45.8	4.9	91.3	0.2	10.4	4.2	1.7	403.4
16RME-0396	21.3	0.4	713.0	1.3	9.5	28.9	25.5	17.3	7.1	128.9	0.3	17.4	6.0	1.1	298.8
16RME-0456	13.8	0.8	551.0	1.5	15.3	56.1	58.5	6.6	14.4	55.1	0.0	18.5	9.3	3.3	34.3
16RME-0558	41.9	0.6	351.0	2.1	22.4	34.2	24.4	6.0	9.1	89.0	0.0	16.4	6.5	3.2	195.8
16RME-0571	16.7	0.6	674.0	1.5	13.6	46.2	33.2	5.7	12.3	127.9	0.0	18.7	8.5	2.7	61.2
15RME-0092	3.5	1.0	53.0	1.2	4.3	31.8	0.7	8.6	8.0	87.5	0.0	4.6	6.8	0.9	73.8
94RME-0016	2.4	0.1	38.0	3.0	2.2	7.9	1.5	0.9	2.1	10.6	0.0	1.3	1.6	0.7	32.1
15RME-0396	3.1	0.2	42.0	3.3	2.9	10.4	2.0	1.3	2.5	12.0	0.0	1.5	2.2	0.6	28.5
16RME-0394	9.1	0.1	133.0	1.1	3.8	6.9	1.1	20.3	1.8	101.2	0.1	2.0	1.5	0.9	355.8
16RME-0491	2.1	0.1	61.0	3.3	1.8	2.1	6.4	1.8	0.6	6.7	0.0	1.7	0.4	0.7	37.0
15RME-0233	7.7	0.1	439.0	0.2	0.2	3.2	8.5	0.5	0.8	1.9	0.0	2.6	0.7	0.1	47.5
15RME-0234	1.4	0.0	239.0	0.1	0.1	2.6	6.6	0.6	0.6	0.8	0.0	1.8	0.5	0.1	61.0
15RME-0331	1.1	0.1	188.0	0.1	0.4	3.6	10.7	7.3	1.0	11.4	0.0	3.0	0.7	0.2	657.4
15RME-0335	1.6	0.0	395.0	0.1	0.1	1.5	7.0	7.7	0.3	0.1	0.1	1.2	0.3	0.2	63.0
15RME-0350	0.8	0.1	284.0	0.1	0.2	12.8	8.4	0.7	3.7	1.4	0.0	1.6	1.9	0.1	246.9
15RME-0351	1.4	0.0	210.0	0.1	0.2	2.7	9.5	0.6	0.7	6.0	0.0	1.5	0.5	0.2	346.3
15RME-0366	3.0	0.0	23.0	0.1	0.1	0.6	10.0	1.9	0.1	1.5	0.0	1.2	0.1	1.4	633.2
15RME-0402	1.8	0.0	50.0	0.1	0.3	0.9	8.2	2.4	0.3	2.7	0.0	1.1	0.2	0.1	581.2
15RME-0410	3.0	0.1	214.0	0.4	0.7	9.8	12.6	2.1	2.5	9.7	0.0	2.0	1.7	0.3	424.8
16RME-0108	0.2	0.5	286.0	0.1	0.0	135.4	16.3	12.6	39.0	0.1	0.0	1.2	19.1	0.1	1560.0
16RME-0115	2.3	0.0	572.0	0.1	0.1	2.9	10.4	1.6	0.7	1.0	0.0	0.6	0.5	0.1	39.4
16RME-0153	1.6	0.0	320.0	0.0	0.0	2.0	9.0	0.7	0.5	0.1	0.0	0.6	0.4	0.1	36.0
16RME-0212	7.6	0.1	226.0	1.1	2.0	29.1	18.6	8.2	8.4	29.7	0.0	2.0	4.1	0.5	1248.1
16RME-0264	0.2	0.0	136.0	0.0	0.1	5.6	14.9	1.5	1.7	2.7	0.0	1.1	0.8	0.1	537.2
16RME-0297	1.2	0.1	160.0	0.8	0.2	12.2	15.4	0.8	3.1	4.5	0.0	0.6	2.0	0.1	682.8
16RME-0298	0.7	0.0	155.0	0.0	0.2	2.4	14.5	1.0	0.5	1.6	0.0	0.6	0.5	0.1	111.1
16RME-0335	0.6	0.0	73.0	0.0	0.1	1.9	15.1	0.8	0.4	1.3	0.0	0.6	0.4	0.2	241.9
16RME-0433	6.2	0.0	317.0	0.2	0.5	4.5	10.2	8.3	1.2	11.9	0.0	1.6	0.8	0.2	744.0
16RME-0557B	6.8	0.0	123.0	0.2	0.3	2.6	11.8	2.1	0.8	3.9	0.0	1.3	0.4	0.4	851.0

reported	*mg/kg*	*mg/kg*	*mg/kg*	*mg/kg*	*mg/kg*	*mg/kg*	*mg/kg*	*mg/kg*	*mg/kg*	*mg/kg*	*mg/kg*	*mg/kg*	*mg/kg*	*mg/kg*	*mg/kg*
Sample Number	**Li**	**Lu**	**Mn**	**Mo**	**Nb**	**Nd**	**Ni**	**Pb**	**Pr**	**Rb**	**Sb**	**Sc**	**Sm**	**Sn**	**Sr**
16RME-0560	8.6	0.2	321.0	0.1	1.0	39.6	11.7	10.2	11.8	2.9	0.0	1.5	5.1	0.3	1560.0
16RME-0573A	2.4	0.1	240.0	0.1	0.5	31.3	11.8	8.8	9.4	9.1	0.0	1.4	4.0	0.2	1272.2
16RME-0591	1.1	0.0	258.0	0.1	0.1	2.0	7.9	2.0	0.4	1.4	0.0	1.3	0.4	0.2	31.3
AKR21															
MP6A															
96TE17															
09PH01B															
09PH04															
09PH05															
09PH10															
09PH18															
09TE09															
09TE21															
09WE12															
09WE17															
96GE02															
96GE09															
96GE20															
96GE22															
96GE24															
96GE27															
96GE30															
96PH04															
96PH06															
96PH07															
96TE15															
96TE23															
96TE25															
96TE26															
96WT03															
96WT04															
96WT15															
96WT27															
809-2A															
809-2B															
809-3															
809-8															
809-9															
809-12															
809-15A															
809-15B															
809-20															
811-7															
811-11															
811-12															
811-14A															
811-14B															

reported	*mg/kg*	*mg/kg*	*mg/kg*	*mg/kg*	*mg/kg*	*mg/kg*	*mg/kg*	*mg/kg*	*mg/kg*	*mg/kg*	*mg/kg*	*mg/kg*	*mg/kg*	*mg/kg*	*mg/kg*
Sample Number	**Li**	**Lu**	**Mn**	**Mo**	**Nb**	**Nd**	**Ni**	**Pb**	**Pr**	**Rb**	**Sb**	**Sc**	**Sm**	**Sn**	**Sr**
811-23															
811-2															
812-11															
812-12															
FA6															
FA7															
802-7															
808-5															
811-13															
811-16															
811-21															
303															
3011															
20CK06B												27.0			152.0
20CK46A												13.0			1065.0
21CK76B		1.0		3.0	21.8	105.0	70.0	13.0	24.4	62.0	0.1	16.0	20.6	3.0	
20CK14A												12.0			518.0
20CK52A												11.0			197.0
20CK25A1												14.0			202.0
21CK43C		0.8		1.0	10.0	41.4	22.0	2.5	10.9	32.0	0.1	14.4	8.4	3.0	190.0
21CK43B		0.4		1.0	15.0	45.5	60.0	14.0	11.9	116.0	0.1	13.0	8.5	4.0	
20CK61A												32.0			64.0
20CK85B												19.0			126.0
20CK16A												13.0			68.0
21CK44A		0.4		2.0	17.6	37.2	90.0	6.0	9.6	144.0	0.1	22.0	6.7	3.0	
21CK46A		0.6		2.0	17.7	33.5	90.0	8.0	8.6	128.0	0.1	22.0	7.0	3.0	
21CK45A		1.9		1.0	18.0	43.0	80.0	2.5	11.1	93.0	0.1	33.0	8.1	3.0	
20CK92B												11.0			368.0
20CK28A1												12.0			391.0
20CK68B												3.0			39.0
21CK36A		0.4		1.0	13.0	46.5	50.0	18.0	11.8	137.0	0.1	14.0	9.0	4.0	59.0
21CK33A		0.3		1.0	16.4	21.1	100.0	2.5	5.7	52.0	0.1	25.0	3.6	2.0	61.0
H-29							35.0			22.0		40.0			125.0
H-60							52.0			29.0		38.0			93.0
H-66							39.0			170.0		42.0			190.0
H-70							50.0			130.0		45.0			68.0
H-90							66.0			190.0		39.0			98.0
H-105							53.0			190.0		20.0			90.0
H-126							54.0			170.0		41.0			68.0
WE-4-58							78.0			68.0		44.0			105.0
WE-10-57															
WE-17-57															

reported	*mg/kg*	*mg/kg*	*mg/kg*	*mg/kg*	*mg/kg*	*mg/kg*	*mg/kg*	*mg/kg*	*mg/kg*	*mg/kg*	*mg/kg*	*mg/kg*	*mg/kg*	*Age*	*Age*	*Age*
Sample Number	**Ta**	**Tb**	**Th**	**Ti**	**Tl**	**Tm**	**U**	**V**	**W**	**Y**	**Yb**	**Zn**	**Zr**	**Zrn**	**Ru**	**Ttn**
FA86-3																
FA86-10																
FA86-1																
FA86-4																
FA86-5																
FA86-6																
105																
114																
125																
127																
128																
129																
131																
132																
133																
135																
137																
144																
148																
155																
156																
161																
173																
182																
183																
185																
186																
189																
190																
194																
211																
212																
229																
61-021																
64-025																
64-002																
64-003																
64-004																
64-007																
64-008																
64-010																
64-011																
64-012																
64-015																
64-020																
64-026																
64-027																

reported	*mg/kg*	*mg/kg*	*mg/kg*	*mg/kg*	*mg/kg*	*mg/kg*	*mg/kg*	*mg/kg*	*mg/kg*	*mg/kg*	*mg/kg*	*mg/kg*	*mg/kg*	*Age*	*Age*	*Age*
Sample Number	**Ta**	**Tb**	**Th**	**Ti**	**Tl**	**Tm**	**U**	**V**	**W**	**Y**	**Yb**	**Zn**	**Zr**	**Zrn**	**Ru**	**Ttn**
64-028																
64-029																
64-49																
64-53																
64-54																
64-55																
64-56																
64-57																
64-65																
FJ46																
FJ45																
FJ25																
FJ26																
FJ9																
FJ12																
FJ44																
FJ67																
FJ2																
FJ60																
FJ22																
FJ8																
FJ78																
FJ7																
FJ63																
FJ64																
FJ4																
FJ3																
FJ97																
FJ21																
R7085																
R7083																
R7070																
R7090																
R7113																
R7062																
R7061																
R7112																
R7071																
FA1										47.0			240.0			
FA2										60.0			219.0			
FA3										31.0			261.0			
.1-3										31.0			216.0			
.1-5										37.0			186.0			
.1-7										41.0			192.0			
.2-0										43.0			246.0	1162.0		1104.0
.2-1										36.0			182.0	1164.0		1129.0
WP2														1164.0		1129.0

reported	*mg/kg*	*mg/kg*	*mg/kg*	*mg/kg*	*mg/kg*	*mg/kg*	*mg/kg*	*mg/kg*	*mg/kg*	*mg/kg*	*mg/kg*	*mg/kg*	*mg/kg*	*Age*	*Age*	*Age*
Sample Number	**Ta**	**Tb**	**Th**	**Ti**	**Tl**	**Tm**	**U**	**V**	**W**	**Y**	**Yb**	**Zn**	**Zr**	**Zrn**	**Ru**	**Ttn**
WP3														1157.0	1028.0	
89-20																1169.0
1157													12.0			
1170													19.0			
1171													13.0			
1173													22.0			
1174													10.0			
1175													10.0			
1176													8.0			
1177													10.0			
1178													14.0			
1179													23.0			
1180													78.0			
1181													12.0			
1182													10.0			
1183													14.0			
1184													10.0			
1185													12.0			
1186													10.0			
1187													11.0			
1188													8.0			
1189													8.0			
1190													6.0			
1191													720.0			
1192													7.0			
1193													66.0			
1194													1680.0			
1195													44.0			
1196													11.0			
1197													10.0			
1198													22.0			
1199													11.0			
1200													12.0			
1201													21.0			
1202													19.0			
1203													10.0			
1204													12.0			
1205													10.0			
1206													10.0			
1207													15.0			
1208													10.0			
1209													22.0			
1210													12.0			
1211													10.0			
1212													12.0			
1213													24.0			
1214													14.0			

reported	*mg/kg*	*mg/kg*	*mg/kg*	*mg/kg*	*mg/kg*	*mg/kg*	*mg/kg*	*mg/kg*	*mg/kg*	*mg/kg*	*mg/kg*	*mg/kg*	*mg/kg*	*Age*	*Age*	*Age*
Sample Number	**Ta**	**Tb**	**Th**	**Ti**	**Tl**	**Tm**	**U**	**V**	**W**	**Y**	**Yb**	**Zn**	**Zr**	**Zrn**	**Ru**	**Ttn**
1215													36.0			
1216													18.0			
1217													10.0			
1218													37.0			
1219													13.0			
1220													24.0			
1221													260.0			
1222													16.0			
1223													32.0			
1224													58.0			
1225													85.0			
1226													12.0			
1227													17.0			
1228													12.0			
1229													400.0			
1230													15.0			
1231													8.0			
1232													18.0			
1233													11.0			
1234													170.0			
1235													29.0			
1236													310.0			
1237													10.0			
1238													14.0			
1239													22.0			
1240													30.0			
1241													17.0			
1242													47.0			
1243													37.0			
1244													30.0			
1246													15.0			
1247													18.0			
1248													36.0			
1249													16.0			
1250													18.0			
1251													25.0			
1252													18.0			
1257													10.0			
1258													24.0			
1259													10.0			
1276													20.0			
1277													46.0			
1278													7.0			
1279													6.0			
1284													13.0			
1285													18.0			
15RME-0247	0.9	0.5	4.4	5787.0	1.0	0.3	0.6	98.5	0.2	18.4	1.9	44.0	231.0	1176.6		

reported	*mg/kg*	*mg/kg*	*mg/kg*	*mg/kg*	*mg/kg*	*mg/kg*	*mg/kg*	*mg/kg*	*mg/kg*	*mg/kg*	*mg/kg*	*mg/kg*	*mg/kg*	*Age*	*Age*	*Age*
Sample Number	**Ta**	**Tb**	**Th**	**Ti**	**Tl**	**Tm**	**U**	**V**	**W**	**Y**	**Yb**	**Zn**	**Zr**	**Zrn**	**Ru**	**Ttn**
15RME-0403	1.6	1.6	7.0	12296.0	0.6	0.5	2.4	87.8	0.2	40.6	3.3	95.0	587.0			1070.0
15RME-0411	0.6	0.6	4.5	3808.0	0.4	0.3	1.1	82.3	0.3	19.0	2.1	5.0	136.0			
15RME-0420	1.0	1.5	17.1	8544.0	0.2	0.7	1.6	165.7	0.8	49.3	4.5	12.0	199.0	1166.1	926.0	
15RME-0452	0.6	1.1	0.2	4406.0	0.1	0.6	0.3	91.6	0.4	40.2	3.9	43.0	149.0			
16RME-0208	0.4	0.6	0.8	6001.0	0.5	0.3	0.6	81.2	0.2	18.6	1.8	29.0	271.0			
16RME-0214	0.9	0.3	2.6	9470.0	0.5	0.3	0.5	187.1	0.1	15.4	2.2	12.0	176.0			
16RME-0222	0.3	0.7	2.3	5655.0	0.4	0.4	0.3	77.4	0.1	25.5	3.1	47.0	271.0			
16RME-0225	0.4	0.8	5.1	6295.0	0.6	0.7	0.7	102.6	0.3	32.3	4.5	147.0	289.0			
16RME-0227	0.1	0.4	1.6	2060.0	0.4	0.3	0.4	36.3	0.2	15.1	2.2	18.0	196.0			
16RME-0230	0.5	1.3	10.7	5033.0	0.6	0.7	0.8	91.5	0.1	46.4	4.6	36.0	247.0			
16RME-0231	0.5	0.8	8.7	5830.0	0.8	0.5	0.4	108.9	0.1	27.5	3.5	77.0	214.0			
16RME-0236	0.3	0.1	0.5	556.0	0.6	0.1	0.5	7.5	0.2	4.3	0.8	7.0	89.0			
16RME-0265	0.7	0.9	6.9	4057.0	0.3	0.5	2.5	80.8	1.5	29.3	3.1	61.0	136.0			
16RME-0358	1.1	1.1	9.9	7613.0	0.3	0.6	1.5	124.4	1.0	37.5	3.7	11.0	230.0			
16RME-0360	1.0	1.1	8.2	6835.0	0.1	0.5	1.4	107.3	0.9	35.5	3.2	5.0	193.0			
16RME-0362	0.3	0.4	3.2	1315.0	0.2	0.2	1.0	16.4	0.2	14.4	1.6	24.0	127.0			
16RME-0371	1.1	0.6	3.3	8162.0	1.0	0.4	0.5	153.7	2.1	20.8	2.6	42.0	200.0			
16RME-0390	0.4	0.7	1.6	3018.0	0.4	0.4	0.5	50.7	0.6	26.9	2.9	19.0	271.0			
16RME-0391	0.3	0.6	0.9	2929.0	0.8	0.4	0.5	53.2	0.7	22.0	2.4	109.0	52.0			
16RME-0396	0.5	0.8	1.2	5047.0	0.8	0.4	0.9	105.1	3.4	29.2	2.9	75.0	143.0			
16RME-0456	0.6	1.0	14.7	9230.0	0.6	0.8	0.7	173.5	0.0	38.4	5.5	75.0	173.0			
16RME-0558	1.1	1.0	9.5	9203.0	0.5	0.6	0.9	139.9	0.6	35.6	3.9	47.0	242.0			
16RME-0571	0.8	1.1	12.8	6944.0	0.7	0.6	0.8	123.9	0.2	35.8	3.9	58.0	187.0			
15RME-0092	0.1	1.3	5.7	1093.0	0.5	1.0	0.8	4.8	0.1	55.7	6.7	14.0	282.0			
94RME-0016	0.2	0.2	1.1	402.0	0.0	0.1	0.3	4.0	0.1	8.4	0.9	5.0	84.0			
15RME-0396	0.2	0.3	2.7	1066.0	0.1	0.2	0.5	10.5	0.1	12.2	1.2	4.0	157.0		1019.0	1158.0
16RME-0394	0.4	0.2	5.0	903.0	0.8	0.1	1.9	10.6	0.2	4.6	0.4	42.0	93.0			
16RME-0491	0.1	0.1	0.4	1750.0	0.0	0.0	0.2	26.3	0.1	2.4	0.3	11.0	93.0			
15RME-0233	0.0	0.1	0.1	225.0	0.0	0.1	0.0	9.5	0.0	4.8	0.4	3.0	7.0			
15RME-0234	0.0	0.1	0.1	61.0	0.0	0.0	0.0	2.7	0.0	3.6	0.2	14.0	7.0			
15RME-0331	0.0	0.1	0.3	427.0	0.1	0.1	0.0	16.4	0.0	5.1	0.4	16.0	9.0			
15RME-0335	0.0	0.1	0.2	76.0	0.0	0.0	0.0	2.2	0.1	3.0	0.2	75.0	6.0			
15RME-0350	0.0	0.2	0.2	80.0	0.0	0.1	0.0	1.8	0.0	7.7	0.6	6.0	9.0			
15RME-0351	0.0	0.1	0.3	105.0	0.0	0.0	0.1	2.5	0.0	3.6	0.3	4.0	9.0			
15RME-0366	0.0	0.0	0.1	54.0	0.0	0.0	0.1	2.4	0.1	0.9	0.1	5.0	3.0			
15RME-0402	0.0	0.0	0.3	92.0	0.0	0.0	0.4	2.0	0.1	0.8	0.1	7.0	3.0			
15RME-0410	0.1	0.2	0.9	347.0	0.1	0.1	0.3	11.7	0.1	7.4	0.7	9.0	12.0			
16RME-0108	0.0	1.4	8.9	3.5	0.0	0.6	0.1	0.4	0.0	43.3	3.7	5.0	3.0			
16RME-0115	0.0	0.1	0.0	94.0	0.0	0.0	0.0	2.4	0.1	4.3	0.3	8.0	3.0			
16RME-0153	0.0	0.1	0.2	22.0	0.0	0.0	0.0	1.6	0.0	3.5	0.2	7.0	3.0			
16RME-0212	0.1	0.3	2.7	568.0	0.2	0.1	0.7	16.2	0.1	10.9	0.9	22.0	29.0			
16RME-0264	0.0	0.1	1.4	92.0	0.0	0.0	0.3	2.5	0.0	1.9	0.2	4.0	3.0			
16RME-0297	0.0	0.2	0.9	71.0	0.0	0.1	0.3	2.1	0.3	7.1	0.5	6.0	3.0			
16RME-0298	0.0	0.1	0.2	93.0	0.0	0.0	0.1	2.5	0.0	3.9	0.3	5.0	10.0			
16RME-0335	0.0	0.1	0.1	76.0	0.0	0.0	0.0	1.7	0.1	3.9	0.2	6.0	3.0			
16RME-0433	0.0	0.1	1.5	204.0	0.1	0.0	0.2	4.8	0.0	3.4	0.3	14.0	8.0			
16RME-0557B	0.0	0.0	0.5	105.0	0.0	0.0	0.2	4.1	0.0	1.7	0.1	12.0	7.0			

reported	*mg/kg*	*mg/kg*	*mg/kg*	*mg/kg*	*mg/kg*	*mg/kg*	*mg/kg*	*mg/kg*	*mg/kg*	*mg/kg*	*mg/kg*	*mg/kg*	*mg/kg*	*Age*	*Age*	*Age*
Sample Number	**Ta**	**Tb**	**Th**	**Ti**	**Tl**	**Tm**	**U**	**V**	**W**	**Y**	**Yb**	**Zn**	**Zr**	**Zrn**	**Ru**	**Ttn**
16RME-0560	0.0	0.4	3.7	183.0	0.0	0.2	0.3	6.4	0.0	13.0	1.0	7.0	13.0			
16RME-0573A	0.0	0.3	2.4	85.0	0.0	0.1	0.2	2.0	0.0	9.3	0.8	7.0	7.0			
16RME-0591	0.0	0.1	0.1	60.0	0.0	0.0	0.0	1.5	0.0	3.9	0.2	12.0	3.0			
AKR21														1195.6		
MP6A														1179.2		
96TE17														1148.4		
09PH01B																
09PH04																
09PH05																
09PH10																
09PH18																
09TE09																
09TE21																
09WE12																
09WE17																
96GE02																
96GE09																
96GE20																
96GE22																
96GE24																
96GE27																
96GE30																
96PH04																
96PH06																
96PH07																
96TE15																
96TE23																
96TE25																
96TE26																
96WT03																
96WT04																
96WT15																
96WT27																
809-2A																
809-2B																
809-3																
809-8																
809-9																
809-12																
809-15A																
809-15B																
809-20																
811-7																
811-11																
811-12																
811-14A																
811-14B																

reported	*mg/kg*	*mg/kg*	*mg/kg*	*mg/kg*	*mg/kg*	*mg/kg*	*mg/kg*	*mg/kg*	*mg/kg*	*mg/kg*	*mg/kg*	*mg/kg*	*mg/kg*	*Age*	*Age*	*Age*
Sample Number	**Ta**	**Tb**	**Th**	**Ti**	**Tl**	**Tm**	**U**	**V**	**W**	**Y**	**Yb**	**Zn**	**Zr**	**Zrn**	**Ru**	**Ttn**
811-23																
811-2																
812-11																
812-12																
FA6																
FA7																
802-7																
808-5																
811-13																
811-16																
811-21																
303																
3011																
20CK06B								126.0		27.0			214.0			
20CK46A								194.0		55.0			301.0			
21CK76B	1.0	2.4	2.3		0.3	1.0	0.6	187.0	1.7	72.8	6.4	150.0	314.0			
20CK14A								69.0		40.0			223.0			
20CK52A								108.0		27.0			155.0			
20CK25A1								101.0		19.0			143.0			
21CK43C	0.9	1.2	5.8		0.1	0.7	1.6	85.0	0.5	41.0	4.8	19.0	439.0			
21CK43B	1.0	0.9	15.3		0.5	0.4	1.0	91.0	0.3	28.4	2.7	80.0	215.0			
20CK61A									132.0	74.0			230.0			
20CK85B									119.0	31.0			259.0			
20CK16A									91.0	27.0			323.0			
21CK44A	0.7	0.9	8.9		0.6	0.4	0.7	175.0	7.4	27.0	2.7	70.0	170.0			
21CK46A	0.8	1.0	8.2		0.5	0.6	0.9	163.0	0.3	34.0	3.8	210.0	201.0			
21CK45A	0.8	1.2	9.9		0.5	1.6	0.8	139.0	0.3	67.8	11.7	40.0	161.0			
20CK92B									70.0	21.0			159.0			
20CK28A1									87.0	46.0			171.0			
20CK68B									17.0	5.0			32.0			
21CK36A	0.6	1.1	11.4		0.6	0.4	1.4	119.0	0.3	32.6	2.5	150.0	208.0			
21CK33A	0.8	0.4	3.7		0.3	0.3	0.4	197.0	0.3	12.7	2.0	240.0	168.0			
H-29								175.0		41.0	7.0		130.0			
H-60								160.0		67.0	11.0		240.0			
H-66								185.0		40.0	8.0		170.0			
H-70								195.0		45.0	11.0		203.0			
H-90								150.0		51.0	11.0		190.0			
H-105								135.0		68.0	10.0		205.0			
H-126								132.0		57.0	9.0		117.0			
WE-4-58								162.0		60.0	13.0		109.0			
WE-10-57																
WE-17-57																

reported	*Age*	*Age*	*Reported*	*Reported*	*Reported*	*Reported*	*Calc*	*Calc*	*Calc*	*Calc*	*Reported*
Sample Number	**Ap**	**Hbl**	**[Sm]**	**[Nd]**	**147Sm/144Nd**	**143Nd/144Nd**	**tDM (Sm-Nd)**	**tCHUR (Sm-Nd)**	**147/144 (i)**	**εNd**	**87Rb/86Sr**
FA86-3	1104	1104									
FA86-10	1007	1007									
FA86-1	1114	1114									
FA86-4	1110	1110									
FA86-5	1108	1108									
FA86-6	1118	1118									
105											
114											
125											
127											
128											
129											
131											
132											
133											
135											
137											
144											
148											
155											
156											
161											
173											
182											
183											
185											
186											
189											
190											
194											
211											
212											
229											
61-021											
64-025											
64-002											
64-003											
64-004											
64-007											
64-008											
64-010											
64-011											
64-012											
64-015											
64-020											
64-026											
64-027											

reported Sample Number	*Age* Ap	*Age* Hbl	*Reported* [Sm]	*Reported* [Nd]	*Reported* 147Sm/144Nd	*Reported* 143Nd/144Nd	*Calc* tDM (Sm-Nd)	*Calc* tCHUR (Sm-Nd)	*Calc* 147/144 (i)	*Calc* εNd	*Reported* 87Rb/86Sr
64-028											
64-029											
64-49											
64-53											
64-54											
64-55											
64-56											
64-57											
64-65											
FJ46			13.45	70.4	0.1155	0.512229	1430.38	768.24	0.51135	4.15	
FJ45			11.82	59.1	0.1209	0.51225	1478.99	780.68	0.51133	3.75	
FJ25			13.42	64.7	0.1255	0.51228	1504.27	766.89	0.51132	3.65	
FJ26			2.53	14.2	0.1076	0.512157	1427.17	823.23	0.51133	3.92	
FJ9			15.55	73.1	0.1286	0.512311	1503.65	732.46	0.51133	3.79	
FJ12			7.51	41.7	0.1088	0.512147	1457.88	851.74	0.51131	3.55	
FJ44			14.65	70.7	0.1253	0.512331	1413.40	656.04	0.51137	4.68	
FJ67			15.36	63	0.1473	0.512545	1391.25	287.59	0.51142	5.57	
FJ2			30.04	120.9	0.1503	0.512546	1454.48	302.87	0.51140	5.14	
FJ60			18.44	76.7	0.1453	0.512507	1434.99	389.20	0.51140	5.13	
FJ22			3.36	17.4	0.117	0.51213	1607.63	971.51	0.51124	1.99	
FJ8			10.58	45.3	0.1412	0.512385	1609.26	695.44	0.51131	3.35	
FJ78			7.71	36.5	0.1278	0.512229	1634.34	904.98	0.51125	2.31	
FJ7			6.84	34.9	0.1185	0.51217	1569.21	912.36	0.51126	2.55	
FJ63			1.87	9.9	0.1141	0.512144	1539.71	911.75	0.51127	2.69	
FJ64			7.58	36.2	0.1266	0.512206	1651.91	939.41	0.51124	2.04	
FJ4			8.32	37.8	0.1331	0.512271	1662.44	879.79	0.51125	2.34	
FJ3			11	49.4	0.1346	0.51228	1676.60	878.95	0.51125	2.29	
FJ97			8.08	39.2	0.1246	0.512236	1563.98	850.17	0.51128	2.92	
FJ21			5.56	31.9	0.1053	0.512041	1559.20	995.49	0.51124	2.00	
R7085											0.079
R7083											0.684
R7070											0.873
R7090											0.394
R7113											2.998
R7062											0.154
R7061											0.822
R7112											1.789
R7071											1.023
FA1			9	42.8	0.1273	0.512	2025.85	1399.25	0.51103	-2.10	5.0794
FA2			9.2	40.4	0.1379	0.51212	2068.45	1341.12	0.51107	-1.34	3.318
FA3			5.9	28.5	0.1257	0.51206	1886.15	1239.74	0.51110	-0.68	0.9798
.1-3			8.1	39.7	0.1235	0.51195	2024.71	1430.43	0.51101	-2.51	9.6295
.1-5			9.2	50.2	0.1105	0.51167	2180.81	1707.51	0.51082	-6.04	4.46
.1-7			8.4	44.9	0.1126	0.51169	2195.98	1713.95	0.51083	-5.96	4.1462
.2-0			7.8	42.9	0.1104	0.51195	1769.17	1214.16	0.51111	-0.55	3.4216
.2-1	990		5.2	24.2	0.1298	0.51218	1761.54	1043.23	0.51119	1.05	0.5963
WP2	990		5.7	29.2	0.118	0.51191	1972.12	1407.92	0.51101	-2.47	

reported	*Age*	*Age*	*Reported*	*Reported*	*Reported*	*Reported*	*Calc*	*Calc*	*Calc*	*Calc*	*Reported*
Sample Number	**Ap**	**Hbl**	**[Sm]**	**[Nd]**	**147Sm/144Nd**	**143Nd/144Nd**	**tDM (Sm-Nd)**	**tCHUR (Sm-Nd)**	**147/144 (i)**	**εNd**	**87Rb/86Sr**
WP3			6.3	32	0.1189	0.51203	1799.37	1190.30	0.51112	-0.25	
89-20											
1157											
1170											
1171											
1173											
1174											
1175											
1176											
1177											
1178											
1179											
1180											
1181											
1182											
1183											
1184											
1185											
1186											
1187											
1188											
1189											
1190											
1191											
1192											
1193											
1194											
1195											
1196											
1197											
1198											
1199											
1200											
1201											
1202											
1203											
1204											
1205											
1206											
1207											
1208											
1209											
1210											
1211											
1212											
1213											
1214											

reported	*Age*	*Age*	*Reported*	*Reported*	*Reported*	*Reported*	*Calc*	*Calc*	*Calc*	*Calc*	*Reported*
Sample Number	**Ap**	**Hbl**	**[Sm]**	**[Nd]**	**147Sm/144Nd**	**143Nd/144Nd**	**tDM (Sm-Nd)**	**tCHUR (Sm-Nd)**	**147/144 (i)**	**εNd**	**87Rb/86Sr**
1215											
1216											
1217											
1218											
1219											
1220											
1221											
1222											
1223											
1224											
1225											
1226											
1227											
1228											
1229											
1230											
1231											
1232											
1233											
1234											
1235											
1236											
1237											
1238											
1239											
1240											
1241											
1242											
1243											
1244											
1246											
1247											
1248											
1249											
1250											
1251											
1252											
1257											
1258											
1259											
1276											
1277											
1278											
1279											
1284											
1285											
15RME-0247											

reported	*Age*	*Age*	*Reported*	*Reported*	*Reported*	*Reported*	*Calc*	*Calc*	*Calc*	*Calc*	*Reported*
Sample Number	**Ap**	**Hbl**	**[Sm]**	**[Nd]**	**147Sm/144Nd**	**143Nd/144Nd**	**tDM (Sm-Nd)**	**tCHUR (Sm-Nd)**	**147/144 (i)**	**εNd**	**87Rb/86Sr**
15RME-0403	993										
15RME-0411											
15RME-0420											
15RME-0452											
16RME-0208											
16RME-0214											
16RME-0222											
16RME-0225											
16RME-0227											
16RME-0230											
16RME-0231											
16RME-0236											
16RME-0265											
16RME-0358											
16RME-0360											
16RME-0362											
16RME-0371											
16RME-0390											
16RME-0391											
16RME-0396											
16RME-0456											
16RME-0558											
16RME-0571											
15RME-0092											
94RME-0016											
15RME-0396											
16RME-0394											
16RME-0491											
15RME-0233											
15RME-0234											
15RME-0331											
15RME-0335											
15RME-0350											
15RME-0351											
15RME-0366											
15RME-0402											
15RME-0410											
16RME-0108											
16RME-0115											
16RME-0153											
16RME-0212											
16RME-0264											
16RME-0297											
16RME-0298											
16RME-0335											
16RME-0433											
16RME-0557B											

reported	*Age*	*Age*	*Reported*	*Reported*	*Reported*	*Reported*	*Calc*	*Calc*	*Calc*	*Calc*	*Reported*
Sample Number	**Ap**	**Hbl**	**[Sm]**	**[Nd]**	**147Sm/144Nd**	**143Nd/144Nd**	**tDM (Sm-Nd)**	**tCHUR (Sm-Nd)**	**147/144 (i)**	**εNd**	**87Rb/86Sr**
16RME-0560											
16RME-0573A											
16RME-0591											
AKR21											
MP6A											
96TE17											
09PH01B											
09PH04											
09PH05											
09PH10											
09PH18											
09TE09											
09TE21											
09WE12											
09WE17											
96GE02											
96GE09											
96GE20											
96GE22											
96GE24											
96GE27											
96GE30											
96PH04											
96PH06											
96PH07											
96TE15											
96TE23											
96TE25											
96TE26											
96WT03											
96WT04											
96WT15											
96WT27											
809-2A											
809-2B											
809-3											
809-8											
809-9											
809-12											
809-15A											
809-15B											
809-20											
811-7											
811-11											
811-12											
811-14A											
811-14B											

reported	*Age*	*Age*	*Reported*	*Reported*	*Reported*	*Reported*	*Calc*	*Calc*	*Calc*	*Calc*	*Reported*
Sample Number	**Ap**	**Hbl**	**[Sm]**	**[Nd]**	**147Sm/144Nd**	**143Nd/144Nd**	**tDM (Sm-Nd)**	**tCHUR (Sm-Nd)**	**147/144 (i)**	**εNd**	**87Rb/86Sr**
811-23											
811-2											
812-11											
812-12											
FA6											
FA7											
802-7											
808-5											
811-13											
811-16											
811-21											
303											
3011											
20CK06B											
20CK46A											
21CK76B											
20CK14A											
20CK52A											
20CK25A1											
21CK43C											
21CK43B											
20CK61A											
20CK85B											
20CK16A											
21CK44A											
21CK46A											
21CK45A											
20CK92B											
20CK28A1											
20CK68B											
21CK36A											
21CK33A											
H-29											
H-60											
H-66											
H-70											
H-90											
H-105											
H-126											
WE-4-58											
WE-10-57											
WE-17-57											

reported	*Reported*	*Reported*	*Reported*	*Calc*	*Calc*	*Calc*	*Calc*	*Reported*	*Reported*	*Calc*	*Calc*
Sample Number	**87Sr/86Sr**	**[Rb]**	**[Sr]**	**tDM (Rb-Sr)**	**tCHUR (Rb-Sr)**	**87/86 (i)**	**εSr**	**δO18**	**δC13**	**Mg#**	**A/NK**
FA86-3											
FA86-10											
FA86-1											
FA86-4											
FA86-5											
FA86-6											
105										0.19	1.31
114										0.19	1.64
125										0.28	1.15
127										0.43	1.64
128										0.32	2.42
129										0.31	1.72
131										0.38	1.45
132										0.34	1.33
133										0.21	1.02
135										0.35	1.35
137										0.53	1.09
144										0.27	1.45
148										0.17	1.81
155										0.21	1.63
156										0.22	1.69
161										0.09	2.22
173										0.24	2.32
182										0.33	1.70
183										0.39	1.42
185										0.40	1.38
186										0.29	1.60
189										0.32	1.37
190										0.38	2.39
194										0.47	2.12
211										0.69	1.50
212										0.38	1.48
229										0.23	2.82
61-021										0.15	2.05
64-025										0.20	2.42
64-002										0.40	1.26
64-003										0.37	1.26
64-004										0.26	0.92
64-007										0.30	1.82
64-008										0.23	1.54
64-010										0.29	1.91
64-011										0.27	1.45
64-012										0.30	1.52
64-015										0.47	1.48
64-020										0.31	1.71
64-026										0.41	1.47
64-027										0.26	1.49

reported	*Reported*	*Reported*	*Reported*	*Calc*	*Calc*	*Calc*	*Calc*	*Reported*	*Reported*	*Calc*	*Calc*
Sample Number	**87Sr/86Sr**	**[Rb]**	**[Sr]**	**tDM (Rb-Sr)**	**tCHUR (Rb-Sr)**	**87/86 (i)**	**εSr**	**δO18**	**δC13**	**Mg#**	**A/NK**
64-028										0.45	2.01
64-029										0.44	1.37
64-49										0.29	2.43
64-53										0.34	1.15
64-54										0.17	1.21
64-55										0.23	1.77
64-56										0.18	1.18
64-57										0.32	2.27
64-65										0.27	1.91
FJ46											
FJ45											
FJ25											
FJ26											
FJ9											
FJ12											
FJ44											
FJ67											
FJ2											
FJ60											
FJ22											
FJ8											
FJ78											
FJ7											
FJ63											
FJ64											
FJ4											
FJ3											
FJ97											
FJ21											
R7085	0.7078	15	530	6364.36		0.70650	47.20				
R7083	0.7203	85	359	1899.29		0.70908	83.79				
R7070	0.7193	140	466	1399.37		0.70498	25.47				
R7090	0.7245	57	417	4112.89		0.71804	211.19				
R7113	0.7628	125	121	1435.90		0.71361	148.23				
R7062	0.7091	24	454	3492.50		0.70657	48.19				
R7061	0.7219	28	99	1715.15		0.70841	74.34				
R7112	0.7393	88	142	1475.47		0.70995	96.15				
R7071	0.7234	63	180	1479.18		0.70661	48.77				
FA1	0.80315			1410.60		0.71981	236.37	23.5	3.9	0.27	1.73
FA2	0.77404			1537.07		0.71960	233.41	13.4		0.39	1.59
FA3	0.72328			1536.40		0.70720	57.15	18.3	-1.1	0.34	1.08
.1-3	0.89179			1396.62		0.73379	435.20	24.1	1.6	0.28	0.29
.1-5	0.7958			1489.27		0.72262	276.38	22.9	2.9	0.24	4.11
.1-7	0.77994			1331.63		0.71191	124.06	25.4	2.6	0.21	2.50
.2-0	0.77748			1561.62		0.72134	258.15			0.51	1.45
.2-1	0.71624			1692.42		0.70646	46.52			0.55	1.30
WP2										0.30	1.39

reported	*Reported*	*Reported*	*Reported*	*Calc*	*Calc*	*Calc*	*Calc*	*Reported*	*Reported*	*Calc*	*Calc*
Sample Number	**87Sr/86Sr**	**[Rb]**	**[Sr]**	**tDM (Rb-Sr)**	**tCHUR (Rb-Sr)**	**87/86 (i)**	**εSr**	**δO18**	**δC13**	**Mg#**	**A/NK**
WP3										0.38	1.26
89-20											
1157										0.99	4.03
1170										0.92	2.21
1171										0.68	5.13
1173										0.83	14.13
1174										0.91	2.94
1175										0.83	2.63
1176										0.98	9.17
1177										0.74	2.51
1178										0.93	2.08
1179										0.88	3.05
1180										0.98	2.13
1181										0.94	17.60
1182										0.98	10.42
1183										0.97	8.80
1184										0.98	7.70
1185										0.89	4.17
1186										0.84	3.92
1187										0.96	1.76
1188										0.97	36.66
1189										0.91	1.96
1190										0.77	5.34
1191										0.80	39.67
1192										0.69	7.23
1193										0.36	3.83
1194										0.88	3.07
1195										0.89	40.70
1196										0.89	49.50
1197										0.97	1.89
1198										0.92	2.19
1199										0.93	29.66
1200										0.91	53.53
1201										0.95	1.62
1202										0.90	10.34
1203										0.92	51.33
1204										0.89	2.34
1205										0.93	4.77
1206										1.00	4.72
1207										0.99	9.90
1208										0.96	4.34
1209										0.89	5.85
1210										1.00	6.23
1211										0.99	3.67
1212										1.00	4.77
1213										0.96	1.76
1214										0.88	27.63

reported	*Reported*	*Reported*	*Reported*	*Calc*	*Calc*	*Calc*	*Calc*	*Reported*	*Reported*	*Calc*	*Calc*
Sample Number	**87Sr/86Sr**	**[Rb]**	**[Sr]**	**tDM (Rb-Sr)**	**tCHUR (Rb-Sr)**	**87/86 (i)**	**εSr**	**δO18**	**δC13**	**Mg#**	**A/NK**
1215										0.80	102.20
1216										0.94	20.90
1217										0.93	25.30
1218										0.92	4.48
1219										1.00	4.03
1220										0.97	1.85
1221										0.76	5.72
1222										0.98	9.65
1223										0.91	19.27
1224										0.96	1.83
1225										0.96	2.46
1226										0.96	31.16
1227										0.97	10.27
1228										0.50	2.62
1229										0.95	8.83
1230										0.94	4.40
1231										0.85	1.93
1232										0.96	6.97
1233										0.95	18.70
1234										0.77	15.77
1235										0.82	112.19
1236										0.90	17.97
1237										0.95	23.10
1238										0.90	8.80
1239										0.96	1.78
1240										0.84	7.19
1241										0.98	3.47
1242										0.87	2.11
1243										0.96	18.11
1244										0.73	8.78
1246										0.98	2.23
1247										0.98	9.90
1248										0.97	9.97
1249										1.00	5.13
1250										0.97	5.50
1251										0.82	13.45
1252										0.98	5.87
1257										0.97	
1258										0.89	
1259										0.97	
1276										0.98	
1277										1.00	
1278										0.99	
1279										0.99	
1284										0.98	
1285										0.97	
15RME-0247										0.31	1.35

reported	*Reported*	*Reported*	*Reported*	*Calc*	*Calc*	*Calc*	*Calc*	*Reported*	*Reported*	*Calc*	*Calc*
Sample Number	**87Sr/86Sr**	**[Rb]**	**[Sr]**	**tDM (Rb-Sr)**	**tCHUR (Rb-Sr)**	**87/86 (i)**	**εSr**	**δO18**	**δC13**	**Mg#**	**A/NK**
15RME-0403										0.34	1.36
15RME-0411										0.64	1.24
15RME-0420										0.30	2.09
15RME-0452										0.72	1.37
16RME-0208										0.28	1.15
16RME-0214										0.34	2.74
16RME-0222										0.23	2.39
16RME-0225										0.43	1.11
16RME-0227										0.39	1.37
16RME-0230										0.34	1.37
16RME-0231										0.37	1.50
16RME-0236										0.29	1.17
16RME-0265										0.56	1.39
16RME-0358										0.59	1.27
16RME-0360										0.52	1.21
16RME-0362										0.56	1.87
16RME-0371										0.33	1.67
16RME-0390										0.40	1.20
16RME-0391										0.36	1.25
16RME-0396										0.55	1.32
16RME-0456										0.25	2.72
16RME-0558										0.35	2.21
16RME-0571										0.28	2.16
15RME-0092										0.06	1.27
94RME-0016										0.58	1.61
15RME-0396										0.39	1.89
16RME-0394										0.21	1.34
16RME-0491										0.11	2.94
15RME-0233										0.97	
15RME-0234										0.99	
15RME-0331										0.84	2.88
15RME-0335										0.99	
15RME-0350										0.98	
15RME-0351										0.93	
15RME-0366										0.97	
15RME-0402										0.98	
15RME-0410										0.65	1.74
16RME-0108										0.82	
16RME-0115										0.98	
16RME-0153										0.98	
16RME-0212										0.72	1.71
16RME-0264										0.97	4.23
16RME-0297										0.93	
16RME-0298										0.97	2.61
16RME-0335										0.98	
16RME-0433										0.94	1.88
16RME-0557B										0.83	1.92

reported	*Reported*	*Reported*	*Reported*	*Calc*	*Calc*	*Calc*	*Calc*	*Reported*	*Reported*	*Calc*	*Calc*
Sample Number	**87Sr/86Sr**	**[Rb]**	**[Sr]**	**tDM (Rb-Sr)**	**tCHUR (Rb-Sr)**	**87/86 (i)**	**εSr**	**δO18**	**δC13**	**Mg#**	**A/NK**
16RME-0560										0.83	3.61
16RME-0573A										0.89	2.65
16RME-0591										0.99	
AKR21											
MP6A											
96TE17											
09PH01B								25.07	2.29		
09PH04								25.73	2.55		
09PH05								26.04	0.87		
09PH10								23.47	2		
09PH18								25.4	2.58		
09TE09								23.63	-1.92		
09TE21								25.13	2.72		
09WE12								26.83	2.62		
09WE17								26.48	3.34		
96GE02								21.47	0		
96GE09								24.12	1.03		
96GE20								25.92	0.93		
96GE22								26.57	3.4		
96GE24								25.26	2.09		
96GE27								26.04	2.51		
96GE30								24.94	1.61		
96PH04								25.47	4.71		
96PH06								20.15	1.03		
96PH07								24.19	4.84		
96TE15								24.39	0.34		
96TE23								21.74	-1.46		
96TE25								23.96	2.29		
96TE26								23.59	0.76		
96WT03								24.34	2.44		
96WT04								21.56	-1.1		
96WT15								24.17	-0.29		
96WT27								22.44	1.34		
809-2A								15.3			
809-2B								16.2			
809-3								12.3			
809-8								12.2			
809-9								14.3			
809-12								12.3			
809-15A								16.9			
809-15B								12.2			
809-20								16.6			
811-7								16.2			
811-11								14.6			
811-12								14.1			
811-14A								15.4			
811-14B								15.7			

reported	*Reported*	*Reported*	*Reported*	*Calc*	*Calc*	*Calc*	*Calc*	*Reported*	*Reported*	*Calc*	*Calc*
Sample Number	**87Sr/86Sr**	**[Rb]**	**[Sr]**	**tDM (Rb-Sr)**	**tCHUR (Rb-Sr)**	**87/86 (i)**	**εSr**	**δO18**	**δC13**	**Mg#**	**A/NK**
811-23								15.5			
811-2								16.2			
812-11								13.4			
812-12								11.9			
FA6								16.2			
FA7								16.6			
802-7								26	2.9		
808-5								23.5	3.9		
811-13								21.4	-0.3		
811-16								18.3	-1.1		
811-21								24.1	1.6		
303								22.9	2.9		
3011								25.4	2.6		
20CK06B										0.33	1.62
20CK46A										0.27	1.40
21CK76B										0.22	1.48
20CK14A										0.39	1.04
20CK52A										0.57	1.14
20CK25A1										0.31	1.40
21CK43C										0.86	1.67
21CK43B										0.21	1.21
20CK61A										0.37	1.73
20CK85B										0.25	1.83
20CK16A										0.31	1.40
21CK44A										0.24	2.21
21CK46A										0.26	3.93
21CK45A										0.31	4.87
20CK92B										0.56	3.12
20CK28A1										0.45	1.54
20CK68B										0.28	1.44
21CK36A										0.35	1.91
21CK33A										0.22	6.09
H-29										0.34	2.67
H-60										0.39	2.33
H-66										0.32	2.63
H-70										0.31	3.17
H-90										0.33	2.09
H-105										0.31	1.89
H-126										0.26	2.47
WE-4-58										0.25	4.82
WE-10-57										0.28	3.59
WE-17-57										0.28	1.36

reported	*Calc*	*Calc*	*Calc*	*Calc*	*Calc*	*Calc*
Sample Number	**ASI**	**N+K-C**	**CIA**	**FeO(t)/FeO(t)+MgO**	**XFe2+**	**HP**
FA86-3						
FA86-10						
FA86-1						
FA86-4						
FA86-5						
FA86-6						
105	1.10	3.40	0.52	0.81	0.42	
114	1.09	4.60	0.52	0.81		
125	0.84	7.50	0.46	0.72	0.18	
127	0.85	1.60	0.46	0.57	0.74	
128	1.84	5.40	0.65	0.68	0.93	
129	1.28	6.40	0.56	0.69	0.66	
131	1.19	7.50	0.54	0.62	0.84	
132	0.99	7.70	0.50	0.66	0.70	
133	0.89	10.30	0.47	0.79	0.75	
135	0.86	5.50	0.46	0.65	0.72	
137	0.91	7.80	0.48	0.47		
144	1.34	7.80	0.57	0.73		
148	1.31	2.10	0.57	0.83	0.46	
155	1.38	7.50	0.58	0.79	0.79	
156	1.43	7.20	0.59	0.78	0.69	
161				0.91	0.52	
173	1.96	5.70	0.66	0.76	0.72	
182	1.48	7.30	0.60	0.67	0.57	
183	0.83	4.60	0.45	0.61	0.70	
185	1.02	6.10	0.51	0.60	0.69	
186	1.03	5.10	0.51	0.71	0.76	
189	0.95	7.10	0.49	0.68	0.65	
190	0.98	-0.10	0.49	0.62	0.40	
194	1.76	5.30	0.64	0.53	0.67	
211	1.17	5.80	0.54	0.31		
212	0.97	4.40	0.49	0.62	0.59	
229	2.47	4.90	0.71	0.77	0.79	
61-021	1.96	7.10	0.66	0.85	0.72	
64-025	1.84	1.70	0.65	0.80	0.56	
64-002	0.84	6.10	0.46	0.60	0.84	
64-003	0.98	6.70	0.49	0.63		
64-004	0.79	9.60	0.44	0.74		
64-007	1.61	7.30	0.62	0.70	0.71	
64-008	1.23	8.00	0.55	0.77	0.78	
64-010	1.51	5.20	0.60	0.71	0.64	
64-011	1.28	7.10	0.56	0.73	0.60	
64-012	1.19	6.60	0.54	0.70	0.62	
64-015	1.33	6.20	0.57	0.53	0.79	
64-020	1.30	5.10	0.57	0.69	0.81	
64-026	1.17	7.00	0.54	0.59	0.58	
64-027	1.16	6.40	0.54	0.74	0.64	

reported	*Calc*	*Calc*	*Calc*	*Calc*	*Calc*	*Calc*
Sample Number	**ASI**	**N+K-C**	**CIA**	**FeO(t)/FeO(t)+MgO**	**XFe2+**	**HP**
64-028	1.13	2.90	0.53	0.55		
64-029	0.87	4.50	0.46	0.56	0.61	
64-49	1.99	4.40	0.67	0.71	0.87	
64-53	0.83	6.20	0.45	0.66		
64-54	1.08	6.60	0.52	0.83	0.69	
64-55	1.29	6.60	0.56	0.77	0.83	
64-56	1.03	5.90	0.51	0.82	0.69	
64-57	1.49	4.20	0.60	0.68	0.83	
64-65	1.23	4.50	0.55	0.73		
FJ46						
FJ45						
FJ25						
FJ26						
FJ9						
FJ12						
FJ44						
FJ67						
FJ2						
FJ60						
FJ22						
FJ8						
FJ78						
FJ7						
FJ63						
FJ64						
FJ4						
FJ3						
FJ97						
FJ21						
R7085						
R7083						
R7070						
R7090						
R7113						
R7062						
R7061						
R7112						
R7071						
FA1	1.16	4.00	0.54	0.73		
FA2	0.94	2.80	0.49	0.61		
FA3	0.74	4.30	0.43	0.66		
.1-3	0.28	50.40	0.22	0.72		
.1-5	3.17	3.30	0.76	0.76		
.1-7	2.02	5.20	0.67	0.79		
.2-0	1.12	7.40	0.53	0.49		
.2-1	0.32	-8.00	0.24	0.45		
WP2	1.13	7.40	0.53	0.70		

reported	*Calc*	*Calc*	*Calc*	*Calc*	*Calc*	*Calc*
Sample Number	**ASI**	**N+K-C**	**CIA**	**FeO(t)/FeO(t)+MgO**	**XFe2+**	**HP**
WP3	0.85	4.70	0.46	0.62		
89-20						
1157	0.00	-44.18	0.43	0.01		
1170	0.01	-45.30	0.43	0.08		
1171	0.01	-55.49	0.43	0.32		
1173	0.01	-51.43	0.43	0.17		
1174	0.06	-28.85	0.43	0.09		
1175	0.10	-24.05	0.43	0.17		
1176	0.00	-54.48	0.43	0.02		
1177	0.04	-41.08	0.43	0.26		
1178	0.02	-29.15	0.43	0.07		
1179	0.03	-27.80	0.43	0.12		
1180	0.01	-41.91	0.43	0.02		
1181	0.01	-27.58	0.43	0.06		
1182	0.01	-29.86	0.43	0.02		
1183	0.00	-30.28	0.43	0.03		
1184	0.00	-59.88	0.43	0.02		
1185	0.00	-55.81	0.43	0.11		
1186	0.02	-30.18	0.43	0.16		
1187	0.01	-25.70	0.43	0.04		
1188	0.02	-29.28	0.43	0.03		
1189	0.04	-27.96	0.43	0.09		
1190	0.02	-24.32	0.43	0.23		
1191	0.03	-37.65	0.43	0.20		
1192	0.01	-31.64	0.43	0.31		
1193	0.10	-24.44	0.43	0.64		
1194	0.02	-31.09	0.43	0.12		
1195	0.02	-40.48	0.43	0.11		
1196	0.02	-32.68	0.43	0.11		
1197	0.05	-24.42	0.43	0.03		
1198	0.01	-43.91	0.43	0.08		
1199	0.02	-31.27	0.43	0.07		
1200	0.03	-31.08	0.43	0.09		
1201	0.02	-44.15	0.43	0.05		
1202	0.01	-49.04	0.43	0.10		
1203	0.03	-28.78	0.43	0.08		
1204	0.01	-39.97	0.43	0.11		
1205	0.00	-32.48	0.43	0.07		
1206	0.00	-56.27	0.43	0.00		
1207	0.00	-50.88	0.43	0.01		
1208	0.00	-57.52	0.43	0.04		
1209	0.01	-54.29	0.43	0.11		
1210	0.00	-52.58	0.43	0.00		
1211	0.00	-57.08	0.43	0.01		
1212	0.00	-51.18	0.43	0.00		
1213	0.00	-47.20	0.43	0.04		
1214	0.03	-30.84	0.43	0.12		

reported	*Calc*	*Calc*	*Calc*	*Calc*	*Calc*	*Calc*
Sample Number	**ASI**	**N+K-C**	**CIA**	**FeO(t)/FeO(t)+MgO**	**XFe2+**	**HP**
1215	0.11	-24.46	0.43	0.20		
1216	0.01	-36.08	0.43	0.06		
1217	0.01	-43.38	0.43	0.07		
1218	0.03	-30.89	0.43	0.08		
1219	0.00	-52.38	0.43	0.00		
1220	0.00	-51.33	0.43	0.03		
1221	0.02	-45.55	0.43	0.24		
1222	0.01	-48.32	0.43	0.02		
1223	0.02	-32.44	0.43	0.09		
1224	0.03	-27.89	0.43	0.04		
1225	0.01	-29.51	0.43	0.04		
1226	0.02	-30.88	0.43	0.04		
1227	0.00	-46.38	0.43	0.03		
1228	0.15	-15.64	0.43	0.50		1.06
1229	0.02	-29.11	0.43	0.05		0.22
1230	0.00	-53.08	0.43	0.06		0.39
1231	0.04	-26.13	0.43	0.15		1.26
1232	0.00	-32.48	0.43	0.04		0.10
1233	0.01	-33.48	0.43	0.05		
1234	0.00	-56.68	0.43	0.23		
1235	0.06	-26.18	0.43	0.18		
1236	0.01	-39.98	0.43	0.10		
1237	0.01	-28.68	0.43	0.05		
1238	0.00	-58.88	0.43	0.10		
1239	0.01	-51.12	0.43	0.04		
1240	0.01	-45.86	0.43	0.16		
1241	0.00	-54.16	0.43	0.02		
1242	0.03	-39.94	0.43	0.13		
1243	0.01	-31.07	0.43	0.04		
1244	0.03	-39.94	0.43	0.27		
1246	0.00	-52.16	0.43	0.02		0.70
1247	0.00	-46.18	0.43	0.02		
1248	0.00	-54.97	0.43	0.03		
1249	0.00	-56.68	0.43	0.00		
1250	0.00	-55.98	0.43	0.03		1.02
1251	0.01	-48.02	0.43	0.18		1.93
1252	0.00	-55.18	0.43	0.02		
1257				0.03		
1258				0.11		
1259				0.03		1.26
1276				0.02		1.19
1277				0.00		1.22
1278				0.01		
1279				0.01		
1284				0.02		
1285				0.03		1.79
15RME-0247	1.06	7.48	0.51	0.69	0.64	1.13

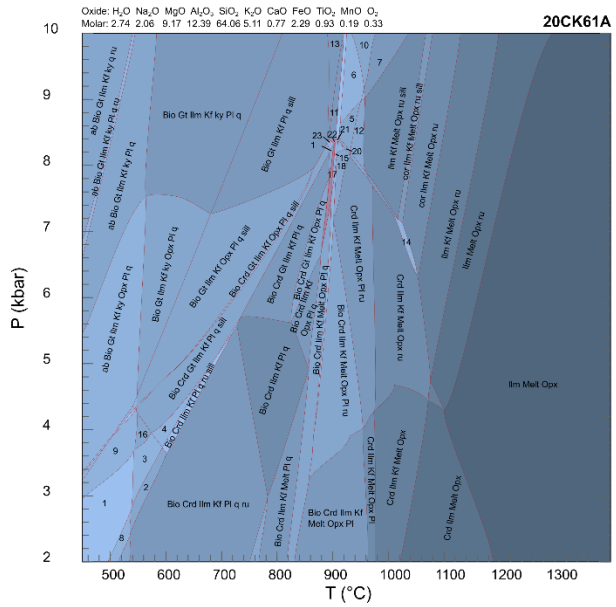
reported	*Calc*	*Calc*	*Calc*	*Calc*	*Calc*	*Calc*
Sample Number	**ASI**	**N+K-C**	**CIA**	**FeO(t)/FeO(t)+MgO**	**XFe2+**	**HP**
15RME-0403	0.92	5.90	0.48	0.66	0.66	1.56
15RME-0411	0.66	3.02	0.40	0.36	0.98	1.15
15RME-0420	1.76	6.19	0.64	0.70	0.81	2.03
15RME-0452	0.68	0.97	0.40	0.28	0.76	0.22
16RME-0208	0.70	4.05	0.41	0.72	0.48	0.75
16RME-0214	2.21	5.63	0.69	0.66	0.86	0.90
16RME-0222	1.13	0.94	0.53	0.77	0.54	0.53
16RME-0225	0.76	6.32	0.43	0.57	0.69	1.17
16RME-0227	0.97	6.34	0.43	0.61	0.63	0.76
16RME-0230	0.81	4.45	0.43	0.66	0.73	1.58
16RME-0231	1.34	8.84	0.43	0.63	0.83	1.48
16RME-0236	1.16	10.70	0.43	0.71	0.19	1.21
16RME-0265	0.34	-7.63	0.43	0.44	0.69	1.52
16RME-0358	1.05	7.57	0.43	0.41	0.55	1.42
16RME-0360	1.08	7.22	0.43	0.48	0.69	1.20
16RME-0362	0.62	-0.84	0.43	0.44	0.60	0.54
16RME-0371	1.52	7.77	0.43	0.67	0.82	1.14
16RME-0390	0.69	2.87	0.43	0.60	0.49	0.69
16RME-0391	0.88	5.30	0.43	0.64	0.58	0.66
16RME-0396	0.58	1.08	0.43	0.45	0.88	0.94
16RME-0456	2.30	5.52	0.43	0.75	0.86	1.78
16RME-0558	1.72	5.18	0.43	0.65	0.88	1.43
16RME-0571	1.63	5.26	0.43	0.72	0.92	1.69
15RME-0092	1.11	6.52	0.43	0.94	0.19	1.06
94RME-0016	1.01	0.65	0.43	0.42	0.71	0.22
15RME-0396	0.81	0.05	0.43	0.61	0.63	0.39
16RME-0394	1.13	7.18	0.43	0.79	0.48	1.26
16RME-0491	2.03	0.35	0.43	0.89	0.28	0.10
15RME-0233				0.03	0.96	0.02
15RME-0234				0.01		0.02
15RME-0331	0.01	-49.63	0.01	0.16	0.98	0.05
15RME-0335				0.01	0.96	0.03
15RME-0350				0.02		0.03
15RME-0351				0.07		0.07
15RME-0366				0.03		0.05
15RME-0402				0.02		0.15
15RME-0410	0.01	-50.35	0.01	0.35		0.19
16RME-0108				0.18	0.76	0.68
16RME-0115				0.02		0.02
16RME-0153				0.02		0.02
16RME-0212	0.03	-42.76	0.03	0.28	0.73	0.49
16RME-0264	0.01	-47.64	0.01	0.03		0.20
16RME-0297				0.07		0.16
16RME-0298	0.00	-48.04	0.00	0.03		0.04
16RME-0335				0.02		0.03
16RME-0433	0.01	-47.11	0.01	0.06	1.01	0.18
16RME-0557B	0.01	-51.06	0.01	0.17		0.11

reported	*Calc*	*Calc*	*Calc*	*Calc*	*Calc*	*Calc*
Sample Number	**ASI**	**N+K-C**	**CIA**	**FeO(t)/FeO(t)+MgO**	**XFe2+**	**HP**
16RME-0560	0.01	-50.48	0.01	0.17	0.91	0.37
16RME-0573A	0.01	-50.13	0.00	0.11	0.93	0.24
16RME-0591				0.01		0.01
AKR21						
MP6A						
96TE17						
09PH01B						
09PH04						
09PH05						
09PH10						
09PH18						
09TE09						
09TE21						
09WE12						
09WE17						
96GE02						
96GE09						
96GE20						
96GE22						
96GE24						
96GE27						
96GE30						
96PH04						
96PH06						
96PH07						
96TE15						
96TE23						
96TE25						
96TE26						
96WT03						
96WT04						
96WT15						
96WT27						
809-2A						
809-2B						
809-3						
809-8						
809-9						
809-12						
809-15A						
809-15B						
809-20						
811-7						
811-11						
811-12						
811-14A						
811-14B						

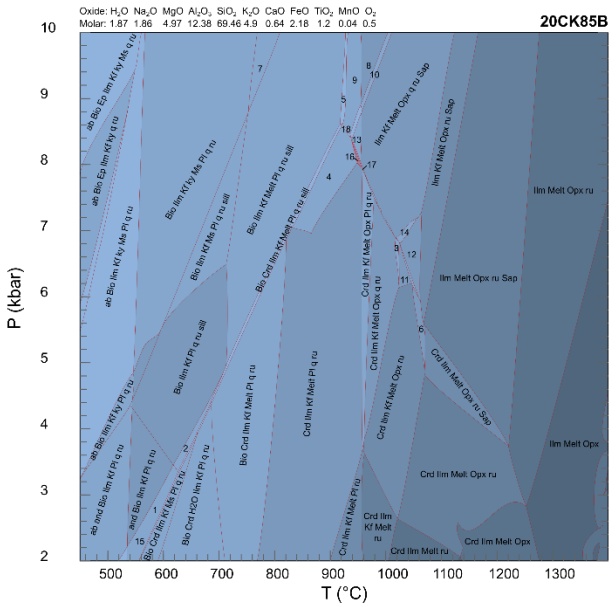
reported	*Calc*	*Calc*	*Calc*	*Calc*	*Calc*	*Calc*
Sample Number	**ASI**	**N+K-C**	**CIA**	**FeO(t)/FeO(t)+MgO**	**XFe2+**	**HP**
811-23						
811-2						
812-11						
812-12						
FA6						
FA7						
802-7						
808-5						
811-13						
811-16						
811-21						
303						
3011						
20CK06B	1.36	6.85	0.43	0.67	0.68	
20CK46A	0.71	2.26	0.43	0.73	0.47	
21CK76B	0.70	1.14	0.43	0.78	0.55	0.70
20CK14A	0.49	2.19	0.43	0.61	0.65	
20CK52A	0.44	-2.42	0.43	0.43	0.63	
20CK25A1	0.97	5.03	0.43	0.69	0.51	
21CK43C	0.46	-4.23	0.43	0.14		1.02
21CK43B	1.16	9.37	0.43	0.79	0.24	1.93
20CK61A	1.56	8.02	0.43	0.63	0.82	
20CK85B	1.67	7.60	0.43	0.75	0.17	
20CK16A	1.14	5.95	0.43	0.69	0.32	
21CK44A	1.34	3.66	0.43	0.76	0.85	1.26
21CK46A	2.36	2.38	0.43	0.74	0.64	1.19
21CK45A	2.58	1.39	0.43	0.69	0.67	1.22
20CK92B	0.31	-15.69	0.43	0.44	0.78	
20CK28A1	0.35	-9.01	0.43	0.55	0.35	
20CK68B	0.75	0.32	0.43	0.72	0.68	
21CK36A	1.66	6.50	0.43	0.65	0.58	1.79
21CK33A	3.84	1.66	0.43	0.78	0.65	0.59
H-29	1.76	3.44	0.43	0.66	0.90	
H-60	2.19	7.04	0.43	0.61	0.60	
H-66	1.97	4.81	0.43	0.68	0.93	
H-70	2.11	3.32	0.43	0.69	0.61	
H-90	1.95	7.12	0.43	0.67	0.64	
H-105	1.69	6.30	0.43	0.69	0.66	
H-126	1.61	3.55	0.43	0.74	0.92	
WE-4-58	3.54	2.46	0.43	0.75	0.82	
WE-10-57	2.36	3.13	0.43	0.72	0.64	
WE-17-57	1.28	8.16	0.43	0.72	0.34	

Appendix S4.4

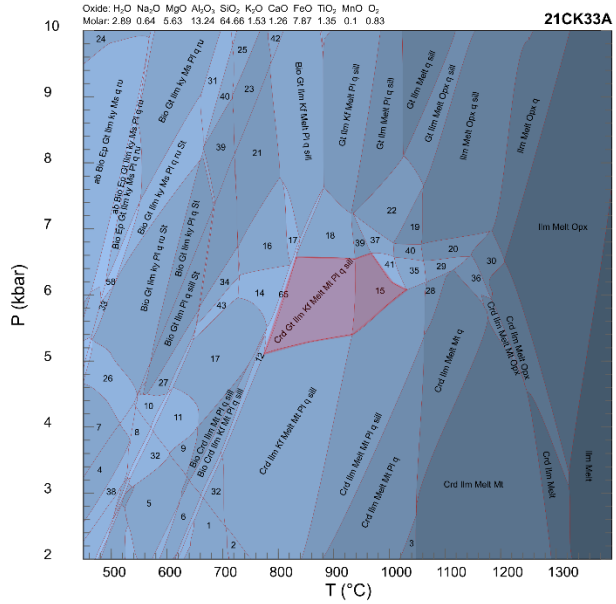
Thermobarometry results for chapter 5



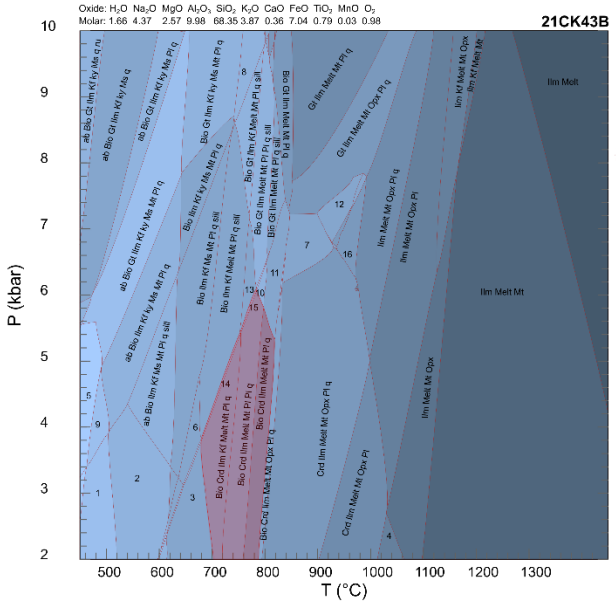
1 ab and Bio Crd Gt Ilm Kf Pl q ru
2 and Bio Crd Ilm Kf Pl q ru
3 and Bio Crd Gt Ilm Kf Pl q ru
4 Bio Crd Gt Ilm Kf Pl q ru sill
5 Ilm Kf Melt Opx Pl q ru sill
6 Gt Ilm Kf Melt Opx Pl q ru sill
7 Gt Ilm Kf Melt Opx ru sill
8 ab and Bio Crd Ilm Kf Pl q ru
9 ab and Bio Crd Gt Ilm Kf Pl q
10 Gt Ilm Kf Melt Opx q ru sill
11 Bio Gt Ilm Kf Melt Opx Pl q sill
12 Ilm Kf Melt Opx Pl ru sill
13 Bio Gt Ilm Kf Melt Pl q sill
14 cor Crd Ilm Kf Melt Opx ru
15 Bio Crd Gt Ilm Kf Melt Opx Pl q
16 and Bio Crd Gt Ilm Kf Pl q
17 **Bio Crd Gt Ilm Kf Melt Opx Pl q sill**
18 Crd Ilm Kf Melt Opx Pl q ru
19 Bio Crd Gt Ilm Kf Melt Pl q sill
20 Crd Ilm Kf Melt Opx Pl q ru sill
21 Crd Gt Ilm Kf Melt Opx Pl q ru sill
22 **Bio Crd Gt Ilm Kf Melt Opx Pl q ru sill**
23 Bio Crd Ilm Kf Melt Opx Pl q ru sill



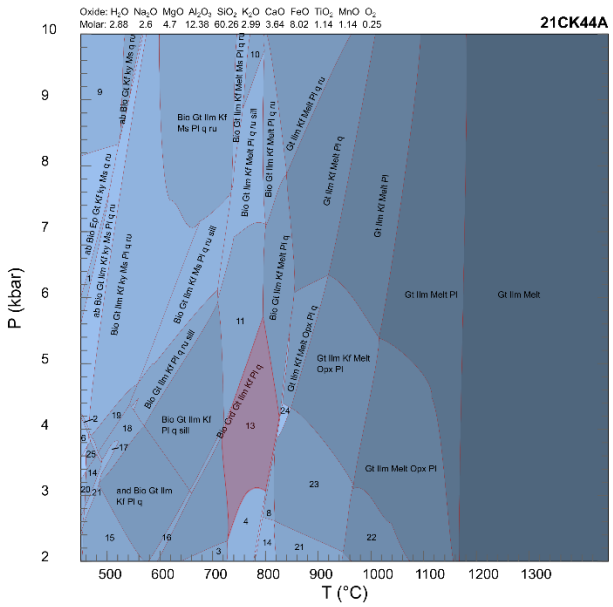
1 and Bio Crd Ilm Kf Pl q ru
2 Bio Crd Ilm Kf Pl q ru sill
3 Crd Ilm Kf Melt Opx osma q ru
4 Crd Ilm Kf Melt Pl q ru sill
5 Bio Ilm Kf Melt Opx Pl q ru sill
6 Crd Ilm Kf Melt Opx ru Sap
7 Bio Ilm Kf ky Melt Pl q ru
8 Ilm Kf Melt Opx q ru sill
9 Ilm Kf Melt Opx Pl q ru sill
10 Ilm Kf Melt Opx q ru Sap sill
11 Crd Ilm Kf Melt Opx osma ru
12 Ilm Kf Melt Opx osma ru Sap
13 Ilm Kf Melt Opx Pl q ru Sap
14 Ilm Kf Melt Opx osma q ru Sap
15 and Bio Crd Ilm Kf Ms Pl q ru
16 **Crd Ilm Kf Melt Pl q ru Sap**
17 Crd Ilm Kf Melt Opx Pl q ru Sap
18 Crd Ilm Kf Melt Opx Pl q ru sill

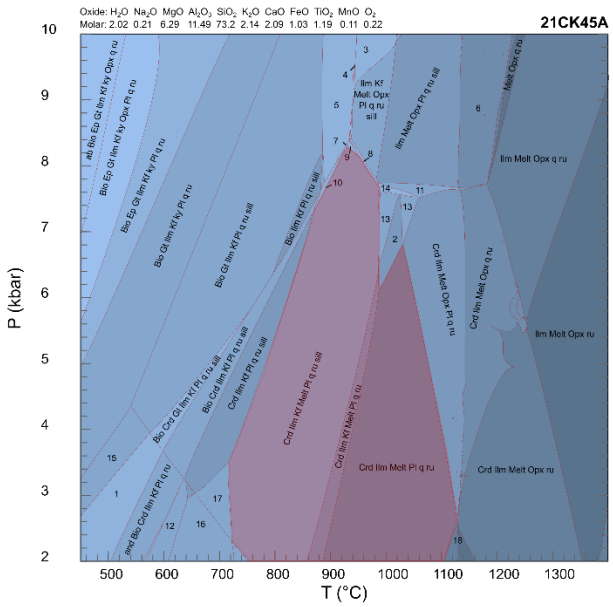


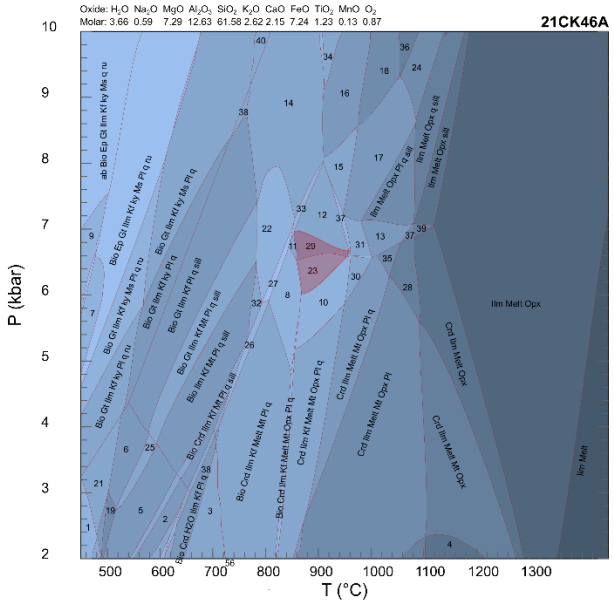
1 and Crd H2O Ilm Kf Mt Pl q
2 and Crd Ilm Kf Melt Mt Pl q
3 Crd Ilm Melt Mt Pl
4 and Bio Gt Mt Pl q ru St
5 and Bio Crd Ilm Ilm Mt Pl q
6 and Bio Crd Ilm Kf Mt Pl q
7 Bio Gt ky Mt Pl q ru St
8 and Bio Gt Ilm Ilm Mt Pl q St
9 Bio Crd Ilm Ilm Mt Pl q sill
10 Bio Gt Ilm Ilm Mt Pl q sill St
11 Bio Crd Gt Ilm Ilm Mt Pl q sill
12 Bio Crd Ilm Kf Melt Mt Pl q sill
13 Bio Crd Gt Ilm Mt Pl q sill
14 Bio Crd Gt Ilm Melt Mt Pl q sill
15 **Crd Gt Ilm Melt Mt Pl q sill**
16 Bio Gt Ilm Melt Mt Pl q sill
17 Bio Gt Ilm Kf Melt Mt Pl q sill
18 Crd Gt Ilm Kf Melt Pl q sill
19 Ilm Melt Opx Pl q sill
20 Crd Ilm Melt Opx q sill
21 Bio Gt Ilm Melt Pl q sill
22 Gt Ilm Melt opx q sill
23 Bio Gt Ilm ky Melt Pl q
24 ab Bio Gt Ilm ky Ms q ru
25 Bio Gt Ilm ky Melt Ms Pl q
26 Bio Gt Ilm ky Melt Pl q ru St
27 Bio Gt Ilm Mt Pl q sill St
28 Bio Gt Ilm ky Mt Pl q ru St
29 Crd Ilm Melt Mt Opx q sill
30 Crd Ilm Melt Opx q
31 Bio Gt H2O Ilm ky Ms Pl q ru
32 and Bio Crd Gt Ilm Ilm Mt Pl q
33 Bio Ep Gt Ilm ky Pl q ru St
34 Bio Gt H2O Ilm Mt Pl q sill
35 Crd Ilm Melt Mt Opx Pl q sill
36 Crd Ilm Melt Mt Opx q
37 Crd Gt Ilm Melt Opx Pl q sill
38 and Bio Gt Ilm Mt Pl q ru St
39 Crd Gt Ilm Melt Kf Pl q sill
40 Crd Ilm Melt Opx Pl q sill
41 Crd Gt Ilm Melt Mt Opx Pl q sill
42 Bio Gt Ilm Kf ky Melt Pl q
43 Bio Crd Gt H2O Ilm Mt Pl q sill

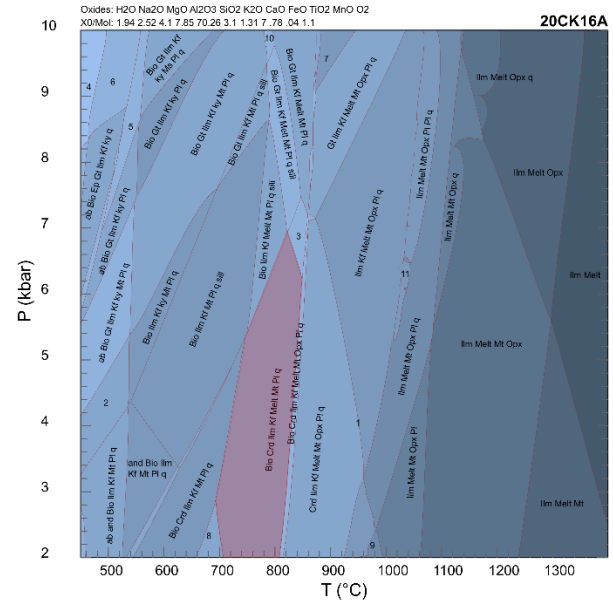


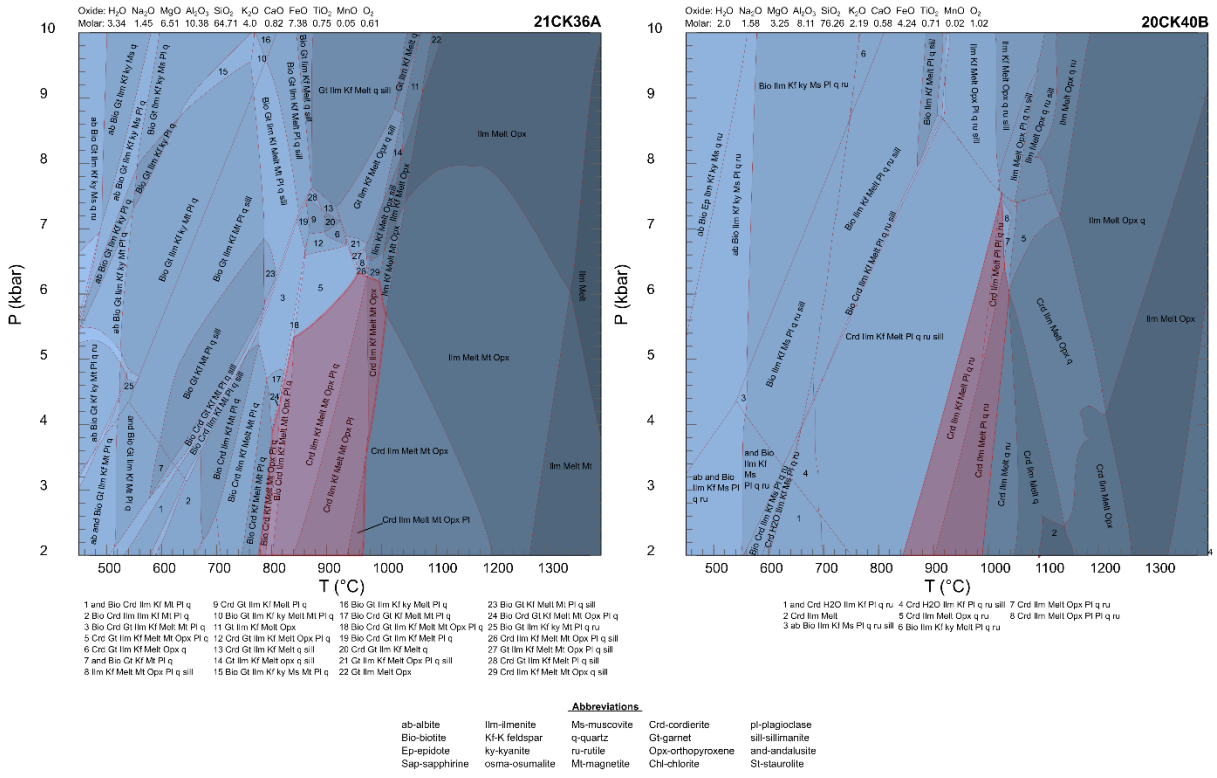
1 ab and Bio Ilm Kf Ms Mt Pl q ru
2 ab and Bio Ilm Kf Ms Mt Pl q
3 Bio Crd H2O Ilm Kf Mt Pl q
4 Crd Ilm Melt Mt Opx
5 ab Bio Gt Ilm Kf ky Ms Mt Pl q ru
6 Bio H2O Ilm Kf Mt Pl q sill
7 Crd Gt Ilm Melt Mt Opx Pl q
8 Bio Gt Ilm Kf ky Melt Mt Pl q
9 ab Bio Ilm Kf ky Ms Mt Pl q ru
10 Bio Crd Gt Ilm Melt Mt Pl Pl q
11 Bio Crd Gt Ilm Melt Mt Pl q
12 Gt Ilm Melt Mt Opx Pl q sill
13 Bio Ilm Melt Mt Pl Pl q sill
14 **Bio Crd Ilm Kf Melt Mt Pl q sill**
15 **Bio Crd Ilm Melt Mt Pl Pl q sill**
16 Crd Ilm Melt Mt Opx Pl q Sap


Oxide: H2O Na2O MgO Al2O3 SiO2 K2O CaO FeO TiO2 MnO O2
Molar: 2.88 2.6 4.7 12.38 60.26 2.99 3.64 8.02 1.14 1.14 0.25
21CK44A
P (kbar)
T (°C)
Bio Gt Ilm Kf Ms Pl q ru
Bio Gt Ilm Kf Pl q sill
and Bio Gt Ilm Kf Pl q
Gt Ilm Kf Melt Pl q
Gt Ilm Melt Pl
Gt Ilm Melt
Gt Ilm Kf Melt Opx Pl
Gt Ilm Melt Opx Pl
Bio Crd Gt Ilm Kf Pl q
1 ab Bio Ep Gt Kf ky Ms Pl q ru
2 ab Bio Gt Ilm Kf ky Ms Mt Pl q ru
3 and Bio Gt Ilm Ilm Kf Pl q ru
4 and Bio Gt Ilm Kf Pl q ru
5 and Bio Gt Ilm Kf Mt Pl q ru
6 ab Bio Gt Kf ky Ms Mt Pl q ru
7 Bio Crd Gt Ilm Kf Melt Mt Opx Pl q
8 Bio Crd Gt Ilm Kf Melt Opx Pl
9 ab Bio Gt Ilm Kf ky Ms q ru
10 Bio Gt Ilm Kf ky Melt Pl q ru
11 Bio Gt Ilm Kf Melt Pl q sill
13 Bio Crd Gt Ilm Kf Melt Pl q
14 and Bio Gt Kf Mt Pl q ru
15 and Bio Gt Ilm Kf Mt Pl q
16 and Bio Crd Gt Ilm Kf Pl q
17 Bio Crd Gt Ilm Kf Mt Pl q
18 Bio Crd Gt Ilm Kf Melt Mt Pl q
19 Bio Gt Ilm Kf ky Pl q ru
20 ab and Bio Gt Kf Mt Pl q ru
21 Crd Gt Ilm Kf Melt Mt Opx Pl
22 Crd Gt Ilm Melt Opx Pl
23 Crd Gt Ilm Kf Melt Opx Pl q
24 Crd Gt Ilm Kf Melt Opx Pl q


Oxide: H2O Na2O MgO Al2O3 SiO2 K2O CaO FeO TiO2 MnO O2
Molar: 2.02 0.21 6.29 11.49 73.2 2.14 2.09 1.03 1.19 0.11 0.22
21CK45A
P (kbar)
T (°C)
Ilm Kf Melt Opx Pl q ru sill
Ilm Melt Opx q ru
Ilm Melt Opx ru
Crd Ilm Melt Pl q ru
Crd Ilm Melt Opx ru
Crd Ilm Kf Melt Pl q ru sill
1 and Bio Gt Ilm Kf Pl q ru
2 Crd Ilm Melt osma Pl q ru
3 Gt Ilm Kf Melt Opx Pl q ru sill
4 Bio Gt Ilm Kf Melt Opx Pl q ru sill
5 Bio Gt Ilm Kf Melt Pl q ru sill
6 Ilm Melt Opx q ru sill
7 Bio Crd Gt Ilm Kf Melt Pl q ru sill
8 Crd Ilm Kf Melt Opx Pl q ru sill
9 Crd Gt Ilm Kf Melt Pl q ru sill
10 Bio Crd Ilm Kf Melt Pl q ru sill
11 Crd Ilm Melt Opx Pl q ru sill
12 Crd Ilm Melt Opx osma Pl q ru
13 Crd Ilm Melt osma Pl q ru sill
14 Crd Ilm Melt Opx osma Pl q ru sill
15 and Bio Crd Gt Ilm Kf Pl q ru
16 and Crd H2O Ilm Kf Pl q ru
17 Crd H2O Ilm Kf Pl q ru sill
18 Crd Ilm Melt Pl ru

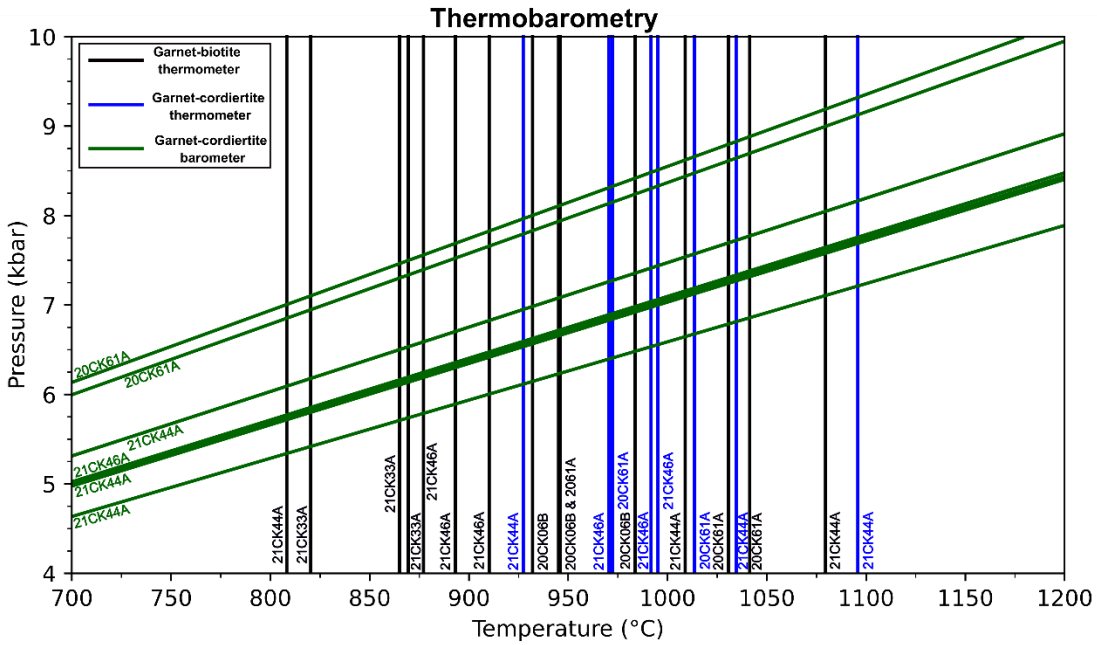

Oxide: H2O Na2O MgO Al2O3 SiO2 K2O CaO FeO TiO2 MnO O2
Molar: 3.66 0.59 7.29 12.63 61.58 2.62 2.15 7.24 1.23 0.13 0.87
21CK46A
P (kbar)
T (°C)
Ilm Melt Opx
Crd Ilm Melt Opx
Ilm Melt
1 and Bio Gt Ilm Kf Mt Pl q ru
2 and Bio Crd Ilm Kf Mt Pl q
3 Bio Crd H2O Ilm Kf Mt Pl q
4 Crd Ilm Melt Mt
5 and Bio Ilm Kf Mt Pl q
6 and Bio Gt Ilm Kf Pl q
7 Bio Ep Gt Ilm Kf ky Pl q ru
8 Bio Crd Gt Ilm Kf Melt Mt Pl q
9 ab Bio Ep Gt Ilm Kf ky q ru
10 Crd Gt Ilm Kf Melt Mt Opx Pl q
11 Bio Crd Gt Ilm Kf Melt Pl q
12 Crd Gt Ilm Kf Melt Pl q sill
13 Crd Ilm Melt Opx Pl q sill
14 Bio Gt Ilm Kf Melt Pl q sill
15 Gt Ilm Kf Melt Opx Pl q sill
16 Gt Ilm Kf Melt Pl q sill
17 Gt Ilm Melt Opx Pl q sill
18 Gt Ilm Melt Pl q sill
19 and Bio Ilm Kf Pl q
21 and Bio Gt Ilm Kf Pl q ru
22 Bio Gt Ilm Kf Melt Mt Pl q sill
23 Crd Gt Ilm Kf Melt Mt Pl q
24 Gt Ilm Melt Opx q sill
25 and Bio Gt Ilm Kf Mt Pl q
26 Bio Crd Ilm Kf Melt Mt Pl q sill
27 Bio Crd Gt Ilm Kf Melt Mt Pl q sill
28 Crd Ilm Melt Opx Pl
29 Crd Gt Ilm Kf Melt Pl q
30 Crd Gt Ilm Melt Mt Opx Pl q
31 Crd Gt Ilm Melt Opx Pl q sill
32 Bio Ilm Kf Melt Mt Pl q sill
33 Bio Crd Gt Ilm Kf Melt Pl q sill
34 Gt Ilm Kf Melt Pl q ru sill
35 Crd Ilm Melt Opx Pl q
36 Gt Ilm Melt q sill
37 Crd Gt Ilm Kf Melt Opx Pl q sill
38 Bio Gt Ilm Kf Ms Pl q sill
52 Crd Ilm Melt Opx sill
40 Bio Gt Ilm Kf ky Melt Ms Pl q


Oxides: H2O Na2O MgO Al2O3 SiO2 K2O CaO FeO TiO2 MnO O2
X0/Mol: 1.94 2.52 4.1 7.85 70.26 3.1 1.31 7 .78 .04 1.1
20CK16A
P (kbar)
T (°C)
Ilm Melt Opx q
Ilm Melt Opx
Ilm Melt
Ilm Melt Mt Opx
Ilm Melt Mt
1 Crd Ilm Melt Mt Opx Pl q
2 ab Bio Ilm Kf ky Mt Pl q
3 Bio Crd Gt Ilm Kf Melt Mt Pl q
4 ab Bio Ep Gt Ilm Kf ky Ms q ru
5 ab Bio Gt Ilm Kf ky Ms Pl q
6 ab Bio Ep Gt Ilm Kf ky Ms q
7 Gt Ilm Kf Melt Opx Pl q
8 Bio Crd H2O Ilm Kf Mt Pl q
9 Crd Ilm Melt Mt Opx Pl
10 Bio Gt Ilm Kf ky Melt Mt Pl q
11Ilm Melt Mt Opx Pl q



Abbreviations

ab-albite	Ilm-ilmenite	Ms-muscovite	Crd-cordierite	pl-plagioclase
Bio-biotite	Kf-K feldspar	q-quartz	Gt-garnet	sill-sillimanite
Ep-epidote	ky-kyanite	ru-rutile	Opx-orthopyroxene	and-andalusite
Sap-sapphirine	osma-osumalite	Mt-magnetite	Chl-chlorite	St-staurolite



Appendix S4.5

Detailed methodology for chapter 5

Electron Microprobe

Electron microprobe analyses were performed at the University of Toronto using a JEOL JXA-8530F electron microprobe.

Correction Method and Mass Absorption Coefficient File: ZAF or Phi-Rho-Z Calculations: FFAST Chantler (NIST v 2.1, 2005)

Current ZAF or Phi-Rho-Z Selection: Armstrong/Love Scott prZ (default)

Correction Selections: Phi(pz) Absorption of Armstrong/Packwood-Brown 1981 MAS, Stopping Power of Love-Scott, Backscatter Coefficient of Love-Scott, Backscatter of Love-Scott, Mean Ionization of Berger-Seltzer, Phi(pz) Equation of Love-Scott, Reed/JTA w/ M-Line Correction and JTA Intensity Mod. Fluorescence by Beta Lines Included.

Perthite

TakeOff = 40.0 KiloVolt = 15.0 Beam Current = 20.0 Beam Size = 15

(Magnification (analytical) = 200000), Beam Mode = Analog Spot, (Magnification (default) = 100, Magnification (imaging) = 500)

Compositional analyses were acquired on an electron microprobe equipped with 5 tunable wavelength dispersive spectrometers. Operating conditions were 40 degrees takeoff angle and a beam energy of 15 keV. The beam current was 20 nA, and the beam diameter was 15 microns. Elements were acquired using analyzing crystals LIF for Fe ka, PETH for Ca ka, K ka, and TAP for Al ka, Si ka, and Na ka. The standards were haematsx1 for Fe ka, albitesx1 for Si ka, Na ka, anorthitesx1 for Ca ka, Al ka, and sanidsx2 for K ka.

albitesx1—Standard Description: locality unknown. Donated by ASTIMEX

sanidsx2—Standard description: Hoenfels. Donated by ASTIMEX

anorthitesx1—Standard Description: USNM 137041

haematsx1—Standard Description: Haematite, Elba, Italy. Donated by ASTIMEX.

The counting time was 10 seconds for Na ka, K ka, 20 seconds for Al ka, Si ka, and 40 seconds for Ca ka, Fe ka. The off-peak counting time was 10 seconds for Na ka, K ka, 20 seconds for Al

ka, Si ka, and 40 seconds for Ca ka, and Fe ka. The off-peak correction method was Linear for all WDS elements. Unknown and standard intensities were corrected for deadtime using the Normal (traditional single term) correction method.

Orthopyroxene

Operating conditions were 40 degrees takeoff angle and a beam energy of 15 keV. The beam current was 20 nA, and the beam diameter was 1 micron. Elements were acquired using analyzing crystals LIFH for Fe ka, PETH for Ca ka, and TAP for Mg ka, Al ka, and Si ka. The standards were pxTiAlsx1 for Ca ka, and Craugitesx1 for Mg ka, Fe ka, Al ka, and Si ka.

Craugitesx1—Standard Description: Chromian augite, USNM164905 Geostandards Newsletter, vol 11, no.2, p.197, 1987

haematsx1—Standard Description: Haematite, Elba, Italy. Donated by ASTIMEX.

pxTiAlsx1—Standard Description: synthetic glass. Donated by Dr. Y. Yusa

pyropKsx1—Standard Description: pyrope, Kakanui, N.Z. USNM143968 E. Jarosevich's analysis. See documentation for alternative analyses.

bustamsx1—Standard Description: bustamite, Broken Hill, NSW, Australia. Donated by ASTIMEX

AlmandineSX2—Fe2+ = 19.78, Fe3+ = 0.83

The counting time was 20 seconds for Mg ka, 40 seconds for Fe ka, Al ka, Si ka, and 80 seconds for Ca ka. The off-peak counting time was 20 seconds for Mg ka, 40 seconds for Fe ka, Al ka, Si ka, and 80 seconds for Ca ka. The off-peak correction method was Linear for all WDS elements.

Garnet

Operating conditions were 40 degrees takeoff angle and a beam energy of 15 keV. The beam current was 20 nA, and the beam diameter was 1 micron. Elements were acquired using analyzing crystals LIF for Fe ka, LIFH for Mn ka, PETH for Ca ka, and TAP for Al ka, Si ka, and Mg ka. The standards were haematsx1 for Fe ka, bustamsx1 for Mn ka, and pyropKsx1 for Ca ka, Al ka, Si ka, and Mg ka.

Craugitesx1—Standard Description: Chromian augite, USNM164905, Geostandards Newsletter, vol 11, no.2, p.197, 1987

haematsx1—Standard Description: Haematite, Elba, Italy. Donated by ASTIMEX.

pxTiAlsx1—Standard Description: synthetic glass. Donated by Dr. Y. Yusa

pyropKsx1—Standard Description: pyrope, Kakanui, N.Z. USNM143968, E. Jarosevich's analysis. See documentation for alternative analyses.

bustamsx1—Standard Description: bustamite, Broken Hill, NSW, Australia. Donated by ASTIMEX

AlmandineSX2—Fe2+ = 19.78, Fe3+ = 0.83

The counting time was 20 seconds for Mg ka, 40 seconds for Fe ka, Al ka, Si ka, 60 seconds for Mn ka, and 80 seconds for Ca ka. The off-peak counting time was 20 seconds for Mg ka, 40 seconds for Fe ka, Al ka, Si ka, 60 seconds for Mn ka, and 80 seconds for Ca ka. The off-peak correction method was Linear for all WDS elements. Unknown and standard intensities were corrected for deadtime using the Normal (traditional single term) correction method.

Cordierite

Operating conditions were 40 degrees takeoff angle and a beam energy of 15 keV. The beam current was 20 nA, and the beam diameter was 1 micron. Elements were acquired using analyzing crystals LIF for Fe ka, LIFH for Mn ka, PETH for Ca ka, and TAP for Al ka, Si ka, and Mg ka. The standards were bustamsx1 for Mn ka, pyropKsx1 for Mg ka, Ca ka, Al ka, Fe ka, and Craugitesx1 for Si ka.

Craugitesx1—Standard Description: Chromian augite, USNM164905, Geostandards Newsletter, vol 11, no.2, p.197, 1987

haematsx1—Standard Description: Haematite, Elba, Italy. Donated by ASTIMEX.

pxTiAlsx1—Standard Description: synthetic glass. Donated by Dr. Y. Yusa

pyropKsx1—Standard Description: pyrope, Kakanui, N.Z. USNM143968, E. Jarosevich's analysis. See documentation for alternative analyses.

bustamsx1—Standard Description: bustamite, Broken Hill, NSW, Australia. Donated by ASTIMEX

AlmandineSX2—Fe2+ = 19.78, Fe3+ = 0.83

Biotite#3_PS03—analyzed by Carmichael, Fe2O3 wt% = 1.8; FeO wt% = 16.51, All the H2O listed here is H2O+, O=F = 1.38

tugtsx1—Standard Description: Tugtupite, Tugtup, Greenland. Donated by ASTIMEX

phlogsx2—Standard Description: fluor phlogopite, synthetic (D. Wones), via D. Ebel. Given %s are from stoichiometry and different from those in Ebel's thesis

MgF2_SX2—stoichiometric calculation

TiO2sx2—Standard Description: synthetic crystal. Atomergic.

The counting time was 20 seconds for Mg ka, 40 seconds for Fe ka, Al ka, Si ka, 60 seconds for Mn ka, and 80 seconds for Ca ka. The off-peak counting time was 20 seconds for Mg ka, 40 seconds for Fe ka, Al ka, Si ka, 60 seconds for Mn ka, and 80 seconds for Ca ka. The off-peak correction method was Linear for all WDS elements. Unknown and standard intensities were corrected for deadtime using the Normal (traditional single term) correction method.

Biotite

Operating conditions were 40 degrees takeoff angle and a beam energy of 15 keV. The beam current was 20 nA, and the beam diameter was 20 microns. Elements were acquired using analyzing crystals LIF for Fe ka, PETH for K ka, Cl ka, and TAP for Al ka, Si ka, F ka, and Mg ka. The standards were phlogsx2 for Mg ka, Si ka, F ka, tugtsx1 for Cl ka, and Biotite#3_PS03 for Fe ka, K ka, Al ka.

Craugitesx1—Standard Description: Chromian augite, USNM164905, Geostandards Newsletter, vol 11, no.2, p.197, 1987

haematsx1—Standard Description: Haematite, Elba, Italy. Donated by ASTIMEX.

pxTiAlsx1—Standard Description: synthetic glass. Donated by Dr. Y. Yusa

pyropKsx1—Standard Description: pyrope, Kakanui, N.Z. USNM143968, E. Jarosevich's analysis. See documentation for alternative analyses.

bustamsx1—Standard Description: bustamite, Broken Hill, NSW, Australia. Donated by ASTIMEX

AlmandineSX2—Fe2+ = 19.78, Fe3+ = 0.83

Biotite#3_PS03—analyzed by Carmichael, Fe2O3 wt% = 1.8; FeO wt% = 16.51. All the H2O listed here is H2O+. O=F = 1.38

tugtsx1—Standard Description: Tugtupite, Tugtup, Greenland. Donated by ASTIMEX

phlogsx2—Standard Description: fluorphlogopite, synthetic (D. Wones), via D. Ebel. Given %s are from stoichiometry and different from those in Ebel's thesis

MgF2_SX2—stoichiometric calculation

TiO2sx2—Standard Description: synthetic crystal. Atomergic.

The counting time was 20 seconds for Mg ka, K ka, F ka, and 40 seconds for Al ka, Si ka, Fe ka, and Cl ka. The off-peak counting time was 20 seconds for Mg ka, K ka, F ka, and 40 seconds for Al ka, Si ka, Fe ka, and Cl ka. The off-peak correction method was Linear for all WDS elements. Unknown and standard intensities were corrected for deadtime using the Normal (traditional single term) correction method.

Oxygen was calculated by cation stoichiometry and included in the matrix correction.

Exchange Thermometers

Garnet-Cordierite Thermometer

Source: Wells (1979); $K_D = \frac{X_{Fe}^{g} * X_{Mg}^{cd}}{X_{Mg}^{g} * X_{Fe}^{cd}}$;

$$\text{Equation: } T(K) = \frac{2789 - 0.0148(P-1)}{\ln K_D + 0.802}$$

Garnet-Cordierite Barometer

Source: Bhattacharya (1993): $K_d = \frac{X_{Mg}^{crd}}{X_{Mg}^{g}}$;

Equation: $P(bar) = 10.46T - 1699.53 - 3.28T\ln K_D - 1.639T\ln\left(1 - X_{H_2O}^{crd}\right)$

Garnet-Biotite Thermometer

Source: Ferry and Spear (1978); $K_D = \frac{\left(X_{Mg}^{g} * X_{Fe}^{bi}\right)}{\left(X_{Fe}^{g} * X_{Mg}^{bi}\right)}$;

Equation: $T(°C) = \frac{-2109}{\ln K_D - 0.782}$

Thermodynamic Modelling using GeoPS

Thermodynamic modelling was performed using the GeoPS software Xiang and Connolly (2022) to construct temperature-composition (varying H2O; T-x) and pressure-temperature (P-T) diagrams. T-x diagrams were calculated from 500–1400ºC and 0–10 wt% H2O at 5 kbar; water saturation at the solidus for the peak mineral assemblage was selected. Using these H2O-corrected compositions, P-T diagrams were calculated from 500–1400ºC and 2–10 kbar. Phase equilibrium modelling was performed in the MnO-N2O-CaO-K2O-FeO-MgO-Al2O3-SiO2-H2O-TiO2-O system using the thermodynamic database of Holland and Powell (2011). Activity-composition models for biotite, cordierite, garnet, ilmenite, melt, and orthopyroxene are from White et al. (2014), whereas feldspar and spinel values are from Holland and Powell (2003), fluid from Powell et al. (1998), and sapphirine from Holland and Powell (2011).

References

Aranovich, L.Ya., and Berman, R.G. 1997. A new garnet-orthopyroxene thermometer based on reversed Al2O3 solubility in FeO-Al2O3-SiO2 orthopyroxene. American Mineralogist, 82: 345–353. doi:10.2138/am-1997-3-413.

Bhattacharya, S. 1993. Refinement of geothermobarometry for cordierite granulites. Journal of Earth System Science, 102: 537–545. doi:10.1007/BF02871952.

Ferry, J.M., and Spear, F.S. 1978. Experimental calibration of the partitioning of Fe and Mg between biotite and garnet. Contributions to Mineralogy and Petrology, 66: 113–117. doi:10.1007/BF00372150.

Holland, T., and Powell, R. 2003. Activity-composition relations for phases in petrological calculations: an asymmetric multicomponent formulation. Contributions to Mineralogy and Petrology, 145: 492–501. doi:10.1007/s00410-003-0464-z.

Holland, T.J.B., and Powell, R. 2011. An improved and extended internally consistent thermodynamic dataset for phases of petrological interest, involving a new equation of state for solids: Thermodynamic dataset fopr phases of petrological interest. Journal of Metamorphic Geology, 29: 333–383. doi:10.1111/j.1525-1314.2010.00923.x.

Powell, R., Holland, T., and Worley, B. 1998. Calculating phase diagrams involving solid solutions via non-linear equations, with examples using THERMOCALC. Journal of Metamorphic Geology, 16: 577–588. doi:10.1111/j.1525-1314.1998.00157.x.

Wells, P.R.A. 1979. Chemical and Thermal Evolution of Archaean Sialic Crust, Southern West Greenland. Journal of Petrology, 20: 187–226. doi:10.1093/petrology/20.2.187.

White, R.W., Powell, R., Holland, T.J.B., Johnson, T.E., and Green, E.C.R. 2014. New mineral activity–composition relations for thermodynamic calculations in metapelitic systems. Journal of Metamorphic Geology, 32: 261–286. doi:10.1111/jmg.12071.

Xiang, H., and Connolly, J.A.D. 2022. GeoPS: An interactive visual computing tool for thermodynamic modelling of phase equilibria. Journal of Metamorphic Geology, 40: 243–255. doi:10.1111/jmg.12626.

Appendix S4.6

Supplementary outcrop and microphotographs for Chapter 5

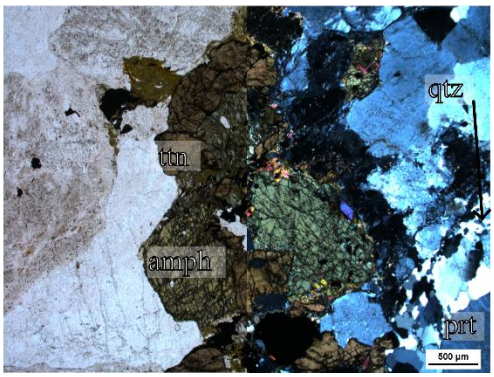
Monzonite-Syenite-Granite



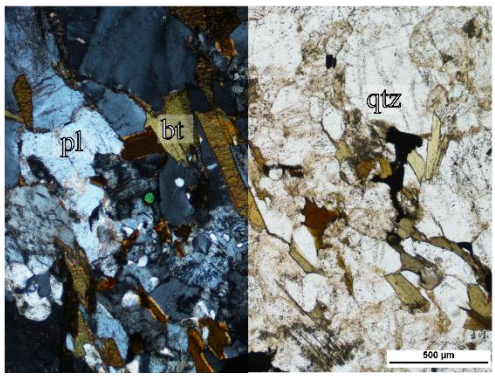
Syenite with K-feldspar phenocrysts.



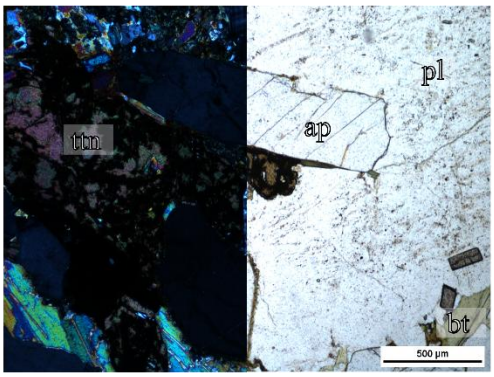
Foliated (defined by biotite) monzogranite.



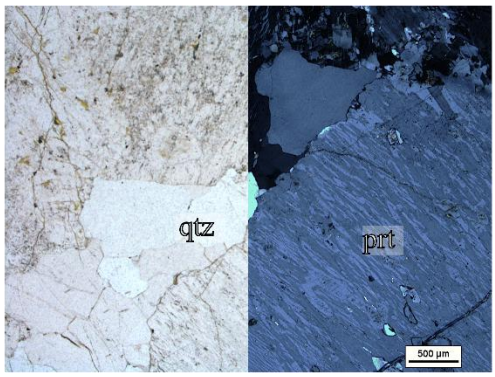
Amphibole, titanite, altered feldspar, and quartz. quartz is in recrystallized ribbons.



Foliation defined by biotite. Altered feldspar.



Large apatite and titanite in altered feldspar and chloritized biotite

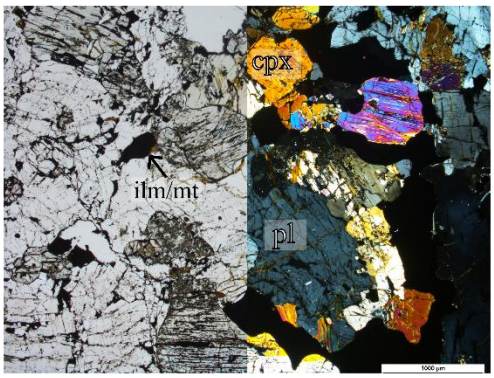


Perthitic feldspar and recrystallized ribbon of quartz.

Gabbro, Anorthosite, and Diorite



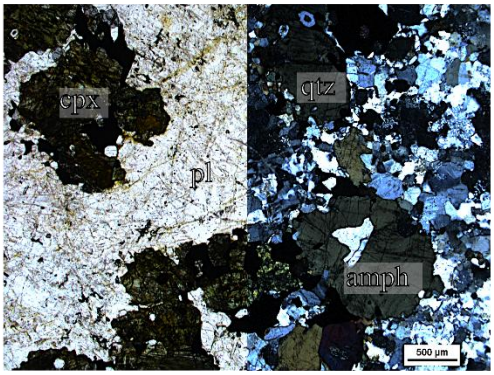
Fresh and weathered surface of fine-grained gabbro.



Slightly altered clinopyroxene and plagioclase with minor ilmenite/magnetite.



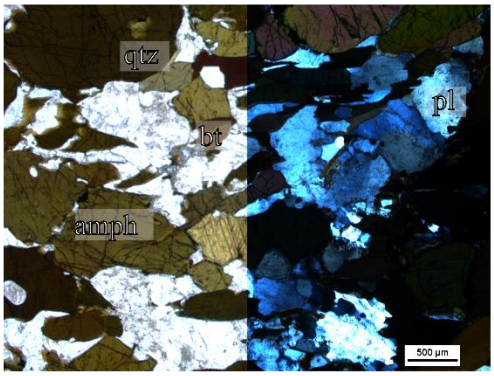
Coarse-grained anorthosite with brownish plagioclase



Altered clinopyroxene, amphibole, and plagioclase with matrix quartz.



Equigranular diorite outcrop with minimal weathering.



Amphibolized diorite with brown amphibole, quartz, and altered feldspar.

Marble and calc-silicate



Paleozoic cover overlying marble.

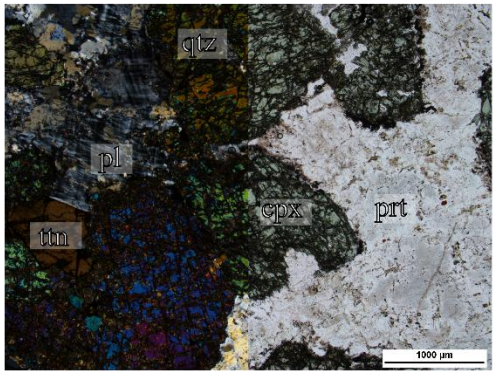


Pod of clinopyroxene and titanite in marble.

Clinopyroxene Aluminous Gneiss



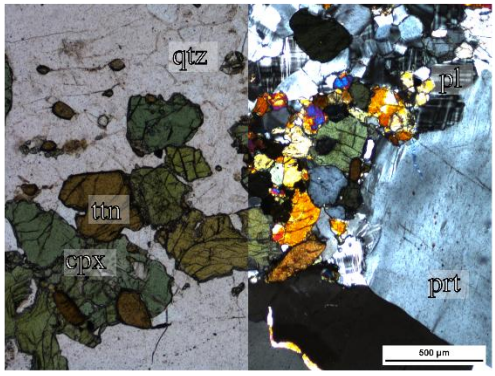
Clinopyroxene in pink leucosome.



Altered clinopyroxene and feldspar with minor titanite.



Stratiform layering of leuco-, meso-, and melanosome with titanite in melanosome.

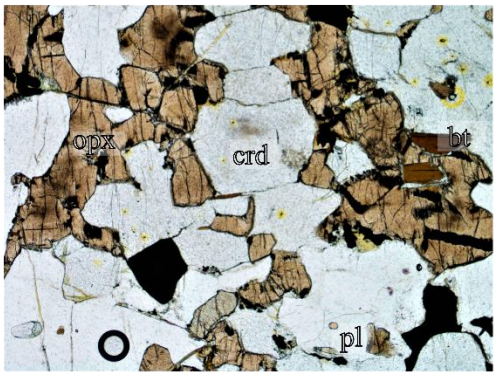


Layer of clinopyroxene and titanite in plagioclase and quartz matrix.

Cordierite and garnet aluminous schist



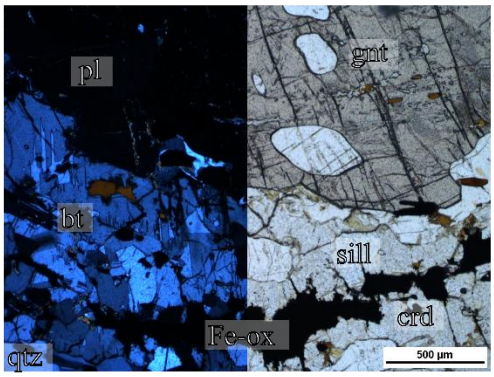
Cordierite in pink leucosome.



Orthopyroxene, cordierite, plagioclase, and quartz matrix with minor biotite.



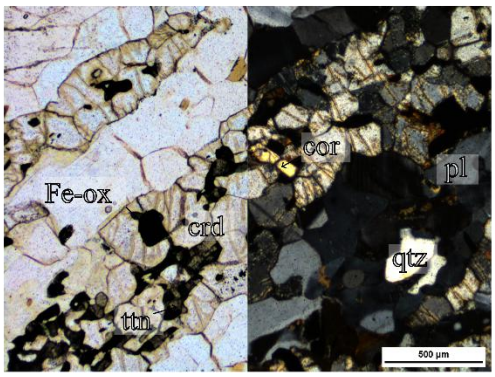
Garnet in white leucosome.



Co-existing garnet and cordierite with sillimanite, biotite, and Fe-oxide inlcusions.



Cordierite and ilmenite accumulations in orangey-white leucosome.

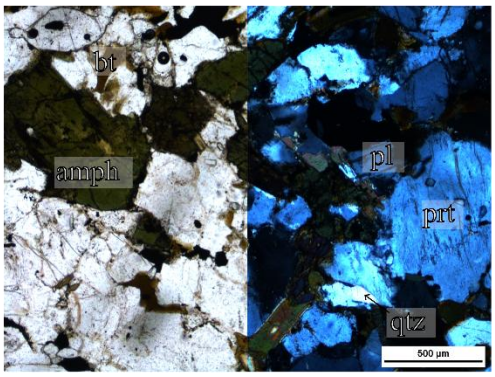


Altered cordierite with inclusions of titanite, corundum, and Fe-oxide.

Mafic Schist



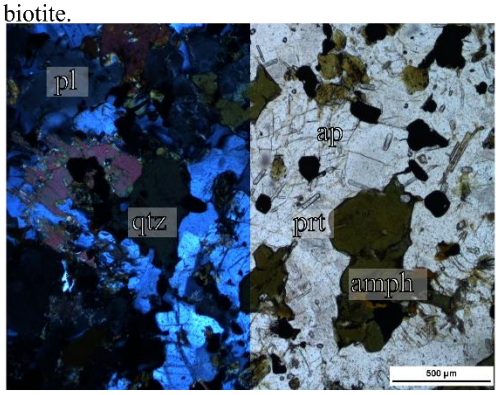
Fine-grained mafic schist with pink leucosome.



Altered amphibole and plagioclase with minor biotite.



Mafic schist interbedded with aluminous gneiss. Pink leucosome is present.

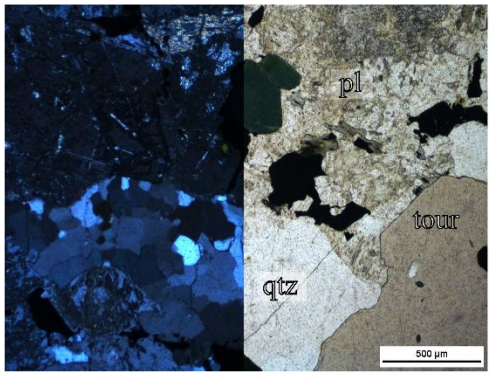


Amphibole, altered feldpar, biotite, and quartz. Note abundant large apatite.

Quartzofeldspathic Schist



Foliation defined by biotite with porphyritic feldspar and minor epidotization.



Altered feldspar with polygonal quartz and large tourmaline grains.

Quartzite

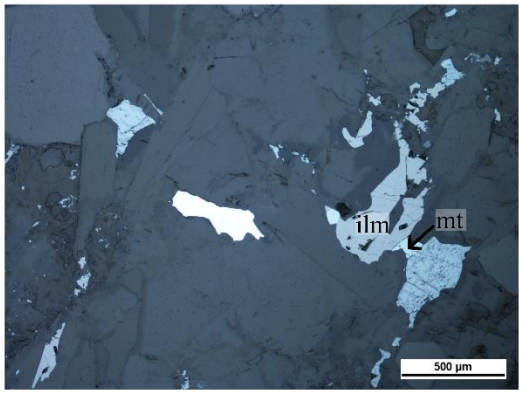


Clean quartzite with heavy mineral layer.

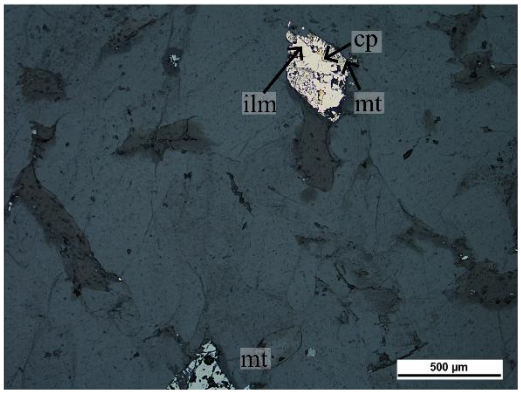


Dirty quartzite with chloritized biotite and K-feldspar.

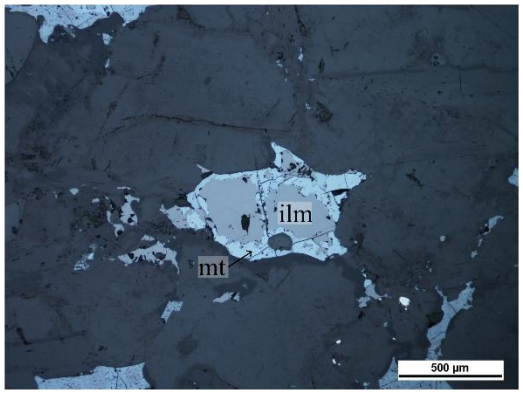
Metallic Minerals



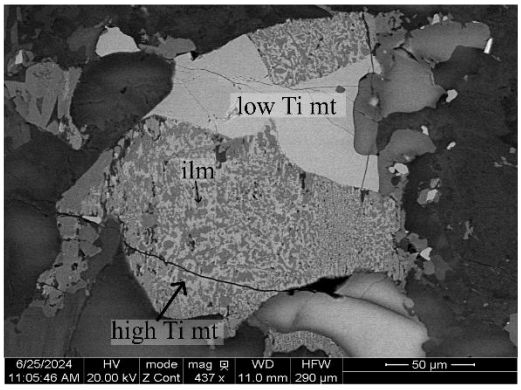
Individual ilmenite and magnetite grains and mixed grains of the two.



Chalcopyrite inclusions in magnetite-ilmenite.



Magnetite rim along ilmenite



Low Ti (1–3 wt%) magnetite with mixture of ilmenite and high (5–10 wt) Ti magnetite.

Deformation



Transposed granitiod and mafic schist



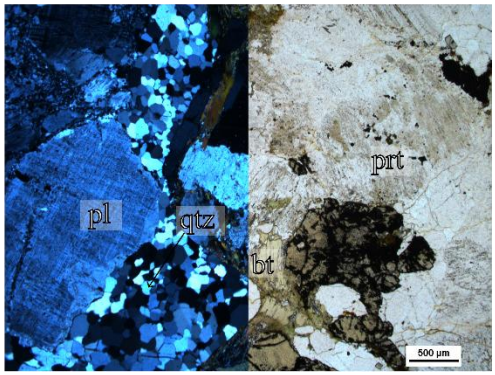
Transposed quartzite, mafic schist, and quartzofeldspathic schist.



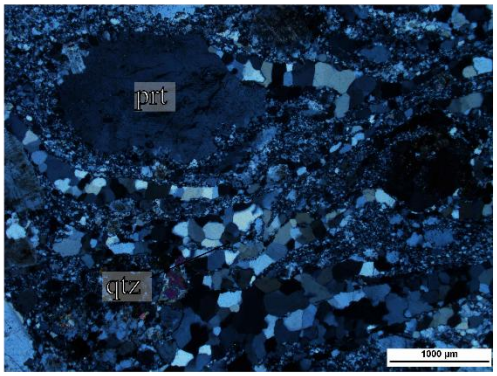
Sheared and folded granitic and mafic schist layers.



Rootless isoclinal folds of mafic and quartzofeldspathic schist in marble.



Recrystallized quartz ribbon between feldspar porphyroblasts in syenogranite.



Recrystallized quartz ribbons between feldspar porphyroblasts in dirty quartzite

Appendix S4.7

Compilation of garnet major element composition for Chapter 5

Paper	Sample	Rock Type	Grain	Number	Line	Distance (um)	Relative Distance	SiO_2	TiO_2	Al_2O_3	FeO	MnO	MgO
This Study	2061A	Gnt/Crd Aluminious	1	27	94	83.8643	0.07	38.23		22.20	26.37	2.32	9.30
This Study	2061A	Gnt/Crd Aluminious	1	27	98	339.203	0.30	38.60		22.45	25.51	2.17	9.90
This Study	2061A	Gnt/Crd Aluminious	1	27	97	566.032	0.49	38.62		22.39	25.80	2.18	9.70
This Study	2061A	Gnt/Crd Aluminious	1	27	95	946.855	0.83	38.60		22.26	26.63	2.33	9.33
This Study	2061A	Gnt/Crd Aluminious	1	27	96	1084.201	0.94	38.65		22.46	26.67	2.29	9.62
This Study	2061A	Gnt/Crd Aluminious	2	28	101	47.863	0.03	38.12		22.16	27.31	2.13	8.53
This Study	2061A	Gnt/Crd Aluminious	2	28	100	326.717	0.22	38.54		22.23	27.17	2.00	8.99
This Study	2061A	Gnt/Crd Aluminious	2	28	103	738.755	0.50	38.46		22.01	26.90	2.05	9.58
This Study	2061A	Gnt/Crd Aluminious	2	28	99	1317.273	0.88	38.49		22.33	27.75	2.22	8.72
This Study	2061A	Gnt/Crd Aluminious	2	28	102	1389.0675	0.93	38.69		22.53	26.43	2.07	9.78
This Study	2061A	Gnt/Crd Aluminious	3	29	104	28.5097	0.02	38.38		22.37	26.82	2.22	9.08
This Study	2061A	Gnt/Crd Aluminious	3	29	108	631.1673	0.33	38.84		22.48	25.68	2.09	9.92
This Study	2061A	Gnt/Crd Aluminious	3	29	106	689.8515	0.37	38.97		22.50	25.18	2.04	10.47
This Study	2061A	Gnt/Crd Aluminious	3	29	105	1458.781	0.77	38.96		22.44	25.46	2.02	10.42
This Study	2061A	Gnt/Crd Aluminious	3	29	107	1888.5075	1.00	38.88		22.56	25.61	2.06	10.43
This Study	2144A	Gnt/Crd Aluminious	1	30	113	166.48	0.09	37.53		21.85	33.92	0.36	5.51
This Study	2144A	Gnt/Crd Aluminious	1	30	110	764.7675	0.40	37.84		21.98	32.54	0.32	6.05
This Study	2144A	Gnt/Crd Aluminious	1	30	112	1300.0007	0.68	37.82		21.94	33.27	0.35	5.61
This Study	2144A	Gnt/Crd Aluminious	1	30	109	1727.23	0.90	37.74		21.92	33.99	0.39	5.48
This Study	2144A	Gnt/Crd Aluminious	2	31	114	145.67	0.06	37.73		21.75	33.51	0.34	5.87
This Study	2144A	Gnt/Crd Aluminious	2	31	115	439.091	0.18	37.81		21.92	33.17	0.34	6.14
This Study	2144A	Gnt/Crd Aluminious	2	31	118	1102.93	0.45	37.92		22.05	32.74	0.30	6.47
This Study	2144A	Gnt/Crd Aluminious	2	31	116	1492.077	0.61	37.72		21.96	33.76	0.35	5.96
This Study	2144A	Gnt/Crd Aluminious	2	31	117	2126.782	0.87	38.25		22.05	33.70	0.34	5.95
This Study	2144A	Gnt/Crd Aluminious	3	32	121	72.835	0.04	37.50		21.76	34.05	0.36	5.35
This Study	2144A	Gnt/Crd Aluminious	3	32	119	561.87	0.33	37.68		21.76	34.06	0.35	5.15
This Study	2144A	Gnt/Crd Aluminious	3	32	123	769.97	0.45	37.43		21.90	34.14	0.35	5.22
This Study	2144A	Gnt/Crd Aluminious	3	32	122	1286.058	0.75	37.80		21.85	33.80	0.35	5.62
This Study	2146A	Gnt/Crd Aluminious	1	33	127	81.159	0.04	38.01		21.78	30.91	1.61	5.97
This Study	2146A	Gnt/Crd Aluminious	1	33	126	582.68	0.29	38.08		21.96	30.59	1.55	6.34
This Study	2146A	Gnt/Crd Aluminious	1	33	125	884.425	0.44	38.00		22.01	31.15	1.59	6.13
This Study	2146A	Gnt/Crd Aluminious	1	33	124	1421.323	0.71	38.01		21.98	30.73	1.53	6.25
This Study	2146A	Gnt/Crd Aluminious	1	33	128	1850.009	0.93	37.89		21.95	32.17	1.66	5.98
This Study	2146A	Gnt/Crd Aluminious	2	34	130	31.215	0.02	37.55		21.81	32.03	1.72	5.42
This Study	2146A	Gnt/Crd Aluminious	2	34	131	390.1875	0.20	37.91		21.89	31.44	1.65	6.19
This Study	2146A	Gnt/Crd Aluminious	2	34	129	894.83	0.46	37.68		21.86	32.20	1.66	5.76
This Study	2146A	Gnt/Crd Aluminious	2	34	132	1467.105	0.76	38.09		22.12	31.15	1.68	6.36
This Study	2146A	Gnt/Crd Aluminious	2	34	133	1841.685	0.96	38.00		22.08	31.35	1.70	6.32
This Study	2146A	Gnt/Crd Aluminious	3	35	135	41.62	0.03	37.48		21.83	31.96	1.74	5.50
This Study	2146A	Gnt/Crd Aluminious	3	35	138	304.8665	0.21	37.73		21.92	31.59	1.77	5.84
This Study	2146A	Gnt/Crd Aluminious	3	35	134	765.808	0.53	37.77		21.93	31.55	1.74	5.94
This Study	2146A	Gnt/Crd Aluminious	3	35	137	1046.743	0.72	37.78		21.85	31.95	1.87	5.69
This Study	2146A	Gnt/Crd Aluminious	3	35	136	1425.485	0.98	37.73		21.91	32.10	1.77	5.80
This Study	2006B	Gnt/Crd Aluminious	1	5	30	214.343	0.10	37.96		22.05	30.26	2.18	6.88
This Study	2006B	Gnt/Crd Aluminious	1	5	31	647.191	0.29	38.40		22.33	28.86	1.85	8.12
This Study	2006B	Gnt/Crd Aluminious	1	5	32	1123.74	0.50	38.64		22.33	27.57	1.85	8.96
This Study	2006B	Gnt/Crd Aluminious	1	5	33	1833.361	0.82	37.80		21.99	31.37	2.18	6.19
This Study	2006B	Gnt/Crd Aluminious	1	5	34	2207.941	0.98	38.13		22.07	30.16	2.17	7.02

Paper	Sample	Rock Type	Grain	Number	Line	Distance (um)	Relative Distance	SiO_2	TiO_2	Al_2O_3	FeO	MnO	MgO
This Study	2006B	Gnt/Crd Aluminious	2	6	35	41.62	0.02	37.93		21.99	31.22	2.39	6.36
This Study	2006B	Gnt/Crd Aluminious	2	6	36	595.166	0.28	38.12		22.06	30.27	1.97	7.14
This Study	2006B	Gnt/Crd Aluminious	2	6	37	1152.874	0.55	38.08		22.09	31.07	2.29	6.67
This Study	2006B	Gnt/Crd Aluminious	2	6	38	1612.775	0.77	38.08		22.16	31.05	2.17	6.65
This Study	2006B	Gnt/Crd Aluminious	2	6	39	2049.785	0.98	38.03		21.97	31.10	2.32	6.53
This Study	2006B	Gnt/Crd Aluminious	3	7	40	57.2275	0.08	38.13		22.23	30.09	2.36	7.11
This Study	2006B	Gnt/Crd Aluminious	3	7	41	338.1625	0.50	38.28		22.22	29.79	2.18	7.60
This Study	2006B	Gnt/Crd Aluminious	3	7	42	603.9062	0.89	37.86		22.14	31.10	2.28	6.40
This Study	2133A	Gnt/Crd Aluminious	1	8	45	93.645	0.06	38.83		22.56	27.65	0.91	9.24
This Study	2133A	Gnt/Crd Aluminious	1	8	46	447.415	0.31	38.80		22.60	27.75	0.88	9.28
This Study	2133A	Gnt/Crd Aluminious	1	8	47	747.079	0.51	38.22		22.40	28.28	0.87	8.83
This Study	2133A	Gnt/Crd Aluminious	1	8	48	1050.905	0.72	38.59		22.42	28.21	0.86	8.87
This Study	2133A	Gnt/Crd Aluminious	1	8	49	1369.298	0.94	38.59		22.36	27.71	0.88	8.99
This Study	2133A	Gnt/Crd Aluminious	2	9	50	135.265	0.06	38.93		22.67	27.20	1.26	9.39
This Study	2133A	Gnt/Crd Aluminious	2	9	51	603.49	0.25	38.80		22.54	27.68	1.23	9.34
This Study	2133A	Gnt/Crd Aluminious	2	9	52	1097.7275	0.45	38.89		22.63	27.27	1.28	9.26
This Study	2133A	Gnt/Crd Aluminious	2	9	53	1666.881	0.69	38.92		22.70	27.26	1.24	9.23
This Study	2133A	Gnt/Crd Aluminious	2	9	54	2408.7575	1.00	38.83		22.74	27.56	1.24	9.39
This Study	2133A	Gnt/Crd Aluminious	3	10	55	104.05	0.05	38.79		22.69	27.56	1.29	9.32
This Study	2133A	Gnt/Crd Aluminious	3	10	56	574.356	0.25	38.92		22.72	26.98	1.26	9.74
This Study	2133A	Gnt/Crd Aluminious	3	10	57	1256.2997	0.56	38.83		22.76	26.90	1.26	9.65
This Study	2133A	Gnt/Crd Aluminious	3	10	58	1995.679	0.88	38.71		22.58	27.94	1.24	8.94
This Study	2133A	Gnt/Crd Aluminious	3	10	59	2252.6825	1.00	38.47		22.48	29.01	1.35	8.20
Reinhart, 1968	D-28	Gnt/Crd Aluminious	g				0.50	39.40	0.14	24.60	25.73	0.23	8.20
Reinhart, 1968	D-56	Gnt/Crd Aluminious	g				0.50	39.10	0.06	23.30	28.20	1.50	6.00
Reinhart, 1968	D-87	Gnt/Crd Aluminious	g				0.50	39.00	0.08	22.70	30.89	0.45	5.00
Reinhart, 1968	D-102	Gnt/Crd Aluminious	g				0.50	37.40	0.07	22.90	29.33	0.62	7.30
Reinhart, 1968	D-175	Gnt/Crd Aluminious	g				0.50	37.80	0.25	23.80	27.18	0.45	8.20
Reinhart, 1968	R-114	Gnt/Crd Aluminious	g				0.50	38.20	0.06	23.20	30.63	0.62	5.40
Reinhart, 1968	R-124	Gnt/Crd Aluminious	g				0.50	39.20	0.12	24.60	27.83	0.45	6.80
Reinhart, 1968	W-53	Gnt/Crd Aluminious	g				0.50	39.00	0.20	25.90	21.75	0.85	10.00
Reinhart, 1968	D-141	Gnt/Crd Aluminious	g				0.50	38.70	0.14	23.40	27.03	0.53	9.60
Reinhart, 1968	D-149	Gnt/Crd Aluminious	g				0.50	38.60	0.11	23.80	24.50	0.39	12.20
Reinhart, 1968	D-165	Gnt/Crd Aluminious	g				0.50	37.80	0.12	23.70	24.50	0.53	11.30
Reinhart, 1968	D-139	Gnt/Crd Aluminious	g				0.50	39.50	0.33	24.40	24.44	0.60	9.90
Reinhart, 1968	D-28	Gnt/Crd Aluminious	g				0.50	39.40	0.14	24.60	25.73	0.23	8.20
Wynne-Edwards & Hay 1963	H-29	Gnt/Crd Aluminious	g				0.50	37.00	0.16	24.30	28.76	0.10	6.70
Wynne-Edwards & Hay 1963	H_66	Gnt/Crd Aluminious	g				0.50	35.45	0.17	23.20	30.87	0.56	7.10
Wynne-Edwards & Hay 1963	H-70	Gnt/Crd Aluminious	g				0.50	37.71	0.11	26.05	27.66	0.80	5.67
Wynne-Edwards & Hay 1963	H-126	Gnt/Crd Aluminious	g				0.50	35.77	0.19	24.47	33.52	0.84	7.95
Wynne-Edwards & Hay 1963	WE-4-58	Gnt/Crd Aluminious	g				0.50	34.60	0.16	23.87	31.23	0.85	6.54
Russell, 2009	AKR-21	Gnt/Crd Aluminious					0.50	38.86	0.27	22.07	27.85	1.32	9.28
Wynne-Edwards, 1967	G1	Gnt/Crd Aluminious					0.50	37.00	0.52	22.20	30.02	0.36	7.80
Wynne-Edwards, 1967	G2	Gnt/Crd Aluminious					0.50	36.40	0.21	21.10	25.98	0.21	12.10
Wynne-Edwards, 1967	G3	Gnt/Crd Aluminious					0.50	36.00	1.72	20.10	30.32	0.39	10.30
Wynne-Edwards, 1967	G4	Gnt/Crd Aluminious					0.50	36.35	0.26	22.97	24.72	0.64	11.80
Wynne-Edwards, 1967	G5	Gnt/Crd Aluminious					0.50	39.17	0.29	21.70	26.93	0.32	10.43
Wynne-Edwards, 1967	G6	Gnt/Crd Aluminious					0.50	39.50	0.42	21.00	26.02	0.80	9.74

Paper	Sample	Rock Type	Grain	Number	Line	Distance (um)	Relative Distance	SiO_2	TiO_2	Al_2O_3	FeO	MnO	MgO
Wynne-Edwards, 1967	G7	Gnt/Crd Aluminious					0.50	39.05		20.42	30.21	0.38	8.97

Sample	CaO	Na_2O	K_2O	Cl	F	H_2O	TOTAL
2061A	0.91						99.34
2061A	0.87						99.49
2061A	0.85						99.54
2061A	0.81						99.96
2061A	0.85						100.54
2061A	0.81						99.06
2061A	0.81						99.73
2061A	0.79						99.79
2061A	0.80						100.30
2061A	0.83						100.33
2061A	0.82						99.69
2061A	0.82						99.83
2061A	0.87						100.02
2061A	0.88						100.19
2061A	0.83						100.38
2144A	1.23						100.40
2144A	1.80						100.54
2144A	1.67						100.67
2144A	1.21						100.73
2144A	1.20						100.39
2144A	1.27						100.65
2144A	1.20						100.67
2144A	1.23						100.98
2144A	1.18						101.46
2144A	1.16						100.18
2144A	1.31						100.32
2144A	1.36						100.39
2144A	1.44						100.86
2146A	1.61						99.88
2146A	1.68						100.20
2146A	1.66						100.54
2146A	2.23						100.72
2146A	1.74						101.40
2146A	1.56						100.10
2146A	1.58						100.66
2146A	1.61						100.76
2146A	1.55						100.96
2146A	1.55						100.99
2146A	1.59						100.10
2146A	1.55						100.40
2146A	1.56						100.50
2146A	1.62						100.76
2146A	1.54						100.84
2006B	0.83						100.17
2006B	0.93						100.50
2006B	0.97						100.31
2006B	0.93						100.48
2006B	0.83						100.38

Sample	CaO	Na_2O	K_2O	Cl	F	H_2O	TOTAL
2006B	0.90						100.80
2006B	0.91						100.47
2006B	0.91						101.12
2006B	0.91						101.02
2006B	0.85						100.81
2006B	0.88						100.79
2006B	0.93						101.00
2006B	0.70						100.48
2133A	1.41						100.60
2133A	1.41						100.72
2133A	1.36						99.96
2133A	1.49						100.44
2133A	1.44						99.97
2133A	1.56						101.00
2133A	1.43						101.03
2133A	1.47						100.81
2133A	1.46						100.82
2133A	1.42						101.18
2133A	1.40						101.04
2133A	1.41						101.03
2133A	1.39						100.78
2133A	1.48						100.89
2133A	1.38						100.88
D-28	2.00	0.00	0.00			0.00	100.30
D-56	1.70	0.00	0.00			0.00	99.86
D-87	1.60	0.00	0.00			0.00	99.72
D-102	1.80	0.00	0.00			0.00	99.42
D-175	1.60	0.00	0.00			0.00	99.28
R-114	2.30	0.00	0.00			0.00	100.41
R-124	1.90	0.00	0.00			0.00	100.90
W-53	1.50	0.00	0.00			0.00	99.20
D-141	1.70	0.00	0.00			0.00	101.10
D-149	1.40	0.00	0.00			0.00	101.00
D-165	2.00	0.00	0.00			0.00	99.95
D-139	1.50	0.00	0.00			0.00	100.67
D-28	2.00	0.00	0.00			0.00	100.30
H-29	1.50						98.52
H_66	1.89						99.24
H-70	1.45						99.45
H-126	1.64						104.38
WE-4-58	1.51						98.76
AKR-21	1.76						101.40
G1	2.15						100.05
G2	2.40						98.40
G3	2.00						100.83
G4	1.87						98.61
G5	1.07						99.91
G6	2.96						100.44

Sample	CaO	Na_2O	K_2O	Cl	F	H_2O	TOTAL
G7	0.72						99.75

Appendix S4.8

Compilation of biotite major element composition for Chapter 5

Paper	Analysis	Sample	Rock Type	Grain	Number	Line	SiO_2	TiO_2	Al_2O_3	FeO	MnO	MgO	CaO	Na_2O
This Study	2133A_bt1	2133A	Gnt/Crd Aluminious	1.00	35.00	114.00	38.58	4.18	14.45	9.84		18.57		
This Study	2133A_bt1	2133A	Gnt/Crd Aluminious	1.00	35.00	115.00	38.42	2.77	14.55	9.19		18.84		
This Study	2133A_bt2	2133A	Gnt/Crd Aluminious	2.00	36.00	116.00	37.67	2.92	14.82	9.19		17.75		
This Study	2133A_bt2	2133A	Gnt/Crd Aluminious	2.00	36.00	117.00	37.80	3.66	15.35	10.36		17.17		
This Study	2133A_bt3	2133A	Gnt/Crd Aluminious	3.00	37.00	118.00	37.87	3.11	15.10	9.94		17.85		
This Study	2133A_bt3	2133A	Gnt/Crd Aluminious	3.00	37.00	119.00	37.76	4.51	14.38	10.68		17.52		
This Study	2006B_bt1	2006B	Gnt/Crd Aluminious	1.00	38.00	120.00	35.45	2.50	14.49	14.56		13.77		
This Study	2006B_bt1	2006B	Gnt/Crd Aluminious	1.00	38.00	121.00	36.09	3.65	15.10	15.69		14.46		
This Study	2006B_bt2	2006B	Gnt/Crd Aluminious	2.00	39.00	122.00	35.95	4.91	15.05	14.96		14.60		
This Study	2006B_bt2	2006B	Gnt/Crd Aluminious	2.00	39.00	123.00	36.09	5.24	15.13	15.45		14.24		
This Study	2006B_bt3	2006B	Gnt/Crd Aluminious	3.00	40.00	124.00	36.18	3.79	15.27	15.62		14.40		
This Study	2006B_bt3	2006B	Gnt/Crd Aluminious	3.00	40.00	125.00	36.04	3.86	15.16	15.16		14.63		
This Study	2061A_bt1	2061A	Gnt/Crd Aluminious	1.00	41.00	126.00	36.38	9.35	15.08	12.47		16.05		
This Study	2061A_bt1	2061A	Gnt/Crd Aluminious	1.00	41.00	127.00	36.28	6.91	14.93	12.78		16.63		
This Study	2061A_bt2	2061A	Gnt/Crd Aluminious	2.00	42.00	128.00	36.58	6.85	15.16	11.58		16.38		
This Study	2061A_bt2	2061A	Gnt/Crd Aluminious	2.00	42.00	129.00	36.71	4.87	15.74	11.02		16.54		
This Study	2061A_bt3	2061A	Gnt/Crd Aluminious	3.00	43.00	130.00	36.44	4.57	15.22	12.34		15.52		
This Study	2061A_bt3	2061A	Gnt/Crd Aluminious	3.00	43.00	131.00	36.57	6.05	16.44	10.37		16.73		
This Study	2061A_bt4	2061A	Gnt/Crd Aluminious	4.00	44.00	132.00	36.37	4.80	14.43	14.27		14.97		
This Study	2061A_bt4	2061A	Gnt/Crd Aluminious	4.00	44.00	133.00	36.77	4.92	15.50	14.06		14.33		
This Study	2144A_bt1	2144A	Gnt/Crd Aluminious	1.00	45.00	134.00	36.07	5.11	16.08	14.70		14.60		
This Study	2144A_bt1	2144A	Gnt/Crd Aluminious	1.00	45.00	135.00	36.27	4.66	15.78	14.11		14.81		
This Study	2144A_bt2	2144A	Gnt/Crd Aluminious	2.00	46.00	136.00	36.53	6.86	15.91	14.25		14.25		
This Study	2144A_bt2	2144A	Gnt/Crd Aluminious	2.00	46.00	137.00	34.99	6.77	15.72	20.68		9.28		
This Study	2144A_bt3	2144A	Gnt/Crd Aluminious	3.00	47.00	138.00	35.49	5.31	15.78	20.18		10.49		
This Study	2144A_bt3	2144A	Gnt/Crd Aluminious	3.00	47.00	139.00	35.35	5.75	15.64	19.98		9.84		
This Study	2146A_bt1	2146A	Gnt/Crd Aluminious	1.00	48.00	140.00	37.20	4.56	16.08	12.92		15.84		
This Study	2146A_bt1	2146A	Gnt/Crd Aluminious	1.00	48.00	141.00	36.30	4.20	15.65	16.38		13.40		
This Study	2146A_bt2	2146A	Gnt/Crd Aluminious	2.00	49.00	142.00	36.61	3.34	15.94	14.47		14.45		
This Study	2146A_bt2	2146A	Gnt/Crd Aluminious	2.00	49.00	143.00	36.68	3.26	16.56	16.15		12.53		
This Study	2146A_bt3	2146A	Gnt/Crd Aluminious	3.00	50.00	144.00	36.07	3.68	15.66	18.54		12.23		
This Study	2146A_bt3	2146A	Gnt/Crd Aluminious	3.00	50.00	145.00	36.82	4.29	15.81	12.93		15.49		
Reinhart, 1968	D-28	D-28	Gnt/Crd Aluminious	bt			38.20	4.80	16.00	14.26	0.01	14.00	0.37	0.18
Reinhart, 1968	D-56	D-56	Gnt/Crd Aluminious	bt			37.30	3.70	18.50	16.19	0.03	11.70	0.38	0.19
Reinhart, 1968	D-87	D-87	Gnt/Crd Aluminious	bt			36.80	3.90	17.30	18.64	0.02	10.30	0.20	0.13
Reinhart, 1968	D-102	D-102	Gnt/Crd Aluminious	bt			37.60	3.50	18.00	17.56	0.01	9.80	0.57	0.10
Reinhart, 1968	D-175	D-175	Gnt/Crd Aluminious	bt			37.60	3.60	16.70	15.22	0.07	12.40	0.16	0.15
Reinhart, 1968	R-114	R-114	Gnt/Crd Aluminious	bt			36.20	4.20	18.00	19.21	0.10	10.00	0.30	0.10
Reinhart, 1968	R-124	R-124	Gnt/Crd Aluminious	bt			38.30	3.50	16.80	15.28	0.03	12.00	0.50	0.18
Reinhart, 1968	W-53	W-53	Gnt/Crd Aluminious	bt			39.10	5.40	15.10	13.86	0.12	13.80	0.40	0.10
Reinhart, 1968	D-141	D-141	Gnt/Crd Aluminious	bt			38.60	3.00	17.30	15.29	0.01	12.10	0.20	0.13
Reinhart, 1968	D-149	D-149	Gnt/Crd Aluminious	bt			38.90	3.70	17.10	13.32	0.01	14.40	0.02	0.29
Reinhart, 1968	D-165	D-165	Gnt/Crd Aluminious	bt			39.10	4.60	16.10	14.72	0.03	13.00	0.20	0.18
Reinhart, 1968	D-139	D-139	Gnt/Crd Aluminious	bt			39.40	4.00	14.70	14.41	0.10	13.70	0.40	0.22
Reinhart, 1968	D-24	D-24	Gnt/Crd Aluminious	bt			39.40	4.60	15.80	13.59	0.11	14.90	0.20	0.16
Reinhart, 1968	D-136	D-136	Gnt/Crd Aluminious	bt			40.80	3.80	14.00	14.71	0.10	15.30	0.10	0.20
Reinhart, 1968	D-34	D-34	Gnt/Crd Aluminious	bt			36.40	4.20	17.20	13.53	0.09	13.80	0.06	0.15
Wynne-Edwards & Hay 1963	H-29	H-29	Gnt/Crd Aluminious	bt			35.59	3.90	19.40	18.89	0.02	9.70		0.10

Paper	Analysis	Sample	Rock Type	Grain	Number	Line	SiO_2	TiO_2	Al_2O_3	FeO	MnO	MgO	CaO	Na_2O
Wynne-Edwards & Hay 1963	H-60	H-60	Gnt/Crd Aluminious	bt			39.50	2.15	20.00	14.43	0.26	11.50		0.15
Wynne-Edwards & Hay 1963	H-66	H-66	Gnt/Crd Aluminious	bt			36.10	2.76	20.00	17.71	0.05	8.70		0.10
Wynne-Edwards & Hay 1963	H-70	H-70	Gnt/Crd Aluminious	bt			34.23	2.76	19.40	21.99	0.13	8.40		0.15
Wynne-Edwards & Hay 1963	H-90	H-90	Gnt/Crd Aluminious	bt			35.00	2.45	19.00	18.75	0.15	10.40		0.13
Wynne-Edwards & Hay 1963	H-105	H-105	Gnt/Crd Aluminious	bt			38.50	2.39	20.00	17.77	0.12	7.50		0.20
Wynne-Edwards & Hay 1963	H-126	H-126	Gnt/Crd Aluminious	bt			36.07	2.37	18.80	17.49	0.06	8.20		0.16
Wynne-Edwards & Hay 1963	WE-4-57	WE-4-58	Gnt/Crd Aluminious	bt			34.50	2.69	20.50	20.03	0.08	7.60		0.09
Grammatikopoulos et al. 2007	LL53	LL53	Granitoid				38.25	5.48	14.68	8.39	0.00	1895.00	0.00	0.33
Grammatikopoulos et al. 2007	LL138	LL138	Granitoid				37.45	7.16	13.51	13.46	0.00	14.82	0.00	0.00
Grammatikopoulos et al. 2007	LL23	LL23	Granitoid				39.62	2.51	12.18	12.46	0.23	18.19	0.41	0.46
Grammatikopoulos et al. 2007	LL25	LL25	Granitoid				39.02	3.04	13.41	14.74	0.32	15.21	0.13	0.12
Grammatikopoulos et al. 2007	LL25	LL25	Granitoid				39.37	2.40	13.70	14.10	0.47	16.17	0.16	0.00
Grammatikopoulos et al. 2007	LL24	LL24	Granitoid				39.32	2.11	12.47	13.26	0.15	17.00	0.09	0.00
Grammatikopoulos et al. 2007	LL24	LL24	Granitoid				38.70	2.42	12.97	14.97	0.24	15.70	0.12	0.00
Grammatikopoulos et al. 2007	LN06	LN06	Granitoid				39.95	0.93	12.28	15.88	0.65	15.93	0.10	0.15
Grammatikopoulos et al. 2007	LN10	LN10	Granitoid				36.46	412.00	16.56	21.51	0.14	9.28	0.14	0.13
Grammatikopoulos et al. 2007	LN10	LN10	Granitoid				36.35	4.21	16.95	21.58	0.00	9.43	0.19	0.15
Russell, 2009	AKR-17	AKR-17	Gnt/Crd Aluminious				37.18	5.36	14.81	11.43	0.05	16491.00	0.00	0.00
Russell, 2009	AKR-19	AKR-19	Gnt/Crd Aluminious				37.19	4.96	14.60	10.63	0.08	17.16	0.02	0.02
Russell, 2009	AKR-20	AKR-20	Gnt/Crd Aluminious				36.84	5.25	14.59	11.20	0.04	16.59	0.02	0.02
Russell, 2009	AKR-21	AKR-21	Gnt/Crd Aluminious				36.81	4.63	14.84	15.33	0.04	14.21	0.00	0.00
Russell, 2009	AKR-26	AKR-26	Gnt/Crd Aluminious				36.05	2.55	16.40	18.65	0.19	10.85	0.02	0.02

Analysis	K_2O	Cl	F	H_2O	TOTAL
2133A_bt1	10.18	0.05	2.32	2.82	100.00
2133A_bt1	10.12	0.05	2.25	4.78	100.00
2133A_bt2	10.36	0.10	1.94	6.08	100.00
2133A_bt2	10.20	0.06	1.84	4.34	100.00
2133A_bt3	10.09	0.08	1.95	4.85	100.00
2133A_bt3	10.00	0.09	1.93	3.96	100.00
2006B_bt1	9.63	0.94	0.93	8.35	100.00
2006B_bt1	10.06	0.98	0.72	3.78	100.00
2006B_bt2	9.86	1.07	0.89	3.34	100.00
2006B_bt2	9.73	0.96	0.79	2.92	100.00
2006B_bt3	10.01	0.91	1.08	3.40	100.00
2006B_bt3	9.99	0.78	0.91	4.03	100.00
2061A_bt1	9.47	0.25	0.93	0.47	100.00
2061A_bt1	9.31	0.23	1.13	2.33	100.00
2061A_bt2	10.07	0.22	1.13	2.56	100.00
2061A_bt2	10.08	0.30	1.04	4.22	100.00
2061A_bt3	10.07	0.22	0.74	5.24	100.00
2061A_bt3	9.85	0.14	0.53	3.57	100.00
2061A_bt4	9.93	0.23	0.87	4.55	100.00
2061A_bt4	10.09	0.24	0.72	3.73	100.00
2144A_bt1	9.83	0.14	1.00	2.92	100.00
2144A_bt1	9.88	0.28	1.32	3.51	100.00
2144A_bt2	10.02	0.32	1.10	1.30	100.00
2144A_bt2	9.51	0.40	0.40	2.52	100.00
2144A_bt3	9.77	0.46	0.78	2.19	100.00
2144A_bt3	9.74	0.43	0.77	2.92	100.00
2146A_bt1	10.21	0.04	1.53	2.28	100.00
2146A_bt1	9.99	0.05	1.39	3.25	100.00
2146A_bt2	10.00	0.06	1.40	4.35	100.00
2146A_bt2	9.29	0.07	1.05	4.88	100.00
2146A_bt3	9.97	0.08	0.87	3.28	100.00
2146A_bt3	10.07	0.08	1.69	3.55	100.00
D-28	9.30			2.20	99.32
D-56	8.50			2.70	99.19
D-87	9.70			2.60	99.59
D-102	8.40			2.50	98.04
D-175	7.70			3.40	97.00
R-114	9.40			3.20	100.71
R-124	9.00			2.50	98.09
W-53	9.50			2.00	99.38
D-141	8.40			2.90	97.93
D-149	8.50			2.90	99.14
D-165	8.80			2.80	99.53
D-139	8.60			2.80	98.33
D-24	9.30			2.20	100.26
D-136	7.80			2.40	99.21
D-34	9.20			4.50	99.13
H-29	9.70				97.30

Analysis	K_2O	Cl	F	H_2O	TOTAL
H-60	9.25				97.24
H-66	9.78				95.20
H-70	9.70				96.76
H-90	10.00				95.88
H-105	9.59				96.07
H-126	9.70				92.85
WE-4-57	9.30				94.79
LL53	9.99				1972.12
LL138	9.95				96.35
LL23	7.93				93.99
LL25	9.14				95.13
LL25	8.44				94.81
LL24	10.28				94.68
LL24	10.07				95.19
LN06	9.87				95.74
LN10	10.08	0.57			506.87
LN10	10.02	0.58			99.46
AKR-17	10.53			4.08	16574.43
AKR-19	10.44			4.06	99.16
AKR-20	10.57			4.04	99.14
AKR-21	9.85			4.01	99.72
AKR-26	10.53			3.92	99.17

Appendix S4.9

Compilation of cordierite major element composition for Chapter 5

Paper	Analysis	Sample	Rock Type	Grain	Number	Line	SiO_2	TiO_2	Al_2O_3	FeO	MnO	MgO	CaO	Na_2O
This Study	2146A_crd1	2146A	Gnt/Crd Aluminious	1	11	60	49.22		34.27	6.98	0.12	9.13	0.02	
This Study	2146A_crd1	2146A	Gnt/Crd Aluminious	1	11	61	49.24		34.09	5.61	0.05	9.78	0.01	
This Study	2146A_crd1_R2	2146A	Gnt/Crd Aluminious	1	12	62	49.06		34.05	6.32	0.09	9.40	0.02	
This Study	2146A_crd1_R2	2146A	Gnt/Crd Aluminious	1	12	63	49.24		34.06	6.84	0.11	9.22	0.02	
This Study	2146A_crd2	2146A	Gnt/Crd Aluminious	2	13	64	49.21		33.78	7.01	0.11	8.90	0.01	
This Study	2146A_crd2	2146A	Gnt/Crd Aluminious	2	13	65	49.41		34.04	6.06	0.06	9.63	0.01	
This Study	2146A_crd3	2146A	Gnt/Crd Aluminious	3	14	66	49.11		34.11	6.74	0.09	9.25	0.01	
This Study	2146A_crd3	2146A	Gnt/Crd Aluminious	3	14	67	49.26		34.19	6.27	0.08	9.43	0.02	
This Study	2144A_crd1	2144A	Gnt/Crd Aluminious	1	15	68	48.67		33.69	7.68	0.02	8.52	0.01	
This Study	2144A_crd1	2144A	Gnt/Crd Aluminious	1	15	69	48.62		33.61	7.98	0.03	8.55	0.01	
This Study	2144A_crd2	2144A	Gnt/Crd Aluminious	2	16	71	49.09		33.81	8.13	0.01	8.44	0.00	
This Study	2144A_crd3	2144A	Gnt/Crd Aluminious	3	17	72	49.07		33.77	6.57	0.01	9.20	0.00	
This Study	2144A_crd3	2144A	Gnt/Crd Aluminious	3	17	73	48.94		33.83	6.45	0.02	9.33	0.01	
This Study	2061A_crd1	2061A	Gnt/Crd Aluminious	1	18	74	49.95		34.45	3.86	0.11	10.93	0.02	
This Study	2061A_crd1	2061A	Gnt/Crd Aluminious	1	18	75	49.82		34.31	3.73	0.09	10.98	0.02	
This Study	2061A_crd2	2061A	Gnt/Crd Aluminious	2	19	77	49.80		34.39	3.60	0.07	11.14	0.02	
This Study	2061A_crd3	2061A	Gnt/Crd Aluminious	3	20	79	49.90		34.61	3.59	0.09	11.05	0.01	
Reinhart, 1968	D-28	D-28	Gnt/Crd Aluminious	crd			50.30	0.02	29.20	5.70	0.01	9.70	0.33	0.30
Reinhart, 1968	D-56	D-56	Gnt/Crd Aluminious	crd			50.00	0.01	34.20	6.04	0.00	7.70	0.00	0.00
Reinhart, 1968	D-87	D-87	Gnt/Crd Aluminious	crd			49.50	0.07	29.00	5.58	0.00	4.40	0.00	0.00
Reinhart, 1968	D-102	D-102	Gnt/Crd Aluminious	crd			50.20	0.10	32.60	6.42	0.09	8.10	0.28	0.14
Reinhart, 1968	D-175	D-175	Gnt/Crd Aluminious	crd			44.40	0.11	27.60	7.40	0.03	8.20	0.81	6.00
Reinhart, 1968	R-114	R-114	Gnt/Crd Aluminious	crd			47.00	0.11	31.30	7.91	0.07	6.60	0.07	0.22
Reinhart, 1968	R-124	R-124	Gnt/Crd Aluminious	crd			49.10	0.01	32.20	6.86	0.05	8.90	0.13	0.20
Reinhart, 1968	W-53	W-53	Gnt/Crd Aluminious	crd			49.30	0.01	33.60	4.58	0.22	10.80	0.00	0.09
Reinhart, 1968	D-24	D-24	Gnt/Crd Aluminious	crd			47.00	0.01	34.60	4.28	0.17	10.90	0.00	0.09
Reinhart, 1968	D-136	D-136	Gnt/Crd Aluminious	crd			50.40	0.03	32.40	4.23	0.11	10.00	0.19	0.46
Reinhart, 1968	D-34	D-34	Gnt/Crd Aluminious	crd			48.50	0.04	32.40	4.24	0.14	9.20	0.00	0.20
Reinhart, 1968	D-115	D-115	Gnt/Crd Aluminious	crd			49.60	0.03	33.00	4.33	0.13	10.30	0.03	0.40
Reinhart, 1968	D-121	D-121	Gnt/Crd Aluminious	crd			50.00	0.07	31.40	7.16	0.15	8.50	0.10	0.10
Reinhart, 1968	D-174	D-174	Gnt/Crd Aluminious	crd			49.00	0.12	32.40	6.46	0.13	8.20	0.19	0.53
Wynne-Edwards & Hay 1963	H-29	H-29	Gnt/Crd Aluminious	crd						8.34	0.20	7.99		
Wynne-Edwards & Hay 1963	H-60	H-60	Gnt/Crd Aluminious	crd						5.68	0.11	6.80		
Wynne-Edwards & Hay 1963	H-70	H-70	Gnt/Crd Aluminious	crd						4.14	0.04	2.11		
Wynne-Edwards & Hay 1963	H-90	H-90	Gnt/Crd Aluminious	crd						6.72	0.02	7.00		
Wynne-Edwards & Hay 1963	H-105	H-105	Gnt/Crd Aluminious	crd						7.35	0.10	6.80		

Analysis	K_2O	Cl	H_2O	TOTAL
2146A_crd1				99.73
2146A_crd1				98.78
2146A_crd1_R2				98.93
2146A_crd1_R2				99.49
2146A_crd2				99.02
2146A_crd2				99.22
2146A_crd3				99.31
2146A_crd3				99.25
2144A_crd1				98.60
2144A_crd1				98.79
2144A_crd2				99.49
2144A_crd3				98.63
2144A_crd3				98.59
2061A_crd1				99.31
2061A_crd1				98.96
2061A_crd2				99.02
2061A_crd3				99.26
D-28	0.60		0.00	96.16
D-56	0.00		0.00	97.95
D-87	0.01		0.00	88.56
D-102	0.58		2.30	100.81
D-175	1.30		5.70	101.55
R-114	2.09		5.70	101.07
R-124	0.97		2.90	101.32
W-53	0.12		2.00	89.92
D-24	0.15		1.90	99.10
D-136	0.96		2.20	100.98
D-34	1.94		3.90	100.56
D-115	0.90		2.60	112.12
D-121	0.40		2.20	100.08
D-174	1.16		2.50	100.69
H-29				16.53
H-60				12.59
H-70				6.29
H-90				13.74
H-105				14.25

Appendix S4.10

Compilation of amphibole major element composition for Chapter 5

Paper	Analysis	Sample	Rock Type	SiO_2	TiO_2	Al_2O_3	FeO	MnO	MgO	CaO	Na_2O	K_2O	Cl	H_2O	TOTAL
Grammatikopoulos et al. 2007	LL23	LL23	Granitoid	44.45	1.31	8.68	14.93	0.36	13.08	11.45	2.04	1.39		2.00	99.69
Grammatikopoulos et al. 2007	LL23	LL23	Granitoid	45.21	1.43	8.50	14.13	0.63	13.36	11.72	2.08	1.36		2.04	100.46
Grammatikopoulos et al. 2007	LL137	LL137	Granitoid	45.52	1.25	8.49	12.80	0.43	14.52	11.32	2.01	1.29		2.03	99.66
Grammatikopoulos et al. 2007	LL137	LL137	Granitoid	45.24	1.53	8.26	13.80	0.37	14.17	11.08	2.40	1.26		2.02	100.13
Grammatikopoulos et al. 2007	LN24	LN24	Granitoid	42.71	1.12	9.76	18.44	0.44	11.17	11.33	2.01	1.60	0.42	1.89	100.89
Grammatikopoulos et al. 2007	LN24	LN24	Granitoid	42.68	1.02	9.94	17.76	0.63	11.03	12.22	1.83	1.75	0.53	1.85	101.24
Grammatikopoulos et al. 2007	LN25	LN25	Granitoid	43.64	4.23	8.16	13.38	0.39	11.19	14.03	1.15	0.79		1.99	98.95
Grammatikopoulos et al. 2007	LN25	LN25	Granitoid	44.47	0.90	9.27	17.64	0.56	11.68	11.80	1.74	1.50		2.03	101.59
Grammatikopoulos et al. 2007	LN06	LN06	Granitoid	43.12	0.59	9.54	21.56	0.91	8.34	11.58	2.04	1.71	0.41	1.86	101.66
Grammatikopoulos et al. 2007	LN06	LN06	Granitoid	38.27	0.24	9.74	22.24	0.78	6.81	14.19	1.71	1.89	0.55	1.72	98.14
Wynne-Edwards, 1967	A1	A1	Mafic Schist	35.60	2.30	16.00	16.52	0.24	10.80	11.30	3.16	0.93			96.85
Wynne-Edwards, 1967	A2	A2	Cpx Aluminious	42.24	2.76	10.47	19.70	0.28	9.22	11.23	1.44	0.89			98.23

Appendix S4.11

Compilation of pyroxene major element composition for Chapter 5

Paper	Analysis	Sample	Rock Type	Grain	NUMBER	LINE	SiO_2	TiO_2	Al_2O_3	FeO	MnO	MgO	CaO	Na_2O	K_2O
This Study	2061A_opx1	2061A	Gnt/Crd Aluminious	1	10	29	47.39		8.59	21.66	0.53	21.37	0.06		
This Study	2061A_opx1	2061A	Gnt/Crd Aluminious	1	10	30	46.70		9.48	21.90	0.49	21.04	0.11		
This Study	2061A_opx1	2061A	Gnt/Crd Aluminious	1	10	31	47.20		8.68	21.68	0.49	20.98	0.07		
This Study	2061A_opx2	2061A	Gnt/Crd Aluminious	2	11	33	49.84		6.55	21.14	0.49	22.29	0.04		
This Study	2061A_opx2	2061A	Gnt/Crd Aluminious	2	13	38	47.81		8.40	21.41	0.48	21.50	0.05		
This Study	2061A_opx2	2061A	Gnt/Crd Aluminious	2	14	39	46.87		8.73	21.58	0.49	21.27	0.06		
This Study	2061A_opx3	2061A	Gnt/Crd Aluminious	3	12	35	50.12		5.18	20.85	0.49	23.24	0.03		
This Study	2061A_opx3	2061A	Gnt/Crd Aluminious	3	12	36	48.35		6.60	21.89	0.47	22.02	0.04		
This Study	2061A_opx3	2061A	Gnt/Crd Aluminious	3	12	37	47.85		7.91	21.60	0.46	21.71	0.04		
Reinhart, 1968	W-53	W-53	Gnt/Crd Aluminious	opx			47.90	0.46	8.60	21.87	0.50	19.80	0.20	0.08	0.41
Reinhart, 1968	D-139	D-139	Gnt/Crd Aluminious	opx			48.40	0.28	7.60	22.12	0.34	18.70	1.30	0.19	0.09
Reinhart, 1968	D-24	D-24	Gnt/Crd Aluminious	opx			48.60	1.50	8.60	21.24	0.38	18.10	0.30	0.28	0.60
Reinhart, 1968	D-136	D-136	Gnt/Crd Aluminious	opx			51.00	0.72	7.20	21.19	0.35	20.10	0.30	0.12	0.24
Grammatikopoulos et al. 2007	LL53		Granitoid	px			53.50	0.32	2.52	14.31	0.41	27.31	1.35	0.28	0.00
Grammatikopoulos et al. 2007	LL138	LL138	Granitoid	px			51.79	0.08	1.77	22.13	0.67	22.40	1.15	0.00	0.00
Grammatikopoulos et al. 2007	LL138	LL138	Granitoid	px			52.15	0.12	1.98	21.72	0.42	21.63	2.25	0.00	0.00
Grammatikopoulos et al. 2007	LL53	LL53	Granitoid	px			50.69	0.61	3.98	7.87	0.32	15.85	19.47	0.83	0.00
Grammatikopoulos et al. 2007	LL53	LL53	Granitoid	px			50.42	0.55	4.38	6.65	0.24	14.51	21.67	0.87	0.03
Grammatikopoulos et al. 2007	LL138	LL138	Granitoid	px			49.44	0.98	2.60	13.93	0.18	14.60	17.42	0.40	0.14
Grammatikopoulos et al. 2007	LL138	LL138	Granitoid	px			49.90	0.83	4.00	9.09	31.00	13.12	22.16	0.59	0.00
Grammatikopoulos et al. 2007	LL138	LL138	Granitoid	px			48.82	0.27	2.81	17.53	0.32	15.57	14.36	0.29	0.00
Grammatikopoulos et al. 2007	LN25	LN25	Granitoid	px			52.11	0.00	0.96	10.88	0.78	11.87	22.89	0.64	0.00
Grammatikopoulos et al. 2007	LN25	LN25	Granitoid	px			51.30	0.07	1.17	13.05	0.80	10.56	22.62	0.82	0.00
Wynne-Edwards, 1967	P1	P1	Cpx Aluminious	px			53.70	0.16	4.82	9.46	0.55	11.60	19.10	1.12	0.30

Sample	Cl	F	H_2O	TOTAL
2061A				99.61
2061A				99.72
2061A				99.11
2061A				100.35
2061A				99.65
2061A				99.01
2061A				99.92
2061A				99.37
2061A				99.56
W-53			0.00	99.82
D-139			0.00	99.02
D-24			0.00	99.60
D-136			0.00	101.22
				100.00
LL138				99.99
LL138				100.27
LL53				99.62
LL53				99.32
LL138				99.69
LL138				130.69
LL138				99.97
LN25				100.13
LN25				100.39
P1				100.81

Appendix S4.12

Compilation of feldspar major element composition for Chapter 5

Paper	Analysis	Sample	Rock Type	Portion	SiO_2	TiO_2	Al_2O_3	FeO	MnO	MgO	CaO	Na_2O	K_2O	Cl
Grammatikopoulos et al. 2007	LL137	LL137	Granitoid	Whole	66.60	0.14	19.07	0.00	0.18	0.00	0.15	5.04	9.59	
Grammatikopoulos et al. 2007	LL137	LL137	Granitoid	Whole	65.02	0.12	19.09	0.00	0.18	0.00	0.43	2.45	12.89	
Grammatikopoulos et al. 2007	LL138	LL138	Granitoid	Whole	57.28	0.00	26.86	0.09	0.00	0.05	9.39	6.13	0.53	
Grammatikopoulos et al. 2007	LL138	LL138	Granitoid	Whole	56.35	0.00	27.65	0.15	0.00	0.00	10.25	5.55	0.47	
Grammatikopoulos et al. 2007	LL23	LL23	Granitoid	Whole	65.04	0.00	22.82	0.00	0.00	0.20	4.17	6.35	0.13	
Grammatikopoulos et al. 2007	LL23	LL23	Granitoid	Whole	65.58	0.00	22.67	0.00	0.00	0.28	4.05	6.30	0.20	
Grammatikopoulos et al. 2007	LL53	LL53	Granitoid	Whole	54.98	0.09	29.06	0.00	0.08	0.19	11.69	4.79	0.11	
Grammatikopoulos et al. 2007	LL53	LL53	Granitoid	Whole	52.68	0.14	30.52	0.18	0.00	0.26	13.26	3.96	0.05	
Grammatikopoulos et al. 2007	LN06	LN06	Granitoid	Whole	65.15	0.00	22.24	0.00	0.00	0.05	3.31	9.73	0.30	
Grammatikopoulos et al. 2007	LN06	LN06	Granitoid	Whole	66.10	0.00	19.65	0.00	0.00	0.06	0.40	5.50	8.48	
Grammatikopoulos et al. 2007	LN06	LN06	Granitoid	Whole	65.06	0.14	18.50	0.00	0.00	0.00	0.17	0.90	15.44	
Grammatikopoulos et al. 2007	LN06	LN06	Granitoid	Whole	65.22	0.00	18.67	0.00	0.00	0.00	0.11	0.75	15.55	
Grammatikopoulos et al. 2007	LN10	LN10	Granitoid	Whole	60.42	0.00	25.55	0.00	0.00	0.08	6.91	7.62	0.19	
Grammatikopoulos et al. 2007	LN10	LN10	Granitoid	Whole	64.15	0.06	19.56	0.00	0.00	0.07	0.78	1.63	13.90	
Grammatikopoulos et al. 2007	LN10	LN10	Granitoid	Whole	64.60	0.08	18.72	0.00	0.00	0.07	0.17	0.97	15.30	
Grammatikopoulos et al. 2007	LN24	LN24	Granitoid	Whole	63.22	0.00	23.70	0.00	0.00	0.00	4.74	8.64	0.16	
Grammatikopoulos et al. 2007	LN24	LN25	Granitoid	Whole	62.47	0.07	23.62	0.24	0.00	0.14	4.71	8.81	0.24	
Grammatikopoulos et al. 2007	LN24	LN24	Granitoid	Whole	64.61	0.12	18.66	0.00	0.10	0.00	0.07	0.99	15.29	
Grammatikopoulos et al. 2007	LN24	LN24	Granitoid	Whole	64.96	0.18	18.66	0.00	0.00	0.00	0.00	1.08	15.04	
Grammatikopoulos et al. 2007	LN25	LN25	Granitoid	Whole	64.96	0.17	22.99	0.00	0.00	0.00	3.82	8.08	0.27	
Grammatikopoulos et al. 2007	LN25	LN26	Granitoid	Whole	63.16	0.08	23.60	0.00	0.00	0.06	4.71	7.68	0.19	
Grammatikopoulos et al. 2007	LN25	LN25	Granitoid	Whole	65.52	0.20	19.02	0.00	0.00	0.00	0.15	1.06	14.49	
Russell, 2009	AKR-17	AKR-17	Gnt/Crd Aluminious	Whole	58.60		25.71	0.03			8.02	6.87	0.22	
Russell, 2009	AKR-17	AKR-17	Gnt/Crd Aluminious	Whole	64.30		18.14	0.85			0.17	1.57	14.50	
Russell, 2009	AKR-19	AKR-19	Gnt/Crd Aluminious	Whole	59.00		25.92	0.02			8.13	6.68	0.21	
Russell, 2009	AKR-19	AKR-19	Gnt/Crd Aluminious	Whole	65.88		18963.00	0.04			0.40	1.50	14.93	
Russell, 2009	AKR-20	AKR-20	Gnt/Crd Aluminious	Whole	61.68		24.60	0.04			6.77	7.28	0.14	
Russell, 2009	AKR-20	AKR-20	Gnt/Crd Aluminious	Whole	65.15		18.61	0.03			0.44	1.67	14.91	
Russell, 2009	AKR-21	AKR-21	Gnt/Crd Aluminious	Whole	55.88		27.59	0.05			10.17	5.72	0.12	
Russell, 2009	AKR-21	AKR-21	Gnt/Crd Aluminious	Whole	66.49		18.86	0.03			0.14	1.19	15.37	
This Study	2085B_1	2085B	Gnt/Crd Aluminious	Integrated	64.36		19.54	0.02	0.00	0.00	0.73	2.29	12.88	0.00
This Study	2085B_2	2085B	Gnt/Crd Aluminious	Integrated	66.07		19.22	0.02	0.00	0.00	0.12	4.17	10.81	0.00
This Study	2085B_3	2085B	Gnt/Crd Aluminious	Integrated	65.84		19.24	0.05	0.00	0.00	0.14	4.76	9.75	0.00
This Study	2085B_Perth1A	2085B	Gnt/Crd Aluminious	Host	64.68		18.89	0.02	0.00	0.00	0.11	1.38	14.67	0.00
This Study	2085B_Perth1B	2085B	Gnt/Crd Aluminious	Lamallae	62.00		24.18	0.04	0.00	0.00	5.16	8.74	0.11	0.00
This Study	2085B_Perth2A	2085B	Gnt/Crd Aluminious	Lamallae	68.53		19.87	0.02	0.00	0.00	0.24	11.60	0.07	0.00
This Study	2085B_Perth2B	2085B	Gnt/Crd Aluminious	Host	65.11		18.97	0.02	0.00	0.00	0.06	1.26	15.03	0.00
This Study	2085B_Perth3A	2085B	Gnt/Crd Aluminious	Host	68.09		19.85	0.07	0.00	0.00	0.29	10.95	0.57	0.00
This Study	2085B_Perth3B	2085B	Gnt/Crd Aluminious	Lamallae	64.59		18.90	0.04	0.00	0.00	0.06	1.35	14.82	0.00
This Study	2133A_1	2133A	Gnt/Crd Aluminious	Integrated	58.91		25.28	0.05	0.00	0.00	6.45	3.65	6.18	0.00
This Study	2133A_2	2133A	Gnt/Crd Aluminious	Integrated	63.91		20.19	0.02	0.00	0.00	1.29	1.44	13.69	0.00
This Study	2133A_3	2133A	Gnt/Crd Aluminious	Integrated	54.96		29.35	0.07	0.00	0.00	10.77	5.09	0.42	0.00
This Study	2133A_Perth1A	2133A	Gnt/Crd Aluminious	Host	54.80		29.46	0.07	0.00	0.00	10.80	5.34	0.17	0.00
This Study	2133A_Perth1B	2133A	Gnt/Crd Aluminious	Lamallae	64.91		19.16	0.02	0.00	0.00	0.09	1.17	14.96	0.00
This Study	2133A_Perth2A	2133A	Gnt/Crd Aluminious	Lamallae	54.52		29.50	0.04	0.00	0.00	10.99	5.18	0.13	0.00
This Study	2133A_Perth2B	2133A	Gnt/Crd Aluminious	Host	65.03		19.09	0.01	0.00	0.00	0.14	1.00	15.30	0.00
This Study	2133A_Perth3A	2133A	Gnt/Crd Aluminious	Lamallae	63.43		19.33	0.65	0.00	0.00	0.12	0.98	14.65	0.00
This Study	2133A_Perth3B	2133A	Gnt/Crd Aluminious	Host	54.78		29.57	0.05	0.00	0.00	11.00	5.18	0.12	0.00

Paper	Analysis	Sample	Rock Type	Portion	SiO_2	TiO_2	Al_2O_3	FeO	MnO	MgO	CaO	Na_2O	K_2O	Cl
This Study	2143B_1	2143B	Gnt/Crd Aluminious	Integrated	67.90		19.66	0.05	0.00	0.00	0.19	9.36	3.28	0.00
This Study	2143B_2	2143B	Gnt/Crd Aluminious	Integrated	66.55		19.32	0.04	0.00	0.00	0.13	5.75	8.53	0.00
This Study	2143B_3	2143B	Gnt/Crd Aluminious	Integrated	67.10		19.52	0.14	0.00	0.00	0.13	6.72	7.06	0.00
This Study	2143B_Perth1A	2143B	Gnt/Crd Aluminious	Host	68.64		19.88	0.05	0.00	0.00	0.23	11.56	0.11	0.00
This Study	2143B_Perth1B	2143B	Gnt/Crd Aluminious	Lamallae	65.23		18.90	0.04	0.00	0.00	0.04	1.38	14.82	0.00
This Study	2143B_Perth2A	2143B	Gnt/Crd Aluminious	Lamallae	68.50		19.92	0.04	0.00	0.00	0.29	11.29	0.42	0.00
This Study	2143B_Perth2B	2143B	Gnt/Crd Aluminious	Host	64.86		18.79	0.03	0.00	0.00	-0.01	0.97	15.52	0.00
This Study	2143B_Perth3A	2143B	Gnt/Crd Aluminious	Host	68.62		20.06	0.03	0.00	0.00	0.25	11.46	0.20	0.00
This Study	2143B_Perth3B	2143B	Gnt/Crd Aluminious	Lamallae	65.13		18.83	0.29	0.00	0.00	-0.02	0.62	15.90	0.00
This Study	2143C_1	2143C	Quartzofeldspathic	Integrated	62.99		22.52	0.13	0.00	0.00	3.83	7.73	2.62	0.00
This Study	2143C_2	2143C	Quartzofeldspathic	Integrated	62.72		22.53	0.05	0.00	0.00	3.84	7.36	2.93	0.00
This Study	2143C_3	2143C	Quartzofeldspathic	Integrated	61.94		23.51	0.12	0.00	0.00	4.36	8.05	1.56	0.00
This Study	2143C_Perth1A	2143C	Quartzofeldspathic	Lamallae	64.63		18.78	0.10	0.00	0.00	0.06	0.50	15.90	0.00
This Study	2143C_Perth1B	2143C	Quartzofeldspathic	Host	62.71		23.18	0.13	0.00	0.00	4.50	9.00	0.28	0.00
This Study	2143C_Perth2A	2143C	Quartzofeldspathic	Lamallae	63.90		18.60	-0.02	0.00	0.00	0.22	0.59	15.72	0.00
This Study	2143C_Perth2B	2143C	Quartzofeldspathic	Host	62.46		23.39	0.06	0.00	0.00	4.64	8.84	0.12	0.00
This Study	2143C_Perth3A	2143C	Quartzofeldspathic	Host	68.16		19.74	0.04	0.00	0.00	0.36	11.60	0.09	0.00
This Study	2143C_Perth3B	2143C	Quartzofeldspathic	Host	62.24		23.59	0.08	0.00	0.00	4.59	8.44	0.98	0.00
This Study	2143C_Perth3C	2143C	Quartzofeldspathic	Lamallae	58.10		22.52	0.61	0.00	0.00	1.00	2.15	10.48	0.00
This Study	2147A_1	2147A	Granitoid	Integrated	62.37		20.09	1.24	0.00	0.00	1.62	3.53	9.57	0.00
This Study	2147A_2	2147A	Granitoid	Integrated	66.73		20.43	0.04	0.00	0.00	2.40	5.77	5.75	0.00
This Study	2147A_3	2147A	Granitoid	Integrated	63.29		22.32	0.08	0.00	0.00	3.54	6.92	3.90	0.00
This Study	2147A_Perth1A	2147A	Granitoid	Lamallae	61.16		22.96	1.51	0.00	0.00	4.45	8.39	0.22	0.00
This Study	2147A_Perth1B	2147A	Granitoid	Host	63.06		18.46	1.08	0.00	0.00	0.00	0.76	14.89	0.00
This Study	2147A_Perth2A	2147A	Granitoid	Host	65.26		18.63	0.02	0.00	0.00	0.01	1.68	14.12	0.00
This Study	2147A_Perth2B	2147A	Granitoid	Lamallae	66.60		21.28	0.05	0.00	0.00	3.94	8.39	0.10	0.00
This Study	2147A_Perth3A	2147A	Granitoid	Lamallae	65.23		18.64	0.01	0.00	0.00	0.00	1.17	15.12	0.00
This Study	2147A_Perth3B	2147A	Granitoid	Host	62.64		23.55	0.11	0.00	0.00	4.73	8.84	0.14	0.00
This Study	2170A_1	2170A	Granitoid	Integrated	64.87		20.97	0.03	0.00	0.00	1.89	5.67	7.10	0.00
This Study	2170A_2	2170A	Granitoid	Integrated	64.57		20.54	0.06	0.00	0.00	1.68	4.87	8.47	0.00
This Study	2170A_3	2170A	Granitoid	Integrated	64.32		21.58	0.05	0.00	0.00	2.60	6.24	5.58	0.00
This Study	2170A_Perth1A	2170A	Granitoid	Host	65.26		18.89	0.01	0.00	0.00	0.01	1.31	14.94	0.00
This Study	2170A_Perth1B	2170A	Granitoid	Lamallae	64.52		22.82	0.04	0.00	0.00	3.55	9.53	0.15	0.00
This Study	2170A_Perth2A	2170A	Granitoid	Lamallae	64.33		22.27	0.04	0.00	0.00	3.11	8.29	2.67	0.00
This Study	2170A_Perth2B	2170A	Granitoid	Host	64.84		18.53	0.09	0.00	0.00	0.02	0.89	15.22	0.00
This Study	2170A_Perth3A	2170A	Granitoid	Host	63.80		23.24	0.05	0.00	0.00	4.11	9.24	0.11	0.00
This Study	2170A_Perth3B	2170A	Granitoid	Lamallae	65.21		18.73	0.06	0.00	0.00	0.01	1.10	14.99	0.00

Analysis	F	H_2O	TOTAL
LL137			100.77
LL137			100.18
LL138			100.33
LL138			100.42
LL23			98.71
LL23			99.08
LL53			100.99
LL53			101.05
LN06			100.78
LN06			100.19
LN06			100.21
LN06			100.30
LN10			100.77
LN10			100.15
LN10			99.91
LN24			100.46
LN24			100.30
LN24			99.84
LN24			99.92
LN25			100.29
LN25			99.48
LN25			100.44
AKR-17			99.46
AKR-17			99.53
AKR-19			99.96
AKR-19			19045.76
AKR-20			100.51
AKR-20			100.82
AKR-21			99.54
AKR-21			102.08
2085B_1	0.00	0.00	99.82
2085B_2	0.00	0.00	100.42
2085B_3	0.00	0.00	99.78
2085B_Perth1A	0.00	0.00	99.76
2085B_Perth1B	0.00	0.00	100.23
2085B_Perth2A	0.00	0.00	100.34
2085B_Perth2B	0.00	0.00	100.45
2085B_Perth3A	0.00	0.00	99.81
2085B_Perth3B	0.00	0.00	99.76
2133A_1	0.00	0.00	100.51
2133A_2	0.00	0.00	100.54
2133A_3	0.00	0.00	100.67
2133A_Perth1A	0.00	0.00	100.64
2133A_Perth1B	0.00	0.00	100.31
2133A_Perth2A	0.00	0.00	100.36
2133A_Perth2B	0.00	0.00	100.56
2133A_Perth3A	0.00	0.00	99.16
2133A_Perth3B	0.00	0.00	100.70

Analysis	F	H_2O	TOTAL
2143B_1	0.00	0.00	100.45
2143B_2	0.00	0.00	100.31
2143B_3	0.00	0.00	100.68
2143B_Perth1A	0.00	0.00	100.47
2143B_Perth1B	0.00	0.00	100.40
2143B_Perth2A	0.00	0.00	100.46
2143B_Perth2B	0.00	0.00	100.17
2143B_Perth3A	0.00	0.00	100.62
2143B_Perth3B	0.00	0.00	100.75
2143C_1	0.00	0.00	99.82
2143C_2	0.00	0.00	99.43
2143C_3	0.00	0.00	99.53
2143C_Perth1A	0.00	0.00	99.96
2143C_Perth1B	0.00	0.00	99.80
2143C_Perth2A	0.00	0.00	99.01
2143C_Perth2B	0.00	0.00	99.52
2143C_Perth3A	0.00	0.00	99.99
2143C_Perth3B	0.00	0.00	99.92
2143C_Perth3C	0.00	0.00	94.85
2147A_1	0.00	0.00	98.42
2147A_2	0.00	0.00	101.11
2147A_3	0.00	0.00	100.05
2147A_Perth1A	0.00	0.00	98.69
2147A_Perth1B	0.00	0.00	98.26
2147A_Perth2A	0.00	0.00	99.72
2147A_Perth2B	0.00	0.00	100.37
2147A_Perth3A	0.00	0.00	100.16
2147A_Perth3B	0.00	0.00	100.01
2170A_1	0.00	0.00	100.53
2170A_2	0.00	0.00	100.19
2170A_3	0.00	0.00	100.38
2170A_Perth1A	0.00	0.00	100.43
2170A_Perth1B	0.00	0.00	100.62
2170A_Perth2A	0.00	0.00	100.72
2170A_Perth2B	0.00	0.00	99.58
2170A_Perth3A	0.00	0.00	100.55
2170A_Perth3B	0.00	0.00	100.10